Automatic Image-Based Adaptive Damage Analysis (AIBADA) with the Scaled Boundary Finite Element Method

Dion Dilina Dissanayake

A thesis submitted for the degree of
Doctor of Philosophy

School of Civil and Environmental Engineering
University of New South Wales
Sydney, Australia

June 2019

Thesis/Dissertation Sheet

Surname/Family Name	:	**Dissanayake**
Given Name/s	:	**Dion Dilina**
Abbreviation for degree as give in the University calendar	:	**PhD**
Faculty	:	**Engineering**
School	:	**School of Civil and Environmental Engineering**
Thesis Title	:	**Automatic Image-Based Adaptive Damage Analysis (AIBADA) with the Scaled Boundary Finite Element Method**

Abstract 350 words maximum: (PLEASE TYPE)

Predicting serviceability and reliability of structures is one of the primary goals in engineering science. In the last few decades Continuum Damage Mechanics (CDM) has risen to prominence providing invaluable insights into the mechanics of deterioration prior to failure. Presently CDM is challenged by poor flexibility and lack of automation in mesh generation, unavailability of Computer Aided Design data, poor solution convergence etc. This thesis presents the development of an Automatic Image-Based Adaptive Damage Analysis (AIBADA) procedure capable of overcoming these difficulties.

Firstly non-linear damage analysis with the Scaled Boundary Finite Element Method (SBFEM) is explored. The SBFE equations are derived incorporating an isotropic thermodynamically congruent elastic damage model. The new simplified damage formulation requires state variable calculations at only one location within a cell. Polygonal (2D) and polyhedral (3D) element formulations are developed for damage analysis. The arbitrary number of edges/faces in these elements assist in meshing complex interfaces. Regularisation is established by exchanging information between model parameters. A line search oriented modified Newton Raphson method with the arc-length technique is adopted to overcome convergence difficulties. The method improves its efficiency by pre-calculating subdomain stiffness matrices, strain modes and weight functions. An adaptive analysis process improves the efficiency and the accuracy of the solution field.

Quadtree and octree image-based mesh generation schemes are utilised to model geometries based on image colour intensities. Mesh balancing limits the number of unique cell patterns reducing the computational burden. Mesh smoothing is carried out by a level set based algorithm. The SBFEM works seamlessly with the pre-processor owing to its inherent compatibility to handle hanging nodes without additional effort. Using these hierarchical meshing algorithms and the SBFE polygonal and polyhedral element formulations mesh automation is achieved.

The computational efficacy, accuracy and the robustness of the proposed fully-automatic framework expands the practical applications of CDM. AIBADA is likely to appeal to engineers and researchers alike in both academia and the industry. Accurate application of the method will enable users to analyse and predict failure with the precursory knowledge on performance deterioration prior to the appearance of macro-cracks.

FOR OFFICE USE ONLY	Date of completion of requirements for Award:

ORIGINALITY STATEMENT

‘I hereby declare that this submission is my own work and to the best of my knowledge it contains no materials previously published or written by another person, or substantial proportions of material which have been accepted for the award of any other degree or diploma at UNSW or any other educational institution, except where due acknowledgement is made in the thesis. Any contribution made to the research by others, with whom I have worked at UNSW or elsewhere, is explicitly acknowledged in the thesis. I also declare that the intellectual content of this thesis is the product of my own work, except to the extent that assistance from others in the project's design and conception or in style, presentation and linguistic expression is acknowledged.’

Signed ……………………………………………..............

Date ……………………………………………..............

INCLUSION OF PUBLICATIONS STATEMENT

UNSW is supportive of candidates publishing their research results during their candidature as detailed in the UNSW Thesis Examination Procedure. **Publications can be used in their thesis in lieu of a Chapter if:** • The student contributed greater than 50% of the content in the publication and is the "primary author", ie. the student was responsible primarily for the planning, execution and preparation of the work for publication • The student has approval to include the publication in their thesis in lieu of a Chapter from their supervisor and Postgraduate Coordinator. • The publication is not subject to any obligations or contractual agreements with a third party that would constrain its inclusion in the thesis

Please indicate whether this thesis contains published material or not.

☐ *This thesis contains no publications, either published or submitted for publication (if this box is checked, you may delete all the material on page 2)*

☒ *Some of the work described in this thesis has been published and it has been documented in the relevant Chapters with acknowledgement (if this box is checked, you may delete all the material on page 2)*

☐ *This thesis has publications (either published or submitted for publication) incorporated into it in lieu of a chapter and the details are presented below*

CANDIDATE'S DECLARATION		
I declare that: • I have complied with the Thesis Examination Procedure • where I have used a publication in lieu of a Chapter, the listed publication(s) below meet(s) the requirements to be included in the thesis.		
Name	**Signature**	**Date (dd/mm/yy)**

Postgraduate Coordinator's Declaration (to be filled in where publications are used in lieu of Chapters)		
I declare that: • the information below is accurate • where listed publication(s) have been used in lieu of Chapter(s), their use complies with the Thesis Examination Procedure • the minimum requirements for the format of the thesis have been met.		
PGC's Name	**PGC's Signature**	**Date (dd/mm/yy)**

COPYRIGHT STATEMENT

'I hereby grant the University of New South Wales or its agents the right to archive and to make available my thesis or dissertation in whole or part in the University libraries in all forms of media, now or here after known, subject to the provisions of the Copyright Act 1968. I retain all proprietary rights, such as patent rights. I also retain the right to use in future works (such as articles or books) all or part of this thesis or dissertation.
I also authorise University Microfilms to use the 350 word abstract of my thesis in Dissertation Abstract International (this is applicable to doctoral theses only).
I have either used no substantial portions of copyright material in my thesis or I have obtained permission to use copyright material; where permission has not been granted I have applied/will apply for a partial restriction of the digital copy of my thesis or dissertation.'

Signed ……………………………………………..........................

Date ………………………………...

AUTHENTICITY STATEMENT

'I certify that the Library deposit digital copy is a direct equivalent of the final officially approved version of my thesis. No emendation of content has occurred and if there are any minor variations in formatting, they are the result of the conversion to digital format.'

Signed ……………………………………………..........................

Date ………………………………...

Abstract

Predicting serviceability and reliability of structures is one of the primary goals in engineering science. In the last few decades Continuum Damage Mechanics (CDM) has risen to prominence providing invaluable insights into the mechanics of deterioration prior to failure. Presently CDM is challenged by poor flexibility and lack of automation in mesh generation, unavailability of Computer Aided Design data, poor solution convergence etc. This thesis presents the development of an Automatic Image-Based Adaptive Damage Analysis (AIBADA) procedure capable of overcoming these difficulties.

Firstly non-linear damage analysis with the Scaled Boundary Finite Element Method (SBFEM) is explored. The SBFE equations are derived incorporating an isotropic thermodynamically congruent elastic damage model. The new simplified damage formulation requires state variable calculations at only one location within a cell. Polygonal (2D) and polyhedral (3D) element formulations are developed for damage analysis. The arbitrary number of edges/faces in these elements assist in meshing complex interfaces. Regularisation is established by exchanging information between model parameters. A line search oriented modified Newton Raphson method with the arc-length technique is adopted to overcome convergence difficulties. The method improves its efficiency by pre-calculating subdomain stiffness matrices, strain modes and weight functions. An adaptive analysis process improves the efficiency and the accuracy of the solution field.

Quadtree and octree image-based mesh generation schemes are utilised to model geometries based on image colour intensities. Mesh balancing limits the number of unique

cell patterns reducing the computational burden. Mesh smoothing is carried out by a level set based algorithm. The SBFEM works seamlessly with the pre-processor owing to its inherent compatibility to handle hanging nodes without additional effort. Using these hierarchical meshing algorithms and the SBFE polygonal and polyhedral element formulations mesh automation is achieved.

The computational efficacy, accuracy and the robustness of the proposed fully-automatic framework expands the practical applications of CDM. AIBADA is likely to appeal to engineers and researchers alike in both academia and the industry. Accurate application of the method will enable users to analyse and predict failure with the precursory knowledge on performance deterioration prior to the appearance of macro-cracks.

Acknowledgements

To my ever loving family; parents Gamini and Sita Dissanayake, and my older brother Christopher Dissanayake, for nurturing and inspiring me to become who I am today. Thank you!

My sincere gratitude to my advisor Prof. Chongmin Song. As my teacher and mentor he has taught me more than I could ever give him credit for here. I am thankful to him for taking me onboard his team and supporting me throughout my doctoral study and related research, for his patience, motivation, and immense knowledge. Also thank you for selecting and supporting me with my research scholarship and stipend. I am forever indebted.

My sincere thanks also goes to my co-supervisor Prof. Wei Gao for always being available to assist me, and opening doors to develop skills in teaching; to Dr. Hossein Talebi for providing guidance through the initial stages of my research; to Dr. Zihua Zhang for adding value and expediting publications; and to Dr. Albert Saputra for being supportive throughout the entire process, and being a great friend.

I am grateful for the ongoing support of all my friends, especially my dearest friend Ms Miley True for showing an inquisitiveness and proactive encouragement of my work, and for being a caring support through the good times and the challenges of this journey.

A special gratitude to the University of New South Wales (UNSW) for offering me the tuition fee scholarship and to the school of Civil and Environmental Engineering who gave access to the laboratory and research facilities, which has been invaluable in carrying out this research. Also a special thank you to Mrs Patricia McLaughlin for being very helpful and understanding.

A big thank you to the Scaled Boundary Finite Element Group for being an inspiring collaborative team, who helped facilitate and propel me to produce and refine excellent research outcomes.

Last but not least I am grateful to all of those individuals with whom I have had the pleasure to work with during my time at UNSW, including students that I had the opportunity and pleasure to guest lecture and tutor passing on knowledge. And a gracious thank you to my employer the NSW Government (Roads and Maritime Service, NSW Department of Finance Services and Innovation, and NSW Department of Planning and Industry) for their ongoing support of me whilst working on my doctoral degree.

Publications

Over the past four years, content for four journal papers has been produced. Two papers have been submitted to date and the last two are to be submitted in mid 2019. These journal papers contribute to the main material of the 4 chapters produced in this thesis. A list of journal papers is presented below:

1. Z. Zhang, Y. Liu, **D. Dissanayake**, A. A. Saputra, and C. Song, “Non-local damage modelling by the Scaled Boundary Finite Element Method (SBFEM),” Engineering Analysis with Boundary Elements, vol. 99, pp. 29-45, 2019.
   https://doi.org/10.1016/j.enganabound.2018.10.006

2. Z. Zhang, **D. Dissanayake**, A. A. Saputra, D. Wu, and C. Song, “Three-dimensional damage analysis by the Scaled Boundary Finite Element Method (SBFEM),” Computers and Structures, vol. 206, pp. 1-17, 2018.
   https://doi.org/10.1016/j.compstruc.2018.06.008

3. **D. Dissanayake**, Z. Zhang, A. A. Saputra, and C. Song, “Two and Three Dimensional Automatic Image-Based Damage Analysis with the Scaled Boundary Finite Element Method,” Computers and Structures. (to be submitted mid 2019)

4. **D. Dissanayake**, A. A. Saputra, and C. Song, “Two Dimensional Automatic Image-Based Adaptive Damage Analysis (AIBADA) with the Scaled Boundary Finite Element Method,” Computers and Structures. (to be submitted mid 2019)

Contents

List of Figures

List of Tables

Nomenclature

$(\hat{x}, \hat{y})$ 2D Cartesian coordinates of an internal point

(x_0, y_0, z_0) global Cartesian coordinates of a scaling centre

(x_g, y_g, z_g) global Cartesian coordinates

α softening branch control parameter

$\alpha(x, \varsigma)$ non-local weight function

$\alpha_0(r)$ monotonically decreasing non-negative distance function

$\bar{t}$ prescribed tractions

$\bar{u}$ prescribed displacements

β softening branch control parameter

Δl path length increment

η SBFE circumferential coordinate (2D) and (3D)

γ hardening-softening parameter

κ equivalent strain parameter

λ_0 load parameter

λ_i eigenvalue

$(\,)_{,i}$ $\frac{d}{di}$

$(\hat{x},\hat{y},\hat{z})$ 3D Cartesian coordinates of an internal point

(x,y,z) local Cartesian coordinates of a point on the boundary

$\Psi_{\sigma}(\eta)$ stress mode

$\mathbf{A}_{grid}$ initial quadtree mesh configuration

$\mathbf{B}_1, \mathbf{B}_2$ strain-displacement matrices

$\mathbf{c}$ integration constants

$\mathbf{D}$ fourth-order constant elasticity tensor

$\mathbf{E}_i^{\mathrm{D}}$ damage incorporated SBFE coefficient matrices, i = 0,1,2

$\mathbf{F}_{\mathrm{bn}}$ equivalent nodal forces from body loads

$\mathbf{I}$ identity matrix

$\mathbf{J}$ Jacobian matrix

$\mathbf{K}$ damage incorporated global stiffness matrix

$\mathbf{K}^{\mathrm{D}}$ damage incorporated stiffness of one subdomain

$\mathbf{K}_{\mathrm{G}}$ global stiffness matrix

$\mathbf{K}_s$ polygon stiffness matrix

$\mathbf{L}$ linear differential operator matrix

$\mathbf{N}_u(\eta)$ vectors of shape functions

$\mathbf{P}$ global force vector

$\mathbf{p}$ body force vector

$\mathbf{P}_{ext}^{i+1}$ external load vector

$\mathbf{r}_{\mathrm{b}}$ nodal coordinates

$\mathbf{S}_{11}, \mathbf{S}_{22}$ eigenvalue sub-matrices

$\mathbf{t}$ traction vector

$\mathbf{U}$ global displacement vector

$\mathbf{u}$ displacement vector

$\mathbf{x}_{\mathrm{b}}, \mathbf{y}_{\mathrm{b}}$ nodal Cartesian coordinates in x and y

$\mathbf{Z}$ Hamiltonian matrix

$\mathbf{E}_i$ SBFE coefficient matrices, i = 0,1,2

$\mathbf{F}_{\mathrm{b}}$ equivalent nodal loads

$\mathrm{d}\mathbf{a}_{n+1}$ displacement increment

H plastic tangential modulus

X_n line search accelerator parameter

∇ Laplacian operator

ν Poisson's ratio

ω isotropic damage variable

ω_0 damage threshold value triggering further mesh refinement

$\bar{\tilde{\varepsilon}}$ non-local equivalent strain

ϕ_n step-length amplification factor

ρ mass density

σ Cauchy stress tensor

σ^* effective stress

$\mathbf{P}_{int,n}$ internal force

$\mathbf{u}(\xi)$ displacement along the radial lines

SL_n line search step length

$\tilde{\varepsilon}$ local equivalent strain

$\triangle\lambda$ scalar proportionality coefficient

$\triangle\varepsilon^{\mathrm{p}}$ incremental plastic strain

ε infinitesimal strain tensor

ε^{p} plastic strain

ε_0 damage initiation threshold

ε_f parameter affecting ductility

ξ SBFE normalised radial coordinate (2D) and (3D)

ζ SBFE circumferential coordinate (3D)

c gradient parameter

D_q percentage of newly damaged elements

E Young′s modulus

$f_n^R, \mathbf{r}_n$ residual force vector

f_t uniaxial tensile strength

$FTOL$ convergence tolerance limit

g_f energy dissipated per unit volume

i Newton Raphson iteration step

I_1^{ε} first invariant of the strain vector

J_2^{ε} second invariant of the deviatoric strain vector

k ratio of the compressive uniaxial strength and the tensile uniaxial strength

l internal length scale

LSC line search counter

$LSTOL$ line search tolerance

n load step

N_{ω} number of damaged elements

N_{ω}^{max} maximum number of damaged elements

R interaction radius

S domain boundary

S_{max} largest element edge size

S_{max}^{allow} maximum allowable element edge size

S_{min} smallest element edge size

S_t boundary where tractions are applied

S_u boundary where displacement boundary conditions are applied

V domain volume

w_t imaginary width of the fracture process zone

z_t actual width of the micro-cracked zone

Chapter 1

Introduction

Preventing failure and predicting the useful service life of mechanical components and structures has always been a challenge that has spurred the curiosity of most engineers and researchers. Conventional design standards relied heavily on safety factors and conservative material characteristics to achieve safe and reliable design outcomes. Modern engineering however focuses on a minimalistic approach whereby reducing cost and time are paramount whilst still focused on strength, safety, and reliability. These constraints have pushed modern design boundaries to better understand and use materials with efficient and accurate analysis frameworks. Continuum Damage Mechanics (CDM) fits perfectly into this space as a accurate, efficient and reliable predictor of material and structural performance subject to the influence of strength deterioration. There are six sections in this chapter. Overall, the chapter highlights the present state of CDM and its challenges which then flows on to the key contributions of this research to overcome these challenges.

Section 1.1 begins with a brief introduction to computational methods in solving engineering problems. This section includes an outline on mathematical modelling, numerical methods, contemporary computational mechanics and damage analysis. Section 1.2 presents an investigation into the current challenges in damage analysis in tandem with the issues faced in computational modelling. These modern day research difficulties inspire the the development of the technique presented in this work. An overview of the approach anticipated to overcome these challenges is documented in section 1.3. Section 1.4 highlights the numerous original contributions in this research. The objectives and scope of this research are presented in section 1.5. Finally, section 1.6 provides an outline of this documented volume.

1.1 Computational mechanics in civil engineering

The age of computers has revolutionized the world enabling computational methods to be in the forefront of many science and engineering fields. These methods enable us to investigate and solve problems of extreme complexities which may never have been viable without the invention of computers.

Applications in civil engineering involve complex geometries, loadings, and material properties. Therefore, it is generally not always possible to obtain an analytical solution. However, engineering systems can be represented by systems of ordinary or partial differential equations which can be solved with the help of numerical techniques.

Numerical methods that were developed prior to the invention of the first commercial computer (Univac, IBM 701 in the early 1950) were not readily adaptable to solving complicated problems. However, with the advent of matrix methods, computers enabled solving large number of algebraic equations. With the developments that followed, these capabilities have come to widespread availability with the invention of the personal computer. Today, numerous special and general purpose programs have become popular applications to handle various complicated civil engineering problems.

1.1.1 Mathematical models of engineering systems

Mathematical models in engineering can be broadly classified into discrete and continuous engineering systems. A discrete system is obtained though amalgamation of a finite number of well-defined components. A continuous model is created through indefinite subdivisions of the problem domain and the model behaviour defined using the mathematical fiction of an infinitesimal. Continuous systems create differential equations or equivalent statements which implicitly describe the behaviour of an infinite number of elements. The discussions that follow focus on mathematical modelling in civil engineering structural systems.

Discrete systems are a simplification of a continuous system with appropriate approximations that approach the limit of a true continuum solution as the number of discrete variables increase. Discrete systems in engineering are created by forming analogies between real discrete elements and finite portions of a continuum domain. Such analogies can be developed for the behaviour of structural engineering elements such as bars, beams and rods. As an example consider the analysis of an electrical pylon. The discrete analysis of such a system can be done through direct stiffness method. The method involves identification of individual elements to develop member stiffness equations. An element stiffness matrix is then formed considering the forces and displacements depending on the geometry and properties of each element. Once the individual element stiffness relations have been developed they are assembled into a global matrix equation consisting of the stiffness matrix, displacement vector, and force vector. The unknown displacements and forces are then obtained by solving this global equation.

Modelling continuous engineering systems involves development of partial differential equations (PDEs) that represent the problem's underlying mechanical principles for an arbitrary infinitesimal element. Building mathematical models that represent an engineering system starts with defining the domain to be analysed and identifying the mechanisms that govern the processes in the system analysed. Then governing physical laws are considered to form PDEs with suitable assumptions on the pertinent variables and properties of the system. In this step it is essential not to overcomplicate the modelling parameters. Therefore, consideration is given to essential problem features that would enable to achieve practical results. Afterwards, restricting initial conditions and boundary conditions are identified and applied to solve the PDEs. An analytical solution may be then achieved by obtaining a fundamental solution containing arbitrary constants, or by separation of variables or by method of characteristics. However in most cases an analytical solution may not be practically achieved due to complexities in the problem geometry or boundary conditions. Therefore, numerous numerical methods have been developed to approximate the solution space formed by PDEs.

1.1.2 Numerical models in engineering systems

Numerical models are adopted in the context of simplifying complex problems in continua through discretisation. Discretisation in numerical modelling refers to the process of transferring continuous geometries, functions and equations into the discrete forms. Thereafter an approximate solution is obtained by employing a numerical method. Numerical models therefore constitute of two important steps: spatial discretisation and numerical analysis.

1.1.2.1 Spatial discretisation techniques

Spatial discretisation of the problem domain can be achieved either through conventional computer-aided-design-based (CAD-based) meshing algorithms or the modern image-based meshing algorithms. In CAD-based meshing the problem geometry is described by Non-Uniform Rational B-Splines (NURBS), whereas in image-based meshing techniques pixels (2D) or voxels (3D) represent the geometrical information and the material distribution of the problem domain. Both CAD-based and image-based meshing algorithms can produce meshes either conforming or non-conforming to the boundary. The former is usually adopted by users to exploit commercial software to produce a required mesh. The latter is often adopted to reduce the amount of human intervention required for creating boundary conforming meshes. In these methods the description of the boundary and local features can be defined implicitly.

Spatial discretisation can be achieved by many different algorithms. These include automatic and semi-automatic techniques. Semi-automatic techniques include techniques such as non-parametric mapping method and the transfinite mapping method. Automatic methods consist of techniques such as Delaunay triangulation method, the advancing front method, and tree methods such as the finite quadtree method in two dimensions (2D) and the finite octree method in three dimensions (3D). Out of which automatic processes are preferred in the current numerical modelling sphere. This is due to the shortcomings of the semi-automatic meshing algorithms in handling three-dimensional complex geometries such as varying size distributions within meshes as the element sizes are controlled by the subdivision of the simple subregions.

The meshes produced can consist of various different types of elements such as line elements (1D), triangular or quadrilateral elements (2D), and tetrahedral or hexahedral elements (3D). These may be regular or higher order elements depending on the interpolation shape functions involved. Therefore, a clear distinction should be made on the appropriateness of each element type by understanding the physical behaviour taking place in a problem. This involves understanding the boundary conditions, loads that must be applied to a body and their magnitudes and locations, computational resources available, and the expected accuracy of the modelling.

Complications in the mesh generation may arise due to complex boundaries that create distorted elements. The meshes that contribute to a bad result may contain elements with large aspect ratios, very large or very small corner angles, elements that are approaching a triangular shape, or elements that are triangular quadrilaterals. Such errors are commonly referred to as discretisation errors.

1.1.2.2 Numerical analysis techniques

Numerical analysis techniques first appeared in applied mathematics in the form of finite difference approximations [1–3], weighted residual procedures [4–6], trial functions to estimate the solutions based on the minimisation of potential energy [7], and approximate techniques for determining the stationarity of properly defined ‘functionals’ [8].

These techniques were directly applicable to the governing equations of a certain system. However, in engineering a relatively different approach was taken by creating an analogy between real discrete elements and finite portions of a continuum domain. This early concept has at present developed to general discretization procedures of continuum problems posed by mathematically defined statements.

Almost all complex engineering analysis follow a standard pattern. The continuum is first divided into a finite number of parts (elements). This step is termed geometrical discretisation or meshing. The outcome of this step is to divide the problem domain into numerous simpler elements. The behaviour of each such element is specified by a finite number of parameters. The behaviour of these parameters is described by piecewise interpolation (shape) functions over the elements. The elements are individually processed and a solution of the complete system is formed after assembly of its elements. Such a treatment on an engineering system was done originally by Turner et al. [9] in 1956. In this work stiffness matrices for truss elements, beam elements, and two dimensional triangular and rectangular elements in plane stress were formulated. The work outlined the commonly known direct stiffness method. With the development of the high-speed digital computer the method developed applications to complex geometries. In 1960, Clough [10] proved with the principal of minimisation of potential energy that refining meshes tend the solution space to converge towards the true continuum solution. The now popular phrase "Finite Element Method" (FEM) was introduced by Clough [10] in 1960 where both triangular and rectangular elements were used for plane stress analysis.

Since the introduction of the FEM, many other numerical methods such as the Boundary Element Method (BEM) [11,12], the eXtended Finite Element Method (XFEM) [13], and the Scaled Boundary Finite Element Method (SBFEM) [14] have emerged. Although different to one another and consist of both advantages and disadvantages in certain applications these methods are based on the original principal of geometry discretisation.

The advancements of these numerical methods have provided the tools for obtaining solutions of mathematical models for various engineering problems concerning elastoplasticity [15], fracture mechanics [16, 17], vibration analysis, fluid dynamics [18, 19], and electromagnetic analysis [20, 21], to name a few.

The FEM included, all the numerical methods mentioned earlier require an accurate geometry representation and an appropriate discretisation of the problem domain. The importance of this step in the process of obtaining agreeable solutions was outlined in section 1.1.2.1.

1.1.3 Digital age computational mechanics

The advent of the computer in the 1950's revolutionised the field of computational mechanics. Since then, computers have come a long way. Gradually computers became more and more powerful moving from the earliest vacuum-tube technology to the transistor-based technology in the 1960s and then to integrated circuit-based technology in the 1970s. With higher processing powers, portability etc. computers have now become a mass-market item. Concepts of mechanics are now integrated into numerous computer programs written to handle various structural and non structural problems. These computer programs have adopted numerical methods for attaining solutions. The large number of equations produced by numerical methods are solved using matrix based computer programs. The humble matrix that was originally developed for simplifying formulations involving large amounts of equations is now used as an efficient technique in computer programming. The use of computers to study phenomena governed by mechanical principles with the help of numerical methods was the beginning of the evolution of computational mechanics.

Over the years computational modelling software have been developed to contain graphical user interfaces that provide accurate representations of various analysis. A few of the modern computational modelling software that enable such functionality are Algor [22], Abaqus [23], ANSYS [24], COSMOS/M [25], GT-STRUDL [26]. LS-DYNA [27], MARC [28], MSC/NASTRAN [29], NISA [30], Pro/MECHANICA [31], SAP2000 [32], and STARDYNE [33]. The popularity of most of these software is due to their efficiency in using minimum hardware enabling users to solve problems in computational mechanics even on a single-processor machine. Their capabilities are such that, with the use of a cluster of computer nodes or modern computers, computational modelling software can solve problems with millions of unknowns.

Computational modelling software allows users to model and analyse mechanical problems. Defining the model geometry via a CAD tool is the first step in the process of creating a computational model. Thereafter, a spatial discretisation method is followed to obtain a mesh. This step may sometimes involve specifying the type of elements to be used in the meshing process, or sometimes the meshing algorithm may run automatically. Then, the material properties of the elements, applied loads, boundary conditions and the kind of analysis to be performed need to be defined as inputs. The software uses this input information to carry out the analysis automatically. Therefore, modern software allows users to solve complex problems with minimum intervention in the solution process.

With time however, the need for more efficient computational methods have heightened as modern research seek to emulate mechanical and structural behaviour of engineering systems to the finest detail. The early 2D computational modelling has now almost fully moved on to the 3D space. The modelling of physical problems in 3D involves a large number of unknowns or Degrees Of Freedom (DOFs) that has pushed the limits of computers and computational techniques. Improvements to existing computational methods and developing new and advanced techniques have thus come to the forefront of engineering research.

One major drawback in the current 3D computational modelling techniques is the lack of fully automated and efficient meshing algorithms. Although automatic techniques are well established in 2D, the lack of mathematical rigour in most spatial discretisation techniques have proven their downfall in 3D space.

The use of an appropriate numerical technique is also a vital component in increasing the efficiency and accuracy of the solution space. To improve the efficiency of the process any numerical technique need to be paired with the most apt mesh generation algorithm that is most compatible with its formulation. This is because every numerical technique has its inherent advantages and disadvantages in application to various problems. The accuracy of the solutions largely weighs on the numerical technique adopted.

This thesis intends to propose and develop a robust technique that is both an efficient and an accurate framework for assessing material damage.

1.1.4 Damage analysis

Damage and deterioration is a common phenomenon experienced by everything around us. It is an irreversible process which causes degradation or reduction in performance. In the field of structural engineering, detection and assessment of damage has come to much prominence in light of evaluating the service life of existing damaged or undamaged structures. Thus, investigations into material damage have been in scientific debate for several decades. The ability to make accurate judgments of whether to run, repair or replace a structure lies in the ability to accurately measure the damage in a structure.

Damage analysis is a field which has applications to many engineering disciplines such as mechanical engineering, aerospace engineering, civil engineering, and structural engineering. A general definition of damage applicable for all these fields is the degradation of a material's physical property due to the presence or the growth of defects. Figure 1.1 is a depiction of the various forms of material damage.

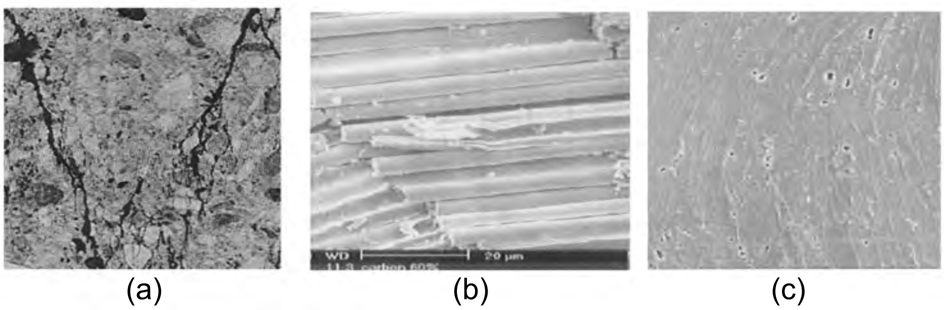

Figure 1.1. Material level damage (a) fracture (b) delamination (c) microcracking

Material damage can be measured in various different ways such as: damage measures using the remaining life concept, damage measures from the microstructure, and damage measures through physical parameters and the effective stress concept. The assessment of material damage through the remaining life concept adopts the damage parameter life ratio, N/N_F. Where, N is the present number of cycles already applied and N_F is the total number of cycles to the limit point of crack initiation for a given loading condition. The second technique measures and quantifies irreversible defects such as inter-granular cavities, surface microcracks, and dimensions of cavities. However, these measurements are destructive and at most times the defects are difficult to observe during the first phase of the damaging processes. The third and final approach to damage measurement is most desired due to the practicality in obtaining measurements. The method involves evaluating the influence of damage on physical quantities such as density, resistivity, acoustic emission, fatigue limit, and mechanical behaviour.

Kachanov [34] was the first to apply damage concepts to model fracture in creep. Fracture, fatigue and creep rupture are all instances of substantial material damage typically associated with exposure to more extreme loading conditions. Damage models are used to describe the evolution of degradation phenomena on the micro-scale from initial (undamaged or pre-damaged) state up to creation of a crack on the meso-scale (material element).

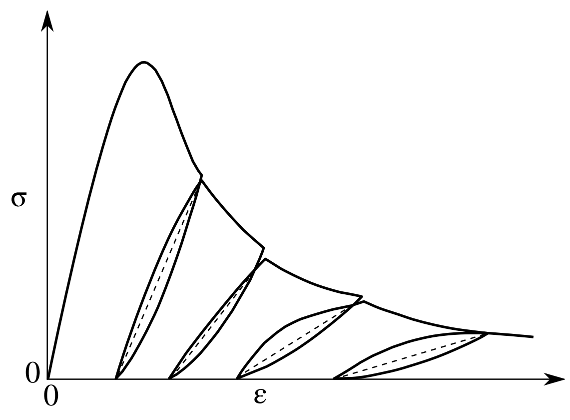

Figure 1.2. Stress-strain response of a concrete specimen in tension.

Figure 1.2 is a typical uniaxial tension stress-strain curve of a concrete specimen if the load is removed at regular intervals [35]. As can be seen, the unloading-reloading curves are not straight-line segments but loops of changing size and the gradient decreases in each loop. If we assume that the average slope is the slope of a straight line connecting the turning points of one cycle and that the material behaviour upon unloading and reloading is linearly elastic (dotted line in figure 1.2), then the elastic modulus degrades with increasing strain. This stiffness degradation behaviour is related to some kind of damage.

In order to analyse this stiffness degradation local and the non-local damage analysis can be considered. Local damage models are models where the evolution of material damage is a function of the stress and strain fields of the same point. Whereas, in non-local damage models the stress and strain fields at a point within the problem domain is dependent on the stress and strain fields of points within a finite neighbourhood. This spatial dependence in the continuum model is achieved by the non-local length parameter l. This parameter contributes to the non-local equivalent strain and must therefore be related to the scale of the microstructure.

1.2 Current challenges

In this section current challenges in the broad fields of modelling material degradation and computational modelling are discussed. The discussions in the computational modelling aspects are based around the FEM. These challenges build the motivation for this research.

1.2.1 Current challenges in modelling material degradation

The fracture mechanics approach to material degradation has proven to be a very powerful theory. In fracture mechanics propagation of cracks are analysed by evaluating the driving forces on a crack by means of analytical solid mechanics and the resistance to fracture by experimental solid mechanics. However, within the theory there is no consideration given to the complexities of the material microstructure and interactions between the various local micro-defects that surround the assumed cracks. To get a better understanding of the phenomenon leading up to the formation of a crack, one can adopt a framework similar to fracture mechanics at a material micromodeling level. The downside to such an approach would be the immense computational cost.

As a solution Continuum Damage Mechanics (CDM) [36] considers material degradation within a Representative Volume Element (RVE) as micro-cavities and microcracks instead of a physically apparent crack. This avoids the requirement to manipulate the structural boundary as required by the fracture mechanics approach to model cracks. The method enables retention of the framework of continuum mechanics by homogenisation of the microscopic defects and describes their growth macroscopically.

If judged by the computational efficiency, CDM is therefore an improvement to the fracture mechanics framework. However, as the reaches of science expand, complex material micro-structures and intricate architecture has inconvenienced the analysis of materials and structures even under the simplified CDM. Although such difficulties have come to light, the extent of damage cannot be disregarded or phased out as damage is a phenomenon which directly affects the response of structures.

Therefore it is important to note, modern CDM frameworks are required to address these complexities in obtaining and modelling material and structural geometries. Such techniques will have the ability to answer questions arising from structural typologies, material properties, boundary conditions, and damage patterns in a robust and efficient framework.

As damage increases within the material it leads to a local softening behaviour as the tangential stiffness becomes negative. Therefore, a local approach to softening phenomena may lead to a physically unacceptable localisation of the deformation [37, 38]. The results obtained through such methods exhibit mesh sensitivity in the finite element context [39, 40]. Consider the tension beam under uniaxial loading conditions is shown in figure 1.3.

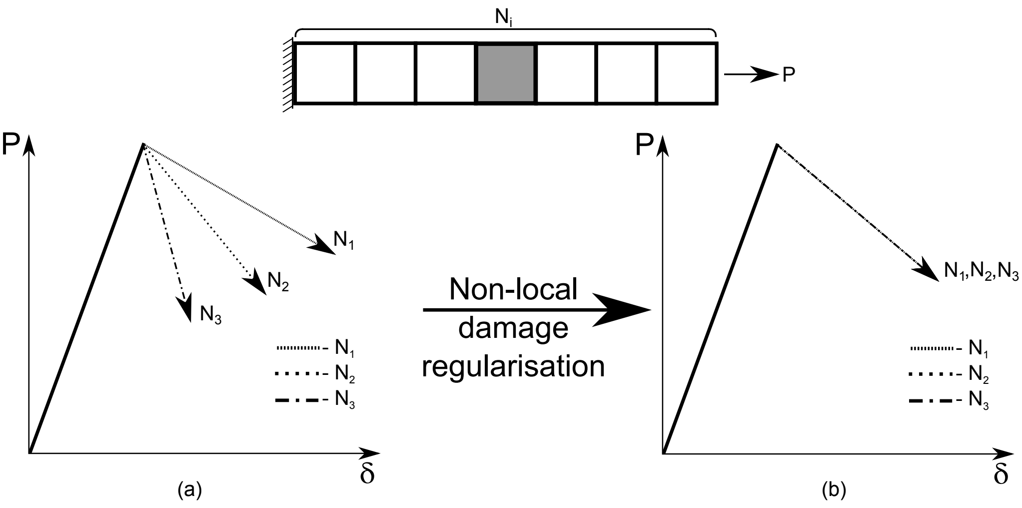

Figure 1.3. Non-local damage regularisation of a uniaxial tension beam for 3 different mesh types with total number of elements increasing from N_1 to N_3. The central element is assumed to be damaged. (a) localised softening curves (b) regularised softening curve.

As the number of elements (N_i) increases from N_1 to N_3 damage localisation takes place as seen in figure 1.3a. This allows more elements to unload contributing to a loss of strain energy. This effect is shown in the reducing area under the curves in figure 1.3a with increasing number of elements. The problem therefore appears to have many solutions dependent on the mesh configuration. If the model is further allowed to localise, the standard strain-softening continuum formulation will lead to an infinitely small softening region and the load-displacement curve may exhibit severe snap-backs.

However, through a regularised model these ill-effects are eradicated and the results become mesh independent (see figure 1.3b). Some of the popular regularisation techniques include non-local modelling of the constitutive behaviour, gradient dependent material description, and local manipulation of material properties depending on the element size. Due to their characteristic mesh independent behaviour these techniques are considered much more reliable than local damage models. Further detail of the formulation can be found in chapter 3, section 3.2.

Regularisation techniques however require transfer of internal variable information between iterations and load steps. This is an additional computational burden that needs to be considered in an efficient modelling technique. Most regularisation techniques may also require considerable alterations to the standard finite element framework. However, it is worthwhile to adopt techniques that require the least amount of such changes to provide an opportunity for these softening models to be used with the standard finite element programs. The methods adopted in this thesis anticipate to avoid this difficulty.

Numerical solvers are a crucial component in accurate modelling of softening behaviour of materials. Most modern damage analysis schemes tend to either fail at limiting and bifurcation points of the softening curve or at certain times become inefficient in the iterative processes. Therefore, this research investigates various mathematical solvers with the intention of adopting a combination of techniques which is most apt for obtaining an accurate equilibrium path efficiently.

Spatial discretisation inefficiencies are another challenge in the current landscape of damage analysis. The inefficiency arises from intermediate steps required to define problem boundaries and through the generation of low accuracy finite elements. If the meshes are further refined to obtain a high quality mesh, large amounts of finite elements are produced as a negative consequence. Due to the iterative nature of the analysis current damage modelling techniques struggle when the number of DOFs increases in the model. To minimise the DOFs produced by increased number of elements an adaptive damage modelling framework can be adopted. A description of the adaptive technique proposed for this research is in section 1.3.3.

1.2.2 Meshing challenges

In modelling geometries CAD tools have become increasingly popular over the last few decades. Even with this popularity there are two main concerns with CAD based techniques. Firstly, there are instances where inabilities occur in obtaining geometrical data of materials, objects, structures, etc. This is due to reasons such as natural formation, defects and so on. Secondly, they fail to exploit the use of inherent surface boundaries of a surface or a volume of interest. However, even if the aforementioned challenges are addressed there are further difficulties in obtaining a high quality mesh. To date, the processes of obtaining high quality meshes have always been a time consuming process and if done manually can be prone to errors. In this section the general difficulties in mesh generation are discussed with the progression to the challenges in automatic mesh generation discussed in section 1.2.3. The FEM forms the baseline for majority of the discussion presented in this section.

Pre-processing (meshing included) is a process that usually consumes almost 50% of the total time required to complete an analysis [41]. This is especially true in the practical applications in engineering computations. Many such practical applications require modelling of problems in 3D. Within the 3D space the difficulty of mesh generation is largely increased when meshes have to be generated for geometries of various different levels of complexity.

Conventional mesh generation processes used in the FEM have difficulties in dealing with curved/irregular boundaries. The elements in the vicinity of such boundaries tend to be ill-shaped. The rectification adopted in these cases is to refine the meshes in regions where the quality of a mesh is compromised. The preprocessing burden in this situation increases resulting in inefficiencies in the succeeding processes in the computational analysis.

Meshing moving boundaries such as in crack propagation problems, large deformation analysis, and adaptive analysis require robust meshing techniques. It is common in most finite element meshing algorithms to use only one type of element for a particular problem. In the case of crack propagation, as elements are cut when the boundary changes to comply with a propagating crack, the resulting elements may not be conforming to the element category of the original mesh. To avoid mesh incompatibilities arising from this scenario complex preprocessing algorithms are employed [42, 43].

h-adaptive mesh refinement techniques with terminating grids struggles from the drawback mainly produced by hanging nodes generated in the process of refinement [44]. As elements are divided into smaller elements, intersections of the refined smaller element and the unrefined larger elements produce nodes between adjacent elements causing mesh incompatibilities. These nodes are typically referred to as hanging nodes. The elements containing hanging nodes are dubbed transitional elements. Various remedies such as using new shape functions or local re-meshing can be adopted to overcome this issue of hanging nodes. However, this additional effort increases the computation burden in the analysis.

Analysis types such as crack propagation, large deformation and damage analysis tend to contribute adversely on the topology of the mesh and therefore more likely to degrade the quality of the mesh by producing ill-shaped elements. Ill-shaped elements cause errors in the element mapping process, which in turn causes numerical instabilities in the analysis [45]. A treatment for this issue involves local removal and replacement of distorted elements. Thereafter, a re-meshing algorithm is employed to produce a mesh with well-shaped elements for the extracted region.

1.2.3 Difficulty in automatic mesh generation

The history of automatic mesh generation dates back to the early 1970s. The initial documented work by Zienkiewicz and Phillips [46] focused on generating a valid finite element spatial discretisation over arbitrary domains by only requiring information of the domain geometric boundaries and the distribution of the element sizes. Automatic meshing algorithms have come a long way since then as most CAD and Computer Aided Engineering (CAE) packages offer automatic meshing capabilities. However, there are still instances in advanced numerical simulations that require the user to craft meshes manually to achieve a high solution accuracy. In these instances where artificial manipulation of the meshing process take place, the user relies on their experience and knowledge on the target physical phenomena to create an ideal mesh. However, such knowledge is not always a luxury. In addition manual alterations are an arduous exercise even if the user is willing to sacrifice the time and effort required. Therefore it is important to make processes in mesh generation fully automatic, and improve upon processes that are inefficient.

In mesh-based numerical methods a geometrical model can be defined by either a CAD drawing or a digital image. In CAD models NURBS are used for boundary definition whereas in image-based models digital images are used for geometrical description.

In CAD-based mesh generation, numerous methods are available for generating automatic meshes with triangular or tetrahedral elements. These techniques include Delaunay triangulation [47] and the advancing front method [48]. However, to model high stress gradients triangular and tetrahedral meshes require higher order formulations which reduces the efficiency of the analysis process. Quadrilateral and hexahedral meshes provide an agreeable solution, as these elements are capable of performing better in modelling high stress gradients. Blacker's [49] attempts to automate hexahedral mesh generation resulted in a semi-automatic process requiring manual adjustments at complicated geometric boundaries.

The lack of control in element anisotropy and directionality are two further constraints obstructing full automation. An anisotropic mesh enables the user to stretch elements in a specified direction with a specified aspect ratio. For example the mesh generated in figure 1.4 for a smooth torus-like piece depicts two possible mesh configurations, an isotropic mesh in figure 1.4a, and an anisotropic mesh in figure 1.4b. The mesh anisotropy reduces the number of elements with minimum compromise in the approximation error and thus yields a superior outcome to that achieved by the isotropic mesh.

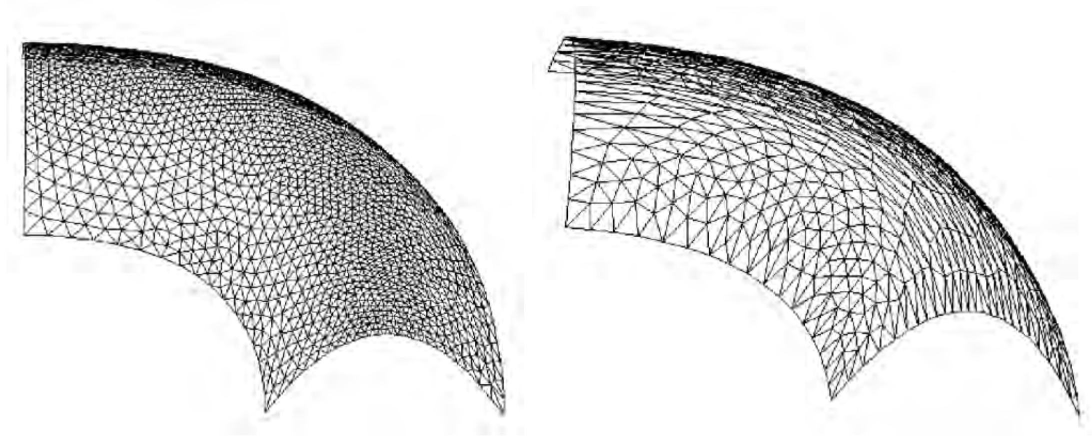

(a) Isotropic triangular mesh (b) Anisotropic triangular mesh

Figure 1.4. (a) An isotropic triangular mesh and (b) an anisotropic triangular mesh that approximate a torus-like piece of smooth surface [50, 51].

Furthermore, applications of anisotropy is not limited to mesh geometrical improvements but also applicable to solution values. For example, anisotropy can be adopted to improve analysis of material damage by increasing the element density in locations of high material damage and decreasing the element density regions of low material damage. Mesh directionality is another factor that contributes to the solution accuracy as element deformation such as angle change and folding dissipate different amounts of energy. Therefore, in highly non-linear analysis types, such as automotive crash simulation and flow simulation, the issues creates solution instabilities.

Automatic mesh generation for moving boundaries is also a tedious operation. The development of changed boundary condition throughout the process of the analysis brings about mesh incompatibility issues in fields that involve analysis of crack propagation, large deformation and adaptive refinement strategies.

In the current CAD and CAE fields the user base is ever expanding from specialized analysis engineers to general design engineers. These users regardless of their expertise are neither interested nor capable of manually adjusting a mesh to obtain acceptable and accurate simulation outputs. Therefore, overcoming these issues can alleviate burden on the user and streamline the process from pre-processing to analysis.

Images produced by non-invasive mesh generation technologies such as X-ray Computed Tomography (X-ray CT) scans, Magnetic Resonance Imaging (MRI), Positron Emission Tomography (PET) and ultrasound provide the geometrical information and the material distribution of the problem domain based on the colour intensity. The traditional approaches used in mesh generation of CAD models are not directly applicable to handle digital images and STL models. Voxelation of images is one of the earliest and the simplest techniques adopted in image-based mesh generation. One of the shortcomings of the technique is the large number of elements produced in the image decomposition stage which then results in large memory requirements and larger processing times. These voxel models also have an unrealistic, stepped, “Lego brick” appearance on the surfaces of mesh domains, which in structural mechanics create stress jumps between surface interfaces of different material. These drawbacks therefore hinder the analysis procedures that has to follow the geometrical modelling stage. An alternative method is the marching cubes algorithm. However, this technique requires adoption of CAD-based meshing techniques as an intermediate process. Inadvertently this step imposes the challenges experienced in CAD-based meshing that were discussed earlier in this section. Quadtree and octree techniques form another alternative to image decomposition. This technique adopts a scheme whereby the mesh is generated through recursively dividing each element. The domain decomposition takes into account geometrical and material boundaries within the problem domain. Although the technique is quite efficient the downside to the process is the generation of hanging nodes as shown in figure 1.5 for a 2D and a 3D domain.

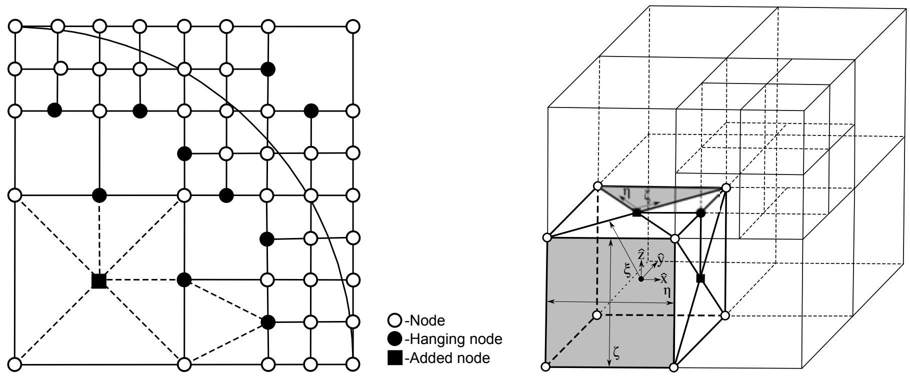

(a) Quadtree mesh of a quadrant of a circular domain

(b) Octree representation of a cube containing hanging nodes

Figure 1.5. SBFEM representation of a (a) quadtree mesh containing a quadrant of a circular domain. Dashed lines indicate subdivisions. (b) octree representation of a cube containing hanging nodes. SBFEM local coordinates in an octree cell shown in bottom left cube. Solid circles represent hanging nodes in both figures (a) and (b).

Essentially, these heirachical structures provide an efficient way to model features at different scales. However, the downside experienced by many numerical methods other than the SBFEM is the creation of hanging nodes on the interface of two neighbouring cells with different sizes (see figure 1.5). Hanging nodes in the standard FEM introduce displacement incompatibilities. The issue is usually handled by triangulation/tetrahedralisation. This solution is not optimal due to the generation of new elements and also the drawbacks associated with triangular and tetrahedral elements.

This work intends to incorporate techniques such as the image-based modelling process that deviate from the classical CAD-based mesh generation technique, and have the capability to overcome the issues outlined earlier in this section and in section 1.2.2. The method adopted should thereafter strive to incorporate a robust and efficient meshing technique that yields a high-accuracy solution with minimum computational expense.

1.2.4 Current challenges in 2D and 3D numerical modelling

Overall there has been a vast advancement in preprocessing techniques apart from the few challenges highlighted in sections 1.2.2 and 1.2.3. However, despite the efficiencies in pre-processing (especially automatic mesh generation) most numerical modelling techniques fail to benefit from these advantages [52, 53].

Automatic mesh generators are an indispensable feature in modern computational modelling software due to their inherent capability, of both reducing the computational burden and also improving the accuracy of the solution field. One of the great introductions to the automatic mesh generation process is the quadtree and the octree algorithms. These methods recursively subdivide square/cubic cells into 4 identical subdivisions by halving the size of the original cell. These algorithms are widely used in applications such as image processing, cartographic data processing, computer animation, and computer-aided architecture due to their simplicity and efficiency. Direct application of these heirachical methods with the FEM is challenging due to two reasons. Firstly, the existence of hanging nodes between elements of different sizes and secondly, the difficulty in representing curved boundaries by square and cubic elements.

Therefore, it is paramount to adopt suitable numerical methods to fully make use of the convenience generated through the advancements in heirachical techniques. The pairing of automatic and adaptive quadtree/octree mesh generation technique with the SBFEM is one such method that complements each other in the pre-processing and the analysis stages of a computational analysis. Further description of this technique can be found in section 1.3.1.

Non-linear mathematical solvers form an integral part in numerical modelling alongside powerful numerical techniques. It is a common practice to adopt displacement control techniques to overcome limit points that are common in softening problems. However, there are many limitation to displacement control techniques when dealing with many DOFs and highly materially non-linear finite elements [54]. The initial equilibrium solution that becomes the basis of further iterations, may sometimes be well away from the final equilibrium state. The following iterations can therefore lead to numerical difficulties and/or divergence of solution process. The numerical solver dealing with softening materials should therefore characteristically avoid such behaviour.

1.3 Proposed approach

This research aims at solving current difficulties faced in the field of damage analysis through an Automatic Image-Based Adaptive Damage Analysis (AIBADA) formulation with the adoption of non-local CDM. A powerful m-NR method with automatic damping and acceleration schemes are implemented with the arc-length technique for accurate representation of the equilibrium path.

1.3.1 Image-based SBFEM implementation

Image-based modelling has revealed exciting new possibilities in material science, structural mechanics, biomechanical and biomedical investigations. As shown in figure 1.6, image-based analysis is abundantly used in modelling objects (see figure 1.6a), materials (see figure 1.6b), analysis of X-ray images in the field of medicine (see figure 1.6c), and in civil engineering (see figure 1.6d). Specifically in civil and structural engineering, images can be used to predict the behaviour of structures under different loading conditions [52]. Many of these fields had problems previously intractable owing to the difficulty in obtaining suitably realistic models.

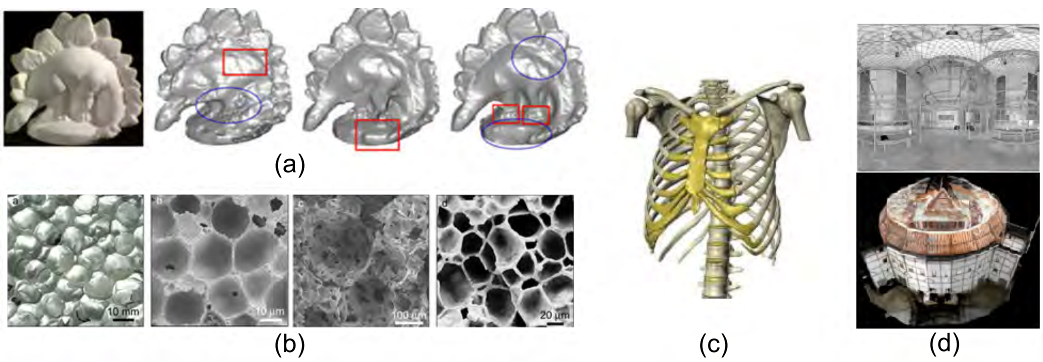

Figure 1.6. Various applications of image-based modelling (a) objects, (b) material, (c) complex living organisms, and (d) structures.

The main principle behind image-based analysis is to use an image and discretise it into a compatible mesh for solving with the use of any numerical method [52]. However, most approaches to convert 3D images into meshes for use in finite element analysis necessitate significant user interaction and often still involve some appreciable simplification of the model geometry [55,56]. A major reason for the lack of automation is the use of traditional approaches to meshing. These meshing techniques involved an intermediary step of surface reconstruction, which is then followed by the use of these traditional CAD-based meshing algorithms [57–59], a process which is time consuming, not very robust, and can be virtually intractable for the complex topologies and geometries typical of image data. Hence a need for a more accurate, robust, and a direct approach that combines the geometric detection and mesh creation stages in one process is in high demand.

At present one of the most useful tools in pre-processing in 2D and 3D image-based analysis is the use of a quadtree and octree mesh structures. Octree structures are an extension of the quadtree in 2D images to 3D images. Here the difference is that the bounding box domain is now in the form of a cube. Unlike the quadtree structure which has four children for each node; octree mesh generation consists of having eight children at each node because a cube is recursively subdivided into eight octants. There are several key advantages in using these heirachical structures because of their inherent ability to generate meshes faster than other available processes and their ability to store grid information efficiently in a hierarchical tree structure [60]. These meshing algorithms also avoid over-refinement of the mesh by only refining the square/cube near the boundaries.

Quadtree-based and octree-based SBFEM is a novel technique to solve problems with complex geometries where standard FEM seems to be inefficient. The SBFEM have several advantages in image-based analysis over the standard FEM. The SBFEM only requires discretization along the boundary of the object and in comparison FEM requires the discretization of the entire domain into finite elements. The SBFEM lines perfectly with the quadtree and octree meshing technique. The combination of the two ensures vital capability between accurate geometric representation and numerical analysis. The use of SBFEM formulation capable of handling hanging nodes without modification to the mesh avoids the triangulation/tetrahedralisation of the quadtree/octree mesh required in the FEM. This reduces the computation costs significantly. This follows up with the ability to use quadtree/octree balancing techniques which reduces the number of elements produced; giving rise to an extremely convenient formulation of the stiffness matrices. Owing to these capabilities the method can be easily extended to an adaptive analysis framework.

Data images are to be obtained first for image-based modelling in two and three dimensional space. For this purpose one of the many geometric data acquisition techniques such as CT, MRI or PET can be used. Figure 1.7 depicts a model of a concrete cube created with the use of images obtained by a CT scan.

(a) CT scan images of a concrete cube

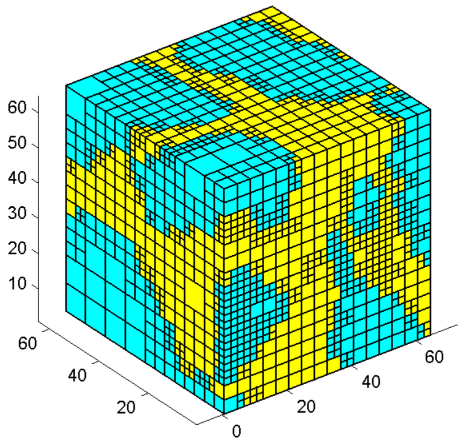

(b) Octree model from figure 1.7a

Figure 1.7. An image-based concrete cube model generation through CT scanned images.

This research intends to develop and improve computer programmes written in MATLAB codes for both quadtree and octree mesh generation. Overall, the procedure adopted for image decomposition starts with importing a data image into MATLAB then recursive decomposition of the image relative to colour intensities. This process is followed by enforcing 2:1 rule on size distribution and material assignment. Finally, geometry information is stored before proceeding to the analysis stage. Further detailed explanations on the process can be found in chapter 5. It is briefly introduced below with an example.

Figure 1.8a is an example of a simple 3D object whose octree block decomposition is given in figure 1.8b and whose tree representation is given in figure 1.8c. The process to obtain the decomposition shown figure 1.8b is by recursively subdividing the original cube in figure 1.8a into eight congruent disjoint cubes (called octants) until blocks of a uniform colour are obtained, or a predetermined level of decomposition is reached.

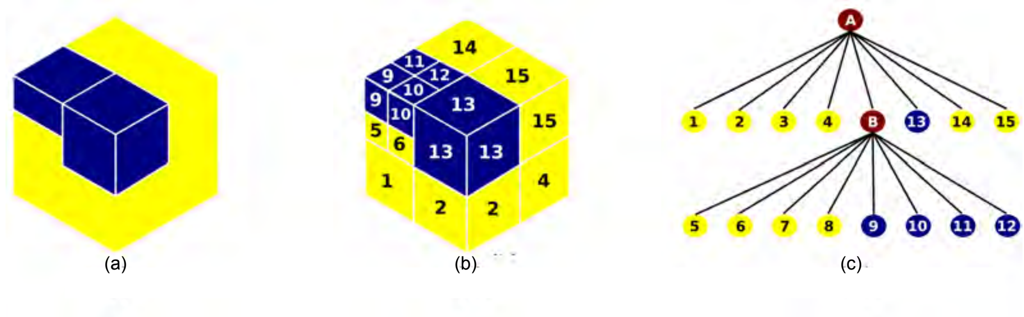

Figure 1.8. (a) 3D object, (b) its octree block decomposition, and (c) tree representation.

The subdivision of an element is called its "children" whereas the subdivided element is called a "parent" element. A cell that is not subdivided is called a "leaf", otherwise it is called an "internal cell". The level of an element corresponds to the number of subdivisions required to obtain this cell from the bounding box. Note that the level of the root cell is zero (no subdivision was needed to obtain it). Two cells are called "neighbour" or "adjacent" if they share a common edge. If two adjacent cells do not share the same level, then so-called hanging nodes appear. In order to manage mesh gradation, the level difference between adjacent cells may not exceed 1. This is also called the 2:1 rule (any element has at most two neighbours along its edges).

The SBFEM is considered in this research to overcome the challenges experienced by other numerical methods when adopted with the quadtree and octree mesh generation techniques. The SBFEM was developed by Song and Wolf [14]. It is a semi-analytical method that reduces partial differential equations to a set of ordinary linear differential equations. The method incorporates advantages of both the BEM and the FEM whereby generating its own salient features. Similar to the BEM numerical discretisation is only performed on the boundary. However, unlike the BEM no fundamental solution is required. Matrix power functions are used to express the internal displacement and stress solutions. The method has proved to be very efficient in solving various types of problems, and outperforms the conventional FEM when solving unbounded domain problems [61–63], and problems involving stress singularities [64, 65] and discontinuities. The applications of the SBFEM range from elastostatics [66], elastodynamics [14], electromagnetics [67], diffusion [68], acoustics [69], fracture [70, 71], crack propagation analysis [72], elasto-plastic analysis [73], piezoelectric materials/plates [74–76], and wave propagation [77, 78].

Automation in meshing for the SBFEM is achieved for 2D and 3D problems through quadtree and octree meshes, respectively. The scaled boundary polygonal and polyhedral formulations on both 2D and 3D analysis provide vital flexibility in formulation process compared to the limited element shapes (triangular and quadrilateral for elements in 2D, and tetrahedral and hexahedral elements in 3D) available in standard FEM. The standard quadtree and the octree elements (squares and cubes) are also included in the vast element library that can be accommodated in this formulation. The SBFEM coordinate systems in both 2D and 3D are as shown in figure 1.9.

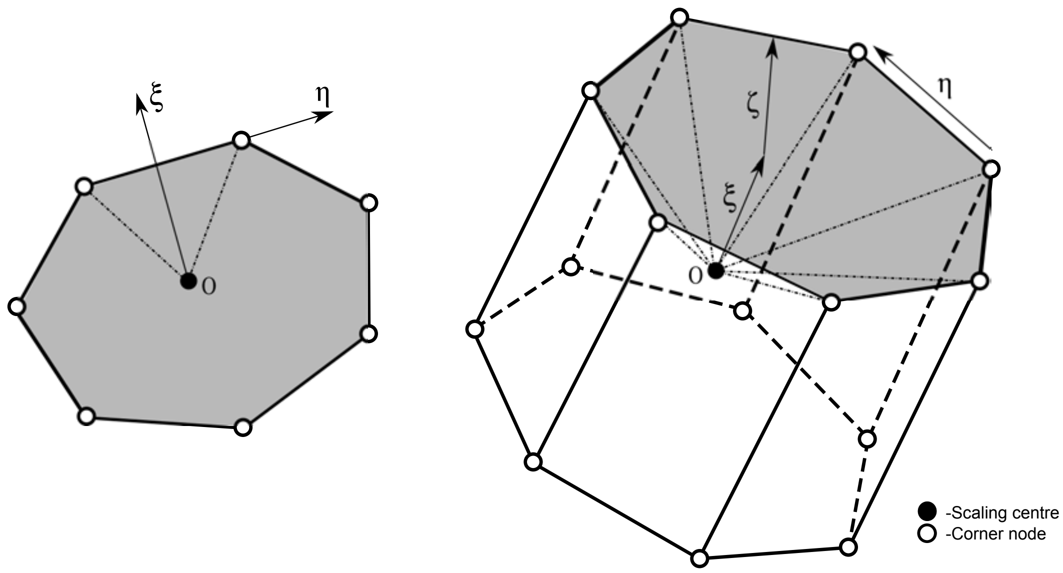

(a) Polygonal element based on the SBFEM.

(b) Polyhedron element based on the SBFEM.

Figure 1.9. Scaled boundary coordinate system for (a) arbitrary polygonal and (b) arbitrary polyhedral elements.

Figure 1.9a represents the 2D coordinate system adopted with a scaling centre at $O(\hat{x}_0, \hat{y}_0)$ and figure 1.9b represents the coordinate system for 3D problems with an additional circumferential coordinate ζ with a scaling centre at $O(\hat{x}_0, \hat{y}_0, \hat{z}_0)$. The scaling centre is selected in such a way that a point within an element where the boundaries of the domain must be visible. The boundary of the element is then scaled relative to the scaling centre. The normalized radial coordinate ξ runs from O towards the boundary, which has values of zero at the scaling centre and unity along the boundary. The circumferential coordinates η, ζ discretise the boundary of domain into arbitrary numbers of elements, and discretisation may take any shape along the boundary with a valid scaling centre, which can be implemented by sub-structuring when it is necessary.

With the generalised polygonal and polyhedral formulation for both 2D and 3D; triangular and quadrilateral (2D), and tetrahedral and hexahedral (3D) elements are automatically included in the element library. The arbitrary polygon and polyhedral elements expand the meshing capabilities to construct boundary conforming meshes around complex boundaries without the requirement of mesh refinement. Any distorted element can easily be combined with the neighbouring elements or divided into more polygons/polyhedrons.

1.3.2 Non-local damage analysis

Assessing material and structural damage forms an important aspect in structural reliability and integrity. Through the advancements in CDM, engineers can now predict the lifetime of structures more accurately. This work focuses on understanding the material and structural behaviour of structural engineering systems by accurately modelling the behaviour of such systems by allowing for material degradation.

A mesh independent integral-type isotropic damage model is considered in this damage formulation. The non-local model is formulated by replacing a local thermodynamics variable by its non-local counterpart obtained by weighted averaging over a spatial neighbourhood of each point under consideration. The non-local weight function is a new parameter for the model. This parameter can be chosen as the Gauss distribution function or the polynomial bell-shaped function. The evolution of damage is assumed to be governed by the equivalent strain with respect to either a linear softening or an exponential softening model.

To perform variable delocalisation the numerical implementation of the constitutive equations require modifications to the classical finite element computer codes. The regularisation technique requires the value of the thermodynamics variables at many Gauss points located at a user specified finite distance outside the considered element. In the SBFEM based damage formulation the non-local integration subroutine efficiently handles this requirement through pre-computing gauss point weights prior to the NR iterations.

Quadtree (2D) and octree (3D) heirachical meshes enable an automatic and efficient process to conduct analyses using the SBFEM. The SBFEM requires only the discretisation of the boundary which simplifies the meshing process. The classical mesh incompatibility issues caused by hanging nodes are overcome by no additional effort in the 2D scheme and by triangulation in the 3D scheme which produces only six surface patterns. The use of the $2:1$ balanced mesh significantly reduces the number of unique cell patterns (master cells) present in the mesh which reduces the computational burden enormously. The damage formulation process with SBFEM can be simplified by assuming the damage degree constant within a subdomain and thus calculating state variables only at one location within a subdomain.

1.3.3 Adaptive analysis

Adaptive analysis improves the accuracy of numerical solution at a lower computational cost. The adoption of the quadtree/octree meshing technique paves the way to the implementation of a highly efficient adaptive scheme. However, the advantages of theses adaptive heirachical structures do not appeal to every numerical modelling technique due to the presence of hanging nodes. The SBFEM posses an inherent capability to handle hanging nodes. Therefore, a simple yet effective damage variable based adaptive h-refinement technique is explored in this work.

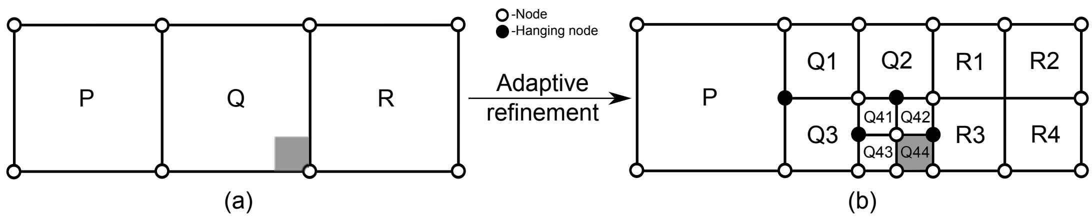

Figure 1.10. The h-refinement process for quadtree mesh illustrating the simplicity of mesh generation assuring the displacement compatibility between adjacent elements.

In the overall process the quadtree mesh is expected to enable rapid local refinement. As an example, assume the lower right corner of element Q in figure 1.10a is damage defected. The adaptive process then recursively subdivides the element Q to obtain the element decomposition shown in figure 1.10b. The damage defected element is now isolated from the rest of the elements to element Q44. To maintain an acceptable aspect ratio and also to limit the number of different types of elements produced in the decomposition, the 2:1 rule is applied. This requires further fragmentation of element R to four separate elements R1-R4. The hanging nodes created in the process are automatically handled by the SBFEM. For example the hanging node created on the left edge of R4 is incorporated in the SBFE formulation by subdividing the edge at the hanging node into two 2-node line elements. This ensures the compatibility with the adjacent smaller quadtree elements Q42 and Q44. In general the SBFEM polygon element formulation allows to incorporate any number of hanging nodes through this process.

1.3.4 Non-linear mathematical solver

When dealing with problems involving softening material, one of the challenges that arises is in tracing the non-linear equilibrium path. This difficulty is solved by continuation methods. The method should be an appropriate non-linear mathematical solver to trace load-deflection path which contain limit points. This work implements an accelerated/dampened m-NR method with line search technique coupled with the arc-length formulation.

In the development of the arc-length formulation Riks [79], Crisfield [80–82], De Borst [83] and Hellweg [84] have made substantial contributions. The crucial advantage of the arc-length method is its ability to trace snap-back behaviour in load-deformation space. The effect is often seen in problems that experience localized failure. This trait is very beneficial for this research as the applicability of the framework is increased substantially. The research therefore intends to look at both localised damage failure mechanisms and also its regularised form.

To overcome the issue of slow convergence typically experienced by the classical NR method, a line search oriented accelerating and damping technique is formulated in this study. The line searches are adopted to calculate an optimum scalar step-length which scales the normal iterative vector. However for efficiency the scheme is only adopted in 'difficult iterations' i.e iterations that do not converge to an acceptable tolerance limit. The method is expected to improve the efficiency of the m-NR method with significant convergence improvements, compared to the standard arc-length method.

Further detail on the arc-length coupled accelerated/dampened m-NR method with line search technique can be found in chapters 3 and 4.

1.4 Research contribution

This research is focused on developing an efficient and robust Automatic Image-Based Adaptive Damage Analysis (AIBADA) framework to simulate structural and material deterioration.

The advances in imaging techniques such as the X-ray CT, MRI and PET have made it possible to obtain high quality images for engineering applications. However image-based structural analysis frameworks adopting the advantages of such rapidly improving technologies are at their early inception. Thus, this contemporary research opens the door to a fascinating field of image-based damage analysis. Furthermore, widely used damage analysis packages in commercial finite element software are not entirely efficient and straightforward in their implementation. Therefore an accurate and effective damage modelling technique built on an input image is expected to spark an interest within both the research community and the industry.

The SBFEM coupled with quadtree/octree mesh generation will most certainly produce a modelling technique which would have the capacity to be highly automated and computationally less costly. Thus, this research has the ability to overcome difficulties faced by many researchers working in the field of damage analysis restrained by the inefficiencies of an analysis framework.

To date, the SBFEM had yet to be expanded to damage analysis. In this thesis the formulation of the SBFEM based damage analysis in both 2D and 3D is explored, with ultimately a successful outcome. Through this extension, the capabilities of the SBFEM will further expand. The ability to model damage influenced material non-linearity will be an enormous advantage to the already burgeoning numerical technique. The investigations into material damage initiation and propagation will allow for better understanding of the two ubiquitous civil engineering materials, steel and concrete. However the formulation will be self contained for future application and expansion to other engineering materials such as rocks, ceramics, granular material, clays, and sands. In structural analysis, modelling damage influenced structures and structural components will lead to important investigations of stability of structures. Since response of a structure is also dependent on its defects, damage analysis will give engineers a better understanding on the structural responses.

The reader can expect to come across the following milestones in this thesis presentation.

- Development and verification of a novel 2D scaling centre based damage formulation by the SBFEM (see chapter 3).

- Development and verification of a novel 3D scaling centre based damage formulation by the SBFEM (see chapter 4).

- Implementation of a robust and efficient automatic image-based damage analysis technique by the SBFEM (see chapter 5).

- Introduction of a novel purely damage variable based Automatic Image-Based Adaptive Damage Analysis (AIBADA) scheme by the SBFEM (see chapter 6).

These milestones capture the intermediate developments along the way to achieving the ultimate goal of an efficient image-based damage modelling framework. These milestones form the originality of the work. Further detail on each of the milestones can be found in the referenced chapters. A high level representation of the developed framework is shown in figure 1.11.

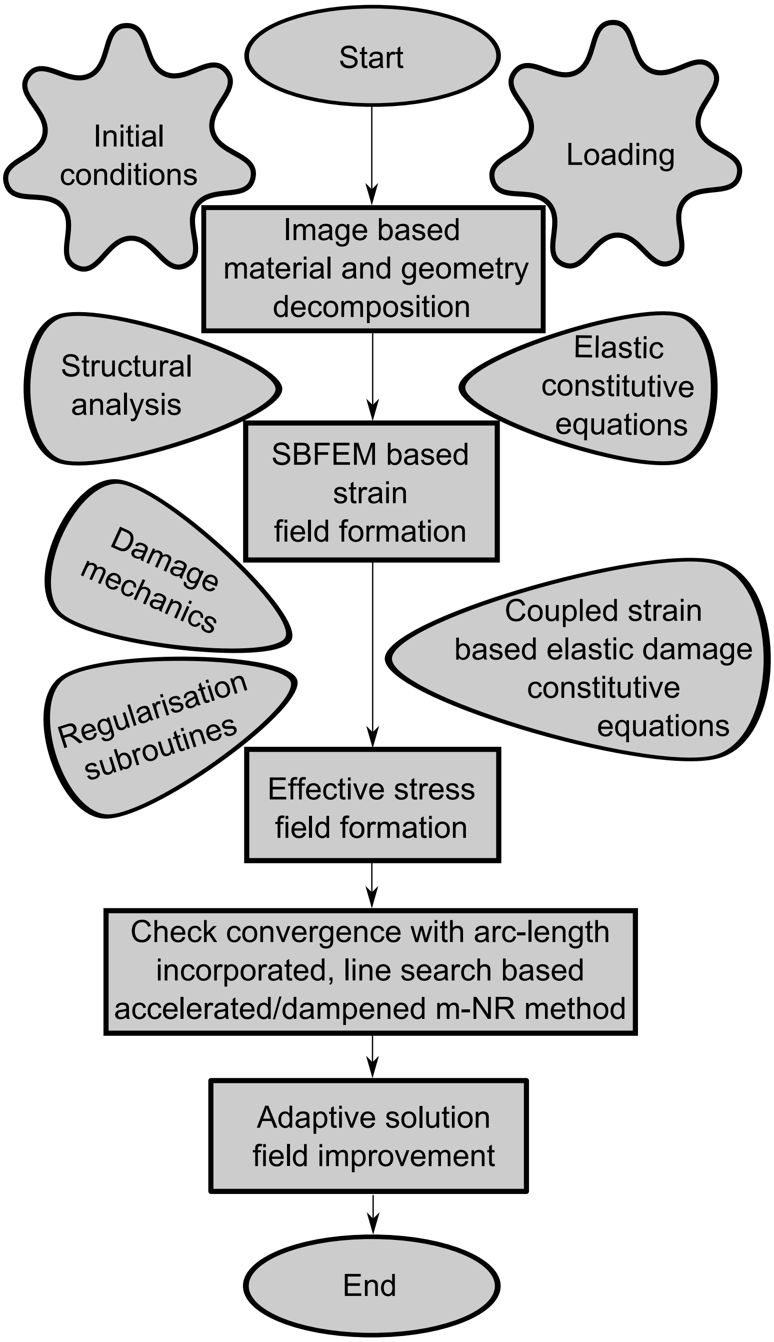

Figure 1.11. High level representation of the automatic image-based damage analysis framework with the SBFEM.

The research outcomes in this thesis contribute to the implementation of an image-based damage analysis scheme, that can be utilised for numerous engineering applications.

1.5 Objectives and scope

This research focuses on developing a novel image oriented adaptive damage analysis technique with the SBFEM. Octree and quadtree heirachical mesh generation structures are employed due to their efficient data storage and rapid computations ability. The SBFEM works in conjunction with the spatial decomposition technique. The method automatically satisfies the compatibility requirement between adjacent quadtree/octree cells irrespective of the presence of hanging nodes. The arc-length incorporated line search oriented accelerated/dampened m-NR method enables accurate and efficient tracking of the equilibrium path.

The first task to investigate in this research is the development of SBFEM framework for 2D damage analysis. Through a thorough validation process the damage formulation is expected to be simplified to a scaling centre formulation. This is expected to largely reduce the computational time. To implement the regularised damage analysis framework the standard SBFEM is to be modified to allow exchange of information between integration points. This part of the work also intends to investigate the effects of damage localisation and where necessary comparisons will be made to the non-local formulations. To accurately trace the softening behaviour of the materials the arc-length technique will be implemented in this initial stage. The scope of this part of work is however limited to only 2D structures and materials.

A natural extension to the 2D framework into 3D damage analysis will then take place. The work will involve the formulation of the damage incorporated SBFE equations in 3D. The method will then be verified thoroughly with the help of published literature. It is expected that in the 3D space the analysis process will be more computationally demanding due to the increased number of DOFs. Various strategies such as pre-computing strain modes and weight functions are considered to improve the efficiency of the programme. To further improve the convergence rate of the analysis and in return to improve the efficiency of the scheme the arc-length technique developed earlier may require improvements such as line search orientated acceleration and damping.

Next the robust and efficient image-based damage analysis framework will be formulated for both two and three dimensional space. Within the image-based formulation automatic meshes are expected to be generated with the quadtree and the octree technique. An assessment of the requirement of mesh smoothing in non-local damage analysis is to be investigated through comparison of results obtained for the smoothened and unsmoothed results. The mesh smoothing for the cells around the boundary will be carried out by the level set method. The process thus is expected to produce arbitrary polygons. These arbitrary polygons will be modelled by the scale boundary polygon formulation. Mesh automation can be effectively achieved through the incorporation of the heirachical mesh generation structures and the SBFEM polygon formulation. The overall technique is expected to enable automatic damage analysis of problems involving curved and complex boundaries. The quadtree and octree balancing techniques will produce a limited number of cell patterns which would effectively reduce the pre-processing and analysis times.

Finally, this research aims to develop a damage variable based adaptive damage analysis formulation to simultaneously improve the solution accuracy and reduce the computational burden. When implemented, the adaptive domain decomposition will automatically refine the Damage Process Zone (DPZ) leaving rest of the problem domain unrefined/unaltered from its original state.

It can be justly ascertained that the scope of this work allows for better understanding of material and structural behaviour in computationally robust and efficient framework. It is an imperative requirement in structural and material analysis to evaluate and trace the evolution of damage within material interfaces and structural systems to fully comprehend the behaviour of these systems. This is because material and structural responses initiated by external agitations are directly related to the inevitable degradation of the material caused by microstructural defects inherent in the material build-up. This research therefore is capable of building the necessary techniques that enable rigorous investigations into material non-linearity. The work therefore has outreaching applications within academia and industrial communities in disciplines such as civil and structural engineering, mechanical engineering, biomedical engineering, material science and aerospace engineering.

1.6 Organisation of the thesis

The thesis consists of seven chapters. Chapter 2 presents a literature review of the past and present developments in CAE preprocessing techniques, numerical modelling techniques, damage analysis techniques, adaptive analysis techniques and mathematical solvers. Each method and technique is investigated within the bounds of this research. Chapter 3 focuses on the formulation and verification of the two dimensional damage analysis using the SBFEM. From two dimensional analysis the research then moves on to three dimensional damage analysis with the SBFEM. The details of which are included chapter 4. In chapter 5 the milestone of formulating the image based damage modelling technique is achieved. The work presented in this chapter builds on the framework established in the previous chapters 3 and 4 by incorporating an automatic image decomposition technique for two and three dimensional damage analysis. The work presented in chapter 5 benefits from the advances in image-based techniques that have gained immense popularity in recent times due to their ability to effectively map complex geometries. The automatic image-based meshing technique adopted to model complex geometries negates the requirement for human intervention in the mesh generation process. The overall formulation benefits from the SBFEM compatibility with the mesh generation technique. An improvement to this overall framework is achieved through the work documented in chapter 6, where the 2D Automatic Image-Based Adaptive Damage Analysis (AIBADA) procedure is introduced. From chapter 3 through to chapter 6 the reader may appreciate a computationally efficient and robust damage modelling framework that can handle diverse problems involving different materials and geometries. The localisation of the damage process zones are prevented through implementing a non-local damage scheme. To capture the softening behaviours of the damaged materials an efficient accelerated/dampened m-NR method is used in conjunction with the arc-length method. At the end of chapters 3-6 numerical examples are presented for verification of the current proposed technique. Where applicable, the examples compare results obtained through this research to that of the results published in the literature. The final conclusions and recommendations of this research are collated in chapter 7.

Chapter 2

Literature Review

This chapter focusses on the most recent contributions of various research studies relevant to this work. Section 2.1 investigates the progressions in Computer Aided Design (CAD) and image-based preprocessing techniques. The focus then moves on to the historical progression in numerical techniques in section 2.2. This review looks at the advantages and shortcomings of the Finite Element Method (FEM), the Boundary Element Method (BEM), the eXtended Finite Element Method (XFEM) and the Scaled Boundary Finite Element Method (SBFEM). Then in section 2.3 various combinations of preprocessing and numerical methods found in the current literature are discussed. In section 2.4 a general overview of damage analysis is presented. At the end of the section regularised and non-regularised damage analysis techniques are discussed. The discussion also includes a section on accurate determination on material parameters in non-local models. To analyse problems involving softening behaviour an efficient process coupled with a robust solver is paramount. Therefore, adaptive analysis techniques and mathematical solvers form the last two components of this chapter. These topics can be found in section 2.5 and section 2.6, respectively. Finally remarks and conclusions are presented in section 2.7.

2.1 Preprocessing techniques

This section presents a review on CAD-based and image-based meshing techniques. It is important to develop an efficient and accurate meshing procedure for the numerical methods explored in section 2.2 to be fully effective. This helps in reducing the spatial discretisation errors within the analysis. Automatic processes are generally preferred in generating high quality meshes as it reduces the human effort in mesh generation. These automated techniques are also useful for applications that require continuous re-meshing such as in topology optimization, adaptive analysis, and problems that involve moving boundaries e.g. crack propagation and phase transition in matter. In general, triangular/tetrahedral meshes are easier to generate automatically compared to the FEM favoured quadrilateral/hexahedral meshes. Therefore, within the finite element process robust and efficient meshing is a challenge.

2.1.1 CAD-based meshing

Automatic mesh generation from CAD models has been an active research field for many years. Therefore, various meshing techniques have been developed in the recent past [48, 85–87].

CAD-based meshing is the conventional method adopted in numerical analysis. To date, there are many different algorithms developed to automate the meshing process based on a CAD geometry input. The geometry of a design is commonly described by Non-Uniform Rational B-Splines (NURBS). Meshes produced through CAD geometry inputs can either be conforming or non-conforming to the boundary.

The traditional approach is to create meshes which conform to the boundary and such meshes are often paired with the FEM. However, for practical problems generating a high-quality finite element mesh conforming to the boundary often requires considerable human interventions. In tetrahedral mesh generation the surface boundaries are first discretised into triangles. Advancing Front (AF) [48] and Delaunay meshing [47] are two popular techniques used in this process. In general both these methods are automatic and simple to implement. The downside to these methods is its high dependence on the initial triangulation of the surface boundary and the poor performance in problems involving stress concentrations. An alternative is to use hexahedral (brick) elements. Blacker in [49] introduced a few methods to construct hexahedral meshes. Compared to the tetrahedral mesh these hexahedral mesh generations are not robust and are semi-automatic i.e they require manual interventions [88]. The process can be cumbersome and time-consuming whereby restricting applications to complicated geometries.

On the other hand, hierarchical mesh generation algorithms such as quadtree (2D) or octree (3D) can be employed to create a mesh structure [89]. The algorithms operate by systematically dividing a square (2D) or a cube (3D). The domain is refined maintaining a hierarchical structure depending on the geometrical discontinuities, complicated boundaries, and material interfaces apparent within the domain. An added advantage of the technique is its ability to model features at different scales. It is a common practice to enable a restriction on the length ratio between neighbouring elements. This is usually maintained at 2:1. In figure 2.1, sub-figure 2.1a depicts a balanced quadtree mesh for a random shape and sub-figure 2.1b illustrates a balanced octree mesh for a cube with a spherical inclusion. In order to obtain boundary conforming meshes, a modified-quadtree or octree technique can be utilised to trim the cells that are cut by the boundary [86, 90].

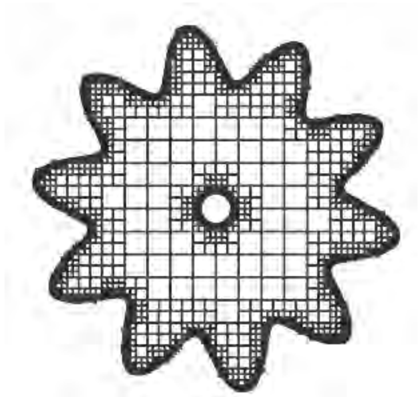

(a) A balanced quadtree mesh generated for random geometry [72]

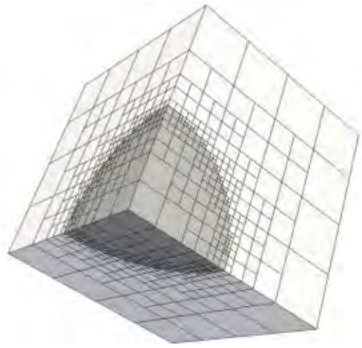

(b) A balanced octree decomposition for one-eighth of a spherical inclusion in a cubic domain [91]

Figure 2.1. Balanced (a) quadtree mesh generated for random geometry and (b) octree decomposition for one-eighth of a spherical inclusion in a cubic domain.

In quadtree or octree implementation in FEM and XFEM hanging nodes between adjacent cells of different size elements create displacement incompatibilities. The most straightforward treatment adopted in the 2D FEM to overcome this incompatibility is to divide each cell into combinations of triangles and quadrilaterals. In the process, FEM uses 5 types of discretisation for a balanced quadtree mesh. However, in 3D a similar treatment becomes less enticing as the types of cells with hanging nodes is very large [89]. Therefore, for octree meshes a Delaunay triangulation-based algorithm for the FEM was proposed by Schroeder et al. [92]. Triangulation (2D) or tetrahedralisation (3D) is however not an ideal solution given the drawbacks associated with these types of elements in the FEM framework. In another recent advancement Lo et al. [93] developed special shape functions for cells with hanging nodes, e.g. transitional quadrilateral (2D) and hexahedral (3D) elements. Further developments recommend adaptive refinement of the FEM basis function [94] and for the XFEM a method to constrain hanging nodes by adjacent nodes on an element edge [89]. Another popular alternative solution is the polygonal element formulation [95] constructed with Wachspress shape functions. Here a mapping procedure is used on each simplex to perform the numerical integration.

As mentioned earlier, the second type of mesh generation is creating meshes non-confirming to the boundary. Although a mesh non-confirming to the boundary will be simpler to obtain compared to a mesh that is confirming, the numerical integration and the calculation of element matrices during the numerical analysis are generally more complicated and time-consuming. However, these boundary non-conforming meshes can be used in the XFEM and the Finite Cell Method (FCM). Similarly, quadtree and octree mesh structures have also been directly used without boundary trimming [89]. The boundary description and local features can be defined implicitly through level sets [96–98].

2.1.2 Image-based meshing

Digital images obtained through non-invasive digital imaging technologies such as X-ray computed tomography (X-ray CT) scans, Magnetic Resonance Imaging (MRI), Single-Photon Emission Computed Tomography (SPECT) and ultrasound have conveniently made their way to engineering and science. This method of processing and segmenting data stored in digital images is popularly known as "image-based processing". The method enables the acquisition of images of the interior structure of objects. These digital images are composed of pixels in 2D and voxels in 3D. The colour intensities of the pixels and voxels represent the geometrical information and the material distribution of the object. Depending on the colour intensities an image is divided into regions, in each of these regions the material characteristics are assumed to be homogeneous. The various image segmentation procedures can be found in [97, 99–102]. The processed information then can be translated into an appropriate mesh for various computer analyses such as material characterization [97, 98, 103, 104], biomedical applications [105–108], and fracture analysis [97, 98, 103, 109].

There are two main categories of image-based mesh development techniques, some techniques involve procedures that require boundary detection prior to meshing and others create meshes directly off a digital image.

In most scenarios boundary detection is opted to make use of the readily available commercial software to produce a required mesh. At present, the most popular method for isosurface extraction and rendering is the marching squares (2D) and marching cubes (3D) algorithms proposed by Lorensen and Cline [110]. Wang et al. [106] later proposed a modified version to treat ambiguity and mesh incompatibility for certain special cases. However, improvements to the algorithm such as, the general study of ambiguity, methods for disambiguation, and how noisy edges/corners can be eliminated is ongoing. A detailed survey on the development of the marching cubes algorithm is presented by Newman and Hong [111]. After detection of the boundary CAD-based meshing techniques outlined in section 2.1.1 can be used to obtain the appropriate mesh. For example, two of the popular techniques involve level sets based on XFEM [97, 98, 112] and level sets based FCM where a fictitious non-conforming voxel-based mesh is used with the boundary defined implicitly using level sets [96].

The second type of image-based meshing technique is a more efficient, simple and a robust approach where mesh elements are generated directly from the image digital data. Keyak in 1990 [107] developed a voxel-based approach where each voxel is assigned to various types of material available in the object (method referred as masking) and then the voxels are simply modelled as a hexahedral finite element. Compared to the techniques discussed earlier Keyak's approach avoids the intermediate step of boundary detection and combines both geometric detection and mesh creation in one process. The method however produces a large number of elements with interface boundary elements containing jagged boundaries for curved geometry. The excessive number of elements then leads to an excessive computational burden. The method is also found to produce inaccurate results when the discretised mesh does not conform to the geometry with smooth representations of surfaces within the meshed domain [113]. The local stress oscillations produced by jagged boundaries [114] are however localised at small elements along each material boundary [98, 108, 115], while the average stresses remain close to the stresses obtained using geometry-based meshes. Volumetric Marching Cubes (VoMaC) method [116] and the Extended Volumetric Marching Cubes (EVoMaC) method [88] superseded Keyak's work and attempted in combining the favourable features of the voxel method and the marching cubes algorithm. EVoMaC is an improvement to VoMaC enabling the technique to consider up to 8 sub-regions meeting at a cube vertex. As shown in figure 2.2 the CT scan of a dry cadaveric bone in figure 2.2a is decomposed into voxel mesh before application of the marching cubes algorithm to produce a smoother surface (refer figure 2.2b). The surface undulation can be further improved by adoption of a partial volume-based interpolation (see figure 2.2c). The process thus has gradually trimmed the jagged edges on the boundary surface and produced a smooth surface.

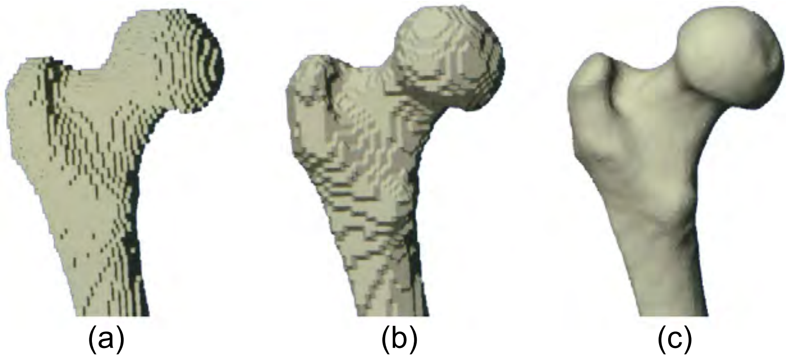

Figure 2.2. Reconstructions from CT scan of a dry cadaveric bone: (a) segmented volume of interest-voxel mesh, (b) surface mesh generated from marching cubes algorithm, (c) rendered view of surface mesh generated from marching cubes algorithm with partial volume-based interpolation [88].

2.2 Numerical modelling techniques

After obtaining a spatial representation of the problem domain Partial Differential Equations (PDEs) governing the problem behaviour are formed to construct a mathematical model. Numerical techniques are employed to obtain practical solutions for these PDEs thereby accurately simulating the behaviour of the model. Due to the vast range of numerical techniques available in the literature only a selected few are discussed here. These include the FEM, the BEM, the XFEM, and the SBFEM. The focus of this review is to highlight the inherent advantages and disadvantages of these techniques based on the concept of discretisation.

2.2.1 Inception of the FEM

In the early days of solid mechanics complex problems were typically solved by modelling the structure as discrete engineering systems of simple well-defined components. For each of these structural parts, a solution is obtained through first principles. These discrete engineering systems can be formulated to give sufficient accuracy for practical applications. For example the direct stiffness method widely used in civil engineering is one such method where well defined conditions for the forces and displacements at joints are used to determine the compatibility between the structural members. Similar displacement based analysis were proposed by Louis Navier in 1826 [117] and documented by Alfred Clebsch in 1862 [118]. Argyris in 1955 [119] developed a matrix based stiffness method which enabled convenient representation of a large number of linear equations. Prior to the advent of modern computer techniques such as the relaxation method developed by Southwell [120] assisted in obtaining solutions for large matrices.

Moving from discrete systems, came the need to approximate the behaviour of a continuum by discrete or "finite elements'. A good example of which is the solution of stress and strain distributions in elastic continua. Although there is no clear transition to modelling the continua, inspirations were drawn from the solution process of discrete engineering systems. Initial approaches discretised a continuum into an assembly of bars in a two or three dimensional space. Such principles were considered in the work published by Hrenikoff [121] which demonstrates modelling of a frame through an assemblage of beams. Later on, the work published by McHenry [122] on a lattice analogy for the solution of stress problems used pin-jointed bars to approximate the solution of an elastic plane. Turner et al. in the early 1950s [9] made a major breakthrough in their publication on stiffness and deflection calculation of complex structures. Turner and his fellow researchers introduced a method subdividing the geometry into numerous elements with triangular or quadrilateral shapes. This is widely regarded as the first application of the finite element approximation.

In continuum mechanics PDEs define the behaviour of a system. Mathematical approximations are often employed to solve these PDEs. One of the earliest such methods was the Finite Difference Method (FDM) [2, 123]. The method is based on Taylor formula expansions on regular grids. The classical finite difference methods commonly restrict applications to irregular unstructured grids or moving boundaries. This limits their application to general engineering problems which have curved (irregular) boundaries and/or multiple material interfaces. However, there have been advances in the FDM from regular grids to general arbitrary and irregular grids or sets. These advancements have revived the method in a different light and has received considerable attention [124–126]. In 1909, Ritz [7] devised a method based on calculus of variations which employs trial functions with unknown variables to represent the solution of the PDE. In this method, to achieve the most optimal approximation to determine the unknown variable, a minimisation of potential energy is performed. In 1915 Galerkin [6] proposed another variational method named the weighted residual method. Essentially, the weighted residual method is a more general technique as different weighting and approximation functions could be used. Later on Courant [127] discretised a 2D domain into triangular elements and the trial functions were defined piecewise over some elements in a problem domain. It was shown that the minimum total potential could be achieved by ensuring the continuity of the function along the boundary.

The phrase "Finite Element Method" was first introduced in 1960 by Clough [10]. Since then FEM has emerged as an intuitive and practical method for solving different types of PDEs in relatively complex geometries which were not accessible previously. Clough's work provided the mathematical backing to the principle behind the success of discretising a continuum into various elements performed by Turner et al. [9]. In this work he further explained how the solutions can converge when a finer mesh is considered due to the minimisation of potential energy.

In the FEM, 'shape functions' or 'basis functions' interpolate the primary mechanical field (e.g. displacement in a stress analysis). These shape functions need to satisfy two requirements to obtain convergence [128]. Firstly, the displacements which are defined by the element's shape functions should not lead to any infinite strains (discontinuities). Secondly, when polynomial shape functions are utilised, the terms producing the constant strain values in each element should be able to take up any arbitrary value.

Subsequently, it was realised that other variational methods can also be used to derive the FEM. Szmelter [129] used an energy based method to formulate FEM. The use of variational principles has allowed FEM to be extended to many different branches of study. These include, problems governed by quasi-harmonic Poisson's equation in fluid mechanics and problems in electromagnetics [130]. In addition to the variational methods, equilibrium equation transformation to a weighted residual form is another way of obtaining FEM solution [131]. Alternatively, Zienkiewicz and Cheung [132, 133] derived FEM based on the principle of virtual work. In the virtual work derivations virtual displacements employed in the formulation can be different to the element shape functions. The virtual work derivation enables FEM formulations for non-symmetric forms of the elasticity matrix [134, 135].

2.2.2 The Finite Element Method (FEM)

The historical development contributing to the inception of the FEM was covered in section 2.2.1. Over the years, since the introduction of the FEM by Turner, Clough, Martin and Topp in 1956, the FEM has grown in leaps and bounds and has become a widely used numerical method to obtain approximate solutions for boundary value problems. FEM has a wide range of applications in fields of fluid flow and fluid dynamics [18, 19, 136], heat transfer [137], soil mechanics [138], acoustics [139], vibration analysis [140, 141], electromagnetic analysis [20, 21, 142, 143], fracture mechanics [16, 17], elastoplasticity [15], etc. It is useful in solving complicated geometries, loading and material properties where analytical solutions cannot be obtained. The method can be accessed through numerous commercial software and has thus become a well known method in Computer Aided Engineering (CAE).

The finite element process starts form generating a mesh by geometrically discretising a problem domain (a continuum). This discretised continuum now consist of 'finite elements' and nodes. Figure 2.3 gives a typical illustration of one, two and three dimensional problem space with forces, supports, elements and nodes labelled for each type.

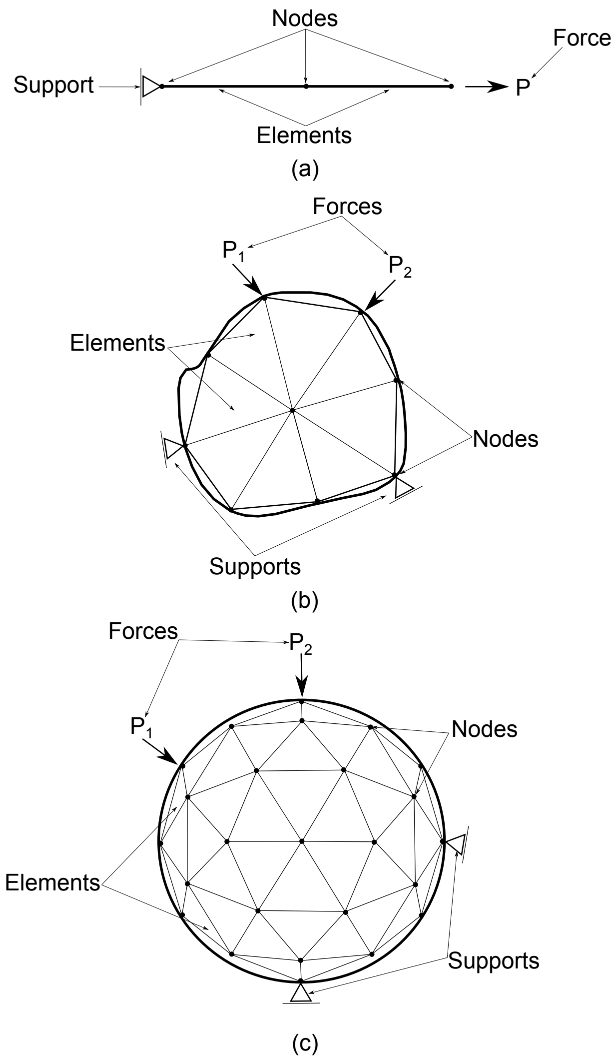

Figure 2.3. Finite elements in (a) 1D problems (b) 2D problems (c) 3D problems with labelled forces, supports, elements and nodes in each type.

The elements are assumed to be interconnected by a discrete number of nodal points situated on their boundaries and sometimes in their interior. The displacements of these nodal points will be the basic unknown parameters of the problem. These meshed elements can be of various different shapes and sizes. As shown in figure 2.3, in structural engineering: linear, planar and solid elements are commonly found in one, two and three dimensional analysis, respectively, These elements are capable of having different material properties. The governing equations vary in accordance with different cases such as truss, beam, torsion, and plates. There are also other types of solid elements developed to cope with particular problems [144], such as pyramid elements, brick elements and shell elements.

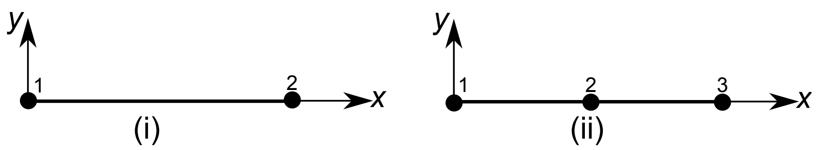

(a) (i) simple two-noded line element (typically used to represent a bar or beam element) and (ii) the higher-order line element.

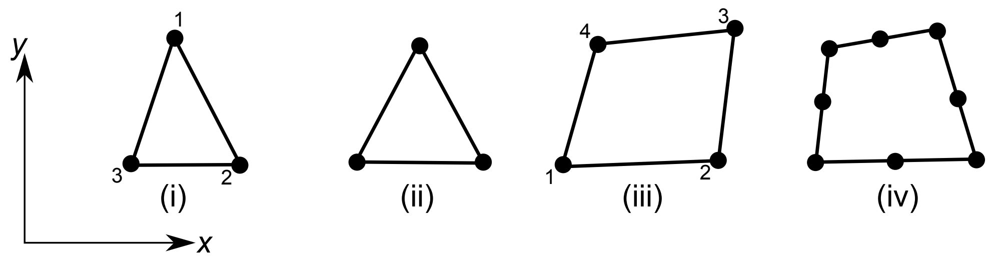

(b) (i, ii and iii) simple two-dimensional elements with corner nodes (typically used to represent plane stress/strain) and (iv) higher-order two-dimensional elements with intermediate nodes along the sides.

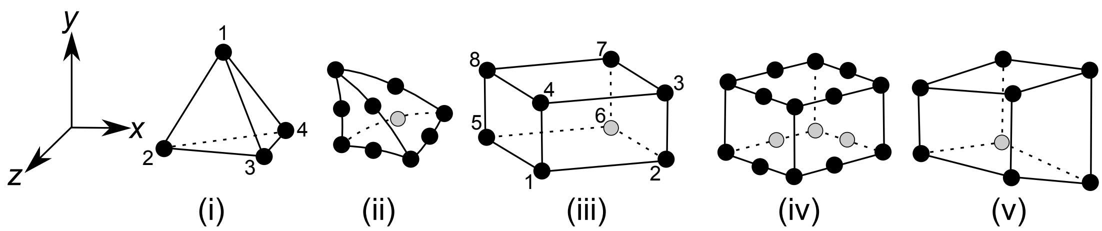

(c) (i, iii and v) simple three-dimensional elements (typically used to represent three-dimensional stress state) and (ii and iv) higher-order three-dimensional elements with intermediate nodes along edges.

Figure 2.4. Various types of simple lowest-order finite elements with corner nodes only and higher-order elements with intermediate nodes [145].

In general, the accuracy of a finite element analysis increases for models that have more elements, elements that have more nodes, nodes that have used higher degree polynomials for shape functions.

After discretising the continuum polynomial shape functions are defined within each element to approximate the state of displacement within each 'finite element' and on its boundaries in terms of its nodal displacements. Thereafter, the state of strain within an element can be defined by using these displacement functions in terms of the nodal displacements. These strains, together with any initial strains and the constitutive properties of the material, define the state of stress within the element and on it's boundaries. A stiffness relationship is formed thereafter considering the "equivalent forces" concentrated at the nodes and equilibrating the boundary stresses and any distributed loads. Finally, an overall solution is sought by bringing together the individual element solutions [146].

Early applications of FEM, elements were required to have straight edges. Therefore curved or complicated boundaries required considerably fine meshes. This generated unnecessarily high number of Degrees Of Freedom (DOF) or unknowns to be solved. As a solution, the geometry transformation technique which is known as the mapping technique was introduced. Through mapping a regular reference element having localised coordinates and straight edges can be mapped onto a physical element containing the global coordinate which have either regular, irregular, or curved edges. This then enables the use of higher order polynomial shape functions to improve the solution accuracy without reducing the element size [147, 148].

However, in the element mapping process, FEM is sensitive to mesh distortion. Meshes are distorted when the element consist of very small acute angles or very large obtuse angles. These unfavourable angles make the determinant of the Jacobian used in the mapping process tend to zero or even negative (non-convex element) which causes inaccuracies in the solution [149]. This issue is observed in simulations where the mesh topology evolves as the analysis progresses such as in crack propagation, large deformation analysis, and adaptive analysis. As a workaround, local re-meshing algorithms which remove and replace the distorted element with new compatible meshes consisting of well-shaped elements are commonly employed.

A possible solution to overcome the issue of mesh distortion is the use of polygonal elements. The introduction of the polygonal element has increased the flexibility of the finite element compatibility with various mesh configurations. The two main challenges in the development of such elements are in obtaining suitable shape functions and finding an efficient integration technique. Various shape functions such as Laplace shape functions, Wachspress shape functions and mean value coordinates have been introduced over the past. These shape functions however, are rational. Therefore no exact integration rule is available. As a workaround, tetrahedralising the polyhedron and integrating each tetrahedral sub-volumes using standard integration rule for a tetrahedron can be adopted. Here the standard integration rules assume that the shape functions to be polynomials which involves a high number of integration points to obtain accurate results. Furthermore, linear shape functions are commonly used in the polyhedral formulations making them not favourable for transient analysis. In section 2.2.5 the SBFEM polygonal element (2D) and polyhedral element (3D) formulation is introduced, which is a simple and efficient method to overcome these concerns.

2.2.3 The Boundary Element Method (BEM)

In the BEM also known as the Boundary Integral Equation Method (BIEM) governing PDEs are formulated as boundary integral equations. Lachat and Watson [150] first realised that the concept of FEM can be applied to solve the boundary integral equations. Later, Brebbia and Dominguez [11] used the method of weighted residuals to obtain the boundary integral equations. These two contributions lead to the publications in 1977 [11, 12] which carried the term "boundary element method".

As the name suggests, in the BEM, the elements are formed on the boundary of the problem domain. This makes the meshing process simpler when compared to the domain discretisation performed in the FEM. Since only the boundary is discretised fewer DOFs are typically produced compared to FEM. Transforming the integral equations with the use of divergence theorem (transforming a volume integral into a boundary integral), Stoke's theorem (transforming a surface integral into a contour integral) or the Green's identities [151] the BEM can reduce the spatial dimensions by one degree, transforming 2D problems to 1D and 3D problems to 2D. However, the method requires the solution of non-symmetrical matrices which results in higher computational cost than the symmetric and banded matrices encountered in FEM.

Contrary to the FEM, the solution process in the BEM starts from outside in. Based on the boundary conditions, boundary values are fitted into the integral equations. These boundary equations are solved simultaneously and the values in the internal domain can be obtained from the results on the boundary through integration. Therefore, in the BEM the accuracy of the internal solution is equal to the solution at the boundary. This is different to the FEM where the optimal solutions inside the element are only located at the quadrature points (superconvergent points). Over the years BEM has become particularly useful in problems involving infinite domains [152] and fracture [153–155].

There are two popular variants of the BEM, the direct BEM and indirect BEM [156]. In the direct BEM, the actual field variables of the problems (displacements, stresses, etc.) are used in the fundamental theorems deriving the boundary integral equations [157–159]. Whereas in the indirect method a fictitious body force distribution over the boundary is considered to compute the boundary integral equations [160, 161]. Out of the two, the indirect approach is preferred as the direct approach is generally harder to formulate and challenging to obtain the internal solutions.

One of the biggest drawbacks of the method is that it requires a fundamental solution or Green's functions to satisfy the governing PDEs which must be obtained a priori. Such a fundamental solution includes the Kelvin's solution for elastostatics problems [162] and the solution for unit point loads acting in an infinite domain [163]. Certain fundamental solutions are much more complicated especially for problems involving anisotropic materials. The application of this method is restricted since non-linearity, non-homogeneity and anisotropy are difficult to handle.

2.2.4 The eXtended Finite Element Method (XFEM)

The XFEM introduced in 1999 by Belytschko and Black [13] and Moes et al. [164] is a numerical technique that enables a local enrichment in addition to the standard finite element method. The method is most widely used and developed to provide an accurate approximation for problems with non smooth domains, discontinuities or domains with different material phases.

The method is highly effective in image-based analysis techniques as traditional methods in mesh generation and numerical analysis produce kinks in the displacement field and jumps in the strain field at the material interfaces. In image-based analysis the straightforward choice in explicit meshing of all heterogeneities requires sophisticated 3D mesh software, and large computational times related to the meshing operation [165, 166]. Therefore, an alternative is to project the phase properties on a mesh, without explicitly representing the interfaces [167, 168]. XFEM usually employs level set and signed distance function for implicit interface representation discontinuities. Then intrinsic and extrinsic enrichment of the finite element scheme is adopted to accurately model the different jumps at the interfaces. In the former, basis vectors are enriched whereas in the latter extrinsic enrichment of the approximation space takes place. Recent developments to the technique have enabled the method to model and compute overall properties of complex microstructures [169].

Another field of applications in the XFEM is in problems involving cracks. Similar to the above XFEM enriches the approximation space in the FEM using discontinuous enrichment functions [13]. Dolbow et al. [170] developed XFEM further by incorporating an enrichment which uses the asymptotic near-tip field for the nodes in the element containing the crack tip. The advantage of the method is that there is no requirement for excessive refinement around the crack tip. As the enrichment function can accurately represent the singular stress field crack growth can be modelled with very little re-meshing. A comprehensive review on this method can be found in [171, 172]. Developments by Daux et al. [173] involved the incorporation of crack branching through an additional discontinuous function. A generalised crack model was subsequently developed by Belytschko et al. [174] to include different types of discontinuities. The implementation of XFEM using level set method for elasto-static fatigue cracks can be found in [175]. Later on, implicit functions were developed by, Belytschko et al. [176] which represent the boundary of the domain along with any inner features such as an interface between two materials, sliding surfaces, and discontinuities. XFEM has also been applied to solve problems concerning crack propagation [177], dynamic fracture analysis [178], and elastoplasticity [179, 180]. The method has also been extended to model planar cracks [181] and non-planar cracks [182] for 3D fracture analysis.

2.2.5 The Scaled Boundary Finite Element Method (SBFEM)

The SBFEM is a semi-analytical method developed by Song and Wolf [14]. Through its development the SBFEM acquires characteristic unique properties of its own. The SBFEM is a semi-analytical method which is based on an analytical solution in the radial direction and a numerical solution in the circumferential direction. Similar to the FEM, the problem domain is divided into various subdomains. Symmetric stiffness and mass matrices for each subdomain are then computed independently. The global system of equations are assembled using these individual stiffness and mass matrices. Similar to BEM, the problem dimension is reduced by one as the numerical discretisation is only performed on the boundary of each subdomain. The solution within each subdomain is expressed as function with respect to a so-called scaling centre. The only requirement for the location of the scaling centre is that from the scaling centre the subdomain's boundary needs to be directly visible. The accuracy of the solution is partly dependent on this condition whereby improving the visibility of the boundary from the scaling centre can improve the accuracy of the solution. Analogous to the effect of small internal angles within elements in the FEM, the angle between the boundary and the line of sight from the scaling centre in SBFEM should not be too small.

Figure 2.5 illustrates the scaled boundary coordinate system, in which the a scaling centre is chosen within the domain with a visible boundary.

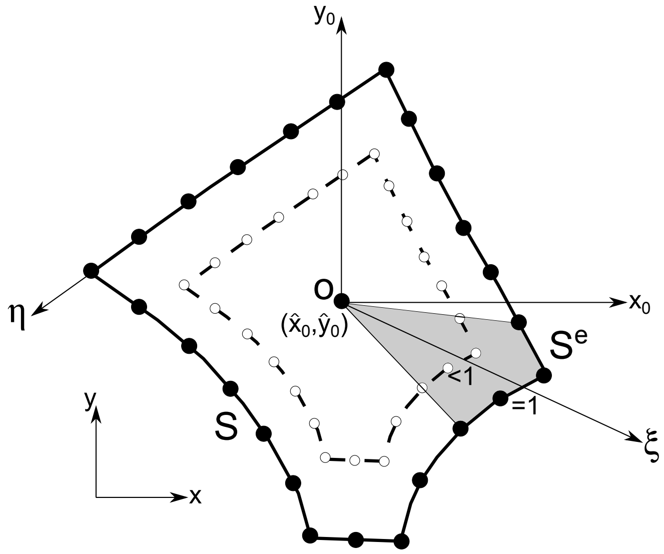

Figure 2.5. A 2D scaled boundary coordinate system with scaling centre O, radial coordinate ξ and circumferential coordinate η [183].

The boundary of the domain can have any number of line elements and the radial coordinate is defined to be infinity in the far field, 1 on the boundary and 0 at the scaling centre [184]. Along the radial direction ξ as shown in figure 2.5 the results are obtained analytically. Unlike in the BEM there is no requirement for fundamental solution to satisfy the governing PDEs. The SBFEM is especially efficient in modelling stress singularities and unbounded medium.

The SBFEM was originally presented as the consistent infinitesimal finite-element cell method in the early 1990s. The method was mechanically derived by making use of a similarity concept to that of the FEM assemblage process. The early applications of the method mainly focused on problems in unbounded media such as scalar wave [185, 186], vector wave [186–189], static [190] and diffusion [188] problems. The applicability of the method was later demonstrated for bounded domains to solve problems in elastostatics and elastodynamics in both 2D and 3D [14].

Song and Wolf [14] in 1997 first coined the phrase "Scaled Boundary Finite Element Method". Their work introduced a novel scaled boundary transformation-based derivation. Similar to the FEM, this formulation transformed the governing partial differential equations to local scaled boundary coordinates. The SBFEM employs the weighted-residual technique (similar to the FEM) to obtain the matrix equations of the original SBFEM. This method found application in problems involving diffusion [68] and body loads [191]. In order to provide a detailed explanation, two primer papers were also published consisting of the SBFE derivations [192] and solution procedure [193] based on a simple example.

In 2004, Song [194] proposed the matrix power function based Schur decomposition technique as an alternative to the conventional eigenvalue decomposition solution method. This numerically robust approach had two main advantages: it enabled the solution to be expressed in terms of a reduced set of orthogonal base functions; and the Schur decomposition prevented solution inaccuracies in problems with multiple eigenvalues with parallel eigenvectors.

A new SBFEM virtual work formulation for elastostatics was published by Deeks and Wolf [66] in 2002. The work followed the traditional virtual work derivation of the standard finite element method. Apart from making the method more accessible the virtual work derivation also provided insights to new techniques to treat side face loads (loading on radial lines from the scaling centre to the points on the boundary), body loads, and axisymmetry.

Adaptive analysis with the SBFEM was first published by Deeks and Wolf [64, 65] in 2002. These two related papers expounded on the stress recovery technique and an error estimator derivation. The SBFEM based h-hierarchical mesh refinement was detailed in a subsequent journal paper by Deeks and Wolf [65]. Later on, with the help of high-order shape functions an adaptive p-refinement technique was introduced by Vu and Deeks [195, 196].

In 2008, the continued-fraction solution [197] was formulated for the unbounded domain and also for the bounded domain [198]. This helped improve the SBFEM solution accuracy for dynamic problems. The original work first formulated by Song and Wolf [199] was only accurate for low frequencies, as the inertial effects related to higher frequencies were neglected in the derivation of the dynamic stiffness. These contributions enabled the construction of symmetric high-order stiffness and mass matrices. The continued-fraction solution allows the response at high frequency to be captured without the need to introduce an internal mesh. Chen et al. [200] later improved the formulations for bounded domain for better stability. In addition the work also demonstrated the possibility for coupling of the continued-fraction solutions for the bounded and the unbounded domains.

For accurate spatial representation of the problem domain the SBFEM was combined with isogeometric analysis using NURBS for 2D problems which allows exact representation of the problem domain [201]. Deeks and Charles [202] has contributed in a meshless method by replacing the conventional shape function on the boundary with a function obtained with the local Petrov-Galerkin approach.

Table 2.1 compares the SBFEM with the FEM, the BEM and the XFEM discussed in this section. It is apparent how the SBFEM benefits from the advantages of both the FEM and the BEM and overall surpass the other three methods in light of the aspects outlined in the table.

Characteristic	FEM	BEM	XFEM	SBFEM
Reduction of the spatial dimension by one as only the boundary is discretised with surface finite elements, reducing the data preparation and computational efforts		x		x
Analytical solution achieved inside domain		x		x
Fundamental solution not required	x		x	x
Radiation condition at infinity satisfied exactly when modelling unbounded (infinite or semi-infinite) media		x		x
No discretisation of free and fixed boundaries and interfaces between different materials			x	x
Approximation required only of the surface finite elements on the boundary		x		x
Symmetric static-stiffness and mass matrices for bounded media	x		x	x
Body loads processed without additional domain discretisation and thus additional approximation	x		x	x
Straightforward calculation of stress concentrations and intensity factors based on their definition			x	x

Table 2.1. Comparison of the FEM, the BEM, the XFEM and the SBFEM.

A major contribution in the field of mesh generation is the introduction of the scaled boundary polygonal (2D) element [203–205] and the polyhedral elements (3D) [91]. This introduction allowed automatic meshing algorithms [72] to be developed with ease and offers greater meshing flexibility. These polygonal elements have thus far been used for crack propagation analysis [72, 205–209], for determination of fracture parameters [70, 71], and image-based analysis [91].

To date, further research continues on unbounded domain [61–63], plates including piezoelectric plates [74–76], fluid-structure interaction [210], electro-magnetics [67], acoustics [69], elasto-plastic material [73], wave propagation [77, 78] and damage analysis [211, 212]. In many of these applications the SBFEM could achieve comparable accuracy to that of the FEM with much lower number of DOF and for some problems involving stress singularities and unbounded domains SBFEM performs better than the FEM [64, 65].

2.3 Combinations of image preprocessing and numerical modelling techniques

The main issues related to image-based analysis occur in the discretisation stage. Therefore, to obtain optimal results researchers have leaned towards combining image-based preprocessing techniques with appropriate numerical modelling techniques that are compatible with one another. Three such popular combinations are voxel-based FEM, image-based XFEM-level set method and the image-based SBFEM-quadtree/octree method.

2.3.1 Image-based analysis using voxel-based FEM

Voxel-based FEM is a popular technique in image-based analysis largely owing to its ease of implementation. The method allows elements to be directly exported from the image.

In voxel-based FEM a voxel-based mesh is first generated. Material assignment is then carried out depending on material phase found at the centroid of a particular element. However, as shown in figure 2.6b the process creates intrinsic jagged surfaces when the material interface does not coincide with element faces.

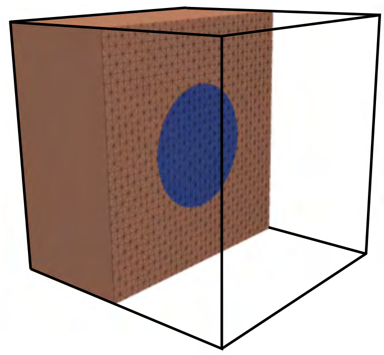

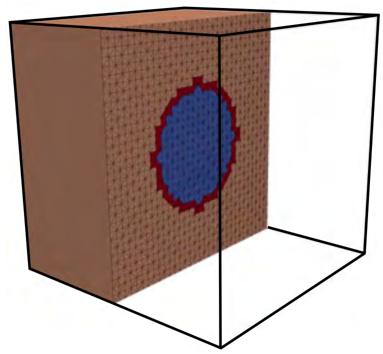

(a) Mesh containing exact material boundaries.

(b) Voxel discretization for analysis.

Figure 2.6. Standard voxel discretization for FEM and XFEM [213].

The elements containing the material interface are represented in dark red. These jagged boundaries result in high local stress oscillations [114]. This is a major disadvantage in the voxel-based finite element especially evident in problems with multiple material phases. The FEM on the other hand is found to produce best results when the underlying mesh conforms to the geometry with smooth representations of physical surfaces within the discretised volume [113]. Therefore, this method show signs of incompatibility between the mesh generation technique and the numerical modelling technique. Since the method is built on the advantage of the efficiency achieved through voxelation, additional treatments to the mesh or the finite element formulation is not usually adopted. Therefore it is not favourable for many applications, as the errors in the stress field close to the interfaces and the inaccuracy of the stress jump across the material interface are not preferred in the solution field in most practical applications.

As a solution, refined meshes can alleviate these issues to a certain degree through better representation of the interface boundaries. However, it is not an ideal solution as it then compromises the efficiency of the method by creating more elements. This drawback gives rise to the development of various smoothing techniques, reconstruction treatments, and implicit boundary definition techniques. One such method is the XFEM-level set method discussed next.

2.3.2 Image-based analysis using XFEM and level set method

The explicit approach of modelling a domain containing interfaces conforming with all internal surfaces is an operation which tends to become highly challenging for complex three dimensional geometries. Typical such situations occur in crack propagation, phase evolution and microstructure modelling. XFEM aims to avoid this issue by enriching the finite element approximation with additional functions to model interfaces or singularities independently of the background mesh. The method adopts the Partition of Unity framework [214] by multiplying the enrichment functions that possess desirable approximation by the nodal shape functions. XFEM coupled with level set functions can effectively handle these issues that create kinks in the unknown displacements and jumps in the derivatives of the unknowns within the interior of finite elements. The method enables to exploit advantages of a regular mesh as the need for an interface aligned mesh is void.

The level set method introduced by Osher and Sethian [215] in 1988 is a numerical technique for tracking moving interfaces. Here a level set curve is represented by a high-dimensional function. In essence, these functions treat interfaces as iso-zero of a ‘distance function’, therefore, the two sides of a boundary, crack path or crack tip will have function values in different signs. In image-based analysis the level set is let to evolve using the image features such as grey scale intensity, gradient magnitude or image edges until it reaches a stop. A successful implementation of such an approach can be found in [216].

As shown in figure 2.6a the XFEM-level set method utilizes the regular voxel mesh considered in voxel-based FEM. The elements marked in dark red represent interface elements which require extra enrichment within the XFEM framework. A comparison of the voxel-based FEM and the XFEM-level set formulation can be found in the following references [113, 213]. In this comparison the latter was found capable of reproducing the jump in the strain component at the material interface. This is a vital attribute to have when modelling complex material behaviour such as interface failure and de-bonding.

Comparing voxel-based FEM to XFEM-level set method, the former is widely used mainly due to the ease of implementation. However, due to its ability to properly define boundaries XFEM-level set approach exhibits higher accuracy than the voxel method. The drawback of the method is the considerable computational cost involved in the meshing process to obtain a good boundary representation with the level set method and the additional enrichments required within XFEM [97].

2.3.3 Image-based analysis using SBFEM and quadtree/octree mesh

Hierarchical data structures such as quadtree (resp. 2D) and octree (resp. 3D) are based on the principle of recursive decomposition. The recursive decomposition of a complex problem into simpler sub problems, known in the literature as the divide-and-conquer paradigm [217, 218].

2.3.3.1 Quadtree technique

The quadtree structure is a hierarchical representation of 2D data. These structures are extensively used in applications like image processing, cartographic data processing. Very-Large-Scale Integration (VLSI) embedding, graphics, computer animation, and computer-aided architecture [217].

Klinger and Dyer [219] and Tanimoto and Pavlidis [220] were the first to successfully implement a hierarchical representation structure for 2D image representation. Their technique recursively decomposed the original image area of a square shape into four identical squares at each step. The resulting data structure represents a 4-array tree, more commonly called a quadtree, (see figure 2.7).

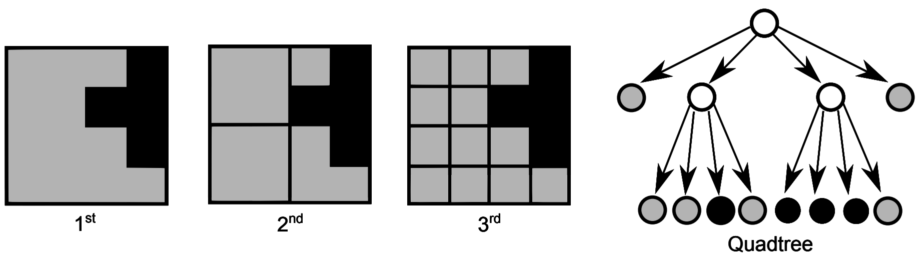

Figure 2.7. First three levels of an image decomposition with its quadtree presentation [221].

In figure 2.7 the initial black and grey image is split into 4 identical squares. Each block can contain either black or grey. Hence, each of the black region that contain either black or grey are split recursively till each leaf represents a uniform area (colour) of the image.

The many advantages of hierarchical image decomposition are discussed in [219,222]. These include rapid and efficient access to any geographical part of the image, retention of image data structure as a hierarchical description of picture patterns, elements and their relationships, and allows recursive analysis of sub-pictures. However, identified limitations of the method consist of the need for large memory for storage and the dependence on location, orientation, and relative size for representation of an object [223]. In recent times the algorithms used for quadtree decomposition have largely improved and these issues are no longer a hindrance to the implementation of the method [224–228].

2.3.3.2 Octree technique

The octree was developed independently by various researchers. In 1978 Hunter [229] mentioned it as a natural extension of the quadtree. Around the same time Reddy and Rubin [230] proposed the equal subdivision of an object in a computer model for generation and representation of solid objects. Srihari [231, 232], Moravec [233], Meagher [234], Jackins and Tanimoto [235], and perhaps others also published octree-based formulations in the early 1980's.

Octree is a 3D generalization of a quadtree by the use of 8-array trees. Similar to the quadtree method octree is a spatial decomposition method that recursively subdivides the bounding-cube of the domain of interest [236]. This cube is first subdivided into four equally sized cubes, each of which may then go through recursive partitioning into cubes that are completely full or empty [237]. Each node in an octree has eight children. Figure 2.8 shows a three level tree representing a three cube object at level 2.

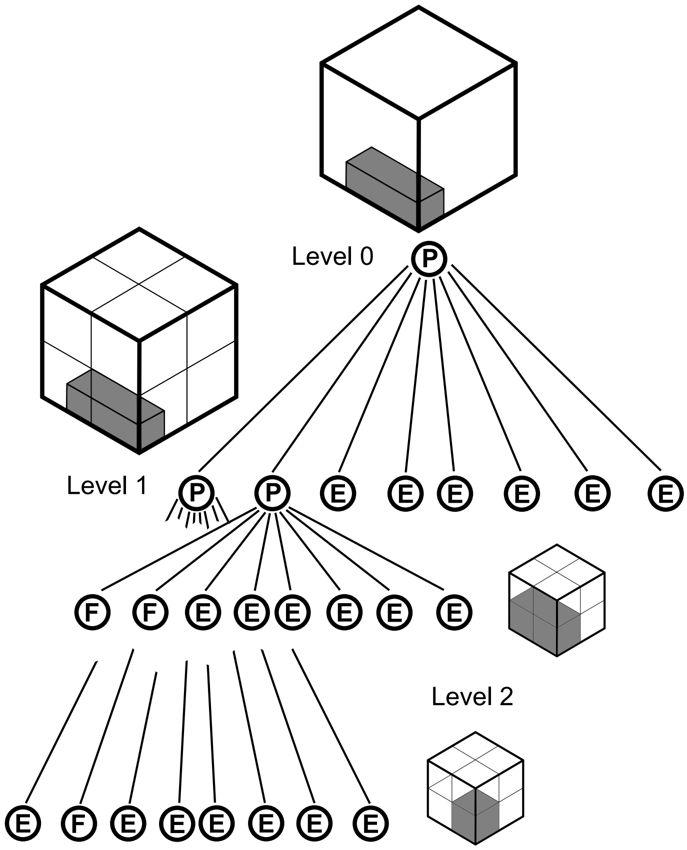

Figure 2.8. Simple object represented in octree encoding format. Three-level tree representation of an object [238]. Grey elements marked ‘F’, white elements marked ‘E’, and elements that require further subdivision marked ‘P’.

There are many advantages to this data structure. Firstly, the method uses a single primitive shape, the cube. Any arbitrary object can thus be represented to the precision of the smallest cube size available in the modelling process. The method uses a single set of manipulation and analysis algorithms for all objects. Unlike other methods, new techniques are not needed to handle complex or sophisticated shapes. The data structure enables efficient storage of 3D data. Octree methods achieve data compression by storing voxel information in a hierarchical tree structure, which is built in a top-down fashion by recursively subdividing inhomogeneous regions of the volume into eight sub-regions until each terminal node of the tree corresponds to a region of the volume in which all voxels share the same value.

Through continuous developments, current quadtree and octree meshing algorithms are able to produce a relatively smooth interface boundary as well as saving the storage for computational speed; but the issue of hanging nodes need to be addressed. Hence, for computational mechanics the two techniques are not a perfect solution on their own. However, they are powerful tools compared to other modelling tools and the aforementioned drawback can be eliminated by using an appropriate numerical modelling tool such as the SBFEM

2.3.3.3 SBFEM and quadtree/octree mesh

Hierarchical mesh generation structures become an attractive option for mesh generation as they have the ability to transition between different cell sizes efficiently [88, 97]. Incorporation of quadtree and the octree mesh generation techniques with FEM and XFEM requires various different treatment techniques to handle hanging nodes that are present between adjacent cells of different sizes. These hanging nodes if left untreated cause displacement incompatibilities at the element interfaces. The FEM treatments to the spatial discretisation or the numerical formulation include Delaunay triangulation [92], 2D polygonal elements [95], use of special shape functions [93], adaptive refinement of finite element basis functions [94], and applying constraints on hanging nodes [89].

On the contrary, treating these problematic hanging nodes within the SBFEM framework is relatively simple. The only requirement for a scaled boundary polygon is that its entire boundary is visible from the scaling centre [14] and only the edges of the polygon are discretised into line elements. The number of line (2D) or surface elements (3D) on an edge can be as many as required. The domain of the scaled boundary polygon is constructed by scaling from its scaling centre to its boundary, and the solution within the polygon is expressed semi-analytically [205, 239].

Quadtree and octree meshing method is based on decomposing the interested area recursively without changing the whole domain. The need for SBFEM in the context of hierarchical meshing is to solve the problem arising from hanging nodes as well as fitting complex boundaries in mesh generation. The technique has been validated to be a powerful approach due to its high accuracy, effectiveness and ease of using.

Hanging nodes in each quadtree/octree cell can be perfectly resolved by considering each of the relevant quadtree/octree cells as a scaled boundary system. As illustrated in figure 2.9 the cells containing hanging nodes are considered in the coordinate system of scaled boundary polygon. Since, the nature of scaled boundary discretisation allows as many numbers of line (2D) and surface (3D) elements as required, the displacement compatibility can be ensured by introducing an appropriate number of elements. As a result of this, the hanging nodes can be treated in the same manner as other nodes. The need for smoothing, reconstruction, etc. is not required. Thus, SBFEM incorporated with the quadtree/octree mesh technique is a viable solution to the difficulties associated with the technique discussed previously.

In order to demonstrate the SBFEM method adopted to handle hanging nodes, consider the octree cell shown in figure 2.9b. The hanging node present on the top right edge is added into the SBFE geometry description by method of triangulation of the polygonal faces adjoining the hanging node. A node is introduced in the face of these adjoining faces to facilitate this process. It is noteworthy, by adopting this method other surfaces in the cell with hanging nodes are not affected as only the cell boundary is discretised.

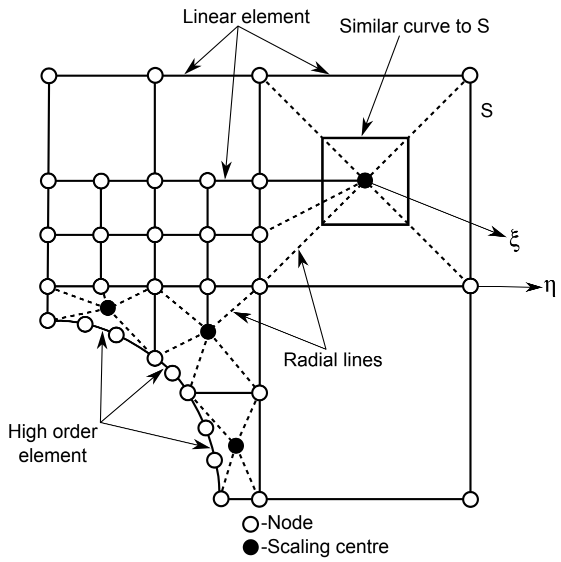

(a) Scaled boundary representation of quadtree cells [183].

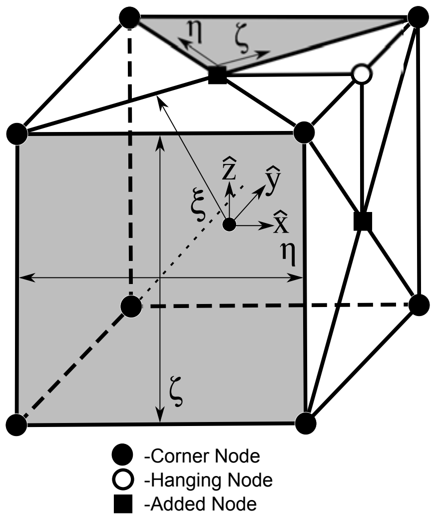

(b) Scaled boundary representation of octree cells [91].

Figure 2.9. Scaled boundary representation of elements in hierarchical meshing structures. Figure 2.9a quadtree cells and figure 2.9b octree cells.

The limitations such as the jaggy interfaces in the voxel method and the high computational costs associated with XFEM-level set method due to frequent requirements of additional treatments are also avoided through this method.

All in all, it can be easily seen that each of the aforementioned approaches has its own advantages over the others. Nevertheless, they all suffer from various limitations in certain areas in the modelling process, and more and more efficient approaches are formulated constantly. However, it is worthwhile to mention an additional treatment process is always needed in all the approaches discussed thus far [183]. The additional treatments required in the image-based SBFEM framework are minimal compared to others. This gives rise to the attention and development of SBFEM in the context of image-based analysis.

Recent applications of SBFEM within quadtree decomposition can be found in crack propagation modelling conducted by Ooi et al. [72] and linear elastic stress analysis covered by Saputra et al. [91] using an octree image-based decomposition algorithm.

2.4 Damage analysis - history and techniques

Material damage is defined as the degradation of its physical properties due to the presence or the growth of defects. There are two basic approaches to measure damage: the conventional method is to quantitatively measure from microscopic observation (Scanning Electron Microscope (SEM), microtomography, etc.), and the indirect approach is to characterise damage from degrading material physical properties induced by the damage phenomenon. When a certain material is under relatively small loads the defects may be too small to be detected by any quantitative measurements. Continuum Damage Mechanics (CDM) provides a platform to indirectly measure damage in materials. Palmgreen (1924), Miner (1945), and Robinson (1952) were the first to introduce the concept of a variable related to the progressive deterioration prior to failure [36]. However, Kachanov's 1958 publication [34] and Rabotnov's work in the year 1969 [240] based on the continuity variable ψ to model metal fracture in creep is regarded as the inception of the modern CDM. After its initial introduction in Russia, CDM moved to Europe where Leckie and Hayhurst [241] applied the damage principles to creep rupture of structures. In France the basic concepts of CDM were described theoretically in particular, through a general thermodynamic formalism [242, 243]. Since then there has been considerable developments in investigating the response of material weakened by micro-defects. This review investigates the various different types of damage analysis techniques and attempts to justify the use of these damage models in a structural level.

Failure of material arises at a diffuse face of damage such as fragmentation, multiple cracking, and micro-voidage. Many models that address these mechanisms are in the framework of deterministic continuum mechanics. In the imitation phase CDM provides a viable tool to account for dilute distribution of voids (e.g. Gurson model [244], cracks [245]). In more recent advancements damage is now formulated by scalars, second and forth-order tensors resulting from systematic studies of the decomposition of the stiffness or compliance tensors [245–248]. These techniques allow for the study of material behaviour to the ultimate state of the damage process which corresponds to the macroscopic crack initiation.

In CDM there are two types of models, phenomenological models and micro-mechanical models. Phenomenological models consider the change of macroscopically observable properties by means of the internal variable(s). Thus, the concept of "effective stress" is used in the formulation. Micro-mechanical models use the mechanical behaviour of a Representative Volume Element (RVE) with defect(s). The constitutive equations are formulated on a meso-scale by homogenization of local stresses and strains in the RVE.

Recently, phenomenological models have come to popularity. These models are able to account for the effects of the interactions between defects. Thus, damage models are used to evaluate the degradation process on the micro-scale from an initial undamaged state up to creation of a crack(s) on the meso-scale. The interaction between such defect formation was first handled through dilute situations [246, 249] to choose the form of the stiffness or compliance tensor. More recently, the kinetic laws have received more attention and the nature of damage interactions is becoming a key element in the choice between a local [36] or a non-local approach [250]. The understanding of these interactions is certainly important for the description of localised objects where spatial gradients are high (e.g. macro-crack initiation, spallation). They also provide rules to decide whether a continuum and local approach is possible.

In CDM elastic damage models or elasto-plastic constitutive laws are the usual approaches taken to describe concrete behaviour. To cite a few, the following papers [251–257] provide evidence of elastic damage models where the mechanical effect of progressive micro cracks and strain softening are represented by a set of internal state variables which intervene with the elastic behaviour at the macroscopic level. Plasticity based models are used in the following papers [258–261], among others. In these formulations softening is directly included in the expression of a plastic yield surface by means of a hardening-softening function. Between the two approaches discussed above plasticity based approaches fail to capture the degradation of the elastic stiffness [258].

Research related to concrete damage then leaned towards including plasticity and damage equations in a single constitutive relation. The paper on ductile failure approaches for metal alloys by Lemaitre [262] first introduced a formulation of damage coupled with plasticity. The formulation is based on the assumption that void nucleation is triggered by plastic strains. Following this many other authors [263–267] produced similar formulations applicable to concrete. The plasticity coupled damage formulation was derived mainly through two approaches; plastic strain based and effective stress based.

One of the challenges in formulating a plastic strain based damage function is the difficulty in realization of plastic strains. The strains vary according to the loading conditions and the development of plastic strains prior to micro cracking is difficult to understand. For example in uniaxial tension there is a lot of damage occurring with less plasticity and comparatively in uniaxial compression the reverse occurs with major plastic strains and less damage. As a remedy two methods can be adopted. One is to assume irreversible strains are due to micro-crack sliding and internal friction. This requires the prior formation of internal surfaces.

A rather more popular approach is an effective stress approach. The plastic yield function is written in the effective configuration pertaining to the stresses in the undamaged material. Many authors [251–253, 268–280] applied this approach to isotropic and anisotropic damage coupled to elastoplasticity. It has then been extended to other sources of damage such as thermal damage [281,282]. The advantage of the effective stress approach is that it provides a simple way to separate the damage and plastic processes. The plastic effects, driven by the effective stresses, can be described independently from damage ones and vice versa. Implicit/explicit numerical implementations can be easily accommodated such that the plastic part is implicit and the damage part is explicit, same as in classical continuum damage computations. As a consequence, existing robust algorithms for integrating the constitutive relations can be implemented. In calibration of the material parameters, it is much easier to handle as a consequence of the separation of damage and plasticity processes. The damage process is (elastic) strain controlled. A similar isotropic damage model was proposed by Tao [255] to describe the damage behaviour of concrete.

However, with the advancement of numerous and sometimes complicated damage models, the elasticity coupled damage model still remains a popular method owing to its simplicity in application and capability to accurately model material deterioration in many engineering applications [283]. In particular for modelling quasi-brittle material such as concrete, rock, ceramics and some fibre reinforced composites, elasticity coupled with damage remains the first choice of consideration [283].

Quasi-brittle damage processes involve deterioration processes which do no undergo large-scale plastic flow. These process however require significantly more energy than needed for the creation of the crack surface. This is due to the process of nucleation, growth and coalescence of microscopic defects in a volume which is much larger than that occupied by the final, macroscopic crack. As a result, a gradual decrease of the deformation resistance is usually observed instead of the sudden loss of strength as observed in perfectly brittle damage.

The applications of the method to quantify and evaluate concrete material damage through calculating stiffness reduction are explored in [284–286]. The Mazar's model [285, 286] is one of the widely accepted isotropic elasticity based scalar damage models. In this formulation damage is only considered to evolve under the presence of tensile strains. Therefore, material damage takes place only if the principal strain tensor contains at least one tensile strain component. It is assumed that local rupture appears according to the fracture mode I or through a combination of fracture modes I and II.

2.4.1 Local damage mechanics

The local approach to isotropic damage formulation for elastic material is described by a damage parameter D. The variable D is a monotonously increasing scalar quantity which expresses the level of material degradation [252, 253, 287–289]. The effect of the damage parameter is treated in CDM through the principle of effective stress [252, 253, 287].

With the development of damage, local softening behaviour is commonly experienced. Consequentially this results in the negative tangential stiffness. Local approaches, if adopted, lead to physically unacceptable localization of the deformation [37, 38]. In a finite element context this results in serious mesh sensitivity [40, 290, 291].

2.4.2 Regularised damage mechanics

There are numerous regularisation approaches to overcome the deficiencies of the classical local damage modelling. These include non-local modelling of the constitutive behaviour [37, 292, 293], gradient dependent material description [37, 294], micropolar (Cosserat) continuum theory [37, 294], viscous regularization [295, 296], and local manipulation of material properties depending on the element size [295]. The key objective of all regularisation techniques is to maintain the well-posedness of the boundary value problems during the softening process. This contributes to remedy the pathological problems encountered in modelling softening materials using conventional continuum mechanics [297].

The gradient dependent models as well as micropolar continuum theory require significant modifications of the typical finite element formulation for elastic analysis. The use of viscous regularisation is inappropriate for solids typically found in solid mechanics. Local alterations to material properties is a debatable concept from a physical point of view although such methods enable global responses to be reasonably predicted. Local strain and damage distributions in such techniques have also been found unrealistic.

The essential idea behind the non-local approach is the substitution of the generally accepted principle of local action, stating that, in the absence of temperature effects, the stress in a material point is fully determined by the deformation and the deformation history at that point by its non-local counterpart. Where in the non-local counterpart, the stress in a material point is now assumed to be dependent on the strain and the strain history in a limited finite area enclosing the particular material point where the stress has to be evaluated.

There are several types of non-local averaging methods [291,298]. However, strategies in line with the microstructural material behaviour are quite prominent. The general idea contributing to a microstructural level formulation is that many materials possess a characteristic volume where the damage distribution is almost uniform [299]. The grid method [299] and the continuous average strain method are two averaging techniques based on a microstructural level formulation. The former, employs a regular cell grid overlay over an element mesh. The size of a grid cell is equal to the characteristic dimension. It is assumed at each cell of the grid the non-local equivalent strain and consequently the non-local damage is considered a constant. In the latter the non-local equivalent strain is calculated through a weighted average of equivalent strains in all material points within a certain radius [292, 293, 300]. In principal this method leads to a continuous damage field.

2.4.3 Selection of non-local model parameters

Concrete, made out of a slurry mix of aggregate, cement and water is one of the most used building materials in civil engineering. For computation purposes, concrete can be assumed to comprise of 3 distinct material phases: aggregate; mortar (made up of sand and cement); and an inter-facial transition zone (ITZ) between the aggregates and the motor. In computation modelling of a quasi-brittle material such as concrete it is important to carefully identify and determine model parameters for the development of constitutive models. This aspect is particularly important for non-local damage models in which model parameters control the local behaviour of the model and also the spatial interaction of material points.

A significant characteristic in concrete micro-structure is that it contains a large number of micro-cracks even prior to application of loads. This is due to various reasons such as shrinkage, segregation, and thermal expansion within the cementitious constituents. Under application of loads the link between the aggregate and cement paste will further undergo micro-cracking. These micro and macro-cracks affect the stress-strain behaviour of the material. In a phenomenological continuum approach these effects are smeared out (i.e averaged) throughout the body where the material is considered as a mechanical continuum with degraded/damaged properties. This concept is adopted in damage regularisation techniques discussed in section 2.4.2.

Damage regularization is an effective technique to overcome softening-related problems in the constitutive modelling and numerical analysis [250, 296, 301, 302]. The methods however deviate from the conventional continuum mechanics by introducing a spatial term in the constitutive relations. This spatial parameter is commonly known as the length parameter related to the characteristic length (or the length scale) of the material. To avoid any confusion between terminologies, the length parameter will be addressed as the characteristic length in this work.

The characteristic length of the non-local continuum is related to the imaginary width w_t of the fracture process zone (see figure 2.10). However, w_t is different from the actual width z_t, of the micro-cracked zone in continuum models.

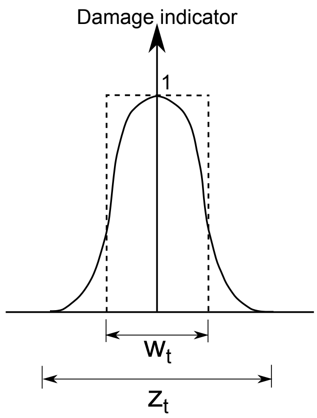

Figure 2.10. Damage profile in a uniaxial test using non-local model, and definition of w_t, and z_t [303].

To obtain model parameters in the presence of a spatial parameter requires the solution of boundary value problems [304]. This is a deviation from the local approach, where a model can be calibrated directly from experimental data. As a result determining non-local model parameters is a challenge that had warranted extensive research [303–308].

To date there are two main techniques adopted for obtaining model parameters: numerical inverse analysis of experimental results; and methods exploiting the correlations between the cohesive crack model and crack band model. In the inverse methods, calibration of model parameters is based on numerical inverse analysis. The common techniques adopted include optimization algorithms [304, 306, 307], and experimental data from real structural tests and size effect laws [304, 306]. In inverse methods, the characteristic length and the local constitutive model are treated equally as general parameters of the non-local constitutive equations in a boundary value problem. Model parameters obtained through drawing similarities between the cohesive crack model and crack band model [309, 310] are commonly found in gradient based damage formulations [308, 311–315].

2.5 Methods in adaptive analysis

In numerical modelling techniques the accuracy of the solutions is determined by the shape of the elements and the spacing of the nodal locations. The traditional method to determine the accuracy of the finite element solution is to analyse the problem at least twice with two or more different uniform or nearly uniform meshes. Determining the accuracy by comparing solutions is not optimal use of computing resources as analysis conducted with uniform meshes are computationally costly. Therefore, attempts to estimate the error without excessively increasing the numerical effort has received considerable attention in the research community [316–342]. The development of the error estimator produced an insight to the accuracy of the solution and information on the distribution of the error in the existing mesh. This gave rise to adaptive mesh refinement as the error distribution can be utilized as an indicator to refine the mesh.

Adaptive mesh refinement techniques were first developed in the FEM framework in the early 1980s [41, 319, 320, 325, 326, 331, 337, 341–419]. The method was termed "adaptive" as it is an iterative process through which a specific error is adaptively estimated in each iteration. Currently, many commercial software packages such as Abaqus FEA [23], ANSYS [24], and LS-DYNA [27] contain adaptive analysis abilities.

To conduct an adaptive process there are four distinct varieties of refinement techniques that are typically employed. These techniques include r-refinement: where position of nodes are modified [363,364,370,374,397,401–404,409,420,421], h-refinement: where size of the elements are reduced [353,361,422–427], p-refinement: where the order of interpolation functions are increased [317,347,384,385,391–394,405–408,428], and hp-refinement: which is a combination of both h-refinement and p-refinement [338,339, 341,342,346,359,360,362,366–368,373,375,377–383,389,411,413–415,418,419,429–431].

The r-refinement/relocation is also termed “grid optimization method”. In this method the nodes are redistributed while keeping the number of elements and the polynomial order of the interpolation functions unchanged. Therefore, for a given number of elements and the fixed interpolation functions the discretization error is reduced by moving the nodal positions to optimal locations. The method leads to an optimal mesh but since the number of nodes are limited the error cannot be reduced too much. Therefore, r-refinements is usually considered with either p-refinement or h-refinement.

The h-refinement is arguably the most widely used adaptive method due to its simplicity. The desired refinement outcome can be achieved by either uniform refinement or adaptive refinement. To improve the efficiency of the method h-refinement can be coupled with r-refinement [338,339,341,342,362,377–383,389,413,415,418,419,429–431].

The p-refinement on the other hand focuses on increasing the order of interpolation functions while keeping the mesh unchanged. With the use of higher order elements a better geometrical description of the domain is obtained. The use of higher order elements are preferred in regions where lower order elements can produce poor aspect ratios. Higher order elements are usually more accurate than their lower order elements but increasing the polynomial order indiscriminately will not always provide point-wise convergence to the exact solution [432]. One disadvantage of the process is that the refinement convergence is highly dependent on the initially selected element mesh. However, by adopting a hp-refinement method this drawback can be resolved.

2.6 Non-linear mathematical solvers

Non-linear solutions, specifically problems that require tracing the complete load deflection response requires tracing of the equilibrium path and proper treatment of limit and bifurcation points. In computational mechanics the Newton-Raphson (NR), the modified Newton-Raphson (m-NR), the quasi-Newton procedure [433–437] and the secant-Newton methods [435, 438–440] are a few of the numerous solvers commonly employed for the task. However, the modified Newton-Raphson (m-NR) is one of the most commonly used non-linear solvers in structural analysis due to the inherent simplicity of the solution method [338].

It is however prudent to first investigate the shortcomings of the NR method and the m-NR method and assess the reasons to which the m-NR method still remains in contention with the alternative methods such as the secant-Newton methods and the quasi-Newton procedure. The first reason supporting its popularity is its improved convergence rate over the NR method. Secondly the technique is adoptable with numerous special techniques that are used to trace the descending branch of the load-displacement path. The incorporation of techniques such as the arc-length method is rather simple and straightforward. Furthermore, these adopted special treatments bring about superior qualities than to those found in ordinary techniques to overcome limit points in the equilibrium path. Therefore, the m-NR method triumphs over other methods due to its aforementioned simplicity compared to other complex methods such as the quasi-Newton procedure and also due to uncompromised accuracy achieved in tracing the equilibrium path.

As mentioned earlier, it is common practice to pair the m-NR and NR methods with acceleration and damping algorithms to improve convergence efficiency. Furthermore, the arc-length method is adopted to trace the softening branch of the load-displacement path. Line search based damping methods are common in mathematical programming [435, 441–445]. These enable for a simple and an effective method for increasing the robustness of the iterative technique [440, 446]. In mechanics damping of the iterative process is initiated when there is an insufficient decrease [446] in the potential energy or the norm of the out-of-balance force vector.

Non-linear solutions, specifically problems that require tracing the complete load deflection response requires tracing of the equilibrium path and proper treatment of limit and bifurcation points. Ordinary techniques may lead to instability near a limit point and also have problems in case of snap through and snap-back behaviour. However, the arc-length technique is able to track the complete load-displacement response even overcoming snap-back and snap-through behaviour.

Load controlled NR method was the earliest method to achieve the solution pattern on the equilibrium but the method failed near the limit point. This gave rise to displacement control techniques [54]. However theses techniques still fail to capture snap-through or snap-back behaviour and thus lead to errors. Various methods can be found in the literature to overcome these issues. Examples of such methods include: switching between load and displacement controls [447]; using the artificial springs [448]; and abandoning the equilibrium iterations in the close vicinity of limit point [449, 450]. However a generalised technique was first developed by Riks [79, 451] and Wempner [452] which was termed the arc-length method for structural analysis.

In the arc-length method, the load-factor at each iteration is modified to allow the solution to converge through some specified path. In contrast, the load or the displacement control method keep the load step or the displacement step constant during increments, respectively. There are two main approaches followed in this technique, fixed and varying arc-length methods. In any increment, the arc-length is kept fixed in the former and whereas the latter evaluates a new arc-length at the beginning of each load step.

Although the initial arc-length formulation gained much acceptance in the field of finite element analysis one of the major drawbacks the method had was that it destroyed the banded nature of the stiffness matrix [80]. Crisfield in 1981 proposed the cylindrical arc-length method [80] where the increment length during load increments was fixed. However, this method was found to be inconsistent in converging to a solution in problems having material non-linearity. Therefore, in 1983 the Crisfield [82] recommend arc-length technique in displacement control with simple line searches to solve problems with material non-linearity with significant strain softening.

Applications of arc-length method in combination with Newton-Raphson method has been successfully applied by researchers [82, 453, 454] for the analysis of reinforced concrete structures. Developments and modifications to the method continues to date. Some of these changes include: non-dimensionalised vectors that define the arc-length constraint equation by introducing scaling matrices [455]; use of the updated hyper-plane technique to evaluate the arc-length [456]; modification to the method of selection of proper root of the non-linear constraint equation by selection of root that is closest to constraint linear solution [457]; Fan's [458] proposal to use three different ways to compute the arc-length (i.e. zero incremental displacement norm, zero residual force norm and zero incremental work norm); a method to compute the initial load increment based on the technique of sign of determinant of current stiffness matrix [459]; inclusion of the displacement of nodes associated with failure zone into the constraint equation; and the modification to the existing arc-length-based on the concept of accumulated arc-length [460].

2.7 Conclusions

The chapter began with a detailed review on preprocessing techniques in section 2.1. Here two main categories of preprocessing namely, CAD-based and image-based methods were discussed. Next the chapter progressed to numerical modelling techniques in section 2.2, where salient features of the FEM, the BEM, the XFEM and the SBFEM were discussed at length. With this knowledge on both preprocessing and numerical modelling techniques the reader was then introduced to commonly used combinations of these techniques, in section 2.3. In line with this work the review focused on image based techniques. Special attention was given to the SBFEM quadtree/octree method due to its unique compatibility. Next numerous damage analysis techniques were reviewed in section 2.4. With the intent on improving the efficiency and the accuracy of the solution field, adaptive analysis procedures were elaborated in section 2.5. Finally, non-linear mathematical solvers were evaluated on their merit in section 2.6.

Mesh automation through classical triangular (2D) or tetrahedral (3D) elements is generally easier compared to quadrilateral (2D) or hexahedral (3D) elements due to their ability to mesh complex boundaries usually encountered in many practical engineering applications. However, standard finite element analysis prefers quadrilateral (2D) or hexahedral (3D) elements as these elements interpolate displacements to a higher degree. Therefore, the discussion on pre-processing techniques focused on methods in both CAD-based and image-based techniques that can be utilised in efficient meshing algorithms without any compromise on the accuracy of the result.

In both CAD-based and image-based mesh generation techniques, meshes non-confirming to the boundary is an appealing option as this then eliminates an additional step for detecting geometrical boundaries. The method also enables to preserve the original mesh structure. Boundary definition for the problem domain can then be incorporated into the solution process through techniques such as XFEM, FCM or defined implicitly through a level set method.

In the presence of numerous meshing algorithms, quadrilateral and hexahedral mesh construction to date is not an efficient process and struggles in achieving full automation. The main issues substantiating this find is the requirement of intermediate steps for achieving final desired mesh, generation of distorted elements causing inaccuracies during the element mapping process, and the requirement of local re-meshing to correct and eradicate distorted elements. Hierarchical mesh generation techniques i.e the quadtree and the octree technique are a suitable alternative to achieve both mesh automation and boundary conformance.

It is a vital to follow the mesh generation process with a compatible numerical modelling technique. Out of the numerous techniques, a selected few were discussed in this chapter. These included the BEM, the FEM, the X-FEM and the SBFEM. The FEM is the most well known method in CAE. Since the introduction of the FEM the numerical method has become a widely used technique to obtain approximate solutions for boundary value problems. This method is useful in yielding an approximate solution for problems with complicated geometries, loading and material properties. The major limitation associated with FEM pertaining to this work is its inability to handle hanging nodes without additional treatments. This drawback creates difficulty to obtain smooth transitions between different meshes. The BEM is a rigorous tool for modelling unbounded media. The method adopts spatial discretisation of the boundary. The disadvantages of the method are: the requirement of a fundamental solution which is usually complicated; exhibits singularities; the resulting equations are fully populated and non-symmetric; and the unsuitability for inhomogeneous and anisotropic material. The XFEM incorporates displacement based finite element approximation with enrichment functions using the framework of partition of unity. The striking two advantages of the method are: the finite element framework (sparsity and symmetry of the stiffness matrix) is retained; and a single-field variational principle is used. The method is specially developed to provide an accurate approximation with non smooth, discontinuities or domains with different material phases. The SBFEM is a method applicable for both bounded and unbounded media which combines advantages of both FEM and BEM. The meshing procedure is simplified as only the boundary is discretised. The method enables the reduction of the spatial dimensions by discretising the boundary alone, which in turn reduces the data preparation and computational effort. The non requirement of a fundamental solution and the ability to exactly satisfy radiation conditions at infinity when modelling unbounded media expands the scope of the applications of the method. The method also does not require discretisation of free and fixed boundaries and interfaces between different materials. Last but not least, it is also possible to obtain straightforward calculations of stress concentrations and intensity factors.

As seen in sections 2.1 and 2.2 preprocessing techniques and numerical modelling techniques have their own inherent advantages and disadvantages. Therefore, to negate the limitations in one method the most compatible combination of preprocessing and numerical modelling techniques need to be united. Three such combinations were examined in this chapter, namely, the voxel-based FEM, the XFEM-level set method and the SBFEM-quadtree/octree mesh technique. The voxel-based FEM suffered from the issues created in the discretisation stage. These issues involve unaligned interfaces, intrinsic jagged surfaces which give rise to considerable local stress oscillations. The shortcomings in voxel-FEM approach of stepped interface boundaries were eliminated in the XFEM-level set method. The local enrichment done through XFEM helps provide an accurate approximation when unsmoothed domains, discontinuities or domains with different material phases arise in a model. Unfortunately, this method often leads to a considerable computational cost. The SBFEM-quadtree/octree technique in essence is a perfect amalgamation of the preprocessing technique and numerical modelling technique.

As noted earlier, hierarchical mesh generation structures are regarded as efficient tools in mesh generation. The classical FEM however is not compatible with both quadtree and octree meshes without an additional treatment to hanging nodes. Such treatments involve: incorporation of transition elements with special shape functions; triangulation (2D) and tetrahedralisation (3D) of the mesh; and the introduction of polyhedral elements. In the finite element framework the introduction of polyhedral elements has created a much needed flexibility in the meshing process as these elements can be cut, merged or split and still result in a polygonal (2D)/polyhedral (3D) shape. Polygonal/polyhedral elements reduce the requirement for re-meshing if the mesh consists of a shape which can be modelled with an element available in the element library. Furthermore, based on Voronoi diagram polyhedral elements can be merged with the neighbouring elements or cut into smaller polyhedrons to resolve the issue of mesh distortion. However, the polygonal and polyhedral formulation in FEM still warrant high number of integration points for an accurate results and the applicability to transient problems is not recommended.

SBFEM has the capabilities to perform efficiently with the incorporation of a hierarchical mesh generation structure to produce accurate solutions with minimum effort. The issue of hanging nodes in quadtree and octree cells is overcome in SBFEM as each cell can be modelled as a polygonal or polyhedral element. This introduction enables automatic meshing algorithm to be developed with ease and offers greater meshing flexibility as the element shapes are not limited to triangles, quadrilaterals, tetrahedrons or tetrahedrals commonly employed in the FEM. Levels sets can be easily incorporated to trim the boundaries to produce boundary conforming meshes. The resulting meshes still conform to the original polygonal/polyhedral formulation and therefore no further re-meshing is warranted. The polygonal formulation in 2D can be adopted as long as any point on the polygon boundary is directly visible from the scaling centre. This requirement is satisfied by any convex polygon and some concave polygons. The polygon elements generated from a Delaunay triangulation automatically satisfy this requirement. In 3D, any arbitrary volume can be modelled based only on surface shape functions on the boundary. In this formulation there is no limitation on the number of surfaces on a polyhedron boundary nor the requirement of a convex polyhedral. Similar to the 2D formulation the only requirement is that all the boundary surfaces are visible from a scaling centre within the polyhedron. This element formulation can therefore be seamlessly integrated with a quadtree or an octree mesh.

To date, CDM has produced theories that lead to powerful methods for the numerical analysis of the behaviour of softening materials. However, precautions need to be taken to limit the localization of the deformation and the consequent damage within material. This issue of localisation and mesh objectivity of finite element solutions is directly related to the correct representation of size effects. The issue of damage localisation can be resolved with the application of non-local approaches. It is also important to adopt techniques that do not require extensive alterations to the finite element framework for convenient integration to existing analysis software. The grid method and the weighted average strain method are two such techniques that can easily be implemented into a classical finite element computer code. The non-local averaging can also alleviate the computational burden by reducing the requirement for mesh refinement in jagged boundaries. Similar observation and conclusion to that of [98, 108, 115] on stress smoothing on jagged boundaries can be extended to strain smoothing in the CDM approach.

In the finite element framework for a linear elastic computation preprocessing takes up approximately 45% of the total time required to complete a conventional analysis, the solution takes 20%, and post-processing 35% [41]. In an adaptive framework the ability to ascertain the distribution of the error in the problem domain enables the user to refine the mesh at locations that require improvements and coarsen the mesh where accuracy of the solution is above expectation. Adaptivity can therefore contribute in reducing pre-processing, processing and post-processing times through reducing the number of DOFs required to obtain solutions with similar or better accuracy compared to a solution obtained through a uniform grid consisting of an equal number of DOFs. Therefore, the benefits of adopting an adaptive analysis framework is twofold, it can contribute heavily to improve the accuracy of the solution and also improve the efficiency of the simulation.

Mathematical solvers especially in the context of softening material must be able to completely follow the equilibrium path. This involves identification and computation of singular points such as limit or bifurcation points, whose secondary branches in the equilibrium path must be examined and followed. Several such techniques to achieve the solution on the equilibrium path were discussed in this chapter. The m-NR is still one of the most commonly used non-linear solvers due to the inherent simplicity of the solution method. The few shortcomings of the m-NR is overcome by dampened and accelerated techniques coupled with the arc-length formulation.

The applications of the SBFEM are numerous. However, damage analysis to date has not been explored through this numerical technique. The SBFEM has performed with comparable accuracy to FEM, but with much lower number of DOFs, and has out performed the conventional FEM when solving unbounded domain problems and problems involving stress singularities and discontinuities. Combination of the SBFEM with the quadtree or the octree mesh generation techniques can overcome the limitations such as the jaggy interfaces in voxel method and the computational costs inheriting XFEM-level set method due to the frequent requirements of additional treatments. The method also has the additional advantage of less storage requirements, high computational speed, ability to be automated, and simplicity in application. Furthermore, through partnering with the SBFEM the issue of hanging nodes is addressed.

This literature review substantially confirms the need for a robust and efficient damage modelling technique. The review also sheds light on the aspired benefits of the use of the SBFEM-quadtree/octree technique for non-local damage analysis. The affect of the softening nature of damage degraded materials can be traced effectively through an arc-length-based accelerated/dampened m-NR method with line search. Adaptive techniques can further improve the solution space.

Chapter 3

Two Dimensional Damage Analysis by the Scaled Boundary Finite Element Method

3.1 Introduction

In this Chapter, the use of the Scaled Boundary Finite Element Method (SBFEM) for analysing progressive damage in structures is introduced. The mathematical derivations of the SBFEM in damage analysis is presented in two dimensional (2D) space with the introduction to the simplified scaling centre damage calculation technique. The integral-type non-local model combined with the isotropic damage model is extended to eliminate the mesh sensitivity caused by the strain localization. Comparative studies of the local and non-local formulations are presented. SBFEM polygonal formulation is implemented owing to its flexibility to mesh arbitrary geometries without any additional effort. Furthermore, the computational effort involved in storing and accessing the strain and stress fields, and damage variables can be considerably reduced in the framework of the SBFEM. Several numerical benchmarks are simulated to demonstrate the effectiveness and robustness of the proposed approach. These examples compare the introduced Scaling Centre (SC) formulation with the Full Gauss Point (FGP) SBFEM formulation and also with an in house finite element formulation. These numerical examples also compare the outputs of the SC formulation with experimental test results and published numerical test results. The numerical examples further investigate the behaviour between local and non-local approaches in damage analysis.

Concrete is one of the most widely used building materials in civil engineering due to its high strength and durability relative to its cost. From a micro-level viewpoint, concrete contains a large number of micro-cracks and micro-voids even prior to application of loads. During the loading process, coalescence of these micro-cracks and micro-voids leads to a degradation of material stiffness observed on the macro scale, and thus the stress strain behaviour of concrete possesses a characteristic of softening [461–464]. In order to describe such a non-linear phenomenon, non-linear fracture mechanics (NFM) and continuum damage mechanics (CDM) were developed. Based on NFM and CDM, studies [465–468] have been carried out to evolve variants of these two methods respectively and a mixed version has also been proposed [469].

Traditional fracture approaches are capable of modelling problems with existing cracks or notches, and the initialization and propagation of cracks are determined by energy or stress-based criterion [465]. In order to accurately describe the cracking behaviour of concrete, the fracture process zone (FPZ) must be properly modelled to consider the gradual energy dissipation during cracking by using smeared crack model [470], or discrete crack model [465,471]. Owing to the strong stress singularity around the crack tip, the finite element size in FPZ should be sufficiently small to obtain relatively accurate stress intensity factors (SIFs). Besides, a re-meshing procedure is required to capture the tortuous crack path along with crack propagation [472]. These two factors may lead to a time-consuming and complicated numerical implementation. As a remedy, higher order and singular finite elements [473] are utilised for the estimation of SIFs. Alternatively, extended finite element method (XFEM) was developed by Belytschko and Moës [13, 164] to improve the finite element method (FEM) concerning problems with strong discontinuities such as cracks and material interfaces, so that re-meshing is avoided.

CDM was introduced by Kachanov [34] in the context of creep rupture, which is a constitutive theory that describes the progressive degradation of material integrity due to the propagation and coalescence of micro-defects. Damage models use internal variables to characterize the density and orientation of micro-defects. For instance the isotropic damage model takes account of the damaged stiffness tensor as a scalar multiple of the initial elastic stiffness tensor. Theoretically there are two scalar parameters to represent two independent elastic constants of standard isotropic elasticity; i.e. the Young's modulus and Poisson's ratio. Assuming that Poisson's ratio is a constant during the damage process, a simple version of the isotropic damage model with only one parameter can be obtained. More sophisticated versions of damage model can be found in [474–476], which represent damage by high-order tensors resulting from systematic studies of the decomposition of the compliance tensors or based on the relationship between damage tensors and crack density distributions.

It is found that excessive damage leads to a local softening behaviour as the tangential stiffness becomes negative. Based on the assumption that stress at a certain point only depends on the state variables at that point, a local damage model may lead to a non-objective strain localization, and thus pathological sensitivity to mesh [477, 478] arises from an ill-posed boundary problem. To overcome the deficiencies of the local damage model, a great variety of non-local models, including integral-type non-local models [250, 477, 479] and gradient-type non-local models [480–482] have been well developed during the last decades. Integral-type non-local models are based on the assumption that the constitutive law at a point of continuum involves weighted averages of a state variable in a certain range of the point by introducing an additional material parameter named the Characteristic Length [483]. While gradient-type non-local models take the field in the immediate vicinity of the point into account, by enriching the local constitutive relations with the first or higher gradients of some state variables. Detailed discussions on these two approaches can be found in [484, 485]. Since non-local damage models impose a non-zero limit on the minimal width of the DPZ and prevent the strain localization into a band of zero width, it is shown to be mesh-independent and thus much more reliable and robust than local damage models. Taking the strain rate into account, non-local damage models have been successfully applied to simulate dynamic damage process [467] and dynamic crack branching [486].

Although a continuous distribution of strain can be achieved by non-local damage models, it is still necessary to use sufficiently fine mesh in the DPZ [467, 477, 479]. Considering that fine mesh is only required in narrow bands and relatively coarse mesh can be used in the rest, finite element meshes are adopted in this chapter with refined meshes around the vicinity of the assumed DPZ. However, as the damage patterns are usually unknown and a uniform fine mesh is an impractical solution imparting excessive computational burden, adaptive procedures becomes an attractive technique to reduce the number of DOFs during the damage evolution. A general algorithm of non-linear adaptive approach includes error estimation, re-meshing and mesh-mapping. A similar approach to [487] has been followed in chapter 6 to produce the Automatic Image-Based Adaptive Damage Analysis (AIBADA) framework.

The scaled boundary finite element method (SBFEM) is a semi-analytical method developed by Wolf and Song in 1990s [199] for the solution of wave propagation problems in unbounded domain. The SBFEM combines some of the advantages of both the FEM and the boundary element method (BEM). The method enables the reduction of the spatial dimensions by discretising only the boundary, which in turn reduces the data preparation and computational effort. Compared to the BEM, there is no requirement for a fundamental solution. The ability to exactly satisfy radiation conditions at infinity makes the method particularly suitable for modelling unbounded media [63]. The method also does not require discretization of free and fixed boundaries and interfaces between different materials [488]. Owing to its capability of obtaining stress concentrations and intensity factors straightforwardly, the SBFEM is also an attractive method to model crack propagation [205, 208, 489, 490]. Furthermore, this method has also been extended to dealing with fluid-structure interaction (FSI) [491], soil-structure interaction (SSI) [492, 493], electro-statics [491] and heat transfer problems [494]. However, neither local nor non-local damage modelling by using SBFEM has been explored prior to this work.

This work aims at developing a SBFEM-based approach to model the non-local damage process. The integral-type non-local model combined with the isotropic damage model is employed and extended to the scaled boundary formulation. There are several advantages of modelling non-local damage in the framework of the SBFEM owing to its salient characteristics:

1. In the SBFEM, a domain is discretised by a set of subdomains (like super-elements in the FEM) with various sizes and different number of edges. For simplicity, the damage degree can be assumed to be uniformly distributed in one subdomain. Correspondingly, only the strain at the scaling centre of the subdomain is used to calculate the equivalent strain and subsequently the damage variable.

2. Since the strain modes for each subdomain is only depended on the geometry of the subdomain, it can be calculated beforehand and utilized at each load step to compute the strain at an arbitrary point in the domain.

3. The weight function can also be calculated beforehand using the distances between subdomains and subdomain areas.

These advantages above make the SBFEM an attractive approach to model the non-local damage process.

The layout of this chapter is as follows. In section 3.2, the isotropic damage model and evolution laws of damage are introduced. The integral-type non-local damage model is also described in the same section. In section 3.3 the governing equations of linear elasticity are described. The concept and equations of the 2D SBFEM are explained in section 3.4. The implicit damage formulation is documented in section 3.5. Section 3.6 introduces the m-NR method incorporated with the arc-length technique. In section

3.7, several benchmarks are modelled to verify the effectiveness and robustness of the proposed approach. Conclusions and remarks are stated in section 3.8.

3.2 Damage model for concrete

3.2.1 Isotropic damage model

Isotropic damage models assume that the stiffness degradation is isotropic, i.e., stiffness modulus corresponding to different directions decrease proportionally. Generally the isotropic damage model should deal with two damage variables, including the Young's modulus and Poisson's ratio. A further simplification can be achieved with the assumption that the Poisson's ratio remains constant during the damage process [34], which is adopted in this study.

3.2.2 Constitutive law

The isotropic damage model with a single scalar variable can be described by the stress-strain law

$$\sigma = (1-\omega)\mathbf{D}\varepsilon, \tag{3.1}$$

in which σ is the stress tensor, ε is the strain tensor, $\mathbf{D}$ is the elasticity matrix, and ω is the damage variable which ranges from 0 to 1 at complete damage and is a function of the damage internal variable κ such that

$$\omega = g(\kappa). \tag{3.2}$$

As shown in figure 3.1 when the deformation is increased after the material undergoes unloading, damage develops approximately at the point where the unloading initiated for that particular cycle. In relation to the damage model in equation (3.1) this suggests that with increasing damage the elastic domain in strain space must grow such that the strain state remains on the loading surface.

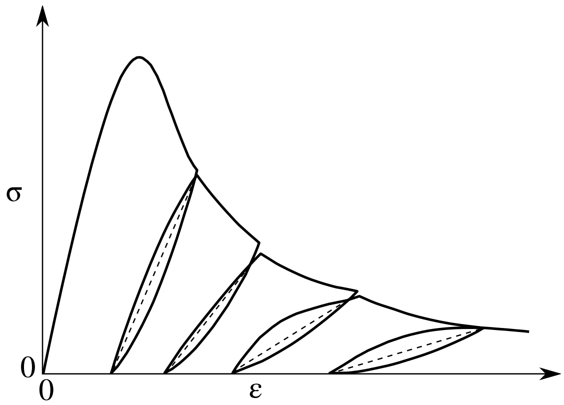

Figure 3.1. The formulation of Kuhn-Tucker relation based on behaviour of stress-strain material response of a concrete specimen in tension.

Mathematically, the loading-unloading condition can be formulated by the set of Kuhn-Tucker relations [495]

$$\begin{aligned} f(\widetilde{\varepsilon},\kappa) &\leq 0 \\ \dot{\kappa} &\geq 0 \ , \\ f(\widetilde{\varepsilon},\kappa)\dot{\kappa} &= 0 \end{aligned} \tag{3.3}$$

in which $f(\widetilde{\varepsilon},\kappa) = \widetilde{\varepsilon}(\varepsilon) - \kappa$ is the damage loading function, $\widetilde{\varepsilon}$ is the equivalent strain, and κ is an internal variable that corresponds to the maximum level of equivalent strain ever reached in the previous history of the material. κ can be locally attained during the loading history. To define the initial elastic domain of the material κ should be supplemented by an initial value $\kappa = \kappa_0$.

3.2.3 Evolution of damage

Damage evolution can be written as

$$\dot{\omega} = \begin{cases} g\,(\omega,\widetilde{\varepsilon})\,\dot{\widetilde{\varepsilon}} & \text{if } f = 0 \text{ and } \dot{f} = 0 \text{ and } \omega < 1, \\ 0 & \text{else,} \end{cases} \tag{3.4}$$

where $\omega < 1$ restricts damage growth beyond the critical value $\omega = 1$. The one to one relationship $\omega = g(\kappa)$ between ω and κ given in equation (3.2) is possible since $\dot{\omega} > 0$ if and only if $f = 0$ and $\dot{\tilde{\varepsilon}} > 0$, and thus $\dot{\kappa} > 0$, and since both ω and κ are semi-monotonic. This relationship can also be obtained by integrating equation (3.4) and through use of the consistency relation $\dot{f} = 0$. However, in quasi-brittle damage models it is specified directly. In this case the corresponding evolution function $g(\omega, \tilde{\varepsilon})$ can be obtained by differentiation with respect to κ.

In this study it is assumed that the damage is governed by the equivalent strain. There are two main variants of the damage function based on the equivalent strain, i.e. linear softening model and exponential softening model [478]. The damage evolution law of the linear softening model is often adopted for theoretical developments where the evolution of damage (refer figure 3.2a) is defined as

$$\omega = \begin{cases} 0 & \text{if } \kappa < \varepsilon_0, \\ \frac{\varepsilon_f}{\kappa}\left(\frac{\kappa - \varepsilon_0}{\varepsilon_f - \varepsilon_0}\right) & \text{if } \kappa < \varepsilon_f, \\ 1 & \text{if } \kappa \geq \varepsilon_f, \end{cases} \tag{3.5}$$

in which $\varepsilon_0 = f_t/\mathrm{E}$ is the limit elastic strain under uniaxial tension, f_t is the tensile strength, E is the Young's modulus, and ε_f is a parameter affecting the ductility of the response and related to the fracture energy. When $\varepsilon = \varepsilon_f$ complete loss of stiffness is experienced, see figure 3.2b.

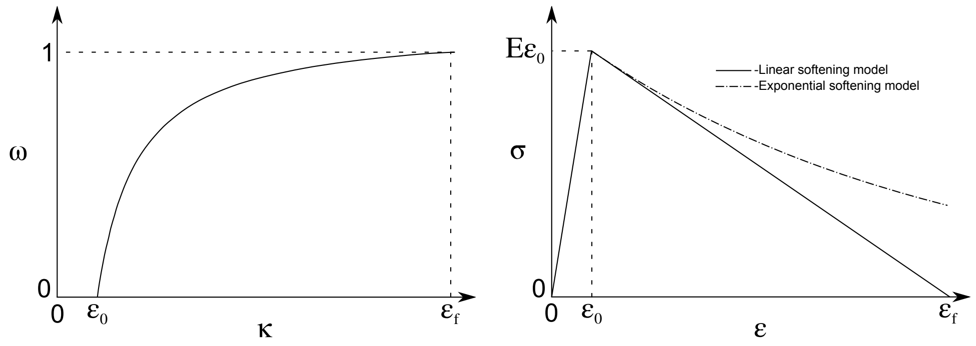

(a) Damage growth with respect to κ

(b) Stress vs strain behaviour in uniaxial tension. Linear (refer equation (3.5)) softening behaviour compared against exponential (refer equation (3.6)) softening law.

Figure 3.2. (a) Damage growth and (b) the corresponding uniaxial stress-strain response for linear (refer equation (3.5)) softening behaviour.

The area under the uniaxial stress-strain curve, $g_f = f_t(\varepsilon_f - \varepsilon_0/2)$, has the meaning of energy dissipated per unit volume of totally damaged material under uniaxial tension.

Softening in real materials is mostly non-linear. The non-linear behaviour is exemplified by a relatively steep initial stress drop followed by a more moderate decrease. Therefore, in most practical situations softening behaviour is represented by exponential softening laws.

The exponential softening model in figure 3.3 is defined as

$$\omega = \begin{cases} 0 & \text{if } \kappa \leq \varepsilon_0, \\ 1 - \frac{\varepsilon_0}{\kappa}\exp\left(\frac{-(\kappa-\varepsilon_0)}{\varepsilon_f-\varepsilon_0}\right) & \text{if } \kappa > \varepsilon_0. \end{cases} \tag{3.6}$$

It can be found that the tangent of the softening branch at the peak stress of the exponential model is coincident with the softening part of the linear model (see figure 3.2b).

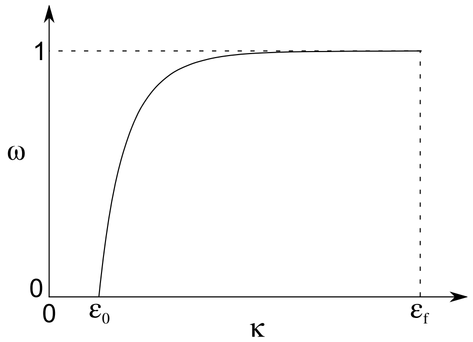

(a) Damage growth with respect to κ.

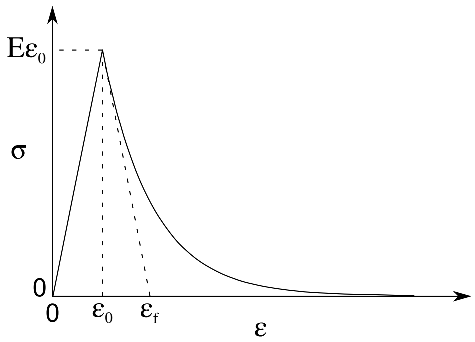

(b) Stress vs strain behaviour in uniaxial tension.

Figure 3.3. (a) Damage growth and (b) the corresponding uniaxial stress-strain response for exponential softening behaviour given in equation (3.6).

There are several variants of exponential softening models, for instance, the following damage law proposed in [481] is defined as

$$\omega = \begin{cases} 0 & \text{if } \kappa \leq \varepsilon_0, \\ 1 - \frac{\varepsilon_0}{\kappa}\left(1 - \alpha + \alpha \times \exp\left(\beta\left(\varepsilon_0 - \kappa\right)\right)\right) & \text{if } \kappa > \varepsilon_0, \end{cases} \tag{3.7}$$

in which α and β are two parameters to control the slope of the softening branch of the curve. The parameter β determines the rate at which the damage grows. A higher value of β results in a more brittle failure as it induces faster growth of damage. The parameter, α on the other hand controls the residual stress. When $\alpha = 1$ there is no residual stress and when $\alpha = 0$ the residual stress is equal to the tensile strength. This expression and the corresponding stress-strain relation have also been plotted in figure 3.4.

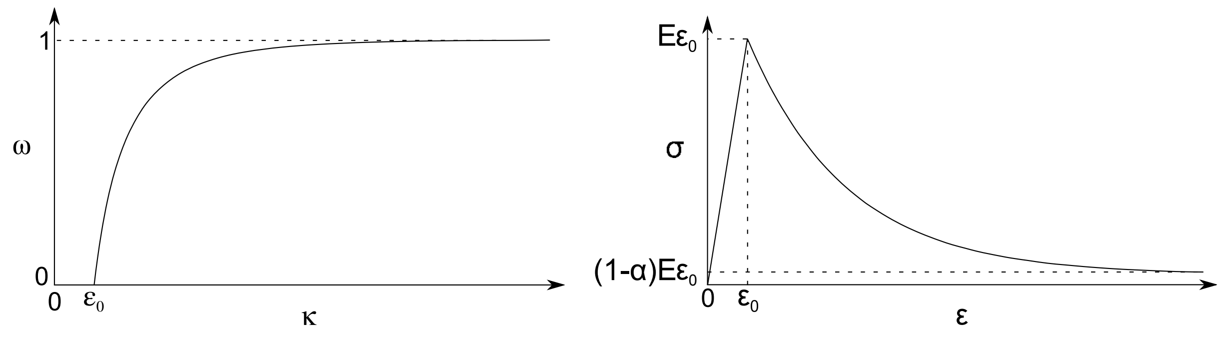

(a) Damage growth with respect to κ.

(b) Stress vs strain behaviour in uniaxial tension.

Figure 3.4. (a) Damage growth and the corresponding (b) uniaxial stress-strain response for linear softening behaviour given in equation (3.7).

In equation (3.7), when $\varepsilon \to \infty$ the uniaxial stress σ approaches $(1-\alpha)\,\mathrm{E}\varepsilon_0$ (figure 3.4b). This asymptote represents the effect of crack bridging [496]. Which is an effect apparent in experimentally obtained load-displacement diagrams in the form of a long tail.

In both damage models given in equations (3.6) and (3.7) the damage variable approaches $\omega = 1$ asymptotically (see figures 3.3a and 3.4a). This characteristic avoids complete fracture. The models also show the characteristic sharp drop in stress initially and thereon a gradual decrease in stiffness, similar to most practically found materials.

To define the complete quasi-brittle damage model next the equivalent strain $\widetilde{\varepsilon}$ definition applicable for both biaxial and triaxial cases is introduced. The equivalent strain parameter maps the strain components onto a scalar variable. The different effects of the strain components on damage growth are accounted within the equivalent strain definition by weighting these components appropriately. The definition of the equivalent strain directly affects the shape of the elastic domain in the strain space.

Damage evolution is usually related to the energy release rate associated to the damage variable since the constitutive relations are derived within the framework of thermodynamics of irreversible processes. Therefore, the equivalent strain could be defined in an energy norm as

$$\widetilde{\varepsilon} = \sqrt{\frac{1}{\mathrm{E}}\varepsilon : \mathbf{D} : \varepsilon}\,. \tag{3.8}$$

Equation (3.8) produces a dimensionless equivalent strain parameter. The value of $\widetilde{\varepsilon}$ equals to the axial strain for the uniaxial tensile stress case. Figure 3.5 is a graphical representation of $\widetilde{\varepsilon}$ in the principal strain space. The plot is produced assuming plane-stress conditions with a Poisson's ratio of $\nu = 0.2$.

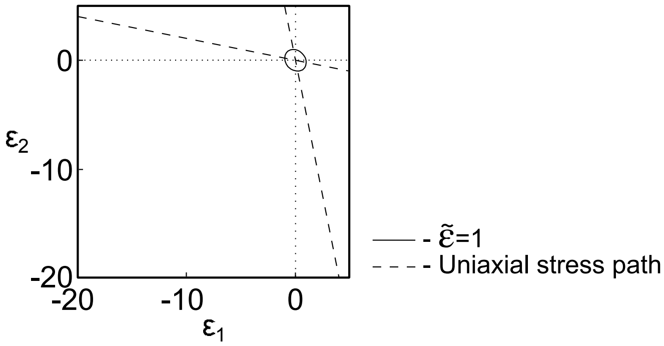

Figure 3.5. Normalised energy release rate definition for equivalent strain, equation (3.8). Principal strain space shown. Plane-stress conditions assumed. Solid line represent $\widetilde{\varepsilon} = 1$ and dashed lines represent uniaxial stress paths. Unit: $10\mu\varepsilon$.

The solid line represents the constant curve $\widetilde{\varepsilon} = 1$ produced by the normalised energy release rate equation (3.8) and the dashed lines in the diagram represent uniaxial stress paths. The downside to this definition as seen in figure 3.5 is the inability to differentiate between tension and compression. The model thus implies equal weight to tensile and compressive strain components. Therefore it is unsuitable to describe the mechanical behaviour of engineering materials, where compressive strength is often higher than the tensile strength.

As a remedy, Mazars and Pijaudier-Cabot [461] proposed a definition for concrete which is more sensitive to positive strains than to negative strains.

$$\widetilde{\varepsilon} = \sqrt{\sum_{i=1}^{3} (< \varepsilon_i >)^2}, \tag{3.9}$$

with ε_i representing the principal strains and the MacAulay brackets $<>$ defined such that $< \varepsilon_i >= \varepsilon_i$ if $\varepsilon_i > 0$ and $\varepsilon_i = 0$ otherwise. Figure 3.6 shows the contour for $\widetilde{\varepsilon} = 1$ associated with equation (3.9). It is evident from the behaviour of the equivalent strain that the sensitivity is solely to tensile strains than to compressive strains.

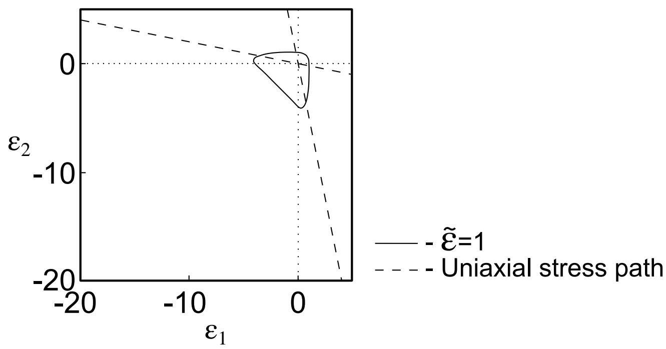

Figure 3.6. Mazars equivalent strain definition (equation (3.9)) in principal strain space. Plane-stress conditions assumed with Poisson's ratio of $\nu = 0.2$. Solid line represent $\widetilde{\varepsilon} = 1$ and dashed lines represent uniaxial stress paths. Unit: $10\mu\varepsilon$.

Another widely used definition of equivalent strain for concrete is proposed by De Vree et al. [497] and termed as the Modified von Mises Definition. The origins of the formulation stems from plasticity models for polymers. The original stress based formulation for modified von Mises definition can be rewritten in terms of strains using Hooke's law, to produce

$$\tilde{\varepsilon} = \frac{k-1}{2k(1-\nu)} I_1^{\varepsilon} + \frac{1}{2k}\sqrt{\frac{(k-1)^2}{(1-2\nu)^2}(I_1^{\varepsilon})^2 + \frac{12k}{(1+\nu)^2} J_2^{\varepsilon}}, \tag{3.10}$$

in which, I_1^{ε} is the first invariant of the strain vector defined below

$$I_1^{\varepsilon} = \varepsilon_{xx} + \varepsilon_{yy} + \varepsilon_{zz}, \tag{3.11}$$

ν is the Poisson's ratio, and J_2^{ε} second invariant of the deviatoric strain vector and defined as

$$J_2^{\varepsilon} = \frac{1}{3}[\varepsilon_{xx}^2 + \varepsilon_{yy}^2 + \varepsilon_{zz}^2 - \varepsilon_{xx}\varepsilon_{yy} + \varepsilon_{yy}\varepsilon_{zz} + \varepsilon_{zz}\varepsilon_{xx} + 3(\varepsilon_{xy}^2 + \varepsilon_{yz}^2 + \varepsilon_{zx}^2). \tag{3.12}$$

k is set equal to the ratio of the compressive uniaxial strength and the tensile uniaxial strength. This parameter therefore governs the sensitivity in compression relative to that in tension. Experimental results range the compressive strength of concrete to be ten to twenty times the tensile strength. The graphical representation in figure 3.8 considers $k = 10$.

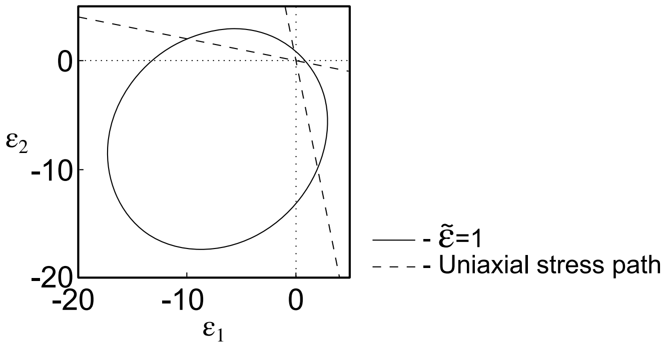

Figure 3.7. Modified von Mises equivalent strain definition (equation (3.10)) in principal strain space. Plane-stress conditions assumed with Poisson's ratio of $\nu = 0.2$. Solid line represent $\widetilde{\varepsilon} = 1$ and dashed lines represent uniaxial stress paths. Unit: $10\mu\varepsilon$.

Another common form of $\widetilde{\varepsilon}$ is the conventional von Mises equivalent strain definition as follows

$$\widetilde{\varepsilon} = \frac{1}{1+\nu}\sqrt{-3J_2^{\varepsilon}}. \tag{3.13}$$

Here, the factor $1/(1+\nu)$ scales the equivalent strain such that it equals the axial strain in the uniaxial stress case. Equation (3.13) is produced when $k = 1$ in the modified von Mises definition given in equation (3.10). A graphical representation of equation (3.13) is given in figure 3.8.

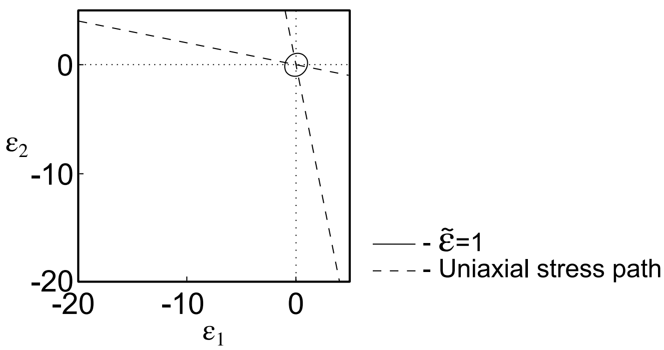

Figure 3.8. Von Mises equivalent strain definition (equation (3.13)) in principal strain space. Plane-stress conditions assumed with Poisson's ratio of $\nu = 0.2$. Solid line represent $\widetilde{\varepsilon} = 1$ and dashed lines represent uniaxial stress paths. Unit: $10\mu\varepsilon$.

3.2.4 Integral-type non-local damage model

The non-local damage model is formulated by replacing a state variable by its non-local counterpart obtained by weighted averaging over a spatial neighbourhood of each point under consideration. Assume in a domain V, $f(x)$ is a specified local field. Then the corresponding non-local field is defined as

$$\overline{f}(x) = \int_v \alpha(x,\varsigma) f(\varsigma) d\varsigma. \tag{3.14}$$

$\alpha(x,\varsigma)$ is a given non-local weight function defined as

$$\alpha(x,\varsigma) = \frac{\alpha_0(||x-\varsigma||)}{\int_v \alpha_0(||x-\varsigma||) d\varsigma}, \tag{3.15}$$

where $\alpha_0(r)$ is a monotonically decreasing non-negative function of the distance $r = ||x-\varsigma||$.

The Gauss distribution function is usually taken as the weight function given by [250].

$$\alpha_0(r) = \exp\left[-0.5 \times \left(\frac{r}{l}\right)^2\right], \tag{3.16}$$

or

$$\alpha_0(r) = \exp\left[-4 \times \left(\frac{r}{R}\right)^2\right], \tag{3.17}$$

in which l is the internal length of the non-local continuum, and R is the interaction radius related to the internal length and denotes the largest distance of point ς that affects the non-local average at point x.

Another alternative form of weight function is the truncated quartic polynomial function in bell-shape [477] given by

$$\alpha_0(r) = \left(1 - \frac{r^2}{R^2}\right)^2. \tag{3.18}$$

3.3 Governing equations of linear elasticity

From the Newton's second law of motion the governing differential equation for equilibrium is

$$\mathbf{L}^{\mathrm{T}}\sigma\left(x,y\right)+\mathbf{b}\left(x,y\right)=\rho\ddot{\mathbf{u}}\left(x,y\right), \tag{3.19}$$

where $\mathbf{b}\left(x,y\right)$ are the body loads, $\rho\ddot{\mathbf{u}}\left(x,y\right)$ are the inertial forces with ρ denoting the mass density, $\ddot{\mathbf{u}}\left(x,y\right)$ is the acceleration field, and $\mathbf{L}^{\mathrm{T}}$ is the linear differential operator for in-plane motion. Equation (3.19) should hold for any point $\left(x,y\right)$ within the domain to satisfy equilibrium in the strong sense.

The linear differential operator $\mathbf{L}$ for the 2D case is written as

$$\mathbf{L}=\begin{bmatrix} \frac{\partial}{\partial x} & \\ & \frac{\partial}{\partial y} \\ \frac{\partial}{\partial y} & \frac{\partial}{\partial x} \end{bmatrix}. \tag{3.20}$$

$\mathbf{L}$ relates the strains $\varepsilon\left(x,y\right)$ and displacements $\mathbf{u}\left(x,y\right)$ as

$$\varepsilon\left(x,y\right)=\mathbf{L}\mathbf{u}\left(x,y\right), \tag{3.21}$$

and stresses, $\sigma\left(x,y\right)$ are related to the strains $\varepsilon\left(x,y\right)$ by

$$\sigma\left(x,y\right)=\mathbf{D}\varepsilon\left(x,y\right), \tag{3.22}$$

where $\mathbf{D}$ is the elastic constitutive matrix. For an isotropic material in plane stress, the constitutive matrix is defined as

$$\mathbf{D}=\frac{\mathrm{E}}{1-\nu^2}\begin{bmatrix} 1 & \nu & 0 \\ \nu & 1 & 0 \\ 0 & 0 & \frac{1-\nu}{2} \end{bmatrix}. \tag{3.23}$$

For an isotropic material in plane strain $\mathbf{D}$ is is defined as

$$\mathbf{D} = \frac{\mathrm{E}}{(1+\nu)(1-2\nu)} \begin{bmatrix} 1-\nu & \nu & 0 \\ \nu & 1-\nu & 0 \\ 0 & 0 & \frac{1-2\nu}{2} \end{bmatrix}. \tag{3.24}$$

In equations (3.23) and (3.24) E is Young's modulus and ν is Poisson's ratio.

A typical problem domain consist of boundary conditions. These include the prescribed displacements

$$\mathbf{u} = \bar{\mathbf{u}} \quad \text{on} \quad \Gamma_{\mathrm{u}} \ , \tag{3.25}$$

and the prescribed tractions

$$\mathbf{t} = \bar{\mathbf{t}} \quad \text{on} \quad \Gamma_{\mathrm{N}} \ . \tag{3.26}$$

In equation (3.25) $\bar{\mathbf{u}}$ are the displacements prescribed on the Dirichlet part of the boundary Γ_{u} and $\bar{\mathbf{t}}$ in equation (3.26) are the tractions prescribed on the Neumann part of the boundary Γ_{N}. The total boundary is therefore specified as $\Gamma = \Gamma_{\mathrm{u}} \bigcup \Gamma_{\mathrm{N}}$.

The governing equation of equilibrium in elastostatics with reference to equation (3.19) is

$$\mathbf{L}^{\mathrm{T}} \sigma(x,y) + \mathbf{b}(x,y) = 0, \tag{3.27}$$

since there is no effect of the inertial force term, $\rho \ddot{\mathbf{u}}(x,y) = 0$.

3.4 The scaled boundary finite element method

In this section, the the standard governing equations in SBFEM for 2D elasticity in Cartesian coordinates are presented.

3.4.1 Geometry of scaled boundary finite elements

3.4.1.1 Overview

To illustrate the modelling in SBFEM, a problem domain divided into three arbitrary polygonal subdomains is considered, as shown in figure 3.9a. Figure 3.9b shows the details of the subdomain 1 in figure 3.9a. The subdomain is represented by scaling a defining curve or boundary *S* relative to a scaling centre. The only requirement is that the entire subdomain boundary has to be visible from the scaling centre. In other words this ensures that every point on the subdomain boundary can be connected to the scaling centre by an unobstructed radial line. When difficulties arise in complex geometries and this requirement is not met, the domain is partitioned into a multiple subdomains.

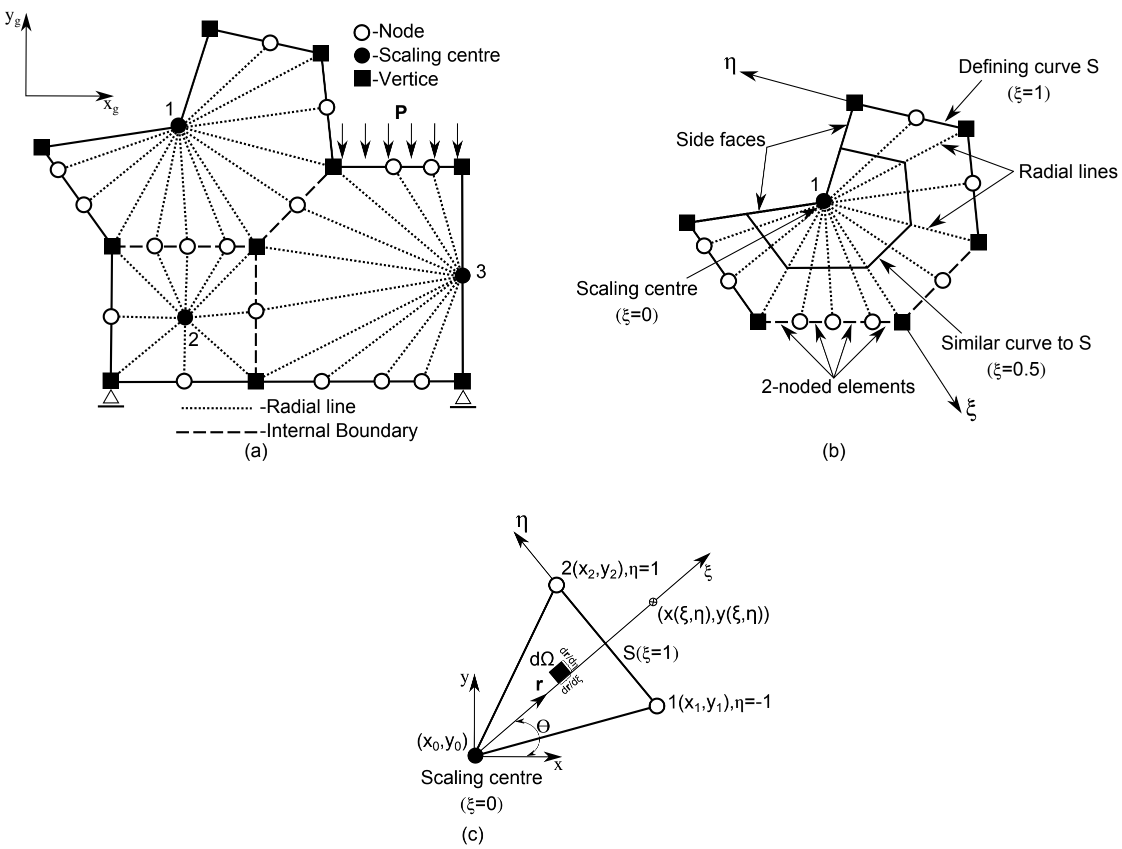

Figure 3.9. Concept of the scaled boundary finite element method, (a) SBFEM problem domain, (b) a scaled boundary subdomain, and (c) a line element on the boundary of a wedge formed by scaling elements on the boundary towards the scaling centre.

A point in a subdomain is described by the scaled boundary coordinates ξ and η.

The normalized radial coordinate ξ varies from zero at the scaling centre to unity on S. A circumferential coordinate η is defined around the defining curve S which pertains to the discretisation of the boundary. A curve similar to S defined by $\xi = 0.5$ is shown in figure 3.9b as well. The boundary can be discretised using any number and/or order of elements, which are connected piece-wise about the scaling centre following the right hand rule. Figure 3.9c depicts the defining curve discretised using one-dimensional SBFE with local coordinate η that ranges from -1 to +1. In this study, two-noded linear elements as shown in figure 3.9c are used. The interpolation along each line element is carried out using standard Gaussian/Gauss-Lobatto shape functions.

3.4.1.2 Scaled boundary finite element transformation of geometry

This thesis adopts the SBFEM formulation for an arbitrary polygonal element. The formulation is applicable to any polygon which satisfy the star convexity or scaling requirement for the SBFEM.

To start with, assume that the local Cartesian coordinate system (x, y) shown in figure 3.9c share the origin with the scaling centre. Then, the global Cartesian coordinate (x_g, y_g) system are related to the local scaled boundary system by

$$x_g = x_0 + x, \tag{3.28a}$$

$$y_g = y_0 + y, \tag{3.28b}$$

where, (x_0, y_0) are the global Cartesian coordinates at the scaling centre.

Any point on the boundary $(x_\mathrm{b}(\eta), y_\mathrm{b}(\eta))$ can be interpolated by using Gauss-Lobatto-Legendre shape functions [195] as

$$x_\mathrm{b}(\eta) = \mathbf{N}(\eta)\mathbf{x}_\mathrm{b}, \tag{3.29a}$$

$$y_\mathrm{b}(\eta) = \mathbf{N}(\eta)\mathbf{y}_\mathrm{b}, \tag{3.29b}$$

where $\mathbf{x}_\mathrm{b} = \begin{bmatrix} x_1 & x_2 & \ldots & x_M \end{bmatrix}^\mathrm{T}$, $\mathbf{y}_\mathrm{b} = \begin{bmatrix} y_1 & y_2 & \ldots & y_M \end{bmatrix}^\mathrm{T}$ are the respective local nodal coordinate vectors for a single M-noded element, and $\mathbf{N}(\eta)$ shape function vector of the M-noded line element. The coordinates $\mathbf{x}_\mathrm{b}$ and $\mathbf{y}_\mathrm{b}$ correspond to the nodes of each line-element used to discretise boundary. The one-dimensional shape function can be expanded as follows

$$\mathbf{N}(\eta) = \begin{bmatrix} N_1(\eta), & N_2(\eta), & \ldots & N_M(\eta) \end{bmatrix}, \tag{3.30}$$

where $\mathbf{N}_i(\eta), i = 1,2,...,M$ are the nodal shape functions.

A point in the domain $(x(\xi,\eta), y(\xi,\eta))$:

$$x(\xi,\eta) = \xi \mathbf{N}(\eta)\mathbf{x}_\mathrm{b}, \tag{3.31a}$$

$$y(\xi,\eta) = \xi \mathbf{N}(\eta)\mathbf{y}_\mathrm{b}, \tag{3.31b}$$

is described by scaling the boundary along the dimensionless radial coordinate, ξ. The radial coordinate attains the values 0 at the scaling centre and 1 at the boundary.

A Jacobian matrix $\mathbf{J}(\xi,\eta)$ is used (similar to standard isoparametric finite elements) for the coordinate transformation between the Cartesian coordinates, (x,y) and the scaled boundary coordinates (ξ,η). The relationship between the Jacobian matrix and the derivatives in the scaled boundary coordinates and the derivatives of the Cartesian coordinates is in the form of

$$\begin{Bmatrix} \frac{\partial}{\partial \xi} \\ \frac{\partial}{\partial \eta} \end{Bmatrix} = \mathbf{J}(\xi,\eta) \begin{Bmatrix} \frac{\partial}{\partial x} \\ \frac{\partial}{\partial y} \end{Bmatrix}, \tag{3.32}$$

where,

$$\mathbf{J}(\xi,\eta) = \begin{bmatrix} x(\xi,\eta)_{,\xi} & y(\xi,\eta)_{,\xi} \\ x(\xi,\eta)_{,\eta} & y(\xi,\eta)_{,\eta} \end{bmatrix}. \tag{3.33}$$

To separate the dependency of the Jacobian matrix on the geometry of the boundary coordinate η, equation (3.32) is rearranged to results in

$$\left\{\begin{array}{c}\frac{\partial}{\partial\xi}\\ \frac{1}{\xi}\frac{\partial}{\partial\eta}\end{array}\right\}=\mathbf{J}(\eta)\left\{\begin{array}{c}\frac{\partial}{\partial x}\\ \frac{\partial}{\partial y}\end{array}\right\}, \tag{3.34}$$

where $\mathbf{J}(\eta)$ is the Jacobian matrix of the boundary as below.

$$\mathbf{J}(\xi,\eta)=\left[\begin{array}{cc}x_{\mathrm{b}}(\eta) & y_{\mathrm{b}}(\eta)\\ x_{\mathrm{b}}(\eta)_{,\eta} & y_{\mathrm{b}}(\eta)_{,\eta}\end{array}\right] \tag{3.35}$$

Making the derivatives of the Cartesian coordinates the subject of the equation (3.34) gives

$$\left\{\begin{array}{c}\frac{\partial}{\partial x}\\ \frac{\partial}{\partial y}\end{array}\right\}=\mathbf{J}^{-1}(\eta)\left\{\begin{array}{c}\frac{\partial}{\partial\xi}\\ \frac{1}{\xi}\frac{\partial}{\partial\eta}\end{array}\right\}, \tag{3.36}$$

where $\mathbf{J}^{-1}(\eta)$ is

$$\mathbf{J}^{-1}(\eta)=\frac{1}{|\mathbf{J}(\eta)|}\left[\begin{array}{cc}y_{\mathrm{b}}(\eta)_{,\eta} & -y_{\mathrm{b}}(\eta)\\ -x_{\mathrm{b}}(\eta)_{,\eta} & x_{\mathrm{b}}(\eta)\end{array}\right] \tag{3.37}$$

According to equation (3.35) the determinant of the matrix $\mathbf{J}(\eta)$, $|\mathbf{J}(\eta)|$ is

$$|\mathbf{J}(\eta)|=x_{\mathrm{b}}(\eta)\,y_{\mathrm{b}}(\eta)_{,\eta}-x_{\mathrm{b}}(\eta)_{,\eta}\,y_{\mathrm{b}}(\eta) \tag{3.38}$$

Expanding equation (3.36) yields

$$\frac{\partial}{\partial x}=\frac{1}{|\mathbf{J}(\eta)|}\left(y_{\mathrm{b}}(\eta)_{,\eta}\frac{\partial}{\partial\xi}-\frac{1}{\xi}y_{\mathrm{b}}(\eta)\frac{\partial}{\partial\eta}\right), \tag{3.39a}$$

$$\frac{\partial}{\partial y}=\frac{1}{|\mathbf{J}(\eta)|}\left(-x_{\mathrm{b}}(\eta)_{,\eta}\frac{\partial}{\partial\xi}+\frac{1}{\xi}x_{\mathrm{b}}(\eta)\frac{\partial}{\partial\xi}\right). \tag{3.39b}$$

As shown in figure 3.9c the position vector $\mathbf{r}$ is defined with the help of the infinitesimal area $\mathrm{d}\Omega$ in scaled boundary coordinates. The position vector $\mathbf{r}$ can be written as

$$\mathbf{r} = x(\xi,\eta)\,\mathbf{i} + y(\xi,\eta)\,\mathbf{j}. \tag{3.40}$$

An infinitesimal area dΩ shown in figure 3.9c is formed by the two vectors

$$\mathbf{r}_{,\xi} = x(\xi,\eta)_{,\xi}\,\mathbf{i} + y(\xi,\eta)_{,\xi}\,\mathbf{j}, \tag{3.41a}$$

$$\mathbf{r}_{,\eta} = x(\xi,\eta)_{,\eta}\,\mathbf{i} + y(\xi,\eta)_{,\eta}\,\mathbf{j}. \tag{3.41b}$$

Therefore dΩ can be obtained by the vector cross product

$$\mathrm{d}\Omega = \left|\mathrm{d}\mathbf{r}_{,\xi} \times \mathrm{d}\mathbf{r}_{,\eta}\right| \tag{3.42a}$$

$$\mathrm{d}\Omega = \left|\begin{bmatrix} \mathbf{i} & \mathbf{j} & \mathbf{k} \\ x(\xi,\eta)_{,\xi} & y(\xi,\eta)_{,\xi} & 0 \\ x(\xi,\eta)_{,\eta} & y(\xi,\eta)_{,\eta} & 0 \end{bmatrix}\right| \mathrm{d}\xi\,\mathrm{d}\eta \tag{3.42b}$$

$$\mathrm{d}\Omega = \begin{vmatrix} x(\xi,\eta)_{,\xi} & y(\xi,\eta)_{,\xi} \\ x(\xi,\eta)_{,\eta} & y(\xi,\eta)_{,\eta} \end{vmatrix} \mathrm{d}\xi\,\mathrm{d}\eta. \tag{3.42c}$$

By substituting from equation (3.35), dΩ can be written as

$$\mathrm{d}\Omega = \xi\,|\mathbf{J}(\eta)|\,\mathrm{d}\xi\,\mathrm{d}\eta \tag{3.43}$$

An infinitesimal change in length dΓ in the circumferential direction can be obtained by Δ_Γ which stands for the magnitude of $\mathbf{r}_{,\eta}$ in equation (3.41b). Therefore

$$\mathrm{d}\Gamma = \Delta_\Gamma \mathrm{d}\eta, \tag{3.44}$$

where,

$$\Delta_\Gamma = \sqrt{\left(x(\xi,\eta)_{,\eta}\right)^2 + \left(y(\xi,\eta)_{,\eta}\right)^2}. \tag{3.45}$$

Equation (3.44) can now be expanded as

$$\mathrm{d}\Gamma = \sqrt{x_{\mathrm{b}}(\eta)_{,\eta}^{2} + y_{\mathrm{b}}(\eta)_{,\eta}^{2}}\mathrm{d}\eta. \tag{3.46}$$

3.4.2 Governing equations of linear elasticity in scaled boundary coordinates

In this section, the governing equations of linear elasticity stated in section 3.3 are transformed into scaled boundary coordinates, and the SBFEM approximation of the displacement field is introduced.

The displacement field $\mathbf{u}(\xi,\eta)$ is represented semi-analytically in the SBFEM formulation. The displacement functions $\mathbf{u}(\xi)$ provides an analytical description of the variation in displacement along a radial line that extends from the scaling centre through to a node on the boundary. Across these radial lines, the shape functions $\mathbf{N}(\eta)$ interpolate the displacement functions piece-wisely in the η-direction using any displacement based shape functions, such as the Gauss-Lobatto-Legendre shape functions. The scaled boundary approximation of the displacement field is given by

$$\mathbf{u}(\xi,\eta) = \mathbf{N}_{\mathrm{u}}(\eta)\mathbf{u}(\xi), \tag{3.47}$$

where

$$\mathbf{N}_{\mathrm{u}}(\eta) = \begin{bmatrix} N_1(\eta) & 0 & N_2(\eta) & 0 & \ldots & 0 & N_M(\eta) & 0 \\ 0 & N_1(\eta) & 0 & N_2(\eta) & 0 & \ldots & 0 & N_M(\eta) \end{bmatrix}. \tag{3.48}$$

$N_i(\eta)$ are the nodal shape functions defined in equation (3.30). These same shape functions apply when interpolating over any lines with a constant radial coordinate ξ.

The linear differential operator given in equation (3.20) as a function of ξ and η can be produced by substituting expressions for $\frac{\partial}{\partial x}$ and $\frac{\partial}{\partial y}$ from equations (3.39a) and (3.39b), respectively.

$$\mathbf{L}=\frac{1}{|\mathbf{J}(\eta)|}\begin{bmatrix} y_{\mathrm{b}}(\eta)_{,\eta}\frac{\partial}{\partial\xi}-\frac{1}{\xi}y_{\mathrm{b}}(\eta)\frac{\partial}{\partial\eta} & \\ & -x_{\mathrm{b}}(\eta)_{,\eta}\frac{\partial}{\partial\xi}+\frac{1}{\xi}x_{\mathrm{b}}(\eta)\frac{\partial}{\partial\xi} \\ -x_{\mathrm{b}}(\eta)_{,\eta}\frac{\partial}{\partial\xi}+\frac{1}{\xi}x_{\mathrm{b}}(\eta)\frac{\partial}{\partial\xi} & y_{\mathrm{b}}(\eta)_{,\eta}\frac{\partial}{\partial\xi}-\frac{1}{\xi}y_{\mathrm{b}}(\eta)\frac{\partial}{\partial\eta}\end{bmatrix}. \tag{3.49}$$

Equation (3.49) can be written concisely as

$$\mathbf{L}=\mathbf{b}_1(\eta)\frac{\partial}{\partial\xi}+\frac{1}{\xi}\mathbf{b}_2(\eta)\frac{\partial}{\partial\eta}, \tag{3.50}$$

where, $\mathbf{b}_1$ and $\mathbf{b}_2$ are

$$\mathbf{b}_1(\eta)=\frac{1}{|\mathbf{J}(\eta)|}\begin{bmatrix} y_{\mathrm{b}}(\eta)_{,\eta} & 0 \\ 0 & -x_{\mathrm{b}}(\eta)_{,\eta} \\ -x_{\mathrm{b}}(\eta)_{,\eta} & y_{\mathrm{b}}(\eta)_{,\eta}\end{bmatrix}, \tag{3.51a}$$

$$\mathbf{b}_2(\eta)=\frac{1}{|\mathbf{J}(\eta)|}\begin{bmatrix} -y_{\mathrm{b}}(\eta) & 0 \\ 0 & x_{\mathrm{b}}(\eta) \\ x_{\mathrm{b}}(\eta) & -y_{\mathrm{b}}(\eta)\end{bmatrix}. \tag{3.51b}$$

The matrices $\mathbf{b}_1$ and $\mathbf{b}_2$ depend only on the geometry of the boundary and are related by the identity

$$(|\mathbf{J}(\eta)|\,\mathbf{b}_2(\eta))_{,\eta}=-\,|\mathbf{J}(\eta)|\,\mathbf{b}_1(\eta). \tag{3.52}$$

The differential operator $\mathbf{L}$ enables transformation of the the governing equation in elastostatics given in equation (3.27) and also the strain-displacement relationship in equation (3.21). Analogous to the expression in equation (3.21), the strain field in scaled boundary coordinates is defined as

$$\varepsilon(\xi,\eta)=\mathbf{Lu}(\xi,\eta), \tag{3.53}$$

where L is the linear differential operator in equation (3.49) and $\mathbf{u}(\xi,\eta)$ is the displacement field given in equation (3.47). Therefore $\varepsilon(\xi,\eta)$ can be expanded as

$$\varepsilon(\xi,\eta) = \mathbf{b}_1(\eta)\frac{\partial}{\partial\xi}\mathbf{u}(\xi,\eta) + \frac{1}{\xi}\mathbf{b}_2(\eta)\frac{\partial}{\partial\eta}\mathbf{u}(\xi,\eta), \tag{3.54a}$$

$$\varepsilon(\xi,\eta) = \mathbf{B}_1(\eta)\mathbf{u}(\xi)_{,\xi} + \frac{1}{\xi}\mathbf{B}_2(\eta)\mathbf{u}(\xi), \tag{3.54b}$$

where $\mathbf{B}_1(\eta)$ and $\mathbf{B}_2(\eta)$ are the strain-displacement matrices

$$\mathbf{B}_1(\eta) = \mathbf{b}_1(\eta)\mathbf{N}_\mathrm{u}(\eta), \tag{3.55a}$$

$$\mathbf{B}_2(\eta) = \mathbf{b}_2(\eta)\mathbf{N}_\mathrm{u}(\eta)_{,\eta}. \tag{3.55b}$$

Similarly with reference to equation (3.22), and using the strain-displacement matrices above the stress field can be written as

$$\sigma(\xi,\eta) = \mathbf{D}\varepsilon(\xi,\eta), \tag{3.56a}$$

$$\sigma(\xi,\eta) = \mathbf{D}\left(\mathbf{B}_1(\eta)\mathbf{u}(\xi)_{,\xi} + \frac{1}{\xi}\mathbf{B}_2(\eta)\mathbf{u}(\xi)\right). \tag{3.56b}$$

Therefore stresses and strains are related by the constitutive matrix $\mathbf{D}$ in equation (3.22) and equation (3.56a), and are independent of the coordinate transformation of the geometry.

3.4.3 2D derivation of the scaled boundary finite element equation based on the principle of virtual work

The D'Alembert's form of the principle of virtual work (also known as the principle of virtual displacements) is used in applying the virtual work method to derive the SBFEM equations in 2D. The method in elastostatics is applied to each subdomain in the following form

$$\Pi_\varepsilon - \Pi_\mathrm{t} - \Pi_\mathrm{b} = 0, \tag{3.57}$$

where Π_ε represent the internal virtual energy, Π_t external work done by the boundary tractions, and Π_b is the external virtual work done by the body loads. These terms can be expanded as

$$\Pi_\varepsilon = \int_\Omega \delta\varepsilon^\mathrm{T}\sigma \mathrm{d}\Omega, \tag{3.58a}$$

$$\Pi_\mathrm{b} = \int_\Omega \delta\mathbf{u}^\mathrm{T}\mathbf{b} \mathrm{d}\Omega, \tag{3.58b}$$

$$\Pi_\mathrm{t} = \int_\Gamma \delta\mathbf{u}^\mathrm{T}\mathbf{t} \mathrm{d}\Gamma, \tag{3.58c}$$

where $\delta\varepsilon$ is the virtual strain field, $\delta\mathbf{u}$ is the virtual displacement field, σ is the stress field, and $\mathbf{t}$ and $\mathbf{b}$ are surface tractions and body loads respectively. Consistent with the previous section, $\mathrm{d}\Gamma$ is an infinitesimal line on the boundary and $\mathrm{d}\Omega$ is an infinitesimal area in the domain. After incorporation of the expanded forms in equations (3.58a-3.58c), (3.57) transforms to

$$\int_\Omega \delta\varepsilon^\mathrm{T}\sigma \mathrm{d}\Omega - \int_\Omega \delta\mathbf{u}^\mathrm{T}\mathbf{b} \mathrm{d}\Omega - \int_\Gamma \delta\mathbf{u}^\mathrm{T}\mathbf{t} \mathrm{d}\Gamma = 0. \tag{3.59}$$

With reference to equation (3.47) the virtual displacement field $\delta\mathbf{u}(\xi,\eta)$ is introduced as

$$\delta\mathbf{u}(\xi,\eta) = \mathbf{N}_\mathrm{u}(\eta)\delta\mathbf{u}(\xi), \tag{3.60}$$

where $\delta\mathbf{u}(\xi)$ is the vector of virtual radial displacement functions. By substituting the virtual displacement field in equation (3.60) into the strain-displacement relationship equation (3.54b) the corresponding virtual strain field is obtained as

$$\delta\varepsilon(\xi,\eta) = \mathbf{B}_1(\eta)\delta\mathbf{u}(\xi)_{,\xi} + \frac{1}{\xi}\mathbf{B}_2(\eta)\delta\mathbf{u}(\xi). \tag{3.61}$$

3.4.3.1 Strain energy (Π_ε)

Equation (3.58a) can be expanded by appropriately substituting for $\delta\varepsilon$, σ, and $\mathrm{d}\Omega$ from equations (3.61), (3.56b), and (3.43), respectively. The expanded full form of Π_ε is therefore

$$\Pi_{\varepsilon}=\underbrace{\int_{0}^{1}\delta\mathbf{u}^{\mathrm{T}}(\xi)_{,\xi}\int_{-1}^{1}\mathbf{B}_1^{\mathrm{T}}(\eta)\mathbf{D}\mathbf{B}_1(\eta)\mathbf{u}(\xi)_{,\xi}\left|\mathbf{J}(\eta)\right|\xi\mathrm{d}\eta\mathrm{d}\xi}_{O1}$$
$$+\underbrace{\int_{0}^{1}\delta\mathbf{u}^{\mathrm{T}}(\xi)_{,\xi}\int_{-1}^{1}\mathbf{B}_1^{\mathrm{T}}(\eta)\mathbf{D}\mathbf{B}_2(\eta)\mathbf{u}(\xi)\left|\mathbf{J}(\eta)\right|\mathrm{d}\eta\mathrm{d}\xi}_{O2}$$
$$+\underbrace{\int_{0}^{1}\delta\mathbf{u}^{\mathrm{T}}(\xi)\int_{-1}^{1}\mathbf{B}_2^{\mathrm{T}}(\eta)\mathbf{D}\mathbf{B}_1(\eta)\mathbf{u}(\xi)_{,\xi}\left|\mathbf{J}(\eta)\right|\mathrm{d}\eta\mathrm{d}\xi}_{O3}$$
$$+\underbrace{\int_{0}^{1}\delta\mathbf{u}^{\mathrm{T}}(\xi)\int_{-1}^{1}\mathbf{B}_2^{\mathrm{T}}(\eta)\mathbf{D}\mathbf{B}_2(\eta)\mathbf{u}(\xi)\left|\mathbf{J}(\eta)\right|\frac{1}{\xi}\mathrm{d}\eta\mathrm{d}\xi}_{O4} \tag{3.62}$$

Since the integral with respect to ξ can be performed independently to the integral in η, the coefficient matrices $\mathrm{E}_0, \mathrm{E}_1$ and E_2 for each line element is formed as

$$\mathrm{E}_0=\int_{-1}^{1}\mathrm{B}_1^{\mathrm{T}}(\eta)\mathbf{D}\mathrm{B}_1(\eta)\left|\mathbf{J}\right|d\eta, \tag{3.63a}$$

$$\mathrm{E}_1=\int_{-1}^{1}\mathrm{B}_2^{\mathrm{T}}(\eta)\mathbf{D}\mathrm{B}_1(\eta)\left|\mathbf{J}\right|d\eta, \tag{3.63b}$$

$$\mathrm{E}_2=\int_{-1}^{1}\mathrm{B}_2^{\mathrm{T}}(\eta)\mathbf{D}\mathrm{B}_2(\eta)\left|\mathbf{J}\right|d\eta, \tag{3.63c}$$

by grouping the integration with respect to η results. O1 and O2 containing $\delta\mathbf{u}(\xi)_{,\xi}$ in equation (3.62) are integrated by parts with respect to ξ as follows

$$O1=\int_{0}^{1}\delta\mathbf{u}^{\mathrm{T}}(\xi)_{,\xi}\mathbf{E}_0\xi\mathbf{u}(\xi)_{,\xi}\mathrm{d}\xi$$
$$O1=\delta\mathbf{u}^{\mathrm{T}}(\xi)\mathbf{E}_0\xi\mathbf{u}(\xi)_{,\xi}\mid_{\xi=1}-\int_{0}^{1}\delta\mathbf{u}^{\mathrm{T}}(\xi)\mathbf{E}_0\left(\mathbf{u}(\xi)_{,\xi}+\xi\mathbf{u}(\xi)_{,\xi\xi}\right)\mathrm{d}\xi$$
$$O1=\delta\mathbf{u}_{\mathrm{b}}^{\mathrm{T}}\mathbf{E}_0\mathbf{u}(\xi)_{,\xi}\mid_{\xi=1}-\int_{0}^{1}\delta\mathbf{u}^{\mathrm{T}}(\xi)\mathbf{E}_0\left(\mathbf{u}(\xi)_{,\xi}+\xi\mathbf{u}(\xi)_{,\xi\xi}\right)\mathrm{d}\xi, \tag{3.64a}$$

$$
\begin{aligned}
O2 =& \int_0^1 \delta \mathbf{u}^{\mathrm{T}}(\xi)_{,\xi} \mathbf{E}_1^{\mathrm{T}} \mathbf{u}(\xi) \mathrm{d}\xi \\
O2 =& \delta \mathbf{u}^{\mathrm{T}}(\xi) \mathbf{E}_1^{\mathrm{T}} \mathbf{u}(\xi) \mid_{\xi=1} - \int_0^1 \delta \mathbf{u}^{\mathrm{T}}(\xi) \mathbf{E}_1^{\mathrm{T}} \mathbf{u}(\xi)_{,\xi} \mathrm{d}\xi \\
O2 =& \delta \mathbf{u}_{\mathrm{b}}^{\mathrm{T}} \mathbf{E}_1^{\mathrm{T}} \mathbf{u}_{\mathrm{b}} - \int_0^1 \delta \mathbf{u}^{\mathrm{T}}(\xi) \mathbf{E}_1^{\mathrm{T}} \mathbf{u}(\xi)_{,\xi} \mathrm{d}\xi.
\end{aligned} \tag{3.64b}
$$

O3 and O4 remain unchanged as they do not contain the term $\delta \mathbf{u}(\xi)_{,\xi}$. Therefore substituting E_1 and E_2 respectively to parts O3 and O4 in equation (3.62), yields

$$
O3 = \int_0^1 \delta \mathbf{u}^{\mathrm{T}}(\xi) \mathbf{E}_1 \mathbf{u}(\xi)_{,\xi} \mathrm{d}\xi, \tag{3.65a}
$$

$$
O4 = \int_0^1 \delta \mathbf{u}^{\mathrm{T}}(\xi) \mathbf{E}_2 \frac{1}{\xi} \mathbf{u}(\xi) \mathrm{d}\xi. \tag{3.65b}
$$

Substituting the results for O1-O4 in equation (3.62) for the total strain energy, provides

$$
\begin{aligned}
\Pi_\varepsilon = \delta \mathbf{u}_{\mathrm{b}}^{\mathrm{T}} \left(\mathbf{E}_0 \mathbf{u}(\xi)_{,\xi} \mid_{\xi=1} + \mathbf{E}_1^{\mathrm{T}} \mathbf{u}_{\mathrm{b}} \right) \\
\ldots - \int_0^1 \delta \mathbf{u}^{\mathrm{T}}(\xi) \left(\mathbf{E}_0 \xi \mathbf{u}(\xi)_{,\xi\xi} + (\mathbf{E}_0 + \mathbf{E}_1^{\mathrm{T}} - \mathbf{E}_1) \mathbf{u}(\xi)_{,\xi} - \mathbf{E}_2 \frac{1}{\xi} \mathbf{u}(\xi) \right) d\xi
\end{aligned} \tag{3.66}
$$

3.4.3.2 Work done by applied forces (Π_{b} and Π_{t})

Work done by applied forces are given in equations (3.58b) and (3.58c).

Equations (3.58b) represent the virtual work done by the applied tractions on the boundary, where $\xi = 1$, which transforms virtual displacement field in equation (3.60) to $\mathbf{N}(\eta) \delta \mathbf{u}_{\mathrm{b}}$. Therefore

$$
\Pi_{\mathrm{t}} = \delta \mathbf{u}_{\mathrm{b}}^{\mathrm{T}} \int_{-1}^{1} \mathbf{N}_{\mathrm{u}}^{\mathrm{T}}(\eta) \mathbf{t}(\eta) \mathrm{d}\eta, \tag{3.67a}
$$

$$
\Pi_{\mathrm{t}} = \delta \mathbf{u}_{\mathrm{b}}^{\mathrm{T}} \mathbf{F}_{\mathrm{t}}, \tag{3.67b}
$$

where $\mathbf{F}_{\mathrm{t}} = \int_{-1}^{1} \mathbf{N}_{\mathrm{u}}^{\mathrm{T}}(\eta) \mathbf{t}(\eta) \mathrm{d}\eta$ is the equivalent nodal forces from tractions.

Equation (3.58c) is a function of (ξ, η) and represents the virtual work from body loads as

$$\Pi_{\mathrm{b}} = \int_0^1 \delta \mathbf{u}^{\mathrm{T}}(\xi) \int_{-1}^1 \mathbf{N}_{\mathrm{u}}^{\mathrm{T}}(\eta) \mathbf{b}(\xi, \eta) |\mathbf{J}(\eta)| \xi \mathrm{d}\eta \mathrm{d}\xi, \tag{3.68a}$$

$$\Pi_{\mathrm{b}} = \int_0^1 \delta \mathbf{u}^{\mathrm{T}}(\xi) \xi \mathbf{F}_{\mathrm{b}}(\xi) \mathrm{d}\xi, \tag{3.68b}$$

where $\mathbf{F}_{\mathrm{b}} = \int_{-1}^1 \mathbf{N}_{\mathrm{u}}^{\mathrm{T}}(\eta) \mathbf{b}(\xi, \eta) |\mathbf{J}(\eta)| \mathrm{d}\eta$ are the equivalent nodal loads for the body loads.

Substituting equations (3.66), (3.67b) and (3.68b) in the initial virtual work expression in equation (3.57) reveals

$$\delta \mathbf{u}_{\mathrm{b}}^{\mathrm{T}} \left(\mathbf{E}_0 \mathbf{u}(\xi)_{,\xi} \mid_{\xi=1} + \mathbf{E}_1^{\mathrm{T}} \mathbf{u}_{\mathrm{b}} - \mathbf{F}_{\mathrm{t}} \right) - \int_0^1 \delta \mathbf{u}^{\mathrm{T}}(\xi) (\mathbf{E}_0 \xi \mathbf{u}(\xi)_{,\xi\xi}$$
$$\ldots + (\mathbf{E}_0 + \mathbf{E}_1^{\mathrm{T}} - \mathbf{E}_1) \mathbf{u}(\xi)_{,\xi} + \frac{1}{\xi} \mathbf{E}_2 \mathbf{u}(\xi) - \xi \mathbf{F}_{\mathrm{b}}(\xi)) \mathrm{d}\xi = 0. \tag{3.69}$$

For the virtual work statement given in equation (3.69) to hold true the following two conditions must be met

$$\delta \mathbf{u}_{\mathrm{b}}^{\mathrm{T}} \left(\mathbf{E}_0 \mathbf{u}(\xi)_{,\xi} \mid_{\xi=1} + \mathbf{E}_1^{\mathrm{T}} \mathbf{u}_{\mathrm{b}} - \mathbf{F}_{\mathrm{t}} \right) = 0, \tag{3.70}$$

and

$$\int_0^1 \delta \mathbf{u}^{\mathrm{T}}(\xi) (\mathbf{E}_0 \xi \mathbf{u}(\xi)_{,\xi\xi} + (\mathbf{E}_0 + \mathbf{E}_1^{\mathrm{T}} - \mathbf{E}_1) \mathbf{u}(\xi)_{,\xi}$$
$$\ldots + \mathbf{E}_2 \frac{1}{\xi} \mathbf{u}(\xi) - \xi \mathbf{F}_{\mathrm{b}}(\xi)) \mathrm{d}\xi = 0. \tag{3.71}$$

Equation (3.70) above provides the nodal force-displacement relationship. Regrouping the two conditions in equations (3.70) and (3.71) produces the following separate conditions that has to be met.

Condition 1:

$$\int_0^1 \delta\mathbf{u}^{\mathrm{T}}(\xi)\left(\mathbf{E}_0\xi\mathbf{u}(\xi)_{,\xi\xi}+(\mathbf{E}_0+\mathbf{E}_1^{\mathrm{T}}-\mathbf{E}_1)\mathbf{u}(\xi)_{,\xi}-\mathbf{E}_2\frac{1}{\xi}\mathbf{u}(\xi)\right)\mathrm{d}\xi=0 \tag{3.72}$$

Condition 2:

$$\delta\mathbf{u}_{\mathrm{b}}^{\mathrm{T}}\left(\mathbf{E}_0\mathbf{u}(\xi)_{,\xi}\,|_{\xi=1}+\mathbf{E}_1^{\mathrm{T}}\mathbf{u}_{\mathrm{b}}-\mathbf{F}_{\mathrm{t}}\right)-\int_0^1 \delta\mathbf{u}^{\mathrm{T}}(\xi)(\xi\mathbf{F}_{\mathrm{b}}(\xi))\mathrm{d}\xi=0 \tag{3.73}$$

Considering the arbitrariness of the virtual displacement $\delta\mathbf{u}(\xi)$ equation (3.73) transforms to the produce a homogeneous second order partial differential equation.

$$\mathbf{E}_0\xi^2\mathbf{u}(\xi)_{,\xi\xi}+(\mathbf{E}_0+\mathbf{E}_1^{\mathrm{T}}-\mathbf{E}_1)\xi\mathbf{u}(\xi)_{,\xi}-\mathbf{E}_2\mathbf{u}(\xi)=0 \tag{3.74}$$

The is termed *the scaled boundary finite element equation in displacement* in statics. To satisfy the conditions set in equations (3.72) and (3.73), the scaled boundary finite element equation in displacement (equation (3.74)) is first solved for the displacement functions $\mathbf{u}(\xi)$.

3.4.4 Solution of the scaled boundary finite element equation in displacement

The second order homogeneous differential equation in $\mathbf{u}(\xi)$ obtained in equation (3.74) is first solved by transforming the equation to a first order linear differential equations by treating $\mathbf{u}(\xi)_{,\xi}$ as an independent variable.

To accomplish this task, first, the internal force vector $\mathbf{q}(\xi)$ is introduced as

$$\mathbf{q}(\xi)=\mathbf{E_0}\xi\mathbf{u}(\xi)_{,\xi}+\mathbf{E}_1^{\mathrm{T}}\mathbf{u}(\xi). \tag{3.75}$$

$\mathbf{q}(\xi)$ represents the force-displacement relationship along the radial lines connecting the scaling centre and the nodes on the boundary. Taking the first derivative of equation (3.75) gives

$$\mathbf{q}(\xi)_{,\xi} = \mathbf{E}_0 \left(\xi \mathbf{u}(\xi)_{,\xi\xi} + \mathbf{u}(\xi)_{,\xi}\right) + \mathbf{E}_1^{\mathrm{T}} \mathbf{u}(\xi)_{,\xi}, \tag{3.76a}$$

$$\mathbf{q}(\xi)_{,\xi} = \xi \mathbf{E}_0 \mathbf{u}(\xi)_{,\xi\xi} + \left(\mathbf{E}_1^{\mathrm{T}} + \mathbf{E}_0\right) \mathbf{u}(\xi)_{,\xi}. \tag{3.76b}$$

Rearranging equation (3.76b) produces

$$\mathbf{E}_0 \xi \mathbf{u}(\xi)_{,\xi\xi} = \mathbf{q}(\xi)_{,\xi} - \left(\mathbf{E}_1^{\mathrm{T}} + \mathbf{E}_0\right) \mathbf{u}(\xi)_{,\xi}. \tag{3.77}$$

Similarly, equation (3.75) can be rearranged as

$$\xi \mathbf{u}(\xi)_{,\xi} = -\mathbf{E}_0^{-1} \mathbf{E}_1^{\mathrm{T}} \mathbf{u}(\xi) + \mathbf{E}_0^{-1} \mathbf{q}(\xi). \tag{3.78}$$

Substituting equation (3.77) into equation (3.74), yields

$$\xi \mathbf{q}(\xi)_{,\xi} = \mathbf{E}_1 \xi \mathbf{u}(\xi)_{,\xi} + \mathbf{E}_2 \mathbf{u}(\xi). \tag{3.79}$$

Substituting equation (3.78) into equation (3.79) results in

$$\xi \mathbf{q}(\xi)_{,\xi} = \left(-\mathbf{E}_1 \mathbf{E}_0^{-1} \mathbf{E}_1^{\mathrm{T}} + \mathbf{E}_2\right) \mathbf{u}(\xi) + \mathbf{E}_1 \mathbf{E}_0^{-1} \mathbf{q}(\xi). \tag{3.80}$$

Now by using equations (3.78), (3.80) and (3.74) is transformed into the first-order ordinary differential equation of the form of

$$\xi \left\{ \begin{array}{c} \mathbf{u}(\xi) \\ \mathbf{q}(\xi) \end{array} \right\}_{,\xi} = \left\{ \begin{array}{cc} -\mathbf{E}_0^{-1} \mathbf{E}_1^{\mathrm{T}} & \mathbf{E}_0^{-1} \\ -\mathbf{E}_1 \mathbf{E}_0^{-1} \mathbf{E}_1^{\mathrm{T}} + \mathbf{E}_2 & \mathbf{E}_1 \mathbf{E}_0^{-1} \end{array} \right\} \left\{ \begin{array}{c} \mathbf{u}(\xi) \\ \mathbf{q}(\xi) \end{array} \right\}. \tag{3.81}$$

Equation (3.81) can be converted to a first order ordinary differential equation as

$$\xi \mathbf{X}(\xi)_{,\xi} = -\mathbf{Z} \mathbf{X}(\xi), \tag{3.82}$$

which can be solved by either eigenvalue or Schur decomposition technique. The Hamiltonian matrix $\mathbf{Z}$ in the equation takes the form of

$$\mathbf{Z} = \left\{ \begin{array}{cc} -\mathbf{E}_0^{-1}\mathbf{E}_1^{\mathrm{T}} & \mathbf{E}_0^{-1} \\ -\mathbf{E}_1\mathbf{E}_0^{-1}\mathbf{E}_1^{\mathrm{T}} + \mathbf{E}_2 & \mathbf{E}_1\mathbf{E}_0^{-1} \end{array} \right\}. \tag{3.83}$$

$\mathbf{Z}$ contains eigenvalues pairs of $(-\lambda, \lambda)$. Also the introduced vector $\mathbf{X}(\xi)$ is in the form of

$$\mathbf{X}(\xi) = \left\{ \begin{array}{c} \mathbf{u}(\xi) \\ \mathbf{q}(\xi) \end{array} \right\}. \tag{3.84}$$

In the thesis, equation (3.82) is solved by the Schur decomposition technique as the eigenvalue method may sometimes produce eigenvectors dependent of each other.

3.4.4.1 Schur decomposition

The Schur decomposition is an intermediate step within the QR algorithm for computing eigenvalues and eigenvectors. The method does not suffer from the numerical pitfalls inherent in computing eigenvectors associated with multiple or near-multiple eigenvalues.

In the Schur decomposition process matrix $\mathbf{Z}$ is transformed into a real Schur matrix, $\mathbf{S}$ as

$$\mathbf{V}^{\mathrm{T}}\mathbf{Z}\mathbf{V} = \mathbf{S}. \tag{3.85}$$

$\mathbf{V}$ is a real orthogonal transformation matrix such that $\mathbf{V}^{\mathrm{T}}\mathbf{V} = \mathbf{I}$. $\mathbf{S}$ is a quasi-upper triangular matrix consisting of 2×2 blocks on the diagonal, corresponding to complex conjugate eigenvalues, or 1×1 blocks corresponding to real eigenvalues.

3.4.4.2 Block diagonalisation of S

To introduce boundary conditions, the Schur decomposition, equation (3.85), is first reordered. Along the diagonal of the Schur matrix $\mathbf{S}$, $\mathbf{S}_{\mathrm{ii}}$ which correspond to the eigenvalues λ of $\mathbf{Z}$, are sorted in ascending order of their real parts as

$$\mathbf{V}^{\mathrm{T}}\mathbf{Z}\mathbf{V} = \mathbf{S} = \begin{bmatrix} \mathbf{S}_{\mathrm{n}} & \diamondsuit \\ & \mathbf{S}_{\mathrm{p}} \end{bmatrix}. \tag{3.86}$$

$\mathbf{S}_{\mathrm{n}}$ and $\mathbf{S}_{\mathrm{p}}$ are two sub-matrices of equal size partitioned in $\mathbf{S}$. The eigenvalues occur in pairs of $(-\lambda, \lambda)$, therefore the diagonal entries in $\mathbf{S}_{\mathrm{n}}$ are negative and are positive in $\mathbf{S}_{\mathrm{p}}$; $\diamondsuit$ stands for a real matrix.

Similarly, the orthogonal matrix $\mathbf{V}$ is partitioned into equal sized sub-matrices as

$$\mathbf{V} = \begin{bmatrix} \mathbf{V}_{11} & \mathbf{V}_{12} \\ \mathbf{V}_{21} & \mathbf{V}_{22} \end{bmatrix}. \tag{3.87}$$

An upper-triangular matrix

$$\mathbf{Y} = \begin{bmatrix} \mathbf{I} & \mathbf{Y}_{12} \\ 0 & \mathbf{I} \end{bmatrix}, \tag{3.88}$$

is introduced for to block diagonalise equation (3.86), where $\mathbf{I}$ are identity matrices. $\mathbf{Y}$ is applied to the matrix $\mathbf{V}$ in the manner such that

$$\Psi = \mathbf{V}\mathbf{Y} = \begin{bmatrix} \mathbf{V}_{11} & \mathbf{V}_{11}\mathbf{Y}_{12} + \mathbf{V}_{12} \\ \mathbf{V}_{21} & \mathbf{V}_{21}\mathbf{Y}_{12} + \mathbf{V}_{22} \end{bmatrix} = \begin{bmatrix} \Psi_{\mathrm{u}}^{(\mathrm{n})} & \Psi_{\mathrm{u}}^{(\mathrm{p})} \\ \Psi_{\mathrm{q}}^{(\mathrm{n})} & \Psi_{\mathrm{q}}^{(\mathrm{p})} \end{bmatrix}, \tag{3.89}$$

where Ψ is an accumulated transformation matrix. Now using $\mathbf{VY}$ from equation (3.89) in equation (3.86) yields

$$(\mathbf{VY})^{-\mathbf{1}}\mathbf{Z}(\mathbf{VY}) = \mathbf{Y}^{-\mathbf{1}}\mathbf{S}\mathbf{Y} = \begin{bmatrix} \mathbf{S}_{\mathrm{n}} & \diamondsuit \\ & \mathbf{S}_{\mathrm{p}} \end{bmatrix}. \tag{3.90}$$

Equation (3.90) becomes

$$\mathbf{Z}\Psi = \Psi\mathbf{S}. \tag{3.91}$$

Expanding equation (3.91), by substituting from equations (3.83) and (3.89) yields

$$\begin{bmatrix} \mathbf{E}_0^{-1}\mathbf{E}_1^{\mathrm{T}} & \mathbf{E}_0^{-1} \\ -\mathbf{E}_2+\mathbf{E}_1\mathbf{E}_0^{-1}\mathbf{E}_1^{\mathrm{T}} & -\mathbf{E}_1\mathbf{E}_0^{-1} \end{bmatrix} \begin{bmatrix} \Psi_{\mathrm{u}}^{(\mathrm{n})} & \Psi_{\mathrm{u}}^{(\mathrm{p})} \\ \Psi_{\mathrm{q}}^{(\mathrm{n})} & \Psi_{\mathrm{q}}^{(\mathrm{p})} \end{bmatrix}$$
$$\ldots = \begin{bmatrix} \Psi_{\mathrm{u}}^{(\mathrm{n})} & \Psi_{\mathrm{u}}^{(\mathrm{p})} \\ \Psi_{\mathrm{q}}^{(\mathrm{n})} & \Psi_{\mathrm{q}}^{(\mathrm{p})} \end{bmatrix} \begin{bmatrix} \mathbf{S}_{\mathrm{n}} & 0 \\ 0 & \mathbf{S}_{\mathrm{p}} \end{bmatrix}. \tag{3.92}$$

It is noted that the block diagonalisation of $\mathbf{S}$ does not modify the diagonal blocks $\mathbf{S}_{\mathrm{n}}$ and $\mathbf{S}_{\mathrm{p}}$. Introducing the function $\mathbf{X}(\xi)$ defined as

$$\mathbf{X}(\xi) = \Psi\mathbf{W}(\xi), \tag{3.93}$$

for which the first derivative is

$$\mathbf{X}(\xi)_{,\xi} = \Psi\mathbf{W}(\xi)_{,\xi}. \tag{3.94}$$

Substituting equations (3.93) and (3.94) into equation (3.82), produces

$$\xi\Psi\mathbf{W}(\xi)_{,\xi} = -\mathbf{Z}\Psi\mathbf{W}(\xi). \tag{3.95}$$

Rearranging equation (3.95) gives

$$\xi\mathbf{W}(\xi)_{,\xi} = -\Psi^{-1}\mathbf{Z}\Psi\mathbf{W}(\xi). \tag{3.96}$$

By comparing this with equation (3.91)

$$\xi\mathbf{W}(\xi)_{,\xi} = -\mathbf{S}\mathbf{W}(\xi), \tag{3.97}$$

where, $\mathbf{S} = \Psi^{-1}\mathbf{Z}\Psi$. Equation (3.97) has a solution of the form

$$\mathbf{W}(\xi) = \xi^{-\mathbf{S}}\mathbf{c}. \tag{3.98}$$

where $\mathbf{c}$ are the integration constants.

3.4.4.3 Solution for the displacement functions

The general solution of $\mathbf{X}(\xi)$ in equation (3.82) in terms of the block diagonalised Schur matrix obtained can be formed by substituting equation (3.98) into equation (3.93).

$$\mathbf{X}(\xi) = \Psi\xi^{-\mathbf{S}}\mathbf{c}. \tag{3.99a}$$

Substituting equations 3.89 and 3.86 in equation 3.99a, gives

$$\mathbf{X}(\xi) = \begin{bmatrix} \Psi_{\mathrm{u}}^{(\mathrm{n})} & \Psi_{\mathrm{u}}^{(\mathrm{p})} \\ \Psi_{\mathrm{q}}^{(\mathrm{n})} & \Psi_{\mathrm{q}}^{(\mathrm{p})} \end{bmatrix} \xi^{-\begin{bmatrix} \mathbf{S}_{\mathrm{n}} & 0 \\ 0 & \mathbf{S}_{\mathrm{p}} \end{bmatrix}} \begin{Bmatrix} \mathbf{c}_{\mathrm{n}} \\ \mathbf{c}_{\mathrm{p}} \end{Bmatrix}. \tag{3.99b}$$

Therefore the general solution for displacements and nodal forces is obtained from equation (3.99b) as

$$\mathbf{u}(\xi) = \Psi_{\mathrm{u}}^{(\mathrm{n})}\xi^{-\mathbf{S}_{\mathrm{n}}}\mathbf{c}_{\mathrm{n}} + \Psi_{\mathrm{u}}^{(\mathrm{p})}\xi^{-\mathbf{S}_{\mathrm{p}}}\mathbf{c}_{\mathrm{p}} \tag{3.100a}$$

$$\mathbf{q}(\xi) = \Psi_{\mathrm{q}}^{(\mathrm{n})}\xi^{-\mathbf{S}_{\mathrm{n}}}\mathbf{c}_{\mathrm{n}} + \Psi_{\mathrm{q}}^{(\mathrm{p})}\xi^{-\mathbf{S}_{\mathrm{p}}}\mathbf{c}_{\mathrm{p}} \tag{3.100b}$$

Eigenvalues with positive real parts are excluded to satisfy the finiteness of the solution at $\xi = 0$. Therefore solution of equation (3.82) for the bounded domain is

$$\mathbf{u}(\xi) = \Psi_{\mathrm{u}}\xi^{-\mathbf{S}_{\mathrm{n}}}\mathbf{c}_{\mathrm{n}}, \tag{3.101a}$$

$$\mathbf{q}(\xi) = \Psi_{\mathrm{q}}\xi^{-\mathbf{S}_{\mathrm{n}}}\mathbf{c}_{\mathrm{n}}, \tag{3.101b}$$

where, for convenience Schur vectors $\Psi_{\mathrm{u}}^{(\mathrm{n})}$ and $\Psi_{\mathrm{q}}^{(\mathrm{n})}$ are referred to as Ψ_{u} and Ψ_{q}, respectively. On the boundary, $\mathbf{u}\,(\xi = 0)$ becomes the nodal displacements

$$\mathbf{u}_{\mathrm{b}} = \Psi_{\mathrm{u}}\mathbf{c}_{\mathrm{n}}. \tag{3.102}$$

These nodal displacements on the boundary can then be used to evaluate the integration constants $\mathbf{c}_{\mathrm{n}}$ as

$$\mathbf{c}_{\mathrm{n}} = \Psi_{\mathrm{u}}^{-1}\mathbf{u}_{\mathrm{b}}. \tag{3.103}$$

Substituting equation (3.103) into equation (3.101a) the relationship between the radial displacement function $\mathbf{u}(\xi)$ and the nodal displacements $\mathbf{u}_{\mathrm{b}}$ can be obtained as

$$\mathbf{u}(\xi) = \Psi_{\mathrm{u}}\xi^{-\mathbf{S}_{\mathrm{n}}}\Psi_{\mathrm{u}}^{-1}\mathbf{u}_{\mathrm{b}}. \tag{3.104}$$

Substituting equation (3.101a) into equation (3.101b) produces the force-displacement relationship along the radial lines

$$\mathbf{q}(\xi) = \Psi_{\mathrm{q}}\xi^{-\mathbf{S}_{\mathrm{n}}}\Psi_{\mathrm{u}}^{-1}\mathbf{u}_{\mathrm{b}}. \tag{3.105}$$

On the boundary where $\xi = 0$, $\mathbf{q}_{\mathrm{b}} = \mathbf{q}\,(\xi = 1)$ and $\mathbf{u}_{\mathrm{b}} = \mathbf{u}\,(\xi = 1)$ represent the nodal forces on the boundary and nodal displacements, respectively. Equation (3.105) is expressed as

$$\mathbf{q}_{\mathrm{b}} = \mathbf{K}_{\mathrm{s}}\mathbf{u}_{\mathrm{b}}, \tag{3.106}$$

where $\Psi_{\mathrm{q}}\Psi_{\mathrm{u}}^{-1}$ are substituted by the static stiffness matrix $\mathbf{K}_{\mathrm{s}}$ of the subdomain. Therefore

$$\mathbf{K}_{\mathrm{s}} = \Psi_{\mathrm{q}}\Psi_{\mathrm{u}}^{-1}. \tag{3.107}$$

3.4.4.4 Solution in elastostatics

Considering the second term of equation (3.73) and substituting $\mathbf{u}(\xi)$ from equation (3.104) produces

$$\int_0^1 \delta\mathbf{u}^{\mathrm{T}}(\xi)(\xi\mathbf{F}_{\mathrm{b}}(\xi))\mathrm{d}\xi = \int_0^1 \left(\Psi_{\mathrm{u}}\xi^{-\mathbf{S}_{\mathrm{n}}}\Psi_{\mathrm{u}}^{-1}\delta\mathbf{u}_{\mathrm{b}}\right)^{\mathrm{T}}\xi\mathbf{F}_{\mathrm{b}}(\xi)\mathrm{d}\xi, \tag{3.108a}$$

$$\int_0^1 \delta\mathbf{u}^{\mathrm{T}}(\xi)(\xi\mathbf{F}_{\mathrm{b}}(\xi))\mathrm{d}\xi = \delta\mathbf{u}_{\mathrm{b}}^{\mathrm{T}}\int_0^1 \Psi_{\mathrm{u}}^{-\mathrm{T}}\xi^{-\mathbf{S}_{\mathrm{n}}^{\mathrm{T}}+\mathbf{I}}\Psi_{\mathrm{u}}^{\mathrm{T}}\mathbf{F}_{\mathrm{b}}(\xi)\mathrm{d}\xi. \tag{3.108b}$$

Substituting equation (3.108b) into equation (3.73) and invoking the arbitrariness of $\delta\mathbf{u}_{\mathrm{b}}$ yields

$$\mathbf{E}_0\mathbf{u}(\xi)_{,\xi}\,|_{\xi=1} + \mathbf{E}_1^{\mathrm{T}}\mathbf{u}_{\mathrm{b}} - \mathbf{F}_{\mathrm{t}} - \int_0^1 \Psi_{\mathrm{u}}^{-\mathrm{T}}\xi^{-\mathbf{S}_{\mathrm{n}}^{\mathrm{T}}+\mathbf{I}}\Psi_{\mathrm{u}}^{\mathrm{T}}\mathbf{F}_{\mathrm{b}}(\xi)\mathrm{d}\xi = 0. \tag{3.109}$$

Evaluating equation (3.75) at the boundary for the internal nodal force $\mathbf{q}_{\mathrm{b}} = \mathbf{q}(\xi = 1)$ gives

$$\mathbf{q}_{\mathrm{b}} = \mathbf{E}_0\mathbf{u}(\xi)_{,\xi}\,|_{\xi=1} + \mathbf{E}_1^{\mathrm{T}}\mathbf{u}_{\mathrm{b}}. \tag{3.110}$$

Substituting equation (3.110) in equation (3.109) generates

$$\mathbf{q}_{\mathrm{b}} = \mathbf{F}_{\mathrm{t}} + \int_0^1 \Psi_{\mathrm{u}}^{-\mathrm{T}}\xi^{-\mathbf{S}_{\mathrm{n}}^{\mathrm{T}}+\mathbf{I}}\Psi_{\mathrm{u}}^{\mathrm{T}}\mathbf{F}_{\mathrm{b}}(\xi)\mathrm{d}\xi. \tag{3.111}$$

This implies equilibrium is sought between internal nodal forces evaluated on the boundary and the applied tractions and body loads calculated at the nodes.

Introducing $\mathbf{F}_{\mathrm{bn}}$ as the equivalent nodal forces from body loads, then $\mathbf{F}_{\mathrm{bn}}$ can be written as

$$\mathbf{F}_{\mathrm{bn}} = \int_0^1 \Psi_{\mathrm{u}}^{-\mathrm{T}}\xi^{-\mathbf{S}_{\mathrm{n}}^{\mathrm{T}}+\mathbf{I}}\Psi_{\mathrm{u}}^{\mathrm{T}}\mathbf{F}_{\mathrm{b}}(\xi)\mathrm{d}\xi. \tag{3.112}$$

Therefore equation (3.111) can condensed to

$$\mathbf{q}_{\mathrm{b}} = \mathbf{F}_{\mathrm{t}} + \mathbf{F}_{\mathrm{bn}}. \tag{3.113}$$

Substituting for $\mathbf{q}_{\mathrm{b}}$ from equation (3.106) gives

$$\mathbf{K}_{\mathrm{s}}\mathbf{u}_{\mathrm{b}} = \mathbf{F}_{\mathrm{A}}. \tag{3.114}$$

Assembling equation (3.114) for all subdomains leads to the global equation system

$$\mathbf{K}_{\mathrm{G}}\mathbf{U} = \mathbf{P}, \tag{3.115}$$

where $\mathbf{K}_{\mathrm{G}}$ is the global stiffness matrix, $\mathbf{U}$ is the nodal displacement vector and $\mathbf{P}$ is the global load vector, respectively.

3.4.4.5 SBFEM Scaling Centre (SC) formulation

Equation (3.102) can also rewritten to calculate the strain at the scaling centre as

$$\varepsilon_{sc}(\xi,\eta) = \sum_{i=1}^{\mathrm{m}} \Psi_{\varepsilon \mathrm{i}}\mathbf{c}_{\mathrm{n}}, \tag{3.116}$$

where, m is the number of strain modes that yield to finite strains, and $\Psi_{\varepsilon \mathrm{i}}$ are the strain modes. $\Psi_{\varepsilon \mathrm{i}}$ depend only on the geometry of the subdomain and can be written in its expanded form as

$$\Psi_{\varepsilon \mathrm{i}}(\xi,\eta) = (\lambda_{\mathrm{i}}\mathrm{B}_1(\eta) + \mathrm{B}_2(\eta))\,\xi^{\lambda_{\mathrm{i}}-1}\varphi_{\mathrm{i}}. \tag{3.117}$$

Equation (3.117) shows that, at the scaling centre, i.e. $\xi = 1$, all the strain modes with $\lambda_i \neq 1$ vanish and only four strain modes with $\lambda_i \neq 1$ lead to a finite strain. Therefore to calculate the strain at the scaling centre for one subdomain

$$\varepsilon_{\mathrm{sc}} = \sum_{j=1}^{4} \left(\lambda_{\mathrm{i}} \mathrm{B}_1(\eta) + \mathrm{B}_2(\eta)\right) \varphi_{\mathrm{i}} \mathrm{c}_{\mathrm{i}}\,,\ (\lambda_{\mathrm{i}} = 1), \tag{3.118}$$

where c_i and φ_i are respectively the integration constants and modal displacements corresponding to λ_i. It is worth noting that equation (3.118) can be considered for any element belonging to one subdomain.

Consequently, the stresses at the scaling centre become

$$\sigma_{sc} = \mathbf{D}\varepsilon_{sc}. \tag{3.119}$$

3.5 Implicit damage formulation in SBFEM

If sufficient refinement is carried out in the DPZ, as an approximation the damage degree can be assumed to be uniform in one subdomain. Substituting equation (3.1) into equations (3.63a - 3.63c), we obtain

$$\mathrm{E}_0^{\mathrm{D}} = (1-\omega)\int_{-1}^{1} \mathrm{B}_1^{\mathrm{T}}(\eta)\mathbf{D}\mathrm{B}_1(\eta)\,|\mathbf{J}|\,d\eta = (1-\omega)\,\mathrm{E}_0 \tag{3.120a}$$

$$\mathrm{E}_1^{\mathrm{D}} = (1-\omega)\int_{-1}^{1} \mathrm{B}_2^{\mathrm{T}}(\eta)\mathbf{D}\mathrm{B}_1(\eta)\,|\mathbf{J}|\,d\eta = (1-\omega)\,\mathrm{E}_1 \tag{3.120b}$$

$$\mathrm{E}_2^{\mathrm{D}} = (1-\omega)\int_{-1}^{1} \mathrm{B}_2^{\mathrm{T}}(\eta)\mathbf{D}\mathrm{B}_2(\eta)\,|\mathbf{J}|\,d\eta = (1-\omega)\,\mathrm{E}_2 \tag{3.120c}$$

where $\mathbf{E}_0^{\mathrm{D}}$, $\mathbf{E}_1^{\mathrm{D}}$and $\mathbf{E}_2^{\mathrm{D}}$ are counterparts of the coefficient matrix with the damage variable ω of one subdomain.

Substituting equations (3.120a-3.120c) into equation (3.74) and (3.75), a similar matrix as equation (3.83) can be obtained

$$\mathbf{Z}^{\mathrm{D}} = \left\{ \begin{array}{cc} -\mathbf{E}_0^{-1}\mathbf{E}_1^{\mathrm{T}} & (1-\omega)^{-1}\mathbf{E}_0^{-1} \\ (1-\omega)\left(-\mathbf{E}_1\mathbf{E}_0^{-1}\mathbf{E}_1^{\mathrm{T}}\right) + \mathbf{E}_2 & \mathbf{E}_1\mathbf{E}_0^{-1} \end{array} \right\}. \tag{3.121}$$

Using the properties of matrix, it can be proven that

$$\mathbf{S}^{\mathrm{D}} = \begin{bmatrix} \mathbf{S}_{\mathrm{n}} & 0 \\ 0 & \mathbf{S}_{\mathrm{p}} \end{bmatrix} \tag{3.122a}$$

$$\mathbf{V}^{\mathrm{D}} = \begin{bmatrix} \mathbf{V}_{11} & (1-\omega)^{-1}\mathbf{V}_{12} \\ (1-\omega)\mathbf{V}_{21} & \mathbf{V}_{22} \end{bmatrix} \tag{3.122b}$$

Substituting equation (3.122a-3.122b) into equation (3.107), the stiffness matrix with damage is given as

$$\mathbf{K}^{\mathrm{D}} = (1-\omega)\mathbf{K}_s \tag{3.123}$$

It should be noted that equation (3.123) implies that, in each load step, the stiffness matrix of each subdomain can be calculated from the original stiffness matrix of the subdomain directly and the computational time for this function is negligible. Unchanged eigenvalues $[\lambda]$ and modal displacements φ_{i} also mean that the strain modes, i.e. equation (3.116), keep the same during damage. In each load step, only the integration constant **c** should be updated according to the displacement field by using equation (3.102) and subsequently the stress and strain field by using equations (3.118) and (3.119) respectively.

Assembling the stiffness matrix of all subdomains leads to the non-linear global equation system

$$\mathbf{KU} = \mathbf{P} \tag{3.124}$$

in which K is the global stiffness matrix with damage.

Equation (3.124) can be solved by means of implicit schemes, such as Newton-Raphson (NR) method and arc-length method [498], or explicit schemes [486, 499]. However, an implicit scheme can provide more control to obtain better convergence compared to a explicit scheme thus an implicit arc-length based scheme is adopted in this work.

3.6 Numerical solver

3.6.1 Modified Newton Raphson (m-NR) method

To maintain computational efficiency the m-NR method described in this work considers the secant stiffness only at the beginning of a load step. Compared to the conventional full NR method, this modified procedure reduces the computational burden on the requirement for decomposing the stiffness matrix in every iteration. A graphical representation of the method is as shown in figure 3.10.

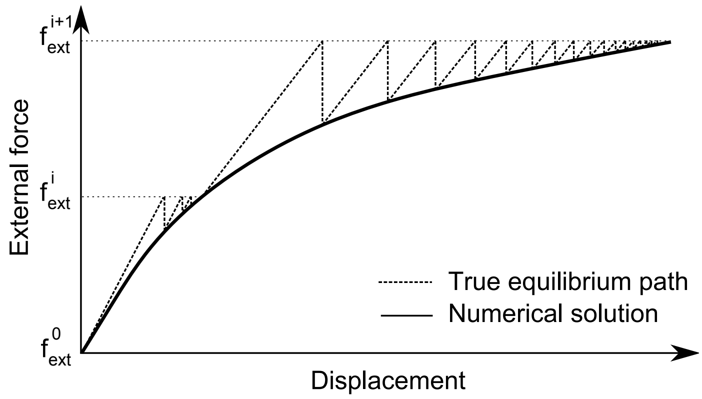

Figure 3.10. Graphical representation of the initial secant stiffness based m-NR iteration scheme.

In this discussion an “iteration” refers to a loop within the m-NR scheme and a “step” refers to an overall increment in the applied force field.

The m-NR procedure adopted in this work is a total-incremental method. Therefore in every iteration the total displacement increment within the step is calculated. This total displacement is then used to increment the total strain and then the total stress increment is calculated. Finally, the new stresses are computed by summing up the stresses at the start of the load step and the total stress increment.

To obtain a solution to equation (3.124) through an incremental iterative m-NR framework, first a set of linearised N equations are formed as shown in equation (3.125).

$$\mathbf{K}^i \Delta \mathbf{a}_n = \mathbf{P}_{ext}^{i+1} - \mathbf{P}_{int,n} \tag{3.125}$$

where $\mathbf{K}^i$ is the damaged stiffness matrix corresponding to the i^{th} load step, $\Delta\mathbf{a}$ is the nodal displacement increment corresponding to the n^{th} incremental NR iteration, $\mathbf{P}_{ext}^{i+1}$ is the external force vector at load step $(i+1)$, and $\mathbf{P}_{int,n}$ is the internal force vector for the n^{th} incremental NR iteration. The vector $\Delta\mathbf{a}_n$ is calculated by

$$\Delta \mathbf{a}_n = \left(\mathbf{K}^i\right)^{-1} \mathbf{r}_n, \tag{3.126}$$

where $\mathbf{r}_n$ is the residual vector for the

$$\mathbf{r}_n = \mathbf{P}_{ext}^{i+1} - \mathbf{P}_{int,n}. \tag{3.127}$$

From the incremental displacement vector $\Delta\mathbf{a}_n$ the strain increment $\Delta\varepsilon_n$ is calculated. Thereafter, using the stress-strain law, the stress increment $\Delta\sigma_n$ is calculated. The stresses formed after the the n^{th} incremental iteration can be therefore written as

$$\sigma_n = \sigma_0 + \Delta\sigma_n, \tag{3.128}$$

where σ_0 relates to the stresses calculated at the beginning of the load step from last the converged load step. The internal force vector $\mathbf{P}_{int,n}$ can be now calculated as

$$\mathbf{P}_{int,n} = \int_{\Omega} \mathbf{B}^{\mathrm{T}}(\xi,\eta)\,\sigma_n(\xi,\eta)\,d\Omega, \tag{3.129}$$

where $\mathbf{B}$ is the scaled boundary strain-displacement matrix given by

$$\mathbf{B}(\xi,\eta) = \Psi_{\varepsilon}(\eta)\,\xi^{-\mathbf{S}_{\mathrm{n}}-\mathbf{I}}\Psi_{\mathrm{u}}^{-1}, \tag{3.130}$$

and strain mode Ψ_ε is

$$\Psi_\varepsilon = \mathbf{B}_1 \Psi_{\mathrm{u}}^{-1} [-\mathbf{S}_n] + \mathbf{B}_2 (\eta) \Psi_{\mathrm{u}}. \tag{3.131}$$

The stresses σ_n is generally not in equilibrium with the external loads $\mathbf{P}_{ext}^{i+1}$. The internal and external force is checked by evaluating the norm of the residual load vector $\mathbf{r}_n$. If $\mathbf{r}_n$ does not meet a user defined tolerance limit (FTOL) a correction to the displacement increment is implemented by $\mathrm{d}\mathbf{a}_{n+1}$ as

$$\mathrm{d}\mathbf{a}_{n+1} = \left(\mathbf{K}^i\right)^{-1} \mathbf{r}_n, \tag{3.132}$$

where $\mathbf{r}_n^i$ is calculated as given in equation (3.127). The iterative procedure then proceeds to the next iterative displacement increment by updating $\Delta \mathbf{a}_n$ to $\Delta \mathbf{a}_{n+1}$

$$\Delta \mathbf{a}_{n+1} = \Delta \mathbf{a}_n + \mathrm{d}\mathbf{a}_{n+1} \tag{3.133}$$

This iterative process can be summarised as follows

$$\mathbf{r}_n = \mathbf{P}_{ext}^{i+1} - \mathbf{P}_{int,n} \tag{3.134a}$$

$$\mathrm{d}\mathbf{a}_{n+1} = \left(\mathbf{K}^i\right)^{-1} \mathbf{r}_n \tag{3.134b}$$

$$\Delta \mathbf{a}_{n+1} = \Delta \mathbf{a}_n + \mathrm{d}\mathbf{a}_{n+1} \tag{3.134c}$$

$$\Delta \varepsilon_{n+1} = \Delta \varepsilon \left(\Delta \mathbf{a}_{n+1}\right) \tag{3.134d}$$

$$\Delta \sigma_{n+1} = \Delta \sigma \left(\Delta \varepsilon_{n+1}\right) \tag{3.134e}$$

$$\sigma_{n+1} = \sigma_0 + \Delta \sigma_{n+1} \tag{3.134f}$$

Afterwords, $\mathbf{P}_{int,n+1}^i$ is calculated. The process repeats until convergence is obtained for the load step i.

3.6.2 Arc-length method

The NR method discussed earlier has a limited radius of convergence. To enlarge the radius of convergence, path-following techniques are used. Arc-length method is one of the advanced solution techniques that belong to this category of techniques. The load and the displacement control methods respectively keep the load and the displacement constant during increments. However in the arc-length method, the load-factor at each iteration is modified. This allows for the solution to follow a specified path until convergence is achieved. To attain this flexibility in solution convergence, the arc-length method treats the load increment λ as an additional unknown. The displacement solution space now contains $n+1$ unknowns when augmented with this new introduction. Since there are now $n+1$ unknowns and only n equations the system becomes indeterminate. The additional equation is supplied by path-following constraint [451]

$$g\left(\mathbf{a}_0, \lambda_0, \Delta\mathbf{a}, \Delta\lambda, \Delta l\right) = 0, \tag{3.135}$$

where $\mathbf{a}_0$ is the nodal displacement at the beginning of a generic load increment, λ_0 is the value of load parameter, $\Delta\mathbf{a}$ is the increment of nodal displacement, $\Delta\lambda$ is the increment of load parameter, and Δl is the path length increment that determines the size of the load increment.

The new equilibrium state of the $n+1$ equations can be determined by simultaneously solving

$$\begin{bmatrix} -\mathbf{r} \\ g \end{bmatrix} = \begin{bmatrix} \mathbf{0} \\ 0 \end{bmatrix}, \tag{3.136}$$

where $\mathbf{r}$ is the residual load vector. The standard NR procedure is adopted to solve equation (3.136). Therefore, to facilitate the NR process this non-linear system in equation

(3.136) is first linearised to give

$$\begin{bmatrix} \mathbf{P}_{int,n} + \frac{\partial \mathbf{P}_{int}}{\partial \mathbf{a}} \mathrm{d}\mathbf{a}_{n+1} \text{-} \lambda_n \mathbf{P}_{ext}^{i+1} - \mathrm{d}\lambda_{n+1} \mathbf{P}_{ext}^{i+1} \\ g_n + \left(\frac{\partial g}{\partial \mathbf{a}}\right)^{\mathrm{T}} \mathrm{d}\mathbf{a}_{n+1} + \left(\frac{\partial g}{\partial \lambda}\right) \mathrm{d}\lambda_{n+1} \end{bmatrix} = \begin{bmatrix} \mathbf{0} \\ 0 \end{bmatrix}. \tag{3.137}$$

The solution thus yields for $(\mathbf{a}, \lambda)$ at $n+1$ iteration

$$\begin{bmatrix} \mathbf{K} & -\mathbf{P}_{ext,}^{i+1} \\ \mathbf{h}^{\mathrm{T}} & s \end{bmatrix} \begin{bmatrix} \mathrm{d}\mathbf{a}_{n+1} \\ \mathrm{d}\lambda_{n+1} \end{bmatrix} = \begin{bmatrix} -\mathbf{r}_n \\ -g_n \end{bmatrix}. \tag{3.138}$$

where, $\mathbf{K}$ is the damage incorporated secant stiffness matrix, and array $\mathbf{h}$ and the scalar s defined as

$$\mathbf{h} = \frac{\partial g}{\partial \mathbf{a}} \tag{3.139}$$

$$s = \frac{\partial g}{\partial \lambda} \tag{3.140}$$

Equation (3.138) destroys the symmetry and the banded nature of the secant stiffness matrix $\mathbf{K}$. Therefore, Crisfield and Ramm [80, 500] proposed a partitioned procedure that leads to a two-stage solution procedure.

To complement this partitioned procedure the following two arrays are computed first.

$$\mathrm{d}\mathbf{a}^{\mathbf{I}}{}_{n+1} \;=\; \left(\mathbf{K}^i\right)^{-1} \mathbf{P}_{ext}^{i+1} \;, \tag{3.141}$$

$$\mathrm{d}\mathbf{a}^{\mathbf{II}}{}_{n+1} \;=\; \left(\mathbf{K}^i\right)^{-1} \mathbf{r}_n \;. \tag{3.142}$$

Considering the first equation of equation (3.137), the new estimate for the displacement increment can be written as

$$\mathrm{d}\mathbf{a}_{n+1} \;= \mathrm{d}\lambda_{n+1} \mathrm{d}\mathbf{a}_{n+1}^{\mathrm{I}} + \; \mathrm{d}\mathbf{a}_{n+1}^{\mathrm{II}} \;. \tag{3.143}$$

Also considering the second equation of equation (3.137), the new estimate for the load increment is given by

$$\mathrm{d}\lambda_{n+1} \quad = -\frac{g_n + \mathbf{h}^{\mathrm{T}}\mathrm{d}\mathbf{a}_{n+1}^{\mathrm{II}}}{s + \mathbf{h}^{\mathrm{T}}\mathrm{d}\mathbf{a}_{n+1}^{\mathrm{I}}}. \tag{3.144}$$

A widely used constraint function is the spherical arc-length constraint [80]

$$g = \Delta\mathbf{a}_{n+1}^{\mathrm{T}}\Delta\mathbf{a}_{n+1} + \beta^2\Delta\lambda_{n+1}^2\left(\mathbf{P}_{ext}^{i+1}\right)^{\mathrm{T}}\mathbf{P}_{ext}^{i+1} - \Delta l^2, \tag{3.145}$$

where β is a user-specified value. This parameter is related to the contributions that stem from the displacement degrees of freedom and the load increment.

If after the first iteration the direction of the tangent normal is kept constant to the hyperplane used to intersect the equilibrium path, equation (3.138) can be written as

$$\Delta\mathbf{a}_1^{\mathrm{T}}\Delta\mathbf{a}_{n+1} + \beta^2\Delta\lambda_1\Delta\lambda_{n+1}\left(\mathbf{P}_{ext}^{i+1}\right)^{\mathrm{T}}\mathbf{P}_{ext}^{i+1} - \Delta l^2 = 0. \tag{3.146}$$

Similarly, the preceding iteration can be written as

$$\Delta\mathbf{a}_1^{\mathrm{T}}\Delta\mathbf{a}_n + \beta^2\Delta\lambda_1\Delta\lambda_n\left(\mathbf{P}_{ext}^{i+1}\right)^{\mathrm{T}}\mathbf{P}_{ext}^{i+1} - \Delta l^2 = 0. \tag{3.147}$$

By substituting equation (3.146) from equation (3.147), Δl can be eliminated to get

$$\Delta\mathbf{a}_1^{\mathrm{T}}\mathrm{d}\mathbf{a}_{n+1} + \beta^2\Delta\lambda_1\mathrm{d}\lambda_{n+1}\left(\mathbf{P}_{ext}^{i+1}\right)^{\mathrm{T}}\mathbf{P}_{ext}^{i+1} = 0. \tag{3.148}$$

Substituting equation (3.148) in equation (3.144)

$$\mathrm{d}\lambda_{n+1} \quad = -\frac{\Delta\mathbf{a}_1^{\mathrm{T}}\mathrm{d}\mathbf{a}_{n+1}^{\mathrm{II}}}{\Delta\mathbf{a}_1^{\mathrm{T}}\mathrm{d}\mathbf{a}_{n+1}^{\mathrm{I}} + \beta^2\Delta\lambda_1\left(\mathbf{P}_{ext}^{i+1}\right)^{\mathrm{T}}\mathbf{P}_{ext}^{i+1}}. \tag{3.149}$$

The arc-length incorporated m-NR is setup in such a way when convergence is found to be difficult for a particular load step the arc-length is automatically halved and the respective load step is repeated. To avoid excessive number of iterations, the maximum number of iterations is fixed. Numerical experience has shown it is optimal to maintain this limit between 30-40 iterations.

The overall framework setup within the SBFE programme is a follows:

1. Pre-process and loop over all subdomains and store the information below in the system memory:

    (a) Compute the original stiffness matrix K_s for each subdomain using equation (3.114);

    (b) Initialize the equivalent strain $\widetilde{\varepsilon}$, internal variable κ and damage variable ω at the scaling centre for each subdomain;

    (c) Compute the weight matrix by using equations (3.14) and (3.15). It should be noted that, considering the damage is assumed to be uniform, the area of each subdomain and the distance between any two scaling centres are used to compute the weight function; and

    (d) Compute the strain modes of each subdomain by using equation (3.116).

2. For $(i+1)^{th}$ displacement step and n^{th} NR iteration, loop over all subdomains:

    (a) Assemble the damaged stiffness matrices (equation (3.123)) based on the damage variables of previous step and the external load vector to obtain the global equation system and solve it (equation (3.124));

    (b) Compute the integration constants $\mathbf{c}_{i+1}$ according to the boundary conditions of the present step by using equation (3.102) ;

    (c) Compute the equivalent strain $\widetilde{\varepsilon}$ by using equations (3.8), (3.9), (3.10) or (3.13) considering the strain at the scaling centre of the present step;

    (d) Modify $\widetilde{\varepsilon}$ by non-local weight matrix;

    (e) Update κ according to loading-unloading conditions, i.e. equation (3.3);

    (f) Compute the damage variables ω according to the damage evolution law (equation (3.5), (3.6) or (3.7)) and save it for the next step;

(g) Calculate $\sigma_{sc,n}^{i+1}$ using equation (3.119); and

(h) Compute internal force vector $(\mathbf{P}_{int,n})$

3. Check convergence, $\left\|\mathbf{P}_{ext}^{i+1} - \mathbf{P}_{int,n}\right\| \leq \text{FTOL}$, where $\mathbf{P}_{ext}^{i+1}$ and FTOL are the external force vector and a user defined force tolerance parameter, respectively.

    (a) If converged; increment the load step and go to step 2(a).

    (b) If not converged; move to arc-length m-NR iterations step 4 .

4. Arc-length incorporated m-NR.

    (a) initialise the data for the loading step $\Delta\mathbf{a}_0 = 0$.

    (b) Solve the linear systems $\mathrm{d}\mathbf{a^I}_{n+1} = \left(\mathbf{K}^i\right)^{-1}\mathbf{P}_{ext}^{i+1}$ and $\mathrm{d}\mathbf{a^{II}}_{n+1} = \left(\mathbf{K}^i\right)^{-1}\mathbf{r}_n$.

    (c) Compute $\mathrm{d}\lambda_{n+1}$ via a constraint equation. Refer to equation (3.149).

    (d) Compute $\Delta\mathbf{a}_{\mathrm{n+1}} = \Delta\mathbf{a}_{\mathrm{n}} + \mathrm{d}\lambda_{n+1}\mathrm{d}\mathbf{a}_{n+1}^{\mathrm{I}} + \mathrm{d}\mathbf{a}_{n+1}^{\mathrm{II}}$.

    (e) Compute $\Delta\varepsilon_{n+1}$ for each integration point $\Delta\mathbf{a}_{n+1} \rightarrow \Delta\varepsilon_{n+1}$.

    (f) Compute $\Delta\sigma_{n+1}$ for each integration point $\Delta\varepsilon_{n+1} \rightarrow \Delta\sigma_{n+1}$.

    (g) Add $\Delta\sigma_{n+1}$ to σ_0 for each integration point $\sigma_{n+1} = \Delta\sigma_0 + \Delta\sigma_{n+1}$.

    (h) Compute internal force vector $(\mathbf{P}_{int,n+1})$.

5. Check convergence, $\left\|\mathbf{P}_{ext}^{i+1} - \mathbf{P}_{int,n+1}\right\| \leq FTOL$.

    (a) If converged; increment the load step and go to step 2(a).

    (b) If not converged and $n <$ NMAX; repeat arc-length incorporated m-NR from step 4(a), where NMAX is a user defined maximum number of arc-length incorporated m-NR iterations.

    (c) If not converged and $n =$ NMAX; discard analysis step, halve the load step length, and restart analysis from step 2(a).

3.7 Numerical simulations

The first two numerical examples uniaxial tension test problem (section 3.7.1), and the three point bending beam problem (section 3.7.2) compare outputs of the SC formulation against the FGP formulation in SBFEM, with the FEM and against respective references in literature. These two examples also investigate the behaviours of local and non-local damage analysis formulations.

The focus then moves primarily towards the non-local damage analysis framework. Therefore the L-shaped specimen (section 3.7.3) and 2D damage characterization in shear band (section 3.7.4) do not investigate the damage localisation trends. However, the results compare the SC formulation to the FGP formulation in SBFEM, to the FEM solution, and to published literature as before.

The in house finite element analysis is conducted with elements modelled as a standard bilinear quadrilateral element with 2×2 integration points. Whereas, for the SBFEM analysis the polygon formulation is employed over each polygon. The polygon boundary is discretised using 1D shape functions along the boundary to approximate the displacement field.

3.7.1 Uniaxial tension test

This example is extracted from the MSc Thesis by Maravalalu [499] where non-local damage models are considered for analysing the effects of impact loads on concrete. The objective of this example is to demonstrate the localization effects of a local damage model in uniaxial loading conditions and then in the latter part of the example the non-local formulation is presented to exemplify its affect in regularization. The example also compares the effectiveness of the SC formulation to the FGP formulation in SBFEM.

The dimensions of the specimen shown in figure 3.11 are selected as considered in the reference [499]. The length of the member is 100 mm with depth equal to 10 mm in dimension . The cross sectional area of the specimen is assumed to be $10\,\text{mm}^2$. The shaded central element in figure 3.11 represent the imperfection introduced in the specimen.

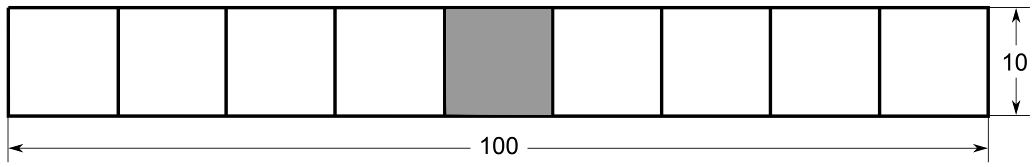

Figure 3.11. Specimen dimensions (mm) used in the 2D local and non-local damage analysis of a uniaxial tension test specimen. Shaded area represent the imperfection.

To implement the loading conditions the left side of the member is encastred and pulled by a force **P** from the unrestrained edge as shown in figure 3.12.

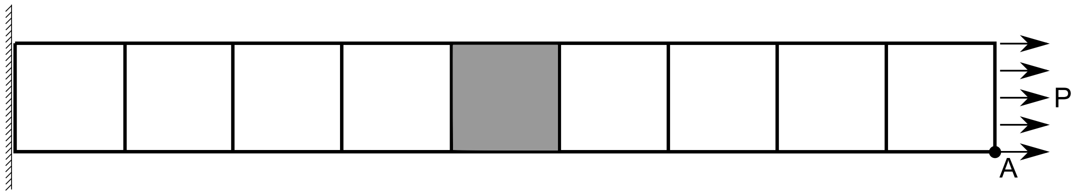

Figure 3.12. Boundary conditions considered in the 2D local and non-local damage analysis of a uniaxial tension test specimen.

The modulus of elasticity for this problem is taken as 30 GPa and Poisson's ratio is considered to be 0.0, where plain strain conditions are assumed. The damage evaluation law is considered as in equation (3.7) with $\alpha = 0.95$ and $\beta = 100$. With reference to equation (3.7) the member is modelled such that the central element has a weaker damage initiation threshold (ε_0) of 145×10^{-6} and the rest of the elements with $\varepsilon_0 = 150 \times 10^{-6}$. The 1D stress-strain variation for the weaker material with respect to the adopted material and damage parameters is shown in figure 3.13.

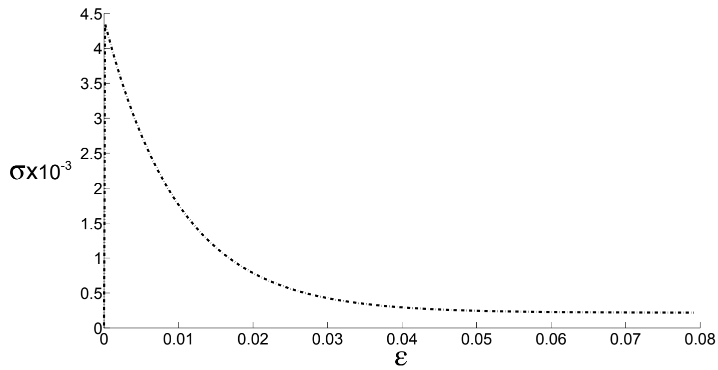

Figure 3.13. 1D element stress (GPa) vs strain profile considered in the 2D uniaxial tension test specimen with respect to the softening law given in equation (3.7) for the weak material with $\varepsilon_0 = 145 \times 10^{-6}$.

The equivalent strain $\widetilde{\varepsilon}$ is calculated according to the Mazar's definition given in equation (3.9).

As mentioned earlier the primary objective of this problem is to demonstrate the mesh sensitivity of local damage models and investigate the accuracy of the SC formulation against the finite element formulation and the SBFE FGP formulation.

Each analysis is run using a force controlled m-NR method coupled with the arc length algorithm. The initial load step is set to 0.001 kN.

3.7.1.1 Local formulation

Firstly, the local damage formulation is modelled considering three different meshes as shown in figure 3.14. Mesh 1, 2 and 3 consist of 21, 51 and 81 elements, respectively. The elements are equally distributed along the length of the model.

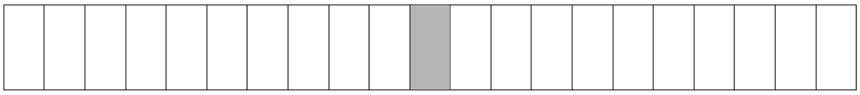

(a) Mesh 1-21 Elements

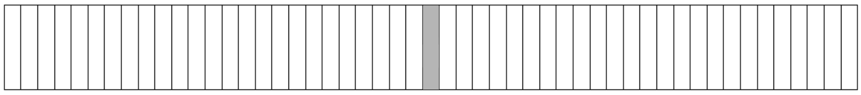

(b) Mesh 2-51 Elements

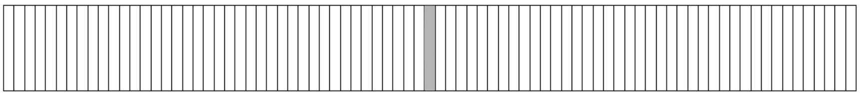

(c) Mesh 3-81 Elements

Figure 3.14. Finite element meshes used in the local analysis of the 2D uniaxial tension specimen.

The load-displacement results obtained for the finite element formulation is given in figure 3.15.

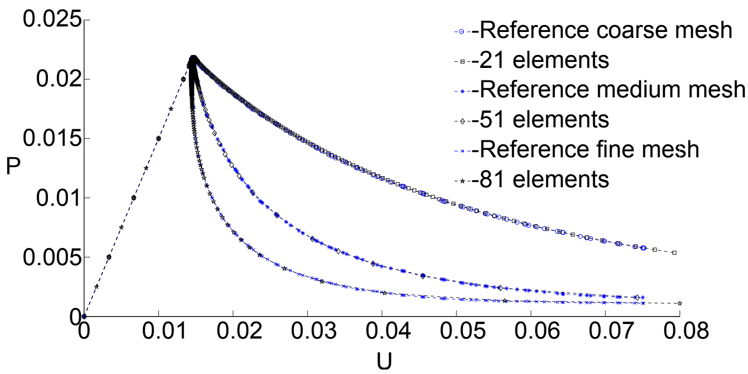

Figure 3.15. Force (kN) vs displacement (mm) curve at node ‘A’ for the FEM-based local damage analysis of the 2D uniaxial tension test specimen.

The results are compared against the reference solution modelled, with identical material and damage parameters. The FEM force-displacement output obtained in figure 3.15 shows good agreement to that of the reference FEM solution.

With use of the same damage parameters and material properties the analysis is next run using the SBFEM FGP formulation and the results are as produced in figure 3.16.

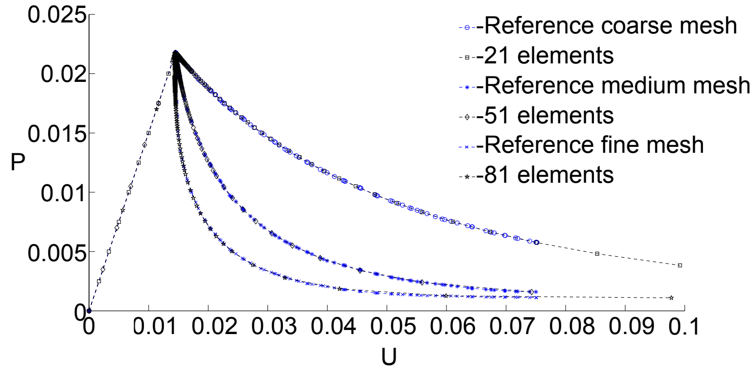

Figure 3.16. Force (kN) vs displacement (mm) curve at node 'A' for the SBFEM-based local damage analysis of the 2D uniaxial tension test specimen.

It is apparent the results obtained through the FGP formulation conforms well with the reference output similar to the observations made for the finite element outputs.

The weak element in the three meshes in figure 3.14 is located the midpoint of the bar. The localised strain in the weaker element increases as the meshes are refined since for smaller elements the deformation is localized to a smaller width. Therefore figures 3.15 and 3.16 display varying force-displacement plots as the larger value of localized strains leads to quicker damage evolution. Overall, the fracture energy dissipation reduces with decrease in the mesh size. The strain at which damage initiates in the central element is 145×10^{-6}. Therefore the force observed in the model at point 'A' can be calculated by $(\mathrm{E} \times \varepsilon \times A)/2$ and is equal to 0.02175 kN . The same value is attained in the analysis as the maximum load capacity of the specimen, validating the formulation.

As a final comparison, the results of the computationally efficient SC formulations are individually compared to the respective finite element and the FGP formulation. In figure 3.17 the force vs displacement outputs for the SC formulation of the three meshes are plotted against the outputs from the FEM and the FGP SBFEM formulation.

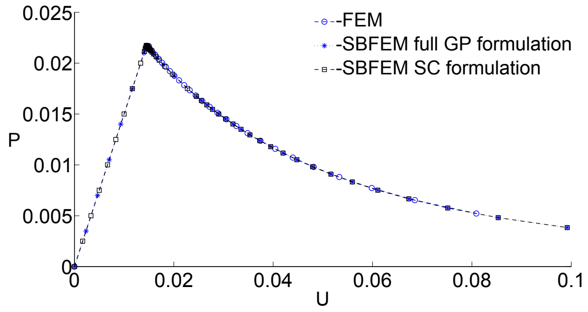

(a) Mesh 1-21 elements

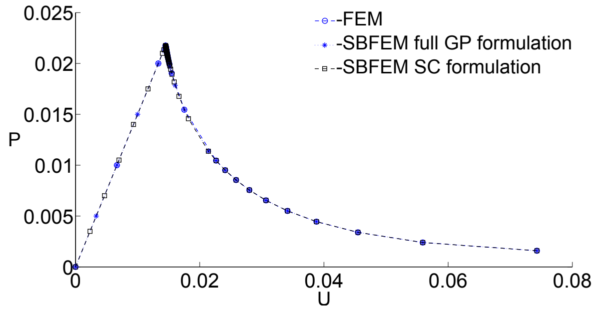

(b) Mesh 1-51 elements

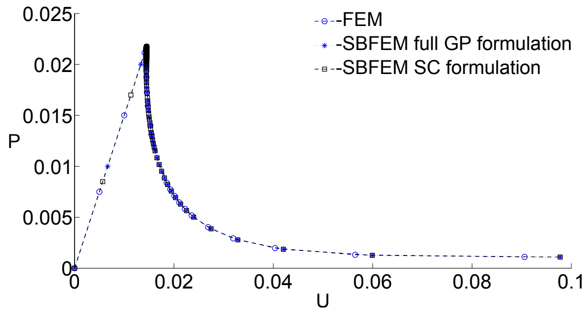

(c) Mesh 3-81 elements

Figure 3.17. Force (kN) vs displacement (mm) output at node 'A' for the 2D uniaxial tension test specimen in axial tension. The SC formulation is compared to the FEM and the FGP formulation.

All three formulations produce comparatively similar outputs almost identical to each other, thus validating the accuracy of the three approaches.

In numerical modelling the descending branches of the load-displacement curve makes the underlying PDEs ill-posed. This in turn causes the loss of ellipticity of the governing differential equations. Ill-posed boundary value problems problems can produce solutions dependent on the given data. This effect can be seen in figures 3.15 and 3.16 where decreasing mesh sizes produce steeper displacement profiles in the descending branch of the force-displacement plots in the post peak regime. Thus, when moving from a lower number of elements to a higher number of elements (21 to 81) the reduction in the dissipated fracture energy is shown in local damage evaluation schemes. The uniqueness of the solutions are determined by the localised strains which limits the damage to the initially damaged elements. These localisation effects bring about numerical convergence issues with the steeper descending gradients. The worst concern however is the incorrect description of the Damage Process Zone (DPZ) width, as it is dependent on the chosen mesh size.

A simple and affective way to overcome mesh sensitivity and related ill-effects is to adopt a non-local formulation.

3.7.1.2 Non-local formulation

In the non-local formulation the tension specimen shown in figure 3.12 is modelled using 4 different meshes as shown in figure 3.18. Mesh 2, 3, 4 and 5 consist of 51, 81,101 and 201 elements, respectively. Similar to the earlier local damage formulation the meshes are obtained by equally distributing the elements along the length of the specimen.

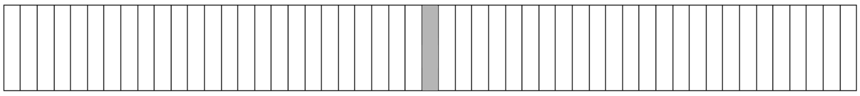

(a) Mesh 2 - 51 Elements

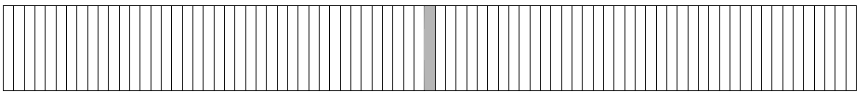

(b) Mesh 3 - 81 Elements

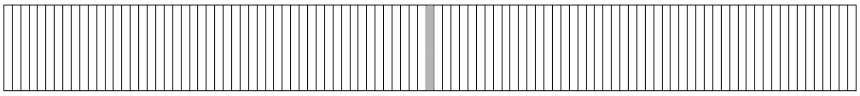

(c) Mesh 4 - 101 Elements

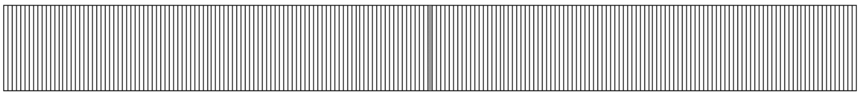

(d) Mesh 5 - 201 Elements

Figure 3.18. Finite element meshes used in the non-local analysis of the 2D uniaxial tension specimen.

To obtain the regularized results independent of the mesh configuration the Gaussian non-local averaging function given in equation (3.17) is used with the interaction radius R set to 6 mm. It is necessary to adopt the interaction radius larger than the largest mesh size. The material properties and the damage evolution are maintained from the local formulation in section 3.7.1.1.

The results obtained through FEM and the SBFEM FGP formulation are given in figures 3.19 and 3.20, respectively. The load-displacement outputs are recorded on the unrestrained end as shown in figure 3.12.

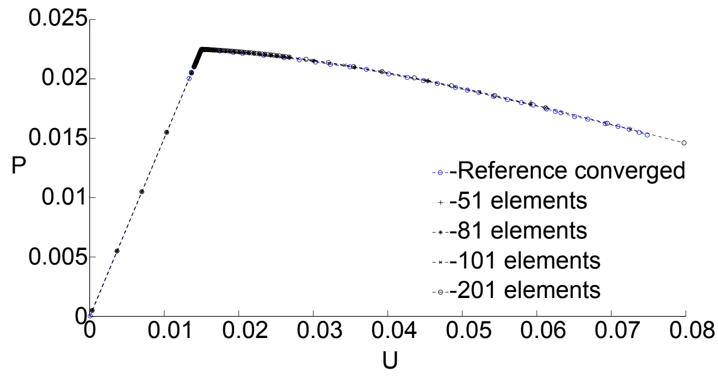

Figure 3.19. Force (kN) vs displacement (mm) curve at node 'A' for the FEM-based non-local damage analysis of the 2D uniaxial tension test specimen.

The regularisation of strains delivers mesh independent force-displacement outputs as seen in figures 3.19 and 3.20. In order to obtain almost identical outputs irrespective of the mesh size the strains and deformation in the continuum must also show converging results irrespective of mesh size.

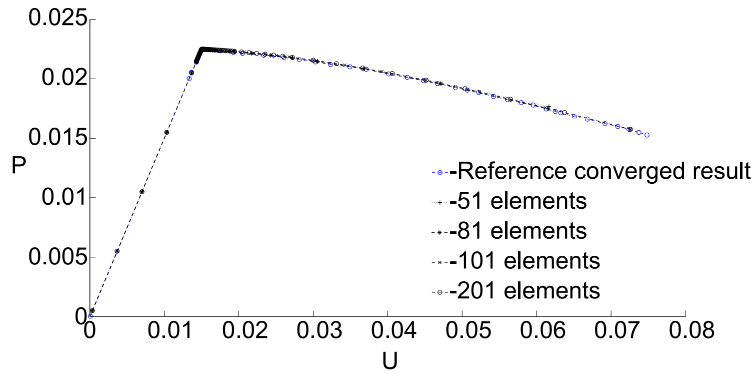

Figure 3.20. Force (kN) vs displacement (mm) curve at node 'A' for the SBFEM-based non-local damage analysis of the 2D uniaxial tension test specimen.

A comparison of the non-local SC formulation alongside the FGP formulation and finite element solution (see figure 3.21) shows that all three formulations yield comparatively similar results.

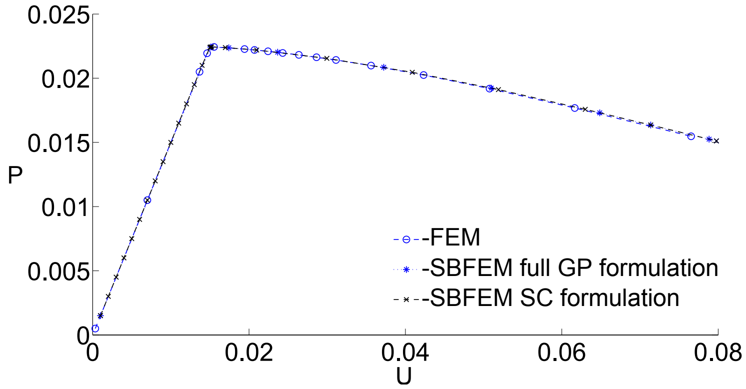

Figure 3.21. Force (kN) vs displacement (mm) output at node ‘A’ for the 2D non-local damage response obtained for a test specimen in axial tension. The SC formulation is compared to the FEM and the SBFE FGP formulation. The mesh considered consist of 201 elements.

As expected the force-displacement plots in figures 3.19 and 3.20 have nearly identical post peak behaviour for all four mesh configurations. They converge as the element size decreases, as the gradient of the strains are better captured with higher number of elements. Hence we can state that this model is mesh independent and has many advantages in comparison with the mesh dependent local models. The mesh independent behaviour is caused by the use of non-local equivalent strains in lieu of their local counterparts. The weighted average formulation of local strains delays the strain concentration in critical elements. This leads to a delay in strain accumulation when using the non-local models. Theoretically, this delay is longer with larger non-local length scales as the influence of the undamaged elements that exhibit unloading is greater.

The contour plots obtained in the simulation for horizontal displacement, x-directional strain, x-directional stress, and for the damage progression are shown in figures 3.22-3.25. These contours are captured at the peak load (0.02249 kN) when the unrestrained edge displacement is 0.01538 mm and just after peak load (0.0191 kN) when displacement is 0.05139 mm, refer figure 3.20.

The horizontal displacement (u_x) contour shown in figure 3.22a depict the linear increase in the displacement field till the peak load is attained before any damage initiates in the centrally located weak element. Thereon as seen in figure 3.22b the non-linear distribution in the displacement field is characteristic of the effects of post peak damage.

(a) Horizontal displacement (u_x) contour for mesh 5. The unrestrained edge displacement is 0.01538 mm.

(b) Horizontal displacement (u_x) contour for mesh 5. The unrestrained edge displacement is 0.05139 mm.

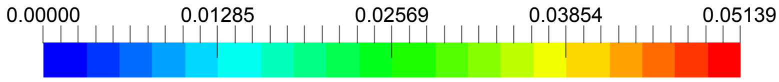

Figure 3.22. Horizontal displacement (u_x) contours obtained for the non-local damage analysis of the 2D uniaxial tension test specimen. Units:mm. Results obtained for mesh 5 consisting of 201 elements.

The strain (ε_{xx}) contours shown in figure 3.23 follow a similar pattern to the displacement field where uniform strain is observed in elements prior to the damage initiation (figure 3.23a). After the initiation of damage, the central portion of the specimen shows the higher strains observed in the weaker element, see figure 3.23b. In order to obtain almost identical force-displacement outputs irrespective of the different mesh sizes the strain localization width shown in figure 3.23b is constant for all 4 mesh configurations.

(a) Strain (ε_{xx}) contour for mesh 5. The unrestrained edge displacement is 0.01538 mm.

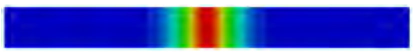

(b) Strain (ε_{xx}) contour for mesh 5. The unrestrained edge displacement is 0.05139 mm.

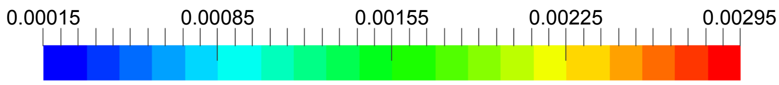

Figure 3.23. Strain (ε_{xx}) contours obtained for the non-local damage analysis of the 2D uniaxial tension test specimen. Results obtained for mesh 5 consisting of 201 elements.

The stress (σ_{xx}) contour shown in figure 3.24 depicts the softening behaviour observed in the specimen. Moving from figure 3.24a to 3.24b damage growth occurs which consequently reduce the stresses due to the stiffness degradation.

(a) Stress (σ_{xx}) contour for mesh 5. The unrestrained edge displacement is 0.01538 mm.

(b) Stress (σ_{xx}) contour for mesh 5. The unrestrained edge displacement is 0.05139 mm.

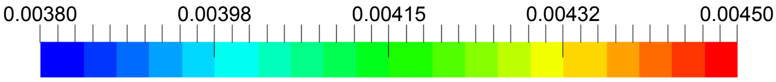

Figure 3.24. Stress (σ_{xx}) contours obtained for the non-local damage analysis of the 2D uniaxial tension test specimen. Units:MPa. Results obtained for mesh 5 consisting of 201 elements.

Damage develops in the specimen when the the strain in the predefined weak element exceeds the tensile strain at peak load. The damage contours shown in figure 3.25 depict the damage developed at an instance after the peak load where the effects of damage is regularised over the central portion of the specimen. This damage profile is consistent between all 4 meshes in order to produce the mesh independent force-displacement output. This guarantees the fracture energy to be same irrespective of the mesh size.

(a) Damage (ω) contour for mesh 5. The unrestrained edge displacement is 0.01538 mm.

(b) Damage (ω) contour for mesh 5. The unrestrained edge displacement is 0.05139 mm.

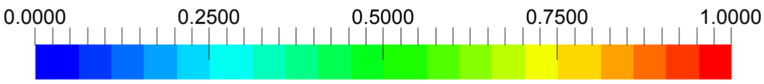

Figure 3.25. Damage (ω) contours obtained for the non-local damage analysis of the 2D uniaxial tension test specimen. Results obtained for mesh 5 consisting of 201 elements.

3.7.2 Three point bending beam

The biaxial bending beam analysis presented in this section is extracted from [501] and [495]. With reference to these publications the model dimensions are considered as given in figure 3.27. These dimensions also correspond to the experiments performed by Kormeling and Reinhardt [502] and the numerical simulations conducted by Grassl et al. [503] with a plastic damage model. .

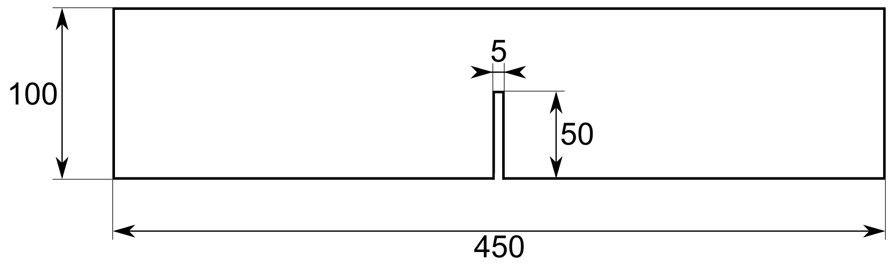

Figure 3.26. Specimen dimensions (mm) for the 2D biaxial bending test.

The specimen dimensions are selected as given in figure 3.26. The length of the beam is 450 mm with a depth and breadth of 100 mm. A central notch of 5 mm is modelled at the centre of the beam. The depth of the notch extends to half way up the beam with 50 mm in dimension. The loading setup replicates a three point bending mechanism as shown in figure 3.27. The bottom left corner of the beam is pinned and thus is restrained in movement in x and y directions. The bottom right corner of the beam is provided with a roller support and thereby is restrained in movement in y direction. A central concentrated load P is applied at the centre of the beam to analyse the structural response.

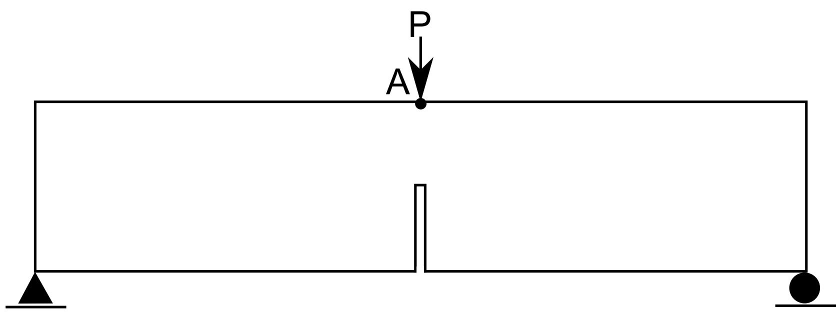

Figure 3.27. Loading and boundary conditions for the 2D biaxial bending test.

The mesh geometry is in accordance to the references mentioned, with a finer mesh around the notch and a coarse mesh away from the notch, refer figure 3.28. In this case three meshes are used with relative small size subdomains, located in a narrow band around the vertical axis of symmetry, where the strains are expected to localise (refer to figure 3.28a-3.28c). The smallest subdomains in mesh 1, mesh 2 and mesh 3 are 5 mm, 1.667 mm and 0.556 mm, respectively.

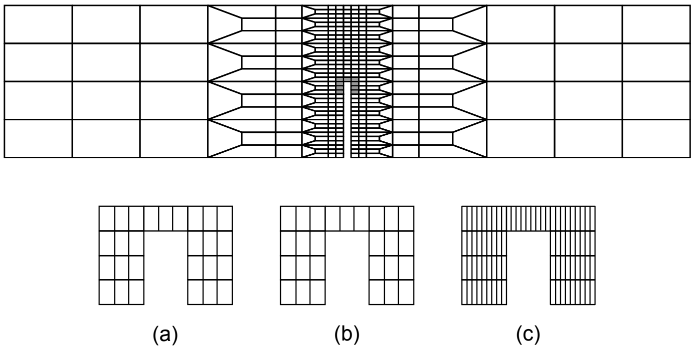

Figure 3.28. Mesh configurations for the 2D biaxial bending test. Zooming the section of the mesh marked in grey show the variation between three meshes. (a) Mesh 1-smallest element size 5 mm, (b) mesh 2-smallest element size 1.667 mm, and (c) mesh 3-smallest element size 0.5556 mm.

Similar to the uniaxial tension problem discussed in section 3.7.1 the analysis is run using a force controlled m-NR method coupled with the arc length method. Each analysis is run using a force controlled algorithm. The initial load step is set to 0.01 kN.

Here too the objective of the analysis is to demonstrate the mesh sensitivity of local damage models and also to explore the accuracy of the SC formulation to that of the finite element formulation and the SBFE FGP formulation.

3.7.2.1 Local formulation

The material properties; modulus of elasticity and Poisson's ratio are taken as 20 GPa and 0.2, respectively. An exponential damage model given in equation (3.6) is considered for the softening law with ε_0 set to 120×10^{-6} and strain at which material is fully damaged ε_f set to 7.0×10^{-3}. The modified von Mises definition given in equation (3.10) is adopted to calculate the equivalent strain parameter with k set to 10 to emulate concrete material properties.

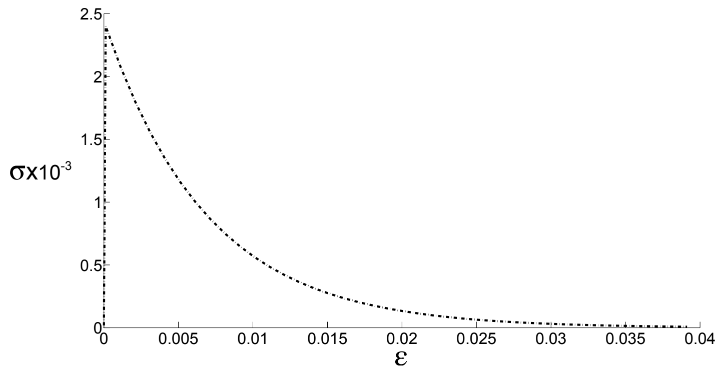

Figure 3.29. 1D element stress (GPa) vs strain profile considered in the 2D local damage simulation of the three point bending beam test with respect to the softening law given in equation (3.6).

With the use of mesh 1 provided in figure 3.28, results are obtained for force-displacement variation at point A in figure 3.26 for both FEM and SBFEM SC formulation (refer figure 3.30). The simulation attains its peak carrying capacity at a displacement value of 0.097 mm.

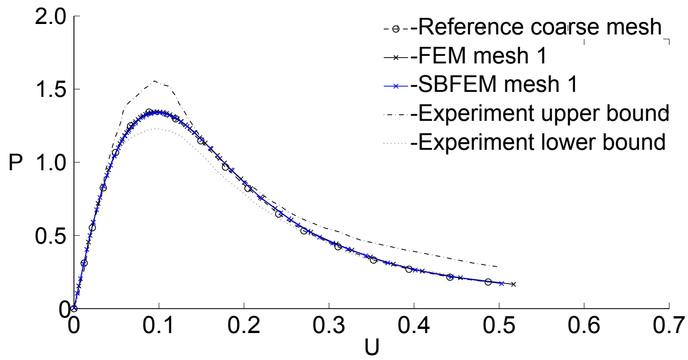

Figure 3.30. Force (kN) vs displacement (mm) curve for the local damage simulation of the three point bending beam test. Mesh 1 considered.

With reference to figure 3.30 there is good agreement in the analysis run through FEM and SBFEM with the given reference result. It is also evident that the simulated peak load is within the experimental bounds and the load-displacement curve favourably agrees with experimental data.

Next an attempt is made to show the variation of the result with respect to varying mesh configuration. Therefore as shown in figure 3.28 three meshes are considered with maximum mesh size of 5 mm and a minimum mesh size of 0.5556 mm. The load-displacement variation at point A in figure 3.26 for both FEM and SBFEM FGP formulation are given in figures 3.31 and 3.32, respectively).

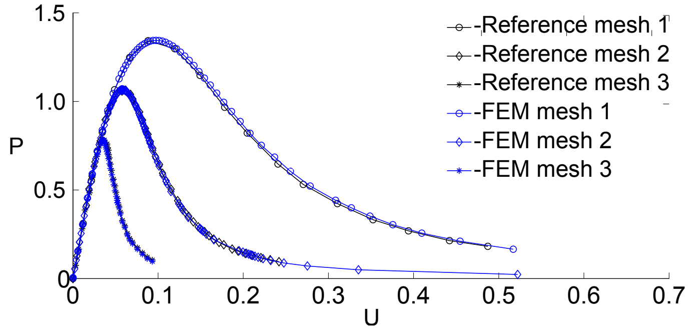

Figure 3.31. Force (kN) vs displacement (mm) curve for the FEM-based local damage simulation of the three point bending beam test compared with the reference [501].

Results for both FEM and SBFEM are verified by comparing with the outputs presented in [501], the results are of satisfactory agreement.

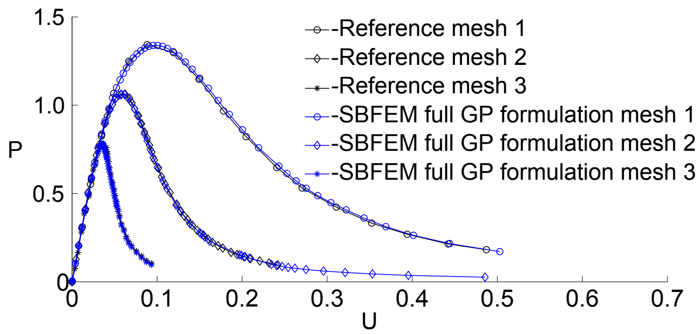

Figure 3.32. Force (kN) vs displacement (mm) curve for the SBFEM-based local damage simulation of the three point bending beam test compared with the reference [501].

In figure 3.33 the load-displacement outputs for the SC formulation of the three meshes are plotted against the outputs from the FEM and the FGP SBFEM formulation. It can be observed that all three formulations produce very similar plots.

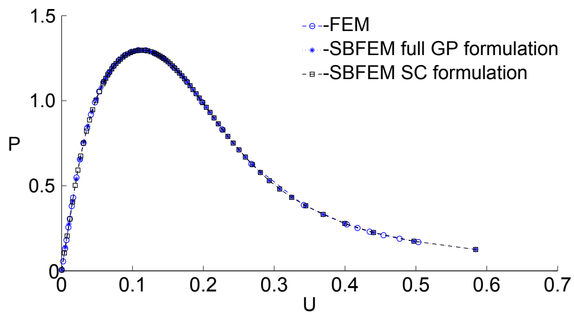

(a) Mesh 1.

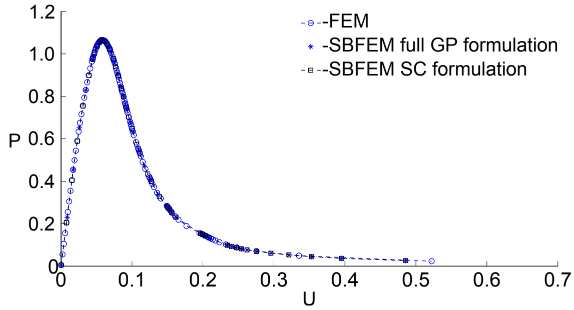

(b) Mesh 2.

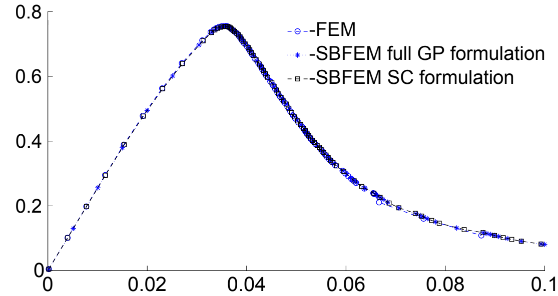

(c) Mesh 3.

Figure 3.33. Force (kN) vs displacement (mm) output for the 2D local response of the three point bending beam. The SC formulation is compared to the FEM and the SBFE FGP formulation.

With reference to figures 3.31 and 3.32, although the material and damage parameters E, ν, ε_0, ε_f and k are kept constant between the three different analysis, as the mesh is refined, the results show considerable variations. The finer element sizes in the DPZ around the axis of symmetry localise damage to the refined elements creating a disparity between the load-displacement diagrams between the respective meshes. The dependence of the total dissipated energy on mesh refinement is unacceptable. Therefore the following section explores the effect of regularisation to negate the ill effects of damage localization.

3.7.2.2 Non-local formulation

The three different meshes shown in figure 3.28 are rerun in the non-local analysis scheme with an equivalent strain based integral-type isotropic damage model. Here, the local strain variables are substituted by their non-local counterpart obtained by a weighted average technique.

With respect to the exponential damage model given in equation (3.6), ε_0 is set to 90×10^{-6} and strain at which material is fully damaged ε_f is set to 7.0×10^{-3}. The 1D element stress-strain behaviour with respect to these parameters is as shown in figure 3.34.

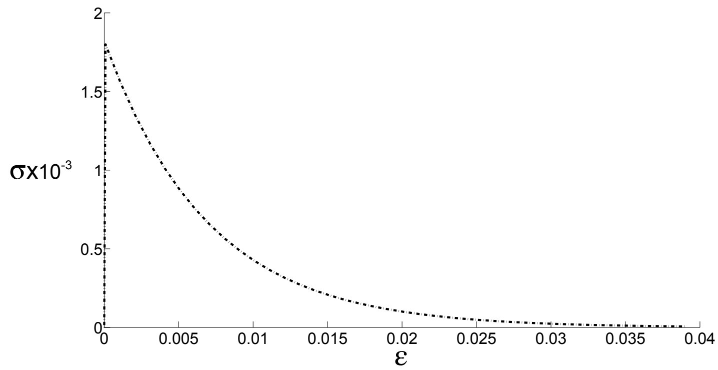

Figure 3.34. 1D element stress (GPa) vs strain profile considered in the 2D non-local damage simulation of the three point bending beam test with respect to the softening law given in equation (3.6).

To calculate the equivalent strain parameter the modified von Mises definition in equation (3.10) is used with $k = 10$. Similar to what is followed in the reference [477] the non-local averaging function given in equation (3.18) is considered with the interaction radius R taken as 4 mm. It is noted that these model parameters aforementioned should be considered as material properties and can be calibrated by experiment [504]. Considering that this section aims at verifying the mesh independence of the proposed method, these parameters are chosen same as those adopted in the reference [477] for finite element modelling.

The load-displacement output for the FEM-based non-local damage analysis is given in figure 3.35 and the SBFEM-based non-local damage analysis results are shown in figure

3.36. With reference to figure 3.26 the force and the displacement are recorded at point 'A'.

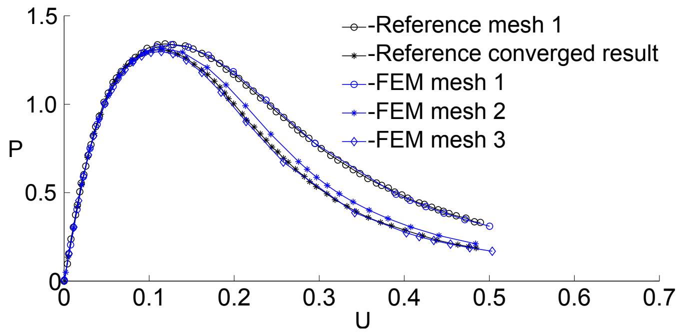

Figure 3.35. Force (kN) vs displacement (mm) curve for the FEM-based non-local damage analysis of the three point bending beam compared with the reference [501].

As the meshes are refined, the finest two meshes produce load-displacement curves with very close agreement to one another thus indicating the solution is converging upon mesh refinement (refer figures 3.35 and 3.36). This convergence eradicates the pathological sensitivity to mesh size observed in the local simulation in section 3.7.2.1.

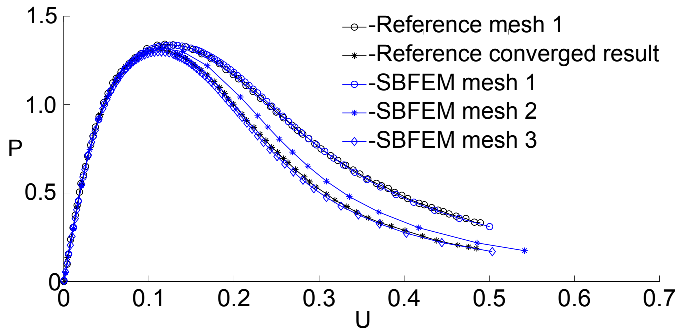

Figure 3.36. Force (kN) vs displacement (mm) curve for the SBFEM-based FGP formulation for the non-local damage analysis of the three point bending beam compared with the reference [501].

When observing the post peak behaviour of the three meshes it is also quite noticeable that the coarse mesh is above the converged result. This is expected due to the fact that the element size of 5 mm in the coarse mesh is larger than the interaction radius of 4 mm and resulting to a localized process zone that cannot be de-regularised with sufficient accuracy.

Overall figures 3.35 and 3.36 show good agreement with the reference solution. The results obtained from the SBFEM SC formulation are then compared alongside the FGP formulation and the finite element formulation. As shown in figure 3.37 , all three formulations yield comparatively similar results.

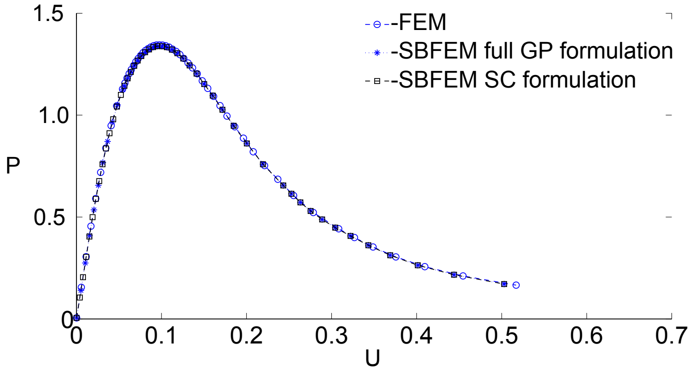

Figure 3.37. Force (kN) vs displacement (mm) output for the 2D non-local damage response obtained for the three point bending beam. The SBFE SC formulation is compared to the FEM and the FGP formulation. Mesh 3 considered for the analysis.

The contour plots given in figure 3.38 correspond to the vertical displacement observed at peak load (1.3 kN) when the recorded vertical displacement reads 0.1187 mm and just after peak load (0.91 kN) when displacement is 0.214 mm.

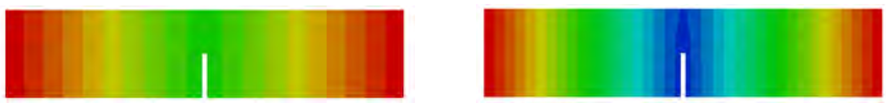

(a) Vertical displacement contour for mesh 3 at mid span displacement of 0.1187 mm.

(b) Vertical displacement contour for mesh 3 at mid span displacement of 0.214 mm.

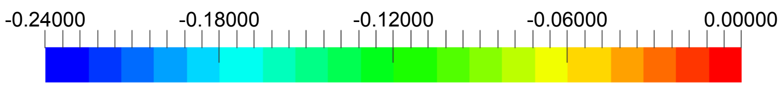

Figure 3.38. Vertical displacement contours for the 2D non-local damage analysis of the three point bending beam. Units:mm. Results obtained for mesh 3.

The stress contours parallel to the beam axis (σ_x) are shown in figure 3.39 for peak load of P = 1.3 kN and just after peak load when P = 0.91 kN. In the two instances it is apparent the highly stressed front propagates from the notch to the top edge of the beam, leaving behind elements that unload elastically as their stiffness has degraded to the limit of maximum damage.

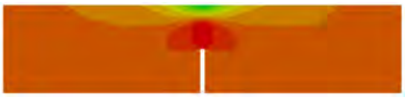

(a) Stress (σ_x) contour for mesh 3 at mid span displacement of 0.1187 mm.

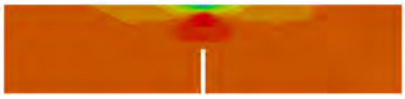

(b) Stress (σ_x) for mesh 3 at mid span displacement of 0.214 mm.

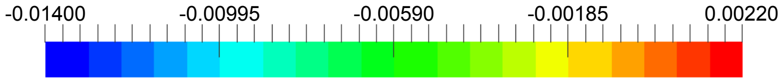

Figure 3.39. Stress (σ_x) contours for 2D non-local damage analysis of the three point bending beam. Units:MPa. Results obtained for mesh 3.

The damage contours are produced at peak load and at the end of the simulation when vertical displacement is 0.563 mm. Since damage is documented at the end of the simulation the damage profile can be clearly observed (refer figure 3.40).

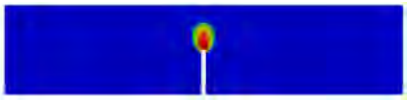

(a) Damage contour for mesh 3 at mid span displacement of 0.1187 mm.

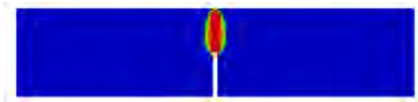

(b) Damage contour for mesh 3 at mid span displacement of 0.563 mm.

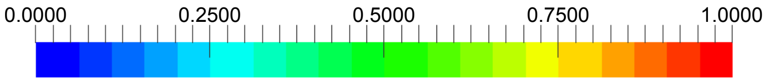

Figure 3.40. Damage (ω) contours for 2D non-local damage analysis of the three point bending beam. Results obtained for mesh 3.

The dark blue regions in figure 3.40 indicate regions with no damage. The evolution of the DPZ simulated on the fine mesh is shown in figure 3.40. It can be observed that at the beginning of loading, damage appears around the tip of notch owing to the high strain singularity. With the applied displacement increasing, the DPZ extends towards the top face of the beam. The damage band keeps a certain thickness while the band of increasing strains becomes progressively thinner so that a macroscopic stress-free crack can be observed as the beam completely fails. Compared to the local formulation the DPZ does not show any mesh-induced directional bias.

As exemplified through the two numerical examples 3.7.1 and 3.7.2, a non-local formulation overcomes the pathological strain localisation issues and thus the non-local regularization method is the preferred choice over local analysis.

3.7.3 L-shaped specimen

As the third example an L-shaped specimen shown in figure 3.41 is analysed with use of a non-local damage model. The objective of this example is to compare and validate the SBFEM FGP and the SC formulation. For this purpose the SBFEM integral-type non-local damage formulation is compared to the outputs of the in house FEM formulation and the reference outputs.

The dimensions of the model are as shown in figure 3.41a. The overall height and the width of the plate is 500 mm. A 250 mm square section of the plate is removed from the lower left quadrant to obtain the L-shaped geometry considered in the analysis. The thickness of the model is set to 200 mm as previously simulated by [482, 505, 506].

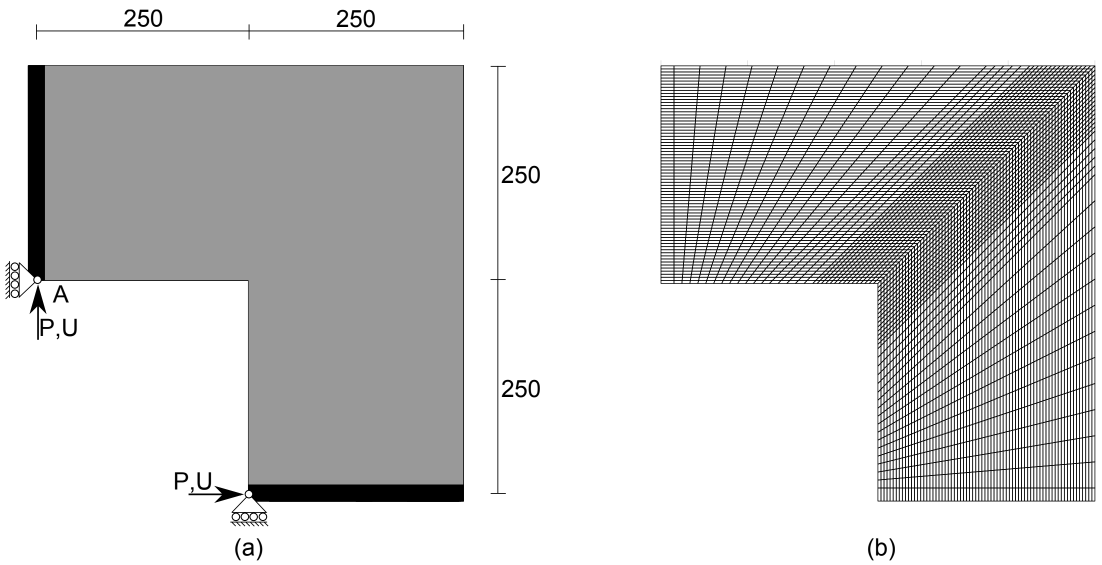

Figure 3.41. (a) Geometry and boundary conditions, and (b) the finite element mesh used in the 2D non-local damage analysis of a L-shaped specimen adopted similar to the reference [505].

Two rigid end plates are modelled in the left and the bottom edges to assist in the application of loads and avoid any undesirable damage around the loading points. These plates are considered to have 1000 times larger modulus of elasticity than the rest of the elements. The free rigid body rotation of the plate is negated by using displacement boundary conditions. The diagonal failure zone resulting from the setup requires mesh refinements in that direction, thus the mesh shown in figure 3.41b has a maximum element size of 1 mm around this process zone.

In the undamaged state a linear isotropic material is considered with the modulus of elasticity E = 10 GPa and Poisson's ratio of 0.2. Plane stress conditions are assumed. The modified von Mises local equivalent strain proposed in equation (3.10) is used with $k = 10$. The damage model considered for the analysis is as given in equation (3.7) with $\varepsilon_0 = 4 \times 10^{-4}$, $\alpha = 0.98$ and $\beta = 80$. With respect to these material and damage parameters the 1D stress-strain profile is produced as shown in figure 3.42.

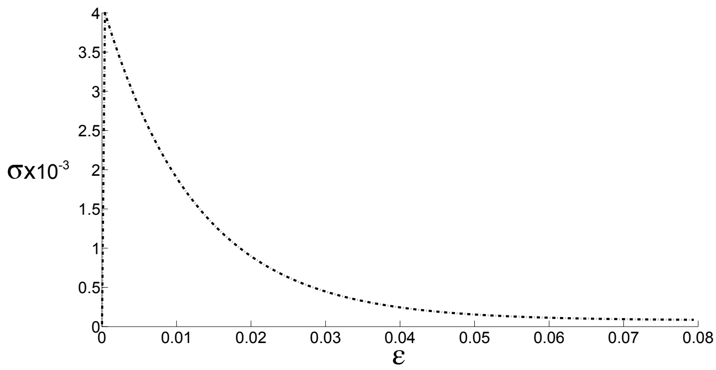

Figure 3.42. 1D element stress (GPa) vs strain profile considered for the 2D L-shaped specimen with respect to the softening law given in equation (3.7).

The adopted non-local averaging function for the simulation is as given in equation (3.16) with the non-local length scale of $l = 7.07$ mm.

Figure 3.43 shows the load-displacement curves of the proposed approach with the mesh configuration in figure 3.41. The force and the displacement are recorded at point 'A' in figure 3.41a. The FEM and SBFEM outputs are obtained through a displacement controlled m-NR method coupled with the arc length method. The initial displacement step is set to 0.01 mm.

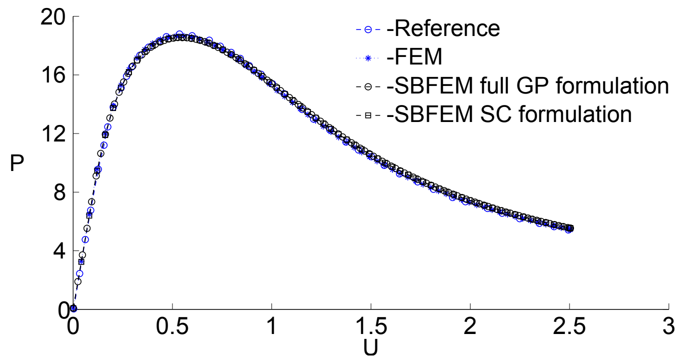

Figure 3.43. Force (kN) vs displacement (mm) output for the 2D L-shaped specimen. SBFEM SC and the FGP formulation compared to the FEM and the reference solution [505].

For comparison, the output of the reference finite element formulation presented in [505] is plotted alongside the findings of this work. The FEM and SBFEM formulations agrees well with the reference solution. More importantly, as seen in figure 3.43, the results obtained through the proposed SC damage formulation yields no noticeable deviation to the SBFEM FGP formulation results.

The contour plots given below are for the displacement magnitude, von Mises stress, and the damage evolution of the plate. Each instance is picked with reference to load-displacement profile in figure 3.43.

The contours for displacement magnitude shown in figure 3.44 correspond to a vertical displacement of 0.5372 mm at node 'A' reflecting a peak load of 18.6 kN and just after the peak load at displacement value of 0.987 mm corresponding to a load of 15.4 kN. The displacement magnitude contours show evidence of the symmetry of the boundary conditions.

(a) Displacement magnitude contour when node 'A' displacement is 0.5372 mm.

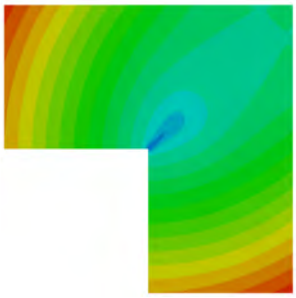

(b) Displacement magnitude contour when node 'A' displacement is 0.987 mm.

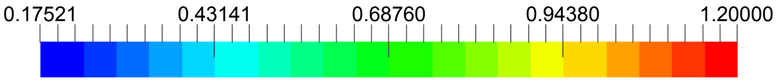

Figure 3.44. Displacement magnitude contours for non-local damage analysis of the 2D L-shaped specimen. Units:mm. Results obtained for the mesh in figure 3.41b.

The contours for von Mises stress are provided corresponding to a the same instances as considered in the displacement magnitude contours in figure 3.44. As the damage process zone propagates diagonally the area of high stress shrinks with elements elastically unloading due to stiffness degradation.

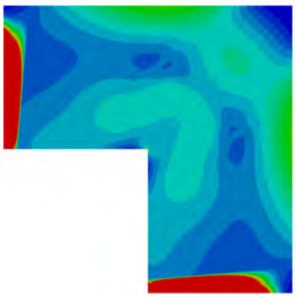

(a) Von Mises stress contour when node 'A' displacement is 0.5372 mm.

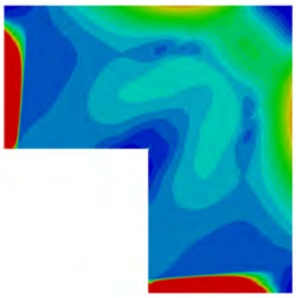

(b) Von Mises stress contour when node 'A' displacement is 0.987 mm.

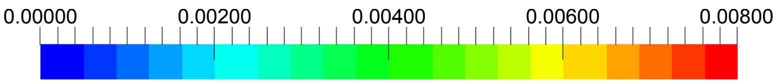

Figure 3.45. Von Mises stress contours for non-local damage analysis of the 2D L-shaped specimen. Units:MPa. Results obtained for the mesh in figure 3.41b.

The edge plates show the amplified stresses expected in the edge plates due to their high modulus of elasticity. The scale shown in the figure 3.44 disregard the amplified stresses for better scaling of the stress variation within the plate.

The damage contours are captured at a vertical displacement of 0.5372 mm at node ‘A’ corresponding to a peak load of 18.6 kN and at the end of the simulation corresponding to displacement of 2.504 mm and force 5.5 kN.

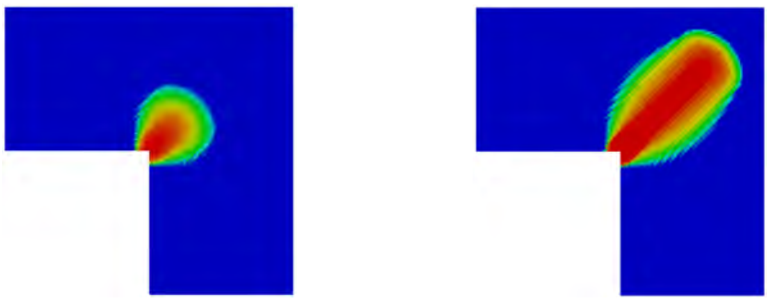

(a) Damage contour for when node ‘A’ displacement is 0.5372 mm.

(b) Damage contour when node ‘A’ displacement is 2.504 mm.

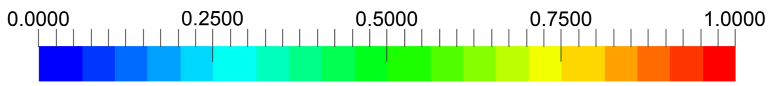

Figure 3.46. Damage (ω) contours for non-local damage analysis of the 2D L-shaped specimen. Results obtained for the mesh in figure 3.41b.

The damage evolution shown in figure 3.46 shows that the damage occurs at the concave corner of the specimen at first, owing to the larger stress singularity in this location. As the damage develops, the area of high stress moves along the diagonal symmetrically until the peak load is reached. During the softening stage, the DPZ keeps advancing as seen in figure 3.46.

3.7.4 Two dimensional damage characterization in shear band

As the final example in this chapter, a commonly investigated problem of a shear band formation is considered, for the verification of the presented formulation. The problem is extracted from the paper by Simone [507] on explicit and implicit gradient-enhanced damage models.

This problem is modelled assuming plane strain conditions as considered in the reference. The 2D plate considered in the analysis is as shown in figure 3.47a. The specimen is of 60×60 mm. To initiate the formation of the shear band an imperfection is introduced at the bottom left corner with dimensions 6×3 mm.

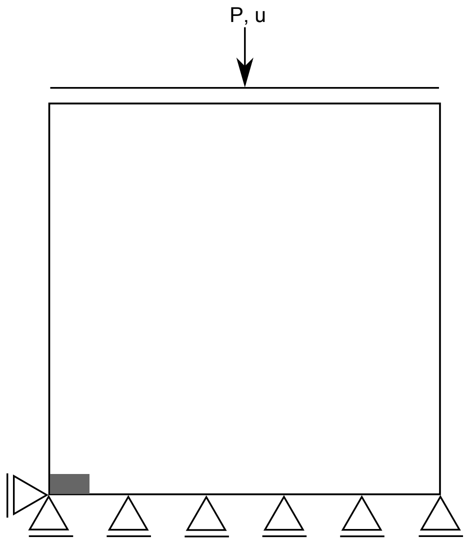

(a) h×h specimen in biaxial compression, where h = 60 mm. The shaded part indicates the imperfection of size h/10 × h/20 mm.

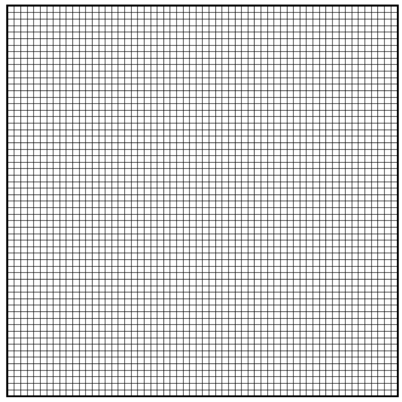

(b) Uniform mesh with element size 1 mm.

Figure 3.47. (a) Geometry and boundary conditions, and (b) the finite element mesh for the 2D non-local damage characterization in shear band.

Figure 3.47a depicts the geometry and boundary conditions, whereas, 3.47b shows the finite element mesh used in the analysis. With reference to figure 3.47a, the bottom edge is restrained from vertical movement, and additionally the bottom left corner of the plate is restrained in horizontal movement. The mesh considered for the analysis consists of a uniform 1 mm element size across the plate. The plate thus consists of 3600 elements as shown in 3.47b. This resolution of the mesh is found to be adequate with the proposed formulation and the non-local length scale considered in this simulation.

Material properties for the plate elements are as follows: Young's modulus E = 20 GPa and Poisson's ration ν = 0.2. The exponential softening law given in 3.7 is adopted with $\varepsilon_0 = 1 \times 10^{-4}$, $\alpha = 0.99$ and $\beta = 300$. The equivalent strain criteria considered is the von

Mises equivalent strain given in equation (3.13). For the imperfection, a reduced damage initiation threshold is considered with $\varepsilon_0 = 5 \times 10^{-5}$ leaving all other material properties same as the plate elements. The 1D stress-strain behaviour for the weaker material after consideration of its material and damage parameters are shown in figure 3.48. The non-local length scale $l = 2$ mm is used with the gauss weighting function given in equation (3.16).

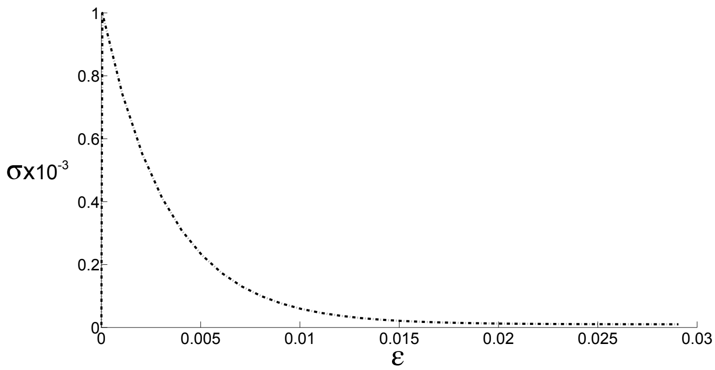

Figure 3.48. 1D element stress (GPa) vs strain profile considered in the 2D damage characterization of a shear band with respect to the softening law given in equation (3.7), for the weaker material with $\varepsilon_0 = 5 \times 10^{-5}$.

A displacement control analysis is carried out for 762 load steps with an initial displacement step of 1×10^{-3}mm. The output load-displacement curve is shown in figure 3.49. The total force on the top edge of the plate is plotted against and the absolute vertical displacement recorded at the centre of the top edge of the plate. Figure 3.49 also compares the proposed SC damage formulation to the FGP formulation, the results of a finite elements simulation, and the reference solution.

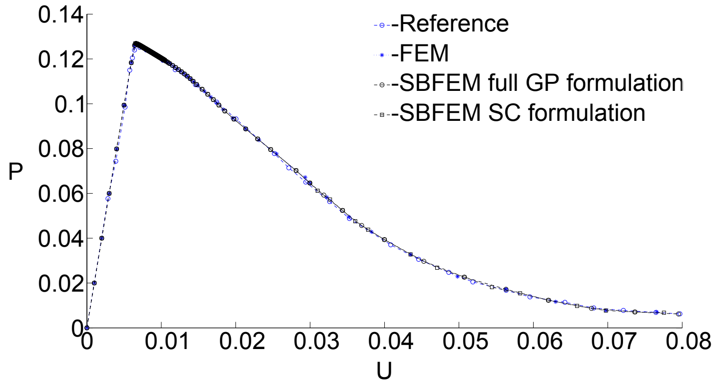

Figure 3.49. Force (kN) vs displacement (mm) output for the 2D damage characterization of a shear band. SBFEM SC and the FGP formulation compared to the FEM and the reference solution.

All results agree well with the reference and there is no noticeable deviation between the SC formulation and the conventional FGP formulation. The peak load of 0.127 kN is attained at a displacement of 0.0066 mm. Gradual softening behaviour is then exemplified till the end of the simulation.

The contour plots are presented for the displacement steps at peak load when the top edge displacement is 0.0066 mm, after peak load when the top edge displacement is 0.03 mm, and at end of simulation when the top edge displacement is 0.08 mm.

The von Mises non-local equivalent strain plots shown in figure 3.50 illustrate the initial strain localisation of the plate and the gradual formation of the high strain concentrated shear band.

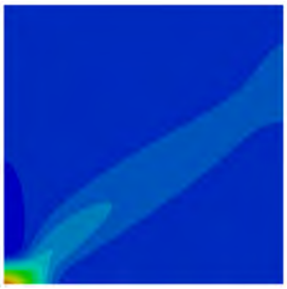

(a) At peak load when top edge displacement is 0.0066 mm.

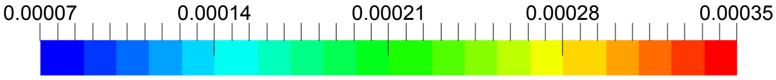

(c) After peak load when top edge displacement at 0.03 mm.

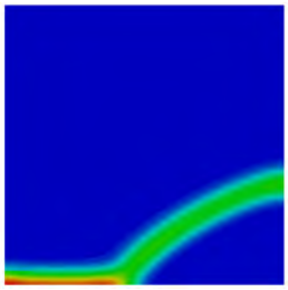

(d) At end of simulation when top edge displacement is 0.0782 mm.

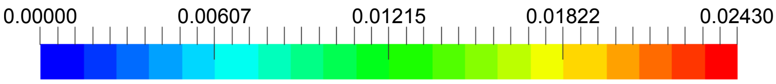

Figure 3.50. Von Mises equivalent strain contours obtained in simulation of the 2D non-local damage characterization in shear band. Results obtained for the mesh shown in figure 3.47b.

As expected [508] these figures also depict further localisation within the shear band after initiation of the shear band . The damage formation shown in figure 3.51 follows the precedent set by the strain localisation. The shear band migrates from the introduced weaker elements to the right hand edge of the plate along the horizontal boundary at first, before veering off diagonally to meet the unrestrained edge.

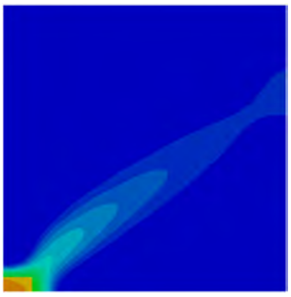

(a) At peak load when top edge displacement is 0.0066 mm.

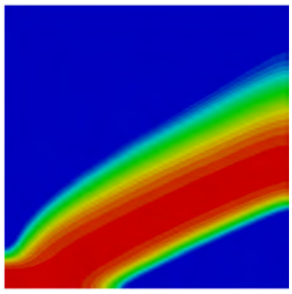

(b) After peak load when top edge displacement is 0.03 mm.

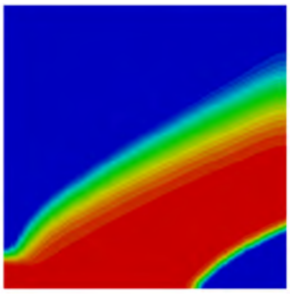

(c) At end of simulation when top edge displacement is 0.0782 mm.

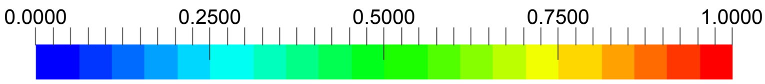

Figure 3.51. Damage (ω) evolution contours obtained in simulation of the 2D non-local damage characterization in shear band. Results obtained for the mesh shown in figure 3.47b.

Most collapse mechanisms in engineering problems are governed by the formation of shear bands. Results similar to the above findings are documents by Engelen et al. [509] and Pamin et al. [510]. However it should be noted that the width of the shear band is dictated by the non-local length parameter. Increasing this parameter will produce a wider shear band. Changes to the non-local length parameter can result in a shift of the shear band [511]. In some instances the failure mode can also be altered through incorrect consideration of the length scale. In this simulation the choice of the non-local length parameter is in accordance with the reference. The results therefore obtained are similar to that published in [507]. Figure 3.52 compares the damage contour obtained with the SBFEM formulation with the reference damage contour output.

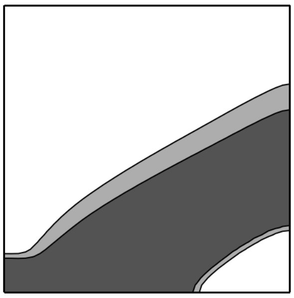

(a) Reference [507] damage contour at the end of the simulation.

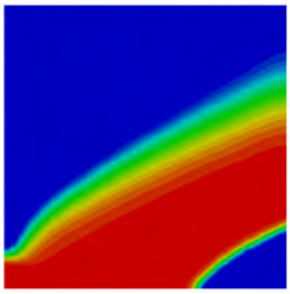

(b) SBFEM damage contour at the end of the simulation.

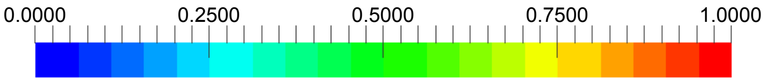

Figure 3.52. Comparison of the (a) reference [507] and the (b) SBFEM formulation damage contours in the 2D non-local damage characterization in shear band. Results obtained for the mesh shown in figure 3.47b.

3.8 Conclusions

The 2D SBFE equations are derived for damage analysis through incorporating the effects of damage degradation thereby extending the applications of the SBFEM to 2D damage analysis. The damage degree is assumed to be uniform in one subdomain, which simplifies the implementation of regularization to overcome strain localization. The work establishes the framework for non-locality within SBFEM, for exchange of information between integration points, a feature not included in standard finite element codes.

The successful implementation of the SBFE scaling centre damage formulation is presented in this chapter. A logical verification process is undertaken for the validation of SBFEM SC damage formulation by comparing results obtained through FEM, SBFEM FGP formulation and also published literature. The SC formulation yields results comparatively similar to that of the FGP formulation. This affirms that the SC formulation is able to capture the deterioration of the simulations considered. Owing to the conformance shown between the SBFEM SC and the SBFEM FGP formulations, the extension of the proposed approach to the 3D SBFEM-based damage analysis will be carried out through the SC formulation.

This chapter also compared the behaviour of local and non-local formulations. The local approach exemplifies severe mesh objectivity, whereas the non-local solutions converge after mesh refinement. Mesh dependency is an undesirable phenomenon, as local simulations allows for models to undergo damage by dissipating different fracture energies and different DPZs under the same loading conditions. Therefore as a solution to this issue the non-local damage modelling is considered in 2D by introducing a length parameter, which distributes the effect of damage and serves as the localization limiter. Only the DPZ is refined with small-sized subdomains to reduce the computational effort. Owing to the salient characteristic of the SBFEM, strain modes, subdomain stiffness matrices and weight functions can be calculated ahead of the damage simulation and thereby the computational efficiency can be considerably improved.

Numerical simulations provide good conformance, and demonstrate that the proposed approach is effective and robust in capturing the 2D damage evolution in structures.

Chapter 4

Three Dimensional Damage Analysis by the Scaled Boundary Finite Element Method

4.1 Introduction

In this chapter a novel and an effective approach within the framework of Scaled Boundary Finite Element Method (SBFEM) is proposed for structural damage analysis in three dimensions. The two dimensional (2D) integral-type non-local damage model introduced in chapter 3 is extended to the three dimensional (3D) SBFEM.

Continuum Damage Mechanics (CDM), initiated by Kachanov [34] in the context of creep rupture, is widely used to simulate the diffuse fracture process at both macroscopic level [250,477,481,483] and meso-scopic level [478,512,513]. CDM models use internal variables to describe the gradual loss of material integrity due to the propagation and coalescence of micro-defects. In CDM the damage stiffness tensor can be represented by a scalar [255], a vector [514] or a tensor [515, 516] combined with the elastic stiffness tensor. Compared with discrete crack models, CDM has become a competitive approach to simulate the progressive failure of structures with no extra effort to re-meshing arising from the strong discontinuity of crack. Based on the assumption that the stress at a specified point only depends on the state variables at that point, a local damage model exhibits an extreme sensitivity to the fineness and orientation of the spatial discretization in a mesh-based formulation [477, 481]. Such a pathological phenomenon is caused by the fact that the mathematical description becomes ill-posed at a certain level of accumulated damage. To overcome the deficiencies of the local damage model, several types of non-local approaches have been proposed during the last decades, among which the integral-type non-local model [477,517] and the gradient-type non-local model [480,518] are mostly used. The integral-type non-local model involves a spatial smoothing function to average the state variable of a point in a certain range of internal length (also called characteristic length), whereas the gradient-type non-local model takes the field in the immediate vicinity of the point into account by enriching the local constitutive relations with gradients of some state variables. Among the gradient-type formulations, the implicit gradient enhancement [301] is found to be more effective and suitable for numerical implementation than the explicit version. A large number of works involving non-local damage simulations have been reported, but only a few of them [479, 519] cover 3D cases, mainly because of the excessive computational cost, especially on the solution of large non-linear equilibrium equations [479].

The SBFEM is a semi-analytical method initiated by Wolf and Song in 1990s [199] for the solution of wave propagation problems in unbounded domain. The SBFEM combines some of the advantages of both the finite element method (FEM) and the boundary element method (BEM). In SBFEM, only the boundary is required to be discretised and the dimensions of the problem can be reduced by one, which in turn reduces the data preparation and computational effort. Compared to the BEM, the SBFEM does not require a fundamental solution. The ability to exactly satisfy radiation conditions at infinity makes this method particularly suitable for modelling unbounded media [63]. Owing to its capability of obtaining semi-analytical stress intensity factors, the SBFEM is also an attractive method for crack initialisation [520] and crack propagation modelling [521,522].

The SBFEM is an extremely versatile approach in terms of meshing. There is no limitation on the number of edges and vertices used for one subdomain, therefore a series of polygonal subdomains with arbitrary shapes and sizes constructed by topological algorithms, e.g. Delaunay triangulation can be used to discretise a domain with complex geometry profiles [205, 523]. The SBFEM can also been combined with the isogeometric analysis to further increase the accuracy of the solution with exact geometric representation [524].

In this contribution a three-dimensional non-local approach for the damage analysis of structures within the framework of SBFEM is proposed. The computationally efficient SBFEM scaling centre formulation introduced in chapter 3 is extended to the 3D space. The integral-type non-local model combined with the isotropic damage constitutive law is employed and extended to the scaled boundary formulation in 3D. Some inherent advantages of SBFEM are exploited for non-local damage modelling, including:

1. The scaling centre damage formulation-

   For damage simulation, the size of subdomains used in DPZ is especially small (typically around one-fourth to one-third of the characteristic length) and the numerical accuracy is mostly dependent on the damage estimation in DPZ. From the numerical point of view, as the mesh is refined the results of simulation would converge to the accurate solution. It is reasonable to assume that the severity of damage is uniform in one subdomain, and only the strain at the scaling centre of the subdomain is used to compute the internal variable. Consequently computational efforts can be considerably saved;

2. Pre-computation of strain modes-

   The strain modes for each subdomain are only dependent on the geometry of the subdomain. Therefore it can be computed beforehand and utilized at each load step to obtain the strain at an arbitrary point within the domain combined with updated integral constants (see section 4.4);

3. Pre-computation of weight function-

   For small deformation situations, the location of each subdomain is assumed to be unchanged during damage process, thus the weight function can also be calculated beforehand and utilized to smooth the internal variable in each load step.

This chapter is organized as follows: A brief description of the constitutive relationship, damage evolution law and the integral-type non-local model are included in section 4.2**.** In section 4.3 the 3D SBFEM derivation for elastostatics is presented. Section 4.4 details the 3D damage formulation with the SBFEM. The implicit accelerated/dampened m-NR method with arc-length algorithm is explained in section 4.5. Several benchmark simulations are presented in section 4.6 to verify the effectiveness and robustness of the proposed approach. The concluding remarks of this chapter are captured in section 4.7.

4.2 Damage model for concrete

This section presents a brief outline of the damage model for concrete. For a detailed explanation the reader is directed to chapter 3, section 3.2.

4.2.1 Evolution of damage

The damage model described in section 3.2.2 contains two relationships which are specific for a material, i.e. the evolution law of damage ω and the equivalent strain definition.

Two types of evolution law are widely used for damage model. The first type of damage models is the linear softening model described as

$$\omega = \begin{cases} 0 & \text{if } \kappa \leq \varepsilon_0, \\ \frac{\varepsilon_f}{\varepsilon_f - \varepsilon_0}\left(1 - \frac{\varepsilon_0}{\kappa}\right) & \text{if } \varepsilon_0 < \kappa < \varepsilon_f, \\ 1 & \text{if } \kappa \geq \varepsilon_f, \end{cases} \tag{4.1}$$

where ε_0 is the threshold of damage, and ε_f is a parameter affecting the ductility of the response and related to the fracture energy. The second type of softening relationships are exponential softening models. One such commonly used exponential softening model is a variant of equation (4.1), which is defined as

$$\omega = \begin{cases} 0 & \text{if } \kappa \leq \varepsilon_0, \\ 1 - \frac{\varepsilon_0}{\kappa} \exp\left(\frac{-(\kappa-\varepsilon_0)}{\varepsilon_f-\varepsilon_0}\right) & \text{if } \kappa > \varepsilon_0. \end{cases} \tag{4.2}$$

However, in this work a modified definition of exponential softening model proposed by Geers et al. [481] is selected

$$\omega = \begin{cases} 0 & \text{if } \kappa \leq \varepsilon_0, \\ 1 - \frac{\varepsilon_0}{\kappa} \left(1 - \alpha + \alpha \times \exp\left(-\beta\left(\kappa - \varepsilon_0\right)\right)\right) & \text{if } \kappa > \varepsilon_0, \end{cases} \tag{4.3}$$

in which α and β are two parameters to control the slope of the softening branch of the curve.

The definition of the equivalent strain directly affects the shape of the elastic domain in the strain space. The equivalent strain could be defined in an energy norm as

$$\tilde{\varepsilon} = \sqrt{\frac{1}{\mathrm{E}} \varepsilon^{\mathrm{T}} \mathbf{D} \varepsilon}. \tag{4.4}$$

It should be noted that such a definition implies equal weights to tensile and compressive strain components and it is unsuitable to describe the mechanical behaviour of quasi-brittle materials, e.g. concrete. Mazars and Pijaudier-Cabot [461] have therefore proposed a definition for concrete as

$$\tilde{\varepsilon} = \sqrt{\sum_{i=1}^{3} (<\varepsilon_i>)^2} \tag{4.5}$$

with ε_i the principal strains, and $<>$ are the MacAulay brackets defined such that $<\varepsilon_i>= \max(0, \varepsilon_i)$.

An alternative form of equation (4.4) with the use of the Mazars definition is

$$\tilde{\varepsilon} = \frac{1}{\mathrm{E}}\sqrt{\langle\varepsilon\rangle^{\mathrm{T}}\mathbf{P}\langle\varepsilon\rangle}, \tag{4.6}$$

where **P** is the diagonal scaling matrix defined as

$$\mathbf{P} = \begin{bmatrix} 1 & 0 & 0 & 0 & 0 & 0 \\ 0 & 1 & 0 & 0 & 0 & 0 \\ 0 & 0 & 1 & 0 & 0 & 0 \\ 0 & 0 & 0 & 0.5 & 0 & 0 \\ 0 & 0 & 0 & 0 & 0.5 & 0 \\ 0 & 0 & 0 & 0 & 0 & 0.5 \end{bmatrix}. \tag{4.7}$$

Incorporating the Rankine criterion of maximum principal stress, equation (4.6) can be written in terms of stress as follows.

$$\tilde{\varepsilon} = \frac{1}{\mathrm{E}}\sqrt{\langle\sigma\rangle^{\mathrm{T}}\mathbf{P}^{-1}\langle\sigma\rangle}. \tag{4.8}$$

Using the relationship $\sigma = \mathbf{D}\varepsilon$ equation (4.8) is transformed into the strain space as

$$\tilde{\varepsilon} = \frac{1}{\mathrm{E}}\sqrt{\langle\mathbf{D}\varepsilon\rangle^{\mathrm{T}}\mathbf{P}^{-1}\langle\mathbf{D}\varepsilon\rangle}. \tag{4.9}$$

Equation (4.9) can be re-written in terms of the principal strains ε_i as

$$\tilde{\varepsilon} = \frac{1}{\mathrm{E}}\sqrt{\langle\mathbf{D}_{nn}\varepsilon_i\rangle^{\mathrm{T}}\mathbf{P}^{-1}\langle\mathbf{D}_{nn}\varepsilon_i\rangle}, \tag{4.10}$$

where $\mathbf{D}_{nn}$ is the left upper block of the elastic stiffness matrix (refer equation (4.7)), related to the normal components of stress and strain.

As pointed out by Peerlings et al. in reference [480], the Mazars definition (equation (4.5)) predicts the propagation of crack in a wrong direction in some cases. Therefore in this study the more reliable conventional von Mises equivalent strain definition

$$\tilde{\varepsilon} = \frac{1}{1+\nu}\sqrt{-3J_2^{\varepsilon}}, \tag{4.11}$$

and the modified von Mises definition

$$\tilde{\varepsilon} = \frac{k-1}{2k(1-\nu)}I_1^{\varepsilon} + \frac{1}{2k}\sqrt{\frac{(k-1)^2}{(1-2\nu)^2}(I_1^{\varepsilon})^2 + \frac{12k}{(1+\nu)^2}J_2^{\varepsilon}}, \tag{4.12}$$

are considered. The modified von Mises definition was first proposed in a strain-based form by de Vree et al. [497]. The parameter k controls the different sensitivity to compressive and tensile strains and usually set equal to the ratio of the compressive and tensile strength, i.e $k = \sigma_{fc}/\sigma_{ft}$, ν is the Poisson's ratio, I_1^{ε}, J_2^{ε} are the strain tensor invariants and defined as

$$I_1^{\varepsilon} = tr(\varepsilon) = \varepsilon_{xx} + \varepsilon_{yy} + \varepsilon_{zz}, \tag{4.13}$$

$$J_2^{\varepsilon} = 3tr(\varepsilon\cdot\varepsilon) = \frac{1}{3}[\varepsilon_{xx}^2 + \varepsilon_{yy}^2 + \varepsilon_{zz}^2 - \varepsilon_{xx}\varepsilon_{yy} + \varepsilon_{yy}\varepsilon_{zz} + \varepsilon_{zz}\varepsilon_{xx} + 3(\varepsilon_{xy}^2 + \varepsilon_{yz}^2 + \varepsilon_{zx}^2). \tag{4.14}$$

4.2.2 Integral-type non-local damage model

As explained in section 3.2.4, the integral-type non-local damage formulation consists of replacing a state variable by its non-local counterpart obtained by weighted averaging over a spatial neighbourhood of each point within the range of the internal length.

This chapter adopts the two Gauss distribution function as the weighting function defined as [250]

$$\alpha_0(r) = \exp\left[-\frac{d^2}{2l^2}\right], \tag{4.15}$$

or as

$$\alpha_0(r) = \exp\left[-4\times\left(\frac{r}{R}\right)^2\right], \tag{4.16}$$

in which R is the interaction radius related to the internal length and denotes the largest distance of point θ that affects the non-local average at point x , and l is the internal length of the non-local continuum.

Another alternative form of weight function is a truncated quartic polynomial function in bell-shape [477]

$$\alpha_0(r) = \left\langle 1 - \frac{r^2}{R^2} \right\rangle^2. \tag{4.17}$$

4.3 The scaled boundary finite element method

This section explains the SBFEM formulation in 3D elastostatics as introduced and explained in [199] and [194].

4.3.1 Governing equations for elastostatics

The displacements $\mathbf{u} = \mathbf{u}(x, y, z)$ for a point in the three-dimensional Cartesian domain (x, y, z) can be denoted as

$$\mathbf{u} = [u_x, u_y, u_z]^{\mathrm{T}}. \tag{4.18}$$

The strains $\varepsilon = \varepsilon(x, y, z)$ can be expressed in terms of the displacements as

$$\varepsilon = [\varepsilon_x, \varepsilon_y, \varepsilon_z, \gamma_{yz}, \gamma_{xz}, \gamma_{xy}]^{\mathrm{T}} = \mathbf{L}\mathbf{u}, \tag{4.19}$$

where the linear differential operator $\mathbf{L}$ is written as

$$\mathbf{L} = \begin{bmatrix} \frac{\partial}{\partial x} & & \\ & \frac{\partial}{\partial y} & \\ & & \frac{\partial}{\partial z} \\ & \frac{\partial}{\partial z} & \frac{\partial}{\partial y} \\ \frac{\partial}{\partial z} & & \frac{\partial}{\partial x} \\ \frac{\partial}{\partial y} & \frac{\partial}{\partial x} & \end{bmatrix}. \tag{4.20}$$

For the linear elastic material, the stresses $\sigma = \sigma(x, y, z)$ can be denoted as

$$\sigma = [\sigma_x, \sigma_y, \sigma_z, \sigma_{yz}, \sigma_{xz}, \sigma_{xy}]^T = \mathbf{D}\varepsilon, \tag{4.21}$$

where $\mathbf{D}$ is the 6×6 elasticity matrix in 3D which can be isotropic or anisotropic in nature. The elasticity matrix for an isotropic material is given as

$$\mathbf{D} = \frac{2G}{1-2\nu} \begin{bmatrix} 1-\nu & \nu & \nu & & & \\ \nu & 1-\nu & \nu & & & \\ \nu & \nu & 1-\nu & & & \\ & & & \frac{1-2\nu}{2} & & \\ & & & & \frac{1-2\nu}{2} & \\ & & & & & \frac{1-2\nu}{2} \end{bmatrix}, \tag{4.22}$$

where G and ν are the material's shear modulus and Poisson's ratio, respectively.

The differential equations to represent equilibrium without body loads and side-face tractions are formulated as

$$\mathbf{L}^{\mathrm{T}}\sigma = 0. \tag{4.23}$$

The prescribed boundary conditions, displacements $\bar{\mathbf{u}}$ and tractions $\bar{\mathbf{t}}$ are applied respectively as

$$\mathbf{u} = \bar{\mathbf{u}} \quad \text{on} \quad S_{\mathrm{u}} \ , \tag{4.24a}$$

$$\mathbf{t} = \bar{\mathbf{t}} \quad \text{on} \quad S_{\mathrm{t}} \ , \tag{4.24b}$$

where $\mathbf{u}$ and $\mathbf{t}$ are the boundary displacements and tractions, respectively. The variable S_u and S_t are the discretised boundary related to the prescribed boundary displacements $\bar{\mathbf{u}}$ and tractions $\bar{\mathbf{t}}$, respectively. At a point on the boundary, either $\bar{\mathbf{u}}$ or $\bar{\mathbf{t}}$ must be prescribed i.e. $S_u \bigcup S_t = S$. In which S is the whole boundary of the problem domain.

4.3.2 Three-dimensional geometry transformation in the SBFEM

4.3.2.1 Modelling an arbitrary polyhedral element

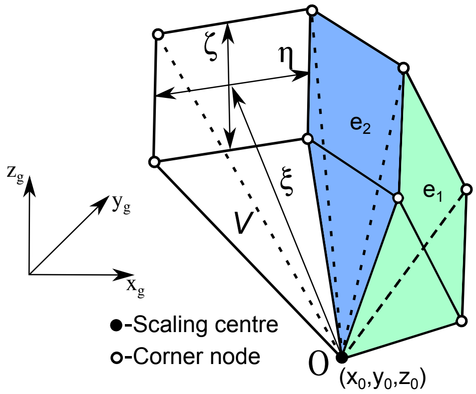

Figure 4.1. Three-dimensional coordinates for a scaled boundary finite element. Bi-material interface (e_1, e_2) shown in green and blue.

A typical problem domain V in 3D, as shown in figure 4.1, is used to illustrate the SBFEM modelling process. In the SBFEM formulation for polyhedral elements, any polyhedron that satisfies the *star convexity* criterion can be modelled by the scaled boundary finite element method. The star convexity criterion requires direct visibility of any point on the polyhedron boundary from a point inside the polyhedron. The scaling centre O is selected such that this requirement is fully satisfied. If this requirement cannot be satisfied, the domain should be further divided into a series of subdomains. This process is called sub-structuring. Therefore any irregular or concave polyhedron can be easily modelled as long as the star convexity criterion is satisfied.

The location of the O of the scaling centre is assumed to be at the local coordinate (x_0, y_0, z_0) and global Cartesian coordinates (x_g, y_g, z_g). The local Cartesian coordinates (x, y, z) with its origin coinciding with the scaling centre O are established as follows

$$x = x_g - x_0, \tag{4.25a}$$

$$y = y_g - y_0, \tag{4.25b}$$

$$z = z_g - z_0. \tag{4.25c}$$

Only the boundary of the domain needs to be discretised with 2D surface elements as depicted in figure 4.1. Each surface element e can be described using 2D interpolation shape functions $\mathbf{N}(\eta,\zeta)$ in which η and ζ represent the two local coordinates on the boundary. The 2D interpolation shape (mapping) functions on the surface element are written as

$$\mathbf{N}(\eta,\zeta)=\left[\begin{array}{cccc} N_1(\eta,\zeta), & N_2(\eta,\zeta), & \ldots & N_Q(\eta,\zeta) \end{array}\right], \tag{4.26}$$

where N_i is the shape function of node i and the subscript Q is the total number of nodes on the surface element.

A point on the boundary ($x(\eta,\zeta)$, $y(\eta,\zeta)$, $z(\eta,\zeta)$) is interpolated using the shape function of the surface element $\mathbf{N}(\eta,\zeta)$ as

$$x(\eta,\zeta)=\mathbf{N}(\eta,\zeta)\mathbf{x}, \tag{4.27a}$$

$$y(\eta,\zeta)=\mathbf{N}(\eta,\zeta)\mathbf{y}, \tag{4.27b}$$

$$z(\eta,\zeta)=\mathbf{N}(\eta,\zeta)\mathbf{z}, \tag{4.27c}$$

where $\mathbf{x}=\left[\begin{array}{cccc} x_1 & x_2 & \ldots & x_Q \end{array}\right]^{\mathrm{T}}$, $\mathbf{y}=\left[\begin{array}{cccc} y_1 & y_2 & \ldots & y_Q \end{array}\right]^{\mathrm{T}}$ and $\mathbf{z}=\left[\begin{array}{cccc} z_1 & z_2 & \ldots & z_Q \end{array}\right]^{\mathrm{T}}$ are the vectors containing the nodal coordinates of the nodes on each surface element in the local Cartesian coordinates.

A point in the internal domain $(x(\xi,\eta,\zeta), y(\xi,\eta,\zeta), z(\xi,\eta,\zeta))$ of the polyhedral element can be described by scaling the boundary $(x(\eta,\zeta), y(\eta,\zeta), z(\eta,\zeta))$ along the dimensionless radial coordinate ξ. The value of the coordinate ξ ranges from 0 at the scaling centre to 1 at the boundary. A specified point (x,y,z) within the domain can be expressed in terms of the scaled boundary local coordinates (ξ,η,ζ) as

$$x(\xi,\eta,\zeta)=\xi x(\eta,\zeta)=\xi\mathbf{N}(\eta,\zeta)x, \tag{4.28a}$$

$$y(\xi,\eta,\zeta)=\xi y(\eta,\zeta)=\xi\mathbf{N}(\eta,\zeta)\mathbf{y}, \tag{4.28b}$$

$$z(\xi,\eta,\zeta)=\xi z(\eta,\zeta)=\xi\mathbf{N}(\eta,\zeta)\mathbf{z}. \tag{4.28c}$$

From here onwards, coordinates (ξ, η, ζ) will be referred to as scaled boundary coordinates in the 3D domain.

If a polyhedral elements contain more than one material as shown in figure 4.1, the scaling is placed at the bi-material interface plane. This avoids the requirement for meshing at the bi-material interface plane. The interface is thereby automatically represented by scaling the edges of the two surface elements e_1 and e_2.

4.3.3 Geometry transformation in terms of scaled boundary coordinates

The local scaled boundary coordinates (ξ, η, ζ) are transformed to the local Cartesian coordinates (x, y, z) by the standard isoparametric mapping technique. Therefore the partial derivatives with respect to Cartesian coordinates can be transformed to partial derivatives with respect to scaled boundary coordinates based on the following equation

$$\left\{ \begin{array}{c} \frac{\partial}{\partial \xi} \\ \frac{\partial}{\partial \eta} \\ \frac{\partial}{\partial \zeta} \end{array} \right\} = \mathbf{J}(\xi, \eta, \zeta) \left\{ \begin{array}{c} \frac{\partial}{\partial x} \\ \frac{\partial}{\partial y} \\ \frac{\partial}{\partial z} \end{array} \right\}, \tag{4.29}$$

where the Jacobian matrix $\mathbf{J}(\xi, \eta, \zeta)$ is obtained as

$$\mathbf{J} = \begin{bmatrix} x(\xi,\eta,\zeta)_{,\xi} & y(\xi,\eta,\zeta)_{,\xi} & z(\xi,\eta,\zeta)_{,\xi} \\ x(\xi,\eta,\zeta)_{,\eta} & y(\xi,\eta,\zeta)_{,\eta} & z(\xi,\eta,\zeta)_{,\eta} \\ x(\xi,\eta,\zeta)_{,\zeta} & y(\xi,\eta,\zeta)_{,\zeta} & z(\xi,\eta,\zeta)_{,\zeta} \end{bmatrix}. \tag{4.30}$$

Therefore 4.29 can be abbreviated to

$$\left\{ \begin{array}{c} \frac{\partial}{\partial \xi} \\ \frac{\partial}{\partial \eta} \\ \frac{\partial}{\partial \zeta} \end{array} \right\} = \begin{bmatrix} 1 & & \\ & \xi & \\ & & \xi \end{bmatrix} \mathbf{J}(\xi, \eta, \zeta) \left\{ \begin{array}{c} \frac{\partial}{\partial x} \\ \frac{\partial}{\partial y} \\ \frac{\partial}{\partial z} \end{array} \right\}. \tag{4.31}$$

The Jacobian matrix at the boundary ($\xi = 1$) is given as

$$\mathbf{J} = \begin{bmatrix} x(\eta,\zeta) & y(\eta,\zeta) & z(\eta,\zeta) \\ x(\eta,\zeta)_{,\eta} & y(\eta,\zeta)_{,\eta} & z(\eta,\zeta)_{,\eta} \\ x(\eta,\zeta)_{,\zeta} & y(\eta,\zeta)_{,\zeta} & z(\eta,\zeta)_{,\zeta} \end{bmatrix}. \tag{4.32}$$

The determinant of the Jacobian matrix $|\mathbf{J}|$ with the arguments (η,ζ) omitted equal to

$$|\mathbf{J}| = x(y_{,\eta}z_{,\zeta} - z_{,\eta}y_{,\zeta}) + y(z_{,\eta}x_{,\zeta} - x_{,\eta}z_{,\zeta}) + z(x_{,\eta}y_{,\zeta} - y_{,\eta}x_{,\zeta}). \tag{4.33}$$

Therefore the inverse of Jacobian matrix at the boundary is

$$\mathbf{J}^{-1}(\eta,\zeta) = \frac{1}{|\mathbf{J}|}\begin{bmatrix} y_{,\eta}z_{,\zeta} - z_{,\eta}y_{,\zeta} & zy_{,\zeta} - yz_{,\zeta} & yz_{,\zeta} - zy_{,\zeta} \\ z_{,\eta}x_{,\zeta} - x_{,\eta}z_{,\zeta} & xz_{,\zeta} - zx_{,\zeta} & zx_{,\zeta} - xz_{,\zeta} \\ x_{,\eta}y_{,\zeta} - y_{,\eta}x_{,\zeta} & yx_{,\zeta} - xy_{,\zeta} & xy_{,\zeta} - yx_{,\zeta} \end{bmatrix}. \tag{4.34}$$

Substituting equation (4.34) in the inverse relationship of 4.31, yields

$$\begin{Bmatrix} \frac{\partial}{\partial x} \\ \frac{\partial}{\partial y} \\ \frac{\partial}{\partial z} \end{Bmatrix} = \frac{1}{|\mathbf{J}|}\begin{bmatrix} y_{,\eta}z_{,\zeta} - z_{,\eta}y_{,\zeta} \\ z_{,\eta}x_{,\zeta} - x_{,\eta}z_{,\zeta} \\ x_{,\eta}y_{,\zeta} - y_{,\eta}x_{,\zeta} \end{bmatrix}\frac{\partial}{\partial \xi}$$
$$\ldots + \frac{1}{\xi}\left(\frac{1}{|\mathbf{J}|}\begin{bmatrix} zy_{,\zeta} - yz_{,\zeta} \\ xz_{,\zeta} - zx_{,\zeta} \\ yx_{,\zeta} - xy_{,\zeta} \end{bmatrix}\frac{\partial}{\partial \eta} + \frac{1}{|\mathbf{J}|}\begin{bmatrix} yz_{,\zeta} - zy_{,\zeta} \\ zx_{,\zeta} - xz_{,\zeta} \\ xy_{,\zeta} - yx_{,\zeta} \end{bmatrix}\frac{\partial}{\partial \zeta}\right). \tag{4.35}$$

The linear differential operator $\mathbf{L}$ in equation (4.20) can be expressed in the local scaled boundary coordinates as

$$\mathbf{L} = \mathbf{b}_1(\eta,\zeta)\frac{\partial}{\partial \xi} + \frac{1}{\xi}\left(\mathbf{b}_2(\eta,\zeta)\frac{\partial}{\partial \eta} + \mathbf{b}_3(\eta,\zeta)\frac{\partial}{\partial \zeta}\right), \tag{4.36}$$

where $\mathbf{b}_1(\eta,\zeta)$, $\mathbf{b}_2(\eta,\zeta)$ and $\mathbf{b}_3(\eta,\zeta)$ with the arguments (η,ζ) of the entries omitted are defined as

$$\mathbf{b}_1(\eta,\zeta) = \frac{1}{|\mathbf{J}|}\begin{bmatrix} y_{,\eta}z_{,\zeta} - z_{,\eta}y_{,\zeta} & 0 & 0 \\ 0 & z_{,\eta}x_{,\zeta} - x_{,\eta}z_{,\zeta} & 0 \\ 0 & 0 & x_{,\eta}y_{,\zeta} - y_{,\eta}x_{,\zeta} \\ 0 & x_{,\eta}y_{,\zeta} - y_{,\eta}x_{,\zeta} & z_{,\eta}x_{,\zeta} - x_{,\eta}z_{,\zeta} \\ x_{,\eta}y_{,\zeta} - y_{,\eta}x_{,\zeta} & 0 & y_{,\eta}z_{,\zeta} - z_{,\eta}y_{,\zeta} \\ z_{,\eta}x_{,\zeta} - x_{,\eta}z_{,\zeta} & y_{,\eta}z_{,\zeta} - z_{,\eta}y_{,\zeta} & 0 \end{bmatrix} \tag{4.37a}$$

$$\mathbf{b}_2(\eta,\zeta) = \frac{1}{|\mathbf{J}|}\begin{bmatrix} zy_{,\zeta} - yz_{,\zeta} & 0 & 0 \\ 0 & xz_{,\zeta} - zx_{,\zeta} & 0 \\ 0 & 0 & yx_{,\zeta} - xy_{,\zeta} \\ 0 & yx_{,\zeta} - xy_{,\zeta} & xz_{,\zeta} - zx_{,\zeta} \\ yx_{,\zeta} - xy_{,\zeta} & 0 & zy_{,\zeta} - yz_{,\zeta} \\ xz_{,\zeta} - zx_{,\zeta} & zy_{,\zeta} - yz_{,\zeta} & 0 \end{bmatrix} \tag{4.37b}$$

$$\mathbf{b}_3(\eta,\zeta) = \frac{1}{|\mathbf{J}|}\begin{bmatrix} yz_{,\eta} - zy_{,\eta} & 0 & 0 \\ 0 & zx_{,\eta} - xz_{,\eta} & 0 \\ 0 & 0 & xy_{,\eta} - yx_{,\eta} \\ 0 & xy_{,\eta} - yx_{,\eta} & zx_{,\eta} - xz_{,\eta} \\ xy_{,\eta} - yx_{,\eta} & 0 & yz_{,\eta} - zy_{,\eta} \\ zx_{,\eta} - xz_{,\eta} & yz_{,\eta} - zy_{,\eta} & 0 \end{bmatrix} \tag{4.37c}$$

The position vector $\mathbf{r}$ of a point on the boundary of a polyhedral element can now be expressed based on the coordinate transformation as

$$\mathbf{r} = x(\eta,\zeta)\,\mathbf{i} + y(\eta,\zeta)\,\mathbf{j} + z(\eta,\zeta)\,\mathbf{k} \tag{4.38}$$

The derivatives of $\mathbf{r}$ with respect to η and ζ representing two of the tangential vectors can be written as

$$\mathbf{r}_{,\eta} = x(\eta,\zeta)_{,\eta}\,\mathbf{i} + y(\eta,\zeta)_{,\eta}\,\mathbf{j} + z(\eta,\zeta)_{,\eta}\,\mathbf{k}, \tag{4.39a}$$

$$\mathbf{r}_{,\zeta} = x(\eta,\zeta)_{,\zeta}\,\mathbf{i} + y(\eta,\zeta)_{,\zeta}\,\mathbf{j} + z(\eta,\zeta)_{,\zeta}\,\mathbf{k}. \tag{4.39b}$$

Alternatively, equation (4.33) can be derived as

$$|\mathbf{J}| = \mathbf{r}\cdot\left(\mathbf{r}_{,\eta}\times\mathbf{r}_{,\zeta}\right) \tag{4.40}$$

The position vector of a point in the polyhedral element $\hat{\mathbf{r}}$ can be written as

$$\hat{\mathbf{r}} = \xi\mathbf{r} = x(\xi,\eta,\zeta)\,\mathbf{i} + y(\xi,\eta,\zeta)\,\mathbf{j} + z(\xi,\eta,\zeta)\,\mathbf{k} \tag{4.41}$$

An infinitesimal volume $\mathrm{d}V$ for an arbitrary ξ can be calculated as

$$\mathrm{d}V = \hat{\mathbf{r}}_{,\xi}\cdot\left(\hat{\mathbf{r}}_{,\eta}\times\hat{\mathbf{r}}_{,\zeta}\right)\mathrm{d}\xi\,\mathrm{d}\eta\,\mathrm{d}\zeta \tag{4.42}$$

where

$$\hat{\mathbf{r}}_{,\xi} = \mathbf{r} = x(\eta,\zeta)\,\mathbf{i} + y(\eta,\zeta)\,\mathbf{j} + z(\eta,\zeta)\,\mathbf{k}, \tag{4.43a}$$

$$\hat{\mathbf{r}}_{,\eta} = \xi\left[x(\eta,\zeta)_{,\eta}\mathbf{i} + y(\eta,\zeta)_{,\eta}\mathbf{j} + z(\eta,\zeta)_{,\eta}\,\mathbf{k}\right], \tag{4.43b}$$

$$\hat{\mathbf{r}}_{,\zeta} = \xi\left[x(\eta,\zeta)_{,\zeta}\,\mathbf{i} + y(\eta,\zeta)_{,\zeta}\,\mathbf{j} + z(\eta,\zeta)_{,\zeta}\,\mathbf{k}\right]. \tag{4.43c}$$

The outward normal vectors $\mathbf{g}_\xi$, $\mathbf{g}_\eta$ and $\mathbf{g}_\zeta$ to the surfaces (η,ζ), (ζ,ξ) and (ξ,η), respectively, with arguments (η,ζ) omitted can be written as

$$\mathbf{g}_\xi = \mathbf{r}_{,\eta}\times\mathbf{r}_{,\zeta} = \left(y_{,\eta}z_{,\zeta} - z_{,\eta}y_{,\zeta}\right)\mathbf{i} + \left(z_{,\eta}x_{,\zeta} - x_{,\eta}z_{,\zeta}\right)\mathbf{j} + \left(x_{,\eta}y_{,\zeta} - y_{,\eta}x_{,\zeta}\right)\mathbf{k}, \tag{4.44a}$$

$$\mathbf{g}_\eta = \mathbf{r}_{,\zeta}\times\mathbf{r} = \left(zy_{,\zeta} - yz_{,\zeta}\right)\mathbf{i} + \left(xz_{,\zeta} - zx_{,\zeta}\right)\mathbf{j} + \left(yx_{,\zeta} - xy\right)\mathbf{k}, \tag{4.44b}$$

$$\mathbf{g}_\zeta = \mathbf{r}\times\mathbf{r}_{,\eta} = \left(yz_{,\zeta} - zy_{,\zeta}\right)\mathbf{i} + \left(zx_{,\zeta} - xz_{,\zeta}\right)\mathbf{j} + \left(xy_{,\zeta} - yx_{,\zeta}\right)\mathbf{k}. \tag{4.44c}$$

Therefore, the dV in equation (4.42) can be expressed as

$$\mathrm{d}V = (x\mathbf{i}+y\mathbf{j}+z\mathbf{k})\cdot\begin{vmatrix}\mathbf{i} & \mathbf{j} & \mathbf{k}\\ \xi x_{,\eta} & \xi y_{,\eta} & \xi z_{,\eta}\\ \xi x_{,\zeta} & \xi y_{,\zeta} & \xi z_{,\zeta}\end{vmatrix}\mathrm{d}\xi\mathrm{d}\eta\mathrm{d}\zeta,$$

$$\mathrm{d}V = \xi^2\left[x\left(y_{,\eta}z_{,\zeta}-z_{,\eta}y_{,\zeta}\right)+y\left(z_{,\eta}x_{,\zeta}-x_{,\eta}z_{,\zeta}\right)+z\left(x_{,\eta}y_{,\zeta}-y_{,\eta}x_{,\zeta}\right)\right]\mathrm{d}\xi\mathrm{d}\eta\mathrm{d}\zeta,$$

$$\mathrm{d}V = \xi^2\left|\mathbf{J}\right|\mathrm{d}\xi\mathrm{d}\eta\mathrm{d}\zeta. \tag{4.45}$$

The infinitesimal surface area dS_ξ, dS_η, and dS_ξ between the coordinates η and ζ, ζ and ξ, and ξ and η, respectively, for an arbitrary ξ is expressed as

$$\mathrm{d}S_\xi = \left|\hat{\mathbf{r}}_{,\eta}\times\hat{\mathbf{r}}_{,\zeta}\right|\mathrm{d}\eta\mathrm{d}\zeta = \left|\xi\mathbf{r}_{,\eta}\times\xi\mathbf{r}_{,\zeta}\right|\mathrm{d}\eta\mathrm{d}\zeta = \xi^2 g_\xi\mathrm{d}\eta\mathrm{d}\zeta, \tag{4.46a}$$

$$\mathrm{d}S_\eta = \left|\hat{\mathbf{r}}_{,\zeta}\times\hat{\mathbf{r}}_{,\xi}\right|\mathrm{d}\zeta\mathrm{d}\xi = \left|\xi\mathbf{r}_{,\zeta}\times\mathbf{r}\right|\mathrm{d}\zeta\mathrm{d}\xi = \xi g_\eta\mathrm{d}\zeta\mathrm{d}\xi, \tag{4.46b}$$

$$\mathrm{d}S_\zeta = \left|\hat{\mathbf{r}}_{,\xi}\times\hat{\mathbf{r}}_{,\eta}\right|\mathrm{d}\xi\mathrm{d}\eta = \left|\mathbf{r}\times\xi\mathbf{r}_{,\eta}\right|\mathrm{d}\xi\mathrm{d}\eta = \xi g_\zeta\mathrm{d}\xi\mathrm{d}\eta, \tag{4.46c}$$

where $g_\xi = \left|\mathbf{r}_{,\eta}\times\mathbf{r}_{,\zeta}\right|$, $g_\eta = \left|\mathbf{r}_{,\zeta}\times\mathbf{r}\right|$, and $g_\zeta = \left|\mathbf{r}\times\mathbf{r}_{,\eta}\right|$.

The unit outward normal vectors for the vectors produced in equations (4.44a-4.44c) can be written as

$$\mathbf{n}_\xi = \frac{\mathbf{g}_\xi}{g_\xi} = n_x^\xi\mathbf{i}+n_y^\xi\mathbf{j}+n_z^\xi\mathbf{k}, \tag{4.47a}$$

$$\mathbf{n}_\eta = \frac{\mathbf{g}_\eta}{g_\eta} = n_x^\eta\mathbf{i}+n_y^\eta\mathbf{j}+n_z^\eta\mathbf{k}, \tag{4.47b}$$

$$\mathbf{n}_\zeta = \frac{\mathbf{g}_\zeta}{g_\zeta} = n_x^\zeta\mathbf{i}+n_y^\zeta\mathbf{j}+n_z^\zeta\mathbf{k}. \tag{4.47c}$$

The amplitudes of the surface tractions $\mathbf{t}$ on any boundary with an outward unit normal vector $\mathbf{n} = n_x\mathbf{i} + n_y\mathbf{j} + n_z\mathbf{k}$ are

$$\mathbf{t} = \begin{bmatrix} t_x \\ t_y \\ t_z \end{bmatrix} = \begin{bmatrix} n_x & 0 & 0 & 0 & n_z & n_y \\ 0 & n_y & 0 & n_z & 0 & n_x \\ 0 & 0 & n_z & n_y & n_x & 0 \end{bmatrix} \sigma. \tag{4.48}$$

Based on equation (4.48) and equations (4.47a-4.47c), the surface tractions on the surfaces (η, ζ), (ζ, ξ) and (ξ, η) can be written as

$$\mathbf{t}_\xi = \begin{bmatrix} n_x^\xi & 0 & 0 & 0 & n_z^\xi & n_y^\xi \\ 0 & n_y^\xi & 0 & n_z^\xi & 0 & n_x^\xi \\ 0 & 0 & n_z^\xi & n_y^\xi & n_x^\xi & 0 \end{bmatrix} \sigma, \tag{4.49a}$$

$$\mathbf{t}_\eta = \begin{bmatrix} n_x^\eta & 0 & 0 & 0 & n_z^\eta & n_y^\eta \\ 0 & n_y^\eta & 0 & n_z^\eta & 0 & n_x^\eta \\ 0 & 0 & n_z^\eta & n_y^\eta & n_x^\eta & 0 \end{bmatrix} \sigma, \tag{4.49b}$$

$$\mathbf{t}_\zeta = \begin{bmatrix} n_x^\zeta & 0 & 0 & 0 & n_z^\zeta & n_y^\zeta \\ 0 & n_y^\zeta & 0 & n_z^\zeta & 0 & n_x^\zeta \\ 0 & 0 & n_z^\zeta & n_y^\zeta & n_x^\zeta & 0 \end{bmatrix} \sigma. \tag{4.49c}$$

Using equations (4.37a-4.37c) and (4.44a-4.44c), equations (4.49a-4.49c) can now be written as

$$\mathbf{t}_\xi = \frac{|\mathbf{J}|}{g_\xi} \mathbf{b}_1^{\mathrm{T}} (\eta, \zeta) \sigma, \tag{4.50a}$$

$$\mathbf{t}_\eta = \frac{|\mathbf{J}|}{g_\eta} \mathbf{b}_2^{\mathrm{T}} (\eta, \zeta) \sigma, \tag{4.50b}$$

$$\mathbf{t}_\zeta = \frac{|\mathbf{J}|}{g_\zeta} \mathbf{b}_3^{\mathrm{T}} (\eta, \zeta) \sigma. \tag{4.50c}$$

4.3.4 Displacements and stresses in terms of the scaled boundary coordinates

The displacement solutions within each polyhedral subdomain $\mathbf{u}(\xi,\eta,\zeta) = [u_x(\xi,\eta,\zeta), u_y(\xi,\eta,\zeta), u_z(\xi,\eta,\zeta)]^{\mathrm{T}}$ at a point (ξ,η,ζ) is obtained by interpolation with shape function

$$\mathbf{u}(\xi,\eta,\zeta) = \mathbf{N}_{\mathrm{u}}(\eta,\zeta)\mathbf{u}(\xi), \tag{4.51}$$

where $\mathbf{u}(\xi)$ denotes the displacement solution in the radial direction. The interpolation shape function $\mathbf{N}_{\mathrm{u}}(\eta,\zeta)$ are defined as

$$\mathbf{N}_{\mathrm{u}}(\eta,\zeta) = [N_1(\eta,\zeta)\mathbf{I}, N_2(\eta,\zeta)\mathbf{I}, ..., N_Q(\eta,\zeta)\mathbf{I},] \tag{4.52}$$

where $\mathbf{I}$ is a 3×3 identity matrix and Q is the total number of nodes on the surface element.

The strains ε in each subdomain expressed in equation (4.19) can be rewritten using equation (4.36) and (4.51) as

$$\varepsilon(\xi,\eta,\zeta) = \mathbf{B}_1(\eta,\zeta)\mathbf{u}(\xi)_{,\xi} + \frac{1}{\xi}\mathbf{B}_2(\eta,\zeta)\mathbf{u}(\xi) \tag{4.53}$$

where

$$\mathbf{B}_1(\eta,\zeta) = \mathbf{b}_1(\eta,\zeta)\mathbf{N}_{\mathrm{u}}(\eta,\zeta), \tag{4.54a}$$

$$\mathbf{B}_2(\eta,\zeta) = \mathbf{b}_2(\eta,\zeta)\mathbf{N}_{\mathrm{u}}(\eta,\zeta)_{,\eta} + \mathbf{b}_3(\eta,\zeta)\mathbf{N}_{\mathrm{u}}(\eta,\zeta)_{,\zeta}. \tag{4.54b}$$

Substituting equation (4.53) into equation (4.21), the stress field is obtained as

$$\sigma(\xi,\eta,\zeta) = \mathbf{D}\left(\mathbf{B}_1(\eta,\zeta)\mathbf{u}(\xi)_{,\xi} + \frac{1}{\xi}\mathbf{B}_2(\eta,\zeta)\mathbf{u}(\xi)\right) \tag{4.55}$$

4.3.5 3D derivation of the scaled boundary finite element equation based on the principle of virtual work

This section presents the SBFE equations based on the principle of virtual displacements. The derivation considers the discretisation of the problem domain to polyhedral elements. The virtual work statement is therefore applied to each individual polyhedral element.

The derivation is based on the virtual displacement field $\delta\mathbf{u}$ written based on equation (4.51) as

$$\delta\mathbf{u}(\xi,\eta,\zeta) = \mathbf{N}_{\mathrm{u}}(\eta,\zeta)\delta\mathbf{u}(\xi). \tag{4.56}$$

The virtual strains based on equation (4.53) are written as

$$\delta\varepsilon(\xi,\eta,\zeta) = \mathbf{B}_1(\eta,\zeta)\delta\mathbf{u}(\xi)_{,\xi} + \frac{1}{\xi}\mathbf{B}_2(\eta,\zeta)\delta\mathbf{u}(\xi). \tag{4.57}$$

The virtual work statement for elastostatics can be written in the following form

$$\int_{v}\delta\varepsilon^{\mathrm{T}}\sigma\mathrm{d}V - \int_{v}\delta\mathbf{u}^{\mathrm{T}}\mathbf{p}\mathrm{d}V - \int_{v}\delta\mathbf{u}^{\mathrm{T}}\mathbf{t}\mathrm{d}S_{\xi} = 0, \tag{4.58}$$

where, the first term corresponds to work done by the internal forces. The second and third terms relate to the work done by the body loads, and surface tractions, respectively. The terms $\mathrm{d}S_{\xi}$ and $\mathrm{d}V$ represent the infinitesimal surface area on the boundary and the infinitesimal volume in the domain, respectively.

4.3.5.1 Internal work (Strain energy)

Applying equations (4.57), (4.55) and (4.45) to the first term of equation (4.58) produces

$$\int_v \left(\mathbf{B}_1(\eta,\zeta)\delta\mathbf{u}(\xi)_{,\xi} + \frac{1}{\xi}\mathbf{B}_2(\eta,\zeta)\delta\mathbf{u}(\xi)\right)^{\mathrm{T}}\mathbf{D}$$

$$\ldots\left(\mathbf{B}_1(\eta,\zeta)\mathbf{u}(\xi)_{,\xi} + \frac{1}{\xi}\mathbf{B}_2(\eta,\zeta)\mathbf{u}(\xi)\right)\xi^2\,|\mathbf{J}|\,d\xi d\eta \mathrm{d}\zeta =$$

$$+\underbrace{\int_0^1 \delta\mathbf{u}^{\mathrm{T}}(\xi)_{,\xi}\int_s \mathbf{B}_1^{\mathrm{T}}(\eta,\zeta)\mathbf{D}\mathbf{B}_1(\eta,\zeta)\,|\mathbf{J}|\,\mathrm{d}\eta\mathrm{d}\zeta\xi^2\mathbf{u}(\xi)_{,\xi}\mathrm{d}\xi}_{P1}$$

$$+\underbrace{\int_0^1 \delta\mathbf{u}^{\mathrm{T}}(\xi)_{,\xi}\int_s \mathbf{B}_1^{\mathrm{T}}(\eta,\zeta)\mathbf{D}\mathbf{B}_2(\eta,\zeta)\,|\mathbf{J}|\,\mathrm{d}\eta\mathrm{d}\zeta\xi\mathbf{u}(\xi)\mathrm{d}\xi}_{P2}$$

$$+\underbrace{\int_0^1 \delta\mathbf{u}^{\mathrm{T}}(\xi)\int_s \mathbf{B}_2^{\mathrm{T}}(\eta,\zeta)\mathbf{D}\mathbf{B}_1(\eta,\zeta)\,|\mathbf{J}|\,\mathrm{d}\eta\mathrm{d}\zeta\xi\mathbf{u}(\xi)_{,\xi}\mathrm{d}\xi}_{P3}$$

$$+\underbrace{\int_0^1 \delta\mathbf{u}^{\mathrm{T}}(\xi)\int_s \mathbf{B}_2^{\mathrm{T}}(\eta,\zeta)\mathbf{D}\mathbf{B}_2(\eta,\zeta)\,|\mathbf{J}|\,\mathrm{d}\eta\mathrm{d}\zeta\mathbf{u}(\xi)\mathrm{d}\xi}_{P4}. \tag{4.59}$$

By introducing the coefficient matrices

$$\mathbf{E}_0 = \int_s \mathbf{B}_1^{\mathrm{T}}(\eta,\zeta)\mathbf{D}\mathbf{B}_1(\eta,\zeta)|\mathbf{J}|d\eta d\zeta, \tag{4.60a}$$

$$\mathbf{E}_1 = \int_s \mathbf{B}_2^{\mathrm{T}}(\eta,\zeta)\mathbf{D}\mathbf{B}_1(\eta,\zeta)|\mathbf{J}|d\eta d\zeta, \tag{4.60b}$$

$$\mathbf{E}_2 = \int_s \mathbf{B}_2^{\mathrm{T}}(\eta,\zeta)\mathbf{D}\mathbf{B}_2(\eta,\zeta)|\mathbf{J}|d\eta d\zeta. \tag{4.60c}$$

The coefficient matrices are constructed for individual surface elements and assembled to obtain the coefficient matrices for each polyhedral element. The assembly process is similar to the construction of the global stiffness matrix from the element stiffness matrices in the finite element method. The integration is performed using standard Gauss-Lobatto quadrature rules [91].

Each part $(P1-P4)$ in equation (4.59) can be simplified as below after integration by parts in the local coordinate ξ.

$$\begin{aligned}
P1 =& \int_0^1 \delta\mathbf{u}^{\mathrm{T}}(\xi)_{,\xi}\mathbf{E}_0\xi^2\mathbf{u}(\xi)_{,\xi}\mathrm{d}\xi \\
=&\delta\mathbf{u}^{\mathrm{T}}(\xi)\mathbf{E}_0\xi^2\mathbf{u}(\xi)_{,\xi}\mid_{\xi=1} - \int_0^1 \delta\mathbf{u}^{\mathrm{T}}(\xi)\mathbf{E}_0\left(2\xi\mathbf{u}(\xi)_{,\xi}+\xi^2\mathbf{u}(\xi)_{,\xi\xi}\right)\mathrm{d}\xi \\
=&\delta\mathbf{u}_{\mathrm{b}}^{\mathrm{T}}\mathbf{E}_0\mathbf{u}(\xi)_{,\xi}\mid_{\xi=1} - \int_0^1 \delta\mathbf{u}^{\mathrm{T}}(\xi)\mathbf{E}_0\left(2\xi\mathbf{u}(\xi)_{,\xi}+\xi^2\mathbf{u}(\xi)_{,\xi\xi}\right)\mathrm{d}\xi
\end{aligned} \tag{4.61a}$$

$$\begin{aligned}
P2 =& \int_0^1 \delta\mathbf{u}^{\mathrm{T}}(\xi)_{,\xi}\mathbf{E}_1^{\mathrm{T}}\xi\mathbf{u}(\xi)\mathrm{d}\xi \\
=&\delta\mathbf{u}^{\mathrm{T}}(\xi)\mathbf{E}_1^{\mathrm{T}}\xi\mathbf{u}(\xi)\mid_{\xi=1} - \int_0^1 \delta\mathbf{u}^{\mathrm{T}}(\xi)\mathbf{E}_1^{\mathrm{T}}\left(\mathbf{u}(\xi)+\xi\mathbf{u}(\xi)_{,\xi}\right)\mathrm{d}\xi \\
=&\delta\mathbf{u}_{\mathrm{b}}^{\mathrm{T}}\mathbf{E}_1^{\mathrm{T}}\mathbf{u}_{\mathrm{b}} - \int_0^1 \delta\mathbf{u}^{\mathrm{T}}(\xi)\mathbf{E}_1^{\mathrm{T}}\left(\mathbf{u}(\xi)+\xi\mathbf{u}(\xi)_{,\xi}\right)\mathrm{d}\xi,
\end{aligned} \tag{4.61b}$$

$$P3 = \int_0^1 \delta\mathbf{u}^{\mathrm{T}}(\xi)\mathbf{E}_1\xi\mathbf{u}(\xi)_{,\xi}\mathrm{d}\xi, \tag{4.61c}$$

$$P4 = \int_0^1 \delta\mathbf{u}^{\mathrm{T}}(\xi)\mathbf{E}_2\mathbf{u}(\xi)\mathrm{d}\xi. \tag{4.61d}$$

In equation (4.61a) and equation (4.61b) $\mathbf{u}_{\mathrm{b}} = u(\xi = 1)$. Now equation (4.59) can now be written as

$$\int_v \delta\varepsilon^{\mathrm{T}}\sigma \mathrm{d}V = \delta\mathbf{u}_{\mathrm{b}}^{\mathrm{T}}\left(\mathbf{E}_0\mathbf{u}(\xi)_{,\xi}\,|_{\xi=1} + \mathbf{E}_1^{\mathrm{T}}\mathbf{u}_{\mathrm{b}}\right)$$
$$\ldots - \int_0^1 \delta\mathbf{u}^{\mathrm{T}}(\xi)(\mathbf{E}_0(2\xi\mathbf{u}(\xi)_{,\xi} + \xi^2\mathbf{u}(\xi)_{,\xi\xi})$$
$$\ldots + \mathbf{E}_1^{\mathrm{T}}(\mathbf{u}(\xi) + \xi\mathbf{u}(\xi)_{,\xi}) - \mathbf{E}_1\xi\mathbf{u}(\xi)_{,\xi} - \mathbf{E}_2\mathbf{u}(\xi))\mathrm{d}\xi$$
$$= \delta\mathbf{u}_{\mathrm{b}}^{\mathrm{T}}\left(\mathbf{E}_0\mathbf{u}(\xi)_{,\xi}\,|_{\xi=1} + \mathbf{E}_1^{\mathrm{T}}\mathbf{u}_{\mathrm{b}}\right)$$
$$\ldots - \int_0^1 \delta\mathbf{u}^{\mathrm{T}}(\xi)(\mathbf{E}_0\xi^2\mathbf{u}(\xi)_{,\xi\xi}$$
$$\ldots + (2\mathbf{E}_0 + \mathbf{E}_1^{\mathrm{T}} - \mathbf{E}_1)\xi\mathbf{u}(\xi)_{,\xi} + (\mathbf{E}_1^{\mathrm{T}} - \mathbf{E}_2)\mathbf{u}(\xi))\mathrm{d}\xi \qquad (4.62)$$

4.3.5.2 Work done by applied body loads

Substituting equation (4.56) and (4.45) to the second term of equation (4.58) produces

$$\int_v (\mathbf{N}_{\mathrm{u}}(\eta,\zeta)\delta\mathbf{u}(\xi))^{\mathrm{T}}\mathbf{p}(\xi,\eta,\zeta)\,\xi^{\mathbf{2}}\,|\mathbf{J}|\,\mathrm{d}\xi\mathrm{d}\eta\mathrm{d}\zeta =$$
$$\int_0^1 \delta\mathbf{u}^{\mathrm{T}}(\xi) - \int_{S_\xi} \mathbf{N}_{\mathrm{u}}^{\mathrm{T}}(\eta,\zeta)\mathbf{p}(\xi,\eta,\zeta)\,|\mathbf{J}|\,\mathrm{d}\eta\mathrm{d}\zeta\xi^2\mathrm{d}\xi, \qquad (4.63)$$

where the applied body loads $\mathbf{p}$ can be a function of any of the scaled boundary coordinates (ξ,η,ζ). The equivalent nodal loads $\mathbf{F}_{\mathrm{b}}$ for the applied body loads can be expressed as

$$\mathbf{F}_{\mathrm{b}} = \int_{S_\xi} \mathbf{N}_{\mathrm{u}}^{\mathrm{T}}(\eta,\zeta)\mathbf{p}(\xi,\eta,\zeta)\,|\mathbf{J}|\,\mathrm{d}\eta\mathrm{d}\zeta. \qquad (4.64)$$

Substituting equation (4.64) in equation (4.63) reveals the second term of equation (4.58) as

$$\int_v \delta\mathbf{u}^{\mathrm{T}}\mathbf{p}\mathrm{d}V = \int_0^1 \delta\mathbf{u}^{\mathrm{T}}(\xi)\mathbf{F}_{\mathrm{b}}\xi^2\mathrm{d}\xi. \qquad (4.65)$$

4.3.5.3 Work done by applied tractions

The applied tractions $\mathbf{t}$ on the boundary $\xi = 1$ can be a function of the scaled boundary coordinates (η,ζ). Substituting equation (4.56) into the third term of equation (4.58) and using $\mathrm{d}S_\xi$ of equation (4.46a) with $\xi = 1$ produces

$$\int_S (\mathbf{N}_\mathrm{u}(\eta,\zeta)\boldsymbol{\delta}\mathbf{u}(\xi=1))^\mathrm{T}\mathbf{t}(\eta,\zeta)\mathrm{d}S_\xi = \boldsymbol{\delta}\mathbf{u}_\mathrm{b}^\mathrm{T}\int_S \mathbf{N}_\mathrm{u}^\mathrm{T}(\eta,\zeta)\mathbf{t}(\eta,\zeta)\,\mathrm{g}_\xi \mathrm{d}\eta\mathrm{d}\zeta. \quad (4.66)$$

Considering $\mathbf{F}_\mathrm{t} = \int_S \mathbf{N}_\mathrm{u}^\mathrm{T}(\eta,\zeta)\mathbf{t}(\eta,\zeta)\,\mathrm{g}_\xi \mathrm{d}\eta\mathrm{d}\zeta$ as the equivalent nodal forces for the applied tractions, equation (4.66) can now be written as

$$\int_s \boldsymbol{\delta}\mathbf{u}^\mathrm{T}\mathbf{t}\mathrm{d}S = \boldsymbol{\delta}\mathbf{u}_\mathrm{b}^\mathrm{T}\mathbf{F}_\mathrm{t}. \quad (4.67)$$

4.3.5.4 Scaled boundary finite element equation in displacement

Considering equations (4.62), (4.65), and (4.67) for the strain energy, for the applied body loads, and for the applied tractions a unified expression for equation (4.58) is obtained in terms of the scaled boundary local coordinates as below.

$$\begin{aligned}&\boldsymbol{\delta}\mathbf{u}_\mathrm{b}^\mathrm{T}\left(\mathbf{E}_0\mathbf{u}(\xi)_{,\xi}\,|_{\xi=1} + \mathbf{E}_1^\mathrm{T}\mathbf{u}_\mathrm{b}\right)\\ &\quad ... - \int_0^1 \boldsymbol{\delta}\mathbf{u}^\mathrm{T}(\xi)(\mathbf{E}_0\xi^2\mathbf{u}(\xi)_{,\xi\xi} + (2\mathbf{E}_0 + \mathbf{E}_1^\mathrm{T} - \mathbf{E}_1)\xi\mathbf{u}(\xi)_{,\xi}\\ &\quad ... + (\mathbf{E}_1^\mathrm{T} - \mathbf{E}_2)\mathbf{u}(\xi))\mathrm{d}\xi - \int_0^1 \boldsymbol{\delta}\mathbf{u}^\mathrm{T}(\xi)\mathbf{F}_\mathrm{b}\xi^2\mathrm{d}\xi - \boldsymbol{\delta}\mathbf{u}_\mathrm{b}^\mathrm{T}\mathbf{F}_\mathrm{t} = 0. \end{aligned} \quad (4.68)$$

Equation (4.68) can be transformed into

$$\begin{aligned}&\boldsymbol{\delta}\mathbf{u}_\mathrm{b}^\mathrm{T}\left(\mathbf{E}_0\mathbf{u}(\xi)_{,\xi}\,|_{\xi=1} + \mathbf{E}_1^\mathrm{T}\mathbf{u}_\mathrm{b} - \mathbf{F}_\mathrm{t}\right)\\ &\quad ... - \int_0^1 \boldsymbol{\delta}\mathbf{u}^\mathrm{T}(\xi)(\mathbf{E}_0\xi^2\mathbf{u}(\xi)_{,\xi\xi} + (2\mathbf{E}_0 + \mathbf{E}_1^\mathrm{T} - \mathbf{E}_1)\xi\mathbf{u}(\xi)_{,\xi}\\ &\quad ... + (\mathbf{E}_1^\mathrm{T} - \mathbf{E}_2)\mathbf{u}(\xi))\mathrm{d}\xi - \int_0^1 \boldsymbol{\delta}\mathbf{u}^\mathrm{T}(\xi)\mathbf{F}_\mathrm{b}\xi^2\mathrm{d}\xi = 0. \end{aligned} \quad (4.69)$$

by rearranging terms containing $\boldsymbol{\delta}\mathbf{u}$ and $\boldsymbol{\delta}\mathbf{u}^\mathrm{T}(\xi)$. To satisfy equation (4.69) for all $\boldsymbol{\delta}\mathbf{u}(\xi)$ with $0 \leq \xi \leq 1$ in all radial and circumferential directions, the following two conditions must be satisfied

$$\delta \mathbf{u}_{\mathrm{b}}^{\mathrm{T}}\left(\mathbf{E}_0\mathbf{u}(\xi)_{,\xi}\,|_{\xi=1} + \mathbf{E}_1^{\mathrm{T}}\mathbf{u}_{\mathrm{b}} - \mathbf{F}_{\mathrm{t}}\right) = 0, \tag{4.70}$$

and

$$\int_0^1 \delta \mathbf{u}^{\mathrm{T}}(\xi)(\mathbf{E}_0\xi^2\mathbf{u}(\xi)_{,\xi\xi} + (2\mathbf{E}_0 + \mathbf{E}_1^{\mathrm{T}} - \mathbf{E}_1)\xi\mathbf{u}(\xi)_{,\xi}$$
$$\ldots + (\mathbf{E}_1^{\mathrm{T}} - \mathbf{E}_2)\mathbf{u}(\xi))\mathrm{d}\xi - \int_0^1 \delta \mathbf{u}^{\mathrm{T}}(\xi)\mathbf{F}_{\mathrm{b}}\xi^2\mathrm{d}\xi = 0. \tag{4.71}$$

Equation (4.70) represents the nodal force-displacement relationship. Rearranging equations (4.70) and (4.71), the following conditions can be obtained

$$\delta \mathbf{u}_{\mathrm{b}}^{\mathrm{T}}\left(\mathbf{E}_0\mathbf{u}(\xi)_{,\xi}\,|_{\xi=1} + \mathbf{E}_1^{\mathrm{T}}\mathbf{u}_{\mathrm{b}} - \mathbf{F}_{\mathrm{t}}\right) - \int_0^1 \delta \mathbf{u}^{\mathrm{T}}(\xi)\mathbf{F}_{\mathrm{b}}\xi^2\mathrm{d}\xi = 0, \tag{4.72}$$

and

$$\int_0^1 \delta \mathbf{u}^{\mathrm{T}}(\xi)(\mathbf{E}_0\xi^2\mathbf{u}(\xi)_{,\xi\xi} + (2\mathbf{E}_0 + \mathbf{E}_1^{\mathrm{T}} - \mathbf{E}_1)\xi\mathbf{u}(\xi)_{,\xi} + (\mathbf{E}_1^{\mathrm{T}} - \mathbf{E}_2)\mathbf{u}(\xi))\mathrm{d}\xi = 0 \tag{4.73}$$

Considering the arbitrariness of $\delta\mathbf{u}(\xi)$, equation (4.73) can be rewritten to obtain the *scaled boundary finite element equation in displacement* as follows

$$\mathbf{E}_0\xi^2\mathbf{u}(\xi)_{,\xi\xi} + (2\mathbf{E}_0 + \mathbf{E}_1^{\mathrm{T}} - \mathbf{E}_1)\xi\mathbf{u}(\xi)_{,\xi} + (\mathbf{E}_1^{\mathrm{T}} - \mathbf{E}_2)\mathbf{u}(\xi) = 0. \tag{4.74}$$

4.3.6 Internal nodal forces on an arbitrary ξ

Equating the internal nodal forces $\mathbf{q}(\xi)$ to the resultant of the surface tractions $\mathbf{t}_\xi$ on a surface with a constant ξ produces the following relationship

$$\delta \mathbf{u}^{\mathrm{T}}(\xi)\mathbf{q}(\xi) = \int_S \delta \mathbf{u}^{\mathrm{T}}(\xi,\eta,\zeta)\mathbf{t}_\xi(\eta,\zeta)\,\mathrm{dS}_\xi. \tag{4.75}$$

Substituting equations (4.56) and (4.46a) into equation (4.75) yields

$$\delta \mathbf{u}^{\mathrm{T}}(\xi)\mathbf{q}(\xi) = \delta \mathbf{u}^{\mathrm{T}}(\xi)\int_S \mathbf{N}_{\mathrm{u}}^{\mathrm{T}}(\eta,\zeta)\mathbf{t}_{\xi}(\eta,\zeta)\xi^2 \mathrm{g}_{\xi}\mathrm{d}\eta\mathrm{d}\zeta. \tag{4.76}$$

Substituting equation (4.50a) into equation (4.76) and using equation (4.55) and the arbitrariness of $\delta\mathbf{u}$ produces

$$\mathbf{q}(\xi) = \int_S \mathbf{N}_{\mathrm{u}}^{\mathrm{T}}(\eta,\zeta)\mathbf{b}_{\mathbf{1}}^{\mathrm{T}}(\eta,\zeta)\left(\mathbf{D}\left(\mathbf{B}_1(\eta,\zeta)\mathbf{u}(\xi)_{,\xi} + \frac{1}{\xi}\mathbf{B}_2(\eta,\zeta)\mathbf{u}(\xi)\right)\right)\xi^2|\mathbf{J}|\,\mathrm{d}\eta\mathrm{d}\zeta$$

$$\mathbf{q}(\xi) = \int_S \mathbf{B}_{\mathbf{1}}^{\mathrm{T}}(\eta,\zeta)\mathbf{D}\left(\mathbf{B}_1(\eta,\zeta)\mathbf{u}(\xi)_{,\xi} + \frac{1}{\xi}\mathbf{B}_2(\eta,\zeta)\mathbf{u}(\xi)\right)\xi^2|\mathbf{J}|\,\mathrm{d}\eta\mathrm{d}\zeta. \tag{4.77}$$

Using equations (4.60a) and (4.60b) in equation (4.77) gives

$$\mathbf{q}(\xi) = \mathbf{E_0}\xi^2\mathbf{u}(\xi)_{,\xi} + \mathbf{E}_1^{\mathrm{T}}\xi\mathbf{u}(\xi). \tag{4.78}$$

Based on equation (4.78), the following relationship for the internal nodal forces on the boundary where $\mathbf{q}_{\mathrm{b}} = \mathbf{q}(\xi = 1)$ is obtained.

$$\mathbf{q}_{\mathrm{b}} = \mathbf{E_0}\mathbf{u}(\xi)_{,\xi}\,|_{\xi=\mathbf{1}} + \mathbf{E}_1^{\mathrm{T}}\mathbf{u}_{\mathrm{b}} \tag{4.79}$$

4.3.7 Solutions of scaled boundary finite element equation for elastostatics

The virtual work derivation for the scaled boundary finite element equation in displacement given in equation (4.74) is a second order homogeneous differential equation in $\mathbf{u}(\xi)$. To solve the scaled boundary finite element equation, equations (4.74) and (4.78) are transformed into a system of first order ordinary differential equations by doubling the number of variables as follows

$$\xi \left\{ \begin{array}{cc} \xi^{0.5} & \mathbf{u}(\xi) \\ \xi^{-0.5} & \mathbf{q}(\xi) \end{array} \right\}_{,\xi} = -\mathbf{Z} \left\{ \begin{array}{cc} \xi^{0.5} & \mathbf{u}(\xi) \\ \xi^{-0.5} & \mathbf{q}(\xi) \end{array} \right\}, \tag{4.80}$$

with the Hamiltonian coefficient matrix $\mathbf{Z}$ defined as

$$\mathbf{Z} = \left\{ \begin{array}{cc} \mathbf{E}_0^{-1}\mathbf{E}_1^{\mathrm{T}} - 0.5\mathbf{I} & \mathbf{E}_0^{-1} \\ -\mathbf{E}_2 + \mathbf{E}_1\mathbf{E}_0^{-1}\mathbf{E}_1^{\mathrm{T}} & -(\mathbf{E}_1\mathbf{E}_0^{-1} - 0.5\mathbf{I}) \end{array} \right\}. \tag{4.81}$$

The eigenvalues of $\mathbf{Z}$ are in pairs. For example $(\lambda, -\lambda)$. A vector $\mathbf{X}$ is introduced as follows

$$\mathbf{X}(\xi) = \left\{ \begin{array}{cc} \xi^{0.5} & \mathbf{u}(\xi) \\ \xi^{-0.5} & \mathbf{q}(\xi) \end{array} \right\} \tag{4.82}$$

Therefore equation (4.80) can be rewritten as

$$\xi \mathbf{X}(\xi)_{,\xi} = -\mathbf{Z}\mathbf{X}(\xi). \tag{4.83}$$

Equation (4.83) can solved by eigenvalue decomposition or through Schur decomposition. In this chapter, the procedure based on the Schur decomposition is explained.

4.3.7.1 Schur decomposition procedure

The details of the Schur decomposition procedure for the solution for the scaled boundary finite element equation in statics can be found in [194]. First matrix $\mathbf{Z}$ is transformed into a real Schur matrix $\mathbf{S}$ as follows

$$\mathbf{V}^{\mathrm{T}}\mathbf{Z}\mathbf{V} = \mathbf{S}, \tag{4.84}$$

where $\mathbf{V}$ is the real orthogonal transformation matrix. Considering matrix orthogonality, $\mathbf{V}^{\mathrm{T}} = \mathbf{V}$. Therefore, the following is also true

$$\mathbf{Z}\mathbf{V} = \mathbf{V}\mathbf{S} \tag{4.85}$$

The matrices **S** produced is a quasi-upper triangular matrix in the following form

$$\mathbf{S} = \begin{bmatrix} \mathbf{S}_{11} & \mathbf{S}_{12} \\ & \mathbf{S}_{22} \end{bmatrix}. \tag{4.86}$$

The diagonal blocks in **S** are sorted in ascending order based on the real parts of their eigenvalues. For the bounded domain, the real parts of all the eigenvalues of the Schur matrix $\mathbf{S}_{11}$ are negative, i.e. $\mathrm{Re}(\lambda(\mathbf{S})) < 0$. The Schur decomposition of the Hamiltonian matrix also possesses the property $\lambda(\mathbf{S}_{11}) = -\lambda(\mathbf{S}_{22})$, i.e. $\mathrm{Re}(\lambda(\mathbf{S}_{22})) > 0$. The transformation **V** is also partitioned conformably similar to matrix **S** as

$$\mathbf{V} = \begin{bmatrix} \mathbf{V}_{11} & \mathbf{V}_{12} \\ \mathbf{V}_{21} & \mathbf{V}_{22} \end{bmatrix}. \tag{4.87}$$

A vector $\mathbf{X}_{\mathrm{m}}(\xi)$ is introduced such that

$$\mathbf{X}(\xi) = \mathbf{V}\mathbf{X}_{\mathrm{m}}(\xi). \tag{4.88}$$

Substituting equation (4.88) into equation (4.83) produces

$$\xi\mathbf{X}_{\mathrm{m}}(\xi)_{,\xi} = -\mathbf{Z}\mathbf{V}\mathbf{X}_{\mathrm{m}}(\xi). \tag{4.89}$$

Pre-multiplying both sides with $\mathbf{V}^{\mathrm{T}}$ produces

$$\xi\mathbf{X}_{\mathrm{m}}(\xi)_{,\xi} = -\mathbf{V}^{\mathrm{T}}\mathbf{Z}\mathbf{V}\mathbf{X}_{\mathrm{m}}(\xi). \tag{4.90}$$

Using equation (4.84), equation (4.90) can be written as

$$\xi\mathbf{X}_{\mathrm{m}}(\xi)_{,\xi} = -\mathbf{S}\mathbf{X}_{\mathrm{m}}(\xi). \tag{4.91}$$

The general solution of equation (4.91) is in the form of

$$\mathbf{X}_{\mathrm{m}}(\xi) = \xi^{-S}\mathbf{c}, \tag{4.92}$$

where $\mathbf{c}$ are the integration constants.

4.3.7.2 Block-diagonalization of the Schur matrix

The procedure explained in [525] is followed to block-diagonalise the quasi-upper triangular matrix $\mathbf{S}$ in equation (4.86). The procedure first involves pre-multiplying equation (4.85) with $\mathbf{Y}^{-1}$ and post-multiplied with $\mathbf{Y}$

$$\begin{aligned}
\mathbf{Y}^{-1}\mathbf{S}\mathbf{Y} &= \mathbf{Y}^{-1}\mathbf{V}^{-1}\mathbf{Z}\mathbf{V}\mathbf{Y}, \\
\mathbf{Y}^{-1}\mathbf{S}\mathbf{Y} &= (\mathbf{Y}\mathbf{V})^{-1}\mathbf{Z}\mathbf{V}\mathbf{Y},
\end{aligned} \tag{4.93}$$

where $\mathbf{Y}$ is an upper triangular transformation matrix in the form of

$$\mathbf{Y} = \begin{bmatrix} \mathbf{I} & \mathbf{Y}_{12} \\ & \mathbf{I} \end{bmatrix}. \tag{4.94}$$

Next, by multiplication of $\mathbf{V}$ and $\mathbf{Y}$ as follows an accumulated transformation matrix Ψ is obtained as below.

$$\begin{aligned}
\Psi = \mathbf{V}\mathbf{Y} &= \begin{bmatrix} \mathbf{V}_{11} & \mathbf{V}_{11}\mathbf{Y}_{12} + \mathbf{V}_{12} \\ \mathbf{V}_{21} & \mathbf{V}_{21}\mathbf{Y}_{12} + \mathbf{V}_{22} \end{bmatrix}, \\
\Psi &= \begin{bmatrix} \Psi_{11} & \Psi_{12} \\ \Psi_{21} & \Psi_{22} \end{bmatrix}.
\end{aligned} \tag{4.95}$$

Equation (4.93) transforms to

$$\mathbf{Y}^{-1}\mathbf{S}\mathbf{Y} = \Psi^{-1}\mathbf{Z}\Psi, \tag{4.96}$$

when $\mathbf{VY}$ is substituted by equation (4.95). Then to determine the sub-matrix $\mathbf{Y}_{12}$ in equation (4.94) the following expression is required to be satisfied

$$\mathbf{Y}^{-1}\mathbf{SY} = \begin{bmatrix} \mathbf{S}_{11} & 0 \\ 0 & \mathbf{S}_{22} \end{bmatrix}. \tag{4.97}$$

The right hand side of equation (4.97) is referred to as the block diagonalised version of the $\mathbf{S}$ matrix $(\mathbf{S}_{\text{block}})$. This is because $\mathbf{S}_{\text{block}}$ resembles $\mathbf{S}$ in equation (4.86) with sub-matrices $\mathbf{S}_{11}$ and $\mathbf{S}_{22}$ with only one difference in $\mathbf{S}_{12}$ sub-matrix being 0. Therefore

$$\mathbf{S}_{\text{block}} = \begin{bmatrix} \mathbf{S}_{11} & 0 \\ 0 & \mathbf{S}_{22} \end{bmatrix}. \tag{4.98}$$

To determine the sub-matrix $\mathbf{Y}_{12}$ in equation (4.94), the expression in equation (4.97) is rearranged as

$$\mathbf{SY} = \mathbf{Y}\begin{bmatrix} \mathbf{S}_{11} & 0 \\ 0 & \mathbf{S}_{22} \end{bmatrix}. \tag{4.99}$$

Substituting equations (4.86) and (4.94), into equation (4.99), then multiplying the matrices on each side produces

$$\begin{bmatrix} \mathbf{S}_{11} & \mathbf{S}_{11}\mathbf{Y}_{12}+\mathbf{S}_{12} \\ 0 & \mathbf{S}_{22} \end{bmatrix} = \begin{bmatrix} \mathbf{S}_{11} & \mathbf{Y}_{12}\mathbf{S}_{22} \\ 0 & \mathbf{S}_{22} \end{bmatrix}. \tag{4.100}$$

The sub-matrix $\mathbf{Y}_{12}$ must be chosen in order for equation (4.100) to hold. Therefore, the following equation must be satisfied

$$\mathbf{S}_{11}\mathbf{Y}_{12}+\mathbf{S}_{12} = \mathbf{Y}_{12}\mathbf{S}_{22}, \tag{4.101}$$

which can be rearranged as

$$\mathbf{S}_{11}\mathbf{Y}_{12} - \mathbf{Y}_{12}\mathbf{S}_{22} = -\mathbf{S}_{12}. \tag{4.102}$$

This last equation is in the form of Sylvester matrix equation. Therefore the solution for $\mathbf{Y}_{12}$ can be obtained by a simple back substitution as the Schur sub-matrices $\mathbf{S}_{11}$ and $\mathbf{S}_{22}$ are quasi-upper triangular matrices.

Subsequently, the expression in equation (4.96) can be written using equation (4.97) as

$$\Psi^{-1}\mathbf{Z}\Psi = \mathbf{S}_{\text{block}}. \tag{4.103}$$

From here on the block diagonalised $\mathbf{S}$ matrix, $\mathbf{S}_{\text{block}}$ will be referred to as just $\mathbf{S}$ in order to simplify the notation. The equation (4.103) can be rearranged into

$$\mathbf{Z}\Psi = \Psi\mathbf{S}. \tag{4.104}$$

The expanded form of equation (4.104) can be written as

$$\begin{aligned}\begin{bmatrix} \mathbf{E}_0^{-1}\mathbf{E}_1^{\mathrm{T}} - 0.5\mathbf{I} & \mathbf{E}_0^{-1} \\ -\mathbf{E}_2 + \mathbf{E}_1\mathbf{E}_0^{-1}\mathbf{E}_1^{\mathrm{T}} & -\left(\mathbf{E}_1\mathbf{E}_0^{-1} - 0.5\mathbf{I}\right) \end{bmatrix} \begin{bmatrix} \Psi_{11} & \Psi_{12} \\ \Psi_{21} & \Psi_{22} \end{bmatrix} \\ = \begin{bmatrix} \Psi_{11} & \Psi_{12} \\ \Psi_{21} & \Psi_{22} \end{bmatrix} \begin{bmatrix} \mathbf{S}_{11} & 0 \\ 0 & \mathbf{S}_{22} \end{bmatrix}.\end{aligned} \tag{4.105}$$

Now a vector $\mathbf{U}(\xi)$ is introduced where

$$\mathbf{X}(\xi) = \Psi\mathbf{U}(\xi). \tag{4.106}$$

Substituting equation (4.106) into equation (4.83) reveals

$$\xi \Psi \mathbf{U}(\xi)_{,\xi} = -\mathbf{Z}\Psi \mathbf{U}(\xi). \tag{4.107}$$

Pre-multiplying both sides with Ψ^{-1} produces

$$\xi \mathbf{U}(\xi)_{,\xi} = -\Psi^{-1}\mathbf{Z}\Psi \mathbf{U}(\xi). \tag{4.108}$$

With the help of equation (4.103), equation (4.108) can be written as

$$\xi \mathbf{U}(\xi)_{,\xi} = -\mathbf{S}\mathbf{U}(\xi). \tag{4.109}$$

The general solution of equation (4.109) must be in the form of

$$\mathbf{U}(\xi) = -\xi^{-\mathbf{S}}\mathbf{c}, \tag{4.110}$$

where $\mathbf{c}$ are the integration constants partitioned conformably as

$$\mathbf{c} = \left\{ \begin{array}{c} \mathbf{c}_1 \\ \mathbf{c}_2 \end{array} \right\}. \tag{4.111}$$

4.3.7.3 Solution for the displacement functions on the radial lines

The solution for $\mathbf{X}(\xi)$ in equation (4.106) can be written using the solution in equation (4.110) as

$$\mathbf{X}(\xi) = \Psi \xi^{-\mathbf{S}}\mathbf{c}. \tag{4.112}$$

Incorporating equations (4.82), (4.95), (4.98), and (4.111), equation (4.112) can be written as

$$\left\{\begin{array}{cc} \xi^{0.5} & \mathbf{u}(\xi) \\ \xi^{-0.5} & \mathbf{q}(\xi) \end{array}\right\} = \begin{bmatrix} \Psi_{11} & \Psi_{12} \\ \Psi_{21} & \Psi_{22} \end{bmatrix} \xi^{-\begin{bmatrix} \mathbf{S}_{11} & 0 \\ 0 & \mathbf{S}_{22} \end{bmatrix}} \left\{\begin{array}{c} \mathbf{c}_1 \\ \mathbf{c}_2 \end{array}\right\}. \tag{4.113}$$

Expanding equation (4.113) reveals the general solutions for the displacements $(\mathbf{u}(\xi))$ and internal nodal forces $(\mathbf{q}(\xi))$ as

$$\mathbf{u}(\xi) = \Psi_{11}\xi^{-\mathbf{S}_{11}-0.5\mathbf{I}}\mathbf{c}_1 + \Psi_{12}\xi^{-\mathbf{S}_{22}-0.5\mathbf{I}}\mathbf{c}_2 \tag{4.114a}$$

$$\mathbf{q}(\xi) = \Psi_{21}\xi^{-\mathbf{S}_{11}+0.5\mathbf{I}}\mathbf{c}_1 + \Psi_{22}\xi^{-\mathbf{S}_{22}+0.5\mathbf{I}}\mathbf{c}_2 \tag{4.114b}$$

The displacement solution must remain finite at the scaling centre i.e. $\mathbf{u}(\xi = 0)$ for a bounded domain. This can only be achieved if $\mathbf{c}_2 = 0$. Therefore, for the bounded domain, the solutions in equations (4.114a) and (4.114b) simplifies to

$$\mathbf{u}(\xi) = \Psi_{11}\xi^{-\mathbf{S}_{11}-0.5\mathbf{I}}\mathbf{c}_1, \tag{4.115a}$$

$$\mathbf{q}(\xi) = \Psi_{21}\xi^{-\mathbf{S}_{11}+0.5\mathbf{I}}\mathbf{c}_1. \tag{4.115b}$$

At the boundary where $\xi = 1$, equations (4.115a) and (4.115b) can be expressed as

$$\mathbf{u}_\mathrm{b} = \Psi_{11}\mathbf{c}_1, \tag{4.116a}$$

$$\mathbf{q}_\mathrm{b} = \Psi_{21}\mathbf{c}_1. \tag{4.116b}$$

The static stiffness matrix $\mathbf{K}_\mathrm{s}$ of each subdomain can be formulated in terms of $\mathbf{u}_\mathrm{b}$ and $\mathbf{q}_\mathrm{b}$ as

$$\mathbf{q}_\mathrm{b} = \mathbf{K}_\mathrm{s}\mathbf{u}_\mathrm{b} \tag{4.117}$$

by substituting equations (4.116a) and (4.116b) into equation (4.117), $\mathbf{K}_\mathrm{s}$ can be written as

$$\mathbf{K}_{\mathrm{s}} = \Psi_{21}\Psi_{11}^{-1}. \tag{4.118}$$

The integration constants $\mathbf{c}_1$ can be evaluated as

$$\mathbf{c}_1 = \Psi_{11}^{-1}\mathbf{u}_{\mathrm{b}}. \tag{4.119}$$

Using equation (4.119), equations (4.115a) and (4.115b) can be written as

$$\mathbf{u}(\xi) = \Psi_{11}\xi^{-\mathbf{S}_{11}-0.5\mathbf{I}}\Psi_{11}^{-1}\mathbf{u}_{\mathrm{b}}, \tag{4.120a}$$

$$\mathbf{q}(\xi) = \Psi_{21}\xi^{-\mathbf{S}_{11}+0.5\mathbf{I}}\Psi_{11}^{-1}\mathbf{u}_{\mathrm{b}}. \tag{4.120b}$$

4.3.7.4 Solution for the strain and stress fields

The strain field is obtained by substituting equation (4.115a) into equation (4.53) as

$$\varepsilon(\xi,\eta,\zeta) = \Psi_{\varepsilon}(\eta,\zeta)\xi^{-(\mathbf{S}_{11}+1.5\mathbf{I})}\mathbf{c}_1, \tag{4.121}$$

where the strain modes $\Psi_{\varepsilon}(\eta,\zeta)$ are denoted as

$$\Psi_{\varepsilon}(\eta,\zeta) = -\mathbf{B}_1(\eta,\zeta)\Psi_{11}(\mathbf{S}_{11}+0.5\mathbf{I}) + \mathbf{B}_2(\eta,\zeta)\Psi_{11}. \tag{4.122}$$

The stress filed can be obtained using equations (4.55) and (4.115a)

$$\sigma(\xi,\eta,\zeta) = \Psi_{\sigma}(\eta,\zeta)\,\xi^{-(\mathbf{S}_{11}+1.5\mathbf{I})}\mathbf{c}_1, \tag{4.123}$$

where the stress modes $\Psi_{\sigma}(\eta,\zeta)$ are given as

$$\Psi_{\sigma}(\eta,\zeta) = \mathbf{D}\left(-\mathbf{B}_1(\eta,\zeta)\Psi_{11}(\mathbf{S}_{11}+0.5\mathbf{I}) + \mathbf{B}_2(\eta,\zeta)\Psi_{11}\right). \tag{4.124}$$

4.3.7.5 Nodal forces on the boundary and the global matrices assembly

The virtual displacement field in the radial direction, $\delta\mathbf{u}(\xi)$ can be written using equation (4.120a) as

$$\delta\mathbf{u}(\xi) = \Psi_{11}\xi^{-\mathbf{S}_{11}-0.5\mathbf{I}}\Psi_{11}^{-1}\delta\mathbf{u}_{\mathrm{b}}. \tag{4.125}$$

Substituting equation (4.125) into equation (4.72) yields

$$\begin{aligned}
&\delta\mathbf{u}_{\mathrm{b}}^{\mathrm{T}}\left(\mathbf{E}_0\mathbf{u}(\xi)_{,\xi}\,|_{\xi=1} + \mathbf{E}_1^{\mathrm{T}}\mathbf{u}_{\mathrm{b}} - \mathbf{F}_{\mathrm{t}}\right)\\
&\qquad\qquad ... - \int_0^1\left(\Psi_{11}\xi^{-\mathbf{S}_{11}-0.5\mathbf{I}}\Psi_{11}^{-1}\delta\mathbf{u}_{\mathrm{b}}\right)^{\mathrm{T}}\mathbf{F}_{\mathrm{b}}\xi^2\mathrm{d}\xi = 0,\\
&\delta\mathbf{u}_{\mathrm{b}}^{\mathrm{T}}\left(\mathbf{E}_0\mathbf{u}(\xi)_{,\xi}\,|_{\xi=1} + \mathbf{E}_1^{\mathrm{T}}\mathbf{u}_{\mathrm{b}} - \mathbf{F}_{\mathrm{t}} - \int_0^1\Psi_{11}^{-\mathrm{T}}\xi^{-\mathbf{S}_{11}^{\mathrm{T}}+1.5\mathbf{I}}\Psi_{11}^{\mathrm{T}}\mathbf{F}_{\mathrm{b}}\mathrm{d}\xi\right) = 0.
\end{aligned} \tag{4.126}$$

By considering the arbitrariness of $\delta\mathbf{u}_{\mathrm{b}}$, equation (4.126) transforms into

$$\mathbf{E}_0\mathbf{u}(\xi)_{,\xi}\,|_{\xi=1} + \mathbf{E}_1^{\mathrm{T}}\mathbf{u}_{\mathrm{b}} - \mathbf{F}_{\mathrm{t}} - \int_0^1\Psi_{11}^{-\mathrm{T}}\xi^{-\mathbf{S}_{11}^{\mathrm{T}}+1.5\mathbf{I}}\Psi_{11}^{\mathrm{T}}\mathbf{F}_{\mathrm{b}}\mathrm{d}\xi = 0. \tag{4.127}$$

The fourth term on the left hand side of equation (4.127) is relevant to the equivalent nodal forces from the body loads $\mathbf{F}_{\mathrm{b}}$. This term is denoted as $\mathbf{F}_{\mathrm{bn}}$ as follows

$$\mathbf{F}_{\mathrm{bn}} = \int_0^1\Psi_{11}^{-\mathrm{T}}\xi^{-\mathbf{S}_{11}^{\mathrm{T}}+1.5\mathbf{I}}\Psi_{11}^{\mathrm{T}}\mathbf{F}_{\mathrm{b}}\mathrm{d}\xi. \tag{4.128}$$

Considering equations (4.79) and (4.128), equation (4.127) can be expressed after re-arrangement as

$$\mathbf{q}_{\mathrm{b}} = \mathbf{F}_{\mathrm{A}}, \tag{4.129}$$

where

$$\mathbf{F}_{\mathrm{A}} = \mathbf{F}_{\mathrm{t}} + \mathbf{F}_{\mathrm{bn}}. \tag{4.130}$$

Substituting equation (4.117) into equation (4.129) and rearranging produces

$$\mathbf{K}_{\mathrm{s}}\mathbf{u}_{\mathrm{b}} = \mathbf{F}_{\mathrm{A}}. \tag{4.131}$$

Judging by the equation (4.131) the contribution of the body loads only affect the nodal force vectors. Therefore the solution of each polyhedral element can be evaluated in the same way as in elastostatic problems with vanishing body loads ($\mathbf{F}_{\mathrm{bn}} = 0$).

The global stiffness matrix can be obtained by assembling the stiffness contributions from the polyhedral elements in the same way as in FEM. A global equation can be expressed as

$$\mathbf{K}_{\mathrm{G}}\mathbf{U} = \mathbf{P}, \tag{4.132}$$

where $\mathbf{K}_{\mathrm{G}}$ is the global stiffness matrix obtained from the assembly of all the polyhedral elements' stiffness matrices $\mathbf{K}_{\mathrm{s}}$, $\mathbf{P}$ is the global nodal force vector obtained from the assembly of all the polyhedral elements' nodal force vectors $\mathbf{F_A}$, and $\mathbf{U}$ are the global nodal displacements of the whole problem domain. After introducing the boundary conditions, a system of linear equations can be solved by direct solver or preconditioned conjugate gradient (PCG) iterative solver [526] to obtain the displacements $\mathbf{U}$.

It should be emphasized that the strain modes depend only on the geometry of the subdomain. At the scaling centre of one subdomain, i.e. $\xi = 0$, all the strain modes with the real parts of the eigenvalues $\mathrm{Re}(\lambda(\mathbf{S}_{11})) \neq -1.5$ vanish and only the modes with $\mathrm{Re}(\lambda(\mathbf{S}_{11})) = -1.5$ lead to a non-zero strain. Consequently, the strains at the scaling centre can be calculated by substituting equation (4.119) in equation (4.121)

$$\varepsilon_{sc}(\xi,\eta,\zeta) = \sum_{\mathrm{j}=1}^{\mathrm{m}} \Psi_{\varepsilon\mathrm{j}}(\eta,\zeta)\,\mathbf{c}_{\mathrm{j}}. \tag{4.133}$$

where $\mathbf{c}_{\mathrm{j}}$ and $\Psi_{\varepsilon\mathrm{j}}$ are the integration constants and strain modes corresponding to $\mathrm{Re}(\lambda(\mathbf{S}_{11})) = -1.5$ and m is the number of modes with $\mathrm{Re}(\lambda(\mathbf{S}_{11})) = -1.5$.

4.4 Damage formulation in SBFEM

From a physical point of view, the material property of each point in the domain is inhomogeneous even before the damage appearing, especially for concrete and geotechnical materials. In the macroscopic level, for the sake of simplicity, the domain is always considered as homogeneous and uniform material properties are assumed. However, owing to the non-integrity of structures and locally applied loading, damage inevitably emerges from local parts of the domain, leading to a non-uniform degradation of material stiffness, i.e. various severity of damage within a finite domain. From a numerical point of view, if sufficiently small subdomains (elements) are used in the DPZ, as an approximation, the damage degree can be assumed to be uniform in one subdomain. Consequently, the coefficient matrix after damage can be obtained by substituting equation (3.1) into equation (4.60a-4.60c) as

$$\mathbf{E}_0^{\mathrm{D}} = (1-\omega)\int_s \mathbf{B}_1^{\mathrm{T}}(\eta,\zeta)\mathbf{D}\mathbf{B}_1(\eta,\zeta)|\mathbf{J}|d\eta d\zeta, \tag{4.134a}$$

$$\mathbf{E}_1^{\mathrm{D}} = (1-\omega)\int_s \mathbf{B}_2^{\mathrm{T}}(\eta,\zeta)\mathbf{D}\mathbf{B}_1(\eta,\zeta)|\mathbf{J}|d\eta d\zeta, \tag{4.134b}$$

$$\mathbf{E}_2^{\mathrm{D}} = (1-\omega)\int_s \mathbf{B}_2^{\mathrm{T}}(\eta,\zeta)\mathbf{D}\mathbf{B}_2(\eta,\zeta)|\mathbf{J}|d\eta d\zeta, \tag{4.134c}$$

where $\mathbf{E}_0^{\mathrm{D}}$, $\mathbf{E}_1^{\mathrm{D}}$ and $\mathbf{E}_2^{\mathrm{D}}$ are counterparts of the coefficient matrix with the damage variable ω of one subdomain.

Substituting equation (4.134a-4.134c) into equations (4.74) and (4.78), a similar matrix as equation (4.81) can be obtained

$$\mathbf{Z}^{\mathrm{D}} = \begin{bmatrix} \mathbf{E}_0^{-1}\mathbf{E}_1^{\mathrm{T}} - 0.5\mathbf{I} & (1-\omega)^{-1}\mathbf{E}_0^{-1} \\ (1-\omega)\left(-\mathbf{E}_2 + \mathbf{E}_1\mathbf{E}_0^{-1}\mathbf{E}_1^{\mathrm{T}}\right) & -\left(\mathbf{E}_1\mathbf{E}_0^{-1} - 0.5\mathbf{I}\right) \end{bmatrix}. \tag{4.135}$$

Using the properties of matrix, it can be proven that

$$\mathbf{S}^{\mathrm{D}} = \begin{bmatrix} \mathbf{S}_{11} & 0 \\ 0 & \mathbf{S}_{22} \end{bmatrix}, \tag{4.136}$$

and

$$\mathbf{V}^{\mathrm{D}} = \begin{bmatrix} \mathbf{V}_{11} & (1-\omega)^{-1}\mathbf{V}_{12} \\ (1-\omega)\mathbf{V}_{21} & \mathbf{V}_{22} \end{bmatrix}. \tag{4.137}$$

Substituting equations (4.136) and (4.137) into equation (4.118), the stiffness matrix for one subdomain with damage is given as

$$\mathbf{K}^{\mathrm{D}} = (1-\omega)\mathbf{K}_{\mathrm{s}}. \tag{4.138}$$

Equation (4.136) and (4.137) also implies that the strain modes, i.e. equation (4.122), do not change during the damage process. In each load step, only the integration constants $\mathbf{c}$ should be updated according to the nodal displacement by using equation (4.119) and subsequently the strain and stress field by using equations (4.121) and (4.123), respectively.

The non-linear global equation system is obtained by assembling the stiffness matrix of all subdomains as

$$\mathbf{KU} = \mathbf{P}, \tag{4.139}$$

where $\mathbf{K}$ is the global stiffness matrix with damage. Equation (4.139) can be solved by either implicit [479] or explicit [499] iterations. These two schemes are compared in order to evaluate the accuracy and efficiency in section 4.6.

4.5 Implicit scheme for damage simulation in the SBFEM

The implicit scheme presented in this section builds on the arc-length incorporated m-NR method presented in chapter 3, section 3.6. The flowchart shown in figure 4.2 depicts the steps involved when acceleration or damping is included in the m-NR method with arc-length [527].

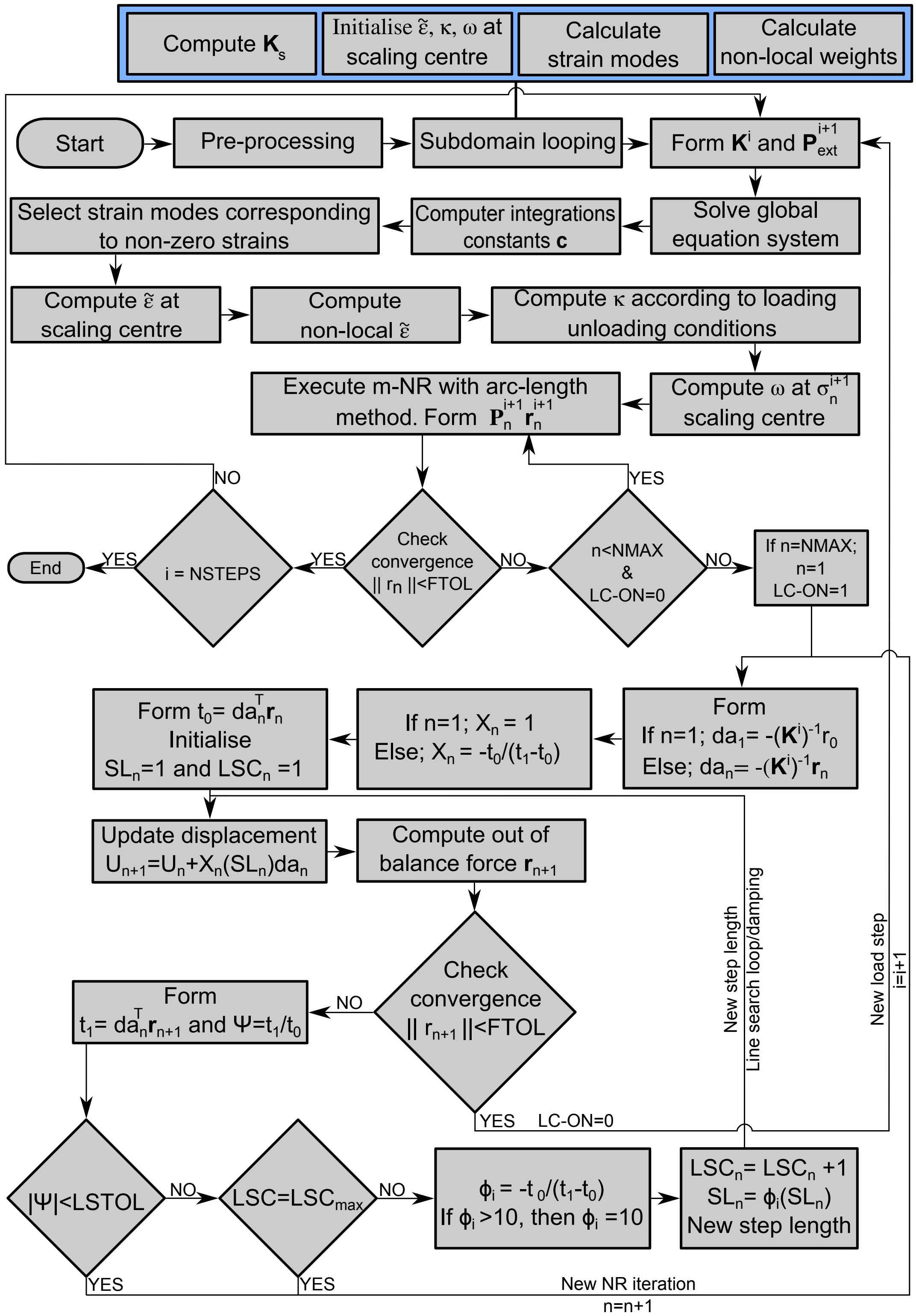

Figure 4.2. Flowchart of the implicit scheme for damage simulation in the SBFEM. Implementation of the acceleration and damping (line searches) m-NR method with arc-length.

After attaining the spatial decomposition of the problem domain, an initial loop over all the subdomains is carried out to calculate the global elastic stiffness matrix $(\mathrm{K_s})$ corresponding to the 0^{th} load step for each subdomain. Along with this process the equivalent strain $\widetilde{\varepsilon}$, internal variable κ, and the damage variable ω are all initialised for the scaling centre formulation. The Gauss point weights are also calculated and stored according to equations (3.14) and (3.15). Simultaneously, the damage variable is initiated to take up a constant value within a subdomain and all the strain modes are computed and stored for each subdomain in accordance with equation (4.122).

Apart from the first load step $(i = 0)$, for a general $(i+1)^{th}$ load step the global elastic stiffness matrix $\left(\mathrm{K}_{\mathrm{G}}^{i}\right)$ is substituted by the damaged stiffness matrix, K^{i} from the previous converged load step i in accordance with equation (4.138). Next the external load vector $\mathbf{P}_{ext}^{i+1}$ is formed and then the global system of equations are formulated by equation (4.139). Thereafter a solution is sought with the help of the iterative m-NR formulation explained in chapter 3, section 3.6. Here the general load step is taken as $(i+1)$ and the NR iteration step is considered as n.

At the end of each NR iteration the residual force norm $\|\mathbf{r}_n\|$ is checked against the user defined tolerance limit FTOL. Here priority is given to the arc-length incorporated m-NR method to obtain a converged solution. At the event a converged solution is not obtained within the permissible maximum number of NR iteration NMAX, the process defaults to the accelerated/dampened line search technique. A logical check is conducted to allow the process to migrate to this loop with the help of a switch on/switch off variable LC-ON. When LC-ON=1, the process moves to the accelerated/dampened line search technique.

The accelerated/dampened line search technique begins with evaluating the correction to the displacement increment $\mathrm{d}\mathbf{a}_n$ as

$$\mathrm{d}\mathbf{a}_n = \left(\mathbf{K}^{i}\right)^{-1}\mathbf{r}_n. \tag{4.140}$$

Afterwords, the accelerator parameter X_n is evaluated by

$$\mathrm{X}_n = \frac{-t_0}{t_1 - t_0}, \tag{4.141}$$

where, X_n is initialized as 1 (no acceleration) for $n = 0$ and for the iterations that follow $t_0 = \mathrm{d}\mathbf{a}_{\mathrm{n}}^{\mathrm{T}}\mathbf{r}_n$ and $t_1 = \mathrm{d}\mathbf{a}_{\mathrm{n}}^{\mathrm{T}}\mathbf{r}_{n+1}$. At the same time the step length (SL_n) and the line search counter (LSC) are both initialised to 1. With the parameters calculated thus far, the displacement is then updated as

$$\mathbf{U}_{n+1} = \mathbf{U}_n + \mathrm{X}_n\,(\mathrm{SL}_n)\,\mathrm{d}\mathbf{a}_n. \tag{4.142}$$

With this updated displacement $\mathbf{U}_{n+1}$ the residual force norm $\|\mathbf{r}_{n+1}\|$ is checked against the user defined tolerance limit FTOL. If converged the analysis proceeds to the next load step by switching off LC-ON. If convergence is not attained, the step-length amplification factor, ϕ_n is formed as $\phi_n = \frac{t_1}{t_0}$. Here, ϕ_n needs to be less than the line search tolerance LSTOL calculated by

$$|\mathrm{LSTOL}| = \left| \frac{\mathrm{d}\mathbf{a}_{\mathrm{n}}^{\mathrm{T}}\mathbf{r}_{n+1}}{\mathrm{d}\mathbf{a}_{\mathrm{n}}^{\mathrm{T}}\mathbf{r}_n} \right|. \tag{4.143}$$

If LSTOL is not exceeded and the maximum user defined number of the line search count (LSC_{max}) is not exceeded the step length SL is modified by ϕ_n as, SL_n=$\phi_n\,(\mathrm{SL}_n)$. Then, ϕ_n is updated to the previously calculated acceleration parameter X_n and a new damping/line search loop executed. In this work the maximum step-length amplification, at each cycle, is set to ten. The process is repeated till a convergence is obtained within the accelerated/dampened line search scheme.

4.6 Numerical examples

In this section, the 3D uniaxial tension beam problem (section 4.6.1) and the 3D damage characterization in shear band problem (section 4.6.2) are two plain strain numerical examples selected from chapter 3 section 3.7 to validate the SBFEM formulation in 3D. The results compare the 3D load vs displacement output to the outputs obtained through the 2D SBFE formulation in chapter 3 and also to that of previously published literature. The 3D uniaxial tension beam problem also investigates the 3D behaviour of local and non-local damage analysis formulations. In the next numerical example a three point bending problem is simulated and presented to further validate the 3D SBFEM in damage analysis by comparing the outputs with a published simulation output of a three point bending beam (see section 4.6.3). The three examples that follow: the double-notched tension beam, the four-point bending beam with a central notch and the L-shaped specimen in sections 4.6.4, 4.6.5 and 4.6.6 respectively compare converged non-local results of the presented formulation to that of experimental data available in published literature. These examples also compare the results obtained through an explicit formulation (courtesy Zihua Zhang) to that of an implicit formulation in SBFEM. The implicit and the explicit simulations are both implemented in MATLAB and performed using an Intel Core i7 @3.4 GHz desktop computer with 8 GB RAM.

4.6.1 Three dimensional uniaxial tension test

The example is extracted from the MSc Thesis [499] and was first introduced in section 3.7.1 of chapter 3 for the validation of the 2D damage formulation in SBFEM. The purpose of this example is to demonstrate under plain strain conditions the validity of the 3D damage formulation in SBFEM by comparing the results obtained through this formulation to that of the plain strain 2D formulation. Similar to what was investigated in section 3.7.1 results of both local and non-local formulations are compared for this purpose. Furthermore, the localization effects of local damage models in 3D space is also investigated in this example.

The length of the model is set to 100 mm and the height considered to be 10 mm. The dimensions are selected similar to the reference with an additional dimension of width introduced for modelling a 3D simulation. To obtain a good aspect ratio in the meshed elements the width of the specimen is set at 10 mm (refer figure 4.3). Therefore, the cross sectional area considered in the 3D analysis is $100\,\text{mm}^2$ compared to that of the assumed $10\,\text{mm}^2$ in the 2D formulation.

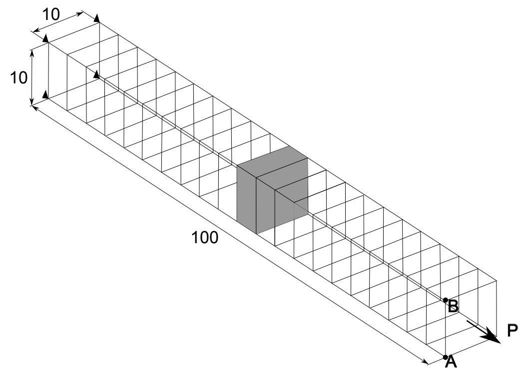

Figure 4.3. Specimen dimensions (mm) and boundary conditions used in the 3D uniaxial tension test. Shaded area represent the imperfection.

To simulate uniaxial loading conditions the bar is clamped at one end with the opposite end subjected to a prescribed displacement, incrementally applied as shown in figure 4.3. Plain strain conditions are modelled by restricting movement on the faces transverse to the direction of loading.

The 5 meshes used in this example are shown in figure 4.4. The meshes 1-5 consist of 21, 51, 81, 101 and 201 elements equally distributed along the length of the member, respectively.

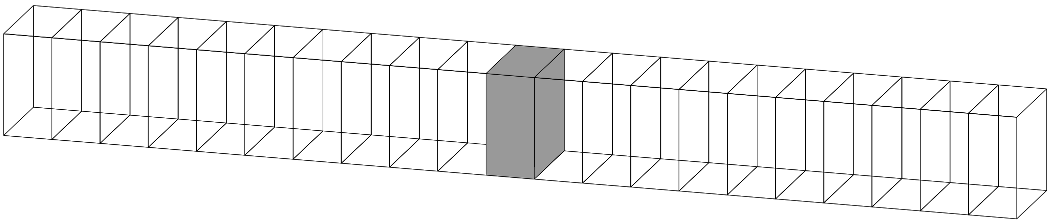

(a) Mesh 1 - 21 Elements

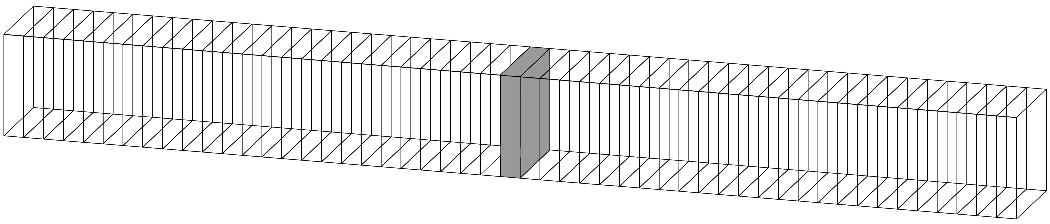

(b) Mesh 2 - 51 Elements

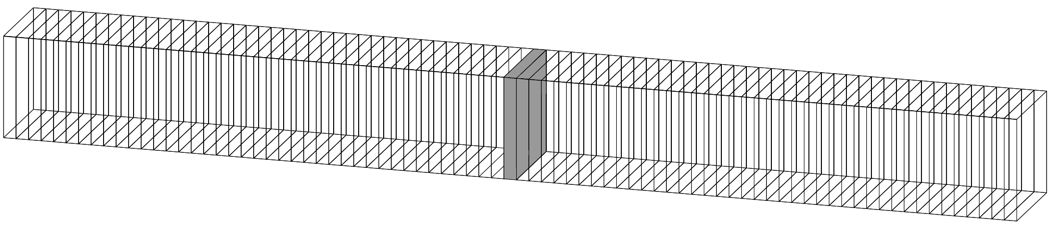

(c) Mesh 3 - 81 Elements

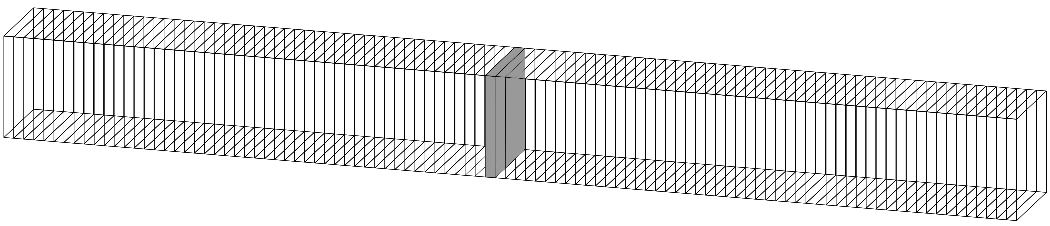

(d) Mesh 4 - 101 Elements

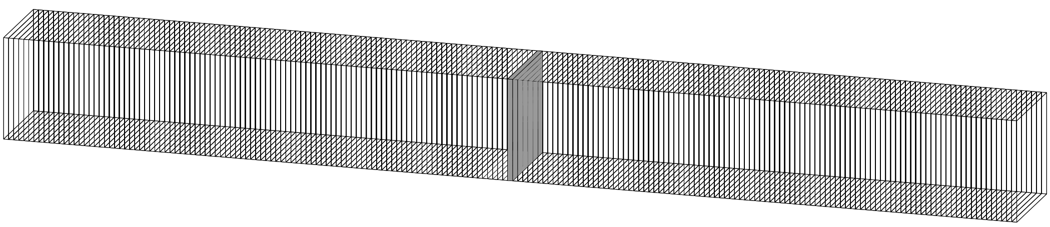

(e) Mesh 5 - 201 Elements

Figure 4.4. SBFE polyhedron meshes used in the local and non-local analysis of the 3D uniaxial tension test.

The modulus of elasticity and the Poisson's ratio are taken 30 GPa and 0.0 respectively. The central element of the member is modelled to carry an imperfection by introducing a weaker martial characteristic. Therefore the damage initiation threshold (ε_0) for the weaker material is set to 145×10^{-6} whereas for the rest of the elements ε_0 is considered as 150×10^{-6}. Figure 4.5 depicts the stress-strain variation for the weaker material by considering the damage variables α - 0.95 and β - 100 in equation (4.3).

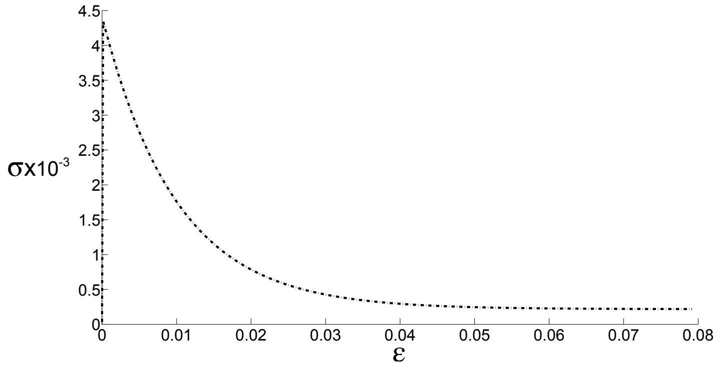

Figure 4.5. 1D element stress (GPa) vs strain profile considered in the 3D damage simulation of the uniaxial tension test with respect to the softening law given in equation (4.3).

The stronger material is considered to have the damage parameters α and β similar to the weaker material. The equivalent strain $\widetilde{\varepsilon}$ is calculated according to the Mazar's definition given in equation (4.5).

This example is simulated using the displacement controlled accelerated/dampened arc-length incorporated m-NR technique. The initial displacement step is set to 0.001 mm.

4.6.1.1 Local formulation

First to illustrate the mesh sensitivity of local damage models the simulation is run using meshes 1, 2 and 3 in figure 4.4. The load-displacement output for the three separate meshes is given in figure 4.6. The load is recorded on edge 'AB' whereas the displacement is recorded at node 'A'.

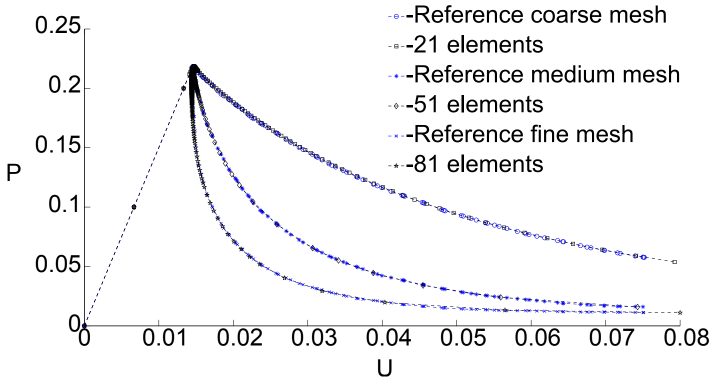

Figure 4.6. Load (kN)-deformation (mm) curves for meshes 1-3 in the 3D uniaxial tension test. Comparison of the SBFEM with the reference output [499]. Local damage analysis with assumed plain strain conditions simulated.

In order to compare the 3D results to that of the 2D results in chapter 3, the 2D results are multiplied by 10 to account for the enlarged cross section adopted in the 3D simulation.

When the mesh is gradually made finer from 21 elements to 81 elements in total, the concentration of strains become larger at the weaker element as the individual element width decreases. As the damage is dependent on the strains experienced by each member, the locations with higher strains experience a higher damage. This creates a sharp variation in the three responses as the coarsest mesh develops damage slower compared to the fine mesh. Therefore the results exhibit a trend of vanishing energy dissipation for smaller mesh sizes. This pathological localization of damage is similar to what was predicted in the local formulation in 2D.

Further to illustrate this phenomenon, contour plots for horizontal displacement, strain and stress parallel to the axis of loading, and damage are shown figures 4.7, 4.8, 4.9 and 4.10, respectively. These contours are captured at a peak load (0.2176 kN) when the right edge displacement is 0.0145 mm and just after peak load (0.06745 kN) when displacement is 0.02066 mm for mesh 3 shown in figure 4.4.

The horizontal displacement contour shown in figure 4.7 depict the variation in displacement distribution between pre (refer figure 4.7a) and post (refer figure 4.7b) damage states. Till the simulation goes beyond the peak load the specimen behaves elastically and therefore a linear distribution of displacement is seen from left hand constrained face to the right hand face. However, immediately after the damage initiates in the central element a non-linear distribution of displacement can be observed where the damaged central element accounts for a large portion of the displacement experienced by the model.

(a) x-directional displacement (u_x) contour for mesh 3 when the right hand face displacement is 0.0145 mm.

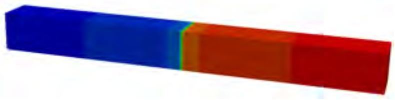

(b) x-directional displacement (u_x) contour for mesh 3 when the right hand face displacement is 0.02066 mm.

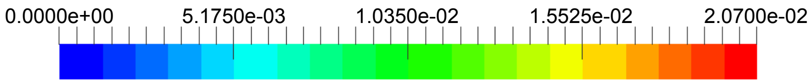

Figure 4.7. x-directional displacement (u_x) contours obtained for the local damage analysis of the 3D uniaxial tension test. Units:mm. Results obtained for mesh 3 consisting of 81 elements.

With the initiation of damage the strains in the central element increase as the central element gradually loses its strength. This effect can be seen in the contour shown in figure 4.8b where the higher strains are localised within the weaker element. As the central damaged element undergo larger deformations the rest of the elements tend to elastically unload to their original undeformed state as the material softens.

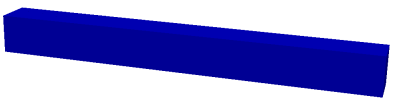

(a) x-directional strain (ε_{xx}) contour for mesh 3 when the right hand face displacement is 0.0145 mm.

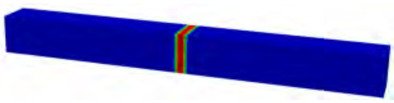

(b) x-directional strain (ε_{xx}) contour for mesh 3 when the right hand face displacement is 0.02066 mm.

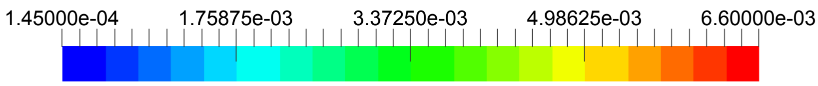

Figure 4.8. x-directional strain (ε_{xx}) contours obtained for the local damage analysis of the 3D uniaxial tension test. Results obtained for mesh 3 consisting of 81 elements.

The overall stress distribution from peak load (figure 4.9a) to the post-peak load instance (figure 4.9b) show the expected trend in unloading.

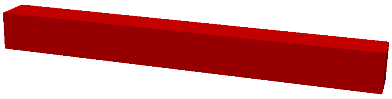

(a) x-directional stress (σ_{xx}) contour for mesh 3 when the right hand face displacement is 0.0145 mm.

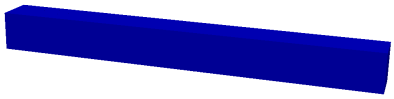

(b) x-directional stress (σ_{xx}) contour for mesh 3 when the right hand face displacement is 0.02066 mm.

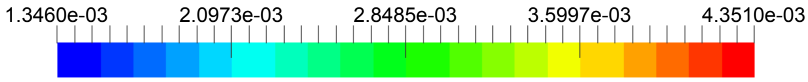

Figure 4.9. x-directional stress (σ_{xx}) contours obtained for the local damage analysis of the 3D uniaxial tension test. Units:GPa. Results obtained for mesh 3 consisting of 81 elements.

Finally the damage distribution shown in figure 4.10a and 4.10b, provides justification to the elastic behaviour observed in the previous contours in the undamaged state and the non-linear softening behaviour seen after the peak load when damage has occurred in the specimen. The characteristic of the localised damage band in the central element can be clearly seen in contour 4.10b.

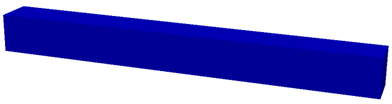

(a) Damage (ω) contour for mesh 3 when the right hand face displacement is 0.0145mm

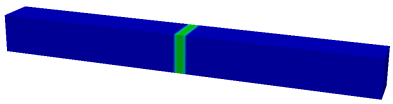

(b) Damage (ω) contour for mesh 3 when the right hand face displacement is 0.02066mm)

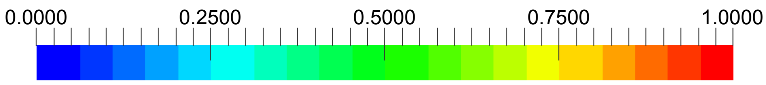

Figure 4.10. Damage (ω) contours obtained for the local damage analysis of the 3D uniaxial tension test. Results obtained for mesh 3 consisting of 81 elements.

4.6.1.2 Non-local formulation

As explained in chapter 3, to obtain a mesh independent behaviour in the model a non-local regularisation scheme is enforced. Material and damage parameters considered for the local analysis of the model remain unchanged.

Similar to the 2D formulation the Gaussian non-local averaging function given in equation (4.16) is used with the non-local interaction radius R taken as 6 mm. The results obtained through the 3D SBFEM formulation are given in figure 4.11. The numerical analysis is carried out using meshes 2, 3, 4 and 5 shown in figure 4.4.

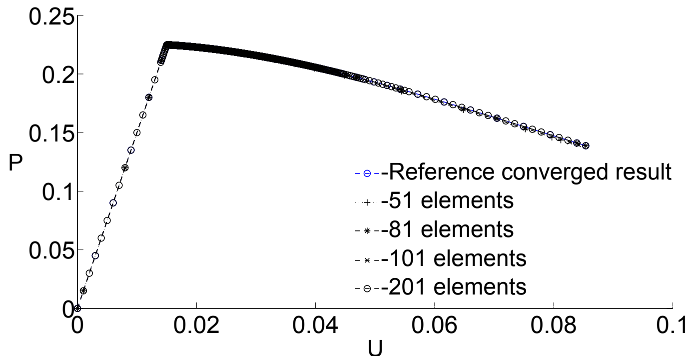

Figure 4.11. Load (kN)-deformation (mm) curves for meshes 2-5 in the 3D uniaxial tension test. Comparison of the SBFEM with the reference output [499]. Non-local damage analysis with assumed plain strain conditions simulated.

The force-displacement plots in figure 4.11 have nearly identical post peak softening behaviour for all 4 mesh sizes. With the regularisation, the effective strain field in damage calculation remains the same irrespective of the mesh configuration. The Gaussian weighting function distributes the localised strains proportional to the distance to each Gauss point. When the strain gradients are well captured through increasing the number of elements the results tend converge to a common result for all meshes. Hence we can fairly conclude the model is mesh independent. This stability in the model behaviour is much advantageous compared to the use of local models.

The contour plots given in figures 4.12, 4.13, 4.14 and 4.15 are respectively for the horizontal displacement (u_x), x-directional strain (ε_{xx}) , x-directional stress (σ_{xx}), and damage (ω) evolution. These contours are captured at a peak load (0.22479 kN) when the right hand face displacement is 0.01538 mm and just after peak load (0.2194 kN) when the free end displacement is 0.042 mm. Refer to the load-displacement output figure 4.12 to appreciate the significance of these instances.

As expected the displacement variation (see figures 4.12a and 4.12b) shows a linear behaviour up until damage initiates in the model. Thereon it is apparent the bar exhibits a non-linear behaviour.

(a) x-directional displacement (u_x) contour for mesh 5 when the right hand face displacement is 0.01538 mm.

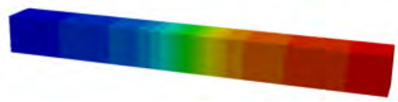

(b) x-directional displacement (u_x) contour for mesh 5 when the right hand face displacement is 0.042 mm.

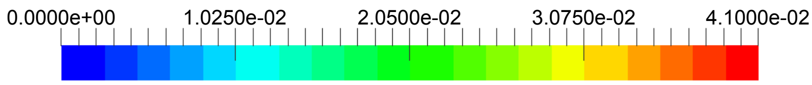

Figure 4.12. x-directional displacement (u_x) contours obtained for the non-local damage analysis of the 3D uniaxial tension test. Units:mm. Results obtained for mesh 5 consisting of 201 elements.

Figures 4.13a and 4.13b show the evolution of axial strain. It can be observed that strains localize in a band which is dictated by the interaction radius. The significance of the interaction radius is such that, the larger the radius selected the wider the influence of damage is spread across the specimen.

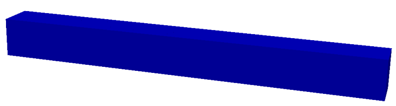

(a) x-directional strain (ε_{xx}) contour for mesh 5 when the right hand face displacement is 0.01538 mm.

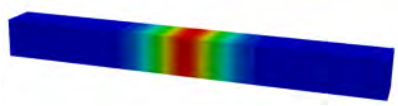

(b) x-directional strain (ε_{xx}) contour for mesh 5 when the right hand face displacement is 0.042 mm.

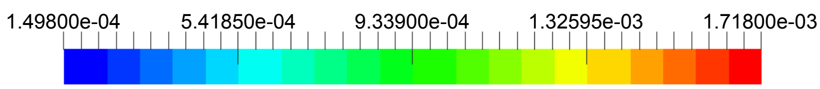

Figure 4.13. x-directional strain (ε_{xx}) contours obtained for the non-local damage analysis of the 3D uniaxial tension test. Results obtained for mesh 5 consisting of 201 elements.

The (σ_{xx}) stress contours in figures 4.14a and 4.14b show evidence of the post peak softening behaviour observed in the analysis. The stress in the elements drops from 4.5

GPa to 4.1 GPa between the two displacement instances (U = 0.01538 mm and U = 0.042 mm) as the material exhibits strain softening induced by damage degradation.

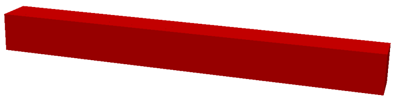

(a) x-directional stress (σ_{xx}) contour for mesh 5 when the right hand face displacement is 0.01538 mm.

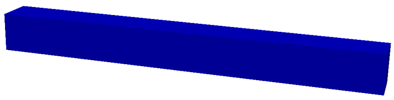

(b) x-directional stress (σ_{xx}) contour for mesh 5 when the right hand face displacement is 0.042 mm.

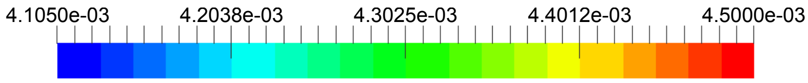

Figure 4.14. x-directional stress (σ_{xx}) contours obtained for the non-local damage analysis of the 3D uniaxial tension test. Units:GPa. Results obtained for mesh 5 consisting of 201 elements.

Figure 4.15 shows the undamaged state of the specimen at peak load and the regularised damage distributed over the region governed by the non-local Gaussian averaging technique used. Compared to localised damage evolution depicted in figure 4.10 the damage distribution in the non-local model helps to eliminate the mesh sensitivity in the localised formulation.

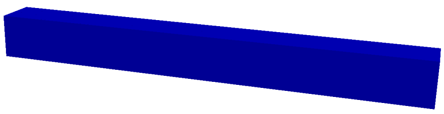

(a) Damage (ω) contour for mesh 5 when right hand face displacement is 0.01538 mm.

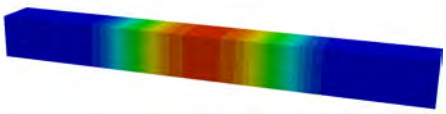

(b) Damage (ω) contour for mesh 5 when the right hand face displacement is 0.042 mm.

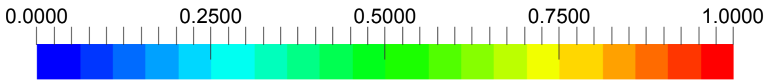

Figure 4.15. Damage (ω) contours obtained for the non-local damage analysis of the 3D uniaxial tension test. Results obtained for mesh 5 consisting of 201 elements.

Similar to what was observed in the 2D formulation the specimen analysed through the non-local model show negligible mesh sensitivity. Therefore moving forward the integral-type non-local modelling is the preferred choice as it overcomes the many pitfalls of the mesh dependent local models.

4.6.2 Three dimensional damage characterization in shear band

The second plain strain example considered in this chapter models the formation of a classical collapse mechanism of a shear band found in many geomaterials. This example was first simulated in 2D in chapter 3, section 3.7.4. The main objective of this example is to compare the accuracy of the 3D formulation by comparing the results to that of the 2D results previously obtained in chapter 3. The simulation is run with reference to the publication by Simone [507] on explicit and implicit gradient-enhanced damage models. Furthermore, certain challenges faced in the description of shear bands are avoided by referring to an earlier publication [511] by the same author which highlights issues related to the use of gradient type continuum damage models for predicting the propagation of shear bands.

The dimensions and boundary conditions used in the model are depicted in figure 4.16a. The height and width of the model is kept at 60 mm with the thickness of the plate considered to be 1 mm. The quasi-static shear band formation simulated in this numerical analysis is triggered by an imperfection placed in the left bottom corner of the plate. This imperfection is modelled with an introduced weaker section as shown (refer figure 4.16a) in the shaded part of the plate with dimensions height, width and thickness set to $3 \times 6 \times 1$ mm, respectively.

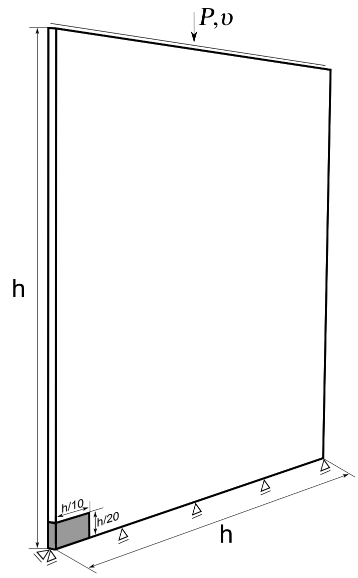

(a) Specimen in biaxial compression, where h = 60. The shaded part indicates the imperfection. Units:mm.

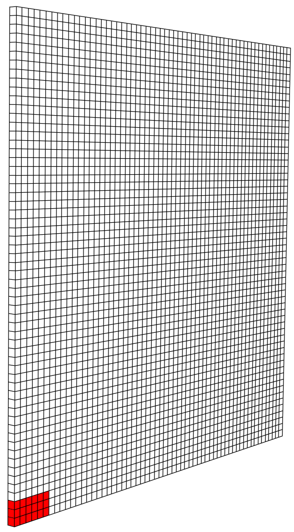

(b) SBFE mesh with uniform 1 mm cubic polyhedral elements.

Figure 4.16. Geometry and boundary conditions, and SBFE mesh for the 3D shear band problem. Figure 4.16a, dimensions h×h×1, where h = 60 mm. The shaded part indicates the imperfection; imperfection size is h/10 × h/20. Figure 4.16b depicts the SBFE polyhedral mesh.

The boundary conditions are set such that the bottom face of the plate is restrained in vertical movement. In addition the left corner nodes resist the movement in the horizontal direction. The vertical downward force is applied on the top face inducing a compressive force. To model plain strain conditions faces transverse to the direction of loading are also restricted in movement. The SBFE polyhedral mesh shown in the sub-figure 4.16b consists of 3600 elements of $1 \times 1 \times 1$ mm to ensure a sufficient resolution of the non-local field.

The material properties considered for the analysis are as shown in table 4.1.

	E (GPa)	ν	ε_0	α	β	l(mm)
Plate	20	0.2	1×10^{-4}	0.99	300	2
Imperfection	20	0.2	5×10^{-5}	0.99	300	2

Table 4.1. Material properties considered in the modelling of the 3D non-local damage characterization of a shear band.

For both the plate and the imperfection, the material properties of the Young's modulus and Poisson's ratio are considered to be identical. The exponential evolution law given in equation (4.3) is adopted with identical α and β values used for both types of material. However, for the weaker imperfection a reduced damage initiation threshold ε_0 is considered. Figure 4.17 depicts the 1D element stress-strain relationship considered as per the softening law given in equation (4.3) for the material parameters used to model the imperfection.

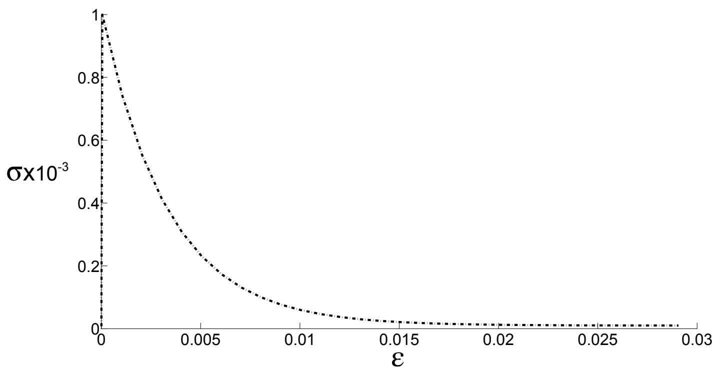

Figure 4.17. 1D element stress (GPa) vs strain profile considered in the 3D damage characterization in shear band with respect to the softening law given in equation (4.3), for the weaker material with $\varepsilon_0 = 5\times10^{-5}$.

The equivalent strain criteria considered for the analysis is the von Mises equivalent strain criteria given in equation (4.11). The Gauss weighting function given in equation (4.3) is used to calculate the non-local weights. The non-local length scale is kept consistent at 2 mm for both the materials.

A displacement control analysis is carried out with an initial displacement step of 1×10^{-3} mm. The automatic acceleration and damping incorporated m-NR method with arc-length technique is run for 426 load steps to produce the output load-displacement curve shown in figure 4.17. The total force on the top edge of the plate is plotted against the absolute vertical downward displacement recorded at the centre of the top edge of the plate.

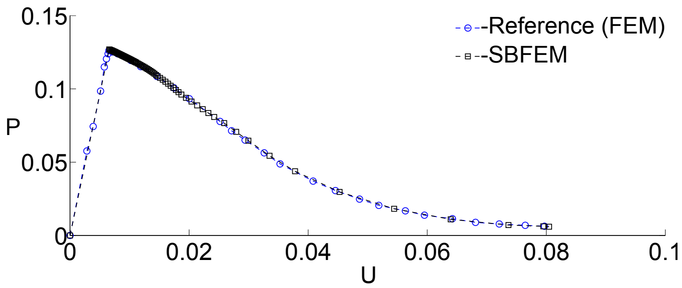

Figure 4.18. Load (kN)-deformation (mm) curves for the 3D simulation of the shear band. Comparison of the SBFEM with the reference output.

Figure 4.18 compares the proposed 3D formulation to the results of the reference finite element simulation given in [507]. The results obtained agree well with the reference solution confirming the accuracy of the formulation.

The contour plots in figures 4.19 and 4.20 are respectively for von Mises stress and the damage formation. These plots are presented for the instance at peak load when the top edge displacement is 0.00656 mm, after peak load when the top edge displacement is 0.03 mm, and at end of simulation when the top edge displacement is 0.0812 mm.

The von Mises non-local equivalent strain plots in figure 4.19 show the initial strain localisation of the plate and the gradual formation of the high strain concentrated shear band. As expected in relation to the reference [508] these figures also depict further localisation within the shear band after initiation of the shear band.

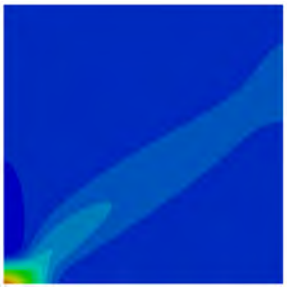

(a) At peak load when top edge displacement is 0.00656 mm.

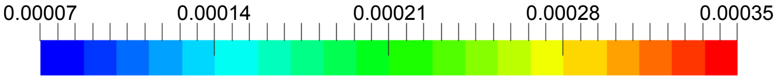

(c) After peak load when top edge displacement is 0.03 mm.

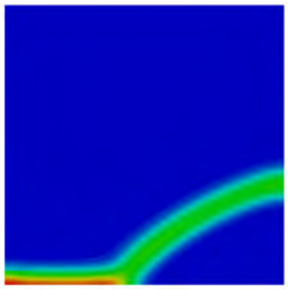

(d) At end of simulation when top edge displacement is 0.0812 mm.

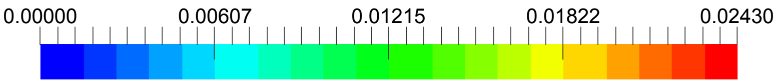

Figure 4.19. Von Mises equivalent strain contours obtained in simulation of the 3D non-local damage characterization in shear band. Results obtained for the mesh shown in figure 4.16b.

The damage formation shown in figure 4.20, follow a similar pattern to the von Mises strain contours shown in figure 4.19. The shear band migrates from the weak spot, where it is initiated and then progress through the elements in the left hand bottom corner till it then gradually moves diagonally towards the mid right hand edge.

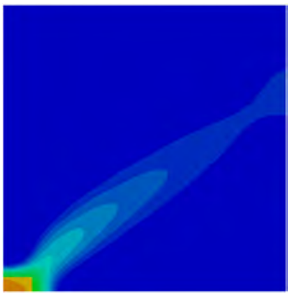

(a) At peak load when top edge displacement is 0.00656mm.

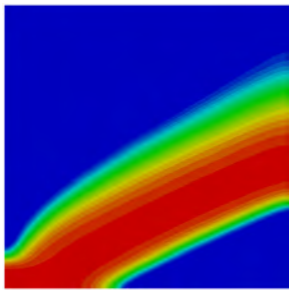

(b) After peak load when top edge displacement is 0.03mm.

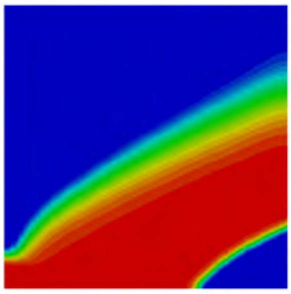

(c) At end of simulation when top edge displacement is 0.0812mm.

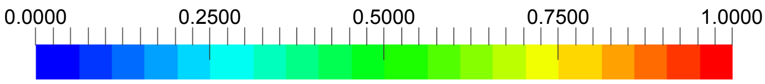

Figure 4.20. Damage (ω) evolution contours obtained in simulation of the 3D non-local damage characterization in shear band. Results obtained for the mesh shown in figure 4.16b.

The simulation represents accurately the shear band propagation in a 3D model of a plate under compressive loading. The results obtained are agreeing to both the 2D simulation in chapter 3 section 3.7.4 and the reference solution [507].

4.6.3 Three dimensional three point bending problem

The third example is extracted from [479] where strain localisation problems are investigated using integral-type non-local continuum damage models. The example explores the behaviour of a simply supported concrete beam loaded by a central concentrated force.

The objective of this example is to validate the SBFEM-based 3D non-local damage formulation and also to exemplify the ability of the arc-length incorporated acceleration and damping m-NR technique to overcome limit points in the post peak softening limb.

The example simulated in this section consist of geometry and boundary conditions as shown in figure 4.21. The beam is 600 mm long 62.5 mm wide and 200 mm in depth. A 4 mm central notch is located midspan up to a depth of 50 mm to induce a weaker section of the beam where damage can initiate in the analysis. The left bottom edge is restrained in horizontal (x) and vertical (y) directional movement and the bottom right edge is retrained in vertical movement.

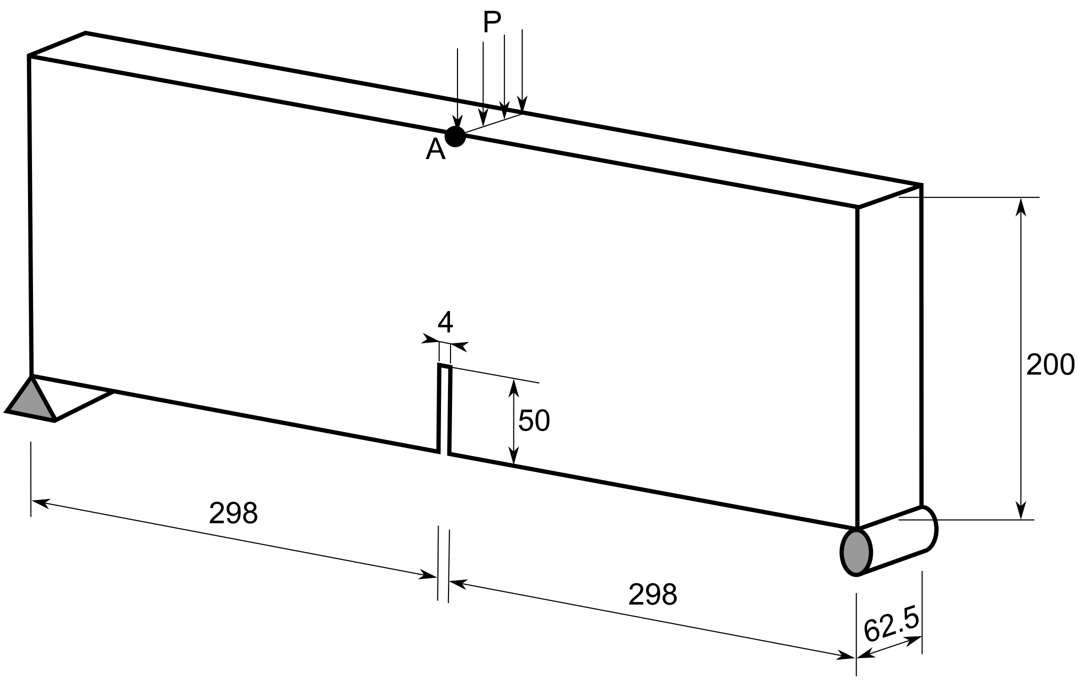

Figure 4.21. Dimensions (mm) and boundary conditions for the 3D non-local damage analysis of the three point bending problem.

In order to develop a similar model to that of the reference the mesh shown in figure 4.22 consists of 40,397 nodes with 121,191 DOFs. Each subdomain is modelled as SBFEM polyhedral element. To ensure compatibility between polyhedral elements of different sizes, only the surfaces between polyhedral elements are discretised with a combination of triangular and quadrilateral elements.

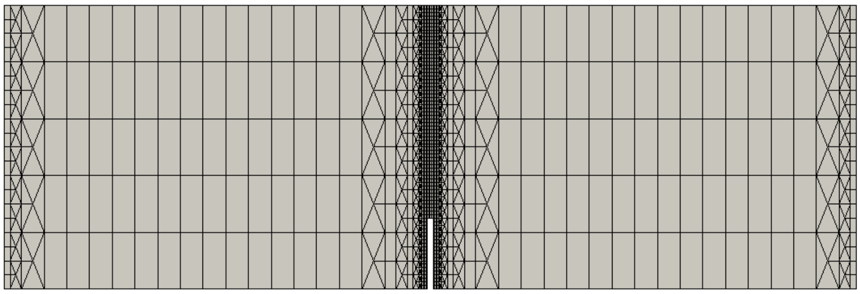

Figure 4.22. SBFE polyhedral mesh for the 3D non-local damage analysis of the three point bending problem. Minimum mesh size 1 mm.

The constitutive properties are set to; Young's modulus E = 30 GPa and Poisson's ratio as $\nu = 0.18$. The damage model given in equation (4.2) with tensile strength (f_t) as 2 MPa, local dissipation density g_f as 28.9 kJ/m^3, where; $f_t = \varepsilon_0 \times \mathrm{E}$ and $g_f = f_t\left(\varepsilon_f - \varepsilon_0/2\right)$. With respect to these parameters the 1D stress-strain relationship is as shown in figure 4.23.

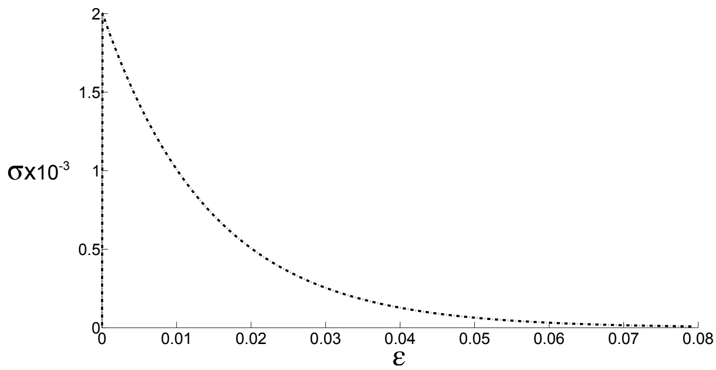

Figure 4.23. 1D element stress (GPa) vs strain profile considered in the 3D non-local damage analysis of the three point bending problem with respect to the softening law given in equation (4.2).

The equivalent strain is calculated using the equation (4.10). The non-local interaction radius R is set to 6 mm for the bell shaped truncated quartic polynomial function in equation (4.17).

The simulation was run using the automatic accelerating and damping m-NR with arc-length technique for 1324 load steps with an initial load step of 0.001 kN. The load-displacement curve in figure 4.24 plots the centrally applied force against the vertical downward displacement of the beam. Figure 4.24 further illustrates the SBFEM 3D damage formulations conformity with the results presented in reference [479]. The curve attains a peak load of 7.116 kN at a central top edge displacement of 0.127 mm and softens gradually there on.

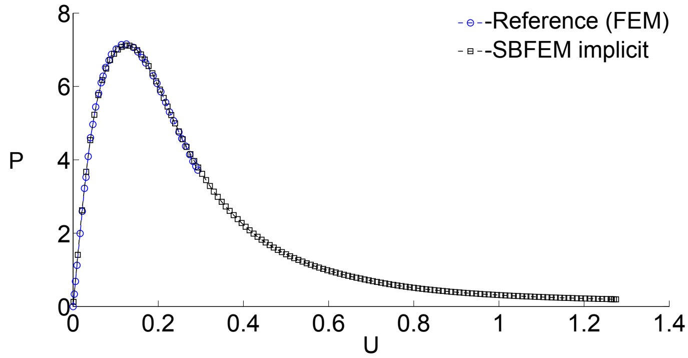

Figure 4.24. Load (kN)-deformation (mm) curves for 3D non-local damage simulation for the three point bending problem. Comparison of the SBFEM with the reference FEM output.

It is evident the force-displacement output obtained in this present formulation is capable of closely tracing the complete softening behaviour overcoming the limit points encountered at instances beyond the simulation end point of the reference solution.

The contour plots in figures 4.25, 4.26 and 4.27 depict the variation in y-directional displacement, x-directional stress and damage evolution respectively. Each sub-figure captures a snapshot in the simulation at point 'A' (refer figure 4.21) displacements of 0.127 mm, 0.332 mm and at 1.34 mm.

The y-directional displacement contour plots in figures 4.25 represent the symmetrical loading conditions applied to the model. As the load is applied central to the mid top face of the beam directly above the notch, the central portion of the beam experiences the maximum amount of deformation as anticipated.

(a) At peak load when vertical displacement at node ‘A’ is 0.127 mm.

(b) After peak load when vertical displacement at nodes ‘A’ is 0.332 mm.

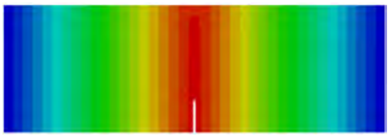

(c) At end of simulation when vertical displacement at node ‘A’ is1.34 mm.

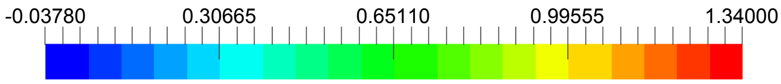

Figure 4.25. y-directional displacement contours for the 3D non-local damage analysis of a beam under three point loading. Units:mm. Results obtained for mesh in figure 4.22.

The stress contours parallel to the axis of the beam shown in figure 4.26 depicts the initial high stress concentration in the immediate vicinity of the notch (see figure 4.26a) and the gradual softening (see figures 4.26b-4.26c).

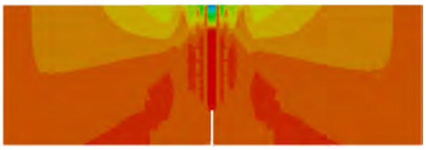

(a) At peak load when vertical displacement at node ‘A’ is 0.127 mm.

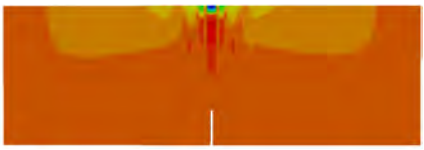

(b) After peak load when vertical displacement at node ‘A’ is 0.332 mm.

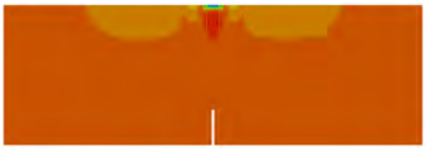

(c) At end of simulation when vertical displacement at node ‘A’ is 1.34 mm.

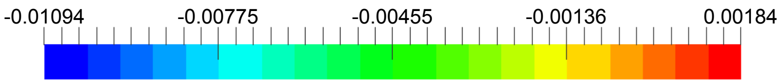

Figure 4.26. x-directional stress (σ_x) contours for the 3D non-local damage analysis of a beam under three point loading. Units:GPa. Results obtained for mesh in figure 4.22.

The final damage evolution contour plots shown in figure 4.27 shows the formation of a narrow damage band.

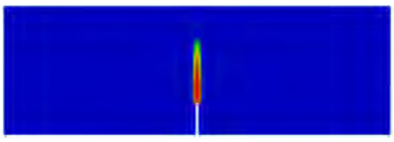

(a) At peak load when vertical displacement at node ‘A’ is 0.127 mm.

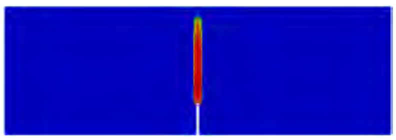

(b) After peak load when vertical displacement at node ‘A’ is 0.332 mm.

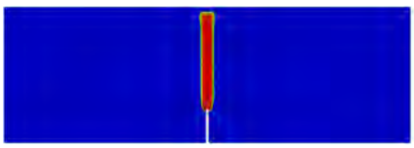

(c) At end of simulation when vertical displacement at node ‘A’ is 1.34 mm.

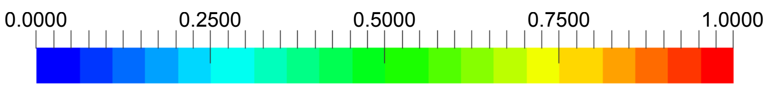

Figure 4.27. Damage (ω) contours for the 3D non-local damage analysis of a beam under three point loading. Results obtained for mesh in figure 4.22.

The degradation initiates from the notched area and gradually migrates towards the top loading edge of the beam. This is the most likely crack path as seen in experiments performed by Kormeling and Reinhardt [502] and by Grassl et al. [503]. Due to symmetry of the process zone the failure mechanism corresponds to pure mode-I fracture.

The final deformed shape is as shown in figure 4.28.

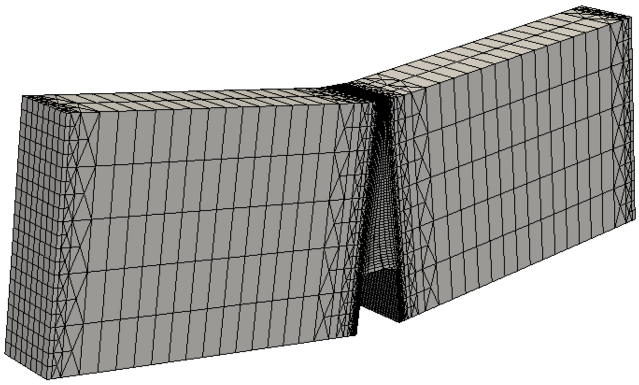

Figure 4.28. Final deformed shape obtained in the 3D non-local damage analysis of a the three point bending beam.

4.6.4 Double-notched tension beam

The mesh-independence of the proposed approach is verified by the simulation of a plain concrete beam with two notches under direct tension. The experiments of Hordijk [528] on lightweight concrete have been taken as a reference. This problem is widely investigated to test the mesh-independence of numerical methods [480, 529–531].

The dimensions and boundary conditions are shown in figure 4.29. The beam is 125 mm in height, 60 mm in depth and 50 mm in width.

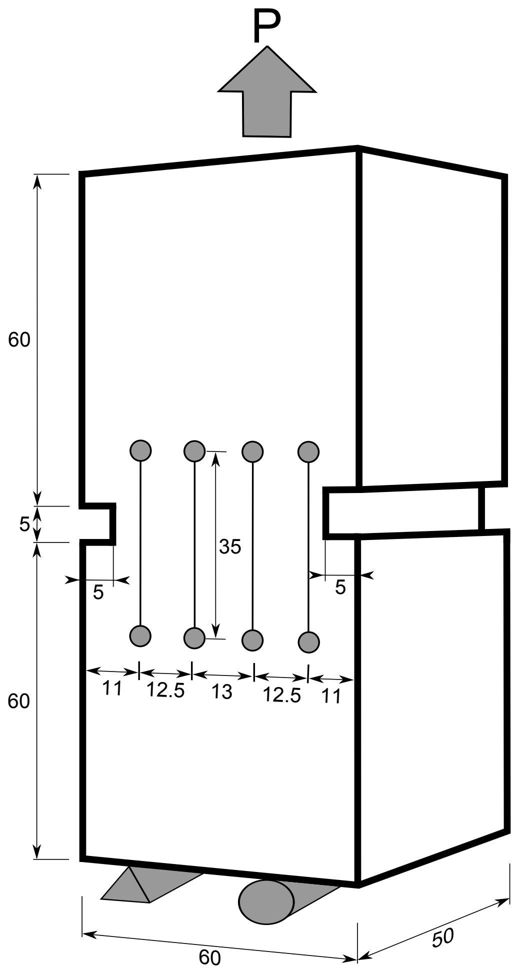

Figure 4.29. Dimensions (mm) and boundary conditions for the 3D non-local damage analysis of a double-notched tension beam.

In order to initialize failure of the specimen, the beam is weakened by two notches with cross-sections 5.0 × 5.0 mm. As demonstrated in reference [531], the numerical results of this example are strongly dependent on the applied boundary conditions. For the sake of simplicity, we only consider the situation in symmetry. Consequently, the bottom surface of the beam is fixed in the vertical direction and the displacement is applied to the top surface.

In order to investigate the mesh-independence of the proposed approach, two different SBFE meshes are employed, as shown in figure 4.30.

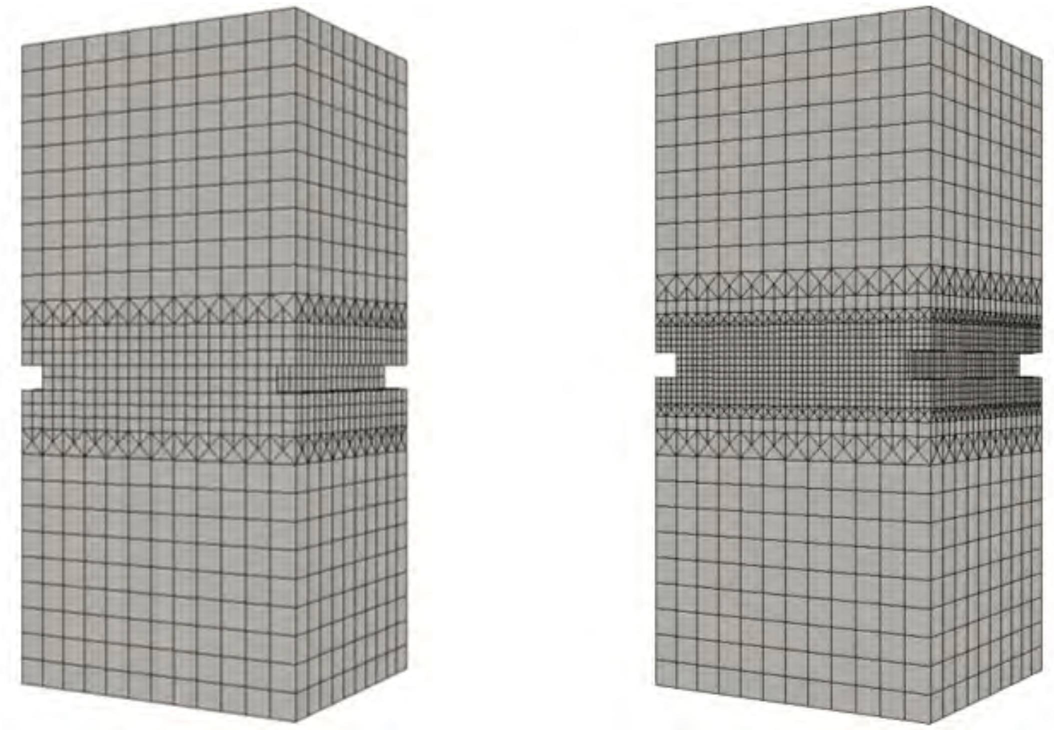

(a) (b)

Figure 4.30. SBFE mesh configurations for the 3D non-local damage analysis of a double-notched tension beam. (a) Mesh-1 and (b) mesh-2.

The details of these two meshes are listed in table 4.2. It can be noted, mesh 2 generates almost 75% more unknowns in the simulation compared to mesh 1.

The model parameters, taken from [528], are as follows: Young's modulus E = 18 GPa, Poisson's ratio $\nu = 0.2$, exponential damage evolution law (equation (4.3)) with $\alpha = 0.96$ and $\beta = 350$, $\varepsilon_0 = 2.1\times10^{-4}$. With regard to these parameters the 1D stress-strain behaviour of the model is shown in figure 4.31.

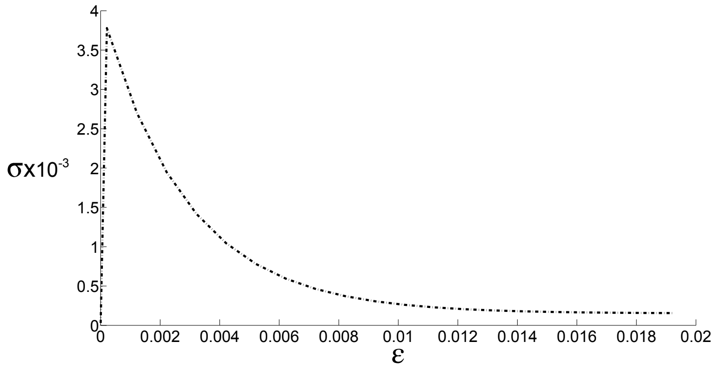

Figure 4.31. 1D element stress (GPa) vs strain profile considered in the 3D non-local damage analysis of a double-notched tension beam with respect to the softening law given in equation (4.3).

The modified von Mises definition of the local equivalent strain (refer equation (4.12)) with k = 10 is used in the analysis. Note that the gradient parameter **c** was set to 1 mm^2 in [517], the internal length for Gauss weight function is approximated as 2.2 mm according to the relationship between gradient damage model and non-local damage model [301].

The analysis was conducted by the implicit arc-length incorporated damage analysis scheme with automatic accelerating and damping capabilities. The experiments by Hordijk [528] were performed under servo-control, with the average deformation over the fracture zone, δ as the control parameter. δ was measured by four pairs of extensometers with gauge length 35 mm, as indicated in figure 4.29. This parameter is also computed during the simulation and compared with experimental results. As seen in figure 4.32 in this simulation the analysis was run till the recorded average displacement δ is 0.06 mm. The number of load steps required for the analysis was 105 with maximum number of iterations per load step being 8.

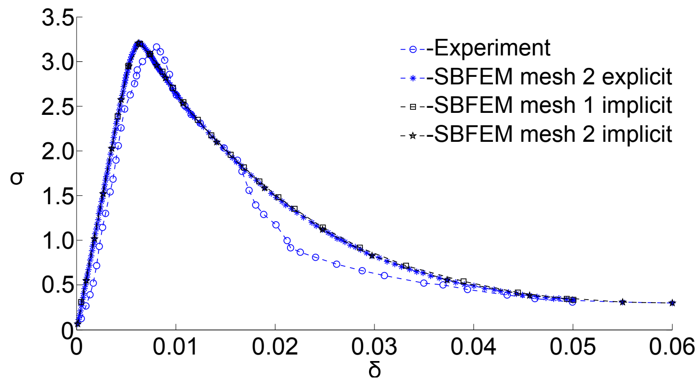

Figure 4.32. Stress (MPa) vs average deformation (mm) curves for 3D non-local damage simulation of the double-notched tension beam. Comparison of the SBFEM implicit formulation with the reference FEM output and the SBFEM explicit formulation.

The computational statistics for the analysis is listed in table 4.2. The implicit and the explicit schemes produce strikingly similar results. Both methods demonstrated capability to map the complete softening behaviour. On average between the two meshes the explicit analysis scheme performed almost 20% faster than the implicit scheme.

Mesh	No. of subdomains	No. of DOFs	Smin (mm)	Smax (mm)	Computational time (sec.) for the implicit formulation	Computational time (sec.) for the explicit formulation
1	6,200	24,504	2.5	10	4,556	3,797
2	26,080	97,875	1.25	10	36,051	29,550

Table 4.2. Computational statistics for the 3D non-local damage analysis of a double-notched tension beam.

Figure 4.32 shows the stress vs average deformation obtained by the proposed approach and experiment results from [528]. The deformation is represented by the average elongation of the 35 mm measuring-section, δ, and the stress is the engineering stress with respect to the smallest cross-section of the beam, i.e. between the notches. It can be observed that the results of the proposed approach remarkably agree with those of experiments, not only at the linear stage but also in the softening regime. Owing to the heterogeneity of concrete, the experimental curve inevitably becomes tortuous, as observed in experimental and numerical studies [480]. It can also be observed in figure 4.32 that the results of mesh 1 and mesh 2 agree well with each other, which indicates the results converge to a solution with finite energy dissipation. It can be concluded that the proposed approach is mesh-independent as sufficient subdomains (two layers or more) are involved in the range of internal length. The explicit and the implicit analysis schemes show conformity to one another. Both the analysis techniques attain a peak stress of 3.27 MPa when $\delta = 0.0063$ mm.

Figure 4.33 contains contours for y directional displacement of mesh 2 at peak load when average displacement is at 0.0063 mm, after peak load when average displacement is at 0.0134 mm and finally at end of simulation when average displacement is at 0.06 mm. With the increase in damage in the notched region of the beam the deformation of the top section of the beam increases as expected.

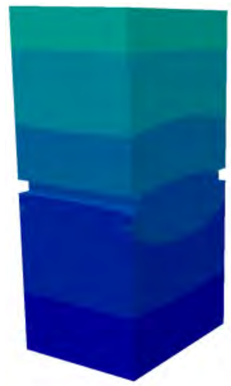

(a) At peak load when average displacement (δ) is 0.0063 mm.

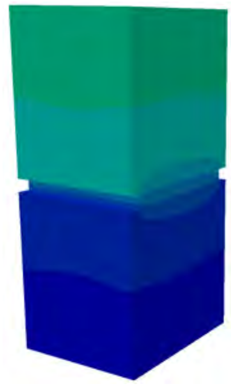

(b) After peak load when average displacement (δ) is 0.0134 mm.

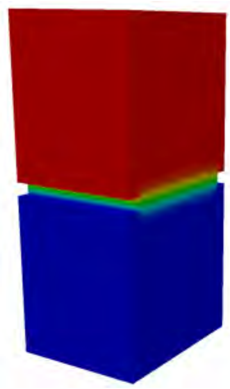

(c) At end of simulation when average displacement (δ) is 0.06 mm.

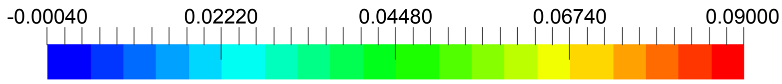

Figure 4.33. y-directional displacement contours for the 3D non-local damage analysis of a double-notched tension beam. Units:mm. Results obtained for mesh 2 in figure 4.30b.

Figure 4.34 shows the von Mises stress contours under three different deformation states. In order to observe the variation of the distribution of stress across the section, only half of the beam is shown. It can be seen that during the loading regime, the high stress regions emerge around the notches and extend to the central portion of the section. After the peak-load, the beam begins to undergo the unloading regime and the high stress regions shrink.

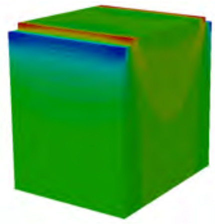

(a) At peak load when average displacement (δ) is 0.0063 mm.

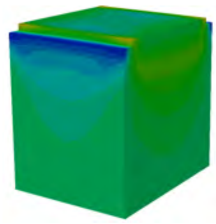

(b) After peak load when average displacement (δ) is 0.0134 mm.

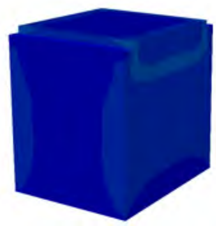

(c) At end of simulation when average displacement (δ) is 0.06 mm.

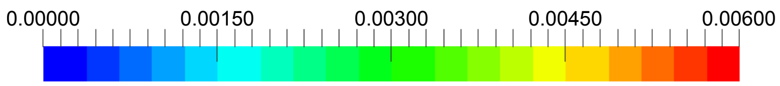

Figure 4.34. Von Mises stress contours for the 3D non-local damage analysis of a double-notched tension beam. Units:GPa. Results obtained for mesh 2 in figure 4.30b.

Figure 4.35 shows the damage evolution corresponding to the same load steps as in figure 4.33. It can be observed that the damage originates at the border of the weakened section and then propagates to the centre of the beam. At the peak-load, about half of the section is damaged in different degrees. When δ reaches 0.06 mm, almost the whole section is damaged.

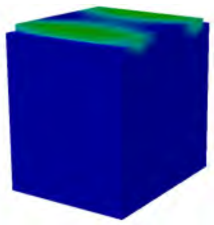

(a) At peak load when average displacement (δ) is 0.0063 mm.

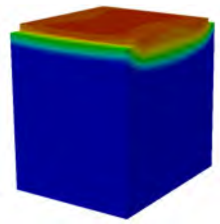

(b) After peak load when average displacement (δ) is 0.0134 mm.

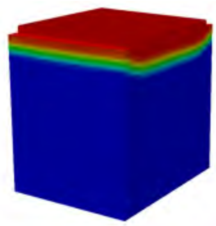

(c) At end of simulation when average displacement (δ) is 0.06 mm.

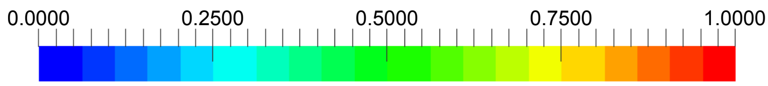

Figure 4.35. Damage (ω) evolution contours for the 3D non-local damage analysis of a double-notched tension beam. Results obtained for mesh 2 in figure 4.30b.

The final deformation of the beam 200 times magnified is given in figure 4.36. It can be seen that the vertical deformation of the beam is mostly contributed by the weaken portion and a necking phenomenon exists in this portion due to the formation of a the damage zone.

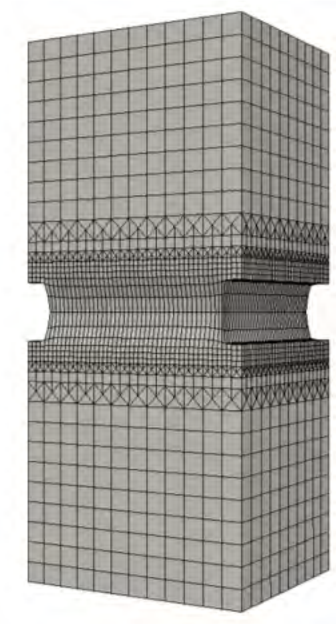

Figure 4.36. Final deformed shape obtained in the 3D non-local damage analysis of a double-notched tension beam. Results obtained for mesh 2 in figure 4.30b. Scaling factor:200.

4.6.5 Four-point bending beam with a central notch

As the fifth example, the behaviour of a four-point bending beam is simulated as shown in figure 4.37. Compared with the three-point bending beam, the four-point bending beam has no support in the damage zone so that no compressive stresses would be introduced parallel to the damage zone. This example is experimentally investigated by Hordijk [528] and numerically simulated by Pamin and de Borst [532] and Simone et al. [533], respectively.

The overall dimensions length, depth and width of the beam are set to 500, 100 and 50 mm, respectively. A 5 mm notch is centrally located to induce damage initiation at the centre of the beam. The depth of the notch L = 10 mm as used in the experimental program.

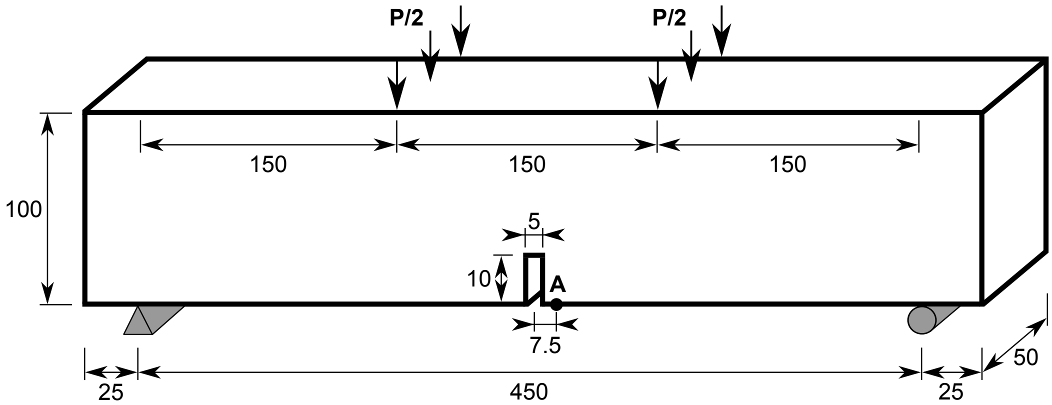

Figure 4.37. Dimensions (mm) and boundary conditions of the 3D non-local damage analysis of a four-point bending beam.

The beam has support conditions modelled 25 mm from the bottom edges of the beam. The left hand support is a pinned support which restrains vertical and horizontal movement, whereas the right hand support is a roller support that restrains only the vertical movement. The vertical loads are applied 150 mm from the centreline of each support.

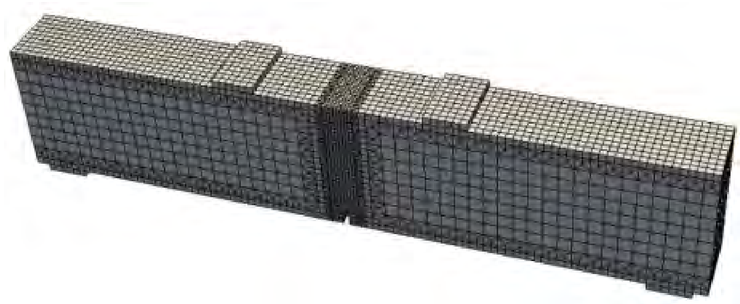

Figure 4.38. SBFE mesh configuration for the 3D non-local damage analysis of a four-point bending beam.

The SBFE mesh used in the analysis is as shown in figure 4.38. The mesh consists of 11,190 subdomains with 51,567 DOFs. It should be noted that the central portion of the beam are refined with small-sized subdomains owing to the expected damage evolution in this region. Plates are used in the top and bottom face of the beam to apply the loading and the displacement restraining boundary conditions.

The following model parameters, 'fitted' for the continuous problem, are adopted for the simulation [532]: Young's modulus E = 40 GPa; Poisson's ratio $\nu = 0.2$; modified exponential damage evolution law (equation (4.3)) with $\varepsilon_0 = 7.5\times10^{-5}$, α = 0.92 and β

= 300. In relation to these parameters the 1D element stress-strain behaviour considered in the simulation is as shown in figure 4.39.

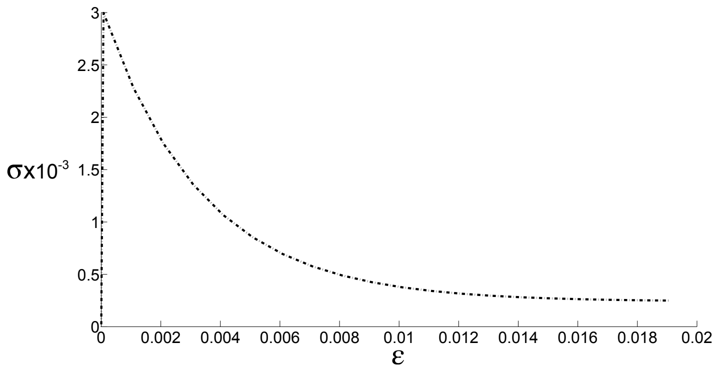

Figure 4.39. 1D element stress (GPa) vs strain profile considered in the 3D non-local damage analysis of a four-point bending beam with respect to the softening law given in equation (4.3).

The plates are modelled by assuming stiffer material properties, Young's modulus E = 1000 GPa; Poisson's ratio $\nu = 0.2$. The modified von Mises definition of the local equivalent strain (equation (4.12)) with $k = 10$ is considered to emulate realistic concrete material properties. To implement the non-local scheme the truncated weight function in equation (4.17) is adopted with the internal radius $R = 10$ mm.

The load-displacement diagrams obtained in the analysis are plotted in figure 4.40. As an indicator of the deflection, the vertical displacement of point 'A' (see in figure 4.37) located at the bottom of the beam and with a distance of 7.5 mm from the centreline of the beam is measured.

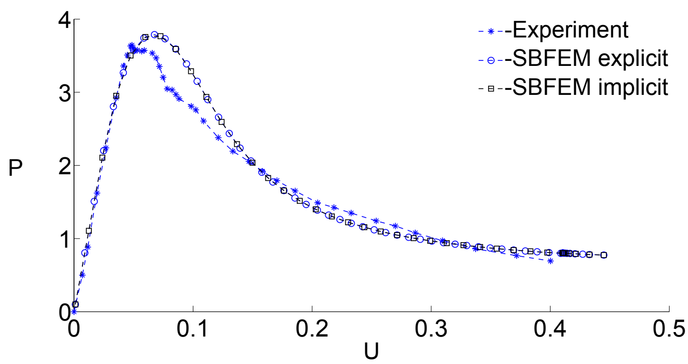

Figure 4.40. Load (kN)-deformation (mm) curves for 3D non-local damage simulation of the four-point bending beam. Comparison of the SBFEM implicit formulation with the experimental results and the SBFEM explicit formulation.

Here the experimental results are from reference [528]. It can be observed that the results of the proposed approach agree well with experimental results. The simulations attains a peak load of 3.79 kN at a displacement of 0.067 mm. As expected there is a strong agreement between the outputs obtained by the explicit and the implicit schemes. Table 4.3 compares the efficiency of the two analysis techniques.

Mesh	No. of subdomains	No. of DOFs	Smin (mm)	Smax (mm)	Computational time (sec.) for the implicit formulation	Computational time (sec.) for the explicit formulation
1	11,190	51,567	2.5	10	8,764	7,967

Table 4.3. Computational statistics for the 3D non-local damage analysis of a four-point bending beam.

In this instance it is found the explicit scheme completes the analysis almost 10% faster than the implicit scheme. Both techniques seem to be able to trace the full softening curve without any difficulty.

The vertical y directional displacement, x directional stress and damage evolutions are shown in figure 4.41, figure 4.42 and figure 4.43, respectively.

The symmetrically distributed displacement contours in figure 4.41 indicate the symmetric boundary and loading conditions applied in the model.

(a) At peak load when vertical displacement at ‘A’ is 0.065 mm.

(b) After peak load when vertical displacement at ‘A’ is 0.202 mm.

(c) At end of simulation when vertical displacement at ‘A’ is 0.445mm.

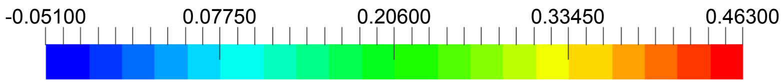

Figure 4.41. y-directional displacement contours for the 3D non-local damage analysis of the four-point bending beam. Units:mm. Results obtained for mesh shown in figure 4.38.

It can be seen from figure 4.42 that the high stress regions emerge around the corners of notch. The high stress regions gradually propagate towards the loading face along with the damage front shown in figure 4.43.

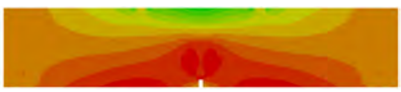

(a) At peak load when vertical displacement at ‘A’ is 0.065 mm.

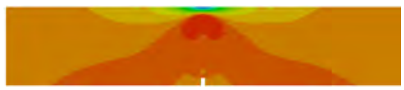

(b) After peak load when vertical displacement at ‘A’ is 0.202 mm.

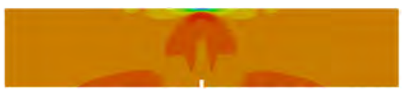

(c) At end of simulation when vertical displacement at ‘A’ is 0.445 mm.

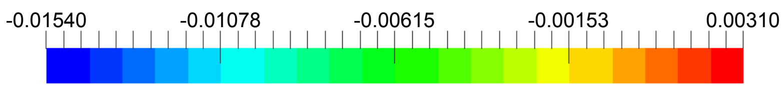

Figure 4.42. x-directional stress (σ_x) contours for the 3D non-local damage analysis of the four-point bending beam. Units:GPa. Results obtained for mesh shown in figure 4.38.

The high strain localisation around the notch results in the damage zone build up around the notch and then propagates along the centreline of the beam.

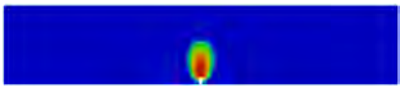

(a) At peak load when vertical displacement at ‘A’ is 0.065 mm.

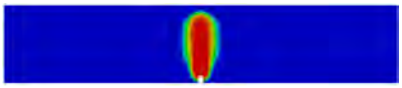

(b) After peak load when vertical displacement at ‘A’ is 0.202 mm.

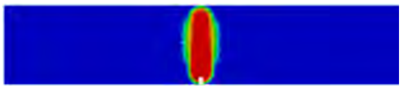

(c) At end of simulation when vertical displacement at ‘A’ is 0.445 mm.

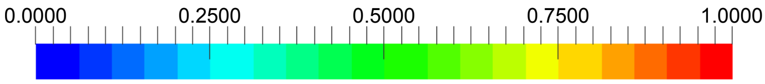

Figure 4.43. Damage (ω) contours for the 3D non-local damage analysis of the four-point bending beam. Results obtained for mesh shown in figure 4.38.

Figure 4.44 shows the final deformed shape of the beam magnified by 100.

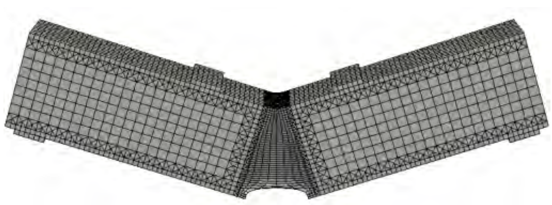

Figure 4.44. Final deformed shape obtained in the 3D non-local damage analysis of the four-point bending beam. Results obtained for mesh shown in figure 4.38. Scaling factor:100.

It can be observed that the central portion has completely failed when the DPZ reaches the top surface of the beam, whereas the deformation of the rest of the beam is negligible.

4.6.6 Three dimensional analysis of an L-shaped specimen

The classical benchmark of the L-shaped concrete specimen (see figure 4.45) is simulated to further demonstrate the performance of the present method. This geometry was experimentally tested and simulated using smeared crack model by Winkler et al. [534]. Dumstorff and Meschke [535], Huang and Yang [490] simulated this benchmark in 2D by using XFEM and cohesive element, respectively. Jäger et al. [536] and Radulovic et al. [537] attempted to model this problem in 3D through a purely deformation-based strategy and embedded strong discontinuity approach, respectively.

The specimen is created off a thick 100 mm plate. The original dimensions of the plate are 500×500 mm. To create the distinct L shape of the model the lower right quarter of the plate is removed. The left bottom face of the specimen is fully restrained in x,y and z movement while the agitation inducing the structural response is introduced as a line load 30 mm from the bottom right free end.

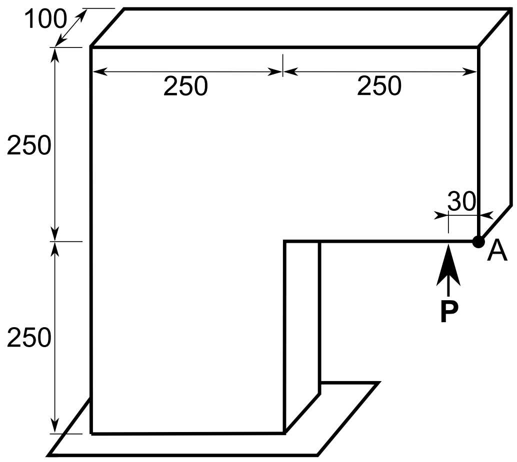

Figure 4.45. Dimensions (mm) and boundary conditions of the 3D non-local damage analysis of a L-shaped specimen.

The SBFE mesh, as shown in figure 4.46, consists of 24,080 subdomains and 89,142 DOFs. The size of the smallest subdomain used for this example is 5 mm and the largest one is 20 mm. Considering that the damage would evolve almost horizontally from the concave corner of the specimen, the mesh is refined in this region correspondingly.

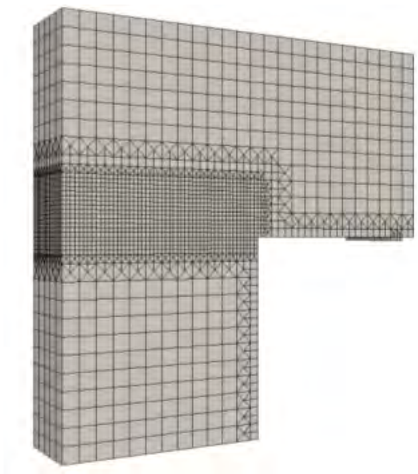

Figure 4.46. SBFE mesh configurations for the 3D non-local damage analysis of a L-shaped specimen.

The model parameters are as follows: Young's modulus E = 25.85GPa; Poisson's ratio $\nu = 0.18$. The exponential damage evolution law presented in equation (4.3) is considered with $\varepsilon_0 = 1.05\times10^{-4}$, $\alpha = 0.96$ and $\beta = 250$. In relation to these parameters the 1D element stress-strain behaviour is as shown in figure 4.47.

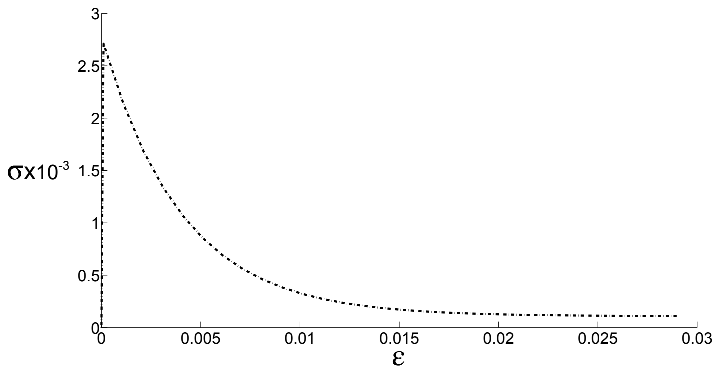

Figure 4.47. 1D element stress (GPa) vs strain profile considered in the 3D non-local damage analysis of an L-shaped specimen with respect to the softening law given in equation (4.3).

The equivalent strain is calculated using the modified von Mises definition given in equation (4.12) with $k = 10$. The truncated weight function (equation (4.17)) with internal radius $R = 10$ mm is used. The plate introduced to apply the load without generating an abnormal stress concentration is assumed to have Young's modulus E = 1000 GPa; Poisson's ratio $\nu = 0.18$.

Figure 4.48 records the load-displacement curves from the present explicit and implicit formulation and experiments with three specimens. The load **P** resembles the total vertical load applied to induce the agitation and the vertical displacement is captured at point 'A' with reference to figure 4.45. The total vertically upward displacement applied is 1.6 mm.

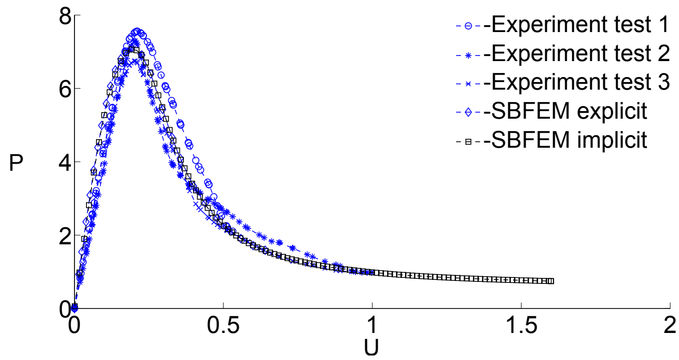

Figure 4.48. Load (kN)-deformation (mm) curves for 3D non-local damage simulation of the L-shaped specimen. Comparison of the SBFEM implicit formulation with the experimental results and the SBFEM explicit formulation.

A satisfactorily consistent result can be observed between the trends of the proposed approach and experiments. The explicit and the implicit formulation produce almost identical results. The simulation reaches its maximum load of 7.067 kN prior to softening at a displacement of 0.198 mm. It should be noted that in this case, the crack initiating load and crack path is strongly dependent on the meso-structure of the concrete, especially the locations and shapes of the aggregates in the failure region [490]. Based on the homogeneous model, the simulated results of numerical model are inevitably different from the experimental observation although the same material properties are assumed.

Mesh	No. of subdomains	No. of DOFs	Smin (mm)	Smax (mm)	Computational time (sec.) for the implicit formulation	Computational time (sec.) for the explicit formulation
1	24,080	89,142	5	20	29,861	28,439

Table 4.4. Computational statistics used in the 3D non-local damage analysis of a L-shaped specimen.

The implicit scheme requires 29,861 seconds to reach to the 0.64 mm displacement reading (see table 4.4). Compared to the explicit formulation the time recorded is 4.7% slower. However, it is clear in this instance the implicit formulation is capable of tracing the complete softening behaviour unlike the explicit scheme which fails to progress beyond the the displacement value of 0.64 mm.

Figure 4.49 shows displacement magnitude at peak load when vertical displacement at ‘A’ is 0.198 mm and after peak load when vertical displacement at ‘A’ is 0.3 mm and at end of simulation when vertical displacement at ‘A’ is 1.6 mm.

(a) At peak load when vertical displacement at ‘A’ is 0.198 mm.

(b) After peak load when vertical displacement at ‘A’ is 0.3 mm.

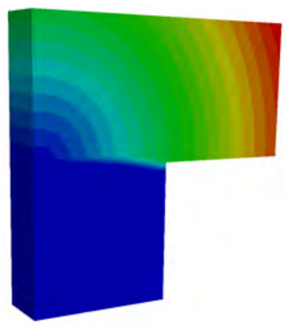

(c) At end of simulation when vertical displacement at ‘A’ is 1.6 mm.

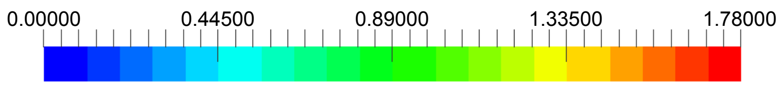

Figure 4.49. Displacement magnitude contours for the 3D non-local damage analysis of an L-shaped specimen. Units:mm. Results obtained for mesh shown in figure 4.46.

The von Mises stress contours in the three different stages are shown in figure 4.50.

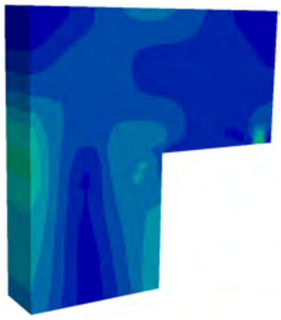

(a) At peak load when vertical displacement at ‘A’ is 0.198 mm.

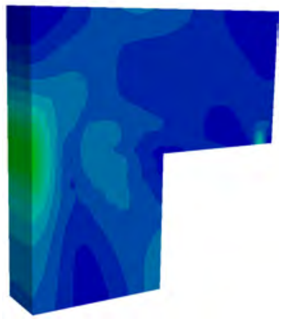

(b) After peak load when vertical displacement at ‘A’ is 0.3 mm.

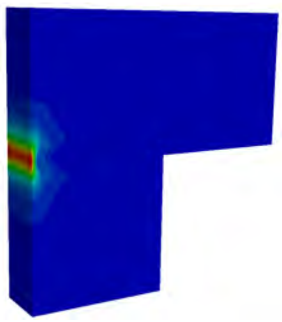

(c) At end of simulation when vertical displacement at ‘A’ is 1.6 mm.

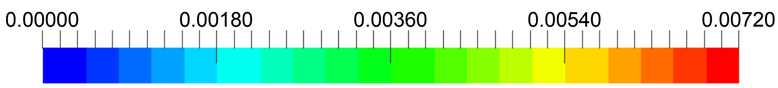

Figure 4.50. Von Mises stress contours for the 3D non-local damage analysis of an L-shaped specimen. Units:GPa. Results obtained for mesh shown in figure 4.46.

Owing to the stress singularity, the highest stress appears around the concave corner of the specimen at the beginning. Thereafter the high stress region extends diagonally to the upper part of the specimen. After the peak-load, it can be observed that the high stress region moves horizontally to the left boundary of the specimen.

Correspondingly, the damage evolutions are depicted in figure 4.51. It can be seen that the DPZ propagates upwards from the concave corner to the left-top of the specimen during the loading stage and then horizontally until the end of the simulation.

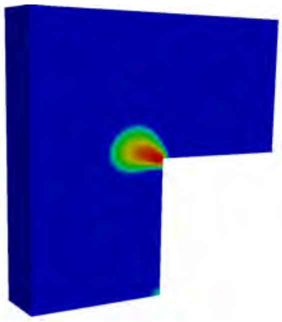

(a) At peak load when vertical displacement at ‘A’ is 0.198 mm.

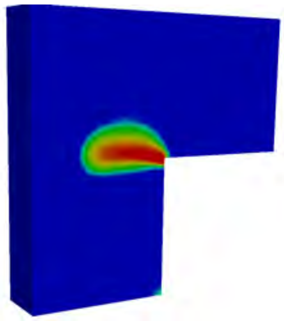

(b) After peak load when vertical displacement at ‘A’ is 0.3 mm.

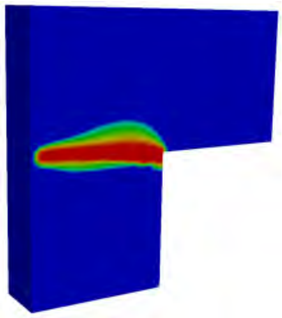

(c) At end of simulation when vertical displacement at ‘A’ is 1.6 mm.

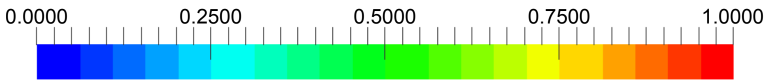

Figure 4.51. Damage (ω) contours for the 3D non-local damage analysis of an L-shaped specimen. Results obtained for mesh shown in figure 4.46.

Figure 4.52 compares the simulated DPZ using present method to the experimental and numerical crack path in the literature. It is apparent in figure 4.52a the location of DPZ predicted by the present method agrees well with the crack path obtained by Winkler et al. [534] (in 2D). The slight difference from the experimental observation seen in figure 4.52b might be caused by the heterogeneous property of real concrete as mentioned above.

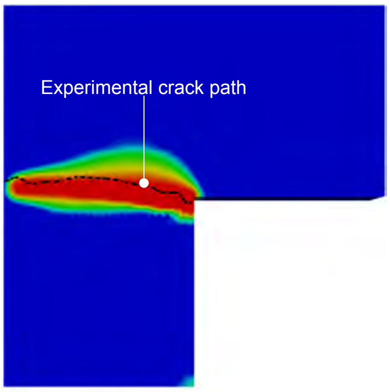

(a) Experimental crack path compared to the damage evolution at the end of simulation when vertical displacement at ‘A’ is 1.6 mm.

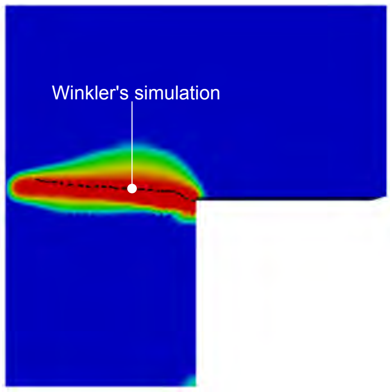

(b) Numerical results from Winkler et al. [534] compared to the damage evolution at the end of simulation when vertical displacement at ‘A’ is 1.6 mm.

Figure 4.52. Comparison of the simulated crack path obtained in the 3D non-local damage analysis of an L-shaped specimen with the (a) experimental crack path and the (b) numerical results from Winkler et al. [534].

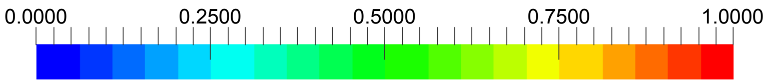

Figure 4.53 shows the final deformed shape of the specimen. Here it is apparent that the failure of the specimen actually initiates from the top of the left leg and then extends layer by layer. Finally, the macro crack propagates horizontally to the left boundary.

Figure 4.53. Final deformed shape when vertical displacement at node 'A' is 1.6 mm obtained in the 3D non-local damage analysis of an L-shaped specimen. Results obtained for mesh shown in figure 4.46. Scaling factor:100.

4.7 Conclusions

This chapter has undertaken the detailed presentation of the extension of the scaled boundary finite element formulation in damage analysis of problems in the three dimensional space. This extension incorporates a non-local damage analysis framework where the ill effects of local damage formulations are avoided. The non-local formulation adopts an enriched continuum description to avoid strain localization to a single element. This enrichment was achieved by introducing a length parameter to regularize the localization process by introducing damage dispersion.

Some advantages of SBFEM are the ability to compute the strain modes and the weight functions prior to the iterative damage analysis process, and the scaling centre estimation of damage variable based on the assumption of uniform damage distribution in one subdomain are exploited to facilitate the damage simulation. A logical verification process was undertaken in the numerical simulation presented in this section. Comparisons were first made with plain strain problems for validation of the proposed 3D damage modelling technique. The technique was then compared with examples and laboratory experiments found in published literature. These numerical simulations show that the proposed non-local approach possesses the characteristic mesh-independent behaviour when sufficient subdomains are included in the internal averaging radius. Concluding from the examples presented in this chapter at least two layers or more are recommended in the non-local averaging scheme to achieve mesh-independent congruent results. The benchmarks are simulated to verify the effectiveness and robustness of the proposed approach, and good agreement with the experimental observations and numerical simulations are obtained.

The accelerated and dampened m-NR technique with arc-length formulation is robust to handle various types of problems. The load vs deflection curves obtained through the method follows the accurate damage process very close to failure. In some numerical simulations the efficiency of implicit accelerated/dampened NR method was compared to the explicit analysis technique. The former revealed accurate results by following the equilibrium path closely whereas the explicit technique in some examples failed at limit points. The overall efficiency of the explicit technique was superior to that of the implicit method. However, the efficiency between the two methods become almost similar in complex problems as the explicit scheme required smaller load steps to overcome limit points.

The result of this study reveals that the SBFEM is a competitive tool to simulate the damage process of structures in the three dimensional space.

Chapter 5

Two and Three Dimensional Automatic Image-Based Damage Analysis with the Scaled Boundary Finite Element Method

5.1 Introduction

In the modern age there are many non-invasive imaging techniques such as X-ray, Computed Tomography (CT) scans, Magnetic Resonance Imaging (MRI), and ultrasound, that aid in obtaining non-intrusive high resolution images of objects. Image-based analysis provides an attractive approach for various numerical analysis by using an image obtained mesh by assessing the colour intensities produced by the geometrical information and the material distribution of the object. This technique is more commonly known as image-based analysis. In this study reference is made to publications in material characterization [97, 103, 104, 113] where techniques such as the level set coupled eXtended Finite Elements Method (XFEM) are applied to solve microstructures with complex geometries and homogenization analysis of composite materials, fracture analysis [109] where an image-based process is implemented to simulate quasi-static crack propagation with the XFEM, and biomedical applications [106–108, 115], where image-based finite element analysis is adopted to analyse the trabecular bone structure, the human femur and the lumbar spine.

The aim of this chapter is to present a robust, automatic, and efficient approach for damage analysis using the SBFEM based damage analysis formulation developed in chapters 3 and 4. This chapter investigates and presents the image-based analysis technique by combining the SBFEM with a quadtree or octree mesh generation algorithm for two dimensional (2D) or three dimensional (3D) images respectively.

The technique developed here attempts to reduce the Degrees Of Freedom (DOFs) through automatically created meshes which saves tremendous human effort typically required for solving complex problems in material and structural damage analysis. The automatic mesh generation algorithm significantly reduces the time and effort typically required to produce an acceptable mesh, especially within the vicinity of the Damage Process Zone (DPZ). Geometrical features of different scales are conveniently captured and modelled through the quadtree and octree structures. These two structures are modelled by scaled boundary polygonal elements and polyhedral elements in quadtree and octree mesh development respectively. The requirement of a visible boundary from the scaling centre is always satisfied. The issue of hanging nodes encountered in the FEM is eliminated in the SBFEM process since one edge or face can be divided into multiple line or surface elements. As only the boundary of the cells require discretisation, the process is simple. Quadtree and octree structures are employed to discretise the domain with multi-level sizes of subdomains without any extra effort to deal with hanging nodes existing between adjacent subdomains of different sizes [72,489]. The refinement of local regions are controlled by certain parameters, and the transition between large and small size subdomains is fast and straightforward. In SBFEM, a problem domain can be discretised by a set of subdomains with various sizes and different number of edges. The use of 1D and 2D shape functions to model respectively 2D and 3D problems reduces the spatial dimensions by one degree. It should be noted heirachical mesh generation structures are adopted in FEM to the algorithms salient advantage to transition between different cell sizes efficiently [88]. However, displacement incompatibility is inevitably introduced by the hanging nodes presented between adjacent cells with different sizes. In order to deal with such a problem, complex shape functions are required for cells with hanging nodes [538] or further discretise the cell with tetrahedralised cells [539].

This chapter starts off with section 5.2 which describes the quadtree and octree decomposition of an image. Then in section 5.3 the process of identifying the cell type and discretisation of each cell on the boundary is described. The next section, section 5.4 explains the numerous damage models. This section also includes a discussion on the effects of non-local averaging over multi-material interfaces. Moving on, section 5.5 presents a summary of SBFEM to analyse quadtree and octree meshes and in section 5.6 solution procedures for geometrically similar cells are detailed for both two and three dimensional space. Section 5.7 illustrates the SBFE formulation in damage analysis. Penultimately, in section 5.8 two and three dimensional numerical examples are presented. Finally, the concluding remarks are given in section 5.9.

5.2 Quadtree and octree decomposition of an image

In image-based analysis images are automatically decomposed on their colour intensity. This section outlines this procedure carried out by evaluating the colour intensity of pixels (2D) or voxels (3D) of an image. Quadtree (in 2D) and octree (in 3D) are hierarchical mesh generations structures adopted to segment the image to square and cubic cells, respectively. The explanations that follow assume that an image has been segmented and stored in a digital file format.

5.2.1 Quadtree decomposition

Quadtree is a spatial decomposition method, which was first developed by Finkel and Bentley [540]. The process of quadtree decomposition starts from a square containing the problem domain. The square is the first cell of the quadtree structure, which is also called the root. Based on specified stopping conditions, the root is recursively subdivided into four new cells. In each subdivision, newly generated cells are called the children of the subdivided cell whereas the subdivided cell is called the parent. A cell without any children is called a leaf. Leaves of a quadtree structure discretise the problem domain into a number of subdomains which are later used as a mesh for analysis.

A typical quadtree structure with three levels is shown in figure 5.1.

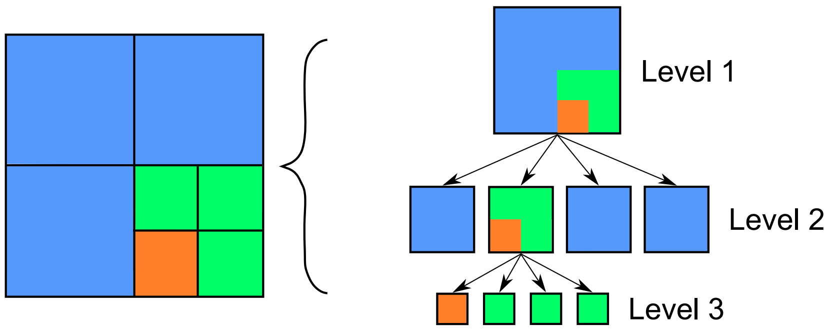

Figure 5.1. A typical three level quadtree structure. Colours blue, green and orange represent 3 different types of material.

In the first root level of the quadtree, three distinctive types of colours (blue, green and orange) can be seen. The children of this root cell are obtained in the second level of quadtree fragmentation. This level yields three leaves containing only the blue colour and one cell containing the colours green and orange. The latter cell therefore requires further quadtree decomposition due to the presence of dissimilar materials. This produces the level three decomposition which yields four leafs constituting three children in green colour and one child in orange colour. Further decomposition is not required beyond this point as each child contains only one type of material.

The image decomposition process starts with storing the colours of each pixel in an image colour matrix $\mathbf{I}_{ori}$. Here a pixel is represented as a square domain of size $h \times$

h where h is the image sampling interval. If the matrix $\mathbf{I}_{ori}$ is not a square matrix of dimensions 2^n, where n is a positive integer such that $n \geq 0$, then a bounding background is introduced to create a $2^n \times 2^n$ matrix $\mathbf{I}_{bound}$. To differentiate the background from the image the background colour is chosen different to the colour intensities appearing in $\mathbf{I}_{ori}$. Thereafter the quadtree decomposition process is carried out on $\mathbf{I}_{bound}$.

Figure 5.2 illustrates the image decomposition process according to the colour intensities appearing in the image. For this example an image of size 6×7 pixels is considered. The colour intensities extracted from the image are assembled in the matrix $\mathbf{I}_{ori}$ shown in figure 5.2b. These colour intensities are assumed to fall within a scale of 0 to 20, where 0 represents the darkest colour and 20 represents the lightest colour in the image. The matrix $\mathbf{I}_{ori}$ is overlapped on a background matrix of size $2^3 \times 2^3$ creating $\mathbf{I}_{bound}$. The value 100 of the newly introduced matrix elements is chosen outside of the colour intensity scale assumed for the image.

(a) A sample 2D image with a size of 6×7 pixels.

$$\begin{bmatrix} 4 & 4 & 4 & 4 & 10 & 10 & 16 \\ 4 & 4 & 4 & 4 & 10 & 10 & 16 \\ 4 & 4 & 4 & 4 & 8 & 10 & 8 \\ 4 & 4 & 4 & 4 & 10 & 9 & 8 \\ 20 & 20 & 20 & 16 & 16 & 12 & 12 \\ 20 & 20 & 20 & 16 & 16 & 12 & 12 \end{bmatrix}_{ori} \rightarrow \begin{bmatrix} 4 & 4 & 4 & 4 & 10 & 10 & 16 & 100 \\ 4 & 4 & 4 & 4 & 10 & 10 & 16 & 100 \\ 4 & 4 & 4 & 4 & 8 & 10 & 8 & 100 \\ 4 & 4 & 4 & 4 & 10 & 9 & 8 & 100 \\ 20 & 20 & 20 & 16 & 16 & 12 & 12 & 100 \\ 20 & 20 & 20 & 16 & 16 & 12 & 12 & 100 \\ 100 & 100 & 100 & 100 & 100 & 100 & 100 & 100 \\ 100 & 100 & 100 & 100 & 100 & 100 & 100 & 100 \end{bmatrix}_{bound}$$

(b) $\mathbf{I}_{ori}$ of size 6×7 representing colour intensities of the image.

(c) $\mathbf{I}_{bound}$ of size 8×8 with an introduced background.

Figure 5.2. Image decomposition of (a) a sample 2D image to produce (b) $\mathbf{I}_{ori}$ of size 6×7 and (c) $\mathbf{I}_{bound}$ of size of 8×8. In $\mathbf{I}_{bound}$ the rows 6-8 and column 8 are filled with the background colour intensity of 100.

The quadtree mesh generation starting from the matrix $\mathbf{I}_{bound}$ is executed by first dividing $\mathbf{I}_{bound}$ into cells of a maximum cell edge length of S_{max}. Here S_{max} is a user defined parameter. After this initial subdivision each cell is tested for homogeneity. A user defined parameter $C_{relative}$ is considered for this process. $C_{relative}$ is input to the process as a value ranging from 0 to 1. This value is first multiplied by the range of the actual colour intensity scale of the image and rounded to the nearest integer to produce a value C_{actual}. Therefore C_{actual} is reflective of the colour intensities present in an image. The cells are recursively divided into four equal-sized cells if the difference between the maximum and minimum colour intensities in a cell is larger than C_{actual}. The process terminates when the homogeneity criterion is satisfied or when the cells reach the minimum user defined cell edge length of S_{min}.

As per the example considered in figure 5.2, the actual colour intensity range is 21 since the intensity scale ranges from 0 to 20. Assuming $C_{relative} = 0.1$ yields $C_{actual} = 2$. Taking S_{max} and S_{min} respectively as 4 and 1 produces the quadtree mesh shown in figure .

4	4	4	4	10	10	16	100
4	4	4	4	10	10	16	100
4	4	4	4	9	10	8	100
4	4	4	4	10	8	8	100
20	20	20	16	16	12	12	100
20	20	20	16	16	12	12	100
100	100	100	100	100	100	100	100
100	100	100	100	100	100	100	100

Figure 5.3. Recursive quadtree decomposition of $\mathbf{I}_{bound}$ shown in figure 5.2c. $C_{actual} = 2$, $S_{max} = 4$ and $S_{min} = 1$.

As seen in figure 5.3, depending on the value set for the parameter C_{actual} there can be instances where pixels of different colours are present in the same cell. If this is an unsuitable outcome as per the expected accuracy for the analysis, C_{actual} can be set to zero to refine the mesh generation to represent exactly the colour intensities available in the image.

Next, specifically for the purpose of limiting the number cell patterns produced in the quadtree decomposition process a limiting 2 : 1 rule is enforced. This ensures the maximum edge length ratio between two neighbouring cells is not greater than 2. This process reduces the number of cell patterns available in the analysis enabling pre-computation of the subdomain stiffness matrices of a handful of cell types reducing the computational burden. The balanced quadtree decomposition of figure 5.3 is shown in figure 5.4.

4	4	4	4	10	10	16	100
4	4	4	4	10	10	16	100
4	4	4	4	9	10	8	100
4	4	4	4	10	8	8	100
20	20	20	16	16	12	12	100
20	20	20	16	16	12	12	100
100	100	100	100	100	100	100	100
100	100	100	100	100	100	100	100

Figure 5.4. The balanced quadtree decomposition of the mesh shown in figure 5.3 after enforcing the 2 : 1 rule. $C_{actual} = 2$, $S_{max} = 4$ and $S_{min} = 1$.

5.2.2 Octree decomposition

An image-based octree decomposition approach is used to generate the 3D meshes required for damage simulation. The process of octree decomposition starts from a cube containing the problem domain. The first cubic cell of the octree structure is also called the root. Based on specified stopping conditions, the root is recursively subdivided into eight new cells. Similar to the quadtree decomposition, newly generated cells are called "children" of the subdivided "parent" cell. A cell without any children is called a leaf. Leaves of an octree structure discretise the problem domain into a number of subdomains which are later used as a mesh for analysis.

A typical octree structure with three levels is shown in figure 5.5. The colours blue, green and orange represent 3 different types of material present in the domain.

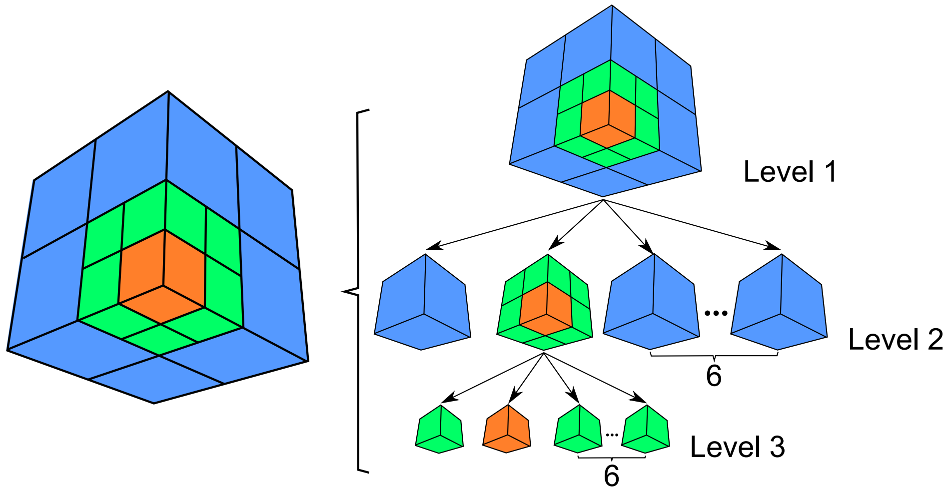

Figure 5.5. A typical three level octree decomposition. Colours blue, green and orange represent 3 different types of material.

The initial root cell is divided into eight cubic cells in the second level of decomposition. One cubic cell in this initial fragmentation is composed of different material. Therefore in the level three decomposition the green and orange cells are separated from one another.

The octree decomposition is developed on similar principles to that of the quadtree decomposition. The 2D image slices are stacked to build the 3D image. A voxel similar to a pixel in 2D represents a cubic domain of size $h \times h \times h$, where h is the image sampling interval. The matrices $\mathbf{I}_{ori}$ and $\mathbf{I}_{bound}$ are constructed similar to the 2D process where $\mathbf{I}_{ori}$ is fitted into a cubic bounding image matrix of size $2^n \times 2^n \times 2^n$ to create $\mathbf{I}_{bound}$. Then the process of octree decomposition recursively divides $\mathbf{I}_{bound}$ into eight equal sized cubic cells. Any cell that does not fall within the the criterion for homogeneity is further subdivided until homogeneity is achieved or the minimum user defined cell edge length of S_{min} is reached. Similar to the quadtree decomposition the octree decomposition also considers the balancing process by enforcing the $2:1$ rule.

A simple octree decomposition of a bar element is demonstrated in figure 5.6. The slender domain is 20 mm in length and 4 mm in breadth and height. A central prismatic portion highlighted in red 2 mm in length and height and 4 mm width is assumed to contain a different material. The octree structure is controlled by two user-defined parameters, maximum cell edge size $S_{max} = 4$ and the minimum cell edge size $S_{min} = 1$. To start the mesh generation, the domain is equally divided into five cells with size $S_{max} = 4$ as shown in figure 5.6b. Then the cells within the red region are subdivided until the cell sizes are equal to $S_{min} = 1$, which is shown in figures 5.6c-5.6d. This process is carried out to isolate the red pigmented portion of the bar into separate cells. Finally, the 2 : 1 balancing constraint is enforced on the octree structure in order to make the transition of mesh relatively smooth. The final mesh based on the proposed algorithm is shown in figure 5.6e.

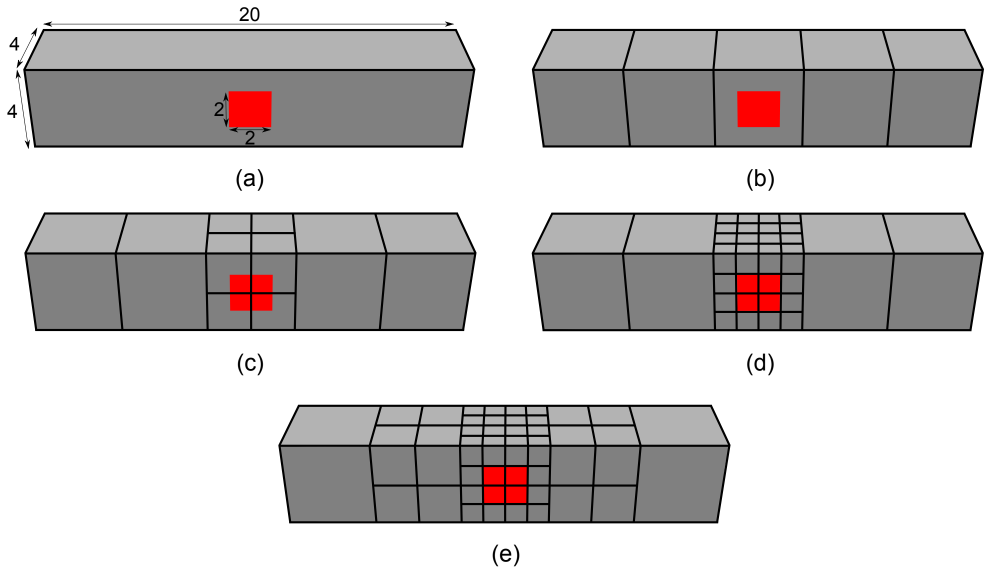

Figure 5.6. Octree decomposition of a bar element. Central prismatic portion marked in red indicate a different type of material.

5.2.3 Material assignment for each quadtree or octree cell

The material assignment procedure follows the balanced quadtree decomposition shown in figure 5.4. The colour intensities in each cell in figure 5.4 is first averaged and rounded up to the nearest positive integer to obtain the representative colour intensity of a cell. This step is as shown in figure 5.7a. Thereafter, material assignment takes place according to a user defined colour intensity range for each material.

4	4	4	4	10	10	16	100
4	4	4	4	10	10	16	100
4	4	4	4	9	9	8	100
4	4	4	4	9	9	8	100
20	20	20	16	16	12	12	100
20	20	20	16	16	12	12	100
100	100	100	100	100	100	100	100
100	100	100	100	100	100	100	100

(a) The average colour intensity for each cell in figure 5.4.

A	A	A	A	A	A	B	C
A	A	A	A	A	A	B	C
A	A	A	A	A	A	A	C
A	A	A	A	A	A	A	C
B	B	B	B	B	B	B	C
B	B	B	B	B	B	B	C
C	C	C	C	C	C	C	C
C	C	C	C	C	C	C	C

(b) The material classification for each cell in figure 5.7a.

Figure 5.7. Quadtree and octree material assignment process. (a) Calculation of the average colour intensity for each cell and (b) material assignment for each cell.

As shown in figure 5.7b material A is classed for all colour intensities ranging from $0-10$, material B belongs to colour intensities ranging from $10-20$. Any colour intensity greater than 20 is classed as the background and designated as material C.

To obtain the final quadtree or octree decomposition the background (material type C) is removed as a final step. The final decomposition for the image in figure 5.2a is shown in figure 5.8.

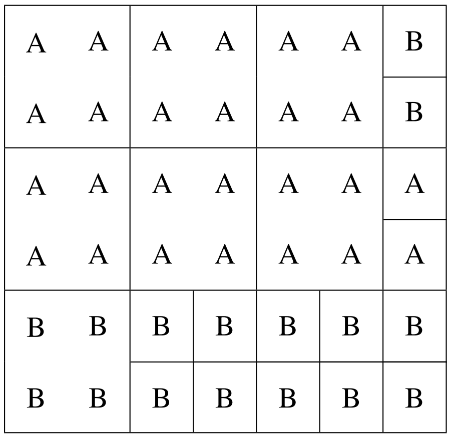

Figure 5.8. The final quadtree decomposition for the image in figure 5.2a. The letters A and B indicating the different material types.

5.3 Quadtree and octree cell patterns

The previous sections, section 5.2.1 and section 5.2.2 describe the process of quadtree and octree mesh generation starting from a simple image. The application of the 2 : 1 rule limits the number of different patterns of node arrangements among the elements produced although the cells can be of different size. This section describes the identification procedure of these unique cell patterns for the SBFE analysis framework later highlighted in this chapter.

In 2D analysis mid-side nodes may exist on the edges of cells. In the 3D space in addition to the mid-side nodes mid-face nodes in the centre of a cell face can also occur. These nodes are commonly referred to as hanging nodes in conventional literature. A typical 2D balanced quadtree decomposition with hanging nodes is shown in figure 5.9a. On the other hand, figure 5.9b depicts a balanced octree decomposition with hanging nodes. Hanging nodes create mesh incompatibilities in the conventional square (2D) or hexahedral (3D) element mapping processes in standard FEM.

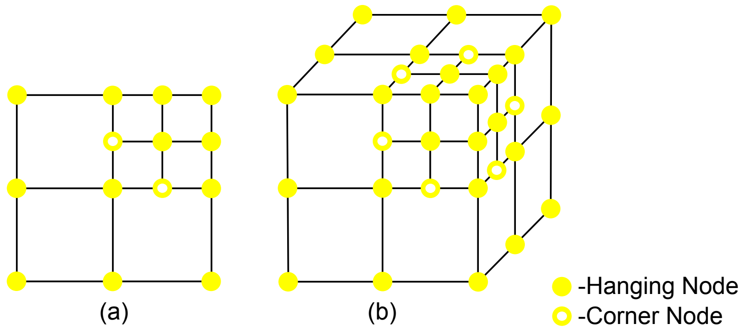

Figure 5.9. Hanging nodes occurring in (a) a segmented balanced quadtree image and (b) a segmented balanced octree image.

5.3.1 Patterns of quadtree cells

Owing to the SBFEM salient capability to handle hanging nodes a mesh typically consisting of hanging nodes as shown in figure 5.9a can be directly used in a analysis without further modification. This ability stems from SBFEM capability to model cells as polyhedral elements. The maximum number nodal configurations for a balanced quadtree mesh structure is 16. The size of these cell patterns can vary. However they are proportional to each other. This feature allows the user to pre-compute stiffness for different types of cell structures.

A four digit binary storage format is used to conveniently store the edge information. An edge consisting a hanging node is given binary 1 else binary 0.

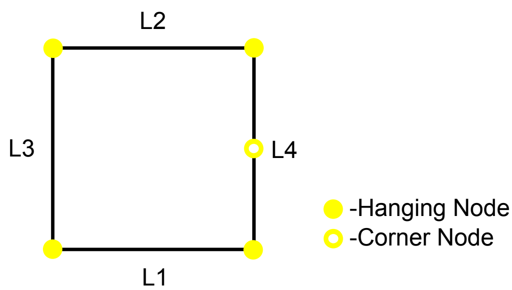

Figure 5.10. Edge numbering and binary coding of cell pattern for storing hanging node information in a quadtree mesh generation.

Figure 5.10 shows a typical cell generated in the meshing process with four edges L1 - L4. The numbering convention is always set such that the first two numbers L1 and L2 represent bottom and top edges respectively, and the preceding numbers L3 and L4 represents left and right edges respectively. Thus, for this example the stored binary cell information will be 0101. This additional step to identify the types of cells is advantageous moving forward when dealing with large problems that have large number of cells by reducing the storage requirements.

When rotational symmetry is considered, the number of cell patterns reduce from 16 to 6 unique types shown in figure 5.11. The identification of these unique cell patterns makes the meshing process extremely simple and quick as most procedures can be performed simultaneously for cells of the same unique node arrangement.

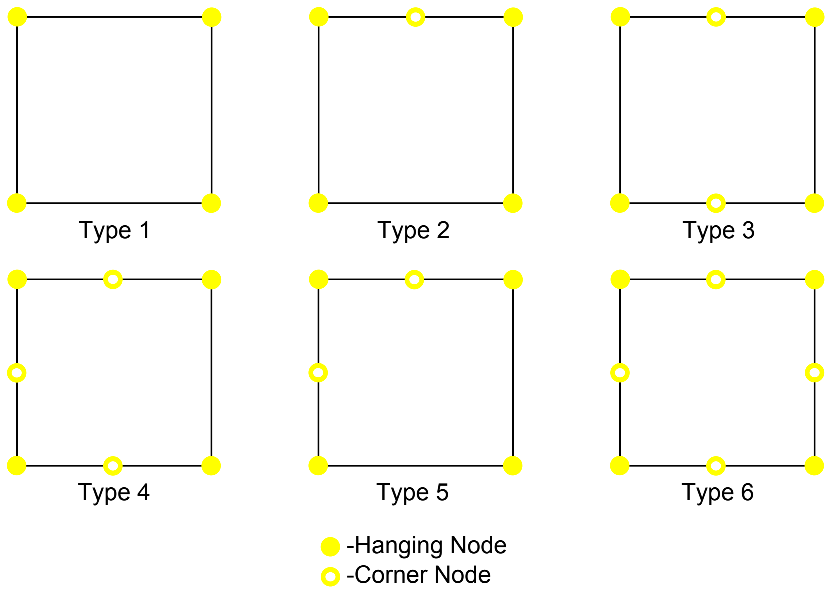

Figure 5.11. 6 types of unique node arrangements of a balanced quadtree decomposition by considering rotational symmetry.

5.3.2 Patterns of octree cells

Polyhedral elements are employed by the SBFEM to model the balanced octree decomposition explained in section 5.2.2. To carry out the method it only requires the 6 squares faces of the boundary to be discretised with surface elements. The work presented here employs standard triangular and quadrilateral 2D finite elements for this purpose.

As shown in figure 5.12 there are 6 types of surface discretisation patterns for different hanging nodes configurations on the face of an octree. In types 1, 2 and 5 a central node is introduced to accommodate the hanging node configuration. This additional node avoids any changes to the other faces of the cell as the discretization of the edges is not modified. The procedure produces only isosceles triangular and rectangular elements on the octree cell faces. A 2D Gauss-Lobatto quadrature integration scheme can produce exact results for all such elements and thus considered in this work.

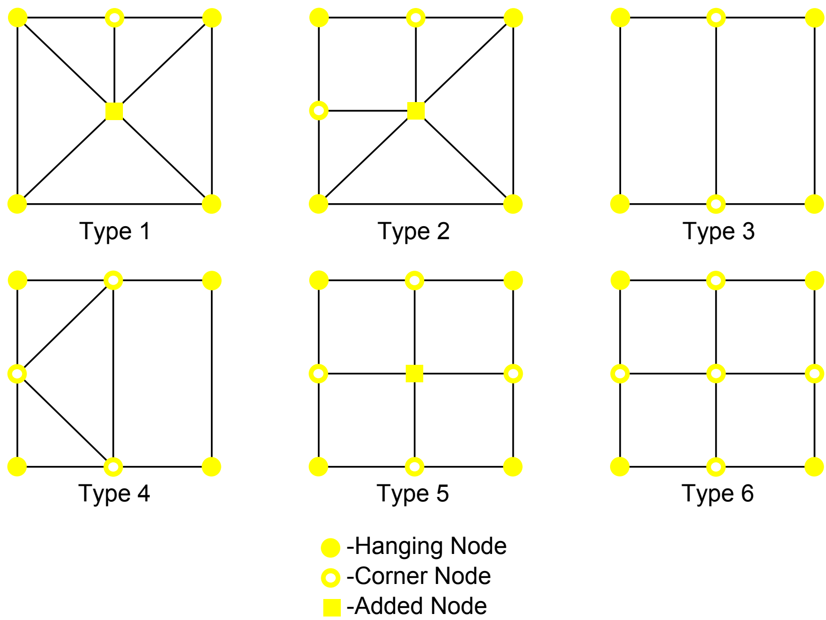

Figure 5.12. 6 types of surface discretization in a balanced octree decomposition on a face of an octree cell.

To identify different cell patterns it is only required to check the hanging node configurations in each of the 12 edges. Midpoint nodes can occur in any of the 12 edges of an octant. Therefore in total 4096 (2^{12}) unique cell nodal configurations are plausible. Despite this large number of cell patterns geometrically similar cells produce identical or proportional matrices to each other. Noting also, types 5 and 6 in figure 5.12 have identical surface discretisation even though the hanging node configurations are different.

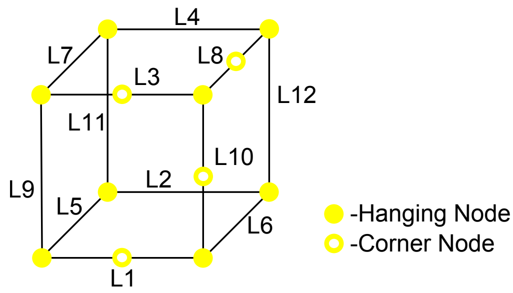

Figure 5.13. Edge numbering and binary coding of cell pattern for storing hanging node information in octree mesh generation.

Similar to the information storage pattern in quadtree mesh generation a twelve digit binary number is used to save the octree hanging node information. The binary 0 and 1 values represents a side without and with a mid-side node, respectively. The eight edges are labelled as L1-L12. The numbering pattern is as shown in figure 5.13. Therefore for the illustration shown in figure 5.13 the binary number 101000010100 represents the cell pattern.

5.4 Damage model for concrete

This section presents a condensed outline of the damage model for concrete. For a detailed explanation the reader can refer to chapter 3 section 3.2.

5.4.1 Evolution of damage

This chapter considers two damage evolution laws for the single scalar isotropic damage model described in section 3.2.2. The first is the linear softening model which is described as

$$\omega = \begin{cases} 0 & \text{if } \kappa \leq \varepsilon_0 \\ \frac{\varepsilon_f}{\varepsilon_f - \varepsilon_0}\left(1 - \frac{\varepsilon_0}{\kappa}\right) & \text{if } \varepsilon_0 < \kappa < \varepsilon_f \\ 1 & \text{if } \kappa \geq \varepsilon_f \end{cases} \tag{5.1}$$

where, ε_0 is the threshold of damage, and ε_f is a parameter affecting the ductility of the response which is related to the fracture energy.

The second type of relationships are exponential softening models. Two types of exponential softening models are considered in this chapter. The first model is defined as

$$\omega = \begin{cases} 0 & \text{if } \kappa \leq \varepsilon_0 \\ 1 - \frac{\varepsilon_0}{\kappa} \exp\left(\frac{-(\kappa-\varepsilon_0)}{\varepsilon_f-\varepsilon_0}\right) & \text{if } \kappa > \varepsilon_0. \end{cases} \tag{5.2}$$

The second model is a modified definition of the exponential softening model proposed by Geers et al. [481] defined as

$$\omega = \begin{cases} 0 & \text{if } \kappa \leq \varepsilon_0 \\ 1 - \frac{\varepsilon_0}{\kappa} \left(1 - \alpha + \alpha \times \exp\left(-\beta(\kappa - \varepsilon_0)\right)\right) & \text{if } \kappa > \varepsilon_0. \end{cases} \tag{5.3}$$

The definition of the equivalent strain directly affects the shape of the elastic domain in the strain space. The equivalent strain could be defined in an energy norm as

$$\tilde{\varepsilon} = \sqrt{\frac{1}{\mathrm{E}} \varepsilon : \mathbf{D} : \varepsilon}. \tag{5.4}$$

However, such a definition is not sensitive to the sign of the principal strains, and the model exhibits a symmetric behaviour in tension and in compression. As a remedy, Mazars and Pijaudier-Cabot [461] have proposed a definition for concrete as

$$\tilde{\varepsilon} = \sqrt{\sum_{i=1}^{3} (< \varepsilon_i >)^2}, \tag{5.5}$$

with ε_i representing the principal strains and the MacAulay brackets ($<>$) defined such that $< \varepsilon_i >= \varepsilon_i$ if $\varepsilon_i > 0$ and $\varepsilon_i = 0$ otherwise. This allows the model to consider only the tension producing principal strains in the analysis.

Also, the more conventional von Mises equivalent strain definition is as follows

$$\tilde{\varepsilon} = \frac{1}{1+\nu} \sqrt{3 J_2^{\varepsilon}}, \tag{5.6}$$

where, ν is the Poisson's ratio, J_2^ε is the second invariant of the deviatoric strain vector defined as

$$J_2^\varepsilon = \frac{1}{3}[\varepsilon_{xx}^2 + \varepsilon_{yy}^2 + \varepsilon_{zz}^2 - \varepsilon_{xx}\varepsilon_{yy} + \varepsilon_{yy}\varepsilon_{zz} + \varepsilon_{zz}\varepsilon_{xx} + 3(\varepsilon_{xy}^2 + \varepsilon_{yz}^2 + \varepsilon_{zx}^2). \tag{5.7}$$

Another widely used definition of equivalent strain for concrete is proposed by De Vree et al. [497] and termed as modified von Mises definition, which is given by

$$\tilde{\varepsilon} = \frac{k-1}{2k(1-\nu)} I_1^\varepsilon + \frac{1}{2k}\sqrt{\frac{(k-1)^2}{(1-2\nu)^2}(I_1^\varepsilon)^2 + \frac{12k}{(1+\nu)^2} J_2^\varepsilon} \tag{5.8}$$

in which k is normally set equal to the ratio between the compressive uniaxial strength and the tensile uniaxial strength, ν is the Poisson's ratio, I_1^ε the first invariant of the strain vector defined below and J_2^ε the second invariant of the deviatoric strain vector and defined in equation (5.7)

$$I_1^\varepsilon = \varepsilon_{xx} + \varepsilon_{yy} + \varepsilon_{zz}. \tag{5.9}$$

5.4.2 Integral-type non-local damage models

With reference to section 3.2.4, the non-local damage model implemented in this chapter uses the Gauss distribution weight function defined by [250]

$$\alpha_0(r) = \exp\left[-\frac{d^2}{2l^2}\right], \tag{5.10}$$

in which l is the internal length of the non-local continuum.

Another alternative form of weight function is a truncated quartic polynomial function in bell-shape given in [477]

$$\alpha_0(r) = \left\langle 1 - \frac{d^2}{R^2} \right\rangle^2. \tag{5.11}$$

In equation (5.11), R is the interaction radius related to the internal length and denotes the largest distance of point θ that affects the non-local average at point x. The Gauss distribution function can also be written in terms of the interaction radius as

$$\alpha_0(r) = \exp\left[-\frac{4d^2}{R^2}\right] \tag{5.12}$$

5.4.3 Discussion on non-local averaging over different material interfaces

In this section the effect of non-local averaging over different types of material is investigated in detail. This discussion is quite vital especially in instances where multi-material interfaces can influence the damage process zone. A typical example for which is concrete. Concrete in most instances modelled by considering the presence of aggregate, mortar and also the presence of inter-facial transition zone (ITZ).

To begin the discussion a two element model is considered with each element having a Young's modulus considerably different to the other.

As shown in figure 5.14 a simple model of a plate with dimensions 2×1 mm is considered for this analysis. Therefore each element is of dimension 1×1 mm. These dimensions are selected purely for the convenience of numerical verification.

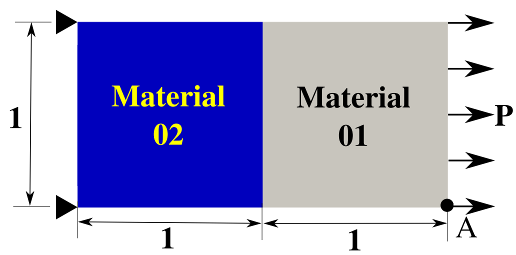

Figure 5.14. Plate dimensions (mm) and loading conditions considered for the 2D local and non-local behaviour analysis of a bi-material interface under uniaxial tension. Material 1 shaded in grey assumed to be 100 times stronger than the material 2 shaded in blue.

The Young's modulus of material 1 is considered to be 100 GPa and material 2 is set to 1 GPa. Thus one material of the two material interface has a Young's modulus which deviates 100 times from the other. The stiffer material (material 1) undergoes material damage whereas the weaker material (material 2) remains elastic throughout the simulation. For simplicity the Poisons ratio for both materials is set to 0.

The linear damage evolution is in accordance to the linear damage model given in equation (5.1) with ε_0 set to 1.2×10^{-4} and strain at which material is fully damaged ε_f set to 7.0×10^{-3}. The 1D stress-strain behaviour for the stronger material with respect to these material and damage parameters is shown in figure 5.15. The equivalent strain parameter $\tilde{\varepsilon}$ is calculated as per equation (5.6).

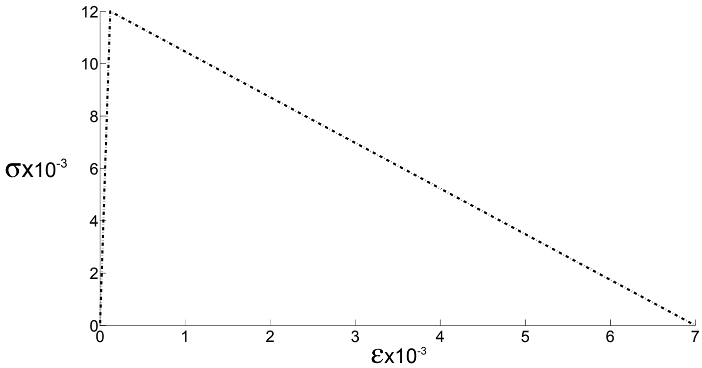

Figure 5.15. 1D element stress (GPa) vs strain profile considered in the discussion on non-local averaging over bi-material interface. The stress-strain profile shown here is related to material 1. Damage evolution considered is with respect to the softening law in equation (5.1).

At first the analysis is run as a local analysis without the consideration of averaging equivalent strains. Next a non-local analysis is performed with the consideration of averaging equivalent strain over both materials. For the non-local analysis a internal length scale of 100 mm is considered such that averaging over the adjacent element is achieved and the averaging weight functions yield close to unity. The non-local weighting considered is according to equation (5.10).

The model is meshed with just two elements, one element for each material type. The single Gauss point SC model is used in each element leading to a 1 mm distance between the gauss points of the two elements (see figure 5.16).

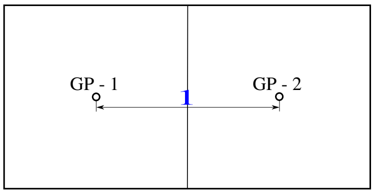

Figure 5.16. SBFEM mesh used in the discussion on non-local averaging over bi-material interface. The analysis considers one element for each material type.

As shown in figure 5.14 the plate is subjected to uniaxial tension by providing horizontal restraints at one end and applying a uniform agitation from the opposite end. A displacement controlled analysis is considered for this simulation. The modified Newton Raphson solver with arc-length control introduced in chapter 3 is used for this analysis. 700 iterations with an initial displacement step of 1×10^{-5} mm is adopted with automatic displacement control analysis. The load-displacement curve produced in the analysis is shown in figure 5.17. Here the computational outputs are compared to the hand calculated quantities of the local and non-local averaging scheme.

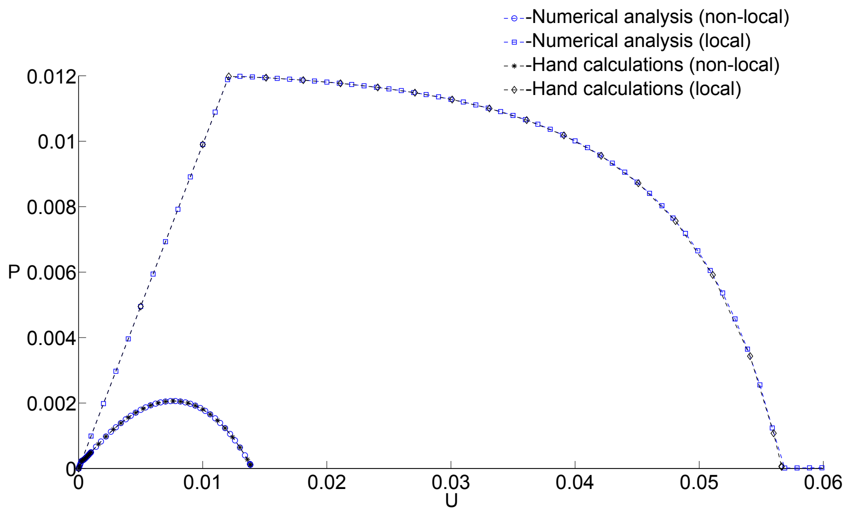

Figure 5.17. Force (kN) vs displacement (mm) output for the discussion on non-local averaging over bi-material interface. Numerical analysis compared to the hand calculations for both local and non-local damage analysis schemes.

The computational results show exact agreement with hand calculated quantities, justifying the accuracy of the computational framework.

The following displacement (figure 5.18), strain (figure 5.19), stress (figure 5.20), and damage (figure 5.19) evolution contour plots correspond to the local analysis. With reference to figure 5.17 these contour plots are recorded at displacement of 0.006 mm at node ‘A’ corresponding to a load of 0.005941 kN on the right edge, at peak load for a displacement value of 0.01212 mm corresponding to a load of 0.012 kN, after peak load for a displacement value of 0.03 mm corresponding to a load of 0.01128 kN and at the end of the simulation for a displacement value of 0.056 mm corresponding to a load of 0 kN.

(a) Horizontal displacement (u_x) contour. The displacement at node A is 0.006 mm.

(b) Horizontal displacement (u_x) contour. The displacement at node ‘A’ is 0.01212 mm.

(c) Horizontal displacement (u_x) contour. The displacement at node ‘A’ is 0.03 mm.

(d) Horizontal displacement (u_x) contour. The displacement at node ‘A’ is 0.056 mm.

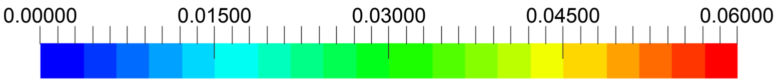

Figure 5.18. Horizontal displacement (u_x) contours obtained for the local damage analysis in the discussion on averaging over bi-material interface. Units:mm. Results are obtained for the mesh shown in figure 5.16.

As evident in figures 5.19a and 5.19b the strain profiles for the two materials show a distinct uniform variation in the magnitude of 100 in the elastic stage (up to the displacement value of 0.01212 mm). This is due to the variation in Young’s modulus in the magnitude of 100 between material 1 and material 2. To exhibit non-linear behaviour material 1 has to reach a strain value equal to 0.00012 (value of ε_0). When material 1 attains this value the total displacement corresponds to 0.01212 mm (see figure 5.19b). This value agrees with the hand calculations as material 2 should depict a strain of 0.012 when material 1 reaches a strain of 0.00012. Beyond the elastic limit the two materials depict a characteristic damage induced non-linear behaviour till the termination of the simulation.

(a) Strain (ε_{xx}) contour. The horizontal displacement at node 'A' is 0.006 mm.

(b) Strain (ε_{xx}) contour. The horizontal displacement at node 'A' is 0.01212 mm.

(c) Strain (ε_{xx}) contour. The horizontal displacement at node 'A' is 0.03 mm.

(d) Strain (ε_{xx}) contour. The horizontal displacement at node 'A' is 0.056 mm.

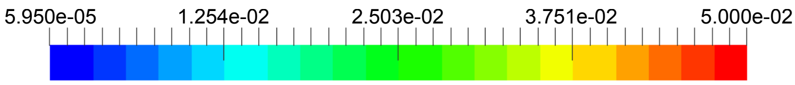

Figure 5.19. Strain (ε_{xx}) contours obtained for the local damage analysis in the discussion on averaging over bi-material interface. Results are obtained for the mesh shown in figure 5.16.

The stresses in the two materials are identical in the linear elastic stage up to node 'A' displacement reaches 0.01212 mm. This is depicted in figures 5.20a and 5.20b. Thereafter due to the degradation material 1 the stress within this material begins to drop. When the simulation reaches a node 'A' displacement of 0.056 mm the total load carrying capacity of the model is lost as the stress within material 1 corresponds to 1.4×10^{-5} GPa.

(a) Stress (σ_{xx}) contour. The horizontal displacement at node 'A' is 0.006 mm.

(b) Stress (σ_{xx}) contour. The horizontal displacement at node 'A' is 0.01212 mm.

(c) Stress (σ_{xx}) contour. The horizontal displacement at node 'A' is 0.03 mm.

(d) Stress (σ_{xx}) contour. The horizontal displacement at node 'A' is 0.056 mm.

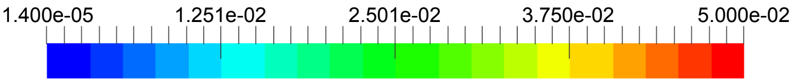

Figure 5.20. Stress (σ_{xx}) contours obtained for the local damage analysis in the discussion on averaging over bi-material interface. Units:GPa. Results are obtained for the mesh shown in figure 5.16.

The damage profiles below show evidence of the gradual degradation experienced by material 1. The model show no signs of damage degradation up to the displacement value of 0.01212 mm corresponding to the peak load 0.012 kN (see figures 5.21a and 5.21b). However from this point onwards (figures 5.21c and 5.21d) the accumulation of strain greater than the damage initiation threshold ε_0 develops damage within material 1.

(a) Damage (ω) contour. The horizontal displacement at node ‘A’ is 0.006 mm.

(b) Damage (ω) contour. The horizontal displacement at node ‘A’ is 0.01212 mm.

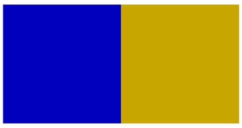

(c) Damage (ω) contour. The horizontal displacement at node ‘A’ is of 0.03 mm.

(d) Damage (ω) contour. The horizontal displacement at node ‘A’ is 0.056 mm.

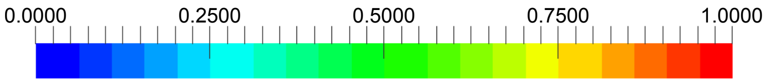

Figure 5.21. Damage (ω) contours obtained for the local damage analysis in the discussion on averaging over bi-material interface. Results are obtained for the mesh shown in figure 5.16.

Next the displacement (figure 5.22), strain (figure 5.23), stress (figure 5.24) and damage (figure 5.25) evolution contour plots, are documented for the non-local simulation. The instances captured in this simulation are of similar significance to that considered in the local analysis. In reference to figure 5.17 these contour plots are recorded at displacement of 2.424×10^{-4} mm at node ‘A’ corresponding to a load of 2.4×10^{-4} kN on the right edge, at peak load for a displacement value of 0.00761 mm corresponding to a load of 2.062×10^{-3} kN, after peak load for a displacement value of 0.01 mm corresponding to a load of 1.806×10^{-3} kN, and at the end of the simulation for a displacement value of 0.01386 mm when the load reaches 0 kN.

(a) Horizontal displacement (u_x) contour. The displacement at node 'A' is 0.0002424 mm.

(b) Horizontal displacement (u_x) contour. The displacement at node 'A' is 0.00761 mm.

(c) Horizontal displacement (u_x) contour. The displacement at node 'A' is 0.01 mm.

(d) Horizontal displacement (u_x) contour. The displacement at node 'A' is 0.01386 mm.

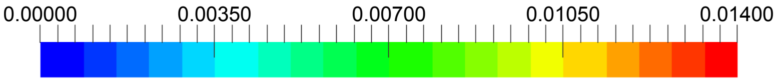

Figure 5.22. Horizontal displacement (u_x) contours obtained for the non-local damage analysis in the discussion on averaging over bi-material interface. Units:mm. Results are obtained for the mesh shown in figure 5.16.

The simulation depicts non-linear behaviour when the non-local strain within material 1 reaches the damage initiation threshold ε_0. Since the non-local averaging internal length parameter is set to 100 mm the non-local weights produced by equation (5.10) are close to unity. Therefore when equivalent strain within material 2 reaches 2.4×10^{-4} the non-local equivalent strain within material 1 reaches ε_0 $(2.4 \times 10^{-4}/2 = 0.00012)$. At this instance the equivalent strain within material 1 reads be 2.4×10^{-6} due to the variation in Young's modulus between material 2 and material 1. Considering these two strain values the node 'A' displacement of the model immediately prior to the beginning of non-linear behaviour is 2.424×10^{-4} mm $((2.4 + 0.0024)\,10^{-4} = 2.424 \times 10^{-4})$. These values are evident in the displacement contour in figure 5.22a. As material 1 degrades through the formation of damage the strains produced by the material became comparatively similar to those of material 2 (see figures 5.23b-5.23d).

(a) Strain (ε_{xx}) contour. The horizontal displacement at node 'A' is 0.0002424 mm.

(b) Strain (ε_{xx}) contour. The horizontal displacement at node 'A' is 0.00761 mm.

(c) Strain (ε_{xx}) contour. The horizontal displacement at node 'A' is 0.01 mm.

(d) Strain (ε_{xx}) contour. The horizontal displacement at node 'A' is 0.01386 mm.

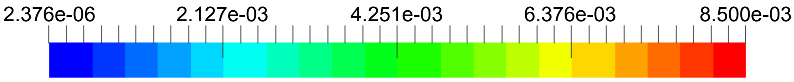

Figure 5.23. Strain (ε_{xx}) contours obtained for the non-local damage analysis in the discussion on averaging over bi-material interface. Results are obtained for the mesh shown in figure 5.16.

In the elastic region (see figure 5.24a) the model depicts a uniform stress distribution. However thereafter the stress within material 1 drops as it degrades with increasing damage until the element can no longer resist any applied loading (see figure 5.24d).

(a) Stress (σ_{xx}) contour. The horizontal displacement at node 'A' is 0.0002424 mm.

(b) Stress (σ_{xx}) contour. The horizontal displacement at node 'A' is 0.00761 mm.

(c) Stress (σ_{xx}) contour. The horizontal displacement at node 'A' is 0.01 mm.

(d) Stress (σ_{xx}) contour. The horizontal displacement at node 'A' is 0.01386 mm.

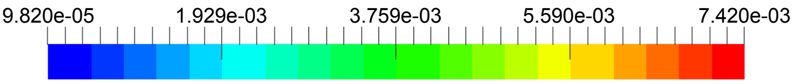

Figure 5.24. Stress (σ_{xx}) contours obtained for the non-local damage analysis in the discussion on averaging over bi-material interface. Units:GPa. Results are obtained for the mesh shown in figure 5.16.

The hardening limb observed in the non-local simulation in figure 5.17 can be attributed to the residual stiffness within material 1. Even though damage initiates soon after node 'A', reaching a displacement of 0.0002424 mm (see figure 5.25a), the residual, damage effected stiffness enables the material to carry further load (see figure 5.24b). However after reaching maximum capacity when node 'A' displacement reaches 0.00761 mm, the model starts to soften gradually (see figures 5.24c-5.24d).

(a) Damage (ω) contour. The horizontal displacement at node 'A' is 0.0002424 mm.

(b) Damage (ω) contour. The horizontal displacement at node 'A' is 0.00761 mm.

(c) Damage (ω) contour. The horizontal displacement at node 'A' is 0.01 mm.

(d) Damage (ω) contour. The horizontal displacement at node 'A' is 0.01386 mm.

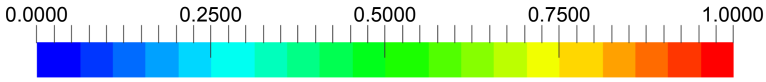

Figure 5.25. Damage (ω) contours obtained for the non-local damage analysis in the discussion on averaging over bi-material interface. Results are obtained for the mesh shown in figure 5.16.

As observed within both the local and non-local analysis, prior to damage inception, strain in both materials increase linearly (see figures 5.19a, 5.19b and 5.23a). When damage initiates in material 1 and subsequent development of damage within the material, the strain in material 1 increases disproportionally to material 2. Due to the degradation of material 1 the strain thus observed by material 1 compromises of a larger proportion of the total strain observed by the composite element as material 2 unloads to maintain external and internal force equilibrium.

In a non-local analysis where averaging is considered within the same material the behaviour of the neighbouring materials does not contribute to the damage development of the material under consideration. However when averaging over different material, the strain observed by the neighbouring materials creeps into the material in consideration. This then transcends to the force-displacement behaviour of the model.

In this simulation material parameters are carefully considered to exemplify the effects of such non-local averaging over different material. Here the variation in the Young's modulus between the two materials contribute to a contrasting change in the load-displacement output seen in figure 5.17. Therefore, it is prudent to carefully consider the affects of non-local averaging between bi-material interfaces as it may have a considerable effect on the results obtained. Furthermore this example also considers the non-local length parameter such that it has less or no affect in the simulation. It is best practice to consider the non-local length scale as a material parameter representative of the material characteristics. This, in turn will lead to disparities in the results as different material types will inherent different characteristic length scales

5.5 Fundamentals of the scaled boundary finite element method

5.5.1 Scaled boundary geometry representation

The 2D SBFEM is based on a coordinate system of two coordinates (ξ, η), where ξ represents the radial coordinates and η represents the circumferential coordinate. Whereas the 3D SBFEM introduces an additional third circumferential coordinate ζ. Arbitrary n-sided polytope elements can be modelled using the SBFEM. The only requirement being every point on the boundary can be connected to the scaling centre by an unobstructed radial line. In situations when this condition is unable to be attained further subdivision is carried out. In this section the discussions are based on elements produced in the quadtree and octree mesh generation. A detailed description of the derivation can be found in chapters 3 and 4, and the original publication by Song and Wolf [199].

5.5.1.1 2D formulation

Quadtree elements are modelled as scaled boundary polygonal elements. The boundary of the element is divided into line elements as shown in figure 5.26. The condition of the visible boundary is satisfied from the scaling centre (O) thus no further subdivision is required.

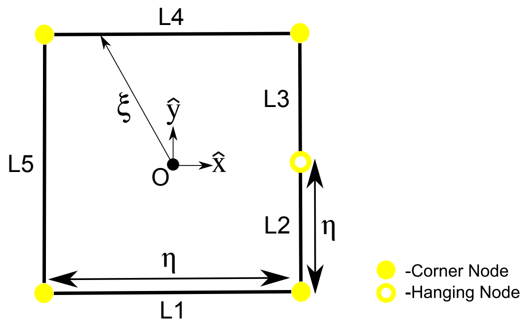

Figure 5.26. Scaled boundary finite element coordinate system for a quadtree element.

Since only the boundaries are required to be discretised the hanging nodes do not require any special treatment. The edge containing the hanging node is modelled with two line elements L2 and L3 (refer fig 5.26). This chapter uses linear line elements to model the examples presented later in section 5.8. Thus the derivations that follow are explicit equations for a linear line element.

The variable ξ varies form 0 to 1. At O $\xi = 0$ and at the boundary $\xi = 1$. Assuming the Cartesian coordinates origin is the same location as the scaling centre, a point $(\hat{x}, \hat{y})$ can be described with respect to the SBFE local coordinates (ξ, η) as

$$\hat{x}(\xi, \eta) = \xi x(\eta) = \xi \mathbf{N}(\eta) x, \tag{5.13a}$$

$$\hat{y}(\xi, \eta) = \xi y(\eta) = \xi \mathbf{N}(\eta) y, \tag{5.13b}$$

where, $\mathbf{N}(\eta)$ is the 1D linear interpolation shape function given by $\mathbf{N}(\eta) = \left[\begin{array}{cc} \frac{1-\eta}{2} & \frac{1+\eta}{2} \end{array} \right]$ and x, y are vectors of the nodal coordinates for each line element. Thus the coordinates of a point in the element boundary $(x(\eta), y(\eta))$ can be written as

$$x(\eta) = \begin{bmatrix} \frac{1-\eta}{2} & \frac{1+\eta}{2} \end{bmatrix} \begin{Bmatrix} x_1 \\ x_2 \end{Bmatrix} = \bar{x} + \eta \frac{\delta x}{2}, \tag{5.14a}$$

$$y(\eta) = \begin{bmatrix} \frac{1-\eta}{2} & \frac{1+\eta}{2} \end{bmatrix} \begin{Bmatrix} y_1 \\ y_2 \end{Bmatrix} = \bar{y} + \eta \frac{\delta y}{2}, \tag{5.14b}$$

where,

$$\bar{x} = \frac{x_2 + x_1}{2} \tag{5.15a}$$

$$\bar{y} = \frac{y_2 + y_1}{2} \tag{5.15b}$$

$$\delta x = x_2 - x_1 \tag{5.15c}$$

$$\delta y = y_2 - y_1 \tag{5.15d}$$

The transformation of the problem domain from $(\hat{x}, \hat{y})$ Cartesian coordinates to the local scaled boundary coordinates (ξ, η) is through the Jacobian matrix $\mathbf{J}$

$$\mathbf{J} = \begin{bmatrix} x & y \\ x_{,\eta} & y_{,\eta} \end{bmatrix}, \tag{5.16}$$

where $x_{,\eta} = \frac{\delta x}{2}$ and $y_{,\eta} = \frac{\delta y}{2}$. Then the determinant of the 2×2 Jacobian matrix $|\mathbf{J}|$ is

$$|\mathbf{J}| = \frac{1}{2}(x_1 y_2 - x_2 y_1). \tag{5.17}$$

The linear differential operator $\mathbf{L}$

$$\mathbf{L} = \mathbf{b}_1 \frac{\partial}{\partial \xi} + \frac{1}{\xi} \mathbf{b}_2 \frac{\partial}{\partial \eta}, \tag{5.18}$$

where $\mathbf{b}_1$ and $\mathbf{b}_2$ are defined as follows

$$\mathbf{b}_1 = \frac{1}{|\mathbf{J}|}\begin{bmatrix} y_{,\eta} & 0 \\ 0 & -x_{,\eta} \\ -x_{,\eta} & y_{,\eta} \end{bmatrix} = \frac{1}{|\mathbf{J}|}\mathbf{C}_1, \tag{5.19a}$$

$$\mathbf{b}_2 = \frac{1}{|\mathbf{J}|}\begin{bmatrix} -y & 0 \\ 0 & x \\ x & -y \end{bmatrix} = \frac{1}{|\mathbf{J}|}\left[\eta\mathbf{C}_1 + \mathbf{C}_2\right]. \tag{5.19b}$$

Therefore $\mathbf{C}_1$ and $\mathbf{C}_2$ in the equations above stand for

$$\mathbf{C}_1 = \frac{1}{2}\begin{bmatrix} \delta y & 0 \\ 0 & -\delta x \\ -\delta x & \delta y \end{bmatrix}, \tag{5.20a}$$

$$\mathbf{C}_2 = \begin{bmatrix} \bar{y} & 0 \\ 0 & -\bar{x} \\ -\bar{x} & \bar{y} \end{bmatrix}. \tag{5.20b}$$

The displacement solutions within each polygonal element

$$\mathbf{u}(\xi,\eta) = \left[\mathbf{u}_x(\xi,\eta), \mathbf{u}_y(\xi,\eta)\right]^{\mathrm{T}}, \tag{5.21}$$

are interpolated as

$$\mathbf{u}(\xi,\eta) = \mathbf{N}_u(\eta)\mathbf{u}(\xi), \tag{5.22}$$

where $\mathbf{u}(\xi)$ is the displacement solution in the radial direction. The shape function $\mathbf{N}_u(\eta)$ is

$$\mathbf{N}_u(\eta) = \begin{bmatrix} \frac{1-\eta}{2}\mathbf{I} & , & \frac{1+\eta}{2}\mathbf{I} \end{bmatrix}, \tag{5.23}$$

where $\mathbf{I}$ is 2×2 identity matrix.

The strain-displacement matrices $\mathbf{B}_1$, $\mathbf{B}_2$ can be written using equation (5.18) as

$$\mathbf{B}_1 = \mathbf{b}_1 \mathbf{N}_u(\eta) = \frac{1}{|\mathbf{J}|} \left[\begin{array}{cc} \frac{1-\eta}{2}\mathbf{C}_1 & , \frac{1+\eta}{2}\mathbf{C}_1 \end{array} \right], \tag{5.24a}$$

$$\mathbf{B}_2 = \mathbf{b}_2 \mathbf{N}_u(\eta)_{,\eta} = -\frac{1}{|\mathbf{J}|} \left[\begin{array}{cc} -\frac{\eta}{2}\mathbf{C}_1 - \frac{1}{2}\mathbf{C}_2 & , \frac{\eta}{2}\mathbf{C}_1 + \frac{1}{2}\mathbf{C}_2 \end{array} \right]. \tag{5.24b}$$

The strains ε can be formed using equation (5.18) and equation (5.22) as

$$\varepsilon = \mathbf{L}\mathbf{u}(\xi, \eta) = \mathbf{B}_1 \mathbf{u}(\xi)_{,\xi} + \frac{1}{\xi}\mathbf{B}_2 \mathbf{u}(\xi). \tag{5.25}$$

5.5.1.2 3D formulation

In the 3D formulation each cubic subdomain is modelled as a scaled boundary polyhedral element as shown in figure 5.27. The element consists of surface elements on the boundary and the scaling centre O is placed at the centroid of each octree element. The surface elements are modelled similar to the 2D elements with local boundary coordinates (η, ζ). The two main types of surface elements created in the mesh generation are triangular and quadrilateral elements. The local boundary representations of these two common types of source elements are also included in figure 5.27.

In this chapter classical finite element triangular and quadrilateral elements with linear shape functions are utilised on the boundaries. Presented below is a summary of the SBFE formulation for a linear triangular surface element.

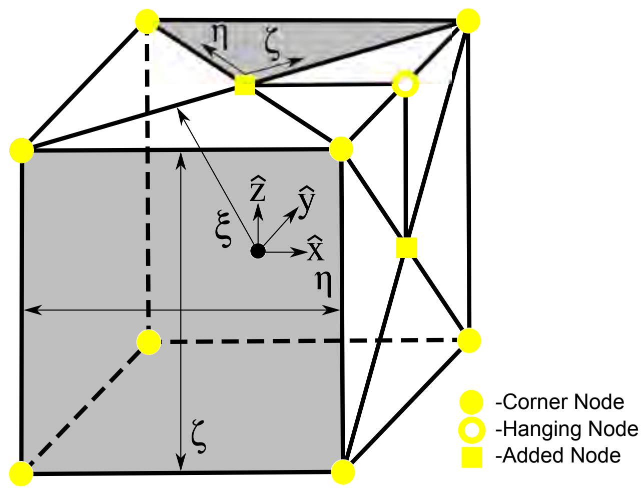

Figure 5.27. The SBFE local coordinates in an octree cell.

A radial coordinate ξ is used to describe the cell's internal domain by scaling the surface elements. At the scaling centre $\xi = 0$ and at a point on the boundary $\xi = 1$. For this instance if the the origin of the Cartesian coordinates coincides with the scaling centre, a point $(\hat{x}, \hat{y}, \hat{z})$ in the cell can be written in terms of the local coordinates (ξ, η, ζ) as

$$\hat{x}(\xi, \eta, \zeta) = \xi x(\eta, \zeta) = \xi \mathbf{N}(\eta, \zeta)\mathbf{x}, \tag{5.26a}$$

$$\hat{y}(\xi, \eta, \zeta) = \xi y(\eta, \zeta) = \xi \mathbf{N}(\eta, \zeta)\mathbf{y}, \tag{5.26b}$$

$$\hat{z}(\xi, \eta, \zeta) = \xi z(\eta, \zeta) = \xi \mathbf{N}(\eta, \zeta)\mathbf{z}, \tag{5.26c}$$

where $\mathbf{N}(\eta, \zeta)$ is the 2D interpolation shape functions and $\mathbf{x}, \mathbf{y}, \mathbf{z}$ are nodal coordinate vectors for each surface element. Since the coordinates of a point on the surface element's boundary can be written using the linear shape function for a triangular element $\mathbf{N}(\eta) = \begin{bmatrix} (1-\eta-\zeta) & \eta & \zeta \end{bmatrix}$ equations (5.26a-5.26c) transforms to

$$x(\eta, \zeta) = \mathbf{N}(\eta, \zeta)\mathbf{x} = x_1 + \delta x_1 + \delta x_2, \tag{5.27a}$$

$$y(\eta, \zeta) = \mathbf{N}(\eta, \zeta)\mathbf{y} = y_1 + \delta y_1 + \delta y_2, \tag{5.27b}$$

$$z(\eta, \zeta) = \mathbf{N}(\eta, \zeta)\mathbf{z} = z_1 + \delta z_1 + \delta z_2, \tag{5.27c}$$

where,

$$\delta x_1 = x_2 - x_1, \tag{5.28a}$$

$$\delta y_1 = y_2 - y_1, \tag{5.28b}$$

$$\delta z_1 = z_2 - z_1, \tag{5.28c}$$

$$\delta x_2 = x_3 - x_1, \tag{5.28d}$$

$$\delta y_2 = y_3 - y_1, \tag{5.28e}$$

$$\delta z_2 = z_3 - z_1, \tag{5.28f}$$

(x_i, y_i, z_i) are the Cartesian coordinates of a local node i on the surface an element.

With the help of the Jacobian matrix $\mathbf{J} = \begin{bmatrix} x & y & z \\ x_{,\eta} & y_{,\eta} & z_{,\eta} \\ x_{,\zeta} & y_{,\zeta} & z_{,\zeta} \end{bmatrix}$ at the boundary $(x = 1)$ with omitted arguments (η, ζ), the problem domain is transformed from the Cartesian coordinates $(\hat{x}, \hat{y}, \hat{z})$ to the local scaled boundary coordinates (ξ, η, ζ) using standard procedures for each surface element.

The derivatives of the coordinates on the surface element are written as

$$x_{,\eta} = \delta x_1, \tag{5.29a}$$

$$y_{,\eta} = \delta y_1, \tag{5.29b}$$

$$z_{,\eta} = \delta z_1, \tag{5.29c}$$

$$x_{,\zeta} = \delta x_2, \tag{5.29d}$$

$$y_{,\zeta} = \delta y_2, \tag{5.29e}$$

$$z_{,\zeta} = \delta z_2, \tag{5.29f}$$

The determinant of the Jacobian matrix $|\mathbf{J}|$ is

$$|\mathbf{J}| = x_1 \left(y_2 z_3 - z_2 y_3\right) + y_1 \left(z_2 x_3 - x_2 z_3\right) + z_1 \left(x_2 y_3 - y_2 x_3\right) \tag{5.30}$$

The linear differential operator $\mathbf{L}$ in the local scaled boundary coordinates can then be written as

$$\mathbf{L} = \mathbf{b}_1 \frac{\partial}{\partial \xi} + \frac{1}{\xi} \left(\mathbf{b}_2 \frac{\partial}{\partial \eta} + \mathbf{b}_3 \frac{\partial}{\partial \zeta} \right) \tag{5.31}$$

where $\mathbf{b}_1$, $\mathbf{b}_2$ and $\mathbf{b}_3$ are defined as

$$\mathbf{b}_1 (\eta, \zeta) = \frac{1}{|\mathbf{J}|} \mathbf{G}_1, \tag{5.32a}$$

$$\mathbf{b}_2 (\eta, \zeta) = \frac{1}{|\mathbf{J}|} [\eta \mathbf{G}_1 + \mathbf{G}_2], \tag{5.32b}$$

$$\mathbf{b}_3 (\eta, \zeta) = \frac{1}{|\mathbf{J}|} [\eta \mathbf{G}_1 + \mathbf{G}_2], \tag{5.32c}$$

and $\mathbf{G}_1$, $\mathbf{G}_2$ and $\mathbf{G}_3$ are defined as

$$\mathbf{G}_1 = \begin{bmatrix} \delta y_1 \delta z_2 - \delta z_1 \delta y_2 & 0 & 0 \\ 0 & \delta z_1 \delta x_2 - \delta x_1 \delta z_2 & 0 \\ 0 & 0 & \delta x_1 \delta y_2 - \delta y_1 \delta x_2 \\ 0 & \delta x_1 \delta y_2 - \delta y_1 \delta x_2 & \delta z_1 \delta x_2 - \delta x_1 \delta z_2 \\ \delta x_1 \delta y_2 - \delta y_1 \delta x_2 & 0 & \delta y_1 \delta z_2 - \delta z_1 \delta y_2 \\ \delta z_1 \delta x_2 - \delta x_1 \delta z_2 & \delta y_1 \delta z_2 - \delta z_1 \delta y_2 & 0 \end{bmatrix}, \tag{5.33a}$$

$$\mathbf{G}_2 = \begin{bmatrix} z_3 y_1 - y_3 z_1 & 0 & 0 \\ 0 & x_3 z_1 - z_3 x_1 & 0 \\ 0 & 0 & y_3 x_1 - x_3 y_1 \\ 0 & y_3 x_1 - x_3 y_1 & x_3 z_1 - z_3 x_1 \\ y_3 x_1 - x_3 y_1 & 0 & z_3 y_1 - y_3 z_1 \\ x_3 z_1 - z_3 x_1 & z_3 y_1 - y_3 z_1 & 0 \end{bmatrix}, \tag{5.33b}$$

$$\mathbf{G}_3 = \begin{bmatrix} y_2 z_1 - z_2 y_1 & 0 & 0 \\ 0 & z_2 x_1 - x_2 z_1 & 0 \\ 0 & 0 & x_2 y_1 - y_2 x_1 \\ 0 & x_2 y_1 - y_2 x_1 & z_2 x_1 - x_2 z_1 \\ x_2 y_1 - y_2 x_1 & 0 & y_2 z_1 - z_2 y_1 \\ z_2 x_1 - x_2 z_1 & y_2 z_1 - z_2 y_1 & 0 \end{bmatrix}. \tag{5.33c}$$

The displacement solutions within each polyhedral element $u(\xi, \eta, \zeta)$ is is defined as

$$u(\xi, \eta, \zeta) = [\ u_x(\xi, \eta, \zeta), \quad u_y(\xi, \eta, \zeta), \quad u_z(\xi, \eta, \zeta)\ ]^{\mathrm{T}}, \tag{5.34}$$

and interpolated as

$$u(\xi, \eta, \zeta) = \mathbf{N}_u(\eta, \zeta) u(\xi), \tag{5.35}$$

where $u(\xi)$ denote the displacement solution in the radial direction. The interpolation shape function $N_u(\eta,\zeta)$ are defined as

$$\mathbf{N}_u(\eta,\zeta) = [\ (1-\eta-\zeta)\,\mathbf{I}, \quad \eta\mathbf{I}, \quad \zeta\mathbf{I}\ ], \tag{5.36}$$

where $\mathbf{I}$ is a 3×3 identity matrix.

The strain-displacement matrices $\mathbf{B}_1$ and $\mathbf{B}_2$ are expressed using equations (5.32a-5.32c) and equation (5.36) as

$$\begin{aligned}
\mathbf{B}_1 &= \mathbf{b}_1\mathbf{N}_u(\eta,\zeta) \\
\mathbf{B}_1 &= \frac{1}{|\mathbf{J}|}\left[(1-\eta-\zeta)\mathbf{G}_1,\eta\mathbf{G}_1,\zeta\mathbf{G}_1\right], \qquad (5.37a) \\
\mathbf{B}_2 &= \mathbf{b}_2\mathbf{N}_u(\eta,\zeta)+\mathbf{b}_3\mathbf{N}_u(\eta,\zeta) \\
\mathbf{B}_2 &= \frac{1}{|\mathbf{J}|}\left[-(\zeta+\eta)\mathbf{G}_1-\mathbf{G}_2-\mathbf{G}_3,\eta\mathbf{G}_1+\mathbf{G}_2,\zeta\mathbf{G}_1+\mathbf{G}_3\right]. \qquad (5.37b)
\end{aligned}$$

Therefore, the strains ε in each cell is expressed using in equations (5.31,5.35 and 5.37a-5.37b) as

$$\varepsilon = \mathbf{L}\mathbf{u}(\xi,\eta,\zeta) = \mathbf{B}_1\mathbf{u}(\xi)_{,\xi} + \frac{1}{\xi}\mathbf{B}_2\mathbf{u}(\xi). \tag{5.38}$$

5.5.2 Scaled boundary finite element equation in displacement

The scaled boundary finite element equations for displacement both in 2D (d = 2) and 3D (d = 3) can be written in terms of $\mathbf{E}_0$, $\mathbf{E}_1$and $\mathbf{E}_2$ as (disregarding the effects of body loads and side-face tractions)

$$\mathbf{E}_0\xi^2\mathbf{u}(\xi)_{,\xi\xi} + \left((d-1)\,\mathbf{E}_0 - \mathbf{E}_1 + \mathbf{E}_1^{\mathrm{T}}\right)\xi\mathbf{u}(\xi)_{,\xi} + \left((\mathrm{d}-2)\,\mathbf{E}_1^{\mathrm{T}} - \mathbf{E}_2\right)\mathbf{u}(\xi) = 0. \tag{5.39}$$

For 2D problems, the coefficient matrices for a line element are written using equations (5.17,5.23 and 5.24a-5.24b).

$$\mathbf{E}_0 = \int_{-1}^{+1}\mathbf{B}_1^{\mathrm{T}}\mathbf{D}\mathbf{B}_1|\mathbf{J}|d\eta, \tag{5.40a}$$

$$\mathbf{E}_1 = \int_{-1}^{+1} \mathbf{B}_2^{\mathrm{T}} \mathbf{D} \mathbf{B}_1 |\mathbf{J}| d\eta, \tag{5.40b}$$

$$\mathbf{E}_2 = \int_{-1}^{+1} \mathbf{B}_2^{\mathrm{T}} \mathbf{D} \mathbf{B}_2 |\mathbf{J}| d\eta, \tag{5.40c}$$

where $\mathbf{D}$ is the elasticity matrix. The coefficient matrices in equations (5.40a-5.40c) can be evaluated analytically for a linear line element yielding

$$\mathbf{E}_0 = \frac{1}{3|\mathbf{J}|} \begin{bmatrix} 2\mathbf{X}_0 & \mathbf{X}_0 \\ \mathbf{X}_0 & 2\mathbf{X}_0 \end{bmatrix}, \tag{5.41a}$$

$$\mathbf{E}_1 = \frac{1}{2|\mathbf{J}|} \begin{bmatrix} -\frac{1}{3}\mathbf{X}_0 + \mathbf{X}_1 & \frac{1}{3}\mathbf{X}_0 + \mathbf{X}_1 \\ \frac{1}{3}\mathbf{X}_0 + \mathbf{X}_1 & -\frac{1}{3}\mathbf{X}_0 + \mathbf{X}_1 \end{bmatrix}, \tag{5.41b}$$

$$\mathbf{E}_2 = \frac{1}{2|\mathbf{J}|} \begin{bmatrix} \frac{1}{3}\mathbf{X}_0 + \mathbf{X}_2 & -\frac{1}{3}\mathbf{X}_0 - \mathbf{X}_2 \\ -\frac{1}{3}\mathbf{X}_0 - \mathbf{X}_2 & \frac{1}{3}\mathbf{X}_0 + \mathbf{X}_2 \end{bmatrix}, \tag{5.41c}$$

where entries $\mathbf{X}_0, \mathbf{X}_1$ and $\mathbf{X}_2$ are

$$\mathbf{X}_0 = \mathbf{C}_1^{\mathrm{T}} \mathbf{D} \mathbf{C}_1, \tag{5.42a}$$

$$\mathbf{X}_1 = \mathbf{C}_2^{\mathrm{T}} \mathbf{D} \mathbf{C}_1, \tag{5.42b}$$

$$\mathbf{X}_2 = \mathbf{C}_2^{\mathrm{T}} \mathbf{D} \mathbf{C}_2. \tag{5.42c}$$

For 3D problems the coefficient matrices for a surface element S are expressed using equations (5.30,5.36 and 5.37a-5.37b) as

$$\mathbf{E}_0 = \int_s \mathbf{B}_1^T \mathbf{D} \mathbf{B}_1 |\mathbf{J}| d\eta d\zeta, \tag{5.43a}$$

$$\mathbf{E}_1 = \int_s \mathbf{B}_2^T \mathbf{D} \mathbf{B}_1 |\mathbf{J}| d\eta d\zeta, \tag{5.43b}$$

$$\mathbf{E}_2 = \int_s \mathbf{B}_2^T \mathbf{D} \mathbf{B}_2 |\mathbf{J}| d\eta d\zeta, \tag{5.43c}$$

The integration in equations (5.43a-5.43c) can be performed either numerically or analytically. Gauss-Lobatto quadrature rules with the same order as the shape function are typically considered when the integration for the coefficient matrices is performed numerically. For a linear triangular element, the integration can be performed analytically. This leads to the following coefficient matrices

$$\mathbf{E}_0 = \frac{4}{3|\mathbf{J}|} \begin{bmatrix} 5\mathbf{Y}_0 & -\mathbf{Y}_0 & -\mathbf{Y}_0 \\ -\mathbf{Y}_0 & \mathbf{Y}_0 & 0 \\ -\mathbf{Y}_0 & 0 & \mathbf{Y}_0 \end{bmatrix}, \tag{5.44a}$$

$$\mathbf{E}_1 = \frac{4}{|\mathbf{J}|} \begin{bmatrix} -\frac{2}{3}\mathbf{Y}_0 + \mathbf{Y}_1 + \mathbf{Y}_2 & \frac{1}{3}\mathbf{Y}_0 & \frac{1}{3}\mathbf{Y}_0 \\ \frac{1}{3}\mathbf{Y}_0 - \mathbf{Y}_1 & -\frac{1}{3}\mathbf{Y}_0 & 0 \\ \frac{1}{3}\mathbf{Y}_0 - \mathbf{Y}_2 & 0 & -\frac{1}{3}\mathbf{Y}_0 \end{bmatrix}, \tag{5.44b}$$

$$\mathbf{E}_2 = \frac{4}{|\mathbf{J}|} \begin{bmatrix} \frac{2}{3}\mathbf{Y}_0 + \mathbf{Y}_3 + \mathbf{Y}_4 + \mathbf{Y}_5 + \mathbf{Y}_6 & -\frac{1}{3}\mathbf{Y}_0 - \mathbf{Y}_3 - \mathbf{Y}_5 & -\frac{1}{3}\mathbf{Y}_0 - \mathbf{Y}_4 - \mathbf{Y}_6 \\ -\frac{1}{3}\mathbf{Y}_0 - \mathbf{Y}_3 - \mathbf{Y}_4 & \frac{1}{3}\mathbf{Y}_0 + \mathbf{Y}_3 & \mathbf{Y}_4 \\ -\frac{1}{3}\mathbf{Y}_0 - \mathbf{Y}_5 - \mathbf{Y}_6 & \mathbf{Y}_5 & -\frac{1}{3}\mathbf{Y}_0 + \mathbf{Y}_6 \end{bmatrix}, \tag{5.44c}$$

where

$$\mathbf{Y}_0 = \mathbf{G}_1^{\mathrm{T}}\mathbf{D}\mathbf{G}_1, \tag{5.45a}$$

$$\mathbf{Y}_1 = \mathbf{G}_2^{\mathrm{T}}\mathbf{D}\mathbf{G}_1, \tag{5.45b}$$

$$\mathbf{Y}_2 = \mathbf{G}_3^{\mathrm{T}}\mathbf{D}\mathbf{G}_1, \tag{5.45c}$$

$$\mathbf{Y}_3 = \mathbf{G}_2^{\mathrm{T}}\mathbf{D}\mathbf{G}_2, \tag{5.45d}$$

$$\mathbf{Y}_4 = \mathbf{G}_3^{\mathrm{T}}\mathbf{D}\mathbf{G}_2, \tag{5.45e}$$

$$\mathbf{Y}_5 = \mathbf{G}_2^{\mathrm{T}}\mathbf{D}\mathbf{G}_3, \tag{5.45f}$$

$$\mathbf{Y}_6 = \mathbf{G}_3^{\mathrm{T}}\mathbf{D}\mathbf{G}_3. \tag{5.45g}$$

The coefficient matrices for 2D or 3D are obtained by assembling the contribution of all line elements or the surface elements respectively. Then equation (5.39) is constructed by assembling the contribution of all elements.

The internal nodal forces on a surface $\mathbf{q}(\xi)$ with a constant ξ can be expressed as

$$\mathbf{q}(\xi) = \xi^{d-2}\left(\mathbf{E}_0\xi\mathbf{u}(\xi)_{,\xi} + \mathbf{E}_1^T\mathbf{u}(\xi)\right) \tag{5.46}$$

5.5.3 Solution of the scaled boundary finite element equation in elastostatics

5.5.3.1 Stiffness matrix for each cell

In order to solve equations (5.39 and 5.46) these equations are transformed into a system of first-order ordinary differential equations by the introduction of variable $\mathbf{X}(\xi)$ as proposed by Song [541].

$$\mathbf{X}(\xi) = \xi\left\{\begin{array}{cc} \xi^{0.5(d-2)} & \mathbf{u}(\xi) \\ \xi^{-0.5(d-2)} & \mathbf{q}(\xi) \end{array}\right\}. \tag{5.47}$$

This produces

$$\xi \mathbf{X}(\xi)_{,\xi} = -\mathbf{Z}\mathbf{X}(\xi), \tag{5.48}$$

with the Hamiltonian coefficient matrix $\mathbf{Z}$ defined as

$$\mathbf{Z}=\begin{bmatrix} \mathbf{E}_0^{-1}\mathbf{E}_1^T - 0.5(d-2)\mathbf{I} & -\mathbf{E}_0^{-1} \\ -\mathbf{E}_2 + \mathbf{E}_1\mathbf{E}_0^{-1}\mathbf{E}_1^T & -(\mathbf{E}_1\mathbf{E}_0^{-1} - 0.5(d-2)\mathbf{I}) \end{bmatrix}. \tag{5.49}$$

Eigenvalue decomposition of the above matrix $\mathbf{Z}$ leads to

$$\mathbf{Z}\begin{bmatrix} \Psi_{11} & \Psi_{12} \\ \Psi_{21} & \Psi_{22} \end{bmatrix} = \begin{bmatrix} \Psi_{11} & \Psi_{12} \\ \Psi_{21} & \Psi_{22} \end{bmatrix}\begin{bmatrix} \mathbf{S}_{11} & 0 \\ 0 & \mathbf{S}_{22} \end{bmatrix}. \tag{5.50}$$

$\mathbf{S}_{11}$ in the equation (5.50) indicates the eigenvalue sub-matrix with the solution for bounded domains where $\mathrm{Re}(\lambda(\mathbf{S})) < 0$ and the $\mathbf{S}_{22}$ eigenvalue sub-matrix indicates the solution for unbounded domains where $\mathrm{Re}(\lambda(\mathbf{S}_{22})) > 0$. These eigenvalues are sorted in ascending order based on their real parts. Accordingly the eigenvectors are separated in a similar manner where the sub-matrices Ψ_{11} and Ψ_{21} are related to the solution in the bounded domain. Thus the bounded domain solutions for each cell is therefore expressed as

$$\mathbf{u}(\xi) = \Psi_{11}\xi^{-(\mathbf{S}_{11}+0.5(d-2)\mathbf{I})}\mathbf{c}_1, \tag{5.51a}$$

$$\mathbf{q}(\xi) = \Psi_{21}\xi^{-(\mathbf{S}_{11}-0.5(d-2)\mathbf{I})}\mathbf{c}_1, \tag{5.51b}$$

where $\mathbf{c}_1$ are the integration constants. The solutions for equations (5.51a-5.51b) at the boundary, $\xi = 1$ i.e $\mathbf{u}_b = \mathbf{u}(\xi = 1)$ and $\mathbf{q}_b = \mathbf{q}(\xi = 1)$ can be expressed as

$$\mathbf{u}_b = \Psi_{11}\mathbf{c}_1, \tag{5.52a}$$

$$\mathbf{q}_b = \Psi_{21}\mathbf{c}_1. \tag{5.52b}$$

The static stiffness matrix $\mathbf{K}_s$ of each cell can be formulated in terms of $\mathbf{u}_b$ and $\mathbf{q}_b$ as

$$\mathbf{q}_b = \mathbf{K}_s \mathbf{u}_b \tag{5.53}$$

Considering equations (5.52a) and (5.52b), $\mathbf{K}_s$ can be written as

$$\mathbf{K}_s = \Psi_{21} \Psi_{11}^{-1}. \tag{5.54}$$

The solutions in each individual cell can be programmed as a parallel algorithm for a faster computation. Then finally the global stiffness matrix $\mathbf{K}_{\mathrm{G}}$ can be obtained by assembling the stiffness matrices of all subdomains in a similar procedure to that of the FEM, and the global equation can be expressed as

$$\mathbf{K}_{\mathrm{G}} \mathbf{U} = \mathbf{P}. \tag{5.55}$$

Here $\mathbf{P}$ is the global nodal force vector and $\mathbf{U}$ is the global nodal displacement vector of the whole domain. After enforcing the boundary conditions, a system of linear equations is solved to obtain the displacements $\mathbf{U}$.

The nodal displacements $\mathbf{u}_b$ on the boundary of each cell is then extracted from the global displacements $\mathbf{U}$ according to the connectivity of the cell. Afterwards, the integration constants $\mathbf{c}_1$ for each cell in equations (5.52a) and (5.52b) can be obtained as

$$\mathbf{c}_1 = \Psi_{11}^{-1} \mathbf{u}_b. \tag{5.56}$$

5.5.3.2 Stress solution in each cell

Using the strain-displacement matrices stresses in each cell can be calculated considering equation (5.25) for 2D problems and equation (5.38) for 3D problems as

$$\sigma = \mathbf{D}\varepsilon = \mathbf{D}\left(\mathbf{B_1}\mathbf{u}(\xi)_{,\xi} + \frac{1}{\xi}\mathbf{B_2}\mathbf{u}(\xi)\right). \tag{5.57}$$

The stress fields can be now expressed by substituting equation (5.51a) into equation (5.57) as

$$\sigma = \Psi_\sigma \xi^{-(\mathbf{S}_{11}+(1+0.5(d-2))\mathbf{I})}\mathbf{c}_1, \tag{5.58}$$

where the stress modes Ψ_σ are given by

$$\Psi_\sigma = \mathbf{D}\left(-\mathbf{B_1}\Psi_{\mathbf{11}}(\mathbf{S_{11}} + \mathbf{0.5}\,(\mathbf{d}-\mathbf{2})\,\mathbf{I}) + \mathbf{B_2}\Psi_{\mathbf{11}}\right). \tag{5.59}$$

5.6 Solutions for geometrically similar cells

In damage analysis, complex geometries are often encountered which result in the generation of large number of cells. Thus, it is advantageous to take use of the inherent quality of producing a very few different types of cells in quadtree or octree mesh generation structures. Many of the matrices formed in the solution will either be identical or scalar multiples of two cells with the same nodal configuration. Therefore, the cell matrices of unique cells are precomputed and stored prior to the Newton Raphson analysis taking place. These unique cells will be referred to as master cells in the context of this chapter. In a balanced quadtree mesh there is a maximum of 16 master cells for a single type of material. In the octree mesh the maximum number of master cells are 4096.

In the discussions that follow, a master cell is designated the letter M and other cells derived from a M are designated by the letter P. Therefore superscript M or superscript P indicates the cell for which the variable belongs to. The ratio R is defined as $\frac{s^{\mathrm{P}}}{s^{\mathrm{M}}}$ where s indicates the edge length of a cell.

5.6.1 2D relationships between a master cell M and a cell P

With reference to equations (5.13a) and (5.13b) the $x^{\mathrm{P}}(\eta)$ and $y^{\mathrm{P}}(\eta)$ for cell P require to satisfy

$$x^{\mathrm{P}}(\eta) = \mathbf{N}(\eta)\left(Rx^{\mathrm{M}}\right) = Rx^{\mathrm{M}}(\eta), \tag{5.60a}$$

$$y^{\mathrm{P}}(\eta) = \mathbf{N}(\eta)\left(Ry^{\mathrm{M}}\right) = Ry^{\mathrm{M}}(\eta). \tag{5.60b}$$

Similar to equation (5.17) the determinant of the 2×2 Jacobian matrix $\left|\mathbf{J}^{P}\right|$ for a cell can be written as

$$\left|\mathbf{J}^{\mathrm{P}}\right| = Rx^{\mathrm{M}}Ry^{\mathrm{M}}_{,\eta} - Ry^{\mathrm{M}}Rx^{\mathrm{M}}_{,\eta} = R^2\left|\mathbf{J}^{\mathrm{M}}\right|. \tag{5.61}$$

The $\mathbf{b}_1^{\mathrm{P}}$ and $\mathrm{b}_2^{\mathrm{P}}$ matrices from equations (5.19a-5.19b) are therefore equal to

$$\mathrm{b}_1^{\mathrm{P}} = \left(\frac{1}{R^2}\times R\right)\mathrm{b}_1^{\mathrm{M}} = \frac{1}{R}\mathrm{b}_1^{\mathrm{M}}, \tag{5.62a}$$

$$\mathrm{b}_2^{\mathrm{P}} = \left(\frac{1}{R^2}\times R\right)\mathrm{b}_2^{\mathrm{M}} = \frac{1}{R}\mathrm{b}_2^{\mathrm{M}}. \tag{5.62b}$$

The strain-displacement matrices $\mathbf{B}_1^{\mathrm{P}}$ and $\mathrm{B}_2^{\mathrm{P}}$ from equations (5.24a) and (5.24b) can be written as

$$\mathbf{B}_1^{\mathrm{P}} = \left(\frac{1}{R}\mathrm{b}_1^{\mathrm{M}}\right)\mathbf{N}_u(\eta) = \frac{1}{R}\mathbf{B}_1^{\mathrm{M}}, \tag{5.63a}$$

$$\mathbf{B}_2^{\mathrm{P}} = \left(\frac{1}{R}\mathrm{b}_2^{\mathrm{M}}\right)\mathbf{N}_u(\eta)_{,\eta} = \frac{1}{R}\mathbf{B}_2^{\mathrm{M}}. \tag{5.63b}$$

Therefore, the coefficient matrices, $\mathbf{E}_0^{\mathrm{P}}$, $\mathbf{E}_1^{\mathrm{P}}$ and $\mathbf{E}_2^{\mathrm{P}}$ from equations (5.40a-5.40c) satisfy

$$\mathbf{E}_0^{\mathrm{P}} = \int_{-1}^{+1}\left(\frac{1}{R}\left(\mathrm{B}_1^{\mathrm{M}}\right)^{\mathrm{T}}\right)\mathbf{D}\left(\frac{1}{R}\mathrm{B}_1^{\mathrm{M}}\right)\left(R^2\left|\mathbf{J}^{\mathrm{M}}\right|\right)d\eta = \mathbf{E}_0^{\mathrm{M}}, \tag{5.64a}$$

$$\mathbf{E}_1^{\mathrm{P}} = \int_{-1}^{+1}\left(\frac{1}{R}\left(\mathrm{B}_2^{\mathrm{M}}\right)^{\mathrm{T}}\right)\mathbf{D}\left(\frac{1}{R}\mathrm{B}_1^{\mathrm{M}}\right)\left(R^2\left|\mathbf{J}^{\mathrm{M}}\right|\right)d\eta = \mathbf{E}_1^{\mathrm{M}}, \tag{5.64b}$$

$$\mathbf{E}_2^{\mathrm{P}} = \int_{-1}^{+1}\left(\frac{1}{R}\left(\mathrm{B}_2^{\mathrm{M}}\right)^{\mathrm{T}}\right)\mathbf{D}\left(\frac{1}{R}\mathrm{B}_2^{\mathrm{M}}\right)\left(R^2\left|\mathbf{J}^{\mathrm{M}}\right|\right)d\eta = \mathbf{E}_2^{\mathrm{M}}. \tag{5.64c}$$

Based on equations (5.64a-5.64c) and (5.49) the Hamiltonian coefficient matrix for cell P, Z^{P} can be written as

$$\mathbf{Z}^{\mathrm{P}} = \begin{bmatrix} \left(\mathbf{E}_0^{\mathrm{P}}\right)^{-1}\left(\mathbf{E}_1^{\mathrm{P}}\right)^{\mathrm{T}} & -\left(\mathbf{E}_0^{\mathrm{P}}\right)^{-1} \\ -\mathbf{E}_2^{\mathrm{P}} + \mathbf{E}_1^{\mathrm{P}}\left(\mathbf{E}_0^{\mathrm{P}}\right)^{-1}\left(\mathbf{E}_1^{\mathrm{P}}\right)^{\mathrm{T}} & -\mathbf{E}_1^{\mathrm{P}}\left(\mathbf{E}_0^{\mathrm{P}}\right)^{-1} \end{bmatrix}$$

$$\mathbf{Z}^{\mathrm{P}} = \begin{bmatrix} \left(\mathbf{E}_0^{\mathrm{M}}\right)^{-1}\left(\mathbf{E}_1^{\mathrm{M}}\right)^{\mathrm{T}} & -\left(\mathbf{E}_0^{\mathrm{M}}\right)^{-1} \\ -\mathbf{E}_2^{\mathrm{M}} + \mathbf{E}_1^{\mathrm{M}}\left(\mathbf{E}_0^{\mathrm{M}}\right)^{-1}\left(\mathbf{E}_1^{\mathrm{M}}\right)^{\mathrm{T}} & -\mathbf{E}_1^{\mathrm{M}}\left(\mathbf{E}_0^{\mathrm{M}}\right)^{-1} \end{bmatrix} = \mathbf{Z}^{\mathrm{M}} \tag{5.65}$$

This relationship between $\mathbf{Z}^{\mathrm{P}}$and $\mathbf{Z}^{\mathrm{M}}$indicates the eigenvalue decomposition yields identical results for both cells P and M. The following relationships are therefore valid

$$\mathbf{S}_{11}^{\mathrm{P}} = \mathbf{S}_{11}^{\mathrm{M}}, \tag{5.66a}$$

$$\Psi_{11}^{\mathrm{P}} = \Psi_{11}^{\mathrm{M}}, \tag{5.66b}$$

$$\Psi_{21}^{\mathrm{P}} = \Psi_{21}^{\mathrm{M}}. \tag{5.66c}$$

The static stiffness matrix of each cell P $\left(\mathbf{K}^{\mathrm{P}}\right)$ can be written in terms of Ψ_{11}^{M} and Ψ_{21}^{M} as

$$\mathbf{K}^{\mathrm{P}} = \Psi_{21}^{\mathrm{M}}\left(\Psi_{11}^{\mathrm{M}}\right)^{-1} = \mathbf{K}^{\mathrm{M}}. \tag{5.67}$$

Finally, the stress modes $\Psi_{\sigma}^{\mathrm{P}}$ are given by

$$\Psi_{\sigma}^{\mathrm{P}} = \mathbf{D}\left(-\left(\frac{1}{R}\mathrm{B}_1^{\mathrm{M}}\right)\Psi_{11}^{\mathrm{M}}\mathbf{S}_{11}^{\mathrm{M}} + \left(\frac{1}{R}\mathrm{B}_2^{\mathrm{M}}\right)\Psi_{11}^{\mathrm{M}}\right) = \frac{1}{R}\Psi_{\sigma}^{\mathrm{M}}. \tag{5.68}$$

5.6.2 3D relationships between a master cell M and a cell P

In relation to equations (5.26a-5.26c) a point $x^{\mathrm{P}}(\eta,\zeta)$, $y^{\mathrm{P}}(\eta,\zeta)$ and $z^{\mathrm{P}}(\eta,\zeta)$ for cell P require to satisfy

$$x^{\mathrm{P}}(\eta,\zeta) = \mathbf{N}(\eta,\zeta)\left(Rx^{\mathrm{M}}\right) = Rx^{\mathrm{M}}(\eta,\zeta), \tag{5.69a}$$

$$y^{\mathrm{P}}(\eta,\zeta) = \mathbf{N}(\eta,\zeta)\left(Ry^{\mathrm{M}}\right) = Ry^{\mathrm{M}}(\eta,\zeta), \tag{5.69b}$$

$$z^{\mathrm{P}}(\eta,\zeta) = \mathbf{N}(\eta,\zeta)\left(Rz^{\mathrm{M}}\right) = Rz^{\mathrm{M}}(\eta,\zeta). \tag{5.69c}$$

The Jacobian matrix $\left|\mathbf{J}^{P}\right|$ for a cell can be written as

$$\left|\mathbf{J}^{\mathrm{P}}\right| = Rx^{\mathrm{M}}\left(R^{2}\left(y^{\mathrm{M}}_{,\eta}z^{\mathrm{M}}_{,\zeta} - z^{\mathrm{M}}_{,\eta}y^{\mathrm{M}}_{,\zeta}\right)\right) + Ry^{\mathrm{M}}\left(R^{2}\left(z^{\mathrm{M}}_{,\eta}x^{\mathrm{M}}_{,\zeta} - x^{\mathrm{M}}_{,\eta}z^{\mathrm{M}}_{,\zeta}\right)\right)\ldots$$
$$+ Rz^{\mathrm{M}}\left(R^{2}\left(x^{\mathrm{M}}_{,\eta}y^{\mathrm{M}}_{,\zeta} - y^{\mathrm{M}}_{,\eta}x^{\mathrm{M}}_{,\zeta}\right)\right) = R^{3}\left|\mathbf{J}^{\mathrm{M}}\right|. \tag{5.70}$$

The $\mathbf{b}^{\mathrm{P}}_{1}$, $\mathrm{b}^{\mathrm{P}}_{2}$ and $\mathrm{b}^{\mathrm{P}}_{3}$ matrices from equations (5.32a-5.32c) are as follows

$$\mathbf{b}^{\mathrm{P}}_{1} = \left(\frac{1}{R^{3}} \times R^{2}\right)\mathrm{b}^{\mathrm{M}}_{1} = \frac{1}{R}\mathrm{b}^{\mathrm{M}}_{1}, \tag{5.71a}$$

$$\mathrm{b}^{\mathrm{P}}_{2} = \left(\frac{1}{R^{3}} \times R^{2}\right)\mathrm{b}^{\mathrm{M}}_{2} = \frac{1}{R}\mathrm{b}^{\mathrm{M}}_{2}, \tag{5.71b}$$

$$\mathrm{b}^{\mathrm{P}}_{3} = \left(\frac{1}{R^{3}} \times R^{2}\right)\mathrm{b}^{\mathrm{M}}_{3} = \frac{1}{R}\mathrm{b}^{\mathrm{M}}_{3}. \tag{5.71c}$$

The strain-displacement matrices $\mathbf{B}^{\mathrm{P}}_{1}$ and $\mathrm{B}^{\mathrm{P}}_{2}$ from equations (5.37a) and (5.37b) are modified as

$$\mathbf{B}^{\mathrm{P}}_{1} = \left(\frac{1}{R}\mathrm{b}^{\mathrm{M}}_{1}\right)\mathbf{N}_{u}(\eta,\zeta) = \frac{1}{R}\mathrm{B}^{\mathrm{M}}_{1}, \tag{5.72a}$$

$$\mathrm{B}^{\mathrm{P}}_{2} = \left(\frac{1}{R}\mathrm{b}^{\mathrm{M}}_{2}\right)\mathbf{N}_{u}(\eta,\zeta)_{,\eta} + \left(\frac{1}{R}\mathrm{b}^{\mathrm{M}}_{3}\right)\mathbf{N}_{u}(\eta,\zeta)_{,\zeta} = \frac{1}{R}\mathrm{B}^{\mathrm{M}}_{2}. \tag{5.72b}$$

The coefficient matrices $\mathbf{E}_0^{\mathrm{P}}$, $\mathbf{E}_1^{\mathrm{P}}$ and $\mathbf{E}_2^{\mathrm{P}}$ from equations (5.43a-5.43c) thus need to satisfy

$$\mathbf{E}_0^{\mathrm{P}} = \int_s \left(\frac{1}{R}\left(\mathrm{B}_1^{\mathrm{M}}\right)^{\mathrm{T}}\right)\mathbf{D}\left(\frac{1}{R}\mathrm{B}_1^{\mathrm{M}}\right)\left(R^3\left|\mathbf{J}^{\mathrm{M}}\right|\right)d\eta d\zeta = R\mathbf{E}_0^{\mathrm{M}}, \tag{5.73a}$$

$$\mathbf{E}_1^{\mathrm{P}} = \int_s \left(\frac{1}{R}\left(\mathrm{B}_2^{\mathrm{M}}\right)^{\mathrm{T}}\right)\mathbf{D}\left(\frac{1}{R}\mathrm{B}_1^{\mathrm{M}}\right)\left(R^3\left|\mathbf{J}^{\mathrm{M}}\right|\right)d\eta d\zeta = R\mathbf{E}_1^{\mathrm{M}}, \tag{5.73b}$$

$$\mathbf{E}_2^{\mathrm{P}} = \int_s \left(\frac{1}{R}\left(\mathrm{B}_2^{\mathrm{M}}\right)^{\mathrm{T}}\right)\mathbf{D}\left(\frac{1}{R}\mathrm{B}_2^{\mathrm{M}}\right)\left(R^3\left|\mathbf{J}^{\mathrm{M}}\right|\right)d\eta d\zeta = R\mathbf{E}_2^{\mathrm{M}}. \tag{5.73c}$$

The Hamiltonian coefficient matrix for cell P, $\mathbf{Z}^{\mathrm{P}}$ can now be written as

$$\mathbf{Z}^{\mathrm{P}} = \begin{bmatrix} \left(\mathbf{E}_0^{\mathrm{P}}\right)^{-1}\left(\mathbf{E}_1^{\mathrm{P}}\right)^{\mathrm{T}} - 0.5\mathbf{I} & -\left(\mathbf{E}_0^{\mathrm{P}}\right)^{-1} \\ -\mathbf{E}_2^{\mathrm{P}} + \mathbf{E}_1^{\mathrm{P}}\left(\mathbf{E}_0^{\mathrm{P}}\right)^{-1}\left(\mathbf{E}_1^{\mathrm{P}}\right)^{\mathrm{T}} & -\left(\mathbf{E}_1^{\mathrm{P}}\left(\mathbf{E}_0^{\mathrm{P}}\right)^{-1} - 0.5\mathbf{I}\right) \end{bmatrix}$$

$$\mathbf{Z}^{\mathrm{P}} = \begin{bmatrix} \left(\mathbf{E}_0^{\mathrm{M}}\right)^{-1}\left(\mathbf{E}_1^{\mathrm{M}}\right)^{\mathrm{T}} - 0.5\mathbf{I} & -R^{-1}\left(\mathbf{E}_0^{\mathrm{M}}\right)^{-1} \\ R\left(-\mathbf{E}_2^{\mathrm{M}} + \mathbf{E}_1^{\mathrm{M}}\left(\mathbf{E}_0^{\mathrm{M}}\right)^{-1}\left(\mathbf{E}_1^{\mathrm{M}}\right)^{\mathrm{T}}\right) & -\left(\mathbf{E}_1^{\mathrm{M}}\left(\mathbf{E}_0^{\mathrm{M}}\right)^{-1} - 0.5\mathbf{I}\right) \end{bmatrix} = \mathbf{Z}^{\mathrm{M}}. \tag{5.74}$$

Next eigenvalue decomposition equation (5.65) can be written in the form of equation (5.50) as

$$\begin{bmatrix} \left(\mathbf{E}_0^{\mathrm{M}}\right)^{-1}\left(\mathbf{E}_1^{\mathrm{M}}\right)^{\mathrm{T}} - 0.5\mathbf{I} & -R^{-1}\left(\mathbf{E}_0^{\mathrm{M}}\right)^{-1} \\ R\left(-\mathbf{E}_2^{\mathrm{M}} + \mathbf{E}_1^{\mathrm{M}}\left(\mathbf{E}_0^{\mathrm{M}}\right)^{-1}\left(\mathbf{E}_1^{\mathrm{M}}\right)^{\mathrm{T}}\right) & -\left(\mathbf{E}_1^{\mathrm{M}}\left(\mathbf{E}_0^{\mathrm{M}}\right)^{-1} - 0.5\mathbf{I}\right) \end{bmatrix}\cdots$$

$$\begin{bmatrix} \Psi_{11}^{\mathrm{P}} & \Psi_{12}^{\mathrm{P}} \\ \Psi_{21}^{\mathrm{P}} & \Psi_{22}^{\mathrm{P}} \end{bmatrix} = \begin{bmatrix} \Psi_{11}^{\mathrm{P}} & \Psi_{12}^{\mathrm{P}} \\ \Psi_{21}^{\mathrm{P}} & \Psi_{22}^{\mathrm{P}} \end{bmatrix}\begin{bmatrix} \mathbf{S}_{11}^{\mathrm{P}} & 0 \\ 0 & \mathbf{S}_{22}^{\mathrm{P}} \end{bmatrix}. \tag{5.75}$$

Dividing the second row of the matrices in equation (5.75) by R yields

$$\begin{bmatrix} \left(\mathbf{E}_0^{\mathrm{M}}\right)^{-1}\left(\mathbf{E}_1^{\mathrm{M}}\right)^{\mathrm{T}} - 0.5\mathbf{I} & -R^{-1}\left(\mathbf{E}_0^{\mathrm{M}}\right)^{-1} \\ \left(-\mathbf{E}_2^{\mathrm{M}} + \mathbf{E}_1^{\mathrm{M}}\left(\mathbf{E}_0^{\mathrm{M}}\right)^{-1}\left(\mathbf{E}_1^{\mathrm{M}}\right)^{\mathrm{T}}\right) & -R^{-1}\left(\mathbf{E}_1^{\mathrm{M}}\left(\mathbf{E}_0^{\mathrm{M}}\right)^{-1} - 0.5\mathbf{I}\right) \end{bmatrix}\cdots$$

$$\begin{bmatrix} \Psi_{11}^{\mathrm{P}} & \Psi_{12}^{\mathrm{P}} \\ \Psi_{21}^{\mathrm{P}} & \Psi_{22}^{\mathrm{P}} \end{bmatrix} = \begin{bmatrix} \Psi_{11}^{\mathrm{P}} & \Psi_{12}^{\mathrm{P}} \\ R^{-1}\Psi_{21}^{\mathrm{P}} & R^{-1}\Psi_{22}^{\mathrm{P}} \end{bmatrix}\begin{bmatrix} \mathbf{S}_{11}^{\mathrm{P}} & 0 \\ 0 & \mathbf{S}_{22}^{\mathrm{P}} \end{bmatrix}. \tag{5.76}$$

Rearranging equation (5.76) gives

$$\begin{bmatrix} \left(\mathbf{E}_0^{\mathrm{M}}\right)^{-1}\left(\mathbf{E}_1^{\mathrm{M}}\right)^{\mathrm{T}} - 0.5\mathbf{I} & -\left(\mathbf{E}_0^{\mathrm{M}}\right)^{-1} \\ \left(-\mathbf{E}_2^{\mathrm{M}} + \mathbf{E}_1^{\mathrm{M}}\left(\mathbf{E}_0^{\mathrm{M}}\right)^{-1}\left(\mathbf{E}_1^{\mathrm{M}}\right)^{\mathrm{T}}\right) & -\left(\mathbf{E}_1^{\mathrm{M}}\left(\mathbf{E}_0^{\mathrm{M}}\right)^{-1} - 0.5\mathbf{I}\right) \end{bmatrix} \cdots$$

$$\begin{bmatrix} \Psi_{11}^{\mathrm{P}} & \Psi_{12}^{\mathrm{P}} \\ R^{-1}\Psi_{21}^{\mathrm{P}}R^{-1} & \Psi_{22}^{\mathrm{P}} \end{bmatrix} = \begin{bmatrix} \Psi_{11}^{\mathrm{P}} & \Psi_{12}^{\mathrm{P}} \\ R^{-1}\Psi_{21}^{\mathrm{P}} & R^{-1}\Psi_{22}^{\mathrm{P}} \end{bmatrix} \begin{bmatrix} \mathbf{S}_{11}^{\mathrm{P}} & 0 \\ 0 & \mathbf{S}_{22}^{\mathrm{P}} \end{bmatrix}. \quad (5.77)$$

Therefore

$$\mathbf{Z}^{\mathrm{M}} \begin{bmatrix} \Psi_{11}^{\mathrm{P}} & \Psi_{12}^{\mathrm{P}} \\ R^{-1}\Psi_{21}^{\mathrm{P}}R^{-1} & \Psi_{22}^{\mathrm{P}} \end{bmatrix} = \begin{bmatrix} \Psi_{11}^{\mathrm{P}} & \Psi_{12}^{\mathrm{P}} \\ R^{-1}\Psi_{21}^{\mathrm{P}} & R^{-1}\Psi_{22}^{\mathrm{P}} \end{bmatrix} \begin{bmatrix} \mathbf{S}_{11}^{\mathrm{P}} & 0 \\ 0 & \mathbf{S}_{22}^{\mathrm{P}} \end{bmatrix}. \quad (5.78)$$

On the other hand the eigenvalue decomposition of master cell M can be written from equation (5.50) as follows

$$\mathbf{Z}^{\mathrm{M}} \begin{bmatrix} \Psi_{11}^{\mathrm{M}} & \Psi_{12}^{\mathrm{M}} \\ \Psi_{21}^{\mathrm{M}} & \Psi_{22}^{\mathrm{M}} \end{bmatrix} = \begin{bmatrix} \Psi_{11}^{\mathrm{M}} & \Psi_{12}^{\mathrm{M}} \\ \Psi_{21}^{\mathrm{M}} & \Psi_{22}^{\mathrm{M}} \end{bmatrix} \begin{bmatrix} \mathbf{S}_{11}^{\mathrm{M}} & 0 \\ 0 & \mathbf{S}_{22}^{\mathrm{M}} \end{bmatrix} \quad (5.79)$$

By comparing equations (5.78) and (5.79) the following relationships can be drawn

$$\mathbf{S}_{11}^{\mathrm{P}} = \mathbf{S}_{11}^{\mathrm{M}}, \quad (5.80a)$$

$$\Psi_{11}^{\mathrm{P}} = \Psi_{11}^{\mathrm{M}}, \quad (5.80b)$$

$$\Psi_{21}^{\mathrm{P}} = R\Psi_{21}^{\mathrm{M}}. \quad (5.80c)$$

Then the static stiffness matrix of each cell P $\left(\mathbf{K}^{\mathrm{P}}\right)$ becomes

$$\mathbf{K}^{\mathrm{P}} = R\Psi_{21}^{\mathrm{M}}\left(\Psi_{11}^{\mathrm{M}}\right)^{-1} = R\mathbf{K}^{\mathrm{M}}. \quad (5.81)$$

Finally, the stress modes $\Psi_{\sigma}^{\mathrm{P}}$ can be written with reference to equation (5.59) as

$$\Psi_{\sigma}^{\mathrm{P}} = \mathbf{D}\left(-\left(\frac{1}{R}\mathrm{B}_{1}^{\mathrm{M}}\right)\Psi_{11}^{\mathrm{M}}\left(\mathbf{S}_{11}^{\mathrm{M}}+0.5\mathbf{I}\right)+\left(\frac{1}{R}\mathrm{B}_{2}^{\mathrm{M}}\right)\Psi_{11}^{\mathrm{M}}\right) = \frac{1}{R}\Psi_{\sigma}^{\mathrm{M}}. \tag{5.82}$$

5.7 Damage formulation in SBFEM

By introducing the damage variable ω in equation (3.1) into the 2D coefficient matrices for a line element are transformed in equations (5.40a-5.40c) as

$$\mathbf{E}_{0}^{\mathrm{D}} = (1-\omega)\int_{-1}^{+1}\mathbf{B}_{1}^{\mathrm{T}}\mathbf{D}\mathbf{B}_{1}|\mathbf{J}|d\eta \tag{5.83a}$$

$$\mathbf{E}_{1}^{\mathrm{D}} = (1-\omega)\int_{-1}^{+1}\mathbf{B}_{2}^{\mathrm{T}}\mathbf{D}\mathbf{B}_{1}|\mathbf{J}|d\eta \tag{5.83b}$$

$$\mathbf{E}_{2}^{\mathrm{D}} = (1-\omega)\int_{-1}^{+1}\mathbf{B}_{2}^{\mathrm{T}}\mathbf{D}\mathbf{B}_{2}|\mathbf{J}|d\eta \tag{5.83c}$$

In the 3D formulation the coefficient matrices for a surface element S are also transformed in a similar manner with the variable ω. Thus, the equations (5.43a-5.43c) as

$$\mathbf{E}_{0}^{\mathrm{D}} = (1-\omega)\int_{s}\mathbf{B}_{1}^{\mathrm{T}}\mathbf{D}\mathbf{B}_{1}|\mathbf{J}|d\eta d\zeta \tag{5.84a}$$

$$\mathbf{E}_{1}^{\mathrm{D}} = (1-\omega)\int_{s}\mathbf{B}_{2}^{\mathrm{T}}\mathbf{D}\mathbf{B}_{1}|\mathbf{J}|d\eta d\zeta \tag{5.84b}$$

$$\mathbf{E}_{2}^{\mathrm{D}} = (1-\omega)\int_{s}\mathbf{B}_{2}^{\mathrm{T}}\mathbf{D}\mathbf{B}_{2}|\mathbf{J}|d\eta d\zeta \tag{5.84c}$$

where $\mathbf{E}_{0}^{\mathrm{D}}, \mathbf{E}_{1}^{\mathrm{D}}$ and $\mathbf{E}_{2}^{\mathrm{D}}$ and are counterparts of the coefficient matrix with the damage variable ω of one subdomain. Now the Hamiltonian coefficient matrix $\mathbf{Z}$ defined as

$$\mathbf{Z}^{\mathrm{D}} = \begin{bmatrix} \mathbf{E}_0^{-1}\mathbf{E}_1^T - 0.5\,(d-2)\,\mathbf{I} & -(1-\omega)^{-1}\mathbf{E}_0^{-1} \\ -(1-\omega)\left(\mathbf{E}_2 + \mathbf{E}_1\mathbf{E}_0^{-1}\mathbf{E}_1^T\right) & -(\mathbf{E}_1\mathbf{E}_0^{-1} - 0.5\,(d-2)\,\mathbf{I}) \end{bmatrix} \tag{5.85}$$

The eigenvalue decomposition of the above matrix $\mathbf{Z}^{\mathbf{D}}$ leads to

$$\mathbf{Z}^{\mathrm{D}} \begin{bmatrix} \Psi_{11} & (1-\omega)^{-1}\Psi_{12} \\ (1-\omega)\Psi_{21} & \Psi_{22} \end{bmatrix} = \begin{bmatrix} \Psi_{11} & (1-\omega)^{-1}\Psi_{12} \\ (1-\omega)\Psi_{21} & \Psi_{22} \end{bmatrix} \begin{bmatrix} \mathbf{S}_{11} & 0 \\ 0 & \mathbf{S}_{22} \end{bmatrix} \tag{5.86}$$

Finally considering equation (5.54) with respect to the transformed equation (5.86) the stiffness matrix with damage is given as

$$\mathbf{K}^{\mathrm{D}} = (1-\omega)\mathbf{K}_s \tag{5.87}$$

The non-linear global equation system is obtained by assembling the stiffness matrix of all subdomains as

$$\mathbf{KU} = \mathbf{P} \tag{5.88}$$

where $\mathbf{K}$ is the global stiffness matrix after considering the effects of damage.

5.8 Numerical simulations

Six numerical examples are presented in this section. The complexity of the examples increases from the first example to the last. The first 3 examples are modelled using the 2D image-based formulation whereas the last three examples are modelled using the 3D image-based formulation.

The first example (refer section 5.8.1) assesses the requirement for mesh smoothing in the automatic mesh generation technique. The second example (refer section 5.8.2) models the behaviour of an actual 2D concrete microstructure imaged by a CT scan. The last 2D example (refer section 5.8.3) analyses an artificially generated concrete microstructure and then compares the result to a published result to validate the formulation presented in this chapter.

The 3D examples start off by analysing the behaviour of a thick plate (refer section 5.8.4) consisting of cylindrical inclusions. The next example (refer section 5.8.5) models a cube with spherical inclusions. The final 3D example (refer section 5.8.6) aims to exemplify the effectiveness of the formulation to handle computationally expensive complex problems by modelling the behaviour of a cubical concrete microstructure procured by means of a CT scan.

5.8.1 2D plate with multiple inclusions of different diameters

This example simulates the behaviour of a thin plate with imperfections. As seen in figure 5.28 the plate has dimensions length and height of 256×256 mm. The thickness of the plate is assumed to be 1 mm. To emulate the imperfections the plate consists of 3 holes of varying diameters.

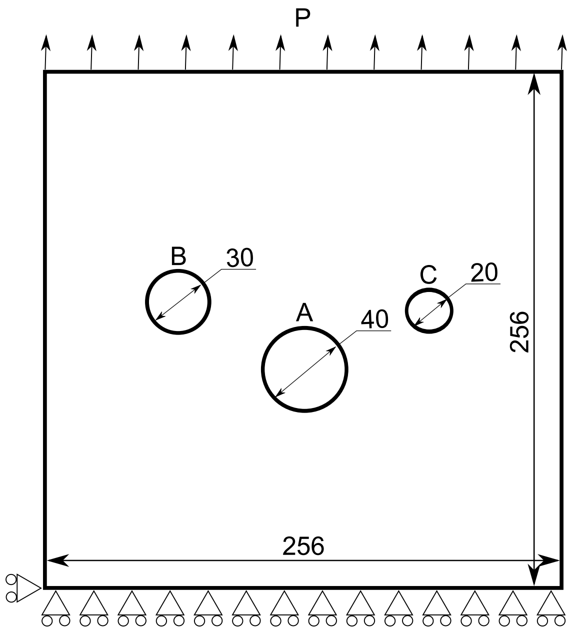

Figure 5.28. Specimen dimensions (mm) and boundary conditions considered in the 2D image-based analysis of a plate with multiple inclusions of different diameters.

The holes in figure 5.28 have dimensions and location coordinates as given in table

5.1. The coordinate system is considered as (0,0) at the bottom left hand corner.

Inclusion notation	Centre coordinates (mm)	Diameter (mm)
A	(128, 108)	40
B	(64, 143)	30
C	(192, 138)	20

Table 5.1. Location and the diameter of circular cavities considered in the 2D image-based analysis of a plate with multiple inclusions of different diameters.

The plate is restrained in the bottom against vertical movement in addition to the restraint in the bottom left corner against horizontal movement. To produce a response in the model an agitation is exerted on the top edge of the plate.

The modulus of elasticity and Poison's ratio of the plate are 20 GPa and 0.2, respectively. Plane stress conditions are assumed for the problem with regard to the dimensions of the model. The damage evolution is with respect to the exponential damage model given in equation (5.2). The variable ε_0 is set to 90×10^{-6} and the variable representing the strain at which material is fully damaged ε_f is set to 7.0×10^{-3}. The behaviour of the damage evolution function with these variables is shown in figure 5.29.

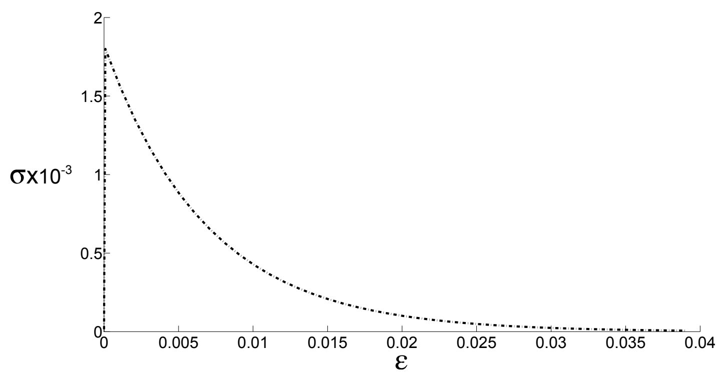

Figure 5.29. 1D element stress (GPa) vs strain profile considered in the 2D image-based analysis of a plate with multiple inclusions of different diameters. Damage evolution considered is with respect to the softening law in equation (5.2).

The equivalent strain parameter is calculated with reference to equation (5.8). The parameter k in the equation is set to 10. This is to emulate more realistic material constants related to concrete. The non-local length scale is considered as 5 mm assuming the maximum particle size in mortar as 1.85 mm [303]. The non-local weighting considered is in accordance to equation (5.10). Table 5.2 below captures all the material properties used in the analysis.

E (GPa)	ν	ε_0	ε_f	l (mm)
20	0.2	90×10^{-6}	7.0×10^{-3}	5

Table 5.2. Material properties and damage parameters adopted in the 2D image-based analysis of a plate with multiple inclusions of different diameters.

The meshes considered for the analysis consist of elements with maximum element size of 4 mm and a minimum element size of 1 mm (see figure 5.30). The finite element mesh shown in figure 5.30a is produced through Abaqus FEA software suite. To control the number of elements produced in the model the top quarter of the plate is manually restricted to only produce 4×4 mm quadrilateral elements. However, the automatically generated central region of the mesh show considerable mesh refinement around the three inclusions.

The automatically generated image-based quadtree meshes are shown in figure 5.30b. For the purpose of comparing the effect of mesh smoothing two types of quadtree meshes have been considered in this analysis; smoothened (figure 5.30b(i)) and unsmoothed (figure 5.30b(ii)). The geometry is meshed such that one pixel represents 1 mm of the problem domain. The quadtree decomposition is automatically set to occur with a maximum size of a cell maintained at 4 pixels and the minimum size of cell fixed at 1 pixel.

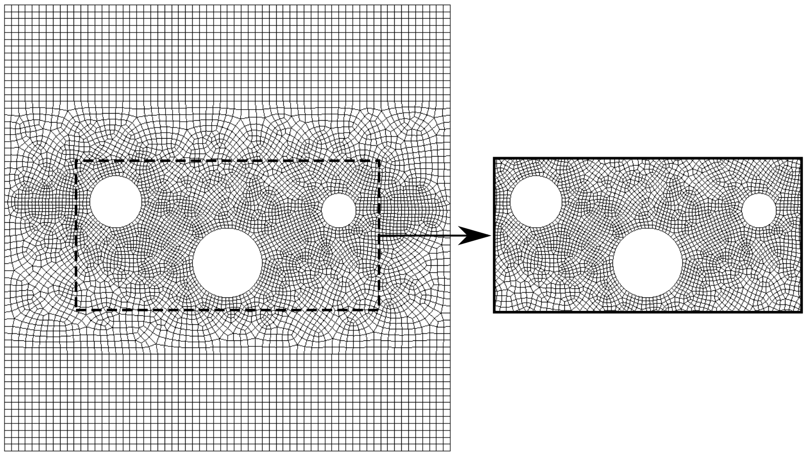

(a) Finite element mesh consisting of 7291 elements produced by Abaqus FEA software suite.

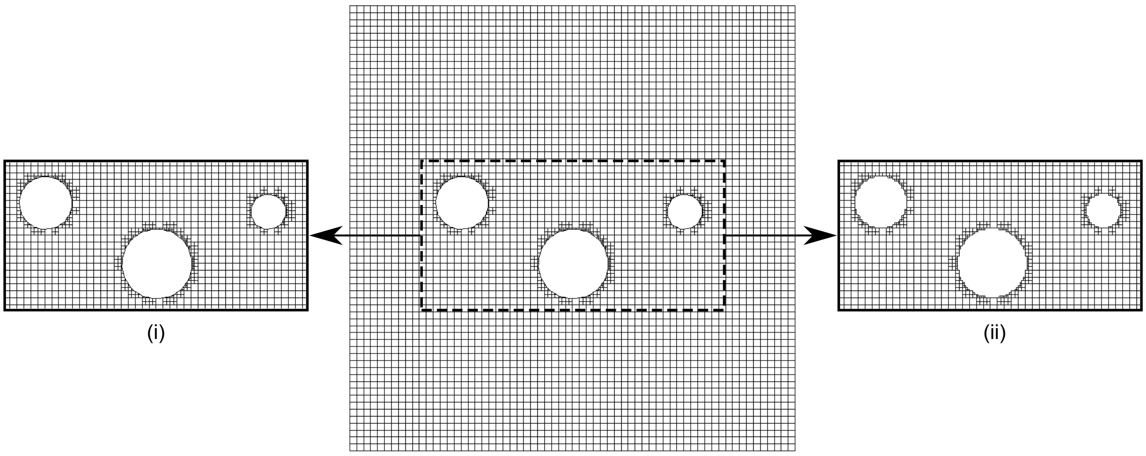

(b) SBFEM (i) smoothened mesh consisting of 4451 elements and (ii) unsmoothed mesh consisting of 4305 elements.

Figure 5.30. (a) The finite element and (b) the automatically generated image-based SBFEM meshes used in the 2D image-based analysis of a plate with multiple inclusions of different diameters. Maximum and minimum element sizes are 4 mm and 1 mm, respectively.

Comparing the finite element mesh to the SBFE meshes, it is evident by using the quadtree mesh generation structure quicker transition between element sizes is achieved. In this example this feature achieved almost a 40% reduction in elements in the quadtree structure compared to the finite element quadrilateral mesh.

The analysis is run using the modified Newton Raphson method. The initial displacement step is kept to 0.002 mm with automatic displacement control the analysis is completed in 180 iterations. The load-displacement curve produced in the analysis is as depicted in figure 5.31.

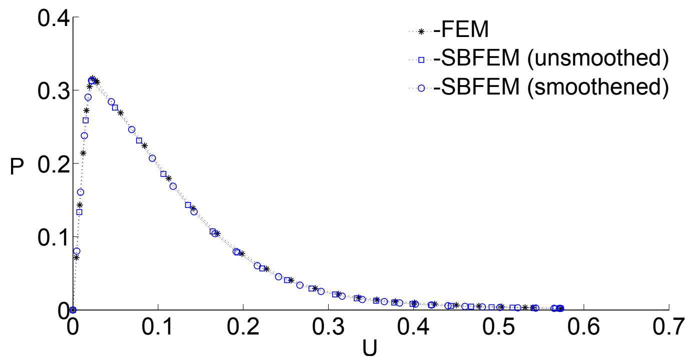

Figure 5.31. Force (kN) vs displacement (mm) output for the 2D image-based non-local damage analysis of a plate with multiple inclusions of different diameters. SBFEM unsmoothed mesh output compared to the smoothened mesh and the FEM-based outputs.

The finite element analysis is performed using first order quadrilateral elements. With reference to figure 5.31 there is good synergy between the finite element results and the SBFEM results. The simulations attains a peak load of 0.3163 kN. At this instance the damage profile shown in figure 5.34a indicates regions where the average damage value is around 0.7 spanning within an approximate 15 mm and 10 mm lengths on either side of inclusions B and C, respectively. As the section passing through holes B and C constitutes the weakest section in the plate the effective reduction in cross section therefore is close to 32%. Assuming an elastic plate in uniaxial tension with the reduction in cross section of 32% and a top edge displacement of 0.02313 mm yields a top edge force of 0.315 kN. This value serves to validate the results obtained in this analysis. What is highly note worthy is that the SBFEM smoothened and unsmoothed meshes produce similar results, thus avoiding the need for mesh smoothing which can be a time consuming exercise in more complex problems. This finding is in line with the observations made by [98, 108, 115] on the effect of stress averaging in the presence of jagged boundaries. Similarly localised strains observed in small elements adjoining the jagged boundaries are in a sense smoothened by the non-local averaging which produces strains close to the strains obtained using geometry-based meshes.

The contour plots are extracted at three critical points in the hardening and softening limbs in the load-displacement curve shown in figure 5.31. The contours for displacement (figure 5.32) and maximum principle stress (figure 5.33) are recorded at a node ‘A’ displacement of 0.02313 mm corresponding to a peak load of 0.3163 kN on the top edge and just after the peak load for displacement value of 0.0543 mm corresponding to a load of 0.2938 kN. In addition the damage contours in figure 5.34 captures an instance corresponding to the end of the simulation when node ‘A’ displacement reads at 0.5727 mm for a corresponding load of 0.0021 kN (figure 5.34c).

The displacement contour in figure 5.32a shows the initial increase in the displacement of the top section of the plate directly above the three imperfections. Thereafter as damage further develops (see figure 5.34b) between the circular inclusions the upper section of the plate displays an amplified state of deformation in figure 5.32b.

(a) Vertical displacement (u_y) contour when node ‘A’ displacement is 0.02313 mm.

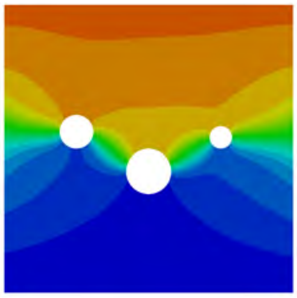

(b) Vertical displacement (u_y) contour when node ‘A’ displacement is 0.0543 mm.

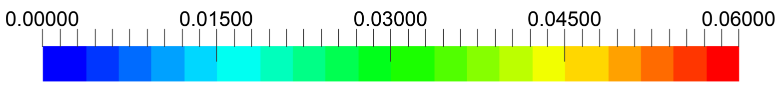

Figure 5.32. Vertical displacement (u_y) contours obtained for the 2D image-based non-local damage analysis of a plate with multiple inclusions of different diameters. Units:mm. Results are recorded for the mesh shown in figure 5.30b-(ii).

The stress contour plots in figure 5.33a-5.33b exhibit the expected stress concentrations at the edges of the horizontal diameter. These concentrated stresses dissipate as the distance increases from the edge of the inclusions.

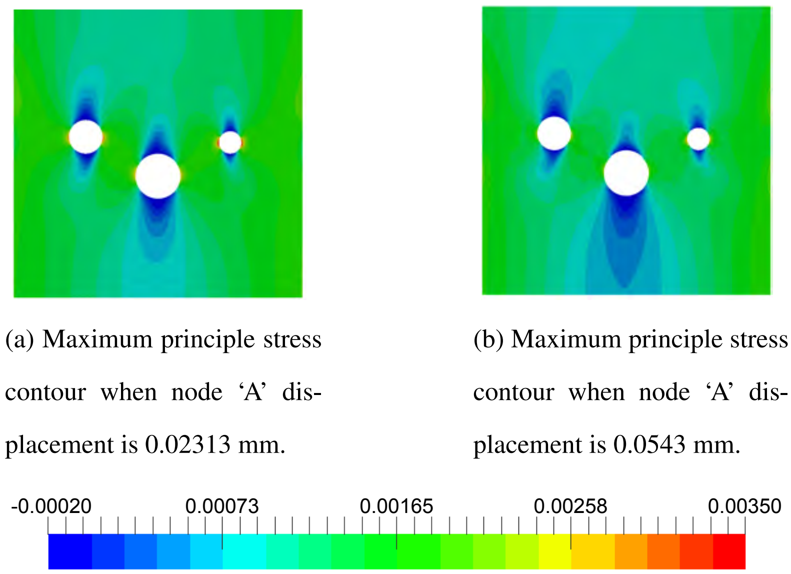

Figure 5.33. Maximum principle stress contours obtained for the 2D image-based non-local damage analysis of a plate with multiple inclusions of different diameters. Units:GPa. Results are recorded for the mesh in figure 5.30b-(ii).

The concentration of strains near to the edges of the horizontal diameter initiates damage in the region as seen in figure 5.34a. This initial damage then fully propagates (see figures 5.34b-5.34c) between the three inclusions following the weakest section of the plate.

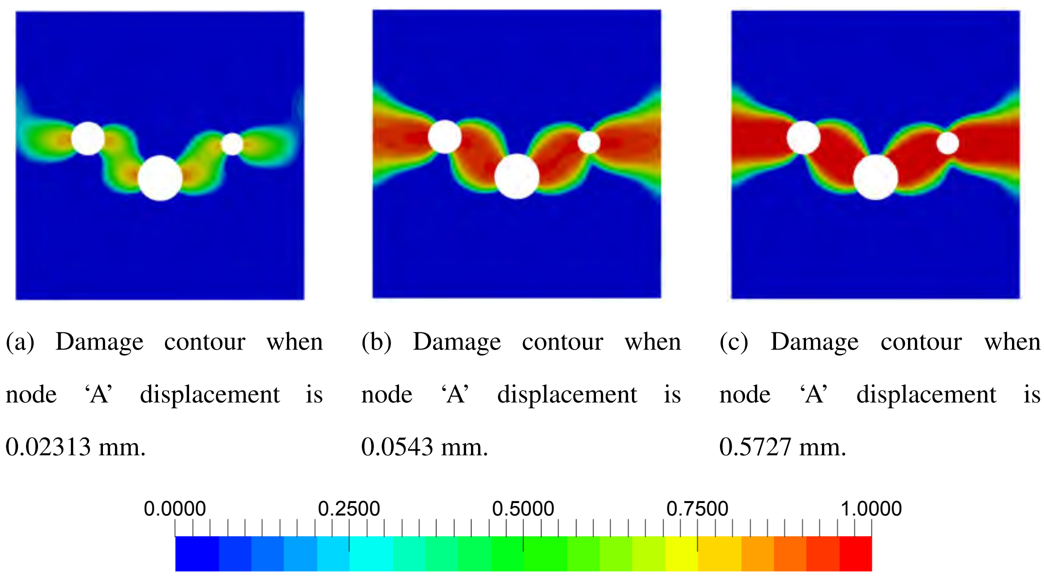

Figure 5.34. Damage (ω) contours obtained for the 2D image-based non-local damage analysis of a plate with multiple inclusions of different diameters. Results are recorded for the mesh in figure 5.30b-(ii).

5.8.2 X-ray CT image generated 2D concrete specimen

This example makes use of an actual image of a concrete specimen published by Ren et. al. [542]. The image shown in figure 5.35 consists of a two phase geometry, made up of the concrete matrix and aggregates represented by grey and black pixels, respectively. The two white specs in the image represent voids generally found in concrete specimens. Figure 5.35 also depicts the dimensions and boundary conditions adopted in the simulation. The specimen is 100×100 mm in length and height with an assumed thickness of 1 mm. The bottom edge of the specimen is restrained in vertical movement while the left bottom corner of the specimen is restrained in horizontal movement. A displacement control agitation is introduced on the top edge of the specimen to generate a response to analyse the structural behaviour of the model.

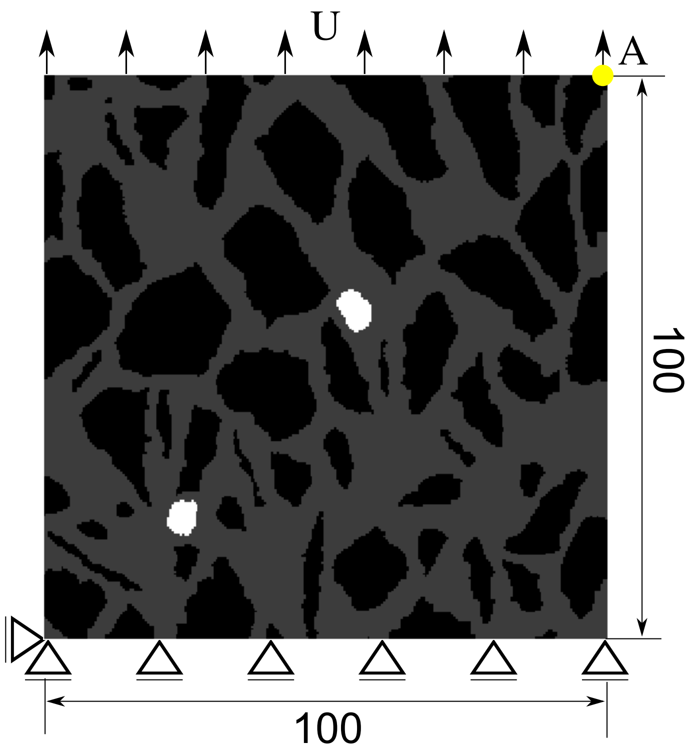

Figure 5.35. Specimen dimensions (mm) and boundary conditions used in the X-ray CT image-based non-local analysis of 2D concrete specimen.

The specimen is considered to have material properties collated in table 5.3. Mortar is considered to be the weaker of the two material interface and thus subject to damage. The aggregate on the other hand is assumed not to undergo damage degradation. The damage evolution is according to the exponential damage model given in equation (5.3). The equivalent strain criteria for non-local averaging is considered through adopting the Mazars formulation given in equation (5.5). Plane stress conditions are considered for the analysis.

	Aggregate	Matrix
Young's modulus (GPa)	35	30
Poisson's ratio	0.2	0.2
Non-local equivalent strain	N/A	Mazars, refer equation (5.5)
Damage initiation threshold	N/A	0.124×10^{-4}
Non-local length (mm)	N/A	2.4
Damage evolution law	N/A	Exponential, refer equation (5.3)
Residual stress parameter	N/A	0.999
Softening rate parameter	N/A	500

Table 5.3. Material properties and damage parameters adopted in the X-ray CT image-based non-local analysis of 2D concrete specimen.

Considering the above damage parameters the behaviour of the damage evolution function is shown in figure 5.36.

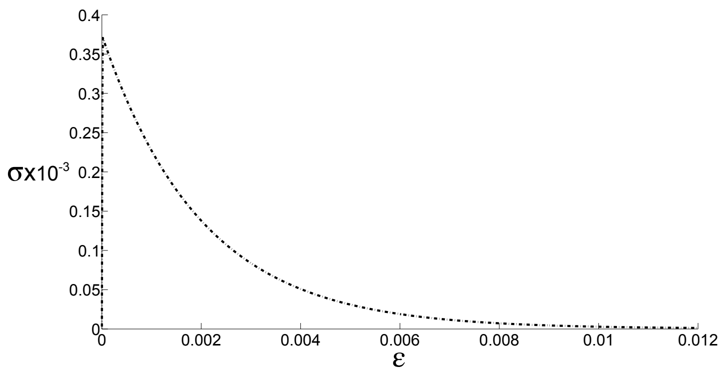

Figure 5.36. 1D element stress (GPa) vs strain profile considered in the X-ray CT image-based non-local analysis of 2D concrete specimen. Damage evolution considered is with respect to the exponential softening law in equation (5.3).

The non-local length parameter is considered as 2.4 mm with non-local weighting considered according to equation (5.10). The non-local length parameter is based on the findings of [303]. With an assumed 0.8 mm maximum particle size of mortar the non-local length parameter is set at 2.4 mm which equates to $3 \times d_0$, where d_0 is the maximum particle size of mortar.

The automatic decomposition of the image to a quadtree mesh is bound by the maximum cell size of 8 pixels and the minimum cell's size is 1 pixel, which resulted in 14,951 cells. The specimen is modelled as a standard 100×100 mm specimen which is achieved by adopting a scaling factor of 0.39. Therefore, minimum and maximum mesh size is 0.39 mm and 1.56 mm. There is a total of 100,031 DOFs in the mesh shown in figure 5.37. All the matrices specified in section 5.6 are pre-computed for all the 32 possible master cells (16 possible master cells in each material), which is less than 0.08% of the total number of cells in the mesh. Pursuant to the observations made in section 5.8.1, this simulation does not consider a smoothened mesh.

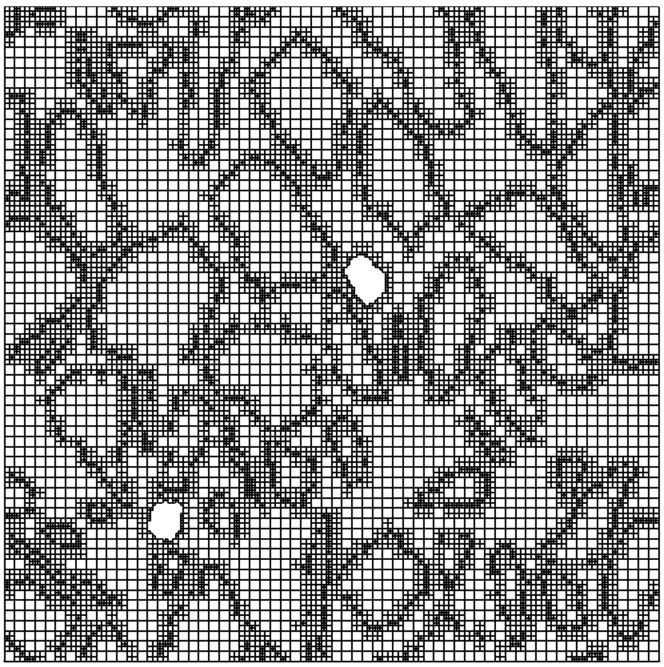

Figure 5.37. SBFEM mesh used in the analysis of an X-ray CT image-based non-local analysis of 2D concrete specimen.

The load-displacement curve produced in the analysis is given in figure 5.38. The analysis is run using the arc-length incorporated modified Newton Raphson method. The initial displacement step is kept to 1×10^{-4} mm with automatic displacement control the analysis is completed in 420 iterations.

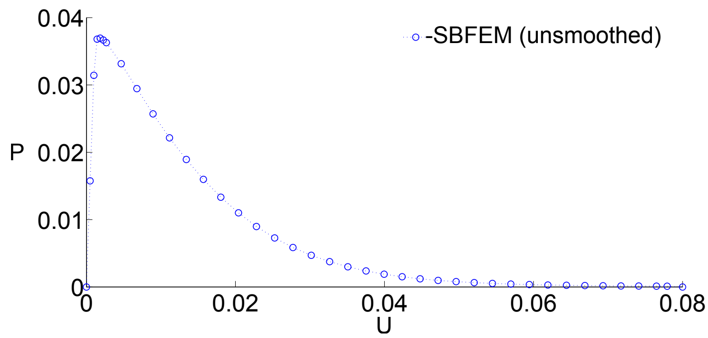

Figure 5.38. Force (kN) vs displacement (mm) output for the X-ray CT image-based non-local analysis of 2D concrete specimen. SBFEM unsmoothed mesh shown in figure 5.30b considered in the analysis.

The contour plots produced below are for displacement (figure 5.39), maximum principle stress in aggregates (figure 5.40) and mortar (figure 5.41), and damage evolution (figure 5.42). The contours for displacement, maximum principle stress and damage are captured when node 'A' reads a displacement of 0.0018 mm corresponding to a peak load of 0.03697 kN on the top edge and just after the peak load for a displacement value of 0.01 mm corresponding to a load of 0.02368 kN (refer figure 5.38). In addition to this these load-displacement instances the damage evolution contains an extra contour corresponding to the end of the simulation at a displacement reading of 0.08 mm and a total force reading of 1.4×10^{-5} kN.

The displacement contours in figure 5.39 depict a clear weak zone formation first in an S shaped form as seen in figure 5.39a and thereon in figure 5.39b the bottom portion of the specimen appears to be separated by the yellow shaded contour indicating larger deformations. This region is therefore most likely to be affected by macro cracks.

(a) Vertical displacement (u_y) contour when node 'A' displacement is 0.0018 mm.

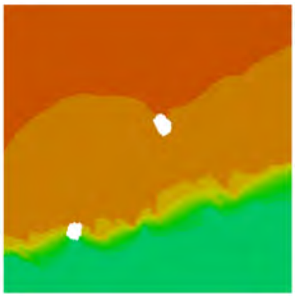

(b) Vertical displacement (u_y) contour when node 'A' displacement is 0.01 mm.

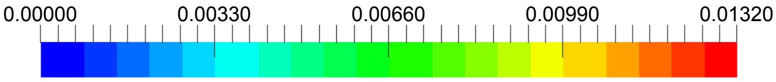

Figure 5.39. Vertical displacement (u_y) contours obtained for the X-ray CT image-based non-local analysis of 2D concrete specimen. Units:mm. Results are obtained for the mesh shown in figure 5.30b.

The aggregate stress contours shown in figure 5.40 capture the distribution of stresses within the aggregate matrix. The sharp edges apparent in the aggregates build stress and strain concentrations in the vicinity of these sharp corners.

(a) Maximum principle stress contour for the aggregates when node 'A' displacement is 0.0018 mm.

(b) Maximum principle stress contour for the aggregates when node 'A' displacement is 0.01 mm.

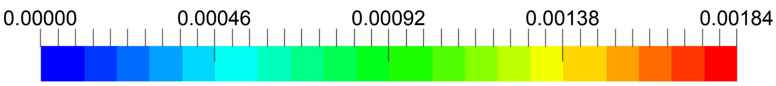

Figure 5.40. Maximum principle stress contours obtained for the aggregate structure in the X-ray CT image-based non-local analysis of 2D concrete specimen. Units:GPa. Results are obtained for the mesh shown in figure 5.30b.

As expected the voids in the mortar tends to concentrate strains and stresses in the edges perpendicular to the direction of loading. This can be seen in figure 5.41a. This initial strain concentration drives the damage formulation around the voids in the matrix (see figure 5.42a). With softening however the stresses in the mortar matrix are expected to reduce. This softening phenomenon within the mortar is apparent in figure 5.41b.

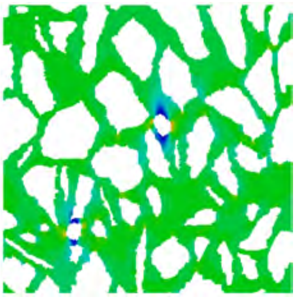

(a) Maximum principle stress contour for the matrix when node 'A' displacement is 0.0018 mm.

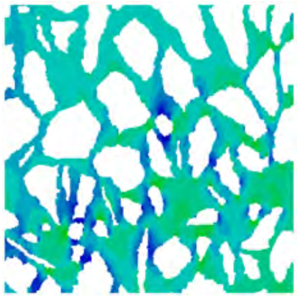

(b) Maximum principle stress contour for the matrix when node 'A' displacement is 0.01 mm.

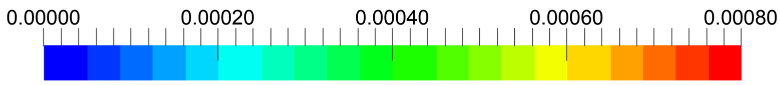

Figure 5.41. Maximum principle stress contours obtained for the matrix structure in the X-ray CT image-based non-local analysis of 2D concrete specimen. Units:GPa. Results are obtained for the mesh shown in figure 5.30b.

After the initial damage formation in the vicinity of the voids further damage accumulation closer to the left edge. This is due to the presence of sharp aggregates (see figure 5.42b) attracting higher strains in the vicinity of sharp corners. The damage then propagates through the mortar meandering around the aggregates following the weakest path within the specimen.

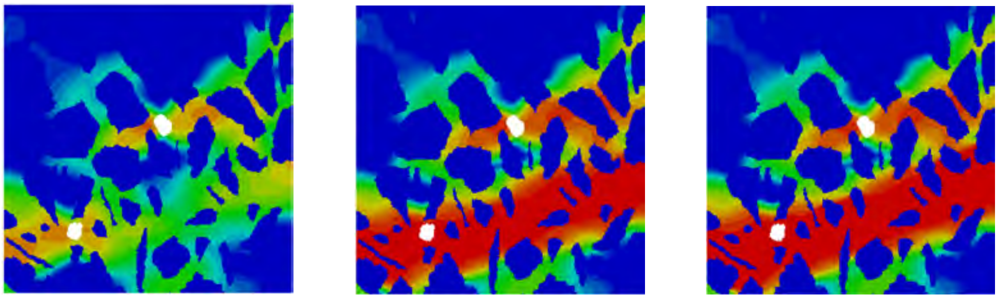

(a) Damage contour when node ‘A’ displacement is 0.0018 mm.

(b) Damage contour when node ‘A’ displacement is 0.01 mm.

(c) Damage contour when node ‘A’ displacement is 0.08 mm.

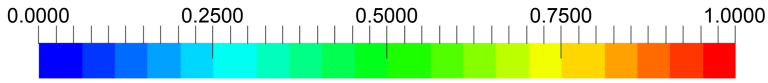

Figure 5.42. Damage (ω) contours obtained for the X-ray CT image-based non-local analysis of 2D concrete specimen. Results are obtained for the mesh shown in figure 5.30b.

5.8.3 Artificially generated 2D concrete specimen

As the final 2D example an automatically generated aggregate distribution is considered with a refined description of the constituents consisting of an inter-facial transition zone (ITZ). The problem description is extracted from the work published by Lloberas et. al. [512], where domain decomposition techniques are studied for efficient modelling of brittle heterogeneous materials.

With reference to figure 5.43 the model consists of a three-phase material description with aggregates (black pixels), matrix (white pixels) and the ITZ (grey pixels) between the aggregates and the matrix. The length and the depth of the specimen is set to 66.67×30 mm. The concrete sample is subjected to a tensile loading by restraining the horizontal movement of the specimen on the left edge while the opposite edge of the specimen is subjected to the application of tensile force. To avoid rigid body movement the lower bottom corner of the model is retrained in vertical movement.

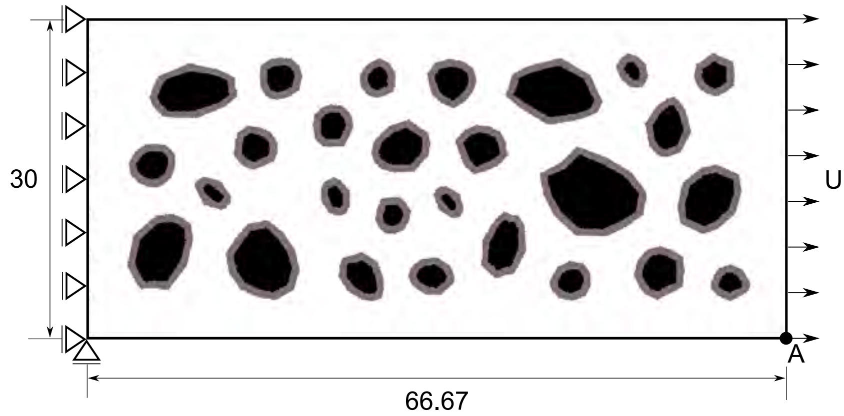

Figure 5.43. Specimen dimensions (mm) and boundary conditions used in the non-local analysis of an artificially generated 2D concrete specimen.

Material properties of the model is as given in table 5.4. The ITZ is assumed as a weak porous region of the material were damage nucleates and propagates through the matrix until complete failure of the specimen. The exponential damage model given in equation (5.3) is used in this formulation. The equivalent strain criteria for non-local averaging is considered as per Mazars formulation given in equation (5.5). The non-local strains are then averaged with the non-local weightings calculated in accordance to equation (5.10).

	Aggregate	Matrix	ITZ
Young's modulus (GPa)	35	30	20
Poisson's ratio	0.2	0.2	0.2
Non-local equivalent strain	N/A	Mazars, refer equation (5.5)	Mazars, refer equation (5.5)
Damage initiation threshold	N/A	0.124×10^{-4}	0.1×10^{-4}
Non-local length (mm)	N/A	0.8	0.8
Damage evolution law	N/A	Exponential, refer equation (5.3)	Exponential, refer equation (5.3)
Residual stress parameter	N/A	0.999	0.999
Softening rate parameter	N/A	500	500

Table 5.4. Material properties and damage parameters adopted in the non-local analysis of an artificially generated 2D concrete specimen.

The stress-strain behaviour of the damage models upon consideration of the parameters in table 5.4 are as shown in figure 5.44. Since both the matrix and the ITZ undergo material damage, figure 5.44 depict the damage induced stress-strain variation between the two material types.

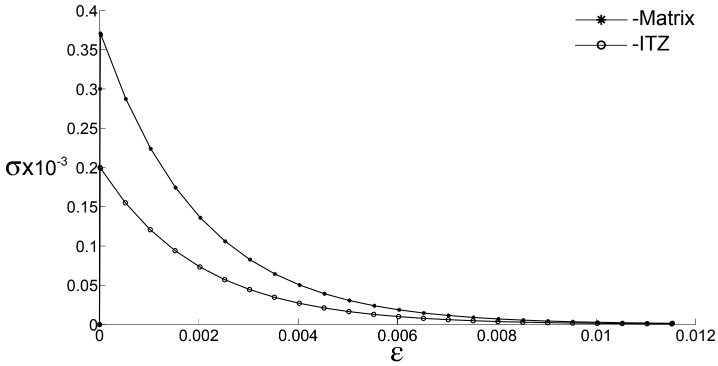

Figure 5.44. 1D element stress (GPa) vs strain profile considered in the 2D image-based analysis of a artificially generated geometry of a concrete specimen. Two different damage evolutions are considered using the exponential softening law in equation (5.3) for the matrix and the ITZ.

The thickness of the ITZ is assumed to be 0.5 mm and therefore the element size distribution within the mesh is considered so that a minimum of at least 2 elements are captured within the ITZ. The final mesh distribution reflect this requirement by setting the maximum and minimum mesh size respectively to 0.78 mm and 0.1 mm, and consist of 28,695 elements (see figure 5.45). As the results for both smooth and unsmoothed mesh configuration was proven to produce similar results in section 5.8.1, this example only considers an unsmoothed mesh.

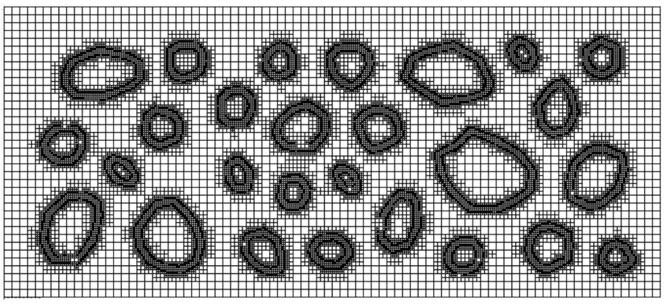

Figure 5.45. SBFEM mesh used in the non-local analysis of an artificially generated 2D concrete specimen. Maximum and minimum mesh sizes are 0.78 mm and 0.1 mm, respectively.

The simulation is run with the arc-length incorporated modified Newton Raphson scheme under assumed plane stress conditions. The load-displacement curve thus produced in the implicit analysis is depicted in figure 5.46.

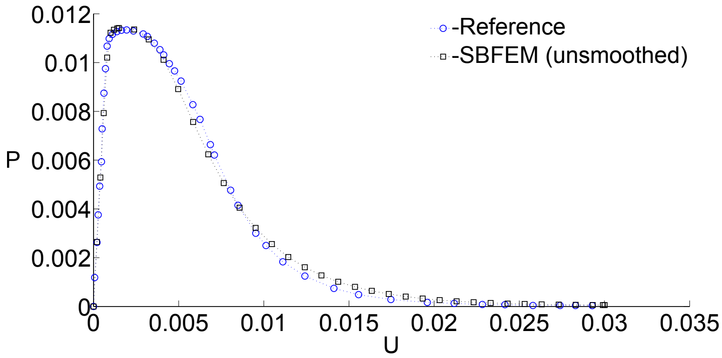

Figure 5.46. Force (kN) vs displacement (mm) output for the 2D image-based non-local damage analysis of a artificially generated geometry of a concrete specimen. SBFEM unsmoothed mesh output compared to the FEM-based output published by [512].

The peak load attained in the simulation is 0.01144 kN. The SBFEM results show a close agreement with the reference solution.

The contour plots for displacement shown in figure 5.47 are captured at instances resembling the peak load and at a point on the softening limb when node 'A' displacement reads 0.005321 mm corresponding to a load of 0.00837 kN. This second displacement contour in figure 5.47b shows a clear definition of the centralised damage process zone distinguished by the yellow shaded contours. As the applied external load increases the deformations to the left of this zone become insignificant due to the phenomenon of unloading.

(a) Horizontal displacement contour when node 'A' displacement is 0.001872 mm.

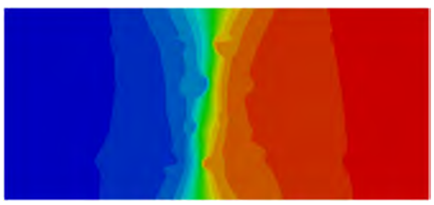

(b) Horizontal displacement contour when node 'A' displacement is 0.005321 mm.

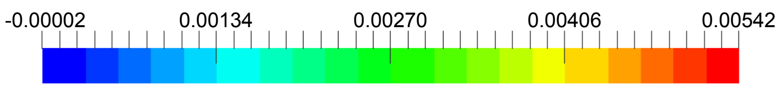

Figure 5.47. Horizontal displacement (u_x) contours obtained for the non-local analysis of an artificially generated 2D concrete specimen. Units:mm. Results are obtained for the mesh shown in figure 5.45.

The maximum principle stress contours shown in figures 5.48, 5.49 and 5.50 respectively belong to the matrix, the ITZ and the aggregate found in the concrete specimen. The instances captured in these figures are similar to those captured in the displacement contours in figure 5.47.

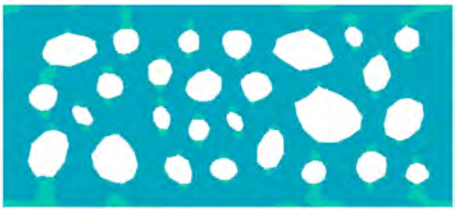

(a) Maximum principle stress contour when node ‘A’ displacement is 0.001872 mm.

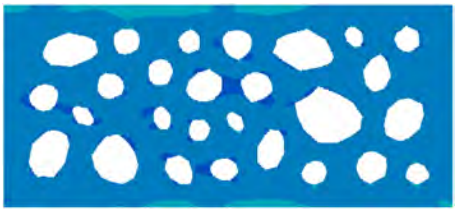

(b) Maximum principle stress contour when node ‘A’ displacement is 0.005321 mm.

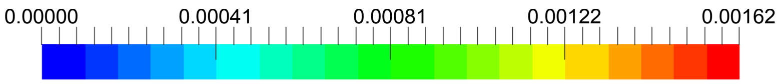

Figure 5.48. Maximum principle stress contours obtained for the matrix structure in the non-local analysis of an artificially generated 2D concrete specimen. Units:GPa. Results are obtained for the mesh shown in figure 5.45.

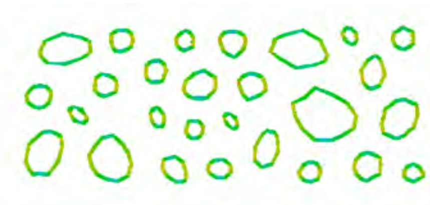

(a) Maximum principle stress contour when node ‘A’ displacement is 0.001872 mm.

(b) Maximum principle stress contour when node ‘A’ displacement is 0.005321 mm.

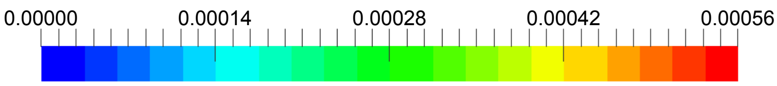

Figure 5.49. Maximum principle stress contours for the ITZ structure in the non-local analysis of an artificially generated 2D concrete specimen. Units:GPa. Results are obtained for the mesh shown in figure 5.45.

As the specimen is subjected to tensile loading the corners of the material constituents perpendicular to the direction of loading garner high stresses due to the accumulation of high strains (see figures 5.49 and 5.50).

(a) Maximum principle stress stress contour when node 'A' displacement is 0.001872 mm.

(b) Maximum principle stress contour when node 'A' displacement is 0.005321 mm.

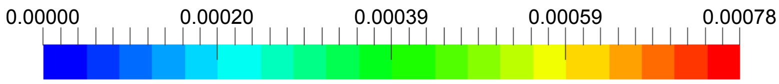

Figure 5.50. Maximum principle stress contours for aggregates structure in the non-local analysis of an artificially generated 2D concrete specimen. Units:GPa. Results are obtained for the mesh shown in figure 5.45.

When the load is increased damage starts at the weak ITZ between aggregates and matrix. These contributes to numerous locations of accumulated strains which results in localised spots of damage. This process cumulatively produces the damage process zone. The damage contours shown in figure 5.51 below depict the formation of this damage process zone at instances similar to that recorded in the displacement contours. In addition a load-displacement instance shown in figure 5.51c correspond to the end of the simulation at a displacement of 0.0287 mm and load of 6.43×10^{-5} kN. This record helps to capture the full extent of the deterioration of the specimen. As the aggregates are assumed to be exempt from damage this assumption is also reflected in the figures 5.51a-5.51c.

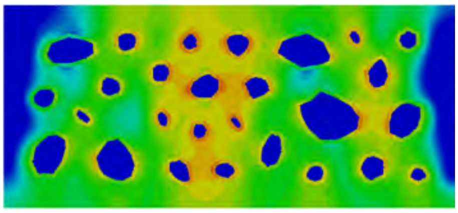

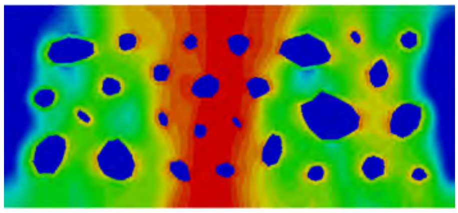

(a) Damage contour when node ‘A’ displacement is 0.001872 mm.

(b) Damage contour when node ‘A’ displacement is 0.005321mm.

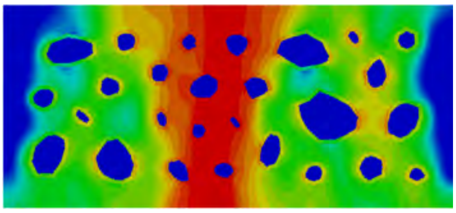

(c) Damage contour when node ‘A’ displacement is 0.0287mm.

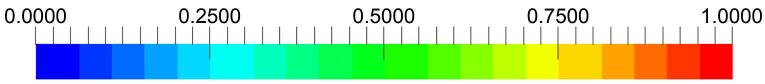

Figure 5.51. Damage (ω) contours obtained for the non-local analysis of an artificially generated 2D concrete specimen. Results are obtained for the mesh shown in figure 5.45.

The central portion of the specimen is made up of small aggregates that are bound by the ITZ. This has contributed to a higher representation of mortar and a lack of representation of the strongest constituent of the model, aggregates. Therefore this section theoretically should contribute to the weakest part of the model as the ITZ and the mortar are the two weakest material constituents in the model. The damage pattern observed in figure 5.51 agrees with this theoretical expectation.

5.8.4 Thick plate with multiple cylindrical cavities of different diameters

The first example in 3D considers a perforated thick plate in uniaxial tension. These perforations intend to act as imperfections that encourage the formation and the evolution of the deterioration of the specimen. This example is similar to the example demonstrated in section 5.8.1.

With reference to figure 5.52 the dimensions of the plate are $128 \times 128 \times 8$ mm. The plate contains 3 cylindrical inclusions (P, Q and R) of varying diameters.

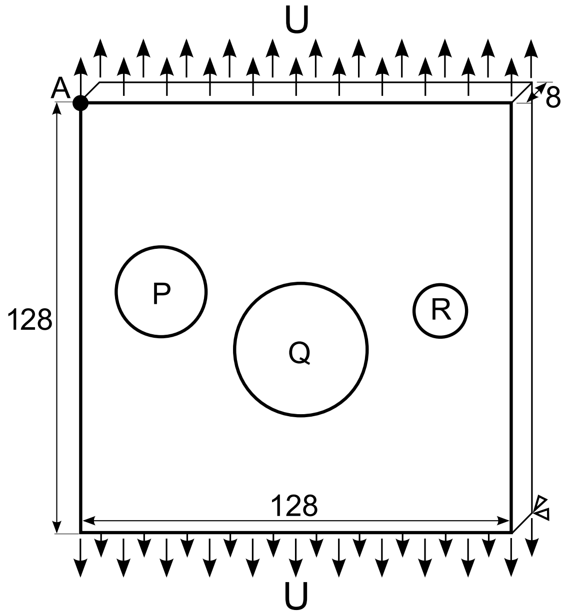

Figure 5.52. Specimen dimensions (mm) and boundary conditions considered in the 3D image-based non-local analysis of a thick plate with 3 cylindrical cavities of different diameters.

The inclusions in figure 5.52 have dimensions and location coordinates as given in table 5.5. The coordinates are given relative to the coordinate (0,0,0) considered at the left hand bottom corner.

Inclusion notation	Centre coordinates (mm)	Diameter (mm)
P	22,72	26
Q	64,53	41
R	105,66	16

Table 5.5. Location and the diameter of cylindrical inclusions considered in the 3D image-based non-local analysis of a thick plate with 3 cylindrical cavities of different diameters.

To emulate the uniaxial loading condition the plate is pulled from both the top and the bottom faces. The horizontal restraint in the bottom right corner restricts any rigid body movements.

The Young's modulus of the plate is considered to be 20 GPa and the Poisson's ratio is set at 0.2. The damage evolution model is according to the exponential damage model given in equation (5.2) with $\varepsilon_0 = 90 \times 10^{-6}$ and strain at which material is fully damaged $\varepsilon_f = 7.0 \times 10^{-3}$. The behaviour of the softening model with respect to these parameters are shown in figure 5.53.

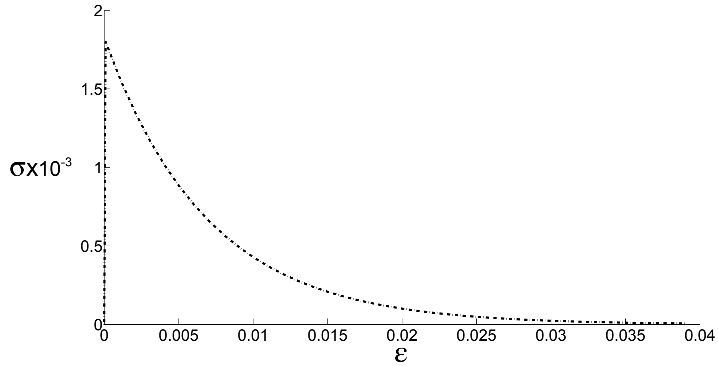

Figure 5.53. 1D element stress (GPa) vs strain profile considered in the 3D image-based analysis of a thick plate with 3 cylindrical cavities of different diameters. The damage evolutions is with respect to the softening law in equation (5.2).

The ratio between the compressive and tensile strength (parameter *k*) in equation (5.8) is set to 10 to obtain an realistic material description while calculating the equivalent strain. The non-local length is taken as 5 mm assuming the maximum particle size of mortar as 1.85 mm. The non-local weighting is implemented using equation (5.10). All the material and damage model parameters used in the analysis are collated in table 5.6.

E (GPa)	ν	ε_0	ε_f	l (mm)
20	0.2	90×10^{-6}	7.0×10^{-3}	5

Table 5.6. Material properties and damage parameters adopted in the 3D image-based non-local analysis of a thick plate with 3 cylindrical cavities of different diameters.

The two meshes considered for the analysis consists of elements with maximum mesh size of 2 mm and 4 mm with a minimum mesh size of 1 mm. Figure 5.54 shows the two meshes considered in the analysis. These meshes are automatically generated through the octree meshing algorithm.

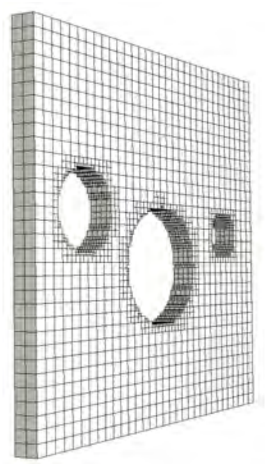

(a) Mesh 1 with maximum element size 4 mm and minimum element size 1 mm.

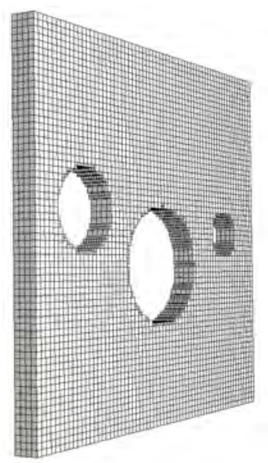

(b) Mesh 2 with maximum element size 2 mm and minimum element size 1 mm.

Figure 5.54. (a) Coarse (mesh 1) and (b) fine (mesh 2) SBFE unsmoothed meshes used in the 3D image-based non-local analysis of a thick plate with 3 cylindrical cavities of different diameters.

The analysis is run using the modified Newton Raphson method with displacement controlled agitations on the top and bottom surfaces. The initial displacement step is kept to 0.001 mm with automatic displacement control the analysis is completed in 350 iterations. The load-displacement curve produced in the analysis is given in figure 5.55.

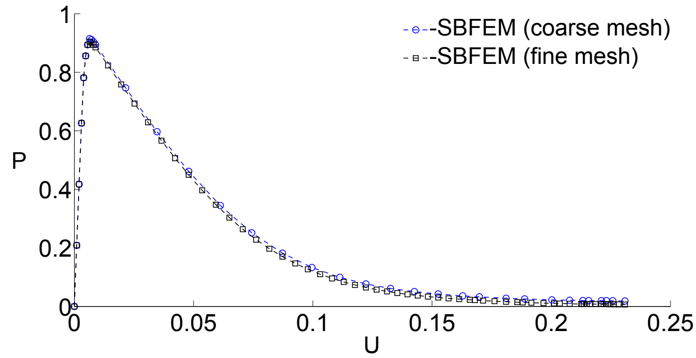

Figure 5.55. Force (kN) vs displacement (mm) output for the 3D image-based non-local analysis of a thick plate with 3 cylindrical cavities of different diameters. SBFEM unsmoothed meshes shown in figure 5.54 considered in the analysis.

With reference to figure 5.55 there is good agreement between the two analysis conducted using the coarse and the fine meshes. Thus, satisfying the expected convergence with mesh refinement in non-local analysis regimes. The simulation attains a peak load of 0.8341 kN. An equivalent elastic plate cross section to attain the recorded maximum load equates to 606.618 mm^2. With the development of damage in the plate, to attain an effective area of 606.618 mm^2 the cross sectional plane passing through the inclusions should therefore have an approximate damage development of 0.78 at the time the simulation attains the maximum load carrying capacity. This damage value is closely reflected in figure 5.58a which can be confidently approximated to fall within 0.75-0.85. Thus, validating the result.

The contour plots depicted in figure 5.56 are for the vertical displacement. The first contour shown in figure 5.56a is captured at displacement of 0.0088 mm corresponding to a peak load of 0.8341 kN whereas the second contour shown in figure 5.56b is associated to an instance where displacement and load values read 0.02245 mm and 0.72574 kN, respectively. Moving from figure 5.56a to figure 5.56b the top part of the plate undergo considerable deformation as damage accumulates in a narrow horizontal band passing through the inclusions (see figures 5.58).

(a) Vertical displacement contour when node 'A' displacement is 0.0088 mm.

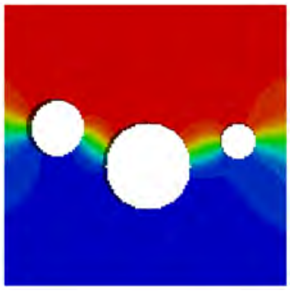

(b) Vertical displacement contour when node 'A' displacement is 0.02245 mm.

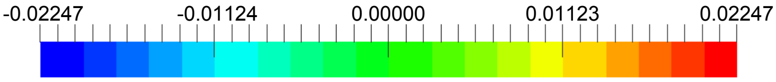

Figure 5.56. Vertical displacement (u_y) contours obtained for the 3D image-based non-local analysis of a thick plate with 3 cylindrical cavities of different diameters. Units:mm. Results are obtained for mesh 2 shown in figure 5.54b.

The von Mises equivalent stress contours in figure 5.57 are captured at similar instances as recorded in the displacement contours. When strains accumulate in the corners of inclusions perpendicular to the direction of loading high stress zones are produced as a consequence. At the same time however edges parallel to the direction of loading undergo unloading.

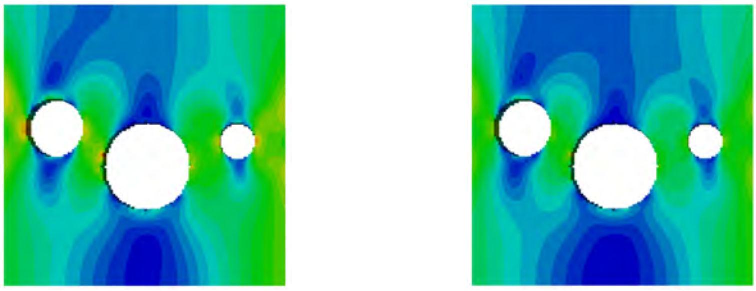

(a) Von Mises stress stress contour when node ‘A’ displacement is 0.0088 mm.

(b) Von Mises stress contour when node ‘A’ displacement is 0.02245 mm.

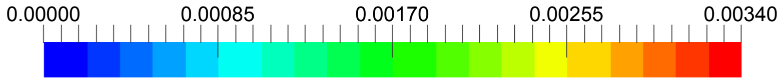

Figure 5.57. Von Mises stress contours obtained in the 3D image-based non-local analysis of a thick plate with 3 cylindrical cavities of different diameters.. Units:GPa. Results are obtained for the mesh 2 shown in figure 5.54b.

For completeness, the damage contours in figure 5.58 captures an additional contour resembling the end of the simulation at a displacement of 0.2338 mm and load of 0.0062 kN. The damage propagates from the high strain and stress accumulated zones evident in the von Mises stress plots in figure 5.57. The damage contour spans from the central larger diameter inclusion to the smaller diameter inclusions on either side.

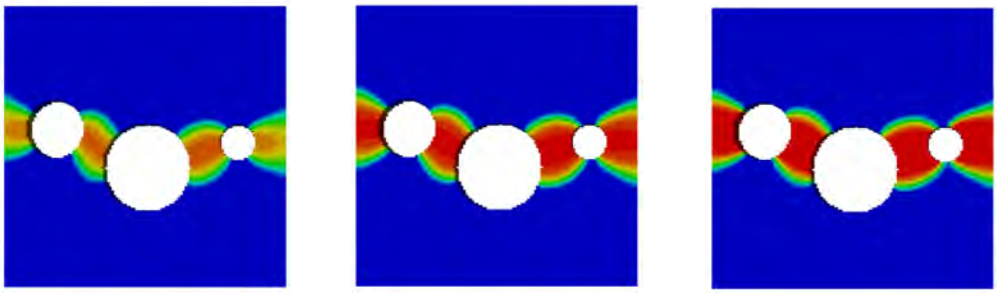

(a) Damage contour when node ‘A’ displacement is 0.0088 mm.

(b) Damage contour when node ‘A’ displacement is 0.02245 mm.

(c) Damage contour when node ‘A’ displacement is 0.2338 mm.

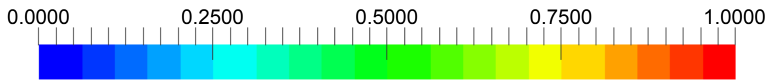

Figure 5.58. Damage (ω) contours obtained in the 3D image-based non-local analysis of a thick plate with 3 cylindrical cavities of different diameters. Results are obtained for the mesh shown in figure 5.54b.

The deformed shape of the specimen at the end of the analysis is as shown in figure 5.59. The result is scaled 100 times to exaggerate the result for better visualisation. As expected the left and right edges of the inclusions undergo significant deformation as damage accumulates in these regions.

Figure 5.59. Deformed shape of the specimen obtained in the 3D image-based non-local analysis of a thick plate with 3 cylindrical cavities of different diameters. Results are obtained for the mesh shown in figure 5.54b.

5.8.5 3D cube with multiple spherical inclusions of different diameters

The uniaxial tensile behaviour of a $128 \times 128 \times 128$ mm cube with 6 spherical inclusions is studied in this section.

As shown in figure 5.60 the inclusions are of varying diameters and are positioned in the central Y plane.

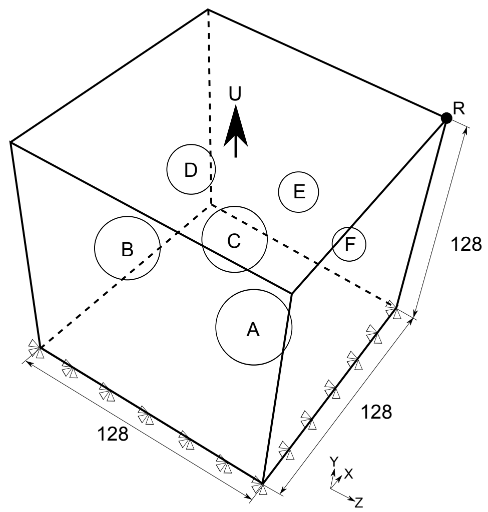

Figure 5.60. Specimen dimensions (mm) and boundary conditions considered in the 3D image-based non-local analysis of a cube with 6 spherical inclusions of different diameters.

These spherical inclusions have dimensions and location coordinates as given in table 5.7. The coordinates given in the table considers (0,0,0) at the bottom left hand corner.

Inclusion notation	Centre coordinates (mm)	Diameter (mm)
A	26,64,100	32
B	30,64,30	28
C	64,64,64	30
D	90,64,20	24
E	110,64,70	20
F	94,64,108	16

Table 5.7. Location and the diameter of spherical cavities considered in the 3D image-based non-local analysis of a cube with 6 spherical inclusions of different diameters.

The cube is restrained in Y directional movement and all rigid body movements through restraints applied on the bottom face. The force applied on the top face of the cube induces the tensile action.

The modulus of elasticity and poisons ratio is set to 20 GPa and 0.2, respectively. The equivalent strain parameter k with reference to equation (5.8) is set to 10. The interaction radius R is set to 7 mm with non-local weighting considered according to equation (5.11). The damage evolution follows the exponential softening model given in equation (5.3) with ε_0 set to 7×10^{-5} , $\alpha = 0.98$ and $\beta = 300$. The stress-strain variation with respect to these damage model parameters is given in figure 5.61.

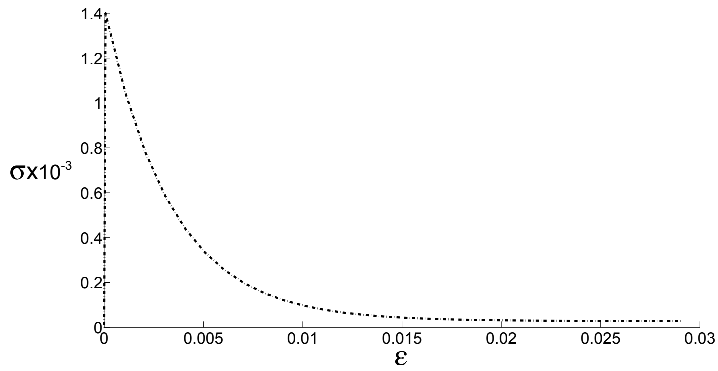

Figure 5.61. 1D element stress (GPa) vs strain profile considered in the 3D image-based non-local analysis of a cube with 6 spherical inclusions of different diameters. The damage evolution is with respect to the softening law in equation (5.3).

Figure 5.62 shows the two meshes automatically generated through image-based octree decomposition. For better visualisation of the mesh details the meshes are shown in the xz plane for one half of the cube. The two meshes are considered to demonstrate the convergence of the results with improved mesh refinement. In mesh 1 the element size varies from 1 mm to 8 mm whereas in mesh 2 the element size varies from 1 mm to 4 mm.

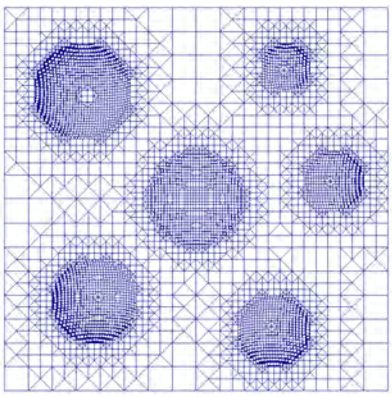

(a) Mesh 1 - minimum element size 1 mm and maximum element size 8 mm.

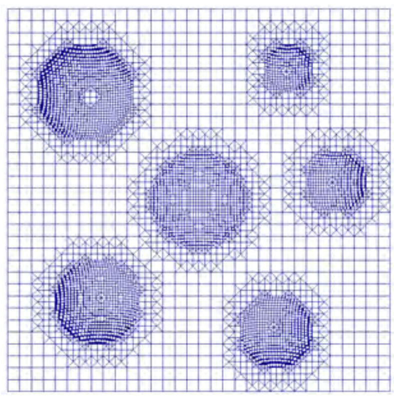

(b) Mesh 2 - minimum element size 1 mm and maximum element size 4 mm.

Figure 5.62. Two octree meshes used in the 3D image-based non-local analysis of a cube with 6 spherical inclusions of different diameters. Minimum element size of 1 mm considered.

The finer mesh is built up of 49,358 cells that generate 213,438 DOFs. The number of cells generated is a mere 2.4% of the voxels present in the original image. The number of unique octree cells identified in the mesh is 168. Therefore, the number of master cells are a 0.34% of the total number of cells.

The analysis is run using the modified Newton Raphson method coupled with the arc-length technique. The initial displacement step is kept to 0.001 mm. The automatic displacement control feature enables the analysis to completed in 198 iterations. The load-displacement curve produced in the analysis with respect to the two meshes in figure 5.62b is shown in figure 5.63.

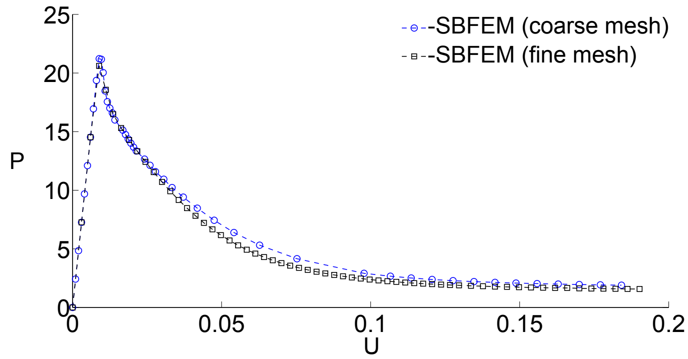

Figure 5.63. Force (kN) vs displacement (mm) output for the 3D image-based non-local analysis of a cube with 6 spherical inclusions of different diameters. Results are obtained for the two SBFEM unsmoothed meshes shown in figure 5.62.

The peak load reached in the simulation is 20.8 kN when the node 'R' displacement is 0.0097 mm. The force-displacement response for the two meshes are comparatively similar. This result is an indication of the analysis converging upon mesh refinement. It can be expected, upon further refinement, the non-local analysis output will produce a similar solution with a finite energy dissipation, independently of the mesh employed.

The contour plots produced below are for displacement (figure 5.64), maximum principle stress (figure 5.65) and damage evolution (figure 5.66). The contours for displacement, maximum principle stress and damage are at peak load and just after the peak load for displacement value of 0.032 mm corresponding to a load of 10.2 kN. In addition to this these contours, the damage evolution contours contains an extra contour corresponding to the end of the simulation at displacement of 0.19 mm and load of 1.58 kN.

Since the spherical inclusions are positioned centrally in the Y plane, the displacement contours show a slight symmetry in the contours. However, due to the inclusions being of different diameter, it is not in a perfect symmetry. As the load increases the central portion of the cube show a clear definition of the differentiation in the magnitude of displacement between the top and the bottom half of the cube. This can be interpreted as the formation of a damage process zone that is evident in the damage contours shown in figure 5.66.

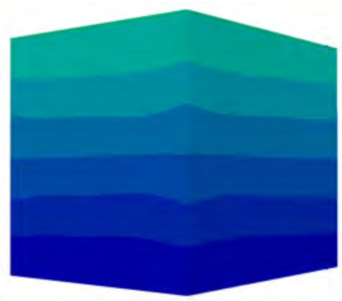

(a) Vertical displacement contour when node 'R' displacement is 0.0097 mm.

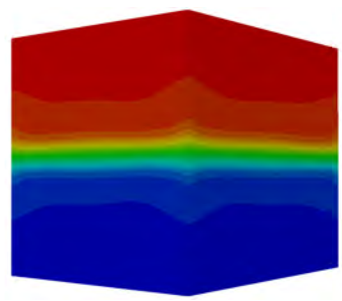

(b) Vertical displacement contour when node 'R' displacement is 0.032 mm.

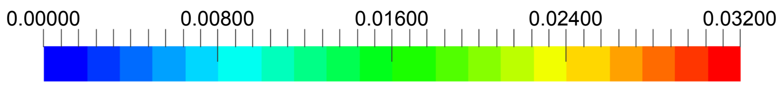

Figure 5.64. Vertical displacement (u_y) contours obtained for the 3D image-based non-local analysis of a cube with 6 spherical inclusions of different diameters. Units:mm. Results shown for the SBFEM unsmoothed mesh in figure 5.62b.

The stress contours in figure 5.65 exemplify the damage induced softening in the specimen. The contour plot in figure 5.65a is captured when the model registered the maximum load therefore this contours show higher stress levels compared to the contour in figure 5.65b which is reflective of the softening stage of the analysis.

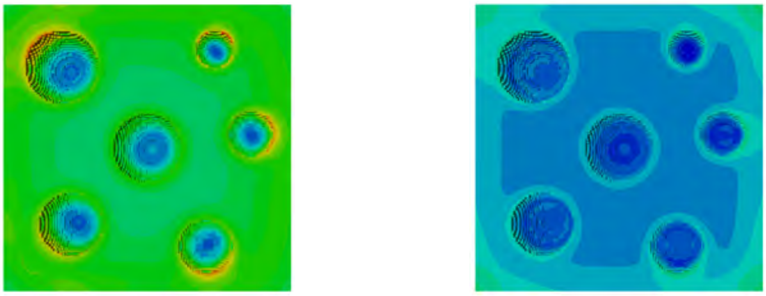

(a) Von Mises stress contour when node ’R’ displacement is 0.0097 mm.

(b) Von Mises stress contour when node ’R’ displacement is 0.032 mm.

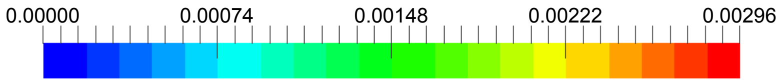

Figure 5.65. Von Mises stress contours obtained for the 3D image-based non-local analysis of a cube with 6 spherical inclusions of different diameters. Units:(GPa). Results shown for the SBFEM unsmoothed mesh in figure 5.62b.

The damage profiles in figures 5.66a-5.66c show the gradual development of damage. Damage first appears between the larger inclusions and then gradually moves towards the smaller inclusions before engulfing the whole section causing the cube to fail.

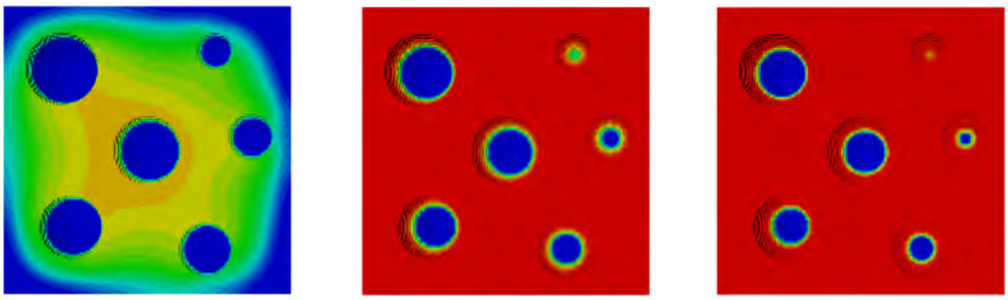

(a) Damage contour when node ’R’ displacement is 0.0097 mm.

(b) Damage contour when node ’R’ displacement is 0.032 mm.

(c) Damage contour when node ’R’ displacement is 0.19 mm.

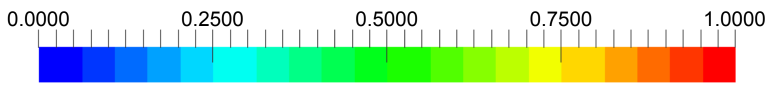

Figure 5.66. Damage (ω) contours obtained for the 3D image-based non-local analysis of a cube with 6 spherical inclusions of different diameters. Results shown for the SBFEM unsmoothed mesh in figure 5.62b.

The final deformed shape of the specimen at the end of the analysis is as shown in figure 5.67. For better visualisation the deformation is magnified by 100.

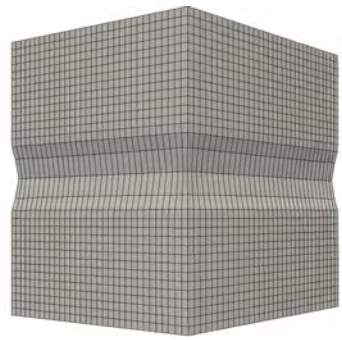

Figure 5.67. Deformed shape of the specimen obtained for the 3D image-based non-local analysis of a cube with 6 spherical inclusions of different diameters. Results shown for the SBFEM unsmoothed mesh in figure 5.62b.

5.8.6 X-ray CT image generated 3D concrete cube

This example simulates the behaviour of a 3D concrete cube obtained by X-ray CT images. The images are courtesy of Huang et al. [490] where meso-scale fracture modelling is investigated.

As shown in figure 5.68 the dimensions of the cube is set to $100 \times 100 \times 100$ mm. The boundary conditions adopted in the analysis is such that the top and the bottom faces are agitated by a displacement U whilst one corner of the cube is restrained in horizontal movement to avoid rigid body motions.

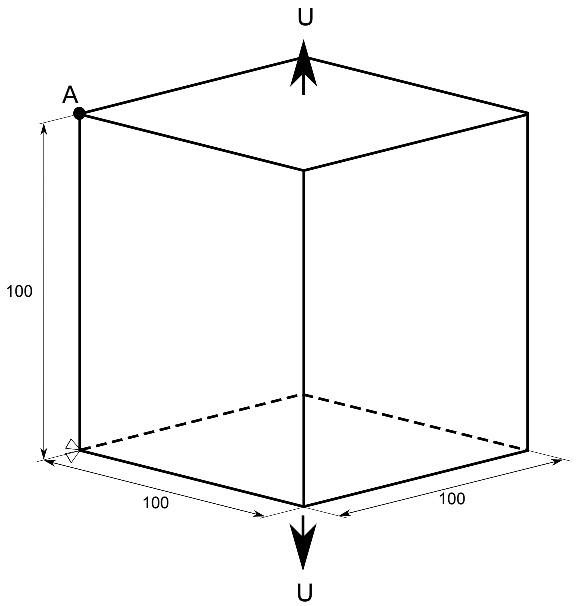

Figure 5.68. Specimen dimensions (mm) and boundary conditions adopted in the 3D X-ray CT image-based non-local analysis of concrete specimen.

The cube consists of aggregates of varying sizes ranging from approximately 4 mm to 16 mm. The specimen is considered to have material properties as given in table 5.8. The constituents of the cube consist of mortar and the aggregate. Mortar is considered weaker of the two material and thus undergo damage, whereas the aggregate on the other hand is assumed not to undergo any material deterioration. The damage evolution is in accordance with the exponential damage model given in equation (5.3). The equivalent strain criteria for non-local averaging is considered with reference to Mazars formulation given in equation (5.5).

	Aggregate	Matrix
Young's modulus (GPa)	35	30
Poisson's ratio	0.2	0.2
Non-local equivalent strain	N/A	Mazars, refer equation (5.5)
Damage initiation threshold	N/A	0.124×10^{-4}
Non-local length (mm)	N/A	5
Damage evolution law	N/A	Exponential, refer equation (5.3)
Residual stress parameter	N/A	0.999
Softening rate parameter	N/A	500

Table 5.8. Material properties and damage parameters adopted in the 3D X-ray CT image-based non-local analysis of concrete specimen.

The non-local length is considered as 5 mm with non-local weighting considered according to equation (5.2). The non-local length is considered as 5 mm assuming the maximum particle size of mortar as 1.85 mm with reference to [303]. The damage evolution is as per the softening model given in equation (5.3). Considering the above damage parameters the behaviour of the damage evolution function is shown in figure 5.69.

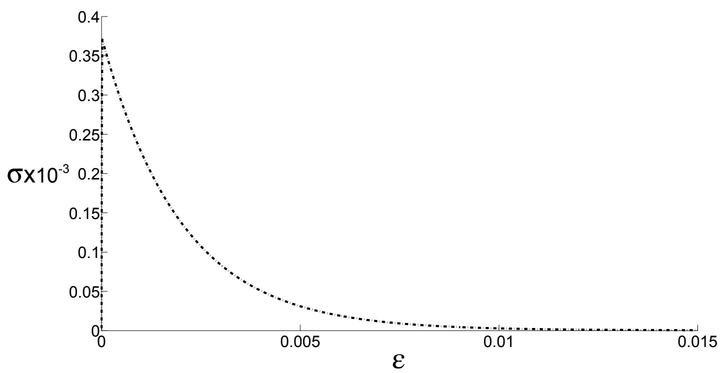

Figure 5.69. 1D element stress (GPa) vs strain profile considered in the 3D X-ray CT image-based non-local analysis of concrete specimen. The damage evolution is with respect to the softening law in equation (5.3).

The meshes considered in the analysis consists of elements with minimum mesh size 1.56 mm (1 voxel), and a maximum mesh size of 3.125 mm (2 voxels) and 6.25 mm (4 voxels) for the fine mesh and the coarse mesh, respectively. Figure 5.70 depict the the two meshes automatically generated by the image-based octree mesh generation algorithm. The finer mesh consists of 72,160 cells that contribute to 519,552 DOFs. Compared to the original $64 \times 64 \times 64$ voxelized image, the total number of cells generated is approximately around 27.5% of the total number of voxels in the image. Out of the 72,160 cells 0.18% are identified as master cells.

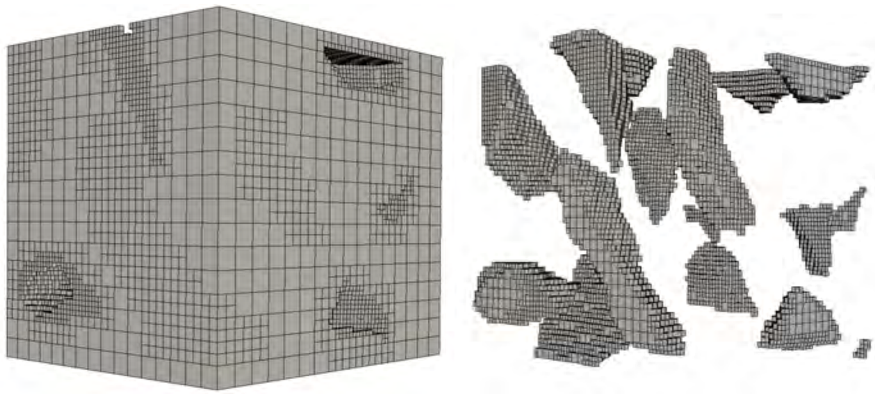

(a) Mesh 1 (coarse mesh) with minimum element size 1.56 mm and maximum element size 6.25 mm.

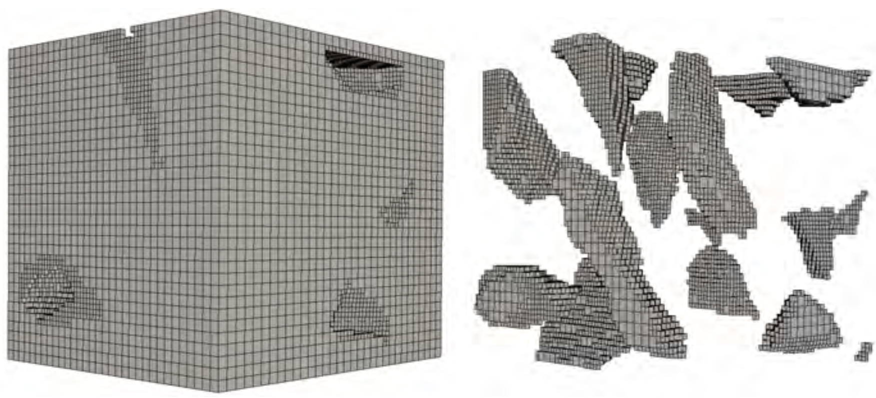

(b) Mesh 2 (fine mesh) with minimum element size 1.56 mm and maximum element size 3.125 mm.

Figure 5.70. Two octree meshes used in the 3D X-ray CT image-based non-local analysis of concrete specimen. Minimum element size of 1.56 mm.

The analysis is run using the modified Newton Raphson method with displacement controlled agitations applied on the top and bottom faces. The initial displacement step is kept to 0.0001 mm. With automatic displacement control the analysis is completed in 1500 iterations. The load-displacement curve produced in the analysis is presented in figure 5.71.

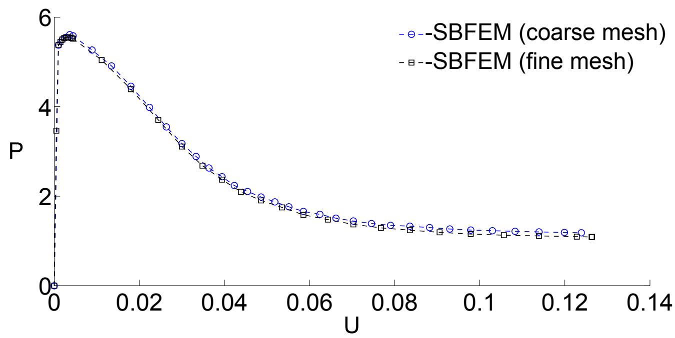

Figure 5.71. Force (kN) vs displacement (mm) output for 3D X-ray CT image-based non-local analysis of concrete specimen. Results are obtained for the two SBFEM unsmoothed meshes shown in figure 5.70.

In regard to figure 5.71 there is good agreement in the force vs displacement curves between the coarse and the fine mesh. The result therefore entails, with the mesh refinement considered from mesh 1 to mesh 2 the overall response of the analysis converges. The simulation exhibits linear behaviour up to a displacement value 0.0006 mm. This displacement induces strains that roughly coincides with the damage initiation threshold strain (ε_0) of 0.124×10^{-4} . As the top and the bottom face displacements reaches a value of 0.0006 mm this then induces a strain in the smallest elements ($1.56 \times 1.56 \times 1.56$ mm) in the mesh very close to ε_0 just prior to damage initiation. At a given cross section of the cube the distribution of mortar to aggregate is approximately 60 to 40. Therefore the load carrying capacity of the concrete block is largely influenced by material properties of the weakest constituent of the concrete matrix (the mortar). With due consideration to the distribution of constituents in the cube, an approximate calculation yields a load of 4 kN at damage initiation. This value is relatable to the simulation attained value of 4.15 kN. Thereon the non-localisation induced hardening helps the concrete cube to attain a peak load of 5.555 kN.

The contour plots below represent contours for displacement (figure 5.72), von Mises stress for mortar (figure 5.73) and aggregates (figure 5.74), and damage evolution (figure 5.75). The contours for displacement, von Mises stress and damage are shown at displacements of 0.00321 mm at node 'A' corresponding to a peak load of 5.555 kN on the top face and just after the peak load for displacement value of 0.019891 mm corresponding to a load of 4.198 kN (refer figure 5.71). In addition to this these load-displacement instances the damage evolution contours contain an extra contour corresponding to the end of the simulation at displacement of 0.1264 mm and load of 1.08 kN.

The displacement contours in figures 5.72a and 5.72b show clear evidence of the non-linear distribution of displacement within the cube.

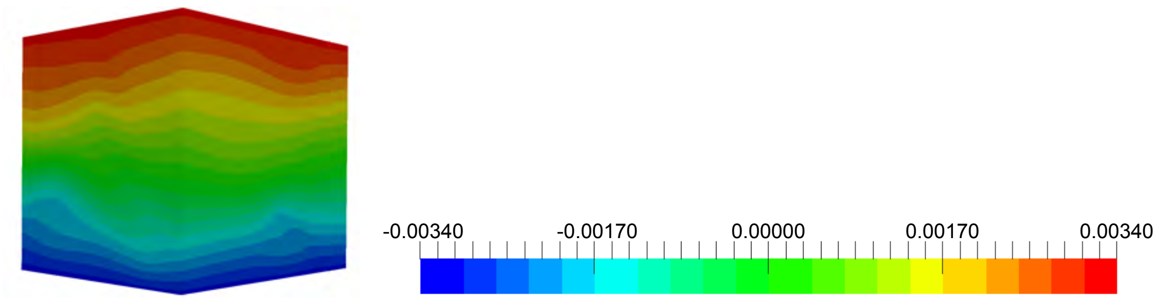

(a) Vertical displacement contour when node 'A' displacement is 0.00321 mm.

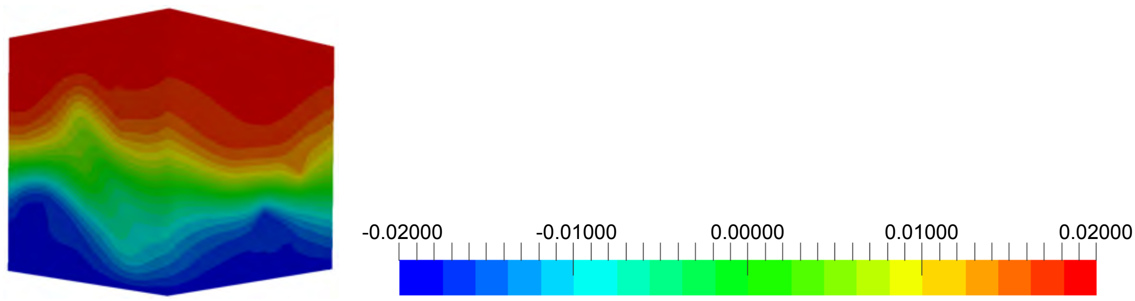

(b) Vertical displacement contour when node 'A' displacement is 0.019891 mm.

Figure 5.72. Vertical displacement (u_y) contours obtained for the 3D X-ray CT image-based non-local analysis of concrete specimen. Units:mm. Results are obtained for the mesh shown in figure 5.70b.

The green-yellow shade of higher displacement contours appear to be expanding in width moving from left vertical edge to the central vertical edge of the cube. This is due to the higher concentration of aggregates around the central vertical edge as evident in figures 5.74a and 5.74b. The higher concentration of the aggregates induce localisation of strains within the mortar that in turn induces damage to initiate within these regions.

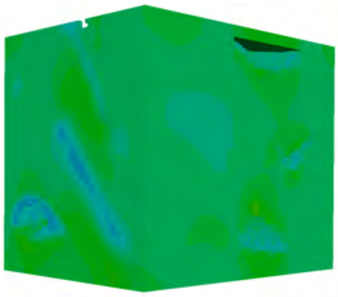

(a) Von Mises stress contour when node ‘A’ displacement is 0.00321 mm.

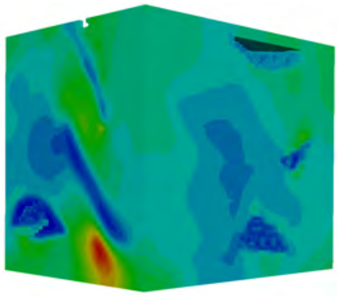

(b) Von Mises stress contour when node ‘A’ displacement is 0.019891 mm.

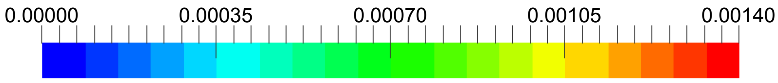

Figure 5.73. Von Mises stress contours for mortar and aggregate obtained for the 3D X-ray CT image-based non-local analysis of concrete specimen. Units:GPa. Results are obtained for the mesh shown in figure 5.70b.

(a) Von Mises stress contour when node ‘A’ displacement is 0.00321 mm.

(b) Von Mises stress contour when node ‘A’ displacement is 0.019891 mm.

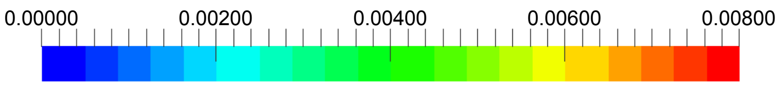

Figure 5.74. Von Mises stress contours for mortar and aggregate obtained for the 3D X-ray CT image-based non-local analysis of concrete specimen. Units:GPa. Results are obtained for the mesh shown in figure 5.70b.

The damage contours show the initial development of damage (see figure 5.75a) in the central portion of the cube and thereafter the damage profile migrates to a wider width within the cube (see figures 5.75b and 5.75c).

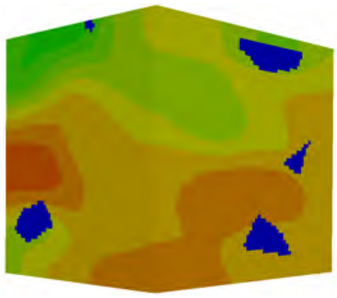

(a) Damage contour when node ‘A’ displacement is 0.00321 mm.

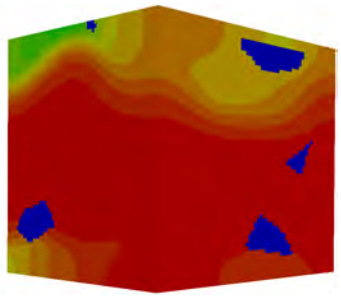

(b) Damage contour when node ‘A’ displacement is 0.019891 mm.

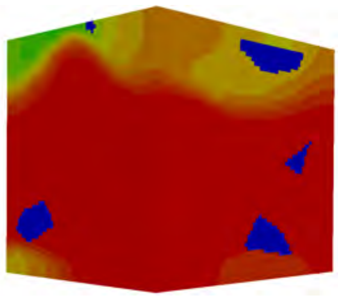

(c) Damage contour when node ‘A’ displacement is 0.1264 mm.

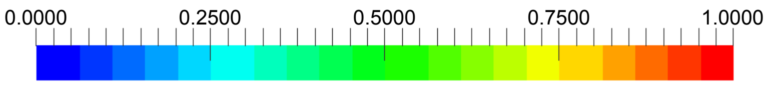

Figure 5.75. Damage (ω) contours obtained for the 3D X-ray CT image-based non-local analysis of concrete specimen. Results are obtained for the mesh shown in figure 5.70b.

The final deformed shape magnified by 25 is shown in figure 5.76.

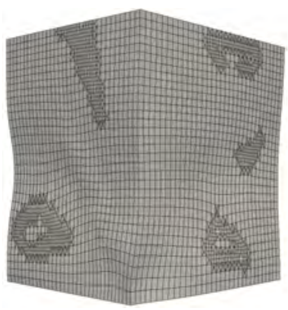

Figure 5.76. Deformed shape of the specimen obtained for the 3D X-ray CT image-based non-local analysis of concrete specimen. Results are obtained for the mesh shown in figure 5.70b.

5.9 Conclusions

This chapter details a novel enhanced image-based damage analysis technique. Throughout the formulation the focus is centred on full automation of the overall damage analysis process. The quadtree and octree meshing technique aids in the development of an automatic yet simple framework to conduct damage analyses using the SBFEM. Hanging nodes created in the mesh generation are handled by the scaled boundary finite element method without any additional meshing requirement.

For damage analysis the effect of mesh smoothing in quadtree proves not to be essential due to the non-localisation of the process zone. An investigation into the effects of strain non-localisation on multi material interfaces contributes to the realisation of the detrimental effect of non-localisation over different material that are composed of largely contrasting material properties.

The numerical simulations build in complexity to exemplify the efficiency of the framework. The last example (refer section 5.8.6) is an epitome to this capability with over half a million DOFs. Computational effort and time are significantly reduced by use of a balanced mesh and storing only the unique cell patterns (master cells) data. This chapter also focuses on and demonstrates the practical application of the technique with 2D and 3D material microstructures modelled in their entirety.

As a continuation of this work the SBFE in elsato-plastic analysis [73] can be easily leveraged into an image-based approach for elsato-plastic damage analysis. The proposed approach can also be extended to incorporate higher-order elements without additional difficulty. The algorithm will also be able to accommodate complex problems in crack propagation [543] and adaptive modelling [544]. Furthermore, the applications can extend to analysis of complex non-linear problems such as the fracture modelling of concrete [542, 545, 546].

Chapter 6

Two Dimensional Automatic Image-Based Adaptive Damage Analysis (AIBADA) with the Scaled Boundary Finite Element Method

6.1 Introduction

In this chapter, a novel quadtree based adaptive damage analysis technique within the framework of the Scaled Boundary Finite Element Method (SBFEM) is detailed. A simple yet effective, damage parameter (ω) based adaptive approach, suitable for modelling highly localized damage zones is introduced in this work. The main focus is to improve the efficiency of the SBFEM two dimensional (2D) formulation in damage analysis by reducing the requirement for mesh refinement beyond the Damage Process Zone (DPZ).

The standard continuum theory for damage analysis consisting of softening stress-strain laws [547] suffers from pathological sensitivity to the spatial discretization. In this light, mesh refinement can cause the energy dissipated by the numerical model to decrease and tend to extremely low values. As a remedy, a regularized model based on generalized continuum theories [250, 501, 548, 549] is used in this work to prevent the localization of strain into an arbitrarily small volume. The integral-type regularisation model used here consists of a continuously differentiable displacement field. High strains accumulate in narrow bands, with a continuous transition to much lower strains in the neighbouring parts of the domain. These narrow bands correspond to the DPZs. The DPZs are largely responsible for the overall behaviour of the simulation. Although non-local damage models enable continuous distribution of strains, it is still necessary to use a sufficiently fine mesh in the DPZ [467, 477, 479] to resolve narrow bands of highly localized strains. Beyond the narrow bands of the DPZ a relatively coarse mesh can be maintained for the efficiency of the computational process. Furthermore, in most cases the localisation pattern is not known in advance. Therefore it is extremely difficult to manually construct a suitably refined mesh around an assumed DPZ. An adaptive procedure becomes an attractive technique to reduce the number of DOFs by mapping and refining the exact locations of these DPZs. The whole process then becomes an automatic technique with much improved computational efficiency.

In numerical simulations a topological map, commonly referred to as a 'mesh', is produced by spatial decomposition of the problem domain. The mesh consists of elements and nodes. The elements are connected by the nodes. A set of algebraic equations which approximate the partial differential equations that describe the system are solved to estimate the values of the unknowns at nodal points. The accuracy of the solutions are determined by the shape of the elements and the spacing of the nodal locations. To improve the accuracy of the solutions four distinct varieties of refinement techniques are typically employed in an adaptive mesh refinement:

1. h-refinement - technique based on reducing the spacing of the nodes [422–427];

2. p-refinement - technique based on increasing the order of the polynomial approximation [428];

3. hp-refinement - a combination of both h and p refinement procedures above [429–431]; and

4. r-refinement - technique based on modifying the location of the nodes considering the local error [420,421].

A h-refinement can be achieved by either uniformly or adaptively. A uniform refinement employs a technique where the nodal spacing in the entire domain is reduced whereas an adaptive refinement refines the mesh locally. A uniform mesh refinement is found to be computationally more expensive than an adaptive refinement. Therefore in this work the adaptive h-refinement technique is employed with the quadtree mesh generation technique. The quadtree mesh refinement technique consists of terminating grids [44] whereas other refinement techniques may have non-terminating or continuous grids (refer figure 6.1).

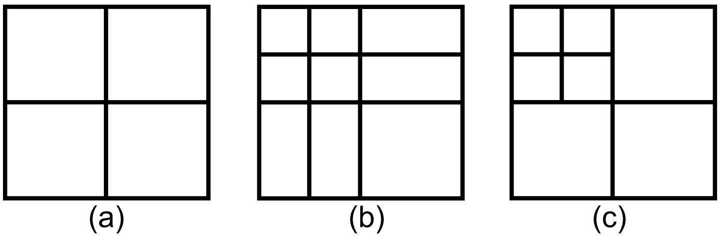

Figure 6.1. Schematic illustration of different refinement techniques: (a) uniform refinement, (b) adaptive refinement without terminating grids, and (c) adaptive refinement with terminating grids - quadtree decomposition.

In a conventional adaptive procedure, a transfer of data structures, i.e. displacements and internal variables, from the old mesh to the new mesh is performed. Thereafter, the old discretization is made redundant and the new mapped configuration is analysed at a constant value of the loading parameter at which a new mesh was generated. A global equilibrium is then sought through internal equilibrium iterations. Thereon, the next load increment is added and a global equilibrium is sought. The process repeats till the requirement for refining the mesh is realised again. In principle, for a purely damage variable based adaptive procedure the conventional transfer of data structures and continuing the computation from the load step from which the mesh refinement algorithm was initiated will not yield satisfactory results. This is because the solution scheme can take different failure trajectories depending on the mesh configuration the analysis is run on. The underlying reason for this observation is due to a certain degree, regularised integral-type formulations are susceptible to variations in the outputs due to the changes in the mesh configurations [487]. This was identified in the numerical examples in chapters 3 and 4. An alternative to avoid the transfer of data structures is to restart the analysis from the initial state after the new discretization [550, 551]. Since the analysis has to now begin from the first load step there is a loss in efficiency. Therefore, the adaptive mesh refinement technique implemented in this work consists of control parameters to improve the efficiency by controlling the frequency of mesh refinement, history variables that store behaviour of past performance for future adaptive iterations, a damage variable based re-meshing criterion and a mesh generator interface. A detailed description of the process can be found in section 6.5.

In this work quadtree decomposition is adopted as a mesh generator interface. A complete detailed description of the quadtree decomposition can be found in section 5.2.1 of chapter 5.

The quadtree structure [552–555] is a hierarchical mesh structure where the parent element is recursively divided into four children. The technique is ideal for adaptive refinement as localised refinement can be adopted with ease. This creates fewer elements which in turn produces a smaller number of Degrees Of Freedom (DOF). The only downside to this technique is the creation of hanging nodes (nodes 12,13,17 and 18) as shown in figure 6.2.

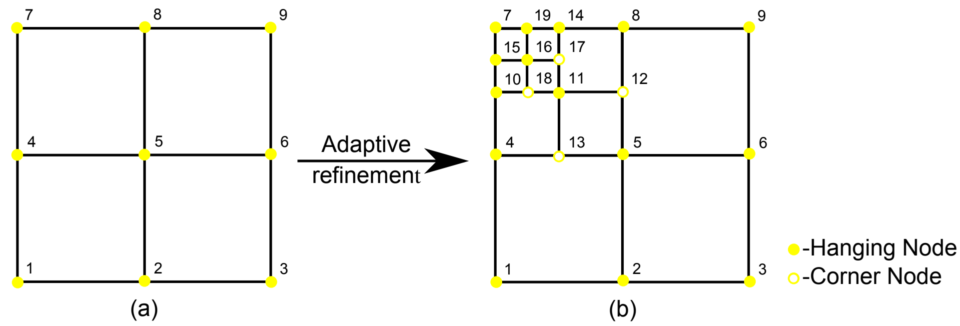

Figure 6.2. Hanging nodes created in adaptive mesh refinement in quadtree decomposition.

These hanging nodes warrant specialised treatments as conventional shape functions are nonconforming at the boundary of these elements [556]. The nonconformity creates displacement incompatibility between the adjacent elements. A few methods are proposed in the literature to resolve this issue. These methods include:

- constraining the displacements at the hanging nodes through Lagrange multipliers or penalty methods [557];
- constraining the hanging nodes to the corner nodes and adding temporary triangular or rectangular elements [539];
- use of special transitional finite elements for the cells [556, 558, 559];
- modification to the shape functions [556]; and
- development of polygonal elements [560].

However, the SBFEM is flexible to be formulated on polygons with arbitrary number of sides [204, 205]. This eliminates the need for any of the treatments outlined above. The SBFEM polygonal formulation in 2D is first explained and utilised in chapter 3 section 3.4.

The SBFEM is a semi-analytical method invented to solve boundary value problems by Song and Wolf [199]. To handle hanging nodes quadtree cells are treated as generic polygons regardless of the presence of hanging nodes. This then requires no modification to the structure of the quadtree mesh. Thus, the efficiency of the quadtree data storage and retrieval can be exploited without any compromises.

In this work accurate representation of the DPZ is achieved by localised refinement of the damaged zones purely through the consideration of the damage variable (ω). The h-adaptive mesh refinement technique is utilised with a quadtree meshing algorithm. The quadtree algorithm enables rapid mesh transition between the DPZ and the rest of the model. The meshing procedure is constrained by the 2:1 rule. This 2:1 rule in quadtree meshing limits the maximum ratio of the size of adjacent quadtree cells to 2. This reduces the number of patterns of cells as described in section 5.2.1 of chapter 5. This rule is favourable as this allows pre-computation of element stiffness which leads to an increase in the efficiency of the analysis.

In this chapter, first an overview of the integral-type damage model is presented in section 6.2. Next an overview of the 2D SBFEM formulation is presented in section 6.3. The implicit damage formulation in SBFEM is documented in section 6.4. Section 6.5 introduces the novel damage variable based adaptive quadtree mesh decomposition technique. Penultimately, in section 6.6, the integral-type continuum damage model is used in tandem with the adaptive approach explained herein to model four benchmark concrete failure experiments and simulations. These problems highlight the computational efficiency of the output generated via the automatic adaptive mesh compared to that of a uniform conventional mesh. Conclusions, remarks and opportunities for future studies are stated in section 6.7.

6.2 Damage model for concrete

An outline of the damage model for concrete is given in this section. For a detailed explanation refer chapter 3 section 3.2.

6.2.1 Isotropic damage model

The stiffness degradation in isotropic damage models is assumed to decrease proportionally in different directions. Therefore, the Young's modulus and the Poisson's ratio can be considered to contribute to the degradation of stiffness. Herein, the Poisson's ratio remains constant for the purpose of simplicity [34] of the formulation.

6.2.2 Evolution of damage

Two major streams of damage evolution functions can be found in the literature, linear softening models and exponential softening models. A detailed description of these models can be found in chapter 3 section 3.2. In the numerical simulations in section 6.6 two exponential softening models that describe the softening behaviour with respect to the equivalent strain parameter are considered.

The exponential model below is extracted from [478] and is defined as

$$\omega = \begin{cases} 0 & \text{if } \kappa \leq \varepsilon_0, \\ 1 - \frac{\varepsilon_0}{\kappa} \exp\left(\frac{-(\kappa - \varepsilon_0)}{\varepsilon_f - \varepsilon_0}\right) & \text{if } \kappa > \varepsilon_0. \end{cases} \tag{6.1}$$

in which $\varepsilon_0 = f_t/\mathrm{E}$ is the limit elastic strain under uniaxial tension, f_t is the tensile strength, E is the Young's modulus, and ε_f is a parameter affecting the ductility of the response and related to the fracture energy. The area under the uniaxial stress-strain curve, $g_f = f_t(\varepsilon_f - \varepsilon_0/2)$, has the meaning of energy dissipated per unit volume of totally damaged material under uniaxial tension. The second variant of the exponential softening model given below is extracted from [481]

$$\omega = \begin{cases} 0 & \text{if } \kappa \leq \varepsilon_0, \\ 1 - \frac{\varepsilon_0}{\kappa} \left(1 - \alpha + \alpha \times \exp\left(-\beta \left(\kappa - \varepsilon_0\right)\right)\right) & \text{if } \kappa > \varepsilon_0, \end{cases} \tag{6.2}$$

in which α and β are two parameters to control the slope of the softening branch of the curve.

Amongst the numerous techniques described in chapter 3 section 3.2 for calculating the equivalent strain parameter $\tilde{\varepsilon}$, two widely used definitions of equivalent strain for concrete are employed in this work.

The modified von Mises definition proposed by De Vree et al. [497] is as follows

$$\tilde{\varepsilon} = \frac{k-1}{2k(1-\nu)} I_1^{\varepsilon} + \frac{1}{2k}\sqrt{\frac{(k-1)^2}{(1-2\nu)^2}(I_1^{\varepsilon})^2 + \frac{12k}{(1+\nu)^2} J_2^{\varepsilon}}, \tag{6.3}$$

in which k is normally set equal to the ratio of the compressive uniaxial strength and the tensile uniaxial strength, ν is the Poisson's ratio, I_1^{ε} is the first invariant of the strain vector defined as

$$I_1^{\varepsilon} = \varepsilon_{xx} + \varepsilon_{yy} + \varepsilon_{zz}, \tag{6.4}$$

and J_2^{ε} is the second invariant of the deviatoric strain vector defined in equation (6.5).

$$J_2^{\varepsilon} = \frac{1}{3}[\varepsilon_{xx}^2 + \varepsilon_{yy}^2 + \varepsilon_{zz}^2 - \varepsilon_{xx}\varepsilon_{yy} + \varepsilon_{yy}\varepsilon_{zz} + \varepsilon_{zz}\varepsilon_{xx} + 3(\varepsilon_{xy}^2 + \varepsilon_{yz}^2 + \varepsilon_{zx}^2) \tag{6.5}$$

The second equivalent strain definition considered in this analysis is a modification to equation (6.3) above. This variant of the modified von Mises definition (refer equation (6.6)) found in [561] has demonstrated an ability to better emulate and represent damage patterns observed in notched beams.

$$\tilde{\varepsilon} = \frac{k-1}{2k(1-2\nu)} I_1^{\varepsilon} + \frac{1}{2k}\sqrt{\frac{(k-1)^2}{(1-2\nu)^2}(I_1^{\varepsilon})^2 + \frac{6k}{(1+\nu)^2} J_2^{\varepsilon}}. \tag{6.6}$$

6.2.3 Integral-type non-local damage models

In non-local integral-type models the stress at a certain point in a domain depends not only on the state variables at that point but also on the distribution of state variables over the whole body or in a finite neighbourhood of the point under consideration.

In this work equivalent strain $\tilde{\varepsilon}$ calculated through either equation (6.3) or equation

(6.6) is replaced by its non-local counterpart obtained by weighted averaging over a spatial neighbourhood of each point under consideration. The weighted averaging procedure is detailed in section 3.2.4.

The commonly used distribution functions are either the Gauss distribution (refer equation (6.7)) or the bell-shaped truncated quartic polynomial function (refer equation (6.8)). The Gauss distribution function in [250], l represents the internal length of the non-local continuum

$$\alpha_0(r) = \exp\left[-0.5 \times \left(\frac{d}{l}\right)^2\right]. \tag{6.7}$$

The bell-shaped distribution function by [477] is as follows

$$\alpha_0(r) = \left\langle 1 - \frac{r^2}{R^2} \right\rangle^2, \tag{6.8}$$

in which R is the interaction radius related to the internal length and denotes the largest distance of point ς that affects the non-local average at point x. However, since the Gauss function 6.7 is unbounded its interaction radius $R = \infty$.

6.3 Overview of scaled boundary finite element method

In this section, a summary of the 2D SBFEM for elastic problems is presented. A comprehensive derivation of the method and detailed explanations are presented in chapter 3 section 3.4. The SBFEM allows discretization with arbitrary sided polygons subjected to a scaling requirement under a unified formulation. This geometric requirement is easily satisfied by sub-structuring i.e. dividing the polygon into smaller subdomains. This flexibility in formulation is most advantageous in the adaptive mesh refinement technique employed in this chapter.

6.3.1 Scaled boundary finite element equation

Formulation of the SBFEM in 2D is demonstrated with reference to figure 6.3. The subdomain is represented by scaling a defining curve S relative to a scaling centre. The only requirement for the location of the scaling centre is that the entire subdomain boundary has to be visible from the scaling centre. A normalised radial coordinate ξ is defined such that at the scaling centre $\xi = 0$ and $\xi = 1$ at the boundary of the polygon. The edges of the polygon boundary is discretised using one-dimensional finite elements with local coordinate η. Similar to the FEM, η varies form $-1 \leq \eta \leq 1$. To interpolate the results to the nodes one-dimensional Lagrange shape functions are used in this study.

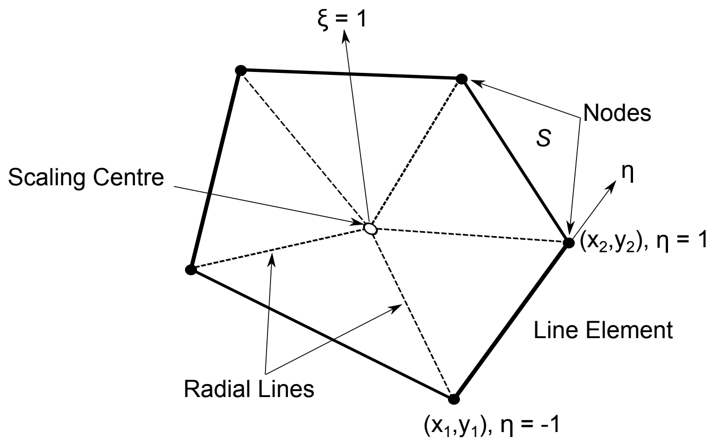

Figure 6.3. Concept of the SBFEM for an arbitrary polygon.

If a quadtree cell with hanging nodes is idealised as a polygon with m nodes, the Cartesian coordinates within a line sector (see figure 6.3) on the boundary can be established through

$$\mathrm{r}(\xi,\eta) = \xi \mathbf{N}_{\mathrm{u}}(\eta)\,\mathbf{r}_{\mathrm{b}}, \tag{6.9}$$

where $\mathbf{N}_u(\eta)$ and $\mathbf{r}_{\mathrm{b}}$ are vectors of shape functions and nodal coordinates, respectively. These $\mathbf{N}_u(\eta)$ and $\mathbf{r}_b$ vectors are represented as

$$\mathbf{N}_u(\eta) = \begin{bmatrix} N_1 & 0 & N_2 & 0 & ... & N_{\mathrm{m}} & 0 \\ 0 & N_1 & 0 & N_2 & ... & 0 & N_{\mathrm{m}} \end{bmatrix}, \tag{6.10}$$

$$\mathbf{r}_b = \begin{bmatrix} x_1 & y_1 & x_2 & y_2 & \dots & x_\mathrm{m} & y_\mathrm{m} \end{bmatrix}^\mathrm{T}. \tag{6.11}$$

The displacements of any point (ξ, η) inside the domain can then be interpolated by

$$\mathbf{u}(\xi, \eta) = \mathbf{N}_\mathrm{u}(\eta)\mathbf{u}(\xi), \tag{6.12}$$

in which $\mathbf{u}(\xi)$ is the displacement along the radial lines calculated from the equilibrium condition of a polygon.

The equilibrium condition in a polygon is formulated either through the principle of virtual work [562] or by the method of weighted residuals [14]. Both formulations lead to the scaled boundary finite element equation in displacement given by

$$\mathbf{E}_0\xi^2\mathbf{u}(\xi)_{,\xi\xi} + \left(\mathbf{E}_0 + \mathbf{E}^\mathrm{T}{}_1 + \mathbf{E}_1\right)\xi\mathrm{u}(\xi)_{,\xi} - \mathbf{E}_2\mathbf{u}(\xi) = 0, \tag{6.13}$$

where the coefficient matrices $\mathbf{E}_0$, $\mathbf{E}_1$ and $\mathbf{E}_2$ for each line element are as follows

$$\mathrm{E}_0 = \int_{-1}^{+1} \mathrm{B}_1^\mathrm{T}\mathbf{D}\mathrm{B}_1|\mathbf{J}|d\eta, \tag{6.14a}$$

$$\mathrm{E}_1 = \int_{-1}^{+1} \mathrm{B}_2^\mathrm{T}\mathbf{D}\mathrm{B}_1|\mathbf{J}|d\eta, \tag{6.14b}$$

$$\mathrm{E}_2 = \int_{-1}^{+1} \mathrm{B}_2^\mathrm{T}\mathbf{D}\mathrm{B}_2|\mathbf{J}|d\eta, \tag{6.14c}$$

where $\mathbf{D}$ is the material constitutive matrix and $\mathbf{B}_1$ and $\mathbf{B}_2$ are the two strain-displacement matrices. $|\mathbf{J}|$ is the determinant of the Jacobian used in coordinate transformation. Once the coefficient matrices are computed for each line element by discretising the polygon boundary they are then assembled in a way similar to the finite element method [14]. The strain-displacement matrices and $\mathbf{B}_1$ and $\mathbf{B}_2$ are as follows

$$\mathbf{B}_1 = \frac{1}{|\mathbf{J}|}\begin{bmatrix} \mathbf{N}(\eta)_{,\eta}\mathbf{y}_\mathrm{b} & 0 \\ 0 & -\mathbf{N}(\eta)_{,\eta}\mathbf{x}_\mathrm{b} \\ -\mathbf{N}(\eta)_{,\eta}\mathbf{x}_\mathrm{b} & \mathbf{N}(\eta)_{,\eta}\mathbf{y}_\mathrm{b} \end{bmatrix}\mathbf{N}_\mathrm{u}(\eta), \tag{6.15a}$$

$$\mathbf{B}_2 = \frac{1}{|\mathbf{J}|}\begin{bmatrix} -\mathbf{N}(\eta)\mathbf{y}_\mathrm{b} & 0 \\ 0 & \mathbf{N}(\eta)\mathbf{x}_\mathrm{b} \\ \mathbf{N}(\eta)\mathbf{x}_\mathrm{b} & -\mathbf{N}(\eta)\mathbf{y}_\mathrm{b} \end{bmatrix}\mathbf{N}_\mathrm{u}(\eta)_{,\eta}, \tag{6.15b}$$

where $\mathbf{N}(\eta)$ is the vector of the shape functions of the line elements, and $\mathbf{x}_\mathrm{b}$ and $\mathbf{y}_\mathrm{b}$ are the nodal Cartesian coordinates in x and y directions of the line elements, respectively.

$$\mathbf{N}(\eta) = \begin{bmatrix} N_1 & N_2 & N_3 & \dots & N_\mathrm{m} \end{bmatrix}, \tag{6.16a}$$

$$\mathbf{x}_\mathrm{b} = \begin{bmatrix} x_1 & x_2 & x_3 & \dots & x_\mathrm{m} \end{bmatrix}^\mathrm{T}, \tag{6.16b}$$

$$\mathbf{y}_\mathrm{b} = \begin{bmatrix} y_1 & y_2 & y_3 & \dots & y_\mathrm{m} \end{bmatrix}^\mathrm{T}. \tag{6.16c}$$

With reference to [562] the Jacobian matrix used in coordinate transformation is

$$\mathbf{J} = \begin{bmatrix} \mathbf{N}(\eta)\mathbf{x}_\mathrm{b} & \mathbf{N}(\eta)\mathbf{y}_\mathrm{b} \\ \mathbf{N}(\eta)_{,\eta}\mathbf{x}_\mathrm{b} & \mathbf{N}(\eta)_{,\eta}\mathbf{y}_\mathrm{b} \end{bmatrix}, \tag{6.17}$$

with determinant $\mathbf{J}$ as

$$|\mathbf{J}| = (\mathbf{N}(\eta)\mathbf{x}_\mathrm{b})(\mathbf{N}(\eta)_{,\eta}\mathbf{y}_\mathrm{b}) - (\mathbf{N}(\eta)\mathbf{y}_\mathrm{b})(\mathbf{N}(\eta)_{,\eta}\mathbf{x}_\mathrm{b}). \tag{6.18}$$

To obtain the solution for equation (6.13), it is transformed into a first order differential equation by introducing a variable $\chi(\xi)$

$$\chi(\xi) = \begin{bmatrix} \mathbf{u}(\xi) & \mathbf{q}(\xi) \end{bmatrix}^{\mathrm{T}}, \tag{6.19}$$

where the analytical functions related to the internal nodal forces in the polygon are represented by $\mathbf{q}(\xi)$. The second order differential equation in equation (6.13) now transforms into

$$\xi\chi(\xi)_{,\xi} = \mathbf{Z}\chi(\xi). \tag{6.20}$$

The Hamiltonian matrix $\mathbf{Z}$ is

$$\mathbf{Z} = \begin{bmatrix} \mathbf{E}_0^{-1}\mathbf{E}_1^{\mathrm{T}} & -\mathbf{E}_0^{-1} \\ -\mathbf{E}_2 + \mathbf{E}_1\mathbf{E}_0^{-1}\mathbf{E}_1^{\mathrm{T}} & -\mathbf{E}_1\mathbf{E}_0^{-1} \end{bmatrix}. \tag{6.21}$$

The Hamiltonian matrix $\mathbf{Z}$ can now be decoupled into pairs of eigenvalues $(-\lambda_i, \lambda_i)$ by considering an eigenvalue decomposition as follows

$$\mathbf{Z}\boldsymbol{\Phi} = \boldsymbol{\Phi}\boldsymbol{\Delta}, \tag{6.22}$$

where $\boldsymbol{\Phi}$ is a transformation matrix with independent column vectors. $\boldsymbol{\Delta}$ is a diagonal matrix with elements corresponding to the eigenvalues for each eigenvector in $\boldsymbol{\Phi}$. $\boldsymbol{\Phi}$ and $\boldsymbol{\Delta}$ are partitioned conformably as

$$\boldsymbol{\Phi} = \begin{bmatrix} \boldsymbol{\Phi}_{\mathrm{n}}^{(u)} & \boldsymbol{\Phi}_{\mathrm{p}}^{(u)} \\ \boldsymbol{\Phi}_{\mathrm{n}}^{(q)} & \boldsymbol{\Phi}_{\mathrm{p}}^{(q)} \end{bmatrix}, \tag{6.23a}$$

$$\boldsymbol{\Delta} = \begin{bmatrix} \boldsymbol{\Delta}_{\mathrm{n}} & \\ & \boldsymbol{\Delta}_{\mathrm{p}} \end{bmatrix}. \tag{6.23b}$$

The diagonal matrix $\boldsymbol{\Delta}$ is sorted in the ascending order of the real parts. $\boldsymbol{\Delta}_{\mathrm{n}}$ and $\boldsymbol{\Delta}_{\mathrm{p}}$

contains the eigenvalues of negative and positive real parts, respectively.

In this work bounded polygons are considered, therefore, only the displacement modes corresponding to Δ_n lead to finite displacements at the scaling centre. Thus, the solution to equation (6.20) considering equation (6.22) is

$$\mathbf{u}(\xi) = \Phi_{\mathrm{n}}^{(u)} \xi^{-\Delta_n} \mathbf{c}, \tag{6.24a}$$

$$\mathbf{q}(\xi) = \Phi_{\mathrm{n}}^{(q)} \xi^{-\Delta_n} \mathbf{c}, \tag{6.24b}$$

where $\mathbf{c}$ denotes the integration constants that depend on the boundary conditions. These constants can be determined by the nodal displacements on the polygon boundary $\mathbf{u}_{\mathrm{b}} = \mathbf{u}(\xi)\,|_{\xi=1}$ as

$$\mathbf{c} = \left(\Phi_{\mathrm{n}}^{(u)}\right)^{-1} \mathbf{u}_{\mathrm{b}}. \tag{6.25}$$

The stiffness matrix of a polygon $\mathbf{K}_{\mathrm{s}}$ can be then formed as

$$\mathbf{K}_{\mathrm{s}} = \Phi_{\mathrm{n}}^{(q)} \left(\Phi_{\mathrm{n}}^{(u)}\right)^{-1}. \tag{6.26}$$

To obtain the complete displacement field, equation (6.24a) is substituted in equation (6.12) to yield

$$\mathbf{u}(\xi,\eta) = \mathbf{N}_{\mathrm{u}}(\eta) \Phi_{\mathrm{n}}^{(u)} \xi^{-\Delta_n} \mathbf{c}. \tag{6.27}$$

The stress field $\sigma(\xi,\eta)$ can now be derived as a product of the the strain ε, linear differential operator matrix $\mathbf{L}$ and the material constitutive matrix $\mathbf{D}$ as

$$\sigma(\xi,\eta) = \mathbf{DL}\varepsilon, \tag{6.28}$$

where

$$\varepsilon = \mathbf{Lu}(\xi,\eta), \tag{6.29}$$

and

$$\mathbf{L} = \mathbf{J}^{-1}\begin{bmatrix} \mathbf{N}(\eta)_{,\eta}\mathbf{y}_{\mathrm{b}} & 0 \\ 0 & -\mathbf{N}(\eta)_{,\eta}\mathbf{x}_{\mathrm{b}} \\ -\mathbf{N}(\eta)_{,\eta}\mathbf{x}_{\mathrm{b}} & \mathbf{N}(\eta)_{,\eta}\mathbf{y}_{\mathrm{b}} \end{bmatrix}\frac{\partial}{\partial\xi}+ \ldots\mathbf{J}^{-1}\begin{bmatrix} -\mathbf{N}(\eta)\mathbf{y}_{\mathrm{b}} & 0 \\ 0 & \mathbf{N}(\eta)\mathbf{x}_{\mathrm{b}} \\ \mathbf{N}(\eta)\mathbf{x}_{\mathrm{b}} & -\mathbf{N}(\eta)\mathbf{y}_{\mathrm{b}} \end{bmatrix}\frac{\partial}{\partial\eta} \tag{6.30}$$

Substituting equation (6.30) into equation (6.28) yields

$$\sigma(\xi,\eta) = \Psi_{\sigma}(\eta)\,\xi^{-\Delta_n-\mathbf{I}}\mathbf{c}, \tag{6.31}$$

where $\Psi_{\sigma}(\eta)$ is the stress mode

$$\Psi_{\sigma}(\eta) = \begin{bmatrix} \Psi_{\sigma_{xx}}(\eta) & \Psi_{\sigma_{yy}}(\eta) & \Psi_{\tau_{xy}}(\eta) \end{bmatrix}^{\mathrm{T}}, \tag{6.32}$$

obtained by

$$\Psi_{\sigma}(\eta) = \mathbf{D}\left(-\mathbf{B}_1(\eta)\Phi_{\mathrm{n}}^{(u)}\Delta_{\mathrm{n}} + \mathbf{B}_2(\eta)\Phi_{\mathrm{n}}^{(u)}\right). \tag{6.33}$$

6.4 Implicit damage formulation in SBFEM

As discussed in detail in section 3.5 of chapter 3, material damage can be assumed to be uniform in one subdomain if the mesh within the DPZ is sufficiently refined. Substituting equation (3.1) into equations (6.14a - 6.14c), we obtain

$$\mathbf{E}_0^{\mathrm{D}} = (1-\omega)\int_{-1}^{+1}\mathbf{B}_1^{\mathrm{T}}\mathbf{D}\mathbf{B}_1|\mathbf{J}|d\eta = (1-\omega)\,\mathbf{E}_0, \tag{6.34a}$$

$$\mathbf{E}_1^{\mathrm{D}} = (1-\omega)\int_{-1}^{+1}\mathbf{B}_2^{\mathrm{T}}\mathbf{D}\mathbf{B}_1\,|\mathbf{J}|\,d\eta = (1-\omega)\,\mathbf{E}_1, \tag{6.34b}$$

$$\mathbf{E}_2^{\mathrm{D}} = (1-\omega)\int_{-1}^{+1} \mathbf{B}_2^{\mathrm{T}}\mathbf{D}\mathbf{B}_2|\mathbf{J}|d\eta = (1-\omega)\,\mathbf{E}_2, \tag{6.34c}$$

where $\mathbf{E}_0^{\mathrm{D}}$, $\mathbf{E}_1^{\mathrm{D}}$ and $\mathbf{E}_2^{\mathrm{D}}$ are substitutes to the elastic coefficient matrices as a result of incorporating material degradation through the damage variable ω of one subdomain.

The degraded stiffness matrix of one subdomain is obtained by factoring out the effect of damage $(1-\omega)$ from the stiffness formulation in equation (6.26). The damage incorporated stiffness of one subdomain $\mathbf{K}^{\mathrm{D}}$ can now be written as

$$\mathbf{K}^{\mathrm{D}} = (1-\omega)\mathbf{K}_{\mathrm{s}}. \tag{6.35}$$

The upside to this formulation is that at each load step, the damage degraded stiffness matrix $\mathbf{K}^{\mathrm{D}}$ of each subdomain can be calculated from the original undamaged stiffness matrix of the subdomain calculated within the preprocessing end of the program. In each load step, only the integration constants $\mathbf{c}$ affected by the boundary conditions (refer equation (6.24a)) are updated according to the displacement field. Thereafter, the stress and strain fields are updated by using equation (6.28) and equation (6.29) respectively.

Finally, assembling the subdomain stiffness matrices leads to the non-linear global equation system

$$\mathbf{K}\mathbf{U} = \mathbf{P} \tag{6.36}$$

in which $\mathbf{K}$ is the global stiffness matrix after considering damage degradation, $\mathbf{U}$ global displacement vector and $\mathbf{P}$ global force vector. To solve this system of equations in equation (6.36) the implicit Newton Raphson method (NRm) with arc-length technique [498] is adopted in this work. For comprehensive details on the solver refer to chapter 3 section 3.5.

6.5 Damage variable ω based adaptive quadtree mesh refinement

The basic concept of this adaptive framework is to adopt a coarse grid initially and then as the simulation progresses to identify and refine regions reaching damage values equal to or greater than the refinement trigger.

The first step of the process is to produce the image-based initial coarse grid $\mathbf{A}_{grid}$. This matrix is formed by taking into consideration the material and geometrical features in the model depending on the colour intensities present in the image. Therefore $\mathbf{A}_{grid}$ represents the initial quadtree mesh configuration obtained through the image decomposition process. The elements in $\mathbf{A}_{grid}$ vary from the user defined smallest element edge size S_{min} to the largest element edge size S_{max}. A typical initial mesh generated around a square inclusion is shown in figure 6.4.

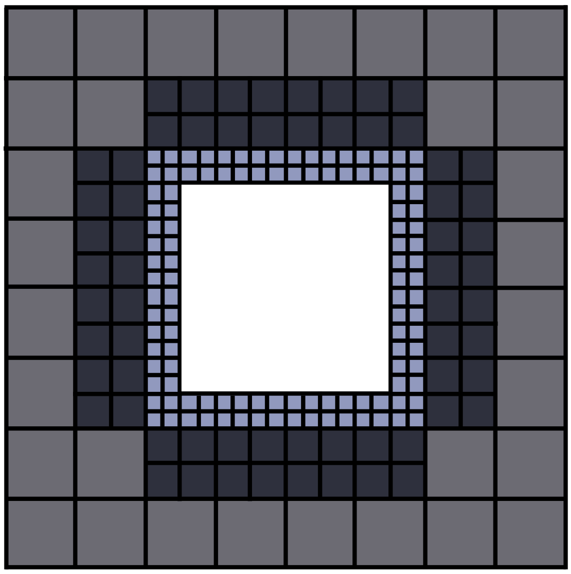

Figure 6.4. Initial coarse mesh around a square inclusion. Element size range from S_{min} to S_{max}. Colour light blue indicate minimum element size S_{min} , colour grey indicate the maximum element size S_{max} and colour dark purple indicate an intermediate element size.

The colour light blue indicates the user defined smallest element size S_{min} and the colour grey indicate the largest user defined element size S_{max}. The colour dark purple is an intermediate element size bridging the gap between S_{min} and S_{max}.

$\mathbf{A}_{grid}$ is the starting point for the adaptive mesh refinement process. Within the adaptive process S_{max} is overwritten by the maximum allowable element edge size S_{max}^{allow}. This variable ensures sufficient elements are produced within the damage process zone. S_{max}^{allow} is governed by the non-local interaction radius R. To achieve affective non-localised results S_{max}^{allow} is kept as a fraction of R such that there are at least four sampling points [487] for regularisation within the domain.

There are two control parameters used in this algorithm. ω_0 controls the damage threshold value triggering further mesh refinement and $\left(D_q\right)$ is the quantifying parameter which governs the percentage of newly damaged elements that is required to trigger mesh refinement. The history variable (N_{ω}^{max}) represents the maximum number of damaged elements $(\omega \geq \omega_0)$ recorded up to the current converged adaptive iteration. The flowchart in figure 6.5 depicts the process of utilizing these parameters with respect to the continuing NR iterations.

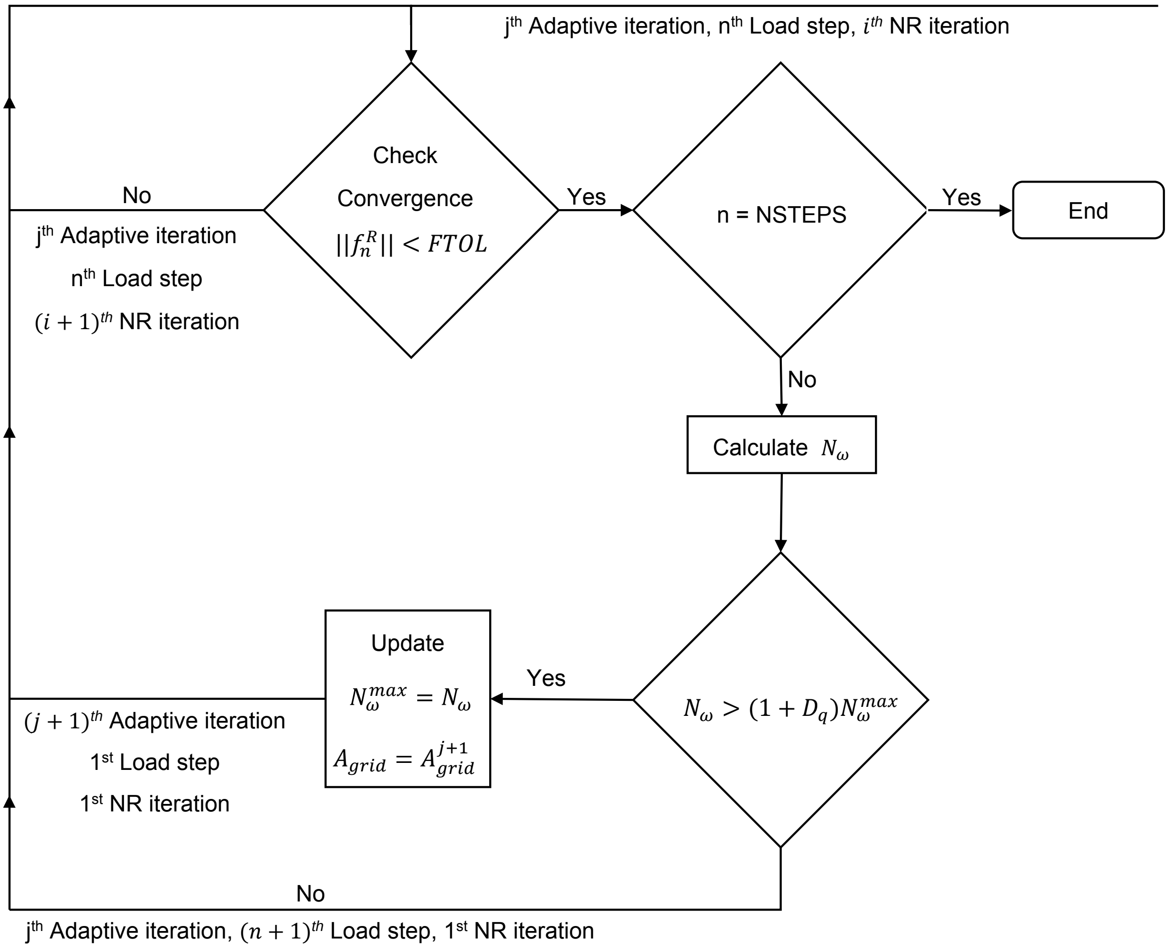

Figure 6.5. Flowchart for the damage parameter ω based adaptive mesh refinement procedure

Upon reaching an equilibrium state $\left|\left|f_n^R\right|\right| < FTOL$ the solution state is updated. Here the $FTOL$ is the convergence tolerance limit which is compared against the the norm of the residual force vector f_n^R corresponding to a given load increment. If the condition is unsatisfied, further iterations within the NR scheme is carried out to obtain an agreeable solution. After passing through $\left|\left|f_n^R\right|\right| < FTOL$, the load step number n is compared against the maximum number of load steps, NSTEPS, if n = NSTEPS the analysis is terminated as the user defined maximum number of load steps has been reached. If n $\neq$ NSTEPS the re-meshing criterion is initiated. First, the number of damaged elements (N_ω) is calculated. The elements that are counted for N_ω require to have their damage value ω equal to or greater than the damage threshold parameter (ω_0). $\mathbf{A}_{grid}$ is then updated to identify the locations of these elements.

Figure 6.6 illustrates the process of updating $\mathbf{A}_{grid}$. Assume the element 'T' marked in red has undergone damage $\omega \geq \omega_0$ and therefore need to be subdivided. In order to trigger mesh refinement a unique decimal value corresponding to the adaptive iteration number 'j' and load step number 'n' is used to overwrite the values at the upper left corner of a damaged element 'T'. It is assumed in this example $S_{min} = 1$ and $S_{max} = 2$.

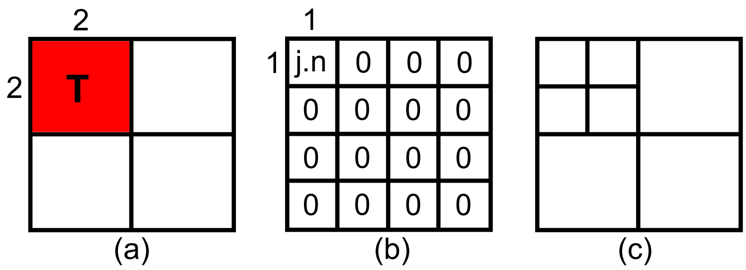

Figure 6.6. Method updating $\mathbf{A}_{grid}$ and the mesh refinement thereafter. (a) Element 'T' marked red assumed damage exceeding the damage threshold parameter (ω_0), (b) substitution of a unique decimal value in the upper left quadrant of the element 'T', and (c) quadtree decomposition of $\mathbf{A}_{grid}$.

In figure 6.6a the element 'T' marked in red is assumed to have undergone damage exceeding the damage threshold parameter (ω_0). Therefore, the upper left quadrant of that element is replaced by a unique decimal value (refer figure 6.6b) corresponding to the adaptive iteration and load step number relevant at the time of identification of the damaged element. The other matrix entries remain zero, as $\mathbf{A}_{grid}$ is initialised to an all zeros matrix. N_ω can now be calculated by summing up the entries in the matrix $\mathbf{A}_{grid}$.

The updated $\mathbf{A}_{grid}$ forms the basis of the automatic quadtree based generation of a new spatial discretization. If $N_\omega > (1+D_q)N_\omega^{max}$ the algorithm proceeds to generate a new refined mesh through which element 'T'in figure 6.6a is subdivided into 4 equal sized elements. Alongside this process of mesh refinement the matrix $\mathbf{A}_{grid}$ and N_ω^{max} is updated and stored. If $N_\omega \not> (1+D_q)N_\omega^{max}$ the analysis continues with the next load increment $n+1$ utilising the current mesh.

6.6 Numerical simulations

Four numerical examples with unique damage formation characteristics are presented to show the robustness of the adaptive damage analysis technique introduced in this work. In all the examples the output produced by the optimised adaptive simulation is compared to an output produced by a uniform or a refined static mesh configuration. All the examples presented in this section deal with conventional problems involving weak singularities.

The objective of the first two examples is to validate the results obtained through the adaptive formulation by comparing them with the results obtained in chapter 3. Thus the three point bending beam problem (refer section 6.6.1) and the L-shaped specimen (refer section 6.6.2) are extracted from 3. The next two examples expand the application of the this procedure through modelling the behaviour of a short cantilever beam (refer section 6.6.3) and a single edge notched beam (refer section 6.6.4).

6.6.1 Three point bending beam

A biaxial bending beam problem presented in this section is extracted from [501] and [495]. With reference to these publications the model dimensions are considered as given in figure 6.7. These dimensions also correspond to the experiments performed by Kormeling and Reinhardt [502] and by Grassl et al. [503] with a plastic damage model.

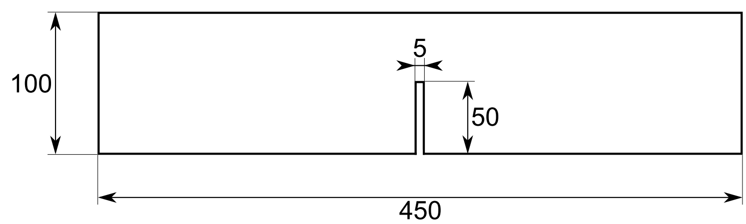

Figure 6.7. Specimen dimensions (mm) for the 2D image-based adaptive non-local damage analysis of the biaxial bending test.

The length of the beam is 450 mm with a depth and breadth of 100 mm. A central notch of 5 mm is modelled. The depth of the notch extends to half way up the beam. The loading is to replicate a three point bending mechanism as shown in figure 6.8. The bottom left corner of the beam is pinned and thus is restrained in movement in x and y directions. The bottom right corner of the beam is modelled as a roller support and thus is restrained in movement in the y direction. A central concentrated load ‘P’ is applied at the centre of the beam to prompt the structural response.

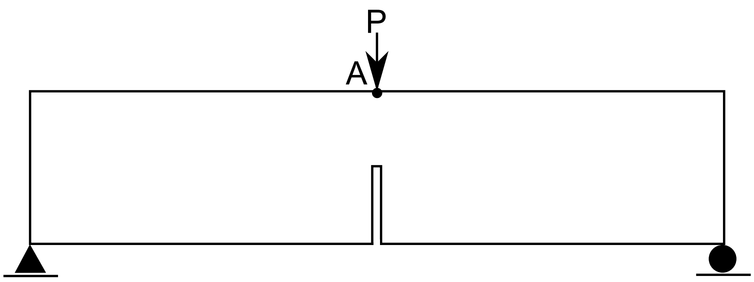

Figure 6.8. Loading configuration for the 2D image-based adaptive non-local damage analysis of the biaxial bending test.

The material properties, Young’s modulus and Poisson’s ratio are set to 20 GPa and 0.2 respectively. A non-local isotropic damage model based on non-local equivalent strain is considered to overcome strain localisation issues. As adopted in the reference the non-local averaging function given in equation (6.8) is considered with internal length parameter R set to 4 mm. The exponential damage model (refer equation (6.1)) considered for this simulation has a stress-strain behaviour as shown in figure 6.9.

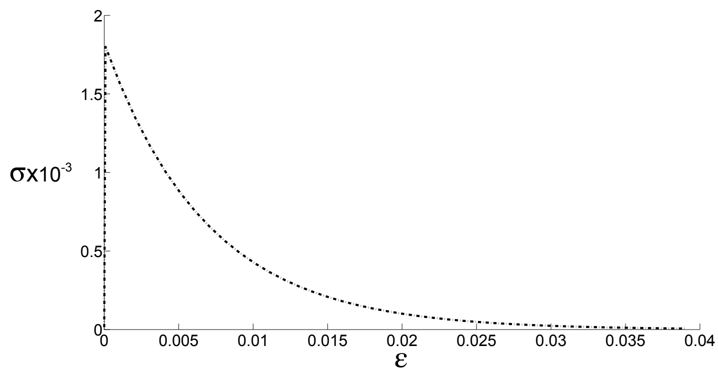

Figure 6.9. 1D element stress (GPa) vs strain profile considered in the 2D image-based adaptive non-local damage analysis of the biaxial bending test. The damage evolution is with respect to the softening law in equation (6.2).

To obtain the above behaviour the parameter ε_0 is set to 90×10^{-6} and strain at which material is fully damaged $\left(\varepsilon_f\right)$ is taken as 7.0×10^{-3}. To calculate the equivalent strain the parameter k with reference to equation (6.3) is set to 10 to emulate more realistic material constants related to concrete. These parameters are chosen to be the same as those used in the finite element modelling carried out in the reference [477].

Prior to the initiation of the adaptive process the initial mesh geometry is obtained by an automatically generated quadtree mesh. Due to the presence of the notch, initial refinement is seen around the notched region (see figure 6.10a). The analysis is then allowed to run automatically, through which meshes shown in figures 6.10b-6.10f are generated adaptively.

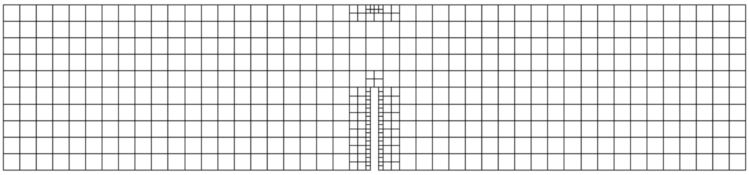

(a) Mesh 1 generated for the biaxial bending test when node ‘A’ vertical displacement is 0.0 mm.

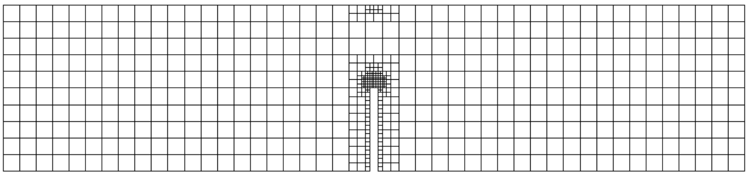

(b) Mesh 2 generated for the biaxial bending test when node ‘A’ vertical displacement is 0.05 mm.

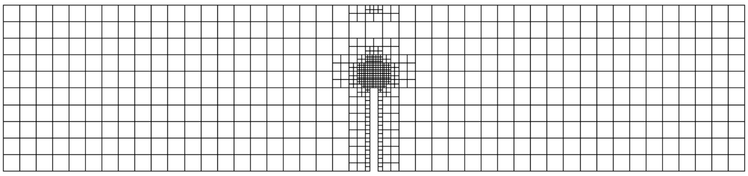

(c) Mesh 3 generated for the biaxial bending test when node ‘A’ vertical displacement is 0.1 mm.

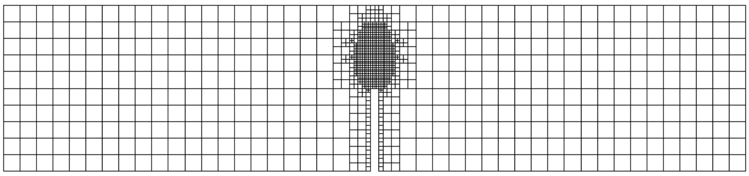

(d) Mesh 4 generated for the biaxial bending test when node ‘A’ vertical displacement is 0.2 mm.

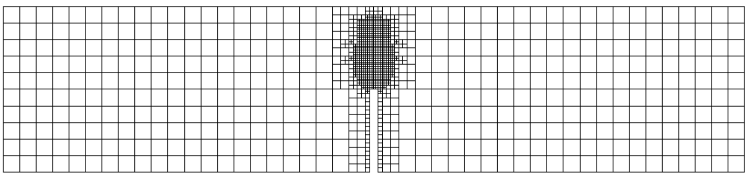

(e) Mesh 5 generated for the biaxial bending test when node ‘A’ vertical displacement is 0.3 mm.

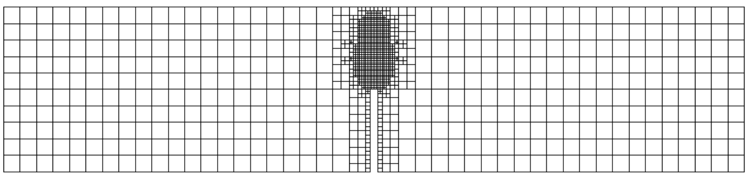

(f) Mesh 6 generated for the biaxial bending test when node ‘A’ vertical displacement is 0.5 mm.

Figure 6.10. Six meshes automatically generated within the simulation for the 2D image-based adaptive non-local damage analysis of the biaxial bending test.

The analysis is run with $\omega_0 = 0.6$ and $D_q = 20\%$. As the damage is controlled by the DPZ a finer mesh around the notch and a coarse mesh away from the notch can be maintained as adopted in the reference [501]. The mesh size varies from the smallest of S_{min}= 1.25 mm within the DPZ and to the largest of S_{max}= 10 mm away from the DPZ.

Next to validate the findings obtained in the adaptive process the finest mesh out of the three reference meshes shown in figure 6.11 is considered. This reference mesh has a smallest subdomain size of 0.556 mm (refer figure 6.11c).

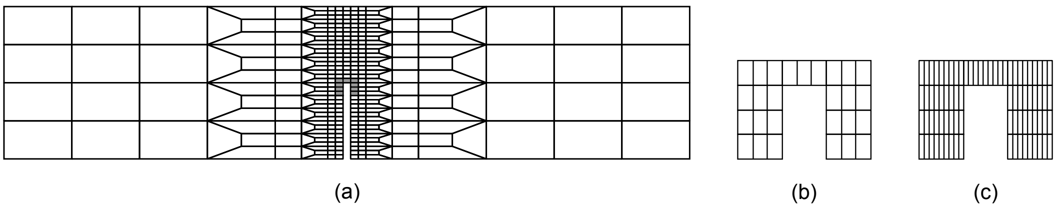

Figure 6.11. Three mesh configurations considered in section 3.7.2 for the biaxial bending test (a) mesh 1 with S_{min}= 5 mm), (b) mesh 2 with S_{min}= 1.667 mm, and (c) mesh 3 with S_{min}= 0.5556mm.

The displacement control analysis is run using the modified Newton Raphson method with arc-length technique. The displacement and the force are both recorded at point 'A' to produce the force-displacement output shown in figure (6.12).

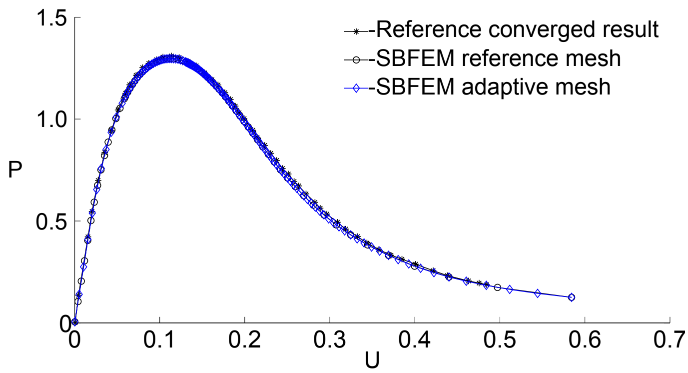

Figure 6.12. Force (kN) vs displacement (mm) output for the 2D image-based adaptive non-local damage analysis of the biaxial bending test. The adaptive formulation in SBFEM compared against the reference output [501] and the mesh 3 result in section 3.7.2.

The most refined mesh shown in figure 6.10f produces the load-displacement curve (refer figure 6.12) closely relatable to the reference solution obtained in chapter 3 section

3.7.2. This conformity validates the result obtained in this work.

The first vertical displacement contour plot shown in figure 6.13a is recorded when the simulation attains a peak load (1.3 kN) when node ‘A’ displacement corresponds to 0.1187 mm. The second contour is captured soon after the model achieves its peak load (0.91 kN) when displacement is 0.214 mm.

The vertical displacement contours show a clear symmetry about the central notch. This is expected of the analysis due to the symmetrical geometry, boundary conditions and loading conditions adopted.

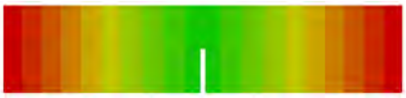

(a) Vertical displacement contour for the adaptive mesh 6 (refer figure 6.10f) when mid span displacement is 0.1187 mm.

(b) Vertical displacement contour for the adaptive mesh 6 (refer figure 6.10f) when mid span displacement is 0.214 mm.

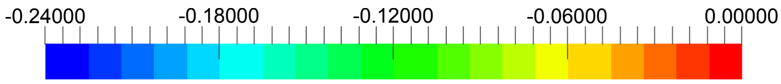

Figure 6.13. Vertical displacement (mm) contours for the 2D image-based adaptive non-local damage analysis of the biaxial bending test. Outputs recorded for the adaptive mesh 6 shown in figure 6.10f.

The stress contour plots shown below are captured at similar instances to that of the displacement contours recorded above. Figure 6.14a depicts the initial stress concentration at the tip of the notch. When the applied external load increases this high stress contour migrates to the top face of the beam in the shape of a plume. This migrating front leaves behind elements that undergo unloading due to the effects of damage.

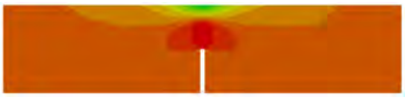

(a) Stress (σ_x) contour for the adaptive mesh 6 (refer figure 6.10f) at mid span displacement of 0.1187 mm.

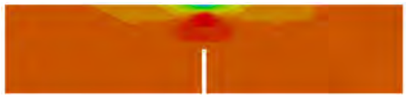

(b) Stress (σ_x) contour for the adaptive mesh 6 (refer figure 6.10f) at mid span displacement of 0.214 mm.

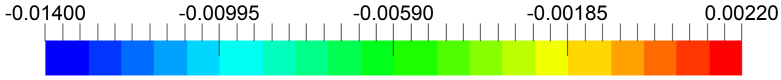

Figure 6.14. Stress (σ_x) contours (MPa) for the 2D image-based adaptive non-local damage analysis of the biaxial bending test. Outputs recorded for the adaptive mesh 6 shown in figure 6.10f.

The contour plots for damage evolution is at a peak load (see figure 6.15a) and at the end of the simulation when vertical displacement is 0.563 mm corresponding to a load of 0.13 kN (see figure 6.15b). This latter contour shows the clear propagation of the DPZ from the tip of the notch to the top face of the beam. Since the adaptive framework is based on the damage variable ω, the damage contours show a close resemblance to the adaptive meshes (see figure 6.10) obtained in the simulation.

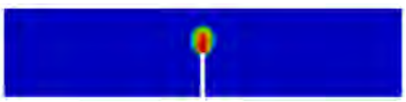

(a) Damage contour for the adaptive mesh 6 (refer figure 6.10f) at mid span displacement of 0.1187 mm.

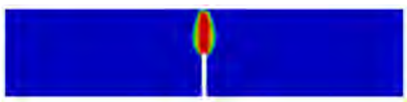

(b) Damage contour for the adaptive mesh 6 (refer figure 6.10f) at mid span displacement of 0.563 mm.

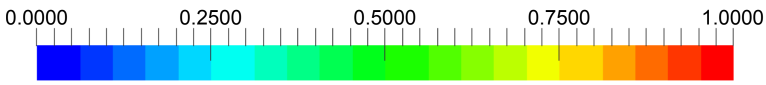

Figure 6.15. Damage (Ω) contours for the 2D image-based adaptive non-local damage analysis of the biaxial bending test. Outputs recorded for the adaptive mesh 6 shown in figure 6.10f.

The adaptive process simulates the evolution of the DPZ precisely as anticipated. The number of elements produced in the adaptive simulation is 1258 compared to the reference mesh (see figure 6.11c) containing 1634 elements. It is also noteworthy the reference mesh is created with considerable human intervention and prior knowledge of the location of the DPZ. Therefore this example a comparably similar result is obtained in the adaptive mesh refinement with a 23% reduction in number of elements and no human intervention in the meshing process.

The final deformed shaped obtained in the simulation is shown in figure 6.16. For better visualisation the deformation is amplified 50 times.

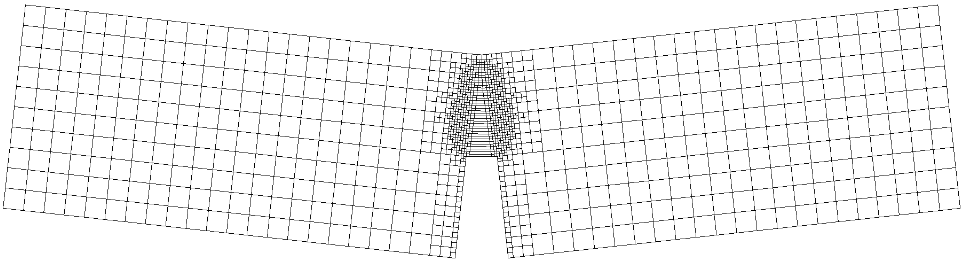

Figure 6.16. The final deformed shape of the specimen obtained in the 2D image-based adaptive non-local damage analysis of the biaxial bending test. Results shown for the mesh shown in figure 6.10f.

6.6.2 L-shaped specimen

As the second example the L-shaped specimen shown in figure 6.17 (previously simulated and analysed in chapter 3 section 3.7.3) is analysed with use of the adaptive non-local damage analysis process. The objective of the simulation is to compare the adaptive formulation to the output obtained through a conventional static mesh generated with a certain amount of human intervention.

The problem is modelled with reference to [482, 505]. The plate has a height and a width of 500 mm with a rectangular 250×250 mm quarter cut out. The thickness considered in the model is 200 mm.

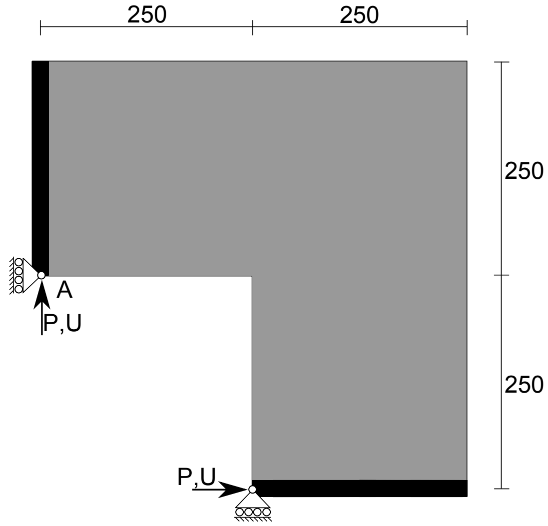

Figure 6.17. Geometry (mm) and boundary conditions adopted with reference to [505] for the 2D image-based adaptive non-local damage analysis of the L-shaped specimen.

Displacement boundary conditions are considered to avoid free rotation of the rigid end-plates. The end plates are modelled by assigning them a modulus of elasticity 1000 times larger than the rest of the plate. This way of modelling the end-plates avoids undesirable damage around the loading points.

The modulus of elasticity of the plate is set to E $=$ 10 GPa in its undamaged state. The Poisson's ratio is considered as ν= 0.2. With reference to equation (6.3) modified von Mises strain is considered for the calculation of the non-local equivalent strain with the parameter k set at 10. As exemplified through the previous problem a non-local formulation is considered to avoid issues related to strain localisation. The Gauss distribution function for non-local averaging considered in this simulation is given in equation (6.7) with the non-local length scale l of 7.07 mm. An exponential damage model is considered for this analysis as given in equation (6.2) with $\varepsilon_0 = 4 \times 10^{-4}$, $\alpha = 0.98$ and $\beta = 80$. Figure 6.18 depicts the behaviour of the damage model in relation to these parameters. Plane stress conditions are assumed.

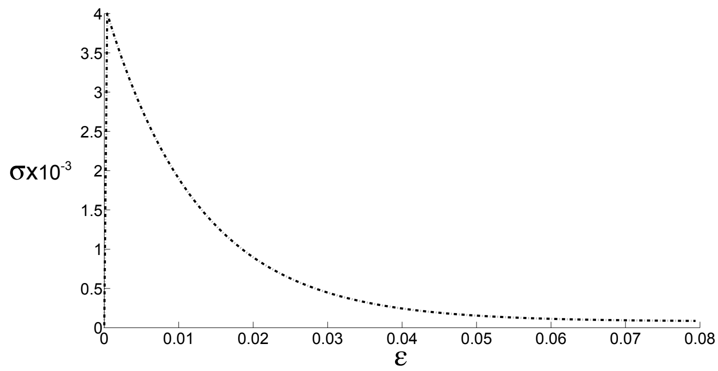

Figure 6.18. 1D element stress (GPa) vs strain profile considered in the 2D image-based adaptive non-local damage analysis of the L-shaped specimen. The damage evolution is with respect to the softening law in equation (6.2).

Similar to the previous example the damage threshold value initiating mesh refinement ω_0 is set to 0.6 and the percentage damage limit $D_q = 20\%$ is considered.

In the adaptive algorithm the damage process zone is automatically refined and no artificial mesh controls need to be set in order to produce the meshes shown in figure 6.19. The user defined element size parameters, smallest element size S_{min}= 3.9 mm and the largest element size is taken 4 times greater than S_{min}. The process refines the mesh diagonally from the convex inner corner to its opposite outer corner (see figure 6.19).

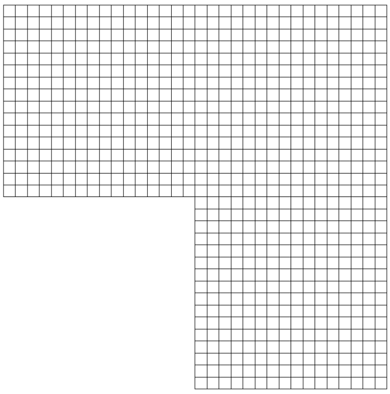

(a) Mesh 1 generated for the L-shaped specimen when node ‘A’ vertical displacement is 0.0 mm.

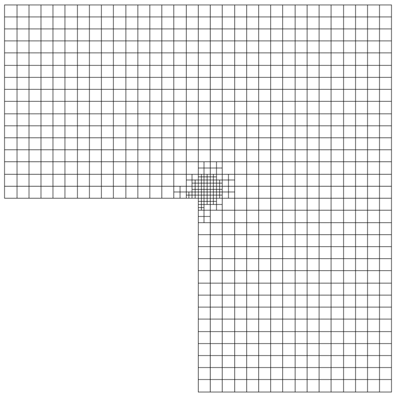

(b) Mesh 2 generated for the L-shaped specimen when node ‘A’ vertical displacement is 0.25 mm.

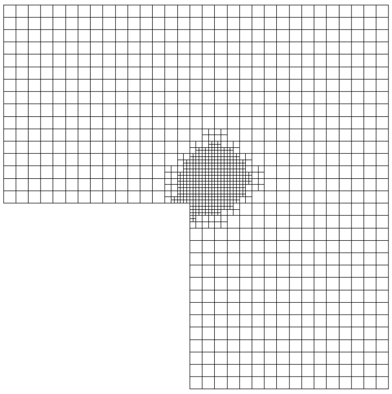

(c) Mesh 3 generated for the L-shaped specimen when node ‘A’ vertical displacement is 0.495 mm.

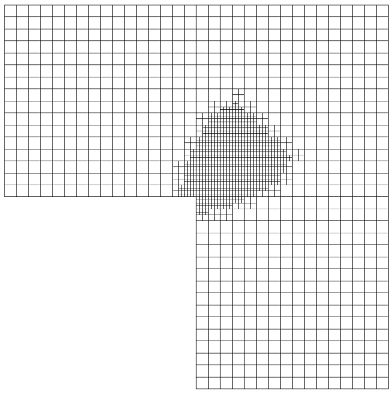

(d) Mesh 4 generated for the L-shaped specimen when node ‘A’ vertical displacement is 0.97 mm.

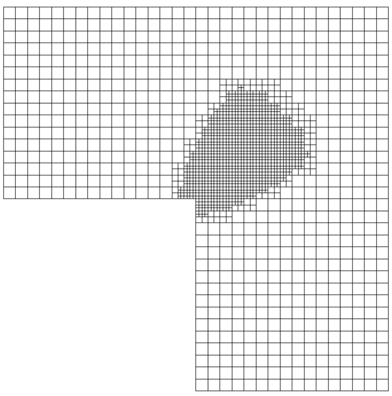

(e) Mesh 5 generated for the L-shaped specimen when node ‘A’ vertical displacement is1.57 mm.

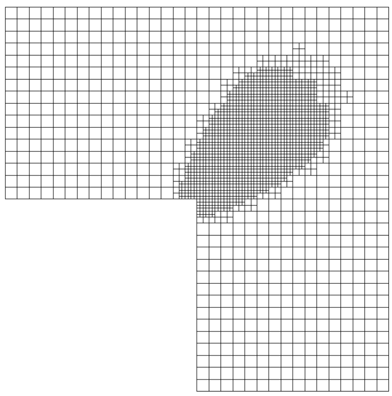

(f) Mesh 6 generated for the L-shaped specimen when node ‘A’ vertical displacement is 2.75 mm.

Figure 6.19. Six meshes automatically generated for the 2D image-based adaptive non-local damage analysis of the L-shaped specimen.

To obtain the reference solution a mesh as shown in figure 6.20 is developed by assuming the DPZ to progress from convex inner corner to the diagonally opposite outer corner.

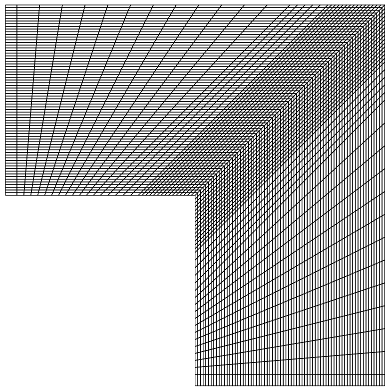

Figure 6.20. Static mesh configuration used in the 2D damage analysis of the L-shaped specimen in section 3.7.3.

The reference mesh in figure 6.20 consists of 4686 elements. In comparison the number of elements produced in the most refined adaptive simulation is 2488. Therefore in this instance the reduction in number of elements in the two meshes is almost 50%.

The arc-length incorporated modified Newton Raphson method is used in the analysis with displacement control agitation. With reference to figure 6.17 the displacement and the force are both recorded at point ‘A’.

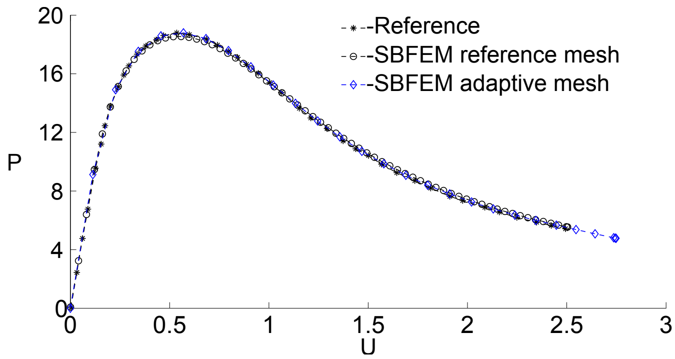

Figure 6.21. Force (kN) vs displacement (mm) output for the 2D image-based adaptive non-local damage analysis of the L-shaped specimen. The adaptive formulation in SBFEM compared against [505] and the force vs displacement output in section 3.7.3.

Figure 6.21 shows the load-displacement curve of the proposed approach obtained with the mesh configuration in figure 6.19f compared against the output obtained in chapter 3 section 3.7.3 using the reference mesh shown in figure 6.20. Furthermore the results obtained through the adaptive and the reference meshes are compared with the solution published by [505]. It is evident that the results obtained through the adaptive formulation agree very closely to the reference force-displacement output. This comparably similar result in the adaptive analysis is achieved by a considerable reduction in the number of elements.

The displacement magnitude (see figure 6.22), von Mises stress (see figure 6.23) and the damage evolution (see figure 6.24) contours are shown in the following figures. The contours for displacement and von Mises stress are presented at a vertical displacement of 0.5372 mm at node 'A' reflecting the peak load of 18.6 kN achieved in the simulation and at a displacement value of 0.987 mm corresponding to a load of 15.4 kN in the softening limb of the force-displacement curve.

The displacement magnitude contours display the symmetry in the simulation attained through the symmetrical loading and boundary conditions implemented in the analysis.

(a) Displacement magnitude contour for the adaptive mesh 6 (refer figure 6.19f) when node 'A' displacement is 0.5372 mm.

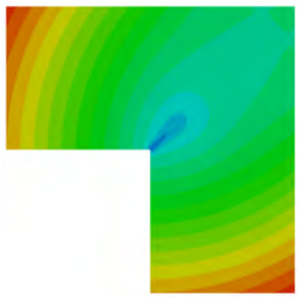

(b) Displacement magnitude contour for the adaptive mesh 6 (refer figure 6.19f) when node 'A' displacement is 0.987 mm.

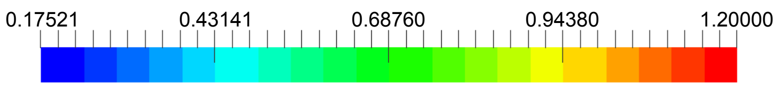

Figure 6.22. Displacement magnitude contours (mm) for the 2D image-based adaptive non-local damage analysis of the L-shaped specimen. Outputs recorded for the adaptive mesh 6 shown in figure 6.19f.

The advancing high stress front moves symmetrically along the diagonal. Similar to the observation in the biaxial bending test in section 6.6.1 this moving front leaves behind elements that unload as the model goes through softening behaviour induced by the spread of damage. When the model approaches the softening stage, the DPZ keeps advancing (refer figure 6.24b) whereas the size of the zone of high stress shrinks (refer figure 6.23b).

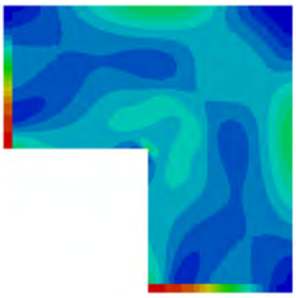

(a) Von Mises stress contour for the adaptive mesh 6 (refer figure 6.19f) when node ‘A’ displacement is 0.5372 mm.

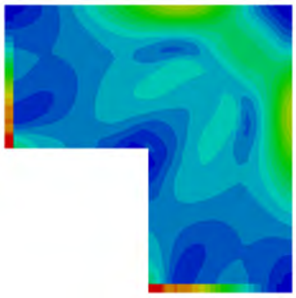

(b) Von Mises stress contour for the adaptive mesh 6 (refer figure 6.19f) when node ‘A’ displacement is 0.987 mm.

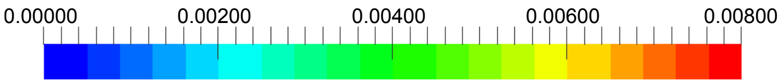

Figure 6.23. Von Mises stress contours (MPa) for the 2D image-based adaptive non-local damage analysis of the L-shaped specimen. Outputs recorded for the adaptive mesh 6 shown in figure 6.19f.

The contour set for damage evolution shown below are recorded at the peak load and at the end of the simulation corresponding to displacement of 2.504 mm and force 5.436 kN.

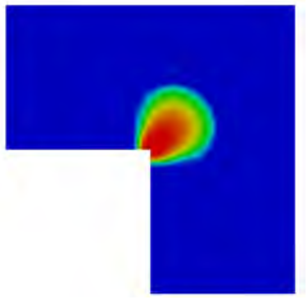

(a) Damage contour for the adaptive mesh 6 (refer figure 6.19f) when node 'A' displacement is 0.5372 mm.

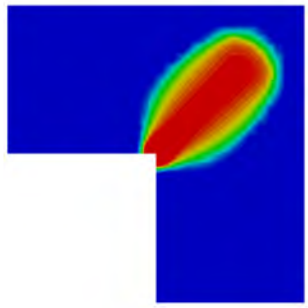

(b) Damage contour for the adaptive mesh 6 (refer figure 6.19f) when node 'A' displacement is 2.504 mm.

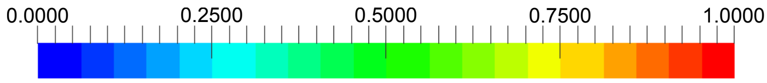

Figure 6.24. Damage (Ω) contours for the 2D image-based adaptive non-local damage analysis of the L-shaped specimen. Outputs recorded for the adaptive mesh 6 shown in figure 6.19f.

The damage evolution in figure 6.24 shows an accurate representation of the failure pattern expected in this analysis. The damage formation developed from the concave corner to the diagonally opposite corner.

The final deformed shape developed in the analysis is shown in figure 6.25. The 100 times amplified result gives evidence to the anticipated large deformation within elements near to the concave corner.

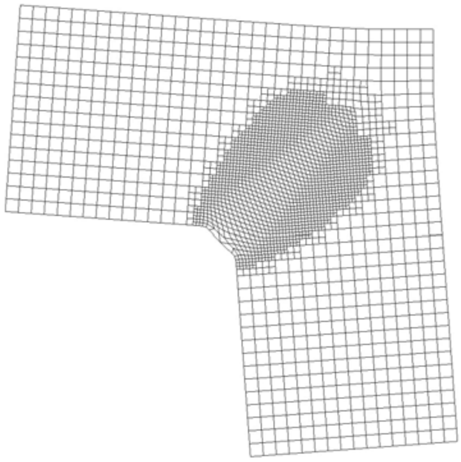

Figure 6.25. The final deformed shape of the specimen obtained in the 2D image-based adaptive non-local damage analysis of the L-shaped specimen. Results shown for the mesh shown in figure 6.19f.

6.6.3 Short cantilever subjected to uniform pressure

This example is inspired by the work published by [44] on an SBFEM based adaptive refinement strategy for linear elasticity problems. The example simulates the behaviour of a short cantilever beam under plane strain conditions. The problem exhibits two strong stress concentrations at the top and bottom left corners restrained in movement.

The dimensions and boundary conditions are considered as given in figure 6.26. The length, breadth and depth of the beam (L) is set to 500 mm.

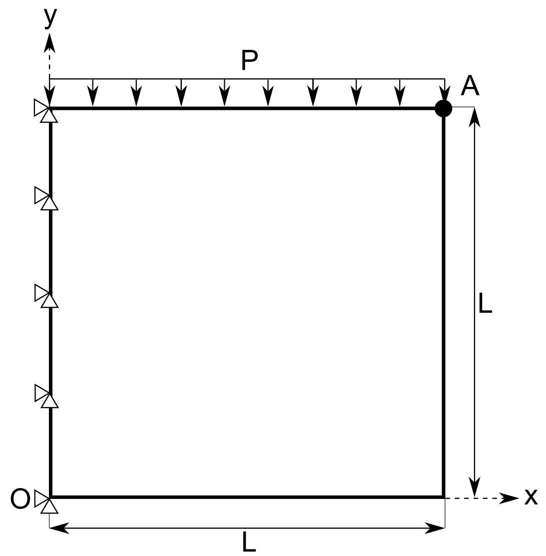

Figure 6.26. Specimen dimensions (mm) and boundary conditions for the 2D image-based adaptive non-local damage analysis of the short cantilever beam subjected to uniform pressure.

The cantilever beam is loaded on the top edge by applying a uniform pressure and it is retrained in movement in both x and y directions on the left edge.

Material properties are considered with reference to the experiments carried out by [563] on fracture processes in concrete. The Young's modulus and Poisson's ratio are thus set to 35 GPa and 0.2. Equivalent strain for the analysis is calculated using the equation (6.3) with parameter k set to 10 to emulate the behaviour of concrete. The non-local averaging function given in equation (6.7) is considered with the characteristic length l set at 8 mm. The damage formulation in the material is governed by the equation (6.1) with ε_0 set to 90×10^{-6} and ε_f set to 7.0×10^{-3}. The stress-strain behaviour of this damage model is as shown in figure 6.27.

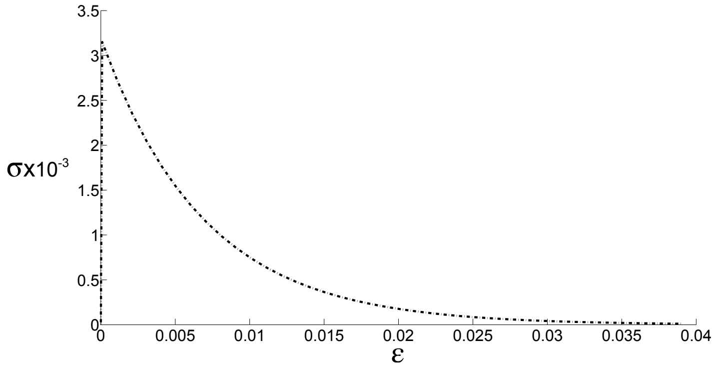

Figure 6.27. 1D element stress (GPa) vs strain profile considered in the adaptive damage analysis of a short cantilever beam subjected to uniform pressure. The damage evolution is with respect to the softening law in equation (6.1).

The automatically generated quadtree mesh is initially controlled by the maximum element size of S_{max} =15.625 mm.To exemplify the convergence of the results a fine mesh and a coarse mesh is analysed by the setting the minimum element size S_{min} of 1.95 mm for the fine mesh and 3.91 mm for the coarse mesh. As the analysis progresses meshes shown in figures 6.28b-6.28f are generated automatically for the fine mesh configuration.

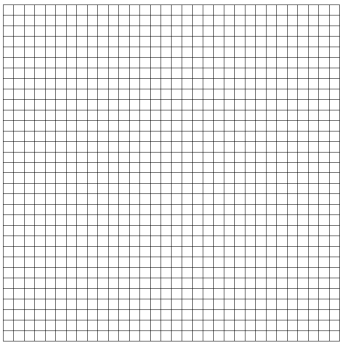

(a) Mesh 1 generated for the short cantilever beam simulation when node 'A' vertical displacement is 0.0 mm.

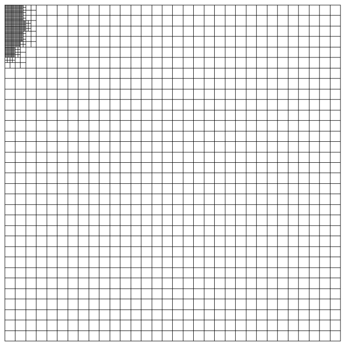

(b) Mesh 2 generated for the short cantilever beam simulation when node 'A' vertical displacement is 0.0055 mm.

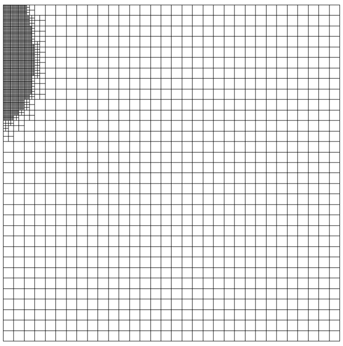

(c) Mesh 3 generated for the short cantilever beam simulation when node 'A' vertical displacement is 0.01 mm.

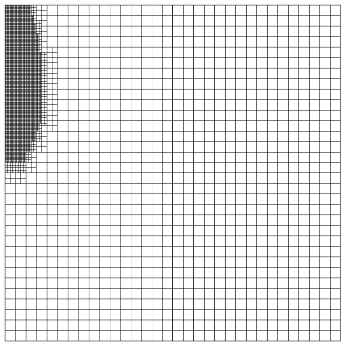

(d) Mesh 4 generated for the short cantilever beam simulation when node 'A' vertical displacement is 0.14 mm.

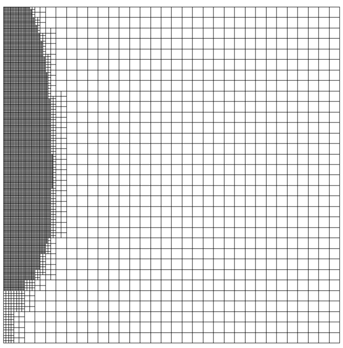

(e) Mesh 5 generated for the short cantilever beam simulation when node 'A' vertical displacement is 0.022 mm.

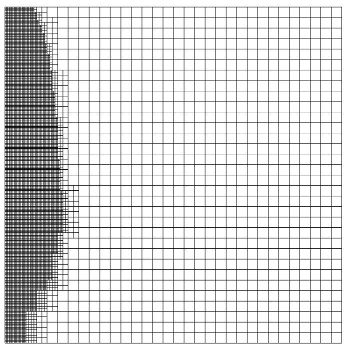

(f) Mesh 6 generated for the short cantilever beam simulation when node 'A' vertical displacement is 0.025 mm.

Figure 6.28. Six meshes automatically generated in the 2D image-based adaptive non-local damage analysis of the short cantilever beam subjected to uniform pressure. Meshes shown for the fine mesh with $S_{min} = 1.95$ mm and $S_{max} = 15.625$ mm.

The mesh refinement is initiated when the number of elements damaged (N_ω) above the damage threshold $\omega_0 = 0.6$ is above the percentage of damaged elements $D_q = 20\%$ compared to history variable N_ω^{max}.

In order to validate the results a uniform mesh is also considered in this example. A comparison of the three meshes are shown in figure 6.29.

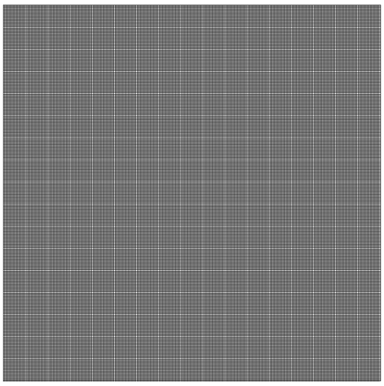

(a) Uniform mesh considered in short cantilever beam simulation. $S_{min} =$ 1.95 mm and $S_{max} = 1.95$.

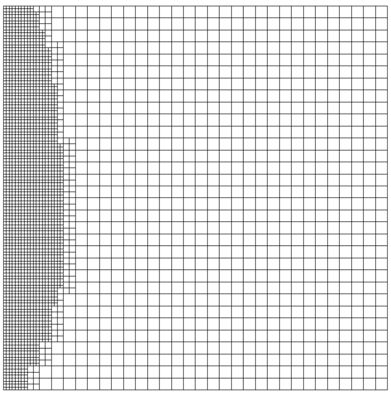

(b) Coarse mesh at the end of the analysis considered in short cantilever beam simulation. $S_{min} = 3.91$ mm and $S_{max} = 15.625$.

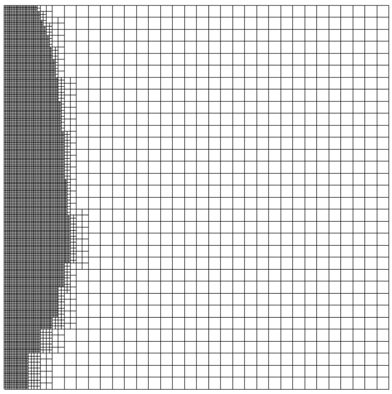

(c) Fine mesh at the end of the analysis considered in short cantilever beam simulation. $S_{min} = 1.95$ mm and $S_{max} =$ 15.625.

Figure 6.29. SBFEM (a) uniform (b) coarse and (c) fine meshes used in the 2D image-based adaptive non-local damage analysis of the short cantilever beam subjected to uniform pressure.

An automatic force controlled analysis is run with the arc-length incorporated modified Newton Raphson method. The load is applied in 0.01 kN increments. Figure 6.30 plots the total load on the top edge against the vertical displacement at point 'A' (see figure 6.26).

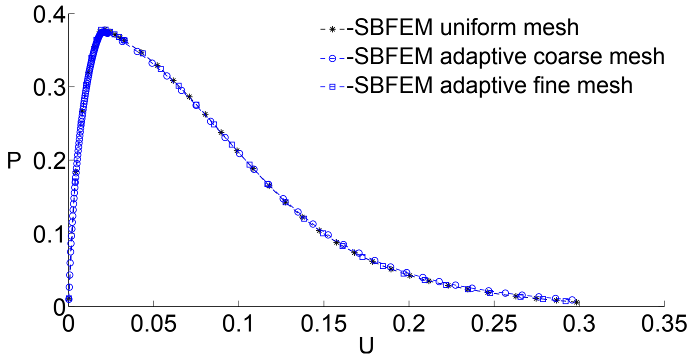

Figure 6.30. Force (kN) vs displacement (mm) output for the 2D image-based adaptive non-local damage analysis of the short cantilever beam subjected to uniform pressure. SBFEM result for the fine mesh (refer figure 6.29c) compared to the coarse mesh (refer figure 6.29b) and the uniform mesh (refer figure 6.29b).

The plots depict a converged result between the coarse and the fine meshes. Both the adaptive mesh outputs are closely relatable to the force-displacement output of the uniform mesh. The three meshes produce similar results due to the adopted mesh configurations producing ample sampling points for the non-local averaging scheme. Confirming to the observations in chapter 3, two or more elements within the non-local radius tend to produce similar results. Therefore S_{min} used in the coarse mesh act as a limiting value to conform to this condition.

The vertical displacement contours in figure 6.31 are captured when the simulation records a peak load of 0.379 kN (corresponding node 'A' displacement is 0.0213 mm) and a load of 0.21 kN (corresponding node 'A' displacement is 0.1 mm) on the top edge.

The beam's cantilevered action results in higher deformations at the free end and no deformations in the restrained end. The restraints in the left edge localises the strains and stresses adjacent to this edge.

(a) Vertical displacement contour for the fine mesh (refer figure 6.29c) when vertical downward displacement at point ‘A’ is 0.0213 mm.

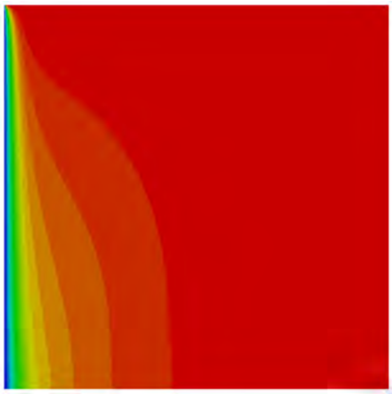

(b) Vertical displacement contour for the fine mesh (refer figure 6.29c) when vertical downward displacement at point ‘A’ is 0.1 mm.

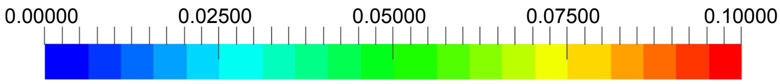

Figure 6.31. Vertical displacement (mm) contours for the 2D image-based adaptive non-local damage analysis of the short cantilever beam subjected to uniform pressure. Outputs recorded for the adaptive mesh shown in figure 6.29c.

The principal stress contours are also captured at similar instances to those considered in the displacement contours.

(a) Principal stress contour for the fine mesh (refer figure 6.29c) when vertical downward displacement at point ‘A’ is 0.0213 mm.

(b) Principal stress contour for the fine mesh (refer figure 6.29c) when vertical downward displacement at point ‘A’ is 0.1 mm.

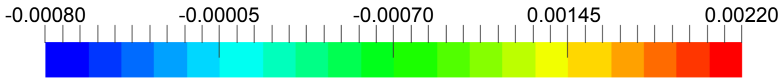

Figure 6.32. Principal stress contours (MPa) for the 2D image-based adaptive non-local damage analysis of the short cantilever beam subjected to uniform pressure. Outputs recorded for the adaptive mesh shown in figure 6.29c.

The damage contours are captured at the peak load and at the end of the simulation when vertical displacement is 0.3 mm corresponding to a load of 0.008 kN. The final damage profile of the simulation is as shown in 6.33b. The initial formation of damage on the top restrained corner of the specimen is characteristic of the tensile strain induced damage formation in concrete.

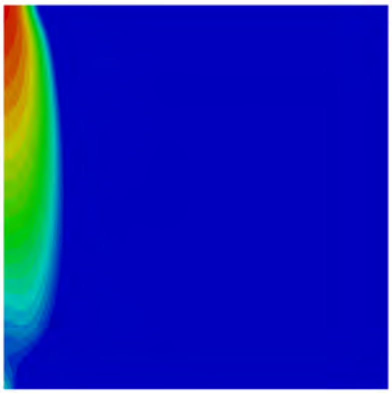

(a) Damage contour for the fine mesh (refer figure 6.29c) when vertical downward displacement at point ‘A’ is 0.0213 mm.

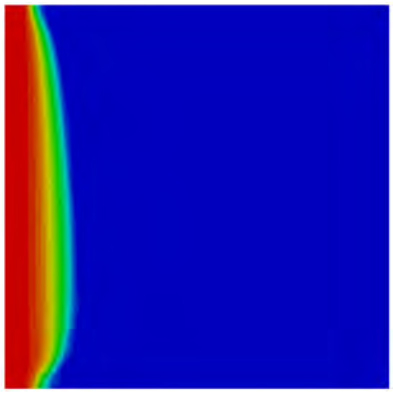

(b) Damage contour for the fine mesh (refer figure 6.29c) when vertical downward displacement at point ‘A’ is 0.3 mm.

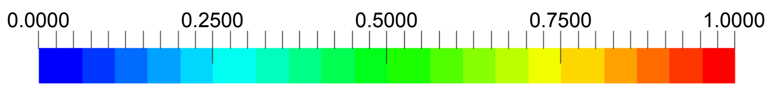

Figure 6.33. Damage (Ω) contours for the 2D image-based adaptive non-local damage analysis of the short cantilever beam subjected to uniform pressure. Outputs recorded for the adaptive mesh shown in figure 6.29c.

The damage variable based adaptive scheme produces meshes shown in figure 6.28 that closely resemble the damage contours above. As the damage develops in the specimen a finer mesh is observed in the restrained end of the cantilever beam .

The deformed shape of the beam is shown in figure 6.34. The output is magnified to better visualise the deformation.

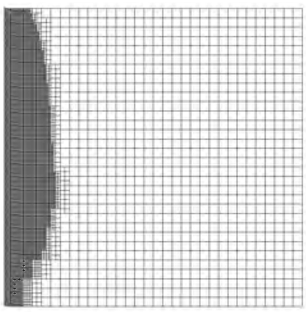

Figure 6.34. The final deformed shape of the specimen obtained in the 2D image-based adaptive non-local damage analysis of the short cantilever beam subjected to uniform pressure. Results shown for the mesh shown in figure 6.29c.

As anticipated the adaptive mesh refinement tracks the damage evolution accurately and by doing so it controls and refines the output of the simulation. The number of elements produced by the uniform mesh is quite large totalling up to a 65536 elements. Compared to this, the coarse mesh saves on the number of elements by 94.7% and the fine mesh by 84.7%.

6.6.4 Single-edge notched beam

As the last example for this chapter a Single Edge Notched Beam (SENB) subject to antisymmetric four-point-shear loading is considered. This problem is previously analysed experimentally and numerically by [563]. Then later numerically simulated by [561] in damage and crack modelling of single and double edge notched concrete beams.

The geometry and the loading conditions shown in figure 6.35 are adopted similar to that of the references for both experimental and numerical simulations. The overall length, width and thickness of the beam are 450, 100 and 50 mm. A 5 mm wide 20 mm deep notch is centrally located in the beam. Four rigid platens located on the top and bottom edges of the beam induce the boundary conditions. At the top left platen near the notch x and y directional movement is restrained centrally whereas at the top right platen vertical y directional movement is restrained centrally. A nodal force is centrally applied on the bottom rigid loading platens. The loading platens at the lower left and right extremities of the beam were applied with a forces such that the bottom right platen experience an agitation 10 times greater than that experienced by the bottom left platen.

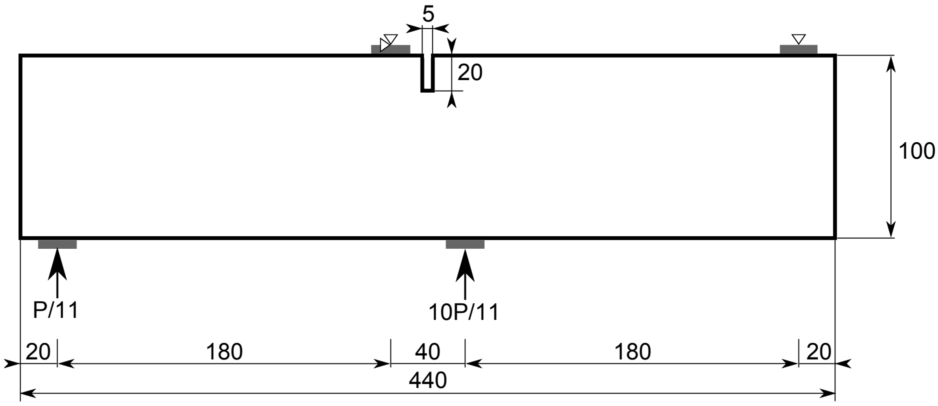

Figure 6.35. Specimen dimensions (mm) and boundary conditions for the 2D image-based adaptive non-local damage analysis of the single-edge notched beam.

The material parameters are set similar to [561] with Young's modulus E = 35 GPa, and Poisson's ratio $\nu = 0.2$. The platens are modelled as rigid bodies with E = 1×10^6 GPa. Equivalent strain is calculated as per equation (6.6) with compression and tension sensitivity parameter k set to 15. The damage model as given in equation (6.2) is considered with the damage initiation history parameter ε_0= 6×10^{-5}. The damage evolution law parameters α and β are set to 0.96 and 100, respectively. The stress-strain behaviour of the damage function is depicted in figure 6.36.

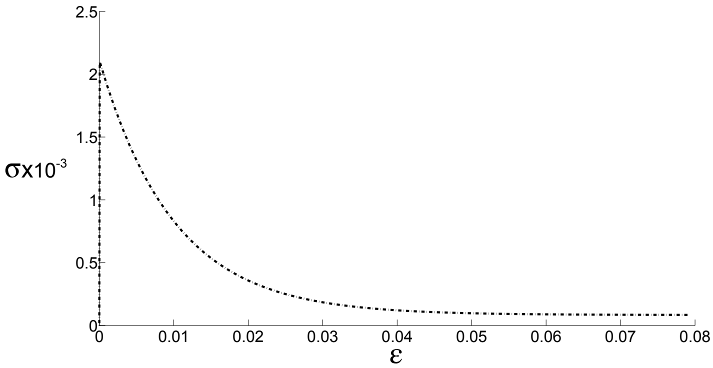

Figure 6.36. 1D element stress (GPa) vs strain profile considered in the 2D image-based adaptive non-local damage analysis of the single-edge notched beam. The damage evolution is with respect to the softening law in equation (6.2).

The characteristic length parameter l is set to 1.7 mm with respect to the non-local averaging function in equation (6.7). Plane stress conditions are assumed upon consideration of the model dimensions.

An automatically generated quadtree mesh is used in the first instance with S_{min} and S_{max} set to of 2.5 mm and 10 mm, respectively. As the analysis progresses, the adaptive refinement around the damage process zone is improved by modifying the smallest mesh size control to 1,25 mm. The adaptive mesh generation occurs during analysis producing the meshes shown in figures 6.37b-6.37f. The mesh refinement is initiated when the damage variable reaches $\omega_0 = 0.6$ and the percentage of damaged elements reach $D_q = 10\%$ beyond the previous converged adaptive iteration.

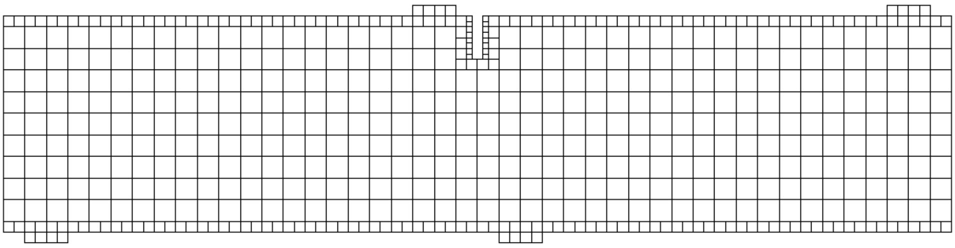

(a) Mesh 1 generated for the single-edge notched beam when CMOD is 0.0 mm.

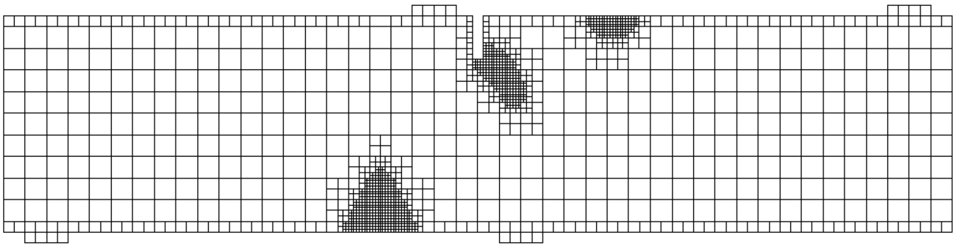

(b) Mesh 2 generated for the single-edge notched beam when CMOD is 0.001 mm.

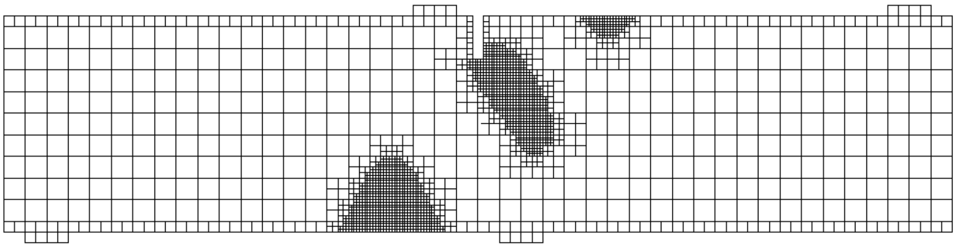

(c) Mesh 3 generated for the single-edge notched beam when CMOD is 0.04 mm.

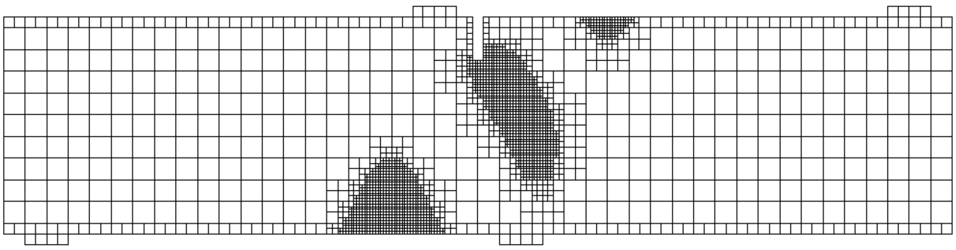

(d) Mesh 4 generated for the single-edge notched beam when CMOD is 0.1 mm.

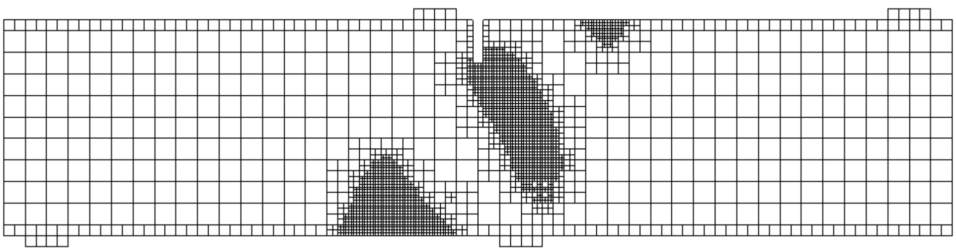

(e) Mesh 5 generated for the single-edge notched beam when CMOD is 0.3 mm.

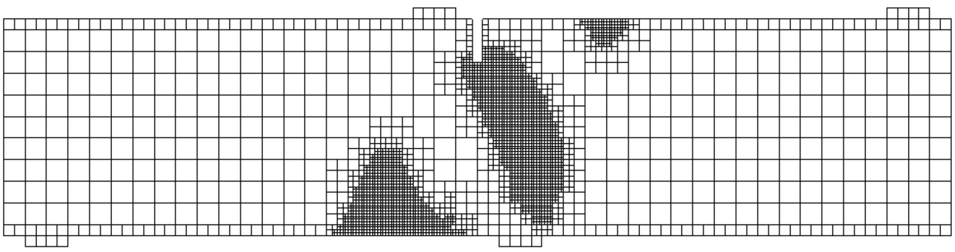

(f) Mesh 6 generated for the single-edge notched beam when CMOD is 0.5 mm.

To validate the results a uniform mesh is considered with an element size of 1.25 mm in addition to the adaptive meshes above. The adaptive mesh in its most refined state produces 3211 elements whereas the uniform mesh produces 28352 elements. These two meshes are shown in figure 6.38.

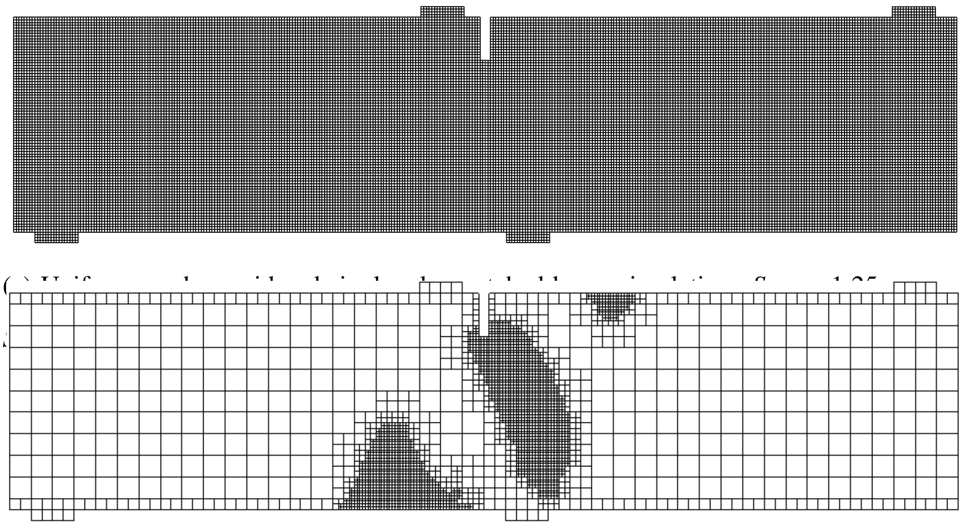

(b) Adaptive mesh considered single-edge notched beam simulation. $S_{min} = 1.25$ mm and $S_{max} = 10$.

Figure 6.38. SBFEM (a) uniform and (b) adaptive meshes used in the 2D image-based adaptive non-local damage analysis of the single-edge notched beam.

The analysis is run using the arc-length algorithm coupled with line search method. The initial agitation ‘P’ is set to 0.025 kN. A total of 763 iterations are run to produce the final load vs Crack Mouth Opening Displacement (CMOD) output below in figure 6.39.

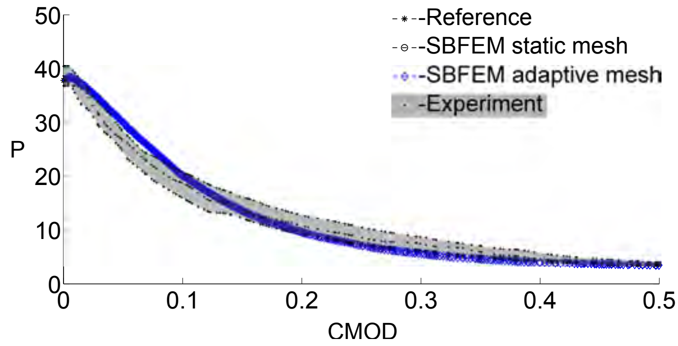

Figure 6.39. Force (kN) vs CMOD displacement (mm) output for the adaptive non-local damage analysis of a Single-edge notched beam beam. Adaptive SBFEM compared to the numerical simulations published by [561], the experimental results of [563], and the static uniform mesh.

As the meshes are refined, the most refined mesh shown in figure 6.38b produces the load vs CMOD displacement curve closely relatable to the reference solution published by [561] and the experimental results published by [563]. Figure 6.39 also validates the mesh independence of the adaptive simulation by producing comparably similar results to the output generated from the SBFEM uniform mesh shown in figure 6.38a.

Displacement magnitude (refer figure 6.40) and damage evolution (refer figure 6.41) results are produced at CMODs of 0.0024 mm at peak load and after peak load at 0.1 mm. Furthermore, the damage contours include an additional instance corresponding to the end of the simulation when CMOD is 0.5 mm to illustrate the full extent of the damage evolution process.

(a) Displacement magnitude contour (mm) for the adaptive mesh 6 (refer figure 6.37f) at CMOD displacement of 0.0024 mm.

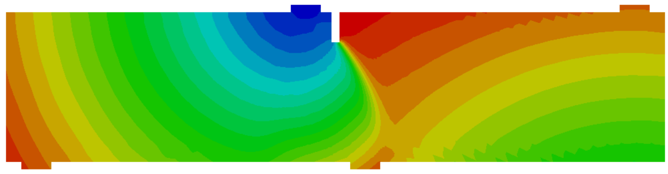

(b) Displacement magnitude contour (mm) for the adaptive mesh 6 (refer figure 6.37f) at CMOD displacement of 0.1 mm.

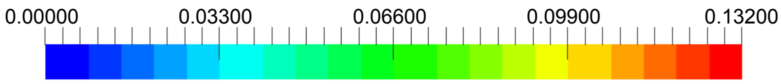

Figure 6.40. Displacement magnitude contours (mm) for the 2D image-based adaptive non-local damage analysis of the single-edge notched beam. Outputs recorded for the adaptive mesh shown in figure 6.37f.

The antisymmetric loading of the beam results in a curved crack path, which starts from the right corner of the notch and ends at the lower right loading platen (see figure 6.41). As the damage grows from the notch damage growth at the bottom of the beam is arrested.

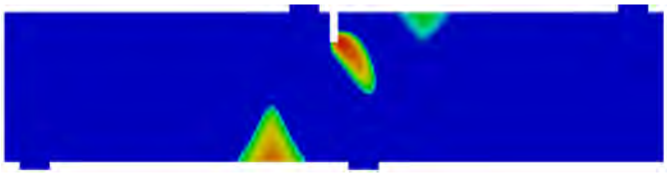

(a) Damage contour for the adaptive mesh 6 (refer figure 6.37f) at CMOD displacement of 0.0024 mm.

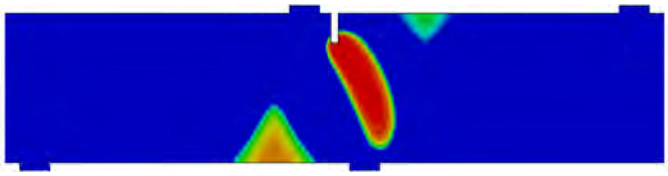

(b) Damage contour for the adaptive mesh 6 (refer figure 6.37f) at CMOD displacement of 0.1 mm.

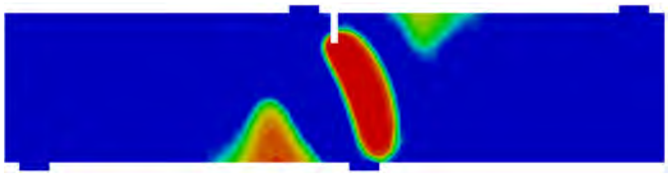

(c) Damage contour for the adaptive mesh 6 (refer figure 6.37f) at CMOD displacement of 0.5 mm.

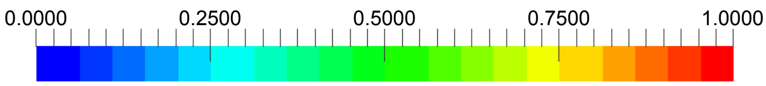

Figure 6.41. Damage (Ω) contours for the 2D image-based adaptive non-local damage analysis of the single-edge notched beam. Outputs recorded for the adaptive mesh shown in figure 6.37f.

Figure 6.41 has a close resemblance with the experimentally observed curve crack path (refer figure 6.42) in [563].

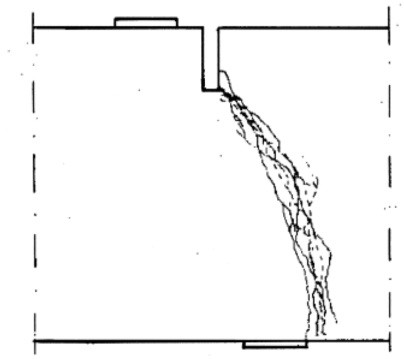

Figure 6.42. Crack path observed by [563] in laboratory experiments conducted on the single-edge notched beam.

The final deformed shape of the beam is shown in figure 6.43. The output confirms the crack path observed in the experimental findings as the highest distorted elements are observed from the right corner of the notch extending towards the lower edge platen.

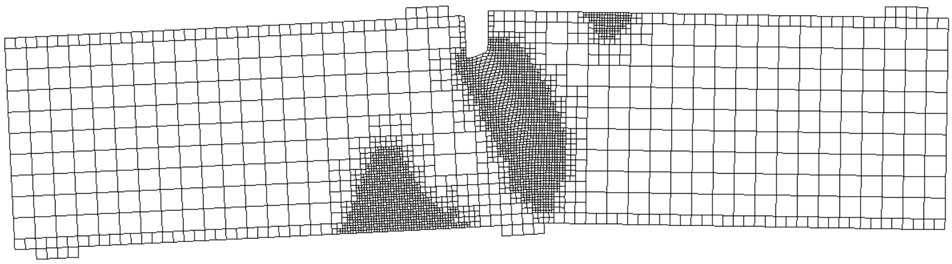

Figure 6.43. The final deformed shape of the specimen obtained in the 2D image-based adaptive non-local damage analysis of the single-edge notched beam. Output recorded for the adaptive mesh shown in figure 6.37f.

There is a good agreement between the numerical model output to that of the experimental results. The adaptive algorithm reduces the number of elements by a mammoth 89% compared to the uniform static mesh. It is also determined that the closeness of the simulation to the experimental observations is a product of proper definition of the equivalent strain in equation (6.6). A considerable influence of the boundary conditions in the loading supports and the effect of the sensitivity to compressive strains versus tensile strains has been observed while setting up this simulation. It is also noted, other definitions [480] in past publications have failed to predict the correct crack path .

6.7 Conclusions

A new highly efficient Automatic Image-Based Adaptive Damage Analysis (AIBADA) is produced in this chapter. AIBADA expands the SBFEM based 2D automatic image-based non-local damage formulation introduced in chapter 5. A simplistic, purely damage variable ω based adaptive algorithm incorporates the salient and efficient features of quadtree decomposition. The new method enables refinement of the DPZ to obtain regularised results. The quadtree based adaptive meshing technique is found to work seamlessly with the SBFEM. The credit is mainly owed to SBFEM's ability to handle hanging nodes through use of polygonal elements, which does not warrant any additional treatments. The efficiency in the computation process is improved by the lesser number of elements produced in the adaptive process. Although it is difficult to generalise the varying computational benefits observed in the four different simulations, an approximate 90% reduction in the number of elements (compared to a uniform mesh) can be attained by adopting an adaptive mesh. The numerical results are verified with both numerical and experimental results in available literature. It is found, the isotropic integral-type damage model adopted is capable in obtaining good agreement between experimental results and numerical simulations. In addition to the type of damage model the effect of proper definition of the equivalent strain parameter has also been critiqued in the SENB example.

The proposed technique is robust and general such that it can be directly extended to adaptive damage analysis in 3D with octree meshing algorithms. Furthermore, there is opportunity to explore the effectiveness of p-refinement, hp-refinement and r-refinement techniques compared to that of h-refinement adopted in this study.

Chapter 7

Conclusions and Recommendations

7.1 Concluding statements – Automatic Image-Based Adaptive Damage Analysis (AIBADA) with SBEFM

Material and structures are constantly susceptible to damage and deterioration. The process of deterioration begins from the development of a process zone in which microcracks emerge and deformations localise. The accumulation of damage in these localised deformation zones eventually leads to the evolution of traction-free macrocracks which results in the loss of load-carrying capacity. The primary intention of this work is to explore this behaviour in materials and structures.

At the beginning of this research the field of Damage Analysis was explored in order to recognise prevailing challenges in the field of computational Continuum Damage Mechanics (CDM). Most methods available to date were found to be computationally expensive which made the application of these frameworks inefficient in handling models with a large number of degrees of freedom especially found in three dimensional (3D) models. Contemporary damage analysis platforms also have difficulties in computer modelling due to the inability to obtain CAD based geometrical data, for example in digital images of materials. These problems also generate a high number of unknowns due to their inherent complex geometries. Therefore these applications have not been thoroughly explored to date. To overcome these issues an Automatic Image-Based Adaptive Damage Analysis (AIBADA) technique has been developed in this thesis, with the novel semi-analytical Scaled Boundary Finite Element Method (SBFEM) as a numerical tool. The adaptive technique minimised mesh refinement, and in turn the number of unknowns introduced in the analysis, which effectively reduced the computational effort. Moreover, the SBFEM polygon (2D) and polyhedral (3D) meshing algorithms assisted in overcoming meshing difficulties around complex material boundaries.

Furthermore, poor solution convergence of numerical solvers in non-linear softening problems is also a difficulty highlighted by many researchers. To overcome this a robust numerical solver incorporated in this study has the capability to accurately trace the equilibrium path beyond limit points till the eventual generation of the macro cracks. The method as a whole provides the user an automatic process with flexibility to analyse numerous types of problems.

The following subsections categorised by each chapter intend to concisely and sequentially present the development of the key outcomes of this research.

7.1.1 Two dimensional damage analysis by the Scaled Boundary Finite Element Method

This thesis first demonstrates in chapter 3 the capability of the SBFEM for material and structural damage analysis in two dimensional space. This extension involves the derivation of the SBFE equations through incorporation of material damage models. The damage analysis framework is built according to the framework of thermodynamics. An elaborate study of damage definitions and measures, damage growth equations, and anisotropy effects are also presented in this chapter.

The geometrical description of the model is through the SBFE polygonal formulation. Each polygonal element is modelled as a linear polygonal element in SBFEM. The boundary of each polygonal element is built up of line elements with one dimensional (1D) shape functions. This polygonal description allows for the elements to have an arbitrary number of edges which can assist in meshing complex geometrical features commonly encountered in CDM.

The investigations involving local damage models are found to be mesh dependent as the damage localisation effects contribute to varying overall responses of the simulations. To overcome this issue non-local models are implemented through exchange of information between integration points. This is a feature not found in standard Finite Element (FE) codes. A comparative study between the local and the non-local damage analysis approaches shows that, while the local approach exhibits severe mesh objectivity, the integral-type non-local model generates solutions that converge to an accurate solution with mesh refinement.

To simplify the modelling process and to reduce the number of unknowns in the solution space the SBFE Scaling Centre (SC) damage formulation is introduced in this chapter. A thorough validation of this novel reduced SC formulation is presented in this chapter with comparisons to the Full Gauss Point (FGP) formulation. This comparison proves the SC damage formulation to be as equally effective as the the FGP formulation. The chapter further validates both the two dimensional (2D) SBFEM SC formulation and the 2D SBFEM FGP formulation through comparisons, with published literature in both regularised and non-regularised analysis techniques.

This part of the research adopts the modified Newton Raphson (m-NR) method with the arc-length technique. The capabilities of the arc-length technique are apparent in the numerical examples presented in this chapter where limit points induced through snap-back behaviour are overcome to follow accurately the damage process of materials and structures very close to failure.

7.1.2 Three dimensional damage analysis by the Scaled Boundary Finite Element Method

The natural continuation of the 2D SBFEM-based damage analysis to 3D SBFEM-based damage analysis is explored in chapter 4. Similar to chapter 3, chapter 4 introduces the derivation of the SBFEM for damage analysis in the 3D space.

The SBFE polyhedral element formulation considered in this section enables the use of elements with arbitrary number of faces, with each face consisting of a n-sided polygon. The formulation accounts for the discretisation of the surfaces of each cell into triangular and quadrilateral elements. Thereafter each surface element is interpolated by adopting standard 2D finite element shape functions for triangles and quadrilateral elements. The formulation assists in the 3D mesh generation of complex features without the restriction of a handful of number of elements (tetrahedral and hexahedral elements), which relaxes the meshing constraints usually experienced in the standard Finite Element Method (FEM).

To maintain the efficiency of the analysis process this chapter continued the use of the 2D SBFE SC formulation by its extension to 3D. The method is validated by comparing the results obtained in the present formulation with published numerical and experimental results found in the CDM literature. The proposed approach demonstrates good synergies with the experimental observations and numerical simulations. The numerical simulations also provide evidence that at least two subdomains are required over the characteristic length of non-local models to obtain mesh independent behaviour.

It is demonstrated that the efficiency of the damage analysis framework is enhanced by the inherent advantageous of the SBFEM to pre-compute strain modes and weight function prior to the iterative solution process, and the reduction of spatial dimension by one requiring only integration on the boundary. These advantages enable the framework to handle 3D problems that involve large number of DOFs.

This chapter also presents the development of the arc-length incorporated m-NR method to include accelerating and damping line search algorithms. A crucial comparison of the effectiveness of the this robust implicit solver to that of an explicit solver is conducted in this chapter. Here the implicit scheme is found to perform better than the explicit scheme as it enabled a higher level of accuracy in tracing the equilibrium path. The efficiency of the implicit scheme although lower than the explicit scheme tend to become comparably similar for problems that exhibit complex softening behaviour. This is owed to the fact that the explicit scheme require small iteration steps to overcome certain “difficult” points in the post peak softening regime.

7.1.3 Two and three dimensional Automatic Image-Based Damage Analysis with the Scaled Boundary Finite Element Method

Chapter 5 introduces the novel Automatic Image-Based Damage Analysis technique with the SBFEM. The most important capability of this presentation is the development of the SBFEM-based damage analysis technique to incorporate a simple image of a structure or a microstructural material composition as the starting point of the spatial description of the modelling process. This capability of the framework extends the computational CDM to numerous practical applications in the 2D and the 3D space.

The study incorporates the automatic quadtree and octree mesh generation algorithm. The polygonal and the polyhedral formulation respectively used in chapters 3 and 4 are used in the quadtree and octree element formulation. The heirachical mesh generation technique is found to be useful to effectively refine the Damage Process Zone (DPZ) and reduce the number of DOFs. The automatic meshing algorithms are found to be capable in modelling features at different scales efficiently through a simple local refinement procedure.

The computational effort and time is significantly reduced by use of a balanced mesh and storing only the unique cell patterns (master cells) data. However, unlike other numerical methods such a approach does not interfere with the efficiency of the technique presented here because the SBFEM’s capability to handle the hanging nodes created in the mesh generation without any additional meshing requirement. The ability to pre-compute the stiffness of the master cells and the calculation of stiffness of other geometrically similar cells by simple scalar multiplication enables the parallelisation of the stiffness calculation for the model. The numerical simulations provides evidence of the efficiency of the technique to model and analyse complex problems consisting of over half a million

DOFs using an Intel Core i7 @3.4 GHz desktop computer with 16 GB RAM.

One of the crucial conclusions of this chapter is revealed by the comparison of the analysis outputs obtained through the smoothened and non-smoothened meshes. Mesh smoothing is concluded to not be a necessary requirement in damage analysis as the damage development is dependent on the equivalent strain parameter calculated by the weighted average of the strain field within a certain radius of influence. This averaging therefore smooths the effects of strain concentration at jagged interfaces. The chapter also explores the effects of the non-local formulations through material interfaces, considering material characteristic length parameter associated with the width of the microstructural damage zone.

7.1.4 Two dimensional Automatic Image-Based Adaptive Damage Analysis (AIBADA) with the Scaled Boundary Finite Element Method

The process of adaptive mesh refinement in damage analysis is explored in chapter 6. This chapter develops a highly efficient damage variable ω based adaptive damage analysis framework in 2D.

This method is found to further reduce the computational burden by only refining the DPZ. The SBFEM's ability to handle hanging nodes within the polygonal formulation aids in eliminating processes such as triangulation or enrichment of interpolation functions. This further enhances the efficiency of the overall framework. The efficiency in the computation process is improved by the less number of elements produced in the adaptive process. The adaptive process is validated by comparing the results to numerical and experimental results found in the CDM research literature.

The research builds an overall efficient image-based damage analysis framework that develops the geometrical description of the model through the colour distribution of an image. The automatic quadtree heirachical mesh generation technique efficiently generates a spatial decomposition of the problem domain which seamlessly functions with the numerical method, the SBFEM. The AIBADA adaptive process enhances and improves the accuracy of the solution space by adaptively refining the DPZ.

7.2 Recommendations for future work

The following subsections highlight the viable future extensions of this work.

7.2.1 Implicit gradient-based damage analysis with the Scaled Boundary Finite Element Method

The integral-type damage models calculate the non-local equivalent strain $\bar{\tilde{\varepsilon}}$ parameter by means spatial averaging over the surrounding domain V with respect to a weight function α_0 such that

$$\bar{\tilde{\varepsilon}}(x) = \frac{\int_v \alpha_0(||x-\theta||)\tilde{\varepsilon}(\theta)\,d\theta}{\int_v \alpha_0(||x-\theta||)d\theta}. \tag{7.1}$$

Usually, an isotropic function such as the Gauss distribution function

$$\alpha_0(r) = \exp\left[-\frac{d^2}{2l^2}\right], \tag{7.2}$$

is chosen as weight function over the domain V. This weight function depends on the distance $r = ||x-\theta||$ between points x and θ and on a parameter l called the internal length scale. This quantity represents a measure of the non-local averaging.

The implicit and the explicit gradient-based damage formulations are differential counterparts of the integral-type damage model. These models incorporate the first or higher order gradients of internal variables into the constitutive relations. The gradient formulation can be derived by considering an alternative description of the local equivalent strain $\tilde{\varepsilon}$ in a Taylor series around x. Substituting the Taylor series expansion into equation (7.1) and considering an isotropic weighting function such as the Gaussian distribution function given in equation (7.2) produces

$$\bar{\tilde{\varepsilon}}(x) = \tilde{\varepsilon}(x) + \frac{1}{2}l^2\nabla^2\tilde{\varepsilon}(x) + \frac{1}{8}l^4\nabla^4\tilde{\varepsilon}(x) + \ldots, \tag{7.3}$$

where the odd terms cancel because of the isotropy of α_0. In equation (7.3), ∇ is the Laplacian operator. Retaining up to the second term in equation (7.3) gives the Helmholtz's equation as

$$\overline{\tilde{\varepsilon}}\,(x) = \tilde{\varepsilon}\,(x) + c\nabla^2\tilde{\varepsilon}\,(x)\,, \tag{7.4}$$

where, $c = l^2/2$. Therefore in relation to equation (7.4) in gradient-based models damage is assumed to be driven by the local equivalent strain $\tilde{\varepsilon}$ and also by its Laplacian, $\nabla^2\tilde{\varepsilon}$. This explicit dependence of the non-local variable $\overline{\tilde{\varepsilon}}$ on the corresponding local variable $\tilde{\varepsilon}$ in equation (7.4) is referred to as the explicit gradient-enhancement.

The presence of the second derivatives of internal variables make the explicit models hard to implement numerically. Therefore the implicit formulation is usually adopted which defines the non-local variable indirectly as the solution of a Helmholtz-type differential equation ([301]).

The implicit form of the inhomogeneous elliptic equation given in equation (7.5) is produced by applying the Laplacian operator to equation (7.3) and multiplying by c. The resultant equation is then subtracted from equation (7.3).

$$\overline{\tilde{\varepsilon}}\,(x) - c\nabla^2\tilde{\varepsilon}\,(x) = \tilde{\varepsilon}\,(x) \tag{7.5}$$

Equation (7.5) can be treated in a weak form and applied a divergence theorem to only impose C^0 continuity requirement on the displacement shape functions.

The boundary value problem can now be formulated in tensorial form by the following coupled governing equations:

$$\overline{\tilde{\varepsilon}}\,(x) - c\nabla^2\tilde{\varepsilon}\,(x) = \tilde{\varepsilon}\,(x)\mathrm{in}V, \tag{7.6a}$$

$$\nabla\cdot\sigma = 0 \qquad \mathrm{in}V, \tag{7.6b}$$

where, σ is the Cauchy stress tensor. The boundary conditions can then be applied such that

$$\sigma n = \bar{t}\,\mathrm{in} S_t, \tag{7.7a}$$

$$u = \bar{u} \mathrm{in} S_u, \tag{7.7b}$$

$$\nabla \bar{\bar{\varepsilon}} \cdot n = 0 \mathrm{in} S, \tag{7.7c}$$

where, n is the unit vector normal to the boundary S, $\bar{t}$ are the prescribed tractions and $\bar{u}$ are the prescribed displacements. S_t represents the boundary where tractions are applied and S_u represents the part of the boundary where displacement boundary conditions are applied. S_t and S_u are disjointed parts of the boundary such that $S_u \bigcup S_t = S$. Similar to the integral-type formulation the Cauchy stress tensor σ is related to the infinitesimal strain tensor ε by

$$\sigma = (1 - \omega)\,\mathbf{D} : \varepsilon, \tag{7.8}$$

where, $\mathbf{D}$ is the fourth-order constant elasticity tensor and ω is the isotropic damage variable.

The gradient enhanced formulation limits the localisation as the curvature of the strain profile is negative around the point in the domain that experiences the largest strain. Therefore with reference to equation (7.4), due to the presence of the Laplacian term the non-local equivalent strain is smaller than the local strain. This slows down the strain growth in the central part of the localized zone where negative curvature of the strain profile is large whereas the adjacent regions will experience an accelerated growth in strain, so the localization zone expands.

7.2.2 Elastoplastic damage analysis with the Scaled Boundary Finite Element Method

In this section the possible future extension of the SBFE elastoplastic analysis framework to an image-based approach for elastoplastic damage analysis is described. The model considers the softening behaviour characterized by degradation of the yield limit. The adoption of the non-local continuum avoids problems of convergence at mesh refinement and spurious mesh sensitivity.

The applications of the SBFEM in elastoplastic material non-linearity was first introduced by Ooi et al. [73] in their 2014 publication on the SBFE polygon-based formulation for elastoplastic analysis. The softening plasticity non-local formulation was first investigated in [300]. This development was subsequent to the development of the non-local elastoplasticity model by Eringen [564, 565].

In this formulation the non-local concept is only applied to parameters which cause the degradation while keeping the definition of the strains local. Therefore the degradation is assumed to affect of the yield limit. The yield limit is associated with the reduction of the areas of cohesive or plastic frictional connections. The formulation therefore does not consider the material stiffness degradation. This consideration produces the unloading slope same as the initial elastic slope as shown in figure 7.1.

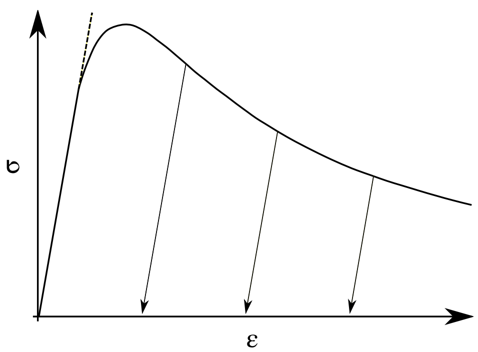

Figure 7.1. Degradation of the yield limit and the resultant unloading slope similar to the initial elastic slope.

7.2.2.1 Non-local elastoplastic continuum formulation

The non-local formulation considers the spatial average of the magnitude of plastic strain ε^{p} . At a location x, ε^{p} may be defined by the equation

$$\langle \varepsilon^{\mathrm{p}}(x) \rangle = \frac{1}{V_r(x)} \int_v \alpha(\mathbf{s}-x)\, \varepsilon^{\mathrm{p}}(\mathbf{s})\, dV = \int_v \alpha^*(x,\mathbf{s})\, \varepsilon^{\mathrm{p}}(\mathbf{s})\, dV, \tag{7.9}$$

where

$$V_r(x) = \int_v \alpha_0(\mathbf{s}-x)\, dV, \tag{7.10}$$

and

$$\alpha^*(x,\mathbf{s}) = \alpha_0(\mathbf{s}-x)/V_r(x). \tag{7.11}$$

In equation (7.9), the $\langle\rangle$ denote the averaging operator, V represents the volume of the body, $\alpha_0(x)$ is the weighting function that defines the averaging, $\mathbf{s}$ is the general coordinate vector, and V_r is the representative volume. The averaging may be specified by the normal (Gaussian) distribution function

$$\alpha(x) = \exp\left[-\left(\frac{k|x|}{l}\right)^2\right], \tag{7.12}$$

where for one, two and three dimensions

$$1\text{D}: |x|^2 = x^2 \qquad k = \sqrt{\pi} \qquad = 1.772, \tag{7.13a}$$

$$2\text{D}: |\mathrm{x}|^2 = x^2 + y^2 \qquad k = 2 \qquad , \tag{7.13b}$$

$$3\text{D}: |x|^2 = x^2 + y^2 + z^2 \qquad k = \left(6\sqrt{\pi}\right)^{1/3} = 2.179, \tag{7.13c}$$

and l is the characteristic length.

7.2.2.2 Non-local generalization of classical incremental plasticity

The derivation presented here begins with the local plasticity model. Thereafter building on the this local plasticity model the generalised non-local plasticity model is presented.

For a typical plasticity model the yield surfaces can be written as

$$\mathrm{F}(\sigma,\kappa) = 0, \tag{7.14}$$

where,

$$\mathrm{F}(\sigma,\kappa) = f(\sigma) - \gamma. \tag{7.15}$$

Here σ denotes the stress tensor, the function $f(\sigma)$ can be taken as the effective stress σ^*, and γ is a hardening-softening parameter. κ may be interpreted as the yield limit which can either increase when hardening or decrease when softening. In a simplified formulation one parameter in the model can be considered to influence the hardening or softening behaviour of the material.

Next the normality rule between the incremental plastic strain $\triangle\varepsilon^{\mathrm{p}}$ and plastic strain tensor ε^{p} can be set as follows

$$\triangle\varepsilon^{\mathrm{p}} = \mathrm{F}_{,\sigma}\triangle\lambda = f_{,\sigma}\triangle\lambda. \tag{7.16}$$

The derivatives $\mathrm{F}_{,\sigma}$ and $f_{,\sigma}$ represent respectively $\partial\mathrm{F}/\partial\sigma$ and $\partial f/\partial\sigma$. The parameter $\triangle\lambda$ is a scalar proportionality coefficient. The loading-unloading condition given by

$$\mathrm{F}\triangle\lambda = 0, \tag{7.17a}$$

$$\triangle\lambda \geq 0, \tag{7.17b}$$

$$\mathrm{F} \leq 0, \tag{7.17c}$$

should hold concurrently.

Considering κ to depend only on ε^{p} , Prager's continuity condition can be introduced as

$$\mathrm{F}_{,\sigma} : \triangle\sigma + \mathrm{F}_{,\kappa}\kappa_{,\varepsilon^{\mathrm{p}}} : \mathrm{F}_{,\sigma}\triangle\lambda = 0. \tag{7.18}$$

Taking H as the plastic tangential modulus given by

$$\mathrm{H} = -\mathrm{F}_{,\kappa}\kappa_{,\varepsilon^{\mathrm{p}}}\varepsilon^{\mathrm{p}}_{,\varepsilon^{\mathrm{p}}} : \mathrm{F}_{,\sigma}, \tag{7.19}$$

equation (7.18) reduces to

$$\mathrm{F}_{,\sigma} : \triangle\sigma - \mathrm{H}\triangle\lambda = 0. \tag{7.20}$$

Rearranging equation (7.20) yields

$$\triangle\lambda = \left(\mathrm{F}_{,\sigma} : \triangle\sigma\right)/\mathrm{H} \tag{7.21}$$

Using equations (7.16) and (7.21) the incremental stress-strain relationship can be written as

$$\triangle\sigma = \mathbf{D} : (\triangle\varepsilon - \triangle\varepsilon^{\mathrm{p}}), \tag{7.22}$$

where, $\mathbf{D}$ is the tensor of elastic moduli. Substituting equation (7.22) into equation (7.21) gives

$$\triangle\lambda = \frac{\mathrm{F}_{,\sigma} : \mathbf{D} : \triangle\varepsilon}{\mathrm{F}_{,\sigma} : \mathbf{D} : \mathrm{F}_{,\sigma} + \mathrm{H}}. \tag{7.23}$$

The effective plastic strain can be considered as the path length of plastic strain, i.e $\triangle\varepsilon^{\mathrm{p}} = \left(\triangle\varepsilon^{\mathrm{p}} : \triangle\varepsilon^{\mathrm{p}}\right)^{1/2}$, or defined by work equivalence $\sigma : \triangle\varepsilon^{\mathrm{p}} = \sigma^{*}\triangle\varepsilon^{\mathrm{p}}$. The latter is considered in this formulation. Making $\triangle\varepsilon^{\mathrm{p}}$ the subject of the equation and substituting from equation (7.16) gives

$$\triangle\varepsilon^{\mathrm{p}} = \frac{1}{\sigma^{*}}\sigma : \mathrm{F}_{,\sigma}\triangle\lambda. \tag{7.24}$$

Considering equation (7.15), function $f(\sigma)$ is assumed to be a homogeneous function of degree n. Therefore by applying Euler's theorem

$$\sigma : f_{,\sigma} = nf. \tag{7.25}$$

Also if the yield function is written in the form such that $n = 1$ and $f(\sigma) = \sigma^{*}$, and the hardening-softening parameter κ assumed as a function of the effective plastic strain ε^{p} such that $k = k(\varepsilon^{\mathrm{p}})$ then the equation (7.18) for H is further simplified as

$$\mathrm{H} = -\mathrm{F}_{,\kappa}\kappa_{,\varepsilon^{\mathrm{p}}}\varepsilon^{\mathrm{p}}_{,\varepsilon^{\mathrm{p}}} : \mathrm{F}_{,\sigma} = \kappa_{,\varepsilon^{\mathrm{p}}}\varepsilon^{\mathrm{p}}_{,\varepsilon^{\mathrm{p}}} : f_{,\sigma}, \tag{7.26a}$$

$$\mathrm{H} = \kappa_{,\varepsilon^{\mathrm{p}}}\frac{1}{\sigma^{*}}\left(\sigma : f_{,\sigma}\right) = \kappa_{,\varepsilon^{\mathrm{p}}}\frac{nf}{\sigma^{*}}, \tag{7.26b}$$

$$\mathrm{H} = \kappa_{,\varepsilon^{\mathrm{p}}}. \tag{7.26c}$$

Now, equation (7.22) can be generalized as

$$\triangle\sigma = \mathbf{D} : (\triangle\varepsilon - \triangle\tilde{\varepsilon}^{\mathrm{p}}), \tag{7.27}$$

by applying the concept of non-local continuum with local strain. Here $\triangle\tilde{\varepsilon}^{\mathrm{p}}$ is the non-local plastic strain increment.

7.2.3 3D adaptive damage analysis and hp-adpative damage analysis with the Scaled Boundary Finite Element Method

A continuation of the 2D adaptive damage analysis framework can be implemented in the 3D adaptive damage analysis space. The general adaptive framework thereafter can be extended to the image-based adaptive quadtree and octree damage analysis technique.

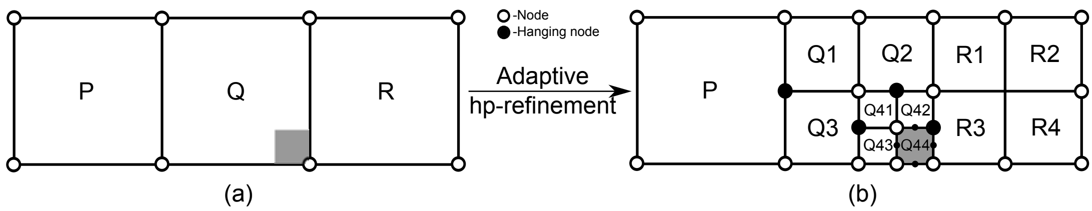

Figure 7.2. Adaptive hp-refinement strategy for non-local damage analysis.

Furthermore, there is an opportunity to also explore the effectiveness of other adaptive refinement strategies such as the p-refinement, hp-refinement and r-refinement techniques. As a demonstration the adaptive hp-refinement strategy is shown in figure 7.2. In this demonstration the lower right corner of element Q in figure 7.2a is assumed to be damaged. The h-adaptive process then recursively subdivides the element Q to generate the element decomposition for element Q shown in figure 7.2b. The h-adaptive process now has separated the damaged element to element Q44. The process also requires the subdivision of the element R to four separate elements R1-R4 in order to maintain the 2:1 rule. In the hp-adpative scheme this stage is followed by the p-adaptive process where order of the polynomial approximation in element Q44 is increased from linear interpolation to quadratic interpolation for better description of the displacement field.

Through the power of persistent curiosity and strategic insight, every process can be refined to be made more efficient, accurate, adaptive and automatic.

Dion Dilina Dissanayake

Bibliography

[1] K. Shimada, A. Yamada, and T. Itoh, "Anisotropic triangulation of parametric surfaces via close packing of ellipsoids," *International Journal of Computational Geometry & Applications*, vol. 10, no. 04, pp. 417–440, 2000.

[2] S. Yamakawa and K. Shimada, "Triangular/quadrilateral remeshing of an arbitrary polygonal surface via packing bubbles," in *Geometric Modeling and Processing, 2004. Proceedings*. IEEE, 2004, pp. 153–162.

[3] P. Young, T. Beresford-West, S. Coward, B. Notarberardino, B. Walker, A. Abdul-Aziz, and Phil.Trans.R.Soc.A, "An efficient approach to converting three dimensional image data into highly accurate computational models," vol. 7, no. 8, 2008.

[4] D. L. Logan, *A first course in the finite element method*. Cengage Learning, 2011.

[5] H. Man., C. Song, S. Natarajan, E. Ooi, and C. Birk, "Towards automatic stress analysis using scaled boundary finite element method with quadtree mesh of high-order elements," *Finite Elements in Analysis and Design*, vol. 6, 2014.

[6] T. Zangmeister, H. Andra, and R. Muller, "Comparison of xfem and voxelbased fem for the approximation of discontinuous stress and strain at material interfaces," 2012.

[7] E. El-Qawasmeh, "A quadtree-based representation technique for indexing and retrieval of image databases," *Journal of Visual Communication and Image Representation*, vol. 14, no. 3, pp. 340–357, 2003.

[8] D. Meagher, “Geometric modeling using octree encoding,” *Computer graphics and image processing*, vol. 19, no. 2, pp. 129–147, 1982.

[9] Z. P. Bazant and G. Pijaudier-Cabot, “Measurement of characteristic length of non-local continuum,” *Journal of Engineering Mechanics*, vol. 115, no. 4, 1989.

[10] M. Jirasek, “Non local damage mechanics,” *Revue Europeenne de Genie Civil*, vol. 11, no. 7-8, pp. 993–1021, 2007.

[11] V. V. Clemens, A. S. Michael, J. R. H. Thomas, and R. de Borst., “An isogeometric analysis approach to gradient damage models,” *International Journal For Numerical Methods In Engineering*, vol. 86, no. 115 -134, 2011.

[12] A. Simone, “Explicit and implicit gradient-enhanced damage models,,” *Revue Europeenne de Genie Civil*, vol. 11, no. 7 - 8, pp. 1023 – 1044, 2007.

[13] R. S. Maravalalu Suresh, “Nonlocal damage models for concrete,” Master’s thesis, Delft University of Technology, 2013.

[14] B. Winkler, G. Hofstetter, and H. Lehar, “Application of a constitutive model for concrete to the analysis of a precast segmental tunnel lining,” *International Journal for Numerical and Analytical Methods in Geomechanics*, vol. 28, pp. 797–819, 2004.

[15] O. Lloberas-Valls, D. Rixen, B. Simone, and S. L.J., “Domain decomposition techniques for the efficient modeling of brittle heterogeneous materials,” *Computer Methods in Applied Mechanical Engineering*, vol. 200, no. 1577 - 1590, 2011.

[16] M. Geers, R. de Borstc, and R. Peerlings, “Damage and crack modeling in single-edge and double-edge notched concrete beams,” *Engineering Fracture Mechanics*, vol. 65, pp. 247–261, 2000.

[17] H. Schlangen, "Experimental and numerical analysis of fracture processes in concrete," Ph.D. dissertation, Delft University of Technology, Delft, The Netherlands, 1993.

[18] R. V. Southwell, "Relaxation methods in theoretical physics: a continuation of the treatise," *Relaxation methods in engineering science, Vol. 2, The Clarendon Press*, 1946.

[19] L. F. Richardson, "Ix. the approximate arithmetical solution by finite differences of physical problems involving differential equations, with an application to the stresses in a masonry dam," *Phil. Trans. R. Soc. Lond. A*, vol. 210, no. 459-470, pp. 307–357, 1911.

[20] D. d. G. Allen, *Relaxation Methods*. McGraw Hill, London, 1955.

[21] S. H. Crandall, *Engineering analysis: A survey of numerical procedures*. Krieger Publishing Co. Inc., 1983.

[22] B. A. Finlayson, *The method of weighted residuals and variational principles*. SIAM, 2013, vol. 73.

[23] B. G. Galerkin, "Series solution of some problems of elastic equilibrium of rods and plates,," *Vestnik inzhenerov i tekhnikov*, vol. 9, no. 7, pp. 897–908, 1915.

[24] W. Ritz, "Uber eine neue methode zur lÃ¶sung gewisser variationsprobleme der mathematischen physik," *Journal fÃŒr die Reine und Angewandte Mathematik*, vol. 135, pp. 1–61, 1909.

[25] K. Washizu, "Variational methods in elasticity and plasticity." *Pergamon Press, New York*, vol. 3, 1982.

[26] M. J. Turner, H. C. Clough, Martin., and L. J. Topp, "Stiffness and deflection analysis of complex structures," *journal of the Aeronautical Sciences*, vol. 23, no. 9, pp. 805–823, 1956.

[27] R. W. Clough, “The finite element method in plane stress analysis,” in *Proceedings of the 2nd ASCE Conference on Electronic Computation*, 1960.

[28] C. Brebbia and J. Dominguez, “Boundary element methods for potential problems,” *Applied Mathematical Modelling*, vol. 1, no. 7, pp. 372–378, 1977.

[29] J. Dominguez, “Stress analysis around anchor plates: a boundary element method application,” Ph.D. dissertation, PhD Thesis. Universidad de Sevilla, 1977.

[30] T. Belytschko and T. Black, “Elastic crack growth in finite elements with minimal remeshing,” *International Journal for Numercal Methods in Engineering*, vol. 56, pp. 601–620., 1999.

[31] C. Song and J. Wolf, “The scaled boundary finite element method-alias consistent infinitesimal finite element cell method for elastodynamics,” *Computational Methods in Applied Mechanical Eng*, vol. 147, 1997.

[32] R. M. McMeeking and J. Rice, “Finite-element formulations for problems of large elastic-plastic deformation,” *International Journal of Solids and Structures*, vol. 11, no. 5, pp. 601–616, 1975.

[33] S. Chan, I. Tuba, and W. Wilson, “On the finite element method in linear fracture mechanics,” *Engineering fracture mechanics*, vol. 2, no. 1, pp. 1–17, 1970.

[34] R. S. Barsoum, “On the use of isoparametric finite elements in linear fracture mechanics,” *International journal for numerical methods in engineering*, vol. 10, no. 1, pp. 25–37, 1976.

[35] T. Chung, “Finite element analysis in fluid dynamics,” *NASA STI/Recon Technical Report A*, vol. 78, 1978.

[36] J. N. Reddy and D. K. Gartling, *The finite element method in heat transfer and fluid dynamics*. CRC press, 2010.

[37] J. Coggon, "Electromagnetic and electrical modeling by the finite element method," *Geophysics*, vol. 36, no. 1, pp. 132–155, 1971.

[38] G. Mur and A. De Hoop, "A finite-element method for computing three-dimensional electromagnetic fields in inhomogeneous media," *IEEE Transactions on Magnetics*, vol. 21, no. 6, pp. 2188–2191, 1985.

[39] *Algor Interactive Systems, 150 Beta Drive, Pittsburgh, PA 15238.*

[40] *Web site http://www.abaqus.com.*

[41] *Swanson, J. A., ANSYS-Engineering Analysis Systems Users Manual, Swanson Analysis Systems, Inc., Johnson Rd., P.O. Box 65, Houston, PA 15342.*

[42] *COSMOS/M, Structural Research & Analysis Corp., 12121 Wilshire Blvd., Los Angeles, CA 90025.*

[43] *web site http://ce6000.cegatech.edu.*

[44] *Hallquist, J. O., LS-DYNA, Theoretical Manual, Livermore Software Technology Corp., 1998.*

[45] *web site http://www.mscsoftware.com.*

[46] *MSC/NASTRAN, MacNeal-Schwendler Corp., 600 Suffolk St., Lowell, MA, 01854.*

[47] *web site http://emrc.com.*

[48] *Toogood, Roger, Pro/MECHANICA Structure Tutorial, SDC Publications, 2001.*

[49] *Computers & Structures, Inc., 1995 University Ave., Berkeley, CA 94704.*

[50] *STARDYNE, Research Engineers, Inc., 22700 Savi Ranch Pkwy, Yorba Linda, CA 92687.*

[51] L. Kachanov, "Time of the rupture process under creep conditions," *Akad. Nauk. SSR. Otd. Tekh*, vol. 8, pp. 26–31, 1958.

[52] B. Sinha, K. Gerstle, and T. L.G., "Stress strain relations for concrete under cyclic loading," *ACI Journal*, vol. 61, pp. 195–211, 1964.

[53] J. Lemaitre, *A Course on Damage Mechanics*, 2nd edn, Ed. Springer, Berlin, 1996.

[54] R. de Borst and H. B. Miihlhaus, "Continuum models for discontinuous media," *Fracture Processes in Concrete, Rock and Ceramics. Proceedings of the International Rilem/Esis Conference*, vol. 2, pp. 601–618, 1991.

[55] M. A. Crisfield, "Local instabilities in the non linear analysis of reinforced concrete beams and slabs." *Inst. Civil Engr.*, vol. 73, pp. 135–I45, 1982.

[56] S. Pietruszczak and Z. Mroz, "Finite element analysis of the deformation of strain-softening materials," *Journal of Numerical Methods in Engineering*, vol. 17, pp. 327–334, 1981.

[57] A. Needleman, "Material rate dependence and mesh sensitivity in localization problems," *Computational. Methods in Applied Mechanics*, vol. 67, pp. 69–85, 1988.

[58] K. Betts, "Adaptivity reshapes fe analysis," *Mechanical Engineering-CIME*, vol. 112, no. 10, pp. 59–65, 1990.

[59] J. F. O'brien and J. K. Hodgins, "Graphical modeling and animation of brittle fracture," Georgia Institute of Technology, Tech. Rep., 1999.

[60] J. F. O'brien, A. W. Bargteil, and J. K. Hodgins, "Graphical modeling and animation of ductile fracture," in *ACM transactions on graphics (TOG)*, vol. 21, no. 3. ACM, 2002, pp. 291–294.

[61] C. Song, E. T. Ooi, L. N. P. Aladurthi, and N. Sundararajan, "A novel error indicator and an adaptive refinement technique using the scaled boundary finite element method," *Engineering Analysis with Boundary Elements*, vol. 94, no. 10-24, 2018.

[62] J. R. Shewchuk, "Updating and constructing constrained delaunay and constrained regular triangulations by flips," in *Proceedings of the nineteenth annual symposium on Computational geometry*. ACM, 2003, pp. 181–190.

[63] O. Zienkiewicz and D. Phillips, "An automatic mesh generation scheme for plane and curved surfaces by isoparametric co-ordinates," *International Journal for Numerical Methods in Engineering*, vol. 3, no. 4, pp. 519–528, 1971.

[64] Q. Du and D. Wang, "Recent progress in robust and quality delaunay mesh generation," *Journal of Computational and Applied Mathematics*, vol. 195, no. 1-2, pp. 8–23, 2006.

[65] R. Löhner and P. Parikh, "Generation of three-dimensional unstructured grids by the advancing-front method," *International Journal for Numerical Methods in Fluids*, vol. 8, no. 10, pp. 1135–1149, 1988.

[66] T. Blacker, "Automated conformal hexahedral meshing constraints, challenges and opportunities," *Engineering with Computers*, vol. 17, no. 3, pp. 201–210, 2001.

[67] P. Reddy, H. Montas, H. Samet, and Shirmohammadi, "Quadtree-based triangular mesh generation for finite element analysis of heterogeneous spatial data," *American Society of Agricultural Engineers (ASAE)*, vol. 01, no. 3072, 2001.

[68] P. Frey and L. Marechal, "Fast adaptive quadtree mesh generation," INRIA, Gamma Project, Tech. Rep., 1998.

[69] J.-L. Batoz and G. Dhatt, "Incremental displacement algorithms for nonlinear problems," *International Journal for Numerical Methods in Engineering*, vol. 14, no. 8, pp. 1262–1267, 1979.

[70] L. Antiga, B. Ene-lordache, L. Caverni, G. P. Cornalba, and A. Remuzzi, "Geometric reconstruction for computational mesh generation of arterial bifurcations from ct angiography," *Comput. Med. Imaging Graph*, vol. 26, pp. 227–235, 2002.

[71] J. Cebral and R. Loehner, “From medical images to anatomically accurate finite element grids,” *International Journal for Numerical Methods in Engineering*, vol. 51, pp. 985–1008, 2001.

[72] M. Viceconti, C. Zannoni, and L. Pierotti, “An application of reverse engineering methods to the creation of cad models of bone segments,” *Comput. Methods Programs Biomed*, vol. 56, pp. 211–220, 1998.

[73] J. Schmitt, J. Meiforth, and M. Lengsfeld, “Development of a hybrid finite element model for individual simulation of intertrochanteric osteotomies,” *Med. Eng. Phys*, vol. 23, pp. 529–539, 2001.

[74] D. C. Wirtz, T. Pandorf, F. Portheine, K. Randermacher, N. Schiffers, A. Prescher, D. Weichert, and F. U. Niethard, “Concept and development of an orthotropic fe model of the proximal femur,” *J. Biomech*, vol. 36, pp. 289–293, 2003.

[75] A. Borthwick and D. Greaves, “Hieararchical tree-based finite element mesh generation,” *International journal for numerical methods in engineering*, vol. 45, pp. 447–471, 1999.

[76] S. Prempramote, C. Song, F. Tin-Loi, and G. Lin, “High-order doubly asymptotic open boundaries for scalar wave equation,” *International Journal for Numerical Methods in Engineering*, vol. 79, no. 3, pp. 340–374, 2009.

[77] X. Chen, C. Birk, and C. Song, “Transient analysis of wave propagation in layered soil by using the scaled boundary finite element method,” *Computers and Geotechnics*, vol. 63, pp. 1–12, 2015.

[78] M. H. Bazyar and C. Song, “Time-harmonic response of non-homogeneous elastic unbounded domains using the scaled boundary finite-element method,” *Earthquake Engineering and Structural Dynamics*, vol. 35, no. 3, pp. 357–384, 2006.

[79] A. Deeks and Wolf, "Stress recovery and error estimation for the scaled boundary finite-element method," *International journal for numerical methods in engineering*, vol. 54, no. 4, pp. 557–583, 2002.

[80] Song and Deeks, "An h-hierarchical adaptive procedure for the scaled boundary finite-element method," *International Journal for Numerical Methods in Engineering*, vol. 54, no. 4, pp. 585–605, 2002.

[81] A. J. Deeks and J. P. Wolf, "A virtual work derivation of the scaled boundary finite-element method for elastostatics," *Computational Mechanics*, vol. 28, no. 6, pp. 489–504, 2002.

[82] J. Liu, G. Lin, F. Wang, and J. Li, "The scaled boundary finite element method applied to electromagnetic field problems," in *IOP Conference Series: Materials Science and Engineering*, vol. 10, no. 1. IOP Publishing, 2010, p. 012245.

[83] C. Song and J. P. Wolf, "The scaled boundary finite element method-alias consistent infinitesimal finite element cell method for diffusion," *International Journal for Numerical Methods in Engineering*, vol. 45, no. 10, pp. 1403–1431, 1999.

[84] L. Lehmann, S. Langer, and D. Clasen, "Scaled boundary finite element method for acoustics," *Journal of Computational Acoustics*, vol. 14, no. 04, pp. 489–506, 2006.

[85] I. Chiong, E. T. Ooi, C. Song, and F. Tin-Loi, "Scaled boundary polygons with application to fracture analysis of functionally graded materials," *International journal for numerical methods in engineering*, vol. 98, no. 8, pp. 562–589, 2014.

[86] I. Chiong, E. T. Ooi, C. Song, and Tin-Loi, "Computation of dynamic stress intensity factors in cracked functionally graded materials using scaled boundary polygons," *Engineering Fracture Mechanics*, vol. 131, pp. 210–231, 2014.

[87] E. T. Ooi, H. Man, S. Natarajan, and C. Song, "Adaptation of quadtree meshes in the scaled boundary finite element method for crack propagation modelling," *Engineering Fracture Mechanics*, vol. 144, pp. 101–117, 2015.

[88] E. Ooi, C. Song, and T. Francis, "A scaled boundary polygon formulation for elasto-plastic analyses," *Computational Methods in Applied Mechanical Engineering*, vol. 268, pp. 905–937, 2014.

[89] H. Man, C. Song, W. Gao, and F. Tin-Loi, "A unified 3d-based technique for plate bending analysis using scaled boundary finite element method," *International Journal for Numerical Methods in Engineering*, vol. 91, no. 5, pp. 491–515, 2012.

[90] H. Man, C. Song, T. Xiang, W. Gao, and F. Tin-Loi, "High-order plate bending analysis based on the scaled boundary finite element method," *International Journal for Numerical Methods in Engineering*, vol. 95, no. 4, pp. 331–360, 2013.

[91] H. Man, C. Song, W. Gao, and F. Tin-Loi, "Semi-analytical analysis for piezoelectric plate using the scaled boundary finite-element method," *Computers & Structures*, vol. 137, pp. 47–62, 2014.

[92] H. Gravenkamp, C. Birk, and C. Song, "Numerical modeling of elastic waveguides coupled to infinite fluid media using exact boundary conditions," *Computers & Structures*, vol. 141, pp. 36–45, 2014.

[93] H. Gravenkamp, C. Birk, and Song, "Simulation of elastic guided waves interacting with defects in arbitrarily long structures using the scaled boundary finite element method," *Journal of Computational Physics*, vol. 295, pp. 438–455, 2015.

[94] E. Riks, "An incremental approach to the solution of snapping and buckling problems," *International journal of solids and structures*, vol. 15, no. 7, pp. 529–551, 1979.

[95] M. A. Crisfield, "A fast incremental/iterative solution procedure that handles "snap -through"," *Computers and Structures*, vol. 13, no. 55-62, 1981.

[96] M. Crisfield, "A fast incremental/iterative solution procedure that handles snap-through," in *Computational Methods in Nonlinear Structural and Solid Mechanics*. Elsevier, 1981, pp. 55–62.

[97] Crisfield, "An arc-length method including line searches and accelerations," *International journal for numerical methods in engineering*, vol. 19, no. 9, pp. 1269–1289, 1983.

[98] R. De Borst, "Computation of post-bifurcation and post-failure behavior of strain-softening solids," *Computers and Structures*, vol. 25, no. 2, pp. 211–224, 1987.

[99] H.-B. Hellweg and M. Crisfield, "A new arc-length method for handling sharp snap-backs," *Computers & Structures*, vol. 66, no. 5, pp. 704–709, 1998.

[100] D. F. Watson, "Computing the n-dimensional delaunay tessellation with application to voronoi polytopes," *The computer journal*, vol. 24, no. 2, pp. 167–172, 1981.

[101] M. A. Yerry and M. S. Shephard, "Automatic three-dimensional mesh generation by the modified-octree technique," *International Journal for Numerical Methods in Engineering*, vol. 20, no. 11, pp. 1965–1990, 1984.

[102] T. D. Blacker and R. J. Meyers, "Seams and wedges in plastering: a 3-d hexahedral mesh generation algorithm," *Engineering with computers*, vol. 9, no. 2, pp. 83–93, 1993.

[103] G. Legrain, R. Allais, and P. Cartraud, "On the use of the extended finite element method with quadtree/octree meshes," *International Journal for Numerical Methods in Engineering*, vol. 86, no. 6, pp. 717–743, 2011.

[104] M. S. Shephard and M. K. Georges, "Automatic three-dimensional mesh generation by the finite octree technique," *International Journal for Numerical methods in engineering*, vol. 32, no. 4, pp. 709–749, 1991.

[105] A. Saputra, H. Talebi, D. Tran, C. Birk, and C. Song, "Automatic image-based stress analysis by the scaled boundary finite element method," *International Journal for Numerical Methods in Engineering*, vol. 109, no. 5, pp. 697–738, 2017.

[106] W. J. Schroeder, B. Geveci, and M. Malaterre, "Compatible triangulations of spatial decompositions," in *IEEE Visualization 2004*. IEEE, 2004, pp. 211–217.

[107] S. Lo, D. Wu, and K. Sze, "Adaptive meshing and analysis using transitional quadrilateral and hexahedral elements," *Finite Elements in Analysis and Design*, vol. 46, no. 1-2, pp. 2–16, 2010.

[108] P. Krysl, E. Grinspun, and P. Schroder, "Natural hierarchical refinement for finite element methods," *International Journal for Numerical Methods in Engineering*, vol. 56, no. 8, pp. 1109–1124, 2003.

[109] A. Tabarraei and N. Sukumar, "Adaptive computations using material forces and residual-based error estimators on quadtree meshes," *Computer methods in applied mechanics and engineering*, vol. 196, no. 25-28, pp. 2657–2680, 2007.

[110] A. Düster, J. Parvizian, Z. Yang, and E. Rank, "The finite cell method for three-dimensional problems of solid mechanics," *Computer methods in applied mechanics and engineering*, vol. 197, no. 45-48, pp. 3768–3782, 2008.

[111] G. Legrain, P. Cartraud, I. Perreard, and N. Moes, "An x-fem and level set computational approach for image-based modelling: Application to homogenization," *International Journal for Numerical Methods in Engineering*, vol. 86, no. 7, pp. 915–934, 2011.

[112] W. Lian, G. Legrain, and P. Cartraud, “Image-based computational homogenization and localization: comparison between x-fem/levelset and voxel-based approaches,,” *Computational Mechanics*, vol. 51, no. 3, pp. 279–293, 2013.

[113] G. B. Coleman and H. C. Andrews, “Image segmentation by clustering,” *Proceedings of the IEEE*, vol. 67, no. 5, pp. 773–785, 1979.

[114] P. K. Sahoo, S. Soltani, and A. K. Wong, “A survey of thresholding techniques,” *Computer vision, graphics, and image processing*, vol. 41, no. 2, pp. 233–260, 1988.

[115] N. R. Pal and S. K. Pal, “A review on image segmentation techniques,” *Pattern recognition*, vol. 26, no. 9, pp. 1277–1294, 1993.

[116] D. L. Pham, C. Xu, and J. L. Prince, “Current methods in medical image segmentation,” *Annual review of biomedical engineering*, vol. 2, no. 1, pp. 315–337, 2000.

[117] K. Terada, N. Miura, and Kikuchi, “Digital image-based modeling applied to the homogenization analysis of composite materials,” *Computational Mechanics*, vol. 20, no. 4, pp. 331–346, 1997.

[118] L. Giraldi, A. Nouy, G. Legrain, and P. Cartraud, “Tensor-based methods for numerical homogenization from high-resolution images,” *Computer Methods in Applied Mechanics and Engineering*, vol. 254, pp. 154–169, 2013.

[119] D. Ulrich, B. van Rietbergen, H. Weinans, and P. Ruegsegger, “Finite element analysis of trabecular bone structure: a comparison of image-based meshing techniques,” *Journal of biomechanics*, vol. 31, no. 12, pp. 1187–1192, 1998.

[120] Z. Wang, J. C.-M. Teo, C.-K. Chui, S. H. Ong, C. H. Yan, S. Wang, H.-K. Wong, and S.-H. Teoh, “Computational biomechanical modelling of the lumbar spine using marching-cubes surface smoothened finite element voxel meshing,” *Computer methods and programs in biomedicine*, vol. 80, no. 1, pp. 25–35, 2005.

[121] J. H. Keyak, J. M. Meagher, H. B. Skinner, and C. D. Mote Jr, "Automated three-dimensional finite element modelling of bone: a new method." *Journal of Biomedical Engineering*, vol. 12, no. 389-397, 1990.

[122] M. Lengsfeld, J. Schmitt, P. Alter, J. Kaminsky, and R. Leppek, "Comparison of geometry-based and ct voxel-based finite element modelling and experimental validation," *Medical engineering & physics*, vol. 20, no. 7, pp. 515–522, 1998.

[123] C. Richardson, J. Hegemann, E. Sifakis, J. Hellrung, and J. Teran, "A xfem method for modeling geometrically elaborate crack propagation in brittle materials," *International Journal for Numerical Methods in Engineering*, no. 88, pp. 1042–1065, 2011.

[124] W. E. Lorensen and H. E. Cline, "Marching cubes: A high resolution 3d surface construction algorithm," in *ACM siggraph computer graphics*, vol. 21, no. 4. ACM, 1987, pp. 163–169.

[125] T. S. Newman and H. Yi, "A survey of the marching cubes algorithm," *Computers & Graphics*, vol. 30, no. 5, pp. 854–879, 2006.

[126] G. Legrain, N. Chevaugeon, and K. Dréau, "High order x-fem and levelsets for complex microstructures: uncoupling geometry and approximation," *Computer Methods in Applied Mechanics and Engineering*, vol. 241, pp. 172–189, 2012.

[127] W. Lian, G. Legrain, and P. Cartraud, "Image-based computational homogenisation and localisation: comparison between xfem / level set and voxel-based approache," *Computational Mechanics*, pp. 1–15, 2012.

[128] R. Guldberg, S. Hollister, and G. Charras, "The accuracy of digital image-based finite element models," *Journal of Biomechanical Engineering*, vol. 289, 1998.

[129] D. Ulrich, B. van Rietbergen, H. Weinans, and P. RÃŒegsegger, "Finite element analysis of trabecular bone structure: a comparison of image-based meshing techniques," *Journal of biomechanics*, vol. 31, no. 12, pp. 1187–1192, 1998.

[130] R. Müller and P. Rüegsegger, "Three-dimensional finite element modelling of non-invasively assessed trabecular bone structures," *Medical engineering & physics*, vol. 17, no. 2, pp. 126–133, 1995.

[131] C. L. M. H. Navier, *Résumé des Leçons sur l'Application de la Mécanique*. Dunod, 1864, vol. 2.

[132] R. F. A. Clebsch, *Theorie der elasticität fester körper*. BG Teubner, 1862.

[133] J. H. Argyris and S. Kelsey, *Energy theorems and structural analysis*. Springer, 1960, vol. 960.

[134] R. V. Southwell, "Stress-calculation in frameworks by the method of systematic relaxation of constraints-iii," *Proc. R. Soc. Lond. A*, vol. 153, no. 878, pp. 41–76, 1935.

[135] A. Hrenikoff, "Solution of problems in elasticity by the framework method,," *Journal of Applied Mechanics*, pp. 169–175, 1941.

[136] D. McHenry, "A lattice analogy for the solution of stress problems," *Journal of the ICE*, pp. 59–82, 1943.

[137] D. d. G. Allen and R. V. Southwell, "Relaxation methods applied to engineering problems xiv. plastic straining in two-dimensional stress-systems," *Phil. Trans. R. Soc. Lond. A*, vol. 242, no. 850, pp. 379–414, 1950.

[138] C. Snell, D. Vesey, and P. Mullord, "The application of a general finite difference method to some boundary value problems," *Computers & Structures*, vol. 13, no. 4, pp. 547–552, 1981.

[139] V. Girault, “Theory of a finite difference method on irregular networks,” *SIAM Journal on Numerical Analysis*, vol. 11, no. 2, pp. 260–282, 1974.

[140] V. Pavlin and N. Perrone, “Finite difference energy techniques for arbitrary meshes applied to linear plate problems,” *International Journal for Numerical Methods in Engineering*, vol. 14, no. 5, pp. 647–664, 1979.

[141] R. Courant *et al.*, “Variational methods for the solution of problems of equilibrium and vibrations,” *Lecture Notes in Pure and Applied Mathematics*, pp. 1–1, 1994.

[142] G. Zienkiewicz, O.and Holister, *Stress analysis*. J. Wiley & Son, 1965.

[143] J. Szmelte, “The energy method of networks of arbitrary shape in problems of the theory of elasticity,,” in *Proceedings of the IUTAM, symposium on nonhomogeneity in elasticity and plasticity, Pergamon Press, New York,*, 1959.

[144] O. C. Zienkiewicz, P. Mayer, and Y. K. Cheung, “Solution of anisotropic seepage by finite elements,” *Journal of the Engineering Mechanics Division*, vol. 92, no. 1, pp. 111–120, 1966.

[145] S. H. Crandall, *Engineering Analysis*. McGraw-Hill, 1956.

[146] O. C. Zienkiewicz and Y. K. Cheung, “The finite element method for analysis of elastic isotropic and orthotropic slabs,” in *ICE Proceedings*, T. Telford, Ed., vol. 28, 1964, pp. 471–488.

[147] Zienkiewicz and Cheung, *Finite element procedures in the solution of plate and shell problems in Stress Analysis*. John Wiley New York, 1965, no. 120-144.

[148] O. Zienkiewicz, S. Valliappan, and I. P. King, “Elasto-plastic solutions of engineering problems initial stress, finite element approach,” *International Journal for Numerical Methods in Engineering*, vol. 1, no. 1, pp. 75–100, 1969.

[149] G. Nayak and O. Zienkiewicz, "Elasto-plastic stress analysis. a generalization for various contitutive relations including strain softening," *International Journal for Numerical Methods in Engineering*, vol. 5, no. 1, pp. 113–135, 1972.

[150] H. C. Martin, "Finite element analysis of fluid flows," in *Proceedings of the Second Conference on Matrix Methods in Structural Mechanics, Wright-Patterson Air Force Base, Ohio*, October 1968, pp. 517–535.

[151] E. L. Wilson and R. E. Nickell, "Application of the finite element method to heat conduction analysis," *Nuclear engineering and design*, vol. 4, no. 3, pp. 276–286, 1966.

[152] C. V. Girijavallabhan and L. C. Reese, "Finite-element method for problems in soil mechanics," *Journal of Soil Mechanics & Foundations Div*, 1968.

[153] C.-I. J. Young and M. J. Crocker, "Prediction of transmission loss in mufflers by the finite- element method," *The Journal of the Acoustical Society of America*, vol. 57, no. 1, pp. 144–148, 1975.

[154] H. Allik and T. J. Hughes, "Finite element method for piezoelectric vibration," *International journal for numerical methods in engineering*, vol. 2, no. 2, pp. 151–157, 1970.

[155] D. Y. Hodges and M. Y. Rutkowski, "Free-vibration analysis of rotating beams by a variable-order finite-element method," *AIAA Journal*, vol. 19, no. 11, pp. 1459–1466, 1981.

[156] O. Zienkiewicz, J. Lyness, and D. Owen, "Three-dimensional magnetic field determination using a scalar potential–a finite element solution," *IEEE Transactions on Magnetics*, vol. 13, no. 5, pp. 1649–1656, 1977.

[157] P. P. Silvester and R. L. Ferrari, *Finite elements for electrical engineers*. Cambridge university press, 1996.

[158] L. Perumal and D. Thet Mon, *Finite Elements for Engineering Analysis: A Brief Review*, 2011, vol. 10.

[159] O. C. Zienkiewicz, R. L. Taylor, and J. Zhu, "The finite element method: its basis and fundamentals," *The Finite Element Method: its Basis and Fundamentals (Seventh Edition), seventh edition ed., Butterworth-Heinemann, Oxford*, 2013.

[160] I. Ergatoudis, B. Irons, and O. Zienkiewicz, "Curved, isoparametric,quadrilateral, elements for finite element analysis," *International Journal of Solids and Structures*, vol. 4, no. 1, pp. 31–42, 1968.

[161] O. Zienkiewicz, B. Irons, J. Ergatoudis, S. Ahmad, and F. Scott, "Isoparametric and associated element families for two and three dimensional analysis," *Finite element methods in stress analysis*, pp. 383–432, 1969.

[162] R. Schneiders and R. Bünten, "Automatic generation of hexahedral finite element meshes," *Computer Aided Geometric Design*, vol. 12, no. 7, pp. 693–707, 1995.

[163] J. Lachat and J. Watson, "Effective numerical treatment of boundary integral equations: a formulation for three-dimensional elastostatics," *International Journal for Numerical Methods in Engineering*, vol. 10, no. 5, pp. 991–1005, 1976.

[164] A. H.-D. Cheng and D. T. Cheng, "Heritage and early history of the boundary element method," *Engineering Analysis with Boundary Elements*, vol. 29, no. 3, pp. 268–302, 2005.

[165] L. Gaul and M. Schanz, "A comparative study of three boundary element approaches to calculate the transient response of viscoelastic solids with unbounded domains," *Computer methods in applied mechanics and engineering*, vol. 179, no. 1-2, pp. 111–123, 1999.

[166] T. Cruse, "Lateral constraint in a cracked, three dimensional elastic body," *International Journal of fracture mechanics*, vol. 6, no. 3, pp. 326–328, 1970.

[167] T. Cruse and W. Vanburen, "Three-dimensional elastic stress analysis of a fracture specimen with an edge crack," *International Journal of Fracture Mechanics*, vol. 7, no. 1, pp. 1–15, 1971.

[168] G. E. Blandford, A. R. Ingraffea, and J. A. Liggett, "Two-dimensional stress intensity factor computations using the boundary element method," *International Journal for Numerical Methods in Engineering*, vol. 17, no. 3, pp. 387–404, 1981.

[169] C. Constanda, B. S. Bertram, and A. A. Struthers, *Integral methods in science and engineering*. Chapman and Hall/CRC, 2000.

[170] F. J. Rizzo, "An integral equation approach to boundary value problems of classical elastostatics," *Quarterly of applied mathematics*, vol. 25, no. 1, pp. 83–95, 1967.

[171] F. Hartmann and R. Zotemantel, "The direct boundary element method in plate bending," *International journal for numerical methods in engineering*, vol. 23, no. 11, pp. 2049–2069, 1986.

[172] B. Birgisson, E. Siebrits, and A. P. Peirce, "Elastodynamic direct boundary element methods with enhanced numerical stability properties," *International journal for numerical methods in engineering*, vol. 46, no. 6, pp. 871–888, 1999.

[173] C. Kipp and R. Bernhard, "Prediction of acoustical behavior in cavities using an indirect boundary element method," *Journal of vibration, acoustics, stress, and reliability in design*, vol. 109, no. 1, pp. 22–28, 1987.

[174] N. Vlahopoulos and S. Raveendra, "Formulation, implementation and validation of multiple connection and free edge constraints in an indirect boundary element formulation," *Journal of Sound and Vibration*, vol. 210, no. 1, pp. 137–152, 1998.

[175] M. H. Aliabadi and D. P. Rooke, *Numerical fracture mechanics*. Springer Science & Business Media, 1991, vol. 8.

[176] J. Telles and C. Brebbia, “On the application of the boundary element method to plasticity,” *Applied Mathematical Modelling*, vol. 3, no. 6, pp. 466–470, 1979.

[177] N. Moes, J. Dolbow, and T. Belytschko, “A finite element method for crack growth without remeshing,” *International Journal for Numerical Methods in Engineering*, vol. 46, pp. 131–150, 1999.

[178] B. Bary, M. B. Haha, E. Adam, and P. Montarnal, “Numerical and analytical effective elastic properties of degraded cement pastes,” *Cement and Concrete Research*, vol. 39, no. 10, pp. 902–912, 2009.

[179] T. Kanit, S. Forest, I. Galliet, V. Mounoury, and D. Jeulin, “Determination of the size of the representative volume element for random composites: statistical and numerical approach,” *International Journal of solids and structures*, vol. 40, no. 13-14, pp. 3647–3679, 2003.

[180] T. Zohdi and P. Wriggers, “Aspects of the computational testing of the mechanical properties of microheterogeneous material samples,” *International Journal for Numerical Methods in Engineering*, vol. 50, no. 11, pp. 2573–2599, 2001.

[181] C. Toulemonde, R. Masson, and J. E. l Gharib, “Modeling the effective elastic behavior of composites: a mixed finite element and homogenisation approach,” *Comptes Rendus Mécanique*, vol. 336, no. 3, pp. 275–282, 2008.

[182] N. Moës, M. Cloirec, P. Cartraud, and J.-F. Remacle, “A computational approach to handle complex microstructure geometries,” *Computer methods in applied mechanics and engineering*, vol. 192, no. 28-30, pp. 3163–3177, 2003.

[183] J. Dolbow, N. Moës, and T. Belytschko, “Discontinuous enrichment in finite elements with a partition of unity method,” *Finite elements in analysis and design*, vol. 36, no. 3-4, pp. 235–260, 2000.

[184] B. L. Karihaloo and Q. Xiao, "Modelling of stationary and growing cracks in fe framework without remeshing: a state-of-the-art review," *Computers & Structures*, vol. 81, no. 3, pp. 119–129, 2003.

[185] Y. Abdelaziz and A. Hamouine, "A survey of the extended finite element," *Computers & structures*, vol. 86, no. 11-12, pp. 1141–1151, 2008.

[186] C. Daux, N. Moës, J. Dolbow, N. Sukumar, and T. Belytschko, "Arbitrary branched and intersecting cracks with the extended finite element method," *International journal for numerical methods in engineering*, vol. 48, no. 12, pp. 1741–1760, 2000.

[187] T. Belytschko, N. Moës, S. Usui, and C. Parimi, "Arbitrary discontinuities in finite elements," *International Journal for Numerical Methods in Engineering*, vol. 50, no. 4, pp. 993–1013, 2001.

[188] M. Stolarska, D. L. Chopp, N. Moes, and T. Belytschko, "Modelling crack growth by level sets in the extended finite element method," *International journal for numerical methods in Engineering*, vol. 51, no. 8, pp. 943–960, 2001.

[189] T. Belytschko, C. Parimi, N. Moës, N. Sukumar, and S. Usui, "Structured extended finite element methods for solids defined by implicit surfaces," *International journal for numerical methods in engineering*, vol. 56, no. 4, pp. 609–635, 2003.

[190] J. Chessa and T. Belytschko, "Arbitrary discontinuities in space–time finite elements by level sets and x-fem," *International Journal for Numerical Methods in Engineering*, vol. 61, no. 15, pp. 2595–2614, 2004.

[191] T. Belytschko, H. Chen, J. Xu, and G. Zi, "Dynamic crack propagation based on loss of hyperbolicity and a new discontinuous enrichment," *International journal for numerical methods in engineering*, vol. 58, no. 12, pp. 1873–1905, 2003.

[192] A. Shamloo, A. Azami, and A. Khoei, "Modeling of pressure-sensitive materials using a cap plasticity theory in extended finite element method," *Journal of materials processing technology*, vol. 164, pp. 1248–1257, 2005.

[193] B. Prabel, A. Combescure, A. Gravouil, and S. Marie, "Level set x-fem non-matching meshes: application to dynamic crack propagation in elastic–plastic media," *International Journal for Numerical Methods in Engineering*, vol. 69, no. 8, pp. 1553–1569, 2007.

[194] N. Sukumar, N. Moës, B. Moran, and T. Belytschko, "Extended finite element method for three-dimensional crack modelling," *International journal for numerical methods in engineering*, vol. 48, no. 11, pp. 1549–1570, 2000.

[195] N. Moes, A. Gravouil, and T. Belytschko, "Non-planar 3d crack growth by the extended finite element and level sets-part i: Mechanical model," *International journal for numerical methods in engineering*, vol. 53, no. 11, pp. 2549–2568, 2002.

[196] S. Shrestha, "Scaled boundary finite element method for various crack problems," *Steel Structures,Japan*, vol. 278, 2007.

[197] C. Song and J. P. Wolf, "Consistent infinitesimal finite-element–cell method: out-of-plane motion," *Journal of Engineering Mechanics*, vol. 121, no. 5, pp. 613–619, 1995.

[198] J. Wolf and C. Song, "Consistent infinitesimal finite element cell method: three-dimensional scalar wave equation," *Journal of applied mechanics*, vol. 63, no. 3, pp. 650–654, 1996.

[199] J. P. Wolf and C. Song, "Consistent infinitesimal finite-element cell method: in-plane motion," *Computer methods in applied mechanics and engineering*, vol. 123, no. 1-4, pp. 355–370, 1995.

[200] C. Song and J. P. Wolf, "Consistent infinitesimal finite-element cell method: three-dimensional vector wave equation," *International Journal for Numerical Methods in Engineering*, vol. 39, no. 13, pp. 2189–2208, 1996.

[201] C. Song and Wolf, "Consistent infinitesimal finite element cell method for incompressible unbounded medium," *Communications in numerical methods in engineering*, vol. 13, no. 1, pp. 21–32, 1997.

[202] J. P. Wolf and C. Song, "Static stiffness of unbounded soil by finite-element method," *Journal of geotechnical engineering*, vol. 122, no. 4, pp. 267–273, 1996.

[203] C. Song and J. P. Wolf, "Body loads in scaled boundary finite-element method," *Computer methods in applied mechanics and engineering*, vol. 180, no. 1-2, pp. 117–135, 1999.

[204] J. P. Wolf and C. Song, "The scaled boundary finite-element method–a primer: derivations," *Computers & Structures*, vol. 78, no. 1-3, pp. 191–210, 2000.

[205] C. Song and J. Wolf, "The scaled boundary finite element method - a primer: solution procedures," *Computers and Structures*, vol. 78, no. 211-225, 2000.

[206] C. Song, "A matrix function solution for the scaled boundary finite-element equation in statics," *Computer Methods in Applied Mechanics and Engineering*, vol. 193, no. 23-26, pp. 2325–2356, 2004.

[207] T. H. Vu and A. J. Deeks, "Use of higher-order shape functions in the scaled boundary finite element method," *International Journal for Numerical Methods in Engineering*, vol. 65, no. 10, pp. 1714–1733, 2006.

[208] T. H. Vu and Deeks, "A p-adaptive scaled boundary finite element method based on maximization of the error decrease rate," *Computational Mechanics*, vol. 41, no. 3, pp. 441–455, 2008.

[209] M. H. Bazyar and C. Song, “A continued-fraction-based high-order transmitting boundary for wave propagation in unbounded domains of arbitrary geometry,” *International Journal for Numerical Methods in Engineering*, vol. 74, no. 2, pp. 209–237, 2008.

[210] C. Song, “The scaled boundary finite element method in structural dynamics,” *International Journal for Numerical Methods in Engineering*, vol. 77, no. 8, pp. 1139–1171, 2009.

[211] C. Song and J. Wolf, “The scaled boundary finite element method alias consistent infinitesimal finite element cell method for elastodynamics,” *Computer Methods in applied mechanics and engineering*, vol. 147, no. 3-4, pp. 329–355., 1997.

[212] D. Chen, C. Birk, C. Song, and C. Du, “A high-order approach for modelling transient wave propagation problems using the scaled boundary finite element method,” *International Journal for Numerical Methods in Engineering*, vol. 97, no. 13, pp. 937–959, 2014.

[213] S. Natarajan, J. Wang, C. Song, and C. Birk, “Isogeometric analysis enhanced by the scaled boundary finite element method,” *Computer Methods in Applied Mechanics and Engineering*, vol. 283, pp. 733–762, 2015.

[214] A. J. Deeks and C. E. Augarde, “A meshless local petrov-galerkin scaled boundary method,” *Computational Mechanics*, vol. 36, no. 3, pp. 159–170, 2005.

[215] E. Ooi, C. Song, F. Tin-Loi, and Z. Yang, “Automatic modelling of cohesive crack propagation in concrete using polygon scaled boundary finite elements,” *Engineering fracture mechanics*, vol. 93, pp. 13–33, 2012.

[216] S. Natarajan, E. Ooi, I. Chiong, and C. Song, “Convergence and accuracy of displacement based finite element formulations over arbitrary polygons: Laplace interpolants, strain smoothing and scaled boundary polygon formulation,” *Finite*

Elements in Analysis and Design, vol. 85, pp. 101–122, 2014. [Online]. Available: http://www.sciencedirect.com/science/article/pii/S0168874X14000407

[217] E. Ooi, C. Song, F. Tin-Loi, and Z. Yang, "Polygon scaled boundary finite elements for crack propagation modelling," *International Journal for Numerical Methods in Engineering*, vol. 91, pp. 319–342, 2012.

[218] C. Zhu, G. Lin, and J. Li, "Modelling cohesive crack growth in concrete beams using scaled boundary finite element method based on super-element remeshing technique," *Computers & Structures*, vol. 121, pp. 76–86, 2013.

[219] S. Dai, C. Augarde, C. Du, and D. Chen, "A fully automatic polygon scaled boundary finite element method for modelling crack propagation," *Engineering Fracture Mechanics*, vol. 133, pp. 163–178, 2015.

[220] Z. J. Yang, "Fully automatic modelling of mixed-mode crack propagation using scaled boundary finite element method," *Engineering Fracture Mechanics,*, vol. 73, no. 12, pp. 1711–1731, 2006.

[221] E. T. Ooi, S. Natarajan, C. Song, and F. Tin-Loi, "Crack propagation modelling in functionally graded materials using scaled boundary polygons," *International Journal of Fracture*, vol. 192, no. 1, pp. 87–105, 2015.

[222] S. Fan, S. Li, and G. Yu, "Dynamic fluid-structure interaction analysis using boundary finite element method–finite element method," *Journal of Applied Mechanics*, vol. 72, no. 4, pp. 591–598, 2005.

[223] Z. Zihua, L. Yan, D. D. Dissanayake, A. A. Saputra, and S. Chongmin., "Nonlocal damage modelling by the scaled boundary finite element method," *Engineering Analysis with Boundary Elements*, 2018.

[224] Z. Zihua, D. Dilina, Dion, S. Albert, Artha, W. Di, and S. Chongmin, "Three-dimensional damage analysis by the scaled boundary finite element method," *Computers and Structures*, 2018.

[225] J. M. Melenk and I. Babuska, "The partition of unity finite element method: basic theory and applications," *Computer methods in applied mechanics and engineering*, vol. 139, no. 1-4, pp. 289–314, 1996.

[226] S. Osher and J. A. Sethian, "Fronts propagating with curvature-dependent speed: algorithms based on hamilton-jacobi formulations," *Journal of computational physics*, vol. 79, no. 1, pp. 12–49, 1988.

[227] L. Lbanez, W. Schroeder, N. L., and J. Cates, *The ITK Software Guide*, 2005th ed. Kitware Inc., 2005.

[228] P. Mazumder, "Planar decomposition for quadtree data structure," *Computer Systems Group, Coordinated Science Laboratory*, June 1986.

[229] A. Aho, J. E. Hopcroft, and J. D. Ullman, "The design and analysis of computer algorithms," *Addison-Wesley, Reading, Mass*, 1974.

[230] A. Klinger and C. Klinger, "Experiments in picture representation using regular decomposition,," *Comput. Graphics Image Process*, vol. 5, no. 68-105, 1976.

[231] S. Tanimoto and T. Pavlidis, "A hierarchical data structure for picture processing," *Comput. Graphics Image Process*, vol. 4, no. 104-119, 1975.

[232] N. Alexandridis and A. Klinger, "Picture decomposition, tree data-structures, and identifying directional symmetries and node combinations," *Comput. Graphics Image Process*, vol. 8, no. 43-47, 1978.

[233] H. Samet, "The quadtree and related hierarchical data structures," *ACM Comput. Suro*, vol. 16, pp. 187–260, 1984.

[234] I. Gargantini, "An effective way to represent quadtrees," *Commun. ACM*, vol. 25, no. 905-910, 1982.

[235] M. Tamminen, "Comment on quad and octtrees," *Commun. ACM*, vol. 27, no. 248-249, 1984.

[236] H. Samet, "Data structures for quadtree approximation and compression," *Commun. ACM*, vol. 28, no. 973-993, 1985.

[237] C. Chien and J. Aggarwal, "A normalized quadtree representation." *Comput. Vision Graphics Image Process.*, vol. 26, pp. 331–346, 1984.

[238] M. Li, W. I. Gorsky, and R. Jain, "Normalized quadtrees with respect to translations, in proceedings." *PRIP-81, Dallas,Texas*, pp. 60–62, 1981.

[239] G. Hunter, "Efficient computation and data structures for graphics," Ph.D. dissertation, Department of Electrical Engineering and Computer Science, Princeton University, Princeton , NJ, 1978.

[240] D. Reddy and S. Rubin, "Representation of 3d objects," *CMU-CS-7S-113,Comp ter Science Department,Carnegie-Mellon University*, April 1978.

[241] N. Sribari, "Representation of three-dimensional digital images,," Technical Report No. 162, Dept. of Computer Science, State University of New York at Buffalo, Tech. Rep., July 1980.

[242] N. Srihari, "Hierarchical representations for serial section images," in *Proceedings of the 5th International Conference on Pattern Recognition*, December 1980.

[243] Moravec, "Three dimensional modelling and graphics with multiprocessors," *internal memo,Robotics Institute, Carnegie-Mellon University*, October 1980.

[244] Meagher, "Octree encoding: A new technique for the representation, manipulation and display of arbitrary 3-d objects by computer, technical report ipl-tr-80-11 i,"

Image Processing Laboratory, Rensselaer Polytechnic Institute, Tech. Rep., October 1980.

[245] C. L. Jackins and S. L. Tanimoto, "Oct-trees and their use in representing three-dimensional objects," *Computer Graphics and Image Processing*, vol. 14, no. 3, pp. 249–270, 1980.

[246] P. J. Frey and P.-L. George, *Mesh generation: application to finite elements*. ISTE, 2007.

[247] C. Prakash and S. Nandy, "Voxel based modeling and rendering irregular solids," *Microprocessing and Microprogramming*, vol. 30, no. 1-5, pp. 341–345, August 1990.

[248] E. Ooi, M. Shi, C. Song, F. Tin-Loi, and Z. J. Yang, "Dynamic crack propagation simulation with scaled boundary polygon elements and automatic remeshing technique," *Engineering Fracture Mechanics*, vol. 106, no. 1-21, 2012 and 2013.

[249] Y. N. Rabotnov, "Creep problems in structural members," 1969.

[250] F. Leckie and D. Hayhurst, "Creep rupture of structures," *Proceedings of the Royal Society of London. A. Mathematical and Physical Sciences*, vol. 340, no. 1622, pp. 323–347, 1974.

[251] P. Germain, Q. S. Nguyen, and P. Suquet, "Continuum thermodynamics," *Journal of Applied Mechanics*, vol. 50, no. 4b, pp. 1010–1020, 1983.

[252] J. Chaboche, "Viscoplastic constitutive equations for description of cyclic and anisotropic behavior of metals," *Bulletin De L Academie Polonaise Des Sciences-Serie Des Sciences Techniques*, vol. 25, no. 1, pp. 39–48, 1977.

[253] A. Gurson, "Continuum theory of ductile rupture by void nucleation and growth," *ASME Journal of Engineering Materials and Technology*, vol. 99, no. 2, 1977.

[254] D. Krajcinovic, *Mechanics of Material*, 1989, vol. 8, no. 117.

[255] E. Onat, *Internaltional Journal for Engineering Sciences*, vol. 22, no. 1013, 1984.

[256] E. Onat and F. Leckie, *ASME Journal of Applied Mechanics*, vol. 55, no. 1, 1988.

[257] L. F.A. and E. Onat, *Proceedings lUTAM Symposium on Physical Nonlinearities in Structures,Springer-Verlag, Berlin (Germany)*, no. 140-155, 1980.

[258] D. Krajcinovic and D. Sumarac, *Continuum Damage Mechanics-Theory and Applications*, D. Krajcinovic and J. Lemaitre, Eds. Springer Verlag,Wien (Austria), 1987, no. 135-194.

[259] G. Pijaudier-Cabot and Z. Bazant, "Non-local damage theory," *ASCE Journal of Engineering Mechanics*, vol. 113, no. 1512, 1987.

[260] J. Mazars and G. Pijaudier Cabot, "Continuum damage theory-application to concrete," *Journal of engineering mechanics*, vol. 115, no. 2, pp. 345–365, 1989.

[261] J. Simo and J. Ju, "Strain and stress-based continuum damage model. part 1 - formulation," *Int. J. Solids Struct.*, vol. 23, no. 7, pp. 821–840, 1987.

[262] J. Simo, "Strain and stress-based continuum damage model. part 2 - computational aspects," *Int. J. Solids Struct.*, vol. 25, no. 7, pp. 841–869, 1987.

[263] Y. Labadi and N. E. Hannachi, "Numerical simulation of brittle damage in concrete," *Strength of Materials*, pp. 268–281., 2005.

[264] X. Tao and D. V. Phillips, "A simplified isotropic damage model for concrete under bi-axial stress states," *Cement and Concrete Composites*, vol. 27, no. 6, pp. 716–726., 2005.

[265] F. S. Junior and W. S. Venturini, "Damage modelling of reinforced concrete beams," *Advances in Engineering Software*, vol. 38, no. 8-9, pp. 538–546, 2007.

[266] A. Khan, A. Al-Gadhib, and M. Baluch, “Elasto-damage model for high strength concrete subjected to multiaxial loading,” *Int. J. of Damage Mech.*, vol. 16, no. 3, pp. 361–398, 2007.

[267] P. Feenstra and R. de Borst, “A composite plasticity model for concrete,” *Int. J. of Solids and Struct.*, vol. 33, no. 5, pp. 707–730, 1996.

[268] N. Bicanic and C. J. Pearce, “Computational aspects of a softening plasticity model for plain concrete,” *Mech. of Cohesive-frictional Mat.*, vol. 1, no. 1, pp. 75–94, 1996.

[269] P. Grassl, K. Lundgren, and K. Gylltoft, “Concrete in compression: a plasticity theory with a novel hardening law,” *Int. J. of Solids and Struct.*, vol. 39, no. 20, pp. 5205–5223, 2002.

[270] H. Park and J. Y. Kim, “Plasticity model using multiple failure criteria for concrete in compression,” *Int. J.of Solids and Struct*, vol. 42, no. 8, pp. 2303–2322, 2005.

[271] J. Lemaitre and J. Chaboche, *Mechanics of Solid Materials*. Cambridge University Press, Cambridge, UK., 1990.

[272] S. Oller, E. Onate, J. Oliver, and J. Lubliner, “Finite element nonlinear analysis of concrete structures using a plastic damage model,” *Eng. Fracture Mech.*, vol. 35, no. 1-3, pp. 219–231, 1990.

[273] Voyiadjis, G. Z., and T. M. Abu Lebdeh, “Damage model for concrete using bounding surface concept,” *J. Eng. Mech.,*, vol. 119, no. 9, pp. 1865–1885, 1993.

[274] G. Z. Voyiadjis and T. M. Abu Lebdeh, “Plasticity model for concrete using the bounding surface concept,” *Int. J. Plast.*, vol. 10, no. 1, pp. 1–21, 1994.

[275] T. Abu-Lebdeh and G. Voyiadjis, “Plasticity-damage model for concrete under cyclic multiaxial loading,” *ASCE J. Eng. Mech.*, vol. 119, no. 7, pp. 1465–1484, 1993.

[276] W. B. Krazig and R. PÃ¶lling, "An elasto-plastic damage model for reinforced oncrete with minimum number of material parameters," *Computers & Structures*, vol. 82, no. 15-16, pp. 1201–1215, 2004.

[277] J. W. Ju, "On energy-based coupled elasto-plastic damage theories:constitutive modeling and computational aspects," *Int. J. Solids and Struct.*, vol. 25, no. 7, pp. 803–833, 1989.

[278] S. Yazdani and H. L. Schreyer, "Combined plasticity and damage mechanics model for plain concrete," *J. Eng. Mech., ASCE*, vol. 116, no. 7, pp. 1435–1450, 1990.

[279] N. R. Hansen and H. Schreyer, "A thermodynamically consistent framework for theories of elastoplasticity coupled with damage," *Int. J. Solids and Struct.*, vol. 31, no. 3, pp. 359–389, 1994.

[280] J. Lee and G. L. Fenves, "A plastic-damage model for cyclic loading of concrete structures," *J. Eng. Mech., ASCE*, vol. 124, pp. 892–900, 1998.

[281] R. Faria, J. Oliver, and M. Cervera, "A strain-based plastic viscous-damage model for massive concrete structures," *Int. J. Solids and Struct.*, vol. 35, no. 14, pp. 1533–1558, 1998.

[282] S. Fichant, C. La Borderie, and G. Pijaudier-Cabot, "Isotropic and anisotropic descriptions of damage in concrete structures," *Int. J. Mech. Cohesive Frictional Matter*, vol. 4, pp. 339–359, 1999.

[283] G. Z. Voyiadjis and P. I. Kattan, *Advances in Damage Mechanics:Metals and Metal Matrix Composites, with an Introduction to Fabric Tensors*, second edition ed. Elsevier, Oxford., 2006.

[284] A. Jefferson, "Craft-a plastic damage contact model for concrete - i.model theory and thermodynamic considerations," *Int. J. Solids Struct.*, vol. 40, pp. 5973–5999, 2003.

[285] M. R. Salari, S. Saeb, K. J. Willam, S. J. Patchet, and R. C. Carrasco, "A coupled elastoplastic damage model for geomaterials," *Comp. Meth. in Applied Mech. and Eng,*, vol. 193, no. 27-29, pp. 2625–2643, 2004.

[286] X. Shen, L. Yang, and F. Zhu, "A plasticity-based damage model for concrete," *Adv. in Struct. Eng.*, vol. 7, no. 5, pp. 461–467, 2004.

[287] L. Jason, A. Huerta, G. Pijaudier-Cabot, and S. Ghavamian, "An elastic plastic damage formulation for concrete:application to elementary tests and comparison with an isotropic damage model," *Comp. Meth. in Applied Mech. and Eng.*, vol. 195, no. 52, pp. 7077–7092, 2006.

[288] G. Z. Voyiadjis, Z. N. Taqieddin, and P. I. Kattan, "Anisotropic damage-plasticity model for concrete," *Int. J. of Plasticity*, 2008.

[289] G. Z. Voyiadjis and P. I. Kattan, *Advances in damage mechanics:Metals and metal-matrix composites*. Elsevier, Oxford., 1999.

[290] W. Nechnech, F. Meftah, and J. M. Reynouard, "An elasto-plastic damage model for plain concrete subjected to high temperatures," *Journal of enigineering structures*, vol. 24, no. 5, pp. 597–611, 2002.

[291] K. Willam, I. Rhee, and G. Beylkin, "Multiresolution analysis of elastic degradation in heterogeneous materials," *Meccanica*, vol. 36, no. 1, pp. 131–150, 2001.

[292] J. Lemaitre and R. Desmorat, *Engineering damage mechanics: ductile, creep, fatigue and brittle failures*. Springer Science & Business Media, 2005.

[293] F. S. Junior and W. S. Venturini, "Damage modelling of reinforced concrete beams," *Advances in Engineering Software*, vol. 38, no. 8-9, pp. 538–546, 2007.

[294] J. Mazars, "Application de la mécanique de l'endommagement au comportement non linéaire et à la rupture du béton de structure," *THESE DE DOCTEUR ES*

SCIENCES PRESENTEE A L'UNIVERSITE PIERRE ET MARIE CURIE-PARIS 6, 1984.

[295] J. Mazars and G. Pijaudier-Cabot, "Continuum damage theory-application to concrete," *Journal of Engineering Mechanics*, vol. 115, no. 2, pp. 345–365, 1989.

[296] J. Chaboche, "Continuum damage mechanics- general concepts (part-1)," *Journal of Applied Mechanics*, vol. 55, March 1988.

[297] J. Lemaitre, "Local approach of fracture," *Engineering Fracture Mechanics*, vol. 25, no. 5-6, pp. 523–537, 1986.

[298] L. M. Kachanov, *Introduction to Continuum Damage Mechanics*. Martinus Nijhoff, Dordrecht, The Netherlands, 1986.

[299] S. Pietruszczak and Z. Mroz, "Finite element analysis of deformation of strain-softening materials," *International Journal for Numerical Methods in Engineering*, vol. 17, no. 3, pp. 327–334, 1981.

[300] Z. P. Bazant, F. B. Lin, and G. Piiaudier-Cabot, "Yield limit degradation: nonlocal continuum model with local strain." in *Proc. Int. Conf: on Compututional Plasticity*, E. Onate, R. Owen, and E. Hinton, Eds., no. 1757-1779, Barcelona, 1987.

[301] Z. P. Bazant and G. Pijaudier-Cabot, "Nonlocal continuum damage, localization instability and convergence." *Journal of Applied Mechanics*, vol. 55, pp. 287–293, 1988.

[302] C. Saouridis and J. . Mazars., "A multiscale approach to distributed damage and its usefulness for capturing structural size effects," *France -U;.S. Workshop on Strain Localizution and Size Effects due to Cracking and Damage*, pp. 391–403, 1988.

[303] N. Triantafyllidis and E. C. Aifantis, "A gradient approach to localization of deformation. i. hyperelastic materials," *Journal of Elasticity*, vol. 16, no. 3, pp. 225–237, 1986.

[304] J. C. . Simo., “Strain softening and dissipation: a unification of approaches.” *France -U;.S. Workshop on Strain Localizution and Size Effects due to Cracking and Damage*, pp. 391–403, 1988.

[305] R. de Borst, “Gradient-dependent plasticity: formulation and algorithmic aspects,” *International Journal for Numerical Methods in Engineering*, vol. 35, no. 3, pp. 521–539, 1992.

[306] M. Jirásek and Z. P. Bazant, *Inelastic analysis of structures*. John Wiley & Sons, 2002.

[307] Z. P. Bazant, “Mechanics of distributed cracking,” *Applied Mechanics Reviews*, vol. 39, no. 5, pp. 675–705, 1986.

[308] F. Hall and D. Hayhurst, “Modelling of grain size effects in creep crack growth using a non-local continuum damage approach,” *Proceedings of the Royal Society of London. Series A: Mathematical and Physical Sciences*, vol. 433, no. 1888, pp. 405–421, 1991.

[309] Z. P. Bažant and F.-B. Lin, “Non-local yield limit degradation,” *International Journal for Numerical Methods in Engineering*, vol. 26, no. 8, pp. 1805–1823, 1988.

[310] R. Peerlings, R. de Borst, W. Brekelmans, and J. de Vree, “Gradient-enhanced damage for quasibrittle materials,” *International Journal for Numerical Methods in Engineering*, vol. 39, pp. 3391–3403, 1996.

[311] R. H. J. Peerlings, “Enhanced damage modelling for fracture and fatigue,” 1999.

[312] C. Le Bellégo, J. F. Dubé, G. Pijaudier-Cabot, and B. Gérard, “Calibration of nonlocal damage model from size effect tests,” *European Journal of Mechanics-A/Solids*, vol. 22, no. 1, pp. 33–46, 2003.

[313] M. Jirasek, "Nonlocal models for damage and fracture: comparison of approaches," *International Journal of Solids and Structures*, vol. 35, no. 31-32, pp. 4133–4145, 1998.

[314] J. Carmeliet, "Optimal estimation of gradient damage parameters from localization phenomena in quasi-brittle materials," *Mechanics of Cohesive-frictional Materials: An International Journal on Experiments, Modelling and Computation of Materials and Structures*, vol. 4, no. 1, pp. 1–16, 1999.

[315] R. Mahnken and E. Kuhl, "Parameter identification of gradient enhanced damage models with the finite element method," *European Journal of Mechanics-A/Solids*, vol. 18, no. 5, pp. 819–835, 1999.

[316] L. Ferrara and M. d. Prisco, "Mode i fracture behavior in concrete: nonlocal damage modeling," *Journal of engineering mechanics*, vol. 127, no. 7, pp. 678–692, 2001.

[317] Z. P. Bažant, Q. Yu, and G. Zi, "Choice of standard fracture test for concrete and its statistical evaluation," *International journal of fracture*, vol. 118, no. 4, pp. 303–337, 2002.

[318] M. Elices, G. Guinea, J. Gomez, and J. Planas, "The cohesive zone model: advantages, limitations and challenges," *Engineering fracture mechanics*, vol. 69, no. 2, pp. 137–163, 2002.

[319] R. De Borst and J. Pamin, "Gradient plasticity in numerical simulation of concrete cracking," *EUROPEAN JOURNAL OF MECHANICS SERIES A SOLIDS*, vol. 15, pp. 295–320, 1996.

[320] M. di Prisco, L. Ferrara, F. Meftah, J. Pamin, R. De Borst, J. Mazars, and J. Reynouard, "Mixed mode fracture in plain and reinforced concrete: some results on benchmark tests," *International journal of fracture*, vol. 103, no. 2, pp. 127–148, 2000.

[321] F. Meftah and J. Reynouard, “A multilayered mixed beam element in gradient plasticity for the analysis of localized failure modes,” *Mechanics of Cohesive-frictional Materials: An International Journal on Experiments, Modelling and Computation of Materials and Structures*, vol. 3, no. 4, pp. 305–322, 1998.

[322] M. Jirásek, “Comparison of nonlocal models for damage and fracture,” *LSC Report*, vol. 98, no. 02, 1998.

[323] M. Jirásek, S. Rolshoven, and P. Grassl, “Size effect on fracture energy induced by non-locality,” *International Journal for Numerical and Analytical Methods in Geomechanics*, vol. 28, no. 7-8, pp. 653–670, 2004.

[324] M. Ainsworth, J. Zhu, A. Craig, and O. Zienkiewicz, “Analysis of the zienkiewicz–zhu a-posteriori error estimator in the finite element method,” *International Journal for numerical methods in engineering*, vol. 28, no. 9, pp. 2161–2174, 1989.

[325] I. Babuska, “Selfadaptive approach in the finite element method.” *Mathematics of Finite Element and Applications, Whiteman JR (ed) Academic Press, London.*, 1975.

[326] I. Babuška and W. C. Rheinboldt, “A-posteriori error estimates for the finite element method,” *International Journal for Numerical Methods in Engineering*, vol. 12, no. 10, pp. 1597–1615, 1978.

[327] I. Babuska and W. C. Rheinboldt, “Reliable error estimation and mesh adaptation for the finite element method.” MARYLAND UNIV COLLEGE PARK INST FOR PHYSICAL SCIENCE AND TECHNOLOGY, Tech. Rep., 1979.

[328] I. Babuska, *Accuracy estimates and adaptive refinements in finite element computations*. John Wiley & Sons, 1986.

[329] I. M. Babuška and R. Rodriguez, "The problem of the selection of an a posteriori error indicator based on smoothening techniques," *International Journal for Numerical Methods in Engineering*, vol. 36, no. 4, pp. 539–567, 1993.

[330] I. Babuška, T. Strouboulis, C. Upadhyay, S. Gangaraj, and K. Copps, "Validation of a posteriori error estimators by numerical approach," *International journal for numerical methods in engineering*, vol. 37, no. 7, pp. 1073–1123, 1994.

[331] R. Durán, M. A. Muschietti, and R. Rodríguez, "On the asymptotic exactness of error estimators for linear triangular finite elements," *Numerische Mathematik*, vol. 59, no. 1, pp. 107–127, 1991.

[332] R. Duran, M. A. Muschietti, and R. Rodriguez, "Asymptotically exact error estimators for rectangular finite elements," *SIAM journal on numerical analysis*, vol. 29, no. 1, pp. 78–88, 1992.

[333] J. Gago, D. Kelly, O. Zienkiewicz, and I. Babuška, "A-posteriori error analysis and adaptive processes in the finite element method. part i: Error analysis. part ii: Adaptive processes," *Int. J. Num. Meth. Engng*, vol. 19, no. 83, pp. 1593–1656, 1983.

[334] N. R. Iyer and T. Appa Rao, "A review of error analysis and adaptive refinement methodologies in finite element applications part-i: Error analysis," 1992.

[335] D. Kelly, "The self-equilibration of residuals and complementary a posteriori error estimates in the finite element method," *International Journal for Numerical Methods in Engineering*, vol. 20, no. 8, pp. 1491–1506, 1984.

[336] D. Kelly, R. Mills, J. Reizes, and A. Miller, "A posteriori estimates of the solution error caused by discretization in the finite element, finite difference and boundary element methods," *International journal for numerical methods in engineering*, vol. 24, no. 10, pp. 1921–1939, 1987.

[337] D. Kelly and J. Isles, "A procedure for a posteriori error analysis for the finite element method which contains a bounding measure," *Computers & Structures*, vol. 31, no. 1, pp. 63–71, 1989.

[338] P. Ladeveze and D. Leguillon, "Error estimate procedure in the finite element method and applications," *SIAM Journal on Numerical Analysis*, vol. 20, no. 3, pp. 485–509, 1983.

[339] P. LadeVeZe, J.-P. Pelle, and P. Rougeot, "Error estimation and mesh optimization for classical finite elements," *Engineering Computations*, vol. 8, no. 1, pp. 69–80, 1991.

[340] A. Mashaie, E. Hughes, and J. Goldak, "Error estimates for finite element solutions of elliptic boundary value problems," *Computers & structures*, vol. 49, no. 1, pp. 187–198, 1993.

[341] E. Rank and O. Zienkiewicz, "A simple error estimator in the finite element method," *Communications in Applied Numerical Methods*, vol. 3, no. 3, pp. 243–249, 1987.

[342] M. S. Shephard, Q. Niu, and P. L. Baehmann, "Some results using stress projectors for error indication and estimation," in *Adaptive Methods for Partial Differential Equations*. SIAM Philadelphia, PA, 1989, pp. 83–99.

[343] N.-E. Wiberg and F. Abdulwahab, "Patch recovery based on superconvergent derivatives and equilibrium," *International Journal for Numerical Methods in Engineering*, vol. 36, no. 16, pp. 2703–2724, 1993.

[344] N. Wiberg and F. Abdulwahab, "Error estimation with post processed fe-solutions," *Advances in Post and Preprocessing for Finite Element Technology*, pp. 1–22, 1994.

[345] J. Wu, J. Zhu, J. Szmelter, and O. Zienkiewicz, "Error estimation and adaptivity in navier-stokes incompressible flows," *Computational mechanics*, vol. 6, no. 4, pp. 259–270, 1990.

[346] Z. OC and T. RL, *The finite element method*, fourth edition ed. McGraw-hill London, 1987, vol. 3.

[347] O. C. Zienkiewicz and J. Z. Zhu, "A simple error estimator and adaptive procedure for practical engineerng analysis," *International journal for numerical methods in engineering*, vol. 24, no. 2, pp. 337–357, 1987.

[348] L.-y. Li and P. Bettess, "Adaptive finite element methods: a review," *Applied Mechanics Reviews*, vol. 50, no. 10, pp. 581–591, 1997.

[349] O. C. Zienkiewicz and J. Z. Zhu, "The superconvergent patch recovery and a posteriori error estimates. part 1: The recovery technique," *International Journal for Numerical Methods in Engineering*, vol. 33, no. 7, pp. 1331–1364, 1992.

[350] O. Zienkiewicz, J. Zhu, and J. Wu, "Superconvergent patch recovery techniques–some further tests," *Communications in Numerical methods in Engineering*, vol. 9, no. 3, pp. 251–258, 1993.

[351] M. H. Aliabadi and C. A. Brebbia, "Adaptive finite and boundary element methods, computational mechanics p," *Elsevier Appl Sci,Southampton, UK.*, 1993.

[352] I. Babuska and W. Rheinboldt, "Analysis of optimal finite-element meshes in r1," *Mathematics of computation*, vol. 33, no. 146, pp. 435–463, 1979.

[353] I. Babuska and A. Miller, "A-posteriori error estimates and adaptive techniques for the finite element method." Maryland Univ College Park Inst for Physical Science and Technology, Tech. Rep., 1981.

[354] I. Babuska and E. Rank, "An expert-system-like feedback approach in the hp-version of the finite element method," *Finite elements in analysis and design*, vol. 3, no. 2, pp. 127–147, 1987.

[355] P. K. Basu and A. Peano, "Adaptivity in p-version finite element analysis," *Journal of Structural Engineering*, vol. 109, no. 10, pp. 2310–2324, 1983.

[356] G. Bugeda and J. Oliver, "Automatic adaptive remeshing for structural shape optimization," in *European Conf on New Advances in Comput Struc Mech*, 1991.

[357] G. Bugeda and E. Onate, "New adaptive techniques for structural problems," in *1st European Conf on Numer Methods in Eng*, 1992.

[358] G. Bugeda and E. Ofiate, "Adaptive mesh refinement techniques for aerodynamic problems," *Numerical Methods in Engineering and Applied Sciences, CIMNE-Barcelona*, 1992.

[359] G. Bugeda and J. Oliver, "A general methodology for structural shape optimization problems using automatic adaptive remeshing," *International Journal for Numerical Methods in Engineering*, vol. 36, no. 18, pp. 3161–3185, 1993.

[360] G. Bugeda and E. Ofiate, "Adaptive techniques for elliptic problems.in: Advances in post and preprocessing for finite element technology," in *Papadrakakis M and Topping BHV (eds), CIVIL-COMP Ltd,Edinburgh, Scotland*, no. 77-84, 1994.

[361] L. Demkowicz, J. Oden, and T. Strouboulis, "Adaptive finite elements for flow problems with moving boundaries. i-variational principles and a posteriori estimates," *Computer methods in applied mechanics and engineering*, vol. 46, pp. 217–251, 1984.

[362] L. Demkowicz and J. Oden, "Extraction methods for second derivatives in finite element approximations of linear elasticity problems," *Communications in applied numerical methods*, vol. 1, no. 3, pp. 137–139, 1985.

[363] L. Demkowicz, P. Devloo, and J. T. Oden, “On an h-type mesh-refinement strategy based on minimization of interpolation errors,” *Computer Methods in Applied Mechanics and Engineering*, vol. 53, no. 1, pp. 67–89, 1985.

[364] L. Demkowicz and J. Oden, “On a mesh optimization method based on a minimization of interpolation error,” *International journal of engineering science*, vol. 24, no. 1, pp. 55–68, 1986.

[365] “An adaptive characteristic petrov-galerkin finite element method for convection-dominated linear and nonlinear parabolic problems in one space variable,” *Journal of Computational Physics*, vol. 67, no. 1, pp. 188–213, 1986.

[366] L. Demkowicz, A. Karafiat, and J. Oden, “Solution of elastic scattering problems in linear acoustics using hp boundary element method,” *Computer Methods in Applied Mechanics and Engineering*, vol. 101, no. 1-3, pp. 251–282, 1992.

[367] L. Demkowicz and J. Oden, “Elastic scattering problems in linear acoustics using an hp boundary/finite element method,” *Adaptive Finite and Boundary Element Methods*, 1993.

[368] Demkowicz and Oden, “Recent progress on application of hp-adaptive be/fe methods to elastic scattering,” *International Journal for Numerical Methods in Engineering*, vol. 37, no. 17, pp. 2893–2910, 1994.

[369] P. Devloo, J. T. Oden, and T. Strouboulis, “Implementation of an adaptive refinement technique for the supg algorithm,” *Computer methods in applied mechanics and engineering*, vol. 61, no. 3, pp. 339–358, 1987.

[370] P. Devloo, “A three-dimensional adaptive finite element strategy,” *Computers & Structures*, vol. 38, no. 2, pp. 121–130, 1991.

[371] A. R. Diaz, N. Klkuchl, P. Papalambros, and J. E. Taylor, “Design of an optimal grid for finite element methods,” *Journal of structural mechanics*, vol. 11, no. 2, pp. 215–230, 1983.

[372] A. R. Díaz, N. Kikuchi, and J. E. Taylor, “A method of grid optimization for finite element methods,” *Computer Methods in Applied Mechanics and Engineering*, vol. 41, no. 1, pp. 29–45, 1983.

[373] L. Gallimard, P. Ladeveze, and J.-P. Pelle, “A posteriori error estimator for nonlinear fe computations: application to elastoplasticity,” *Computational Plasticity Fundamentals and Applications. I*, pp. 373–382, 1995.

[374] M. Georges and M. Shephard, “Automated adaptive two-dimensional system for the hp-version of the finite element method,” *International journal for numerical methods in engineering*, vol. 32, no. 4, pp. 867–893, 1991.

[375] I. Babuska and W. Gui, “The h, p and hp versions of the finite element method in 1 dimension. part i. the error analysis of the p-version.” *Numerische Mathematik*, vol. 49, pp. 577–612, 1986.

[376] B. Guo and I. Babuška, “The hp version of the finite element method,” *Computational Mechanics*, vol. 1, no. 1, pp. 21–41, 1986.

[377] J.-F. Hetu and D. H. Pelletier, “Adaptative remeshing for viscous incompressible flows,” *AIAA journal*, vol. 30, no. 8, pp. 1986–1992, 1992.

[378] T.-S. Hsu and S. Saxena, “New guidelines for optimization of finite element solutions,” *Computers & structures*, vol. 31, no. 2, pp. 203–210, 1989.

[379] C. Johnson and P. Hansbo, “Adaptive finite element methods in computational mechanics,” *Computer methods in applied mechanics and engineering*, vol. 101, no. 1-3, pp. 143–181, 1992.

[380] C. Johnson and Hansbo, “Adaptive finite element methods for small strain elasto-plasticity,” in *Finite Inelastic Deformations-Theory and Applications*. Springer, 1992, pp. 273–288.

[381] N. Kikuchi, “Adaptive grid-design methods for finite element analysis,” *Computer Methods in Applied Mechanics and Engineering*, vol. 55, no. 1-2, pp. 129–160, 1986.

[382] M. G. Kittur and R. L. Huston, “Mesh refinement in finite element analysis by minimization of the stiffness matrix trace,” 1989.

[383] M. Kittur and Huston, “Finite element mesh refinement criteria for stress analysis,” *Computers and Structures*, vol. 34, no. 2, pp. 251–255, 1990.

[384] C. Lee, J. Oden, and M. Ainsworth, “Local a posteriori error estimates and numerical results for contact problems and problems of flow through porous media,” *Nonlinear Computational Mechanics*, pp. 671–689, 1991.

[385] L.-Y. Li, P. Bettess, J. Bull, T. Bond, and I. Applegarth, “Theoretical formulations for adaptive finite element computations,” *Communications in Numerical Methods in Engineering*, vol. 11, no. 10, pp. 857–868, 1995.

[386] L.-Y. Li and P. Bettess, “Notes on mesh optimal criteria in adaptive finite element computations,” *Communications in numerical methods in engineering*, vol. 11, no. 11, pp. 911–915, 1995.

[387] L. Li, P. Bettess, I. Applegarth, J. Bull, and T. Bond, “New mesh refinement formulation for h-adaptive finite element computations,” pp. 443–454, 1995.

[388] L. Li, I. Applegarth, J. Bull, P. Bettess, T. Bond, and P. Thompson, “An auto-adaptive finite element analysis software for stiffened plate and shell structures,” *Advances in Engineering Software*, vol. 28, no. 5, pp. 285–291, 1997.

[389] L. Li, P. Bettess, J. Bull, and T. Bond, “Mesh refinement formulations in adaptive finite element methods,” *Proceedings of the Institution of Mechanical Engineers, Part C: Journal of Mechanical Engineering Science*, vol. 210, no. 4, pp. 353–361, 1996.

[390] L.-Y. Li, I. Applegarth, J. Bull, P. Bettess, and T. Bond, “Adaptive analysis of stiffened structures using stiffened plate bending elements,” *International journal of pressure vessels and piping*, vol. 65, no. 2, pp. 117–125, 1996.

[391] L.-Y. Li and P. Bettess, “Error estimates and adaptive remeshing techniques in elasto–plasticity,” *Communications in numerical methods in engineering*, vol. 13, no. 4, pp. 285–299, 1997.

[392] J. Oden and L. Demkowicz, “Adaptive finite element methods for complex problems in solid and fluid mechanics,” *Computational Mechanics*, 1985.

[393] J. Oden, L. Demkowicz, and T. Strouboulis, “Adaptive methods for problems in solid and fluid mechanics,” 1986.

[394] J. Oden, L. Demkowicz, W. Rochowicz, T. Westermann, and O. Gardy, “Toward a univeral h-p adaptive finite element strategy - part i,ii,iii,” *Comput Meth Appl Mech Eng*, vol. 7, no. 79-21, 1989.

[395] P. A. Oden JT and F. Y, “H-p adaptive strategy,” in *Proc Symp on Adaptive, Multilevel, and Hierarchical Computational Strategies, ASME Winter Annual Meeting, Anaheim CA.*, vol. 8-13, November 1992.

[396] E. Onate and J. Castro, “Adaptive mesh refinement techniques for structural problems,” in *The finite element method in the 1990s*. Springer, 1991, pp. 133–145.

[397] E. Oñate and G. Bugeda, “A study of mesh optimality criteria in adaptive finite element analysis,” *Engineering computations*, vol. 10, no. 4, pp. 307–321, 1993.

[398] M. Ortiz and J. Quigley Iv, "Adaptive mesh refinement in strain localization problems," *Computer Methods in Applied Mechanics and Engineering*, vol. 90, no. 1-3, pp. 781–804, 1991.

[399] A. Peano, "Hierarchies of conforming finite elements," *Doctoral dissert*, 1975.

[400] Peano, "Hierarchies of conforming finite elements for plane elasticity and plate bending," *Computers & Mathematics with Applications*, vol. 2, no. 3-4, pp. 211–224, 1976.

[401] A. Peano, *Automated discretization error control in finite element analysis*, 1978.

[402] A. Peano, A. Pasini, R. Riccioni, and L. Sardella, "Adaptive approximations in finite element structural analysis," *Computers & Structures*, vol. 10, no. 1-2, pp. 333–342, 1979.

[403] J. Peraire, M. Vahdati, K. Morgan, and O. C. Zienkiewicz, "Adaptive remeshing for compressible flow computations," *Journal of computational physics*, vol. 72, no. 2, pp. 449–466, 1987.

[404] D. Perić, J. Yu, and D. Owen, "On error estimates and adaptivity in elastoplastic solids: Applications to the numerical simulation of strain localization in classical and cosserat continua," *International Journal for Numerical Methods in Engineering*, vol. 37, no. 8, pp. 1351–1379, 1994.

[405] W. Prager, "A note on the optimal choice of finite element grids," *Computer Methods in Applied Mechanics and Engineering*, vol. 6, no. 3, pp. 363–366, 1975.

[406] A. Selman, E. Hinton, and W. Atamaz-Sibai, "Edge effects in mindlin-reissner plates using adaptive mesh refinement," *Engineering computations*, vol. 7, no. 3, pp. 217–226, 1990.

[407] M. S. Shephard, "Finite-element grid optimization with interactive computer graphics." 1979.

[408] M. Shephard, "Finite element grid optimization - a review. in:finite element grid optimization," *ASME*, 1979.

[409] M. S. Shephard, R. H. Gallagher, and J. F. Abel, "The synthesis of near-optimum finite element meshes with interactive computer graphics," *International Journal for Numerical Methods in Engineering*, vol. 15, no. 7, pp. 1021–1039, 1980.

[410] M. S. Shephard and M. A. Yerry, "Finite element mesh generation for use with solid modeling and adaptive analysis," in *Solid Modeling by Computers*. Springer, 1984, pp. 53–80.

[411] M. S. Shephard, M. A. Yerry, and P. L. Baehmann, "Automatic mesh generation allowing for efficient a priori and a posteriori mesh refinement," *Computer methods in applied mechanics and engineering*, vol. 55, no. 1-2, pp. 161–180, 1986.

[412] M. S. Shephard, "Approaches to the automatic generation and control of finite element meshes," *Applied Mechanics Reviews*, vol. 41, no. 4, pp. 169–185, 1988.

[413] B. A. Szabo, "Implementation of a finite element software system with h and p extension capabilities," *Finite Elements in Analysis and Design*, vol. 2, no. 1-2, pp. 177–194, 1986.

[414] Szabo, "Estimation and control error based on p-convergence," Washington Univ St Louis MO Center for Computatinal Mechanics, Tech. Rep., 1984.

[415] B. A. Szabó, "Computation of sress field parameters in areas of steep stress gradients," *Communications in applied numerical methods*, vol. 2, no. 2, pp. 133–137, 1986.

[416] B. Szabó, B. A. Szabo, and I. Babuška, *Finite element analysis*. John Wiley & Sons, 1991.

[417] D. Turcke and G. McNeice, "Guidelines for selecting finite element grids based on an optimization study," *Computers & Structures*, vol. 4, no. 3, pp. 499–519, 1974.

[418] J. Yu, D. Peric, and D. Owen, “Adaptive" finite element analysis of a strain localization problem for the elastoplastic cosserat continuum,” in *Proceeding of the 3rd International Conference on Computational Plasticity*, vol. 551. Pineridge Press: Swansea, 1992, p. 566.

[419] J. Zhu and O. Zienkiewicz, “Adaptive techniques in the finite element method,” *Communications in applied numerical methods*, vol. 4, no. 2, pp. 197–204, 1988.

[420] O. Zienkiewicz, D. Kelly, J. Gago, and I. Babuska, “Hierarchical finite element approaches error estimates and adaptive refinement,” Maryland Univ College Park Inst for Physical Science and Technology, Tech. Rep., 1981.

[421] O. Zienkiewicz, J. Zhu, Y. Liu, K. Morgan, and J. Peraire, “Error estimates and adaptivity from elasticity to high speed compressible flow,” *The mathematics of Finite Elements and Applications VI*, pp. 473–511, 1988.

[422] O. Zienkiewicz, J. Zhu, and N. Gong, “Effective and practical h–p-version adaptive analysis procedures for the finite element method,” *International Journal for Numerical Methods in Engineering*, vol. 28, no. 4, pp. 879–891, 1989.

[423] O. Zienkiewicz and J. Zhu, “Error estimates and adaptive refinement for plate bending problems,” *International Journal for Numerical Methods in Engineering*, vol. 28, no. 12, pp. 2839–2853, 1989.

[424] O. Zienkiewicz and D. Lefebvre, “A robust triangular plate bending element of the reissner–mindlin type,” *International journal for numerical methods in engineering*, vol. 26, no. 5, pp. 1169–1184, 1988.

[425] O. Zienkiewicz and J. Zhu, “The three r’s of engineering analysis and error estimation and adaptivity,” *Computer Methods in Applied Mechanics and Engineering*, vol. 82, no. 1-3, pp. 95–113, 1990.

[426] O. C. Zienkiewicz and J. Z. Zhu, "The superconvergent patch recovery (spr) and adaptive finite element refinement," *Computer Methods in Applied Mechanics and Engineering*, vol. 101, no. 1-3, pp. 207–224, 1992.

[427] E. Onate, J. Castro, and R. Kreiner, "Error estimations and mesh adaptivity techniques for plate and shell problems," in *3rd lnt Conf on Quality Assurance and Standards in Finite Element Methods, Stratfordupon-Avon, England.*, 1991.

[428] W. Cao, M. Huang, and R. D. Russell, "Anr-adaptive finite element method based upon moving mesh pdes," *Journal of Computational Physics*, vol. 149, no. 2, pp. 221–244, 1999. [Online]. Available: http://www.sciencedirect.com/science/article/pii/S0021999198961514

[429] B. Pierre, J. Koko, and R. Touzani, "Mesh r -adaptation for unilateral contact problems." *international journal applied mathematics and statistics*, vol. 12, pp. 9–16, 2002.

[430] M. Burgarelli, D.and Kischinhevsky and R. J. Biezuner, "A new adaptive mesh refinement strategy for numerically solving evolutionary pde's," *Journal of Computational and Applied Mathematics*, vol. 196, no. 1, pp. 115–131, 2006. [Online]. Available: http://www.sciencedirect.com/science/article/pii/S0377042705005212

[431] R. W. Douglass, "Laplace-beltrami enhancement for unstructured two-dimensional meshes having dendritic elements and boundary node movement," *Journal of Computational and Applied Mathematics*, vol. 236, no. 18, pp. 4952–4963, 2012.

[432] M. Feischl, M. Page, and D. Praetorius, "Convergence and quasi-optimality of adaptive fem with inhomogeneous dirichlet data," *Journal of Computational and Applied Mathematics*, vol. 255, pp. 481 – 501, 2014. [Online]. Available: http://www.sciencedirect.com/science/article/pii/S0377042713003051

[433] G. Cheng and H. Li, “New method for graded mesh generation of quadrilateral finite elements,” *Computers and Structures*, vol. 59, no. 5, pp. 823–829, 1996, cited By 14. [Online]. Available: https://www.scopus.com/inward/record.uri?eid=2-s2.0-0030567666&doi=10.1016%2f0045-7949%2895%2900316-9&partnerID=40&md5=2c7ea1996876a85f8a52d348a19edccd

[434] P. Areias, M. Msekh, and T. Rabczuk, “Damage and fracture algorithm using the screened poisson equation and local remeshing,” *Engineering Fracture Mechanics*, vol. 158, pp. 116–143, 2016. [Online]. Available: http://www.sciencedirect.com/science/article/pii/S0013794415007079

[435] P. Areias, J. Reinoso, P. Camanho, J. Cesar de Sa, and T. Rabczuk, “Effective 2d and 3d crack propagation with local mesh refinement and the screened poisson equation,” *Engineering Fracture Mechanics*, vol. 189, pp. 339 – 360, 2018. [Online]. Available: http://www.sciencedirect.com/science/article/pii/S0013794417307804

[436] B. Szabo and A. Mehta, “p-convergence finite element approximations in fracture mechanics,” *International journal for numerical methods in engineering*, vol. 12, no. 551- 60, 1978.

[437] P. Solin, J. Cerveny, and I. Dolezel, “Arbitrary-level hanging nodes and automatic adaptivity in the hp-fem,” *Mathematics and Computers in Simulation*, vol. 77, no. 1, pp. 117 – 132, 2008. [Online]. Available: http://www.sciencedirect.com/science/article/pii/S0378475407001504

[438] M. Ainsworth and B. Senior, “Aspects of an adaptive hp-finite element method: Adaptive strategy, conforming approximation and efficient solvers,” *Computer Methods in Applied Mechanics and Engineering*, vol. 150, no. 1, pp. 65 – 87, 1997, symposium on Advances in Computational Mechanics. [Online]. Available: http://www.sciencedirect.com/science/article/pii/S0045782597001011

[439] L. Demkowicz, *Computing with hp-Adaptive Finite Elements*. New York Chapman and Hall/CRC, 2007.

[440] P. M. Prenter *et al.*, *Splines and variational methods*. Courier Corporation, 2008.

[441] K. J. Bathe and A. P. Cimento, "Some practical procedures for the solution of nonlinear finite element equations," *Computer methods in applied mechanics and engineering*, vol. 22, no. 1, pp. 59–85, 1980.

[442] H. Matthies and G. Strang, "The solution of nonlinear finite element equations," *International journal for numerical methods in engineering*, vol. 14, no. 11, pp. 1613–1626, 1979.

[443] M. Crisfield, "Iterative solution procedures for linear and non-linear structural analysis," Tech. Rep., 1979.

[444] D. Owen and C. Gomez, "An appraisal of numerical solution techniques for elasto-plastic and elasto-viscoplastic material problems," in *Structural mechanics in reactor technology. Vol. M*, 1981.

[445] E. Hinton, H. A. Rahman, and O. Zienkiewicz, "Computational strategies for reinforced concrete slab systems," in *Int. Assoc. Bridge Struc. Eng. Colloquium on adanced mechanics of reinforced concrete, Delft*, 1981, pp. 303–313.

[446] M. Crisfield, "A faster modified newton-raphson iteration," *Computer Methods in Applied Mechanics and Engineering*, vol. 20, no. 3, pp. 267–278, 1979.

[447] Crisfield, "Incremental/iterative solution procedures for non-linear structural analysis," *Numerical methods for non-linear problems*, pp. 261–290, 1980.

[448] M. A. Crisfield, "Accelerated solution techniques and concrete cracking," *Computer Methods in Applied Mechanics and Engineering*, vol. 33, no. 1-3, pp. 585–607, 1982.

[449] C. G. Broyden, “The convergence of a class of double-rank minimization algorithms 1. general considerations,” *IMA Journal of Applied Mathematics*, vol. 6, no. 1, pp. 76–90, 1970.

[450] R. Fletcher, “A new approach to variable metric algorithms,” *The computer journal*, vol. 13, no. 3, pp. 317–322, 1970.

[451] M. A. Wolfe, *Numerical methods for unconstrained optimization: An introduction*. Van Nostrand Reinhold, 1978.

[452] P. E. Gill and W. Murray, “Safeguarded steplength algorithms for optimization using descent methods,” 1974.

[453] M. Crisfield, “Variable step-lengths for non-linear structural analysis,” Tech. Rep., 1982.

[454] Crisfield, “The automatic non-linear analysis of stiffened plates and shallow shells using finite elements,” in *Institution of Civil Engineers, Proceedings, Pt2*, vol. 69, no. PT2, 1980.

[455] A. Sabir and A. Lock, “The applications of finite elements to large deflection geometrically nonlinear behaviour of cylindrical shells,” 1972.

[456] E. W. Wright and E. H. Gaylord, “Analysis of unbraced multistory steel rigid frames,” *Journal of the Structural Division*, vol. 94, no. 5, pp. 1143–1164, 1968.

[457] P. Bergan and T. Soreide, “Solution of large displacement and instability problems using the current stiffness parameter,” *Finite elements in nonlinear mechanics*, vol. 2, pp. 647–669, 1978.

[458] P. Bergan, G. Horrigmoe, B. Brkeland, and T. Sreide, “Solution techniques for non-linear finite element problems,” *International Journal for Numerical Methods in Engineering*, vol. 12, no. 11, pp. 1677–1696, 1978.

[459] E. Riks, "The application of newtons method to the problem of elastic stability," *Journal of Applied Mechanics*, vol. 39, no. 4, pp. 1060–1065, 1972.

[460] G. A. Wempner, "Discrete approximations related to nonlinear theories of solids," *International Journal of Solids and Structures*, vol. 7, no. 11, pp. 1581–1599, 1971.

[461] S. Foster, "An application of the arc length method involving concrete cracking," *International Journal for Numerical Methods in Engineering*, vol. 33, no. 2, pp. 269–285, 1992.

[462] W. Lam and C. Morley, "Arc-length method for passing limit points in structural calculation," *Journal of structural engineering*, vol. 118, no. 1, pp. 169–185, 1992.

[463] S. Al-Rasby, "Solution techniques in nonlinear structural analysis," *Computers & Structures*, vol. 40, no. 4, pp. 985–993, 1991.

[464] M. Fafard and B. Massicotte, "Geometrical interpretation of the arc- length method." *Computers and Structures*, vol. 46, no. 4, pp. 603–615, 1993.

[465] E. Carrera, "A study on arc-length-type methods and their operation failures illustrated by a simple model," *Computers & structures*, vol. 50, no. 2, pp. 217–229, 1994.

[466] F. Zhiliang, "A study of variable step-length incremental/iterative methods for nonlinear finite element equations," *Computers & structures*, vol. 52, no. 6, pp. 1269–1275, 1994.

[467] Y. Feng, D. Perić, and D. R. J. Owen, "A new criterion for determination of initial loading parameter in arc-length methods," *Computers & structures*, vol. 58, no. 3, pp. 479–485, 1996.

[468] J. Teng and Y. Luo, "A user-controlled arc-length method for convergence to predefined deformation states," *Communications in numerical methods in engineering*, vol. 14, no. 1, pp. 51–58, 1998.

[469] J. Mazars and G. Pijaudier-Cabot, "From damage to fracture mechanics and conversely: a combined approach," *International Journal of Solids and Structures*, vol. 33, pp. 3327–3342, 1996.

[470] Z. Bazant, "Instability, ductility, and size effect in strain-softening concrete," *Journal of the Engineering Mechanics Division*, vol. 102, no. 2, pp. 331–344, 1976.

[471] G. Markeset and A. Hillerborg, "Softening of concrete in compression-localization and size effects," *Cement and Concrete Research*, vol. 25, no. 4, pp. 702–708, 1995.

[472] J. G. Van Mier, "Strain-softening of concrete under multiaxial loading conditions," *Technische Hogeschool Eindhoven*, 1984.

[473] Z. J. Yang and J. Chen, "Finite element modelling of multiple cohesive discrete crack propagation in reinforced concrete beams," *Engineering Fracture Mechanics*, vol. 72, no. 14, pp. 2280–2297, 2005.

[474] A. L. Saleh and M. H. Aliabadi, "Crack growth analysis in concrete using boundary element method," *Engineering fracture mechanics*, vol. 51, no. 4, pp. 533–545, 1995.

[475] L. Pereira, J. Weerheijm, and L. Sluys, "A new rate-dependent stress-based nonlocal damage model to simulate dynamic tensile failure of quasi-brittle materials." *International Journal of Impact Engineering*, vol. 94, pp. 83–95, 2016.

[476] D. Gregoire, L. B. Rojas-Solano, and G. Pijaudier-Cabot, "Failure and size effect for notched and unnotched concrete beams." *International Journal for Numerical and Analytical Methods in Geomechanics*, vol. 37, no. 10, pp. 1434–1452, 2013.

[477] M. Kurumatani, K. Terada, J. Kato, and K. Kyoya, T. Kashiyama, "An isotropic damage model based on fracture mechanics for concrete. ." *Engineering Fracture Mechanics*, vol. 155, pp. 49–66, 2016.

[478] J. Rots and R. de Borst, "Analysis of concrete fracture in direct tension," *international journal for solids structures*, vol. 25, no. 12, pp. 1381–1394, 1985.

[479] M. V. K. V. Prasad and C. S. Krishnamoorthy, "Computational model for discrete crack growth in plain and reinforced concrete," *Computer Methods in Applied Mechanics and Engineering*, vol. 191, no. 25, pp. 2699–2725, 2002.

[480] P. O. Bouchard, F. Bay, and Y. Chastel, "Numerical modelling of crack propagation: automatic remeshing and comparison of different criteria." *Computer Methods in Applied Mechanics and Engineering,*, vol. 192, no. 35, pp. 3887–3908, 2003;.

[481] K. B. Narayana, B. Dattaguru, T. S. Ramamurthy, and K. Vijayakumar, "Modified crack closure integral using six-noded isoparametric quadrilateral singular elements." *Engineering Fracture Mechanics,*, vol. 36, no. 6, pp. 945–955, 1990.

[482] J. W. Ju, "Isotropic and anisotropic damage variables in continuum damage mechanics," *Journal of Engineering Mechanics*, vol. 16, no. 12, pp. 2764–2770, 1990.

[483] G. Z. Voyiadjis and T. Park, "Anisotropic damage effect tensors for the symmetrization of the effective stress tensor," *Journal of Applied Mechanics*, vol. 64, no. 1, pp. 106–110, 1997.

[484] V. A. Lubarda and D. . Krajcinovic, "Damage tensors and the crack density distribution," *International Journal of Solids and Structures*, vol. 30, no. 20, pp. 2859–2877, 1993.

[485] M. Jirasek, "Non-local damage mechanics with application to concrete," *Revue Francaise de Genie Civil*, vol. 8, no. 5-6, pp. 683–707, 2004.

[486] V. Palmieri and L. De Lorenzis, "Multiscale modeling of concrete and of the frp-concrete interface," *Engineering Fracture Mechanics*, vol. 131, pp. 150–175, 2014.

[487] M. Jirasek and B. Patzak, “Consistent tangent stiffness for nonlocal damage models,” *Computers and Structures*, vol. 80, no. 14, pp. 1279–1293., 2002.

[488] R. Peerlings, R. de Borst, W. Brekelmans, and M. Geers, “Gradient enhanced damage modelling of concrete fracture,” *Mechanics of Cohesive frictional Materials*, pp. 323–342, 1998.

[489] M. Geers, R. De Borst, W. A. M. Brekelmans, and P. R. H. J., “Strain-based transient-gradient damage model for failure analyses.” *Computer Methods in Applied Mechanics and Engineering*, vol. 160, no. 1, pp. 133–153, 1998.

[490] C. V. Verhoosel, M. A. Scott, T. J. Hughes, and R. De Borst, “An isogeometric analysis approach to gradient damage models.” *International Journal for Numerical Methods in Engineering*, vol. 86, no. 1, pp. 115–134, 2001.

[491] Z. P. Bazant, M. Tabbara, M. T. Kazemi, and G. Pijaudier-Cabot, “Random particle model for fracture of aggregate or fiber composites,” *Journal of engineering Mechanics*, no. 116, pp. 1686–1705, 1990.

[492] R. H. J. Peerlings, G. M. G. D., R. De Borst, and W. A. M. Brekelmans, “A critical comparison of nonlocal and gradient-enhanced softening continua.” *International Journal of Solids and Structures,*, vol. 38, no. 44, pp. 7723–7746, 2001.

[493] Z. P. Bazant and M. Jirasek, “Nonlocal integral formulations of plasticity and damage: survey of progress,” *Journal of Engineering Mechanics,*, vol. 128, no. 11, pp. 1119–1149, 2002.

[494] C. Wolff, N. Richart, and J. Molinari, “A non-local continuum damage approach to model dynamic crack branching,” *International Journal for Numerical Methods in Engineering*, vol. 101, no. 12, pp. 933–949, 2015.

[495] B. Patzak and M. Jirasek, “Adaptive resolution of localized damage in quasi-brittle materials,” *Journal of Engineering Mechanics*, vol. 130, no. 6, pp. 720–732, 2004.

[496] C. Song, F. Tin-Loi, and W. Gao, "A definition and evaluation procedure of generalized stress intensity factors at cracks and multi-material wedges," *Engineering Fracture Mechanics*, vol. 77, no. 12, pp. 2316–2336, 2010.

[497] A. A. Saputra, C. Birk, and C. Song, "Computation of three-dimensional fracture parameters at interface cracks and notches by the scaled boundary finite element method," *Engineering Fracture Mechanics*, vol. 148, pp. 213–242, 2015.

[498] Y. J. Huang, Z. J. Yang, G. H. Liu, and X. W. Chen, "An efficient fe-sbfe coupled method for mesoscale cohesive fracture modelling of concrete," *Computational Mechanics*, pp. 1–21, 2016.

[499] J. Liu, G. Lin, and J. Li, "Short-crested waves interaction with a concentric cylindrical structure with double-layered perforated walls," *Ocean Engineering*, vol. 40, pp. 76–90, 2012.

[500] M. C. Genes, "Dynamic analysis of large-scale ssi systems for layered unbounded media via a parallelized coupled finite-element/boundary-element/scaled boundary finite-element model," *Engineering Analysis with Boundary Elements*, vol. 36, no. 5, pp. 845–857, 2012.

[501] C. Birk and R. Behnke, "A modified scaled boundary finite element method for three-dimensional dynamic soil-structure interaction in layered soil." *International Journal for Numerical Methods in Engineering,*, vol. 89, no. 3, pp. 371–402, 2012.

[502] Y. He, H. Yang, and A. J. Deeks, "An element-free galerkin scaled boundary method for steady-state heat transfer problems," *Numerical Heat Transfer - Part B - Fundamentals*, vol. 64, no. 3, pp. 199–217, 2013.

[503] R. De Borst, M. A. Crisfield, J. J. Remmers, and C. V. Verhoosel, "Nonlinear finite element analysis of solids and structures." *John Wiley & Sons*, 2012.

[504] D. Hordijk, "Local approach to fatigue of concrete(ph. d. thesis)," 1991.

[505] J. De Vree, W. Brekelmans, and M. Van Gils, "Comparison of nonlocal approaches in continuum damage mechanics," *Computers and Structures*, vol. 55, no. 581-588, 1995.

[506] G. Pijaudier-Cabot and A. Huerta, "Finite element analysis of bifurcation in nonlocal strain softening solids." *Computer methods in applied mechanics and engineering*, vol. 90, no. 1, pp. 905–919, 1991.

[507] E. Ramm, "Strategies for tracing the nonlinear response near limit points," in *Nonlinear finite element analysis in structural mechanics*. Springer, 1981, pp. 63–89.

[508] H. A. Kormeling and H. Reinhardt, "Determination of the fracture energy of normal concrete and epoxy-modified concrete." *Stevin Laboratory, Delft University of Technology,*, 1982.

[509] P. Grassl, D. Xenos, U. NystrÃ¶m, R. Rempling, and K. Gylltoft, "A damage-plasticity approach to modelling the failure of concrete," *International Journal of Solids and Structures*, vol. 50, no. 24, pp. 3805–3816, 2013.

[510] J. Lee, "Assessment of modal damping from full scale structural testing," Master's thesis, School of Engineering, University of Auckland, 2003.

[511] E. Kuhl, "Numerical models for cohesive frictional materials," Ph.D. dissertation, University of Stuttgart, 2000.

[512] A. Zervos, P. Papanastasiou, and I. Vardoulakis, "A finite element displacement formulation for gradient elastoplasticity," *International Journal for Numerical Methods in Engineering*, vol. 50, pp. 1369–1388, 2001.

[513] R. A. B. Engelen, M. G. D. Geers, and F. P. T. Baaijens, "Nonlocal implicit gradient-enhanced elasto-plasticity for the modelling of softening behaviour," *International Journal of Plasticity*, vol. 19, pp. 403 – 433, 2003.

[514] J. Pamin, H. Askes, and R. de Borst, “Two gradient plasticity theories discretized with the element-free galerkin method,” *Computer Methods in Applied Mechanics and Engineering,*, vol. 192, pp. 2377 – 2403, 2003.

[515] A. Simone, H. Askes, and L. J. Sluys, “Incorrect initiation and propagation of failure in non-local and gradient-enhancedmedia,” *International Journal of Solids and Structures*, vol. 41, pp. 351–363, 2004.

[516] P. Wriggers and S. O. Moftah, “Mesoscale models for concrete: Homogenisation and damage behaviour,” *Finite Elements in Analysis and Design*, vol. 42, pp. 623–636, 2006.

[517] D. Krajcinovic and G. U. Fonseka, “The continuous damage theory of brittle materials, part i: General theory,” *J. Appl. Mech*, vol. 8, pp. 809–815, 1981.

[518] A. Brencich and L. Gambarotta, “Isotropic damage model with different tensile-compressive response for brittle materials,” *International Journal of Solids and Structures*, vol. 38, pp. 5865–5892, 2001.

[519] G. Swoboda and Q. Yang, “An energy-based damage model of geomaterials - formulation and numerical results,” *International journal of solids and structures*, vol. 36, pp. 1719–1734, 1999.

[520] G. Pijaudier Cabot and J. Mazars, “Steel-concrete bond analysis with nonlocal continuous damage,” *Journal of Structural Engineering*, vol. 117, pp. 862–882, 1991.

[521] E. Kuhl, E. Ramm, and R. de Borst, “An anisotropic gradient damage model for quasi-brittle materials,” *Computer Methods in Applied Mechanics and Engineering*, vol. 183, pp. 87–103, 2000.

[522] J. Velde, U. Kowalsky, T. Zumendorf, and D. Dinkler, “3d-fe-analysis of ct-specimens including viscoplastic material behavior and nonlocal damage,” *Computational Materials Science*, vol. 46, pp. 352–357, 2009.

[523] E. T. Sun, Z. C. and. Ooi and C. Song, "Finite fracture mechanics analysis using the scaled boundary finite element method," *Engineering Fracture Mechanics*, vol. 134, pp. 330–353, 2015.

[524] S. R. Chidgzey, J. Trevelyan, and A. J. Deeks, "Coupling of the boundary element method and the scaled boundary finite element method for computations in fracture mechanics," *Computers and Structures*, vol. 86, pp. 1198–1203, 2008.

[525] H. Zhong, G. Lin, X. Li, and J. Li, "Seismic failure modeling of concrete dams considering heterogeneity of concrete," *Soil Dynamics and Earthquake Engineering*, vol. 31, pp. 1678–1689, 2001.

[526] Z. Zhang, Z. Yang, G. H. Liu, and Y. Hu, "An adaptive scaled boundary finite element method by subdividing subdomains for elastodynamic problems." *Science China - Technological Sciences*, vol. 54, no. 1, pp. 101–110, 2011.

[527] G. Lin, Y. Zhang, Z. Q. Hu, and H. Zhong, "Scaled boundary isogeometric analysis for 2d elastostatics," *Science China Physics, Mechanics and Astronomy*, vol. 57, pp. 286–300, 2014.

[528] G. H. Golub *et al.*, "Cf van loan, matrix computations," *The Johns Hopkins*, 1996.

[529] M. 2015b, The MathWorks Inc., Natick, Massachusetts, 2015., Tech. Rep.

[530] M. Crisfield, "Accelerating and damping the modified newton-raphson method," *Computers & structures*, vol. 18, no. 3, pp. 395–407, 1984.

[531] D. A. Hordijk, "Local approach to fatigue of concrete," Ph.D. dissertation, Delft University of Technology, Delft, The Netherlands, 1991.

[532] T. Gasser and G. A. Holzapfel, "Modeling 3d crack propagation in unreinforced concrete using pufem," *Computer Methods in Applied Mechanics and Engineering*, vol. 194, pp. 2859–2896, 2005.

[533] G. N. Wells and L. J. Sluys, "Three-dimensional embedded discontinuity model for brittle fracture," *International Journal of Solids and Structures*, vol. 38, pp. 897–913, 2001.

[534] E. W. V. Chaves, "A three dimensional setting for strong discontinuities modelling in failure mechanics," *Ph.D. Thesis, Escuela Tenica Superior de Ingenieros de Caminos, Universidad Politcnica de Catalua, Spain*, 2003.

[535] J. Pamin and R. de Borst, "Gradient-enhanced damage and plasticity models for plain and reinforced concrete,," *Proceedings of the European Conference on Computational Mechanics-ECCM 99, paper no. 636, Munich, Technical University of Munich,*, pp. 482–483, 1999.

[536] A. Simone, G. N. Wells, and L. Sluys, "From continuous to discontinuous failure in a gradient-enhanced continuum damage model," *Computer Methods in Applied Mechanics and Engineering*, vol. 192, pp. 4581–460, 2003.

[537] P. Dumstorff and G. Meschke, "Crack propagation criteria in the framework of x-fem-based structural analyses," *International Journal for Numerical and Analytical Methods in Geomechanics*, vol. 31, no. 2, pp. 239–259, 2007.

[538] P. Jager, P. Steinmann, and E. Kuhl, "Modeling three-dimensional crack propagation - a comparison of crack path tracking strategies," *International Journal for Numerical Methods in Engineering*, vol. 76, pp. 1328–1352, 2008.

[539] R. Radulovic, O. Bruhns, and J. Mosler, "Effective 3d failure simulations by combining the advantages of embedded strong discontinuity approaches and classical interface elements," *Engineering Fracture Mechanics*, vol. 78, pp. 2470–2485, 2011.

[540] W. J. Schroeder, B. Geveci, and M. Malaterre, "Compatible triangulations of spatial decompositions," *Proceedings of the Conference on Visualization 04, IEEE Computer Society, Austin, Texas, USA*, pp. 211–218, 2004.

[541] P. Krysl, E. Grinspun, and P. Schroder, “Natural hierarchical refinement for finite element methods,” *International Journal for Numerical Methods in Engineering*, vol. 56, pp. 1109–1124, 2003.

[542] R. A. Finkel and J. L. Bentley, “Quad trees a data structure for retrieval on composite keys.” *Acta informatica*, vol. 4, no. 1, pp. 1–9, 1974.

[543] C. Song, “Evaluation of power-logarithmic singularities, t-stresses and higher order terms of in-plane singular stress fields at cracks and multi-material corners,” *Engineering Fracture Mechanics*, vol. 72, no. 10, pp. 1498–1530, 2005.

[544] W. Ren, Z. Yang, R. Sharma, C. Zhang, and P. J. Withers, “Two-dimensional x-ray ct image based meso-scale fracture modelling of concrete,” *Engineering Fracture Mechanics*, vol. 133, pp. 24–39, 2015.

[545] Z. Ooi and E. Yang, “Modelling dynamic crack propagation using the scaled boundary finite element method,,” *International Journal for Numerical Methods in Engineering*, vol. 88, no. 4, pp. 329–349, 2011.

[546] Z. Yang, Z. Zhang, G. Liu, and E. Ooi, “An h-hierarchical adaptive scaled boundary finite element method for elastodynamics,,” *Computers & Structures*, vol. 89, no. 13, pp. 1417–1429, 2011.

[547] E. Ooi and Z. Yang, “A hybrid finite element-scaled boundary finite element method for crack propagation modelling,,” *Computer Methods in Applied Mechanics and Engineering*, vol. 199, no. 17, pp. 1178–1192, 2010.

[548] Y. Huang, Z. Yang, W. Ren, G. Liu, and C. Zhang, “3d meso-scale fracture modelling and validation of concrete based on in-situ x-ray computed tomography images using damage plasticity model,” *International Journal of Solids and Structures*, no. 67-68, pp. 340–352, 2015.

[549] M. Jirasek, "Mathematical analysis of strain localization," *Revue Europeenne de Genie Civil*, vol. 11, pp. 997–991, 2007.

[550] Z. Bazant, T. Belytschko, and C. Ta-Peng, "Continuum theory for strain-softening," *Journal of Engineering Mechanics*, vol. 110, no. 12, 1984.

[551] V. Tvergaard and A. Needleman, "Effects of nonlocal damage in porous plastic solids," *International Journal of Solids and Structures*, vol. 32, no. 8-9, pp. 1063–1077, 1995.

[552] A. Rodrguez-Ferran and Huerta, "Error estimation and adaptivity for nonlocal damage models," *International Journal of Solids and Structures*, vol. 37, no. 48, pp. 7501–7528, 2000. [Online]. Available: http://www.sciencedirect.com/science/article/pii/S0020768300002092

[553] M. Jirasek and T. Zimmermann, "Rotating crack model with transition to scalar damage," *Journal of Engineering Mechanics*, vol. 124, no. 3, pp. 277–284, 1998.

[554] F. Pascal and J. L. Marechal, "Fast adaptive quadtree mesh generation," *7th International Meshing Roundtable*, pp. 211–224, 1998.

[555] S. Popinet, "Quadtree-adaptive tsunami modelling," *Ocean Dynamics*, vol. 61, no. 9, pp. 1261–285, Sep 2011. [Online]. Available: https://doi.org/10.1007/s10236-011-0438-z

[556] K. Yiu, D. Greaves, A. Cruz, S.and Saalehi, and A. Borthwick, "Quadtree grid generation: Information handling, boundary fitting and cfd applications," *Computers & Fluids*, vol. 25, no. 8, pp. 759 –769, 1996. [Online]. Available: http://www.sciencedirect.com/science/article/pii/S0045793096000291

[557] Y. Morvan, D. Farin, and P. De With, "Depth-image compression based on an r-d optimized quadtree decomposition for the transmission of multiview images," vol. 5, 2007, pp. V105–V108, cited By 105. [Online]. Available: https://www.

scopus.com/inward/record.uri?eid=2-s2.0-48149099106&doi=10.1109%2fICIP.2007.4379776&partnerID=40&md5=939258146f90426f966e0e1a354c8540

[558] A. K. Gupta, “A finite element for transition from a fine to a coarse grid,” *International Journal for Numercal Methods*, vol. 12, pp. 35–45, 1978.

[559] J. Bielak, O. Ghattas, and E. Kim, “Parallel octree-based finite element method for large-scale earthquake ground motion simulation,” *CMES-Computer Modeling in Engineering and Sciences*, vol. 10, no. 2, pp. 99–112, 2005, cited By 70. [Online]. Available: https://www.scopus.com/inward/record.uri?eid=2-s2.0-32944479604&partnerID=40&md5=7a2919e420f1a7a640d8abb5f3b7cebf

[560] S. Lo, K. Wan, and K. Sze, “Adaptive refinement analysis using hybrid-stress transition elements,” *Computers & Structures*, vol. 84, no. 31, pp. 2212 – 2230, 2006. [Online]. Available: http://www.sciencedirect.com/science/article/pii/S0045794906002422

[561] K. Sze and D. Wu, “Transition finite element families for adaptive analysis of axisymmetric elasticity problems,” *Finite Elements in Analysis and Design*, vol. 47, no. 4, pp. 360 – 372, 2011. [Online]. Available: http://www.sciencedirect.com/science/article/pii/S0168874X10001897

[562] N. Sukumar and A. Tabarraei, “Conforming polygonal finite elements.” *International Journal for Numercal Methods in Engineering*, vol. 61, pp. 2045–66, 2004.

[563] A. J. Deeks. and J. P. Wolf, “A virtual work derivation of the scaled boundary finite-element method for elastostatics.” *Computational Mechanics*, vol. 28, no. 6, pp. 489–504, 2002.

[564] A. C. Eringen, “On nonlocal plasticity,” *International Journal of Engineering Science*, vol. 19, no. 12, pp. 1461–1474, 1981.

[565] Eringen, “Theories of nonlocal plasticity,” *International Journal of Engineering Science*, vol. 21, no. 7, pp. 741–751, 1983.